UNIVERSITY OF CALIFORNIA
RIVERSIDE

Narcissistic Self-Sorting, Reactivity and Post-Assembly Modification of Metal-Ligand Cage Complexes

A Dissertation submitted in partial satisfaction
of the requirements for the degree of

Doctor of Philosophy

in

Chemistry

by

Lauren Renee Holloway

September 2018

Dissertation Committee:
Dr. Richard J. Hooley, Chairperson
Dr. Christopher Switzer
Dr. Dave Martin

The Dissertation of Lauren Renee Holloway is approved:

_____

_____

_____

Committee Chairperson

University of California, Riverside

ACKNOWLEDGMENTS

First and foremost, I would like to thank my parents, Frank and Janice Holloway, my sister, Shannon Holloway and my grandmother, Dorothy Edie for their loving support. I am especially grateful for your encouragement, your endless patience, and your unshakeable faith in my abilities, particularly when I encountered those inevitable roadblocks. I would also like to thank Jackie Lotspeich and Stephanie Lopez for their enduring friendship through the years. You all mean the world to me.

I have been influenced by several amazing professors throughout my undergraduate and graduate years. I would like to thank Dr. Samir Anz for advising me and happily answering my every question at Cal Poly Pomona. I would also like to thank Dr. Francis Flores for his patience and training during my undergraduate research project. Finally, I would like to thank Dr. Lijuan Li for being an awesome PI and showing me a multitude of new techniques at CSU Long Beach.

I am especially grateful to Dr. Richard Hooley, who has had an enormous impact on my career development at UCR. I truly appreciate you taking the time to explain new techniques and concepts over the last five years. Your extensive knowledge and ability to turn a single curious result into a fully-fledged publication is phenomenal and I thoroughly enjoyed the time spent working in your lab.

Spending five years working in close proximity with the same people inevitably leads to close friendships, and I would like to thank my coworkers for their support and collaboration. Mike Young and Amber Johnson acted as amazing mentors during my first year and I am grateful to them for encouraging me to aim high with our assemblies. The

rest of the “Hooligans,” especially Tabitha Miller and Courtney Ngai deserve thanks for their assistance with our never-ending list of cage-y things to investigate. Paul Bogie also deserves a special thank you for his hard work assisting me with the most recent projects, for helping me plan out reaction steps, and for his superhuman ability when it comes to Suzuki couplings. I wish you all the best of luck with your PhD careers.

I would also like to thank my classmates Lizeth Perez, Eric Commendatore and Keegan Nelson for their camaraderie from those first few days of classes onward. To Zack Palchak and his amazing wife Emily, I would like to say thank you for all the good times and wonderful memories. I will sorely miss spending time with you both. Finally, I would like to thank the rest of the Martin, Larsen and Morton labs for the company during late worknights, for those unforgettable lunch conversations and for keeping our wing of the 4th floor interesting.

The text of this dissertation, in part or in full, is a reprint of the material as they appear in the following publications:

Chapter 2: Holloway, L. R.; Young, M. C.; Beran, G. J. O.; Hooley, R. J. "High Fidelity Sorting of Remarkably Similar Components via Metal-Mediated Assembly" *Chem. Sci*., **2015**, *6*, 4801-4806.

Chapter 3: Wiley, C. A.; Holloway, L. R.; Miller, T. F.; Lyon, Y.; Julian, R. R.; Hooley, R. J. "Electronic Effects on Narcissistic Self-Sorting in Multicomponent Self-Assembly of Fe-Iminopyridine meso-Helicates" *Inorg. Chem.*, **2016**, *55*, 9805-9815.

Chapter 4: Holloway, L. R.; McGarraugh, H. H.; Young, M. C.; Sontising, W.; Beran, G. J. O.; Hooley, R. J. "Structural Switching in Self-Assembled Metal-Ligand Helicate Complexes via Ligand-Centered Reactions" *Chem. Sci*., **2016**, *7*, 4423-4427.

Chapter 5: Holloway, L. R.; Bogie, P. M.; Lyon, Y.; Julian, R. R.; Hooley, R. J. "Stereoselective Postassembly CH Oxidation of Self-Assembled Metal-Ligand Cage Complexes" *Inorg. Chem*., **2017**, *56*, 11435-11442.

Chapter 6: Holloway, L. R.; Bogie, P. M.; Lyon, Y.; Ngai, C.; Miller, T. F.; Julian, R. R.; Hooley, R. J. "Tandem Reactivity of a Self-Assembled Cage Catalyst with Endohedral Acid Groups." *J. Am. Chem. Soc*. **2018**, *140*, 8078–8081.

The co-author Richard J. Hooley listed in these publications directed and supervised the research which forms the basis for this dissertation. All other co-authors listed in these publications contributed technical expertise.

DEDICATION

This dissertation is dedicated to my loving mother, Janice Ileane Holloway.

You will always be in my heart.

ABSTRACT OF THE DISSERTATION

Narcissistic Self-Sorting, Reactivity and Post-Assembly Modification of Metal-Ligand Cage Complexes

by

Lauren Renee Holloway

Doctor of Philosophy, Graduate Program in Chemistry
University of California, Riverside, September 2018
Dr. Richard J. Hooley, Chairperson

Metal assisted self-assembly is a useful tool for the creation of supramolecular structures that can function as molecular switches, cavity containing hosts, and sensors. A wide variety of unfunctionalized supramolecular cages bearing large internal cavities have been synthesized to date, and these hosts are able to effectively bind substrates, but molecular hosts containing internal functionalization are still rare. The use of symmetrical, aromatic ligands is often necessary to control the assembly process, and the presence of reactive functional groups can complicate or interfere with the synthesis. To overcome these challenges and develop useful internally functionalized complexes, new methods for precisely controlling the assembly process must be investigated.

This work explores various methods of controlling the assembly process, with an overarching goal of creating useful endohedrally functionalized species for molecular recognition and biomimetic catalysis. High fidelity narcissistic self-sorting of near identical ligands leads to selective and sequential formation of specific homocomplexes from multicomponent reaction mixtures and provided insight into what traits govern the

favorability of certain assemblies. Small variations to the electronic nature of the coordinating motif were found to increase the thermodynamic stability or the formation rate, and these simple modifications can be used to tune the properties of the final products. Post assembly modifications were performed and lead to the discovery of a structural switch between a polymeric aggregate and a discrete cage. This method was also utilized to oxidize doubly benzylic methylene units in a stereoselective manner to form unusual products. The post-assembly oxidation is directed by the structure of the cages themselves, involves catalytic metal arising from the reversible dissociation of the chelating groups, and occurs in high yield without degradation of the structural iron atoms. In addition, a large Fe^{II}-iminopyridine cage was synthesized bearing twelve internal carboxylic acid groups and effected a 1000-fold rate enhancement in the hydrolysis of aromatic acetals. The compartmentalized nature of the acid groups allowed a cage-to-cage tandem reaction in the presence of sensitive complexes, whereas control acid catalysts were too weak to allow for transformation or caused decomposition of the complexes.

TABLE OF CONTENTS

LIST OF FIGURES

LIST OF TABLES

Chapter 1 - Introduction to the Controlled Assembly of Supramolecular Cage Complexes

1.1 Design and Assembly of Metal-Ligand Supramolecular Cages

The creation of useful metal-organic cages for molecular recognition and biomimetic catalysis is an area of growing popularity within the field of supramolecular chemistry.[1] These cages can act as hosts, with internal cavities capable of influencing the behavior of chemical systems. Recent work has produced many examples of assemblies containing isolated cavities that can be used to stabilize reactive species, shift reaction equilibria, or achieve previously unobserved conformations of guest molecules.[2,3] Confinement within the internal cavities of supramolecular host molecules creates a new method for controlling the outcomes of chemical reactions in the same manner that biological systems use microenvironments to promote specific reactions.[4]

Metal-ligand cage complexes are a subclass of supramolecular assemblies, composed of structural organic ligands bearing two or more metal coordinating or chelating groups bound to metal atoms. The coordinating groups can vary between monodentate pyridyl coordinators, or bidentate chelators such as pyridyl pyrazoles,[5] iminopyridines,[6] or O-donors such as catechols[7] (Figure 1.1). The organic ligands are coordinated to metal salts, frequently transition metals such as Fe^{II}, Pt^{II}, Pd^{II}, or Co^{II}, and more rarely lanthanides and actinides. The resulting metal-ligand combinations can form interesting supramolecular structures such a 2D polygons[8] and 3D polyhedra. By varying the combinations of metal, coordinating group and ligands, a wide range of structures from small M_2L_3 complexes to huge supercontainers[9] can be created (Figure 1.1).

The self-assembly process involves multiple interactions between the metal and ligand structural components, resulting in the formation of discrete products. The metal-ligand interactions must be reversible to allow for equilibration to the thermodynamically favored product. Metal-ligand coordination is rapid, initially forming disordered aggregates or incomplete cage fragments.[10] However, the reversible nature of the metal-ligand coordination allows for ligand dissociation and equilibration, with small structures usually being favored over larger assemblies.

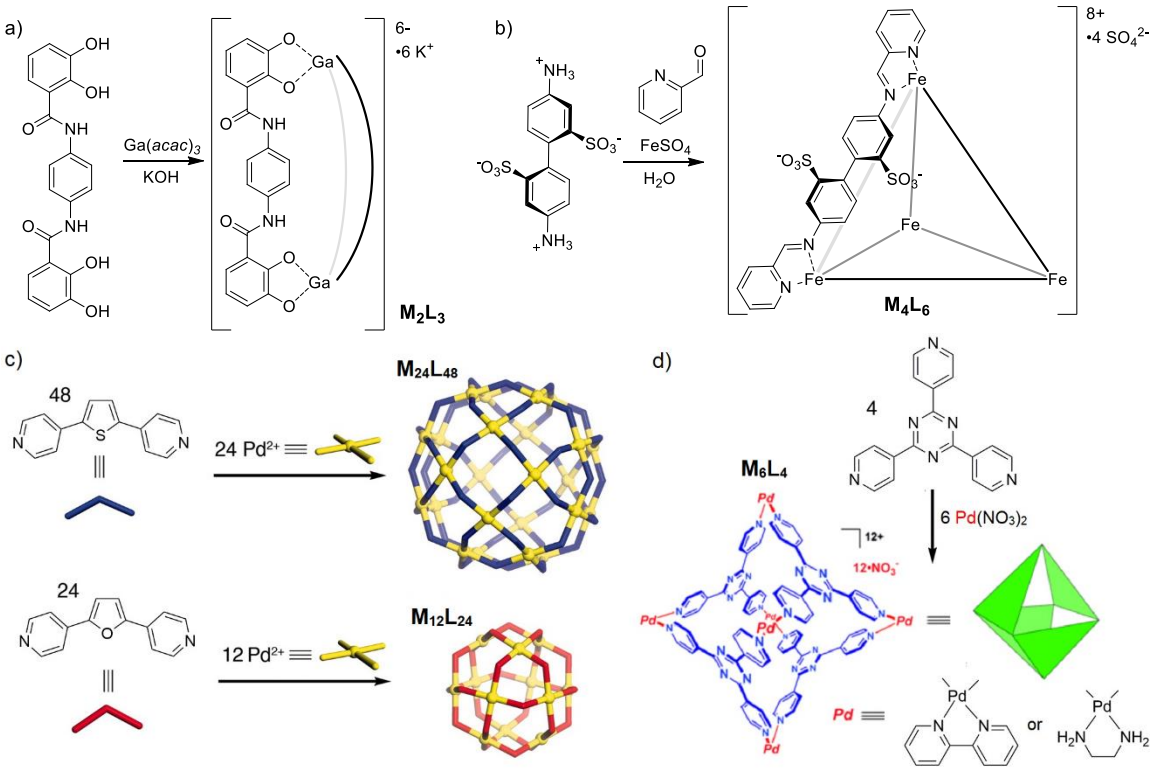

Figure 1.1. Synthesis of metal-organic species: a) a M_2L_3 structure utilizing Ga^{III} and a deprotonated catechol chelator, b) a M_4L_6 cage using Fe^{II} and a self-assembled iminopyridine chelator, and Pd^{II}-pyridyl structures that form either c) $M_{24}L_{48}$ and $M_{12}L_{24}$ supercontainers[9] or d) a large M_6L_4 octahedral cage.[11]

The topology of the assembled products is most greatly affected by the nature of the structural ligands. The directionality, number of coordinating groups and rigidity of the ligand are all important considerations: too flexible and the structural integrity of the resulting assembly may be compromised.[12] If the ligand is too rigid or the geometry is mismatched for the coordinating groups and metal, discrete products may not form. Linear ligand cores that contain aromatic ring[13] or alkyne groups as the main structural components are a favorite among supramolecular chemists. The benefit of rigid structural components is that the stereochemical communication between metal centers is better controlled and the resulting products maintain a high degree of symmetry.[14] Ligands with a non-180° coordination angle can be used to direct functional handles towards the complex interior, or create specific stoichiometries of product.[15] Handles for external modifications, which can tune the solubility of the cage products, may also be introduced to the ligand scaffold.

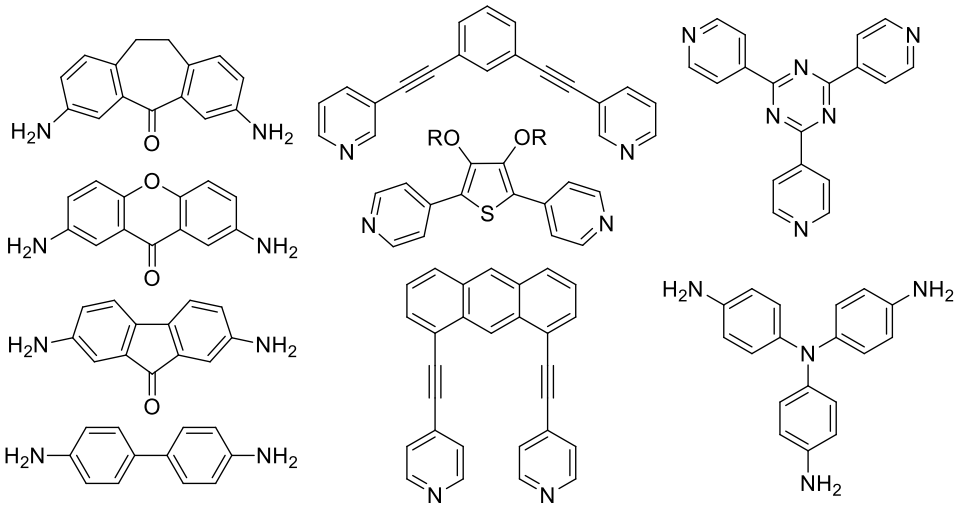

Figure 1.2. A variety of *bis*- and *tris*-coordinating aniline or pyridyl ligands of varying coordination angles.

The self-assembly process can be utilized to create a variety of structures depending on the combination of ligand, metal and coordinating group used. The structural components must be well matched, as non-discrete aggregates can form if incompatibilities exist (e.g. catechol coordinating groups are better suited to oxophilic metals).[16] The coordination sphere of the metal can be used to direct the stoichiometry of the products, but can also lead to synthetic challenges. Octahedral metals coordinated to unsymmetrical bidentate chelators such as iminopyridines can give rise to multiple isomeric possibilities.[17] The chelating groups can be oriented in the facial or meridional configurations, with two enantiomers for each connective possibility arising from the directional rotation of the ligands about the metal center (Figure 1.3). As the stoichiometry of the supramolecular assemblies become larger, the opportunities for multiple isomeric products increases and greater control is necessary.

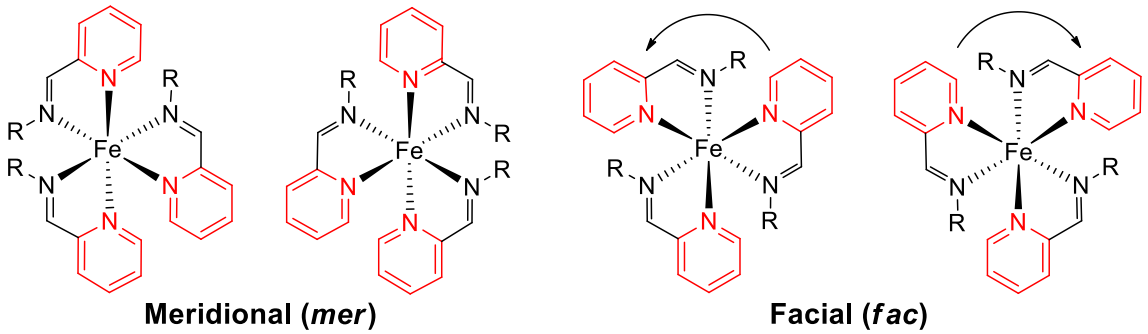

Figure 1.3. The two isomeric connective possibilities of Fe^{II}-iminopyridine centers, and the two possible enantiomers of each with Λ (left) and Δ (right) rotation of the *fac* centers.

The smallest structure that can result from complete assembly of *bis* coordinating iminopyridine ligands and Fe^{II} atoms is the M_2L_3 complex, which has two basic structural possibilities. The symmetrical mesocate structure contains one *fac*-Δ center and one *fac*-Λ

center. The second possibility is a M_2L_3 helicate, where the two *fac* metal centers are matched with ΔΔ or ΛΛ rotation. The meridional configuration is generally not observed in M_2L_3 species, as a high degree of ligand flexibility would be necessary. However, *mer* centers can exist in larger M_4L_6 assemblies, which leads to a greater number of isomeric possibilities. As the coordination angle of the ligand approaches 180°, tetrahedral all-*fac* species are frequently observed. These tetrahedra can form three isomers arising from the presence of Δ or Λ rotation at the metal centers.[18] The T-symmetric species exists with matched *fac*-ΔΔΔΔ or *fac*-ΛΛΛΛ, the achiral S_4 isomer contains *fac*-ΛΛΔΔ metal centers and the C_3 isomer exists with *fac*-ΛΔΔΔ or *fac*-ΔΛΛΛ centers. This can complicate the analysis of cages in the best cases, and lead to difficulties when attempting to track small changes or reaction progress over time. While the use of rigid and symmetrical ligands can minimize the number of isomers observed for an assembly, aromatic panels can be difficult to functionalize or are incapable of directing functional groups towards the cage interior. In order to develop cages containing reactive internal functionality, new ligands will have to be combined with alternate methods for increasing control over the assembly process.

1.2 Fe^{II}-Iminopyridine Assemblies

One frequently used subclass of metal-ligand complex is the Fe^{II}-iminopyridine assembly. These cages are usually synthesized via one-pot reaction, where a ligand bearing two or more amine or aniline groups, a pyridyl aldehyde, (such as 2-formylpyridine, PyCHO) and metal salts are combined simultaneously (Figure 1.4). The presence of the metal facilitates the condensation between aldehyde and amine, provides both an increased

yield and shortened reaction times, and stabilizes the imine functional group. The iminopyridine scaffold is an ideal chelating group for self-assembly, as the neutral bidentate structure readily provides strong metal chelation and forms robust products. However, the metal-iminopyridine coordination is not so strong as to prevent ligand dissociation from occurring. In addition to the typical iminopyridine synthesis (Figure1.4b, c and e), "reverse" variations exist (Figure 1.4d) where pyridyl aldehyde ligands are used in the presence of aniline[19] or chiral amines[20] to form a wide variety of novel structures.[21]

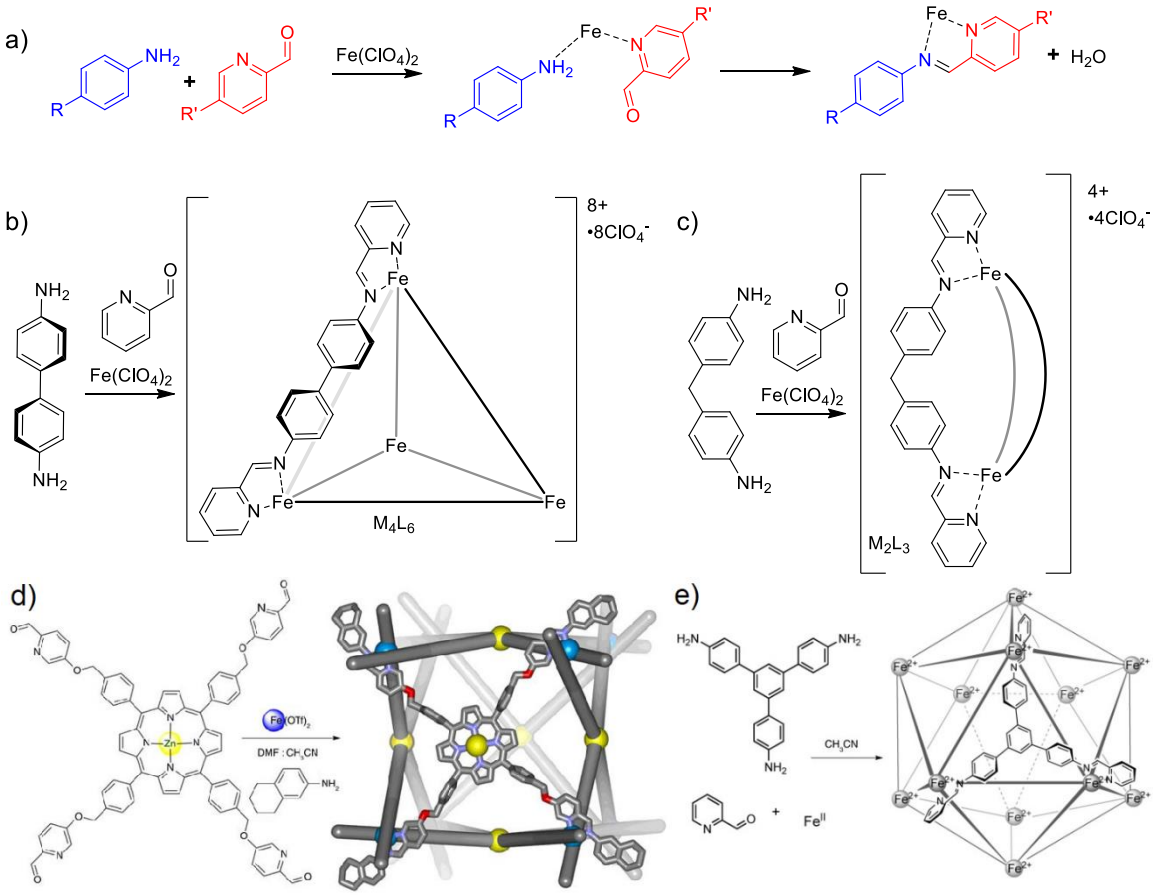

Figure 1.4. a) The one-pot multicomponent self-assembly reaction between amine, aldehyde and metal salt, provides acceleration and higher yields over the stepwise alternative where separate condensation and chelation reactions are performed. Formation of an iminopyridine b) M_4L_6 tetrahedron, c) M_2L_3 mesocate, d) M_8L_6 cube[21] and e) $M_{12}L_{12}$ icosahedron[22] via multicomponent self-assembly.

Iminopyridine assemblies have been successfully utilized for a variety of applications from molecular recognition to catalysis. The properties of the structure and internal cavity of these metal-ligand complexes can be tuned through a variety of subtle, non-ligand modifications. A variety of new stoichiometries can be formed via modification of the guest template.[23] The reaction solvent can tune the host-guest properties,[24,25] and the choice of metal atom can drastically modify the size of the internal cavity.[26] In addition to solvent, guest and metal, changing typically overlooked components of the reaction, such as the counterion of the metal salt, can induce the formation of two different stoichiometries (M_4L_4 or $M_{12}L_{12}$) of product arising from the same ligand (Figure 1.4e).[22] Small modifications to the reaction conditions such as time or temperature can also lead to the formation of multiple structures such as the M_4L_6 tetrahedron or $M_{10}L_{15}$ prism from the same ligand.[27]

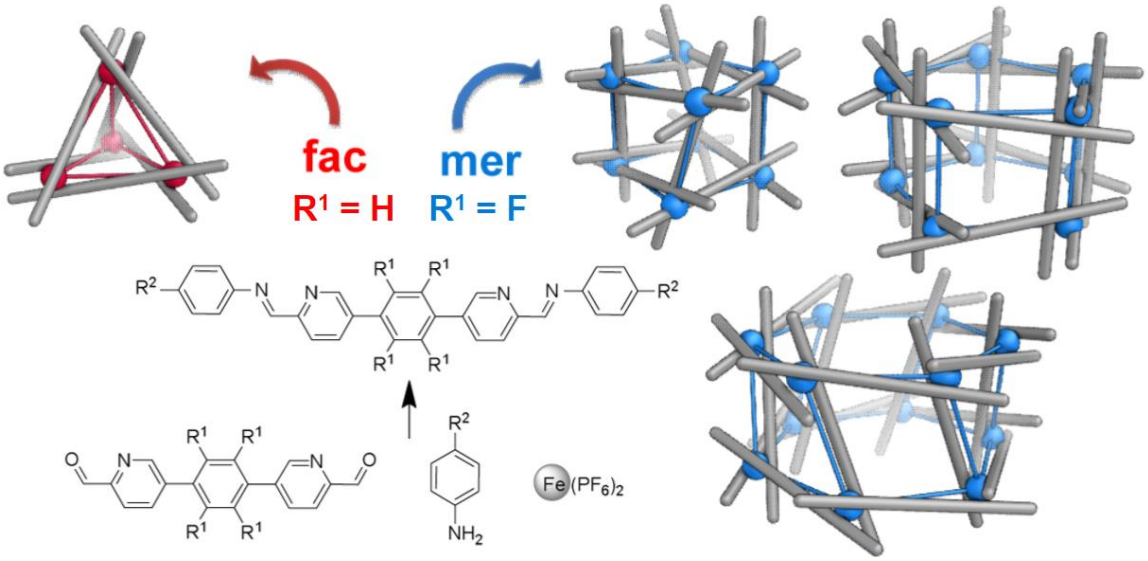

Figure 1.5. Synthesis of unusual M_8L_{12}, $M_{10}L_{15}$ and $M_{12}L_{18}$ prisms via addition of electron-withdrawing fluorine atoms to the structural ligand.[28]

The ability to tune the assembly structure through means other than ligand modification can be very useful. However, varying the structural ligand(s) remains the most powerful method for generating new and useful iminopyridine assemblies. Small modifications to properties such as electron-donating ability can effect large differences in structure (Figure 1.5). Here, the addition of electron withdrawing fluorene groups to the central aromatic panel leads to exclusive formation of the rarely observed *mer* isomer at the metal centers over the more common *fac* isomer.[28] The energetic preference of fluorinated ligands to form *mer* vertices was quantified, and found to be greater than the preference of nonfluorinated ligands towards *fac* centers. The assembly reaction can be further biased towards a specific prism structure over others through modification of the electron-donating capabilities of the aniline component. The equilibrium between the M_8L_{12} cube and the $M_{10}L_{15}$ pentagonal prism follows a linear free-energy relationship, with the ratio between structures correlating with the Hammett σ_p^+ parameter of the aniline group. In addition, changing the metal counterion was also found to influence the formation of one prismatic structure over another, suggesting that counterions can exhibit a directing role in metal-ligand assemblies.

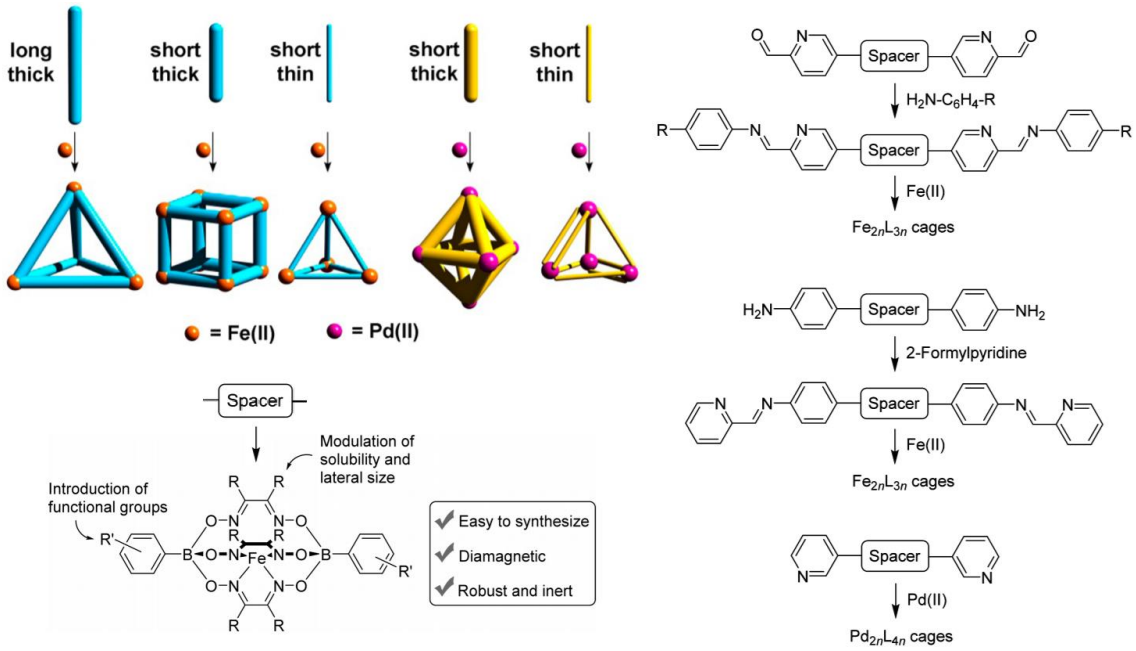

Figure 1.6. Synthesis of different stoichiometries of assembly through modification of steric bulk via clathrochelate groups built into the ligand scaffolds.[29]

It is also possible to control the geometry and composition of self-assembled metal-ligand assemblies via modification of the aspect ratio of the ligands. This is demonstrated by a series of iron- and palladium-based coordination cages utilizing ligands that vary slightly in length and steric bulk (Figure 1.6). Increasing the length or decreasing the ligand width drives the formation of tetrahedral iminopyridine M_4L_6 cages, while shorter or wider ligands lead to M_8L_{12} cubes.[29] It was also possible to control the geometry of Pd-pyridyl cages: ligands with large aspect ratios yielded a tetrahedral M_4L_8 assembly, while an octahedral M_6L_{12} cage was formed upon increasing the ligand width. From these studies it was determined that structural features such as steric bulk or the electron donating nature can be used to bias the assembly process towards new structures. More interesting,

however, are ligands that can form multiple stoichiometries under identical reaction conditions.

When a single ligand is able to equilibrate between two stoichiometries of assembled product, a greater amount of control is necessary in order to select for one product over another. Here, a *tris*-aniline ligand can form the thermodynamically favored M_4L_4 structure, or the kinetically favored M_2L_3.[30] In order to favor the kinetic product, covalent modification was used to prevent the kinetic M_2L_3 species from reorganizing to the thermodynamically favored M_4L_4 tetrahedral cage. The trapping was completed through formation of the amide or azide products. This demonstrates how covalent modification can be used as a means to alter the structural outcomes without having to design new ligands prior to assembly.

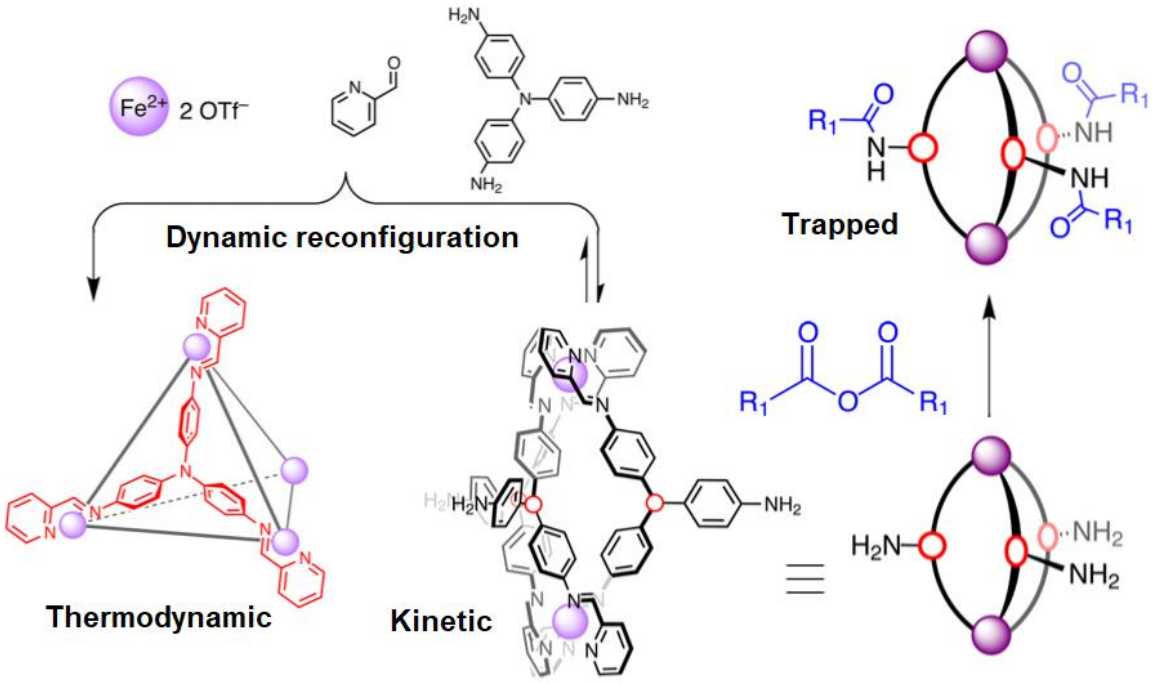

Figure 1.7. Covalent modification of the kinetically formed M_2L_3 complex prevents equilibration to the thermodynamically favored M_4L_4.[30]

Iminopyridine structures can be highly useful, in that altering the cage properties provides multiple opportunities to discover novel host-guest interactions.[31,32] Reversible iminopyridine scaffolds have the potential to form a variety of structures, making them useful as cargo transport systems for separation, drug delivery and stimuli responsive systems.[33] A wide variety of interactions are capable of affecting guest binding,[34] and reversible iminopyridine scaffolds are ideal for the creation of cooperative networks.[35] One such example is a chemical network made up of two different sized cages that were able to selectively shuffle cargo anions upon addition of a suitable guest (Figure 1.8a).[36] Reverse iminopyridine M_4L_6 cages **1.1** and **1.2** will selectively bind anionic guests of a specific size. The addition of a competitive anion (hexafluorophosphate) to a solution of both cages with their respective guests lead to displacement of perchlorate from the smaller cage **1.1**, which then enters the larger cage **1.2**. The incoming perchlorate guest causes the triflimide anion bound with **1.2** to be ejected from the complex.

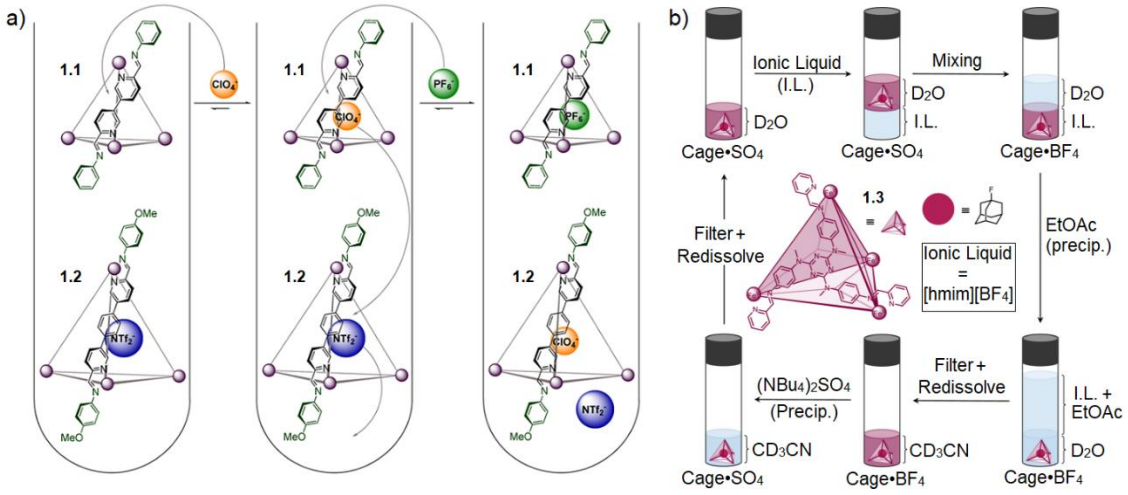

Figure 1.8. a) Cargo shuffling of anions between Complexes **1.1** and **1.2**[36] and b) cargo delivery between varying solvents via Cage **1.3**.[37]

In addition to selective guest shuffling, Fe^{II}-iminopyridine complexes can transport cargo between different solvent systems by modification of cage solubility via anion exchange.[38] Fe^{II}-iminopyridine complexes bearing SO_4^{2-} anions are frequently soluble in water, while complexes using ClO_4^-, BF_4^-, or NTf_2^- anions are soluble in polar organic solvents such as acetonitrile. Figure 1.8b shows how 1-fluoroadamantane guest can be transported between solvent layers via a sequence of salt metathesis steps using M_4L_4 cage **1.3**.[37] The initial **1.3**•SO_4 complex in D_2O is transported into an ionic liquid 1-Hexyl-3-methylimidazolium tetrafluoroborate, through mixing and metathesis of the anions. The **1.3**•BF_4 complex can be precipitated from the ionic liquid using ethyl acetate (EtOAc), redissolved in acetonitrile, and a second metathesis using tetrabutyl ammonium sulfate ($(NBu_4)_2SO_4$) regenerates the starting complex, which is soluble in D_2O. This demonstrates the great potential for iminopyridine assemblies to be used for cargo delivery and molecular recognition.

1.3 Hydrogen-Bonding as a Form of Structural Control

Hydrogen bonding is a powerful interaction that can be exploited for many useful purposes such as guest binding, and examples of this are well precedented in the literature.[39] Several examples of M_4L_6 complexes containing symmetrical urea groups have been previously synthesized using iminopyridine[40] or bipyridine[41] coordinating groups. The iminopyridine assemblies selectively encapsulated one sulfate ion, and the bipyridyl complexes could be extended to other tetrahedral oxoanions of selenium, phosphorous, tungsten, molybdenum and chromium through directed hydrogen bonding. The tetrahedral

M_4L_6 complexes were synthesized by incorporating the urea groups and flexible sp^3 methylene spacers into the ligand cores. The internal cavity of the complexes is complementary in shape to that of the tetrahedral guests, and the urea hydrogen bond donor groups are directed towards the cage interior, allowing for binding to occur. However, in the absence of suitable guests, the flexible nature of the ligands does not allow for the formation of discrete assemblies.

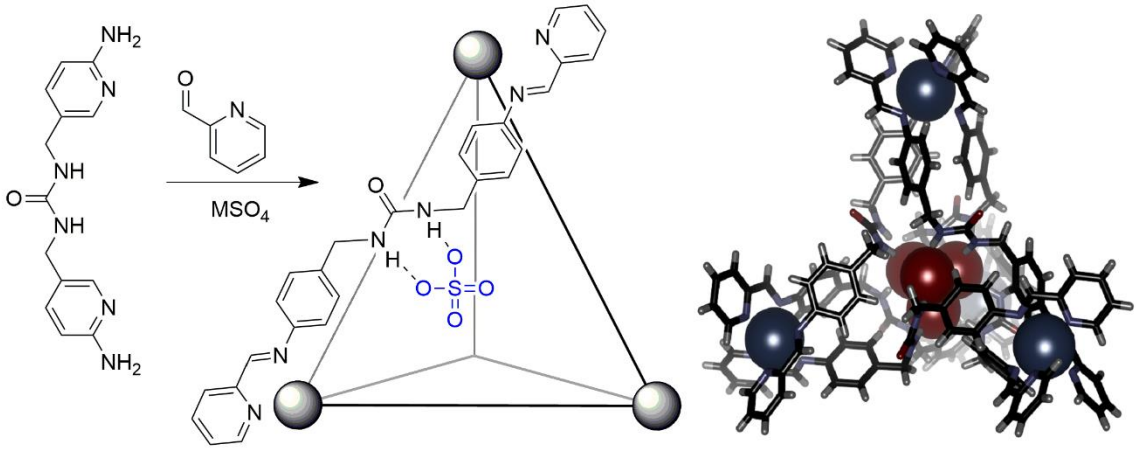

Figure 1.9. Synthesis of a urea-containing iminopyridine M_4L_6 structure and binding of a sulfate anion.

Hydrogen bonding has the potential to be useful as a form of structural control in addition to directed anion binding. If the assembly of complex unsymmetrical ligands containing reactive functional groups could be simplified, a library of functional supramolecular cages could be easily accessible. The challenge is overcoming the daunting complexity arising from the use of desymmetrized non-linear ligands in addition to the possibility of multiple isomers. One solution to this is to exploit intermolecular interaction as an alternative for control over chemical reactivity. Hydrogen bonding can be useful for selective guest binding, but more importantly, this intermolecular force can be used to drive

the assembly process towards the formation of fewer isomers of product. The use of hydrogen bonding as a means of structural control is a well-precedented strategy within the field of multicomponent self-assembly,[42] but is far less common in metal-ligand self-assembled systems.

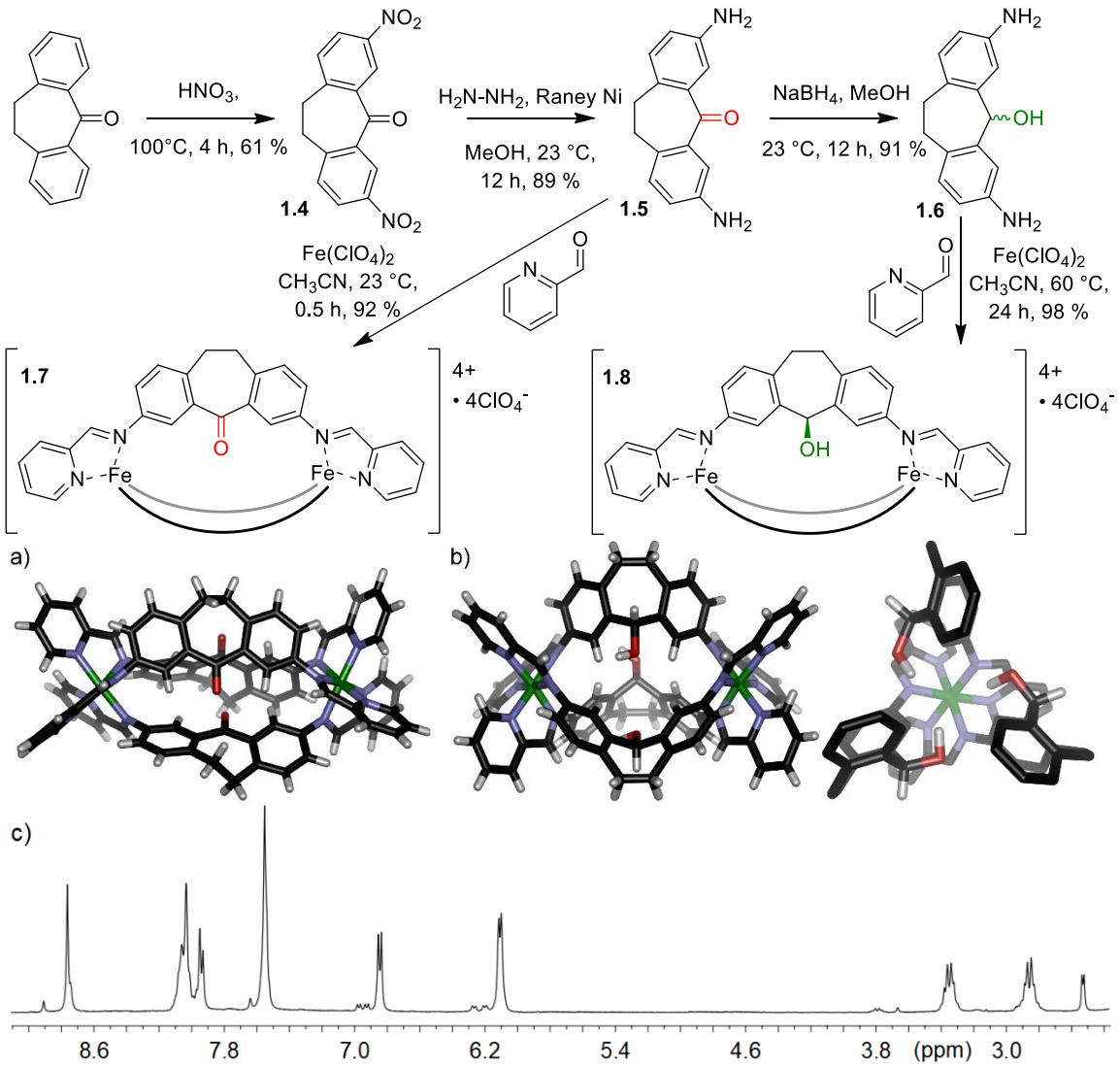

Figure 1.10. Synthesis of 3,7-diaminodibenzosuberone derivatives, X-ray crystal structures of the single isomers of cages a) **1.7** and b) **1.8** and c) ^{1}H NMR of **1.8** displaying the major single isomer of product along with ~10 % of the remaining possibilities observed in the baseline.[43]

Dianiline ligands **1.5** and **1.6** easily assemble into their respective *fac*-ΔΛ mesocate structures **1.7** and **1.8** (as opposed to previously published M_2L_3 structures that favor the matched ΔΔ/ΛΛ helicate isomers).[44] The rigid suberone core **1.5** forms a single mesocate complex, whereas the prochiral center on core **1.6** has the potential to introduce multiple isomeric products if the alcohol group is oriented in different, asymmetrical combinations of "in" and "out" of the complex.[43] However, upon multicomponent assembly with $Fe(ClO_4)_2$ and PyCHO, a single isomer is formed, although very small amounts of the other isomers can be observed in the baseline of the ^{1}H NMR spectrum (Figure 1.10c). This selectivity is possible due to inter-ligand hydrogen bonds that direct the mesocate structure to the most favorable, symmetrical product wherein all three alcohol groups are directed inwards. If the hydrogen bonding capabilities of the pro-chiral group are lost through post-assembly modification with an isocyanate, the absence of any directing effects lead to the formation of multiple isomers.

If applied correctly, directing effects from hydrogen bonding have the potential to simplify the assembly of much larger and more complicated systems, such as M_4L_6 tetrahedra. Ligands that are more rigid, or linear in geometry preferably form larger stoichiometries, as they cannot accommodate the bend necessary to form M_2L_3 species. Perfectly linear and rigid ligands will form a single isomer with tetrahedral symmetry, but non-linear ligands such as the fluorenone scaffold usually form multiple isomers of product. As these larger species contain a greater number of metal centers, along with the added possibility of *mer* connectivity, the number of possible isomers increases significantly, and greater control becomes necessary.

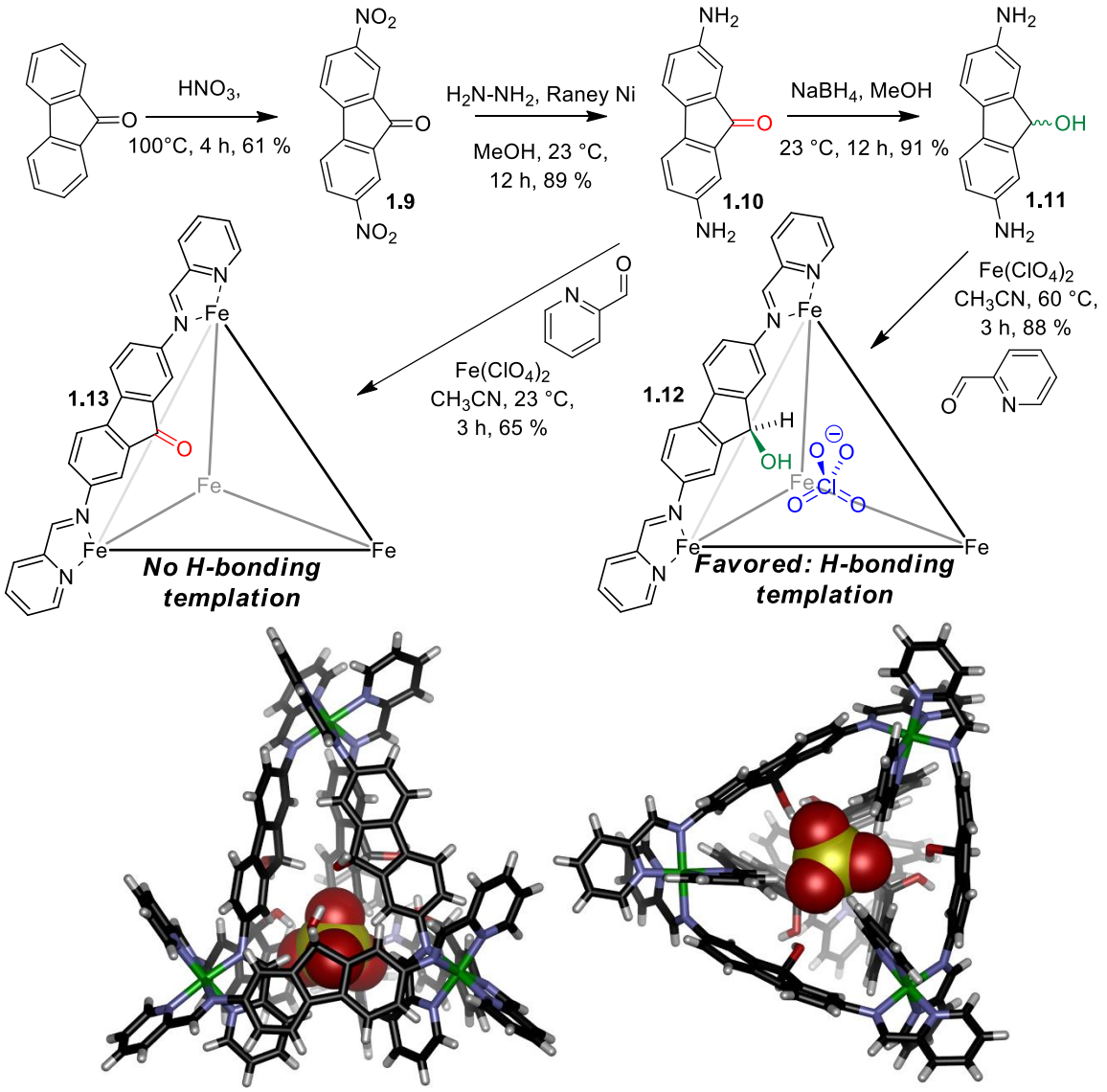

Figure 1.11. Synthesis of 2,7-diaminofluorenone derivatives and two M_4L_6 complexes **1.12** and **1.13**, and X-ray crystal structure of **1.12** illustrating the bound ClO_4^- anion.[45]

The 2,7-diaminofluorenol core **1.11** (Figure 1.11) forms a M_4L_6 structure upon multicomponent assembly with $Fe(ClO_4)_2$ and PyCHO. Given that the M_4L_6 contains four metal atoms that can be oriented in the *fac* or *mer* connectivity with enantiomers of each possibility, the number of products increases. In addition, **1.11** contains a prochiral center

that can be oriented in or out of the cavity. When all isomeric possibilities are accounted for, this ligand can assemble into > 100 possible M_4L_6 products.[45] However, upon assembly with $Fe(ClO_4)_2$ and PyCHO, a single C_3 symmetric isomer is formed and X-Ray crystallography revealed the M_4L_6 structure contained three *mer* centers and one *fac* center. This impressive result is due to templation with a single perchlorate anion bound within the complex, which hydrogen bonds with the alcohol groups and selectively forms the unique *mer*$_3$*fac* structure. Conversely, when the ketone derivative is assembled in the same manner, no favorable hydrogen bonding exists as a driving force, and a complex unassignable mixture of isomers is formed. This impressive structural control demonstrates that hydrogen bonding may be able to direct the assembly of larger, more complex structures. As such, amides, carboxylic acids, thiols and other groups capable of hydrogen bonding are attractive targets for endohedral functionalization.

1.4 Self-Sorting of Supramolecular Cages

The formation of supramolecular complexes from multiple components relies on many small beneficial interactions in order to overcome the entropic penalties associated with assembly formation.[46] To favor one assembly over another many intermolecular forces can be exploited such as hydrogen bonding,[47] π-π/CH-π interactions[48] or solvation effects.[49] When the goal is to create larger and more complex assemblies, exploiting large energetic differences arising from these multiple interactions can bias a reaction towards the desired outcome. As these supramolecular structures become larger and more complex,

greater control over the assembly process becomes necessary, and new methods must be investigated.

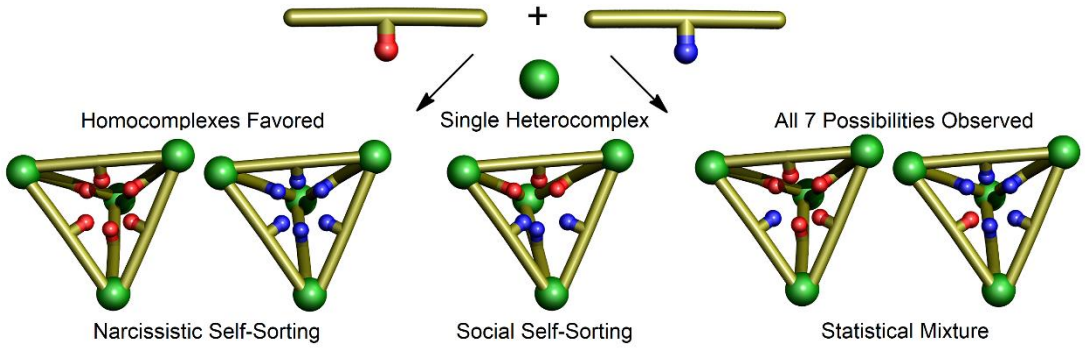

Figure 1.12. Three possible outcomes when multiple ligands are used during the self-assembly process.

Self-sorting is an interesting phenomenon observed when assemblies are formed in the presence of multiple different ligands[50,51] and can be used to exert control over which products are formed. There are three different sorting possibilities that can occur when attempting to combine multiple ligand types into self-assembled complexes (Figure 1.12). The first is narcissistic self-sorting, which is the selective incorporation of only one structural component (e.g. ligand, coordinating motif or metal) leading to the formation of only homocomplex products. The second, and less common possibility is social[52] or integrative[53] self-sorting, which involves selective incorporation of multiple different components.[54] The final possibility is when there is no control over the sorting and a statistical mixture is formed. These mixtures are frequently referred to as dynamic combinatorial libraries and have applications as adaptive systems.[55]

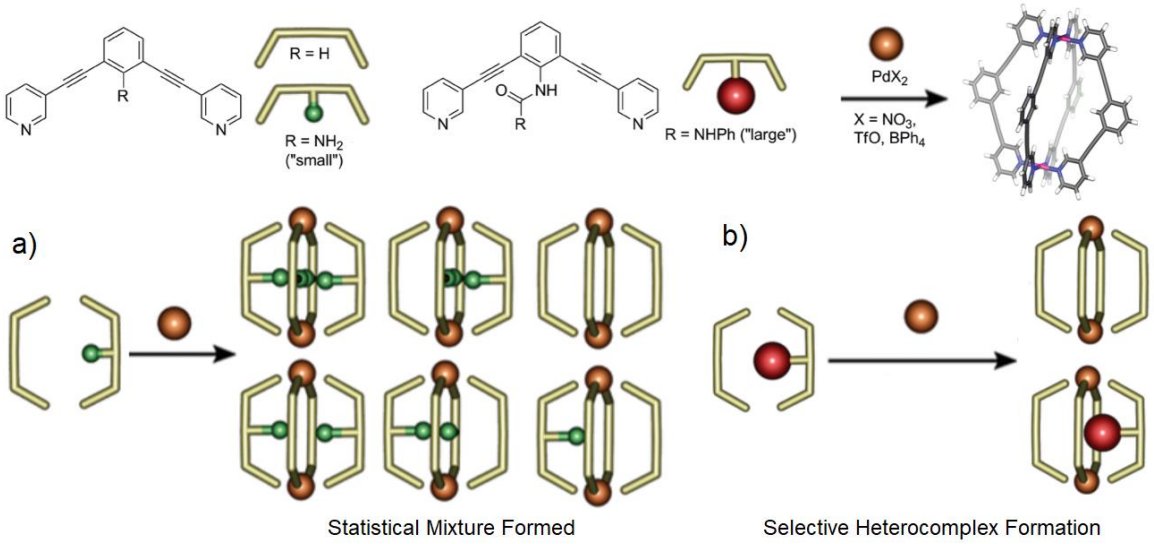

Figure 1.13. a) Formation of a statistical mixture of products due to minimal influence from the small amine functional groups and b) the selective formation of a heterocomplex due to the presence of a sterically demanding phenyl group.[56]

There are several methods that can be used to control self-sorting, such as varying the metal coordinator, changing the ligand length or angle, and modifying the number of donors in the coordination motif.[57] If the components in a system are too similar, typically a complex mixture of species results including non-discrete aggregates, heterocomplexes, stereoisomers and different stoichiometries (e.g. M_2L_3 vs M_4L_6 species). Social self-sorting relies on complementarity between ligand functional groups[58] or coordinating angles.[59] The challenge in selective social self-sorting is that ligand matching cannot be used, as self-complementary ligands favor narcissistic self-sorting. One method of driving the formation of heterocomplexes is the inclusion of endohedral steric bulk (Figure 1.13).[56] When small internal groups such as amines were introduced to bent *bis*-pyridyl ligands, and the functionalized core was complexed with Pd^{II} in the presence of the unfunctionalized derivative, a statistical mixture was observed (Figure 1.13a). However,

when the size of the functional group was increased (i.e. substituted with a sterically demanding phenyl urea group) a single heterocomplex was formed. Here three unfunctionalized ligands and a single phenyl urea decorated ligand were incorporated into the M_2L_4 heterocomplex (Figure 1.13b). This behavior can be extended to much larger scaffolds to form highly complex systems.[60]

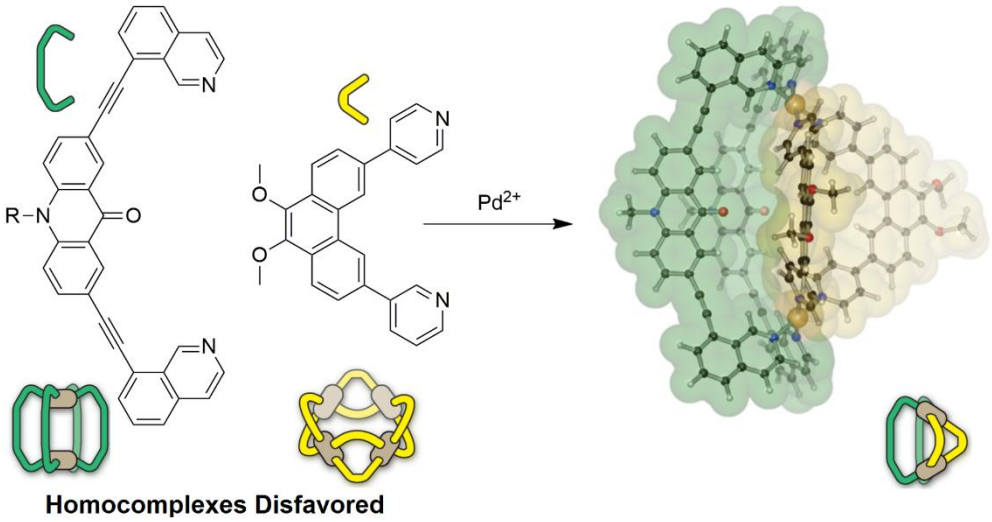

Figure 1.14. Formation of a *cis* $Pd_2L1_2L2_2$ heterocomplex through complementary angles of two bent ligands.[61]

While the use of steric bulk within an assembly to form heterocomplexes is interesting, the internal cavities of the resultant complexes are blocked, and thus cannot function as hosts. A far more interesting method for the formation of heterocomplexes is through careful planning of complimentary ligand angles. The key to this strategy, is the use of ligands that, when assembled into their respective homocomplexes, created strained and unfavorable products (Figure 1.14). Two ligands with bite angles of 120° and 60° were synthesized, and these form disfavored homocomplexes.[61] When a mixture of the two ligands was complexed with Pd^{2+} salts, a *cis*-$Pd_2L1_2L2_2$ complex could be reliably formed.

When a third ligand with a bite angle of 75° was used,[62] two more heterocomplexes could be generated and in each case, only the cis isomers were formed.

When ligands are highly self-complimentary, narcissistic self-sorting occurs, and homocomplexes are favored from ligand mixtures.[63,64] To date, most narcissistic self-sorting studies focus on differentiation between the coordinating groups or large differences in the ligand cores in order to exert maximum control over the systems.[65,66] However, it has been demonstrated that subtle differences between otherwise identical ligands can be enough to encourage narcissistic self-sorting. Small changes in length or the presence of pendant functional groups far from the metal coordinating groups can have drastic effects on self-sorting behavior.[67] Here, ligands varying slightly in angle and length were shown to selectively form homocomplexes in solution, but more impressive was the high fidelity narcissistic self-sorting observed between ligands of identical length that vary only in the pendant functional groups (Figure 1.15). From these studies, methods for greater control over the assembly system can be developed.

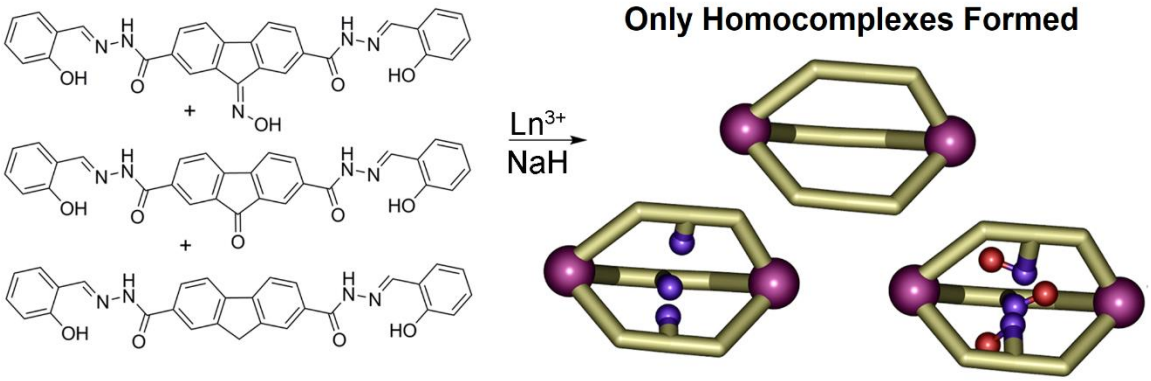

Figure 1.15. Narcissistic self-sorting observed from a mixture of three ligands of identical angle, length and chelating groups.[67]

1.5 Post-Assembly Modification Towards Reactive Functionalization

Many supramolecular systems can mimic the behavior of proteins, in that they are capable of recognizing and binding specific guests. Some metal-ligand assemblies display characteristics similar to enzymes, and can accelerate[68] and catalyze[69] simple reactions of their bound guest molecules. In addition, they can be used to stabilize reactive species and favor regioselective outcomes that cannot occur in solution.[70] However, many of these systems do not involve the use of reactive functional groups, which is the cornerstone of enzymatic activity. In order to introduce reactive functionality to assembly structures, new methods must be investigated, including post-assembly modification of preformed complexes.[71]

Post-assembly modifications (PAM) have been thoroughly studied for metal-organic frameworks,[72] but these reactions are less common in reversibly formed self-assembled cage complexes, and the majority of studies completed to date have focused on mild external modifications.[73] This is likely due to the fact that performing reactions on the interior of reversible systems is challenging.[74] Most known examples of PAM on self-assembled cage systems rely on mild transformations such as ring closing metathesis,[75] CuAAC "click" reactions[76] or the addition of species such as isocyanates.[77] While there are numerous examples of reactivity in self-assembled cages, the reactions only make use of pre-organization of the substrates within the cavity and do not make use of reactive endohedral functionality.

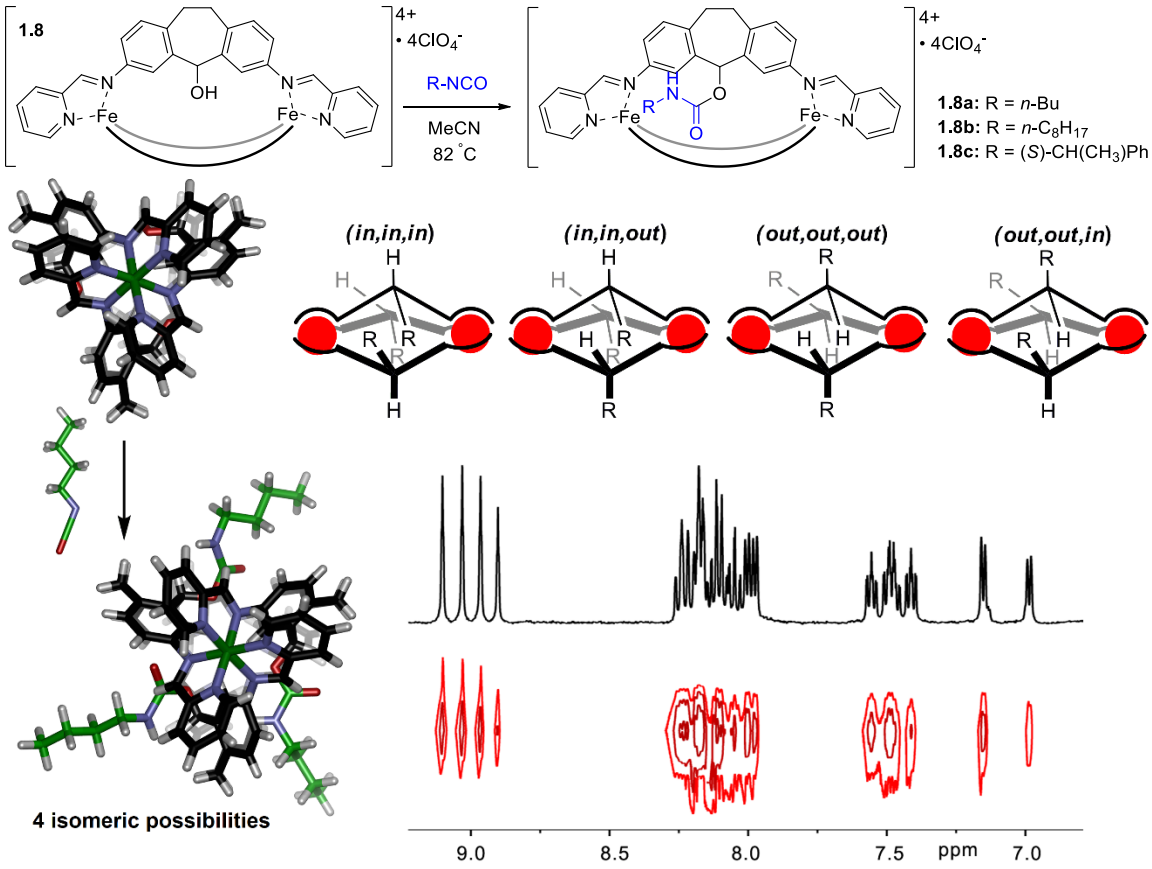

Figure 1.16. Synthesis of the three carbamate substituted structures via PAM with suitable isocyanates, molecular models of one of the four possible isomeric possibilities, and the ^{1}H NMR and DOSEY spectrum of the carbamate product.[43]

The introduction of endohedral functionalization via PAM is difficult and requires matching of the complex and the functional group. Previously it was discussed how the addition of endohedral hydrogen bonding groups could direct the formation of a single isomer. In addition to this, the alcohol groups were found to self-catalyze their addition to suitable isocyanates (Figure 1.16).[43] The complex ^{1}H NMR spectrum indicates that the carbamate groups are not all oriented towards the cage interior in this case, but DOSY NMR analysis[78] confirms that all peaks present arise from complexes of roughly the same size.

Cycloadditions are an ideal form of PAM due to the mild nature of the reaction and the inert nature of the reagents.[79] One interesting example of a ligand-based post-assembly modification is the inverse electron-demand Diels-Alder (IEDDA) of a tetrazine complex (Figure 1.17).[80] Here it was found that, the electron-donating or -withdrawing nature of the of the substituent on the aniline components could influence the IEDDA reactivity of the ligand. Electron withdrawn substituents increased the Diels-Alder rates and followed a linear relationship. The rate of the Diels-Alder PAM could be adjusted by varying the electronics of the aniline component substituents. This form of post-assembly modification can also be applied to more complicated systems to create signaling pathways.[81]

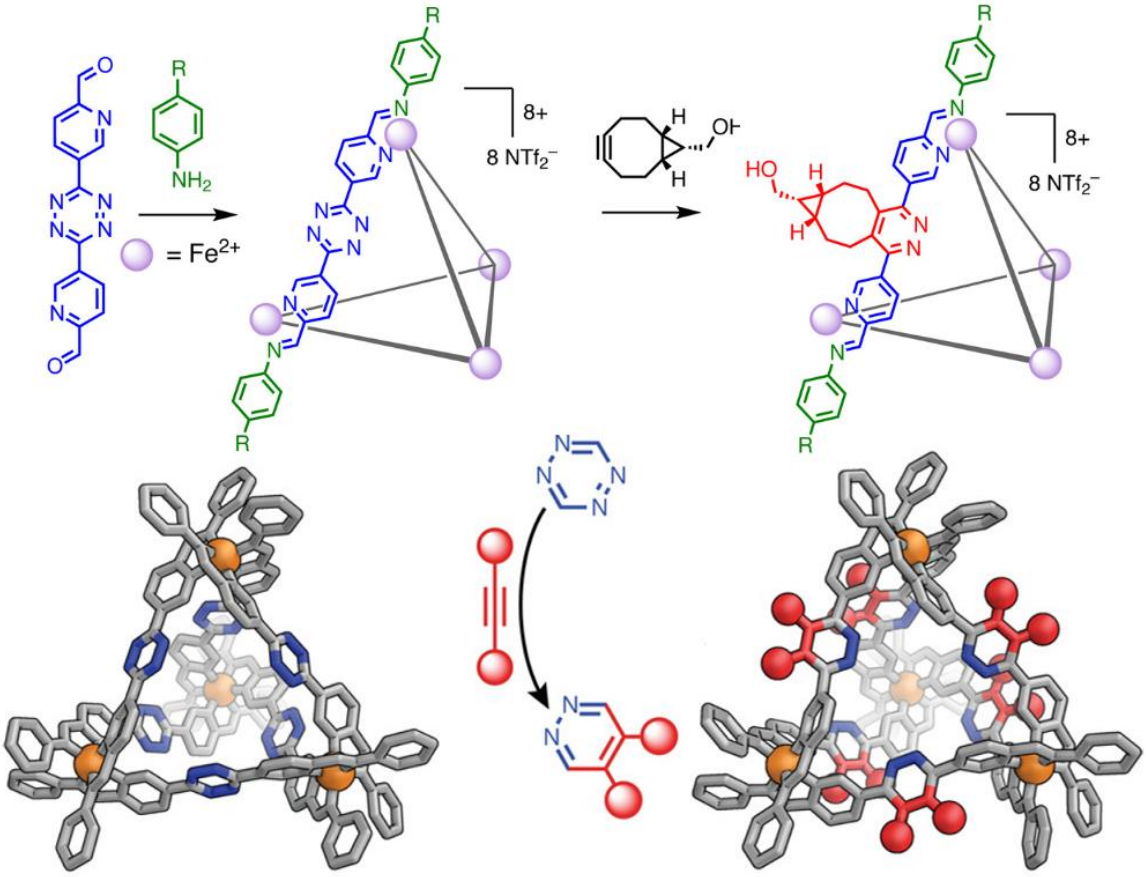

Figure 1.17. The inverse electron-demand Diels-Alder reaction of a tetrazine edged M_4L_6.[80]

In addition to installing controlled functionality, PAMs have the potential to create enzyme mimics in a different manner. Conformational changes of enzymes are a frequently observed mechanism within biosystems.[82] A molecular recognition or binding event at a particular site of a metal-ligand complex can theoretically effect structural changes at a secondary position of the structure, which can cascade into multiple other changes within a system. Supramolecular chemists have been successful in mimicking this effect to create allosteric catalysts and host molecules.[83] The concept of controlling structural changes via external stimuli or recognition processes has also been applied in the construction of molecular machines and switches.[84] The design of these structures has several requirements: the system must contain a specific site where a recognition event will occur, and the system must undergo a predictable change in conformation or stoichiometry via extremal stimuli. Coupling of a structural switch with a reactive functionalized assembly could lead to the formation of highly useful products for targeted drug delivery or signaling. Self-assembled metal-ligand cage complexes are an enticing target for this concept: by performing a reaction on the structural cage ligands, a change in geometry or cage stoichiometry (i.e. M_2L_3 to M_4L_6) could be induced that leads to a change in the host-guest properties.[85]

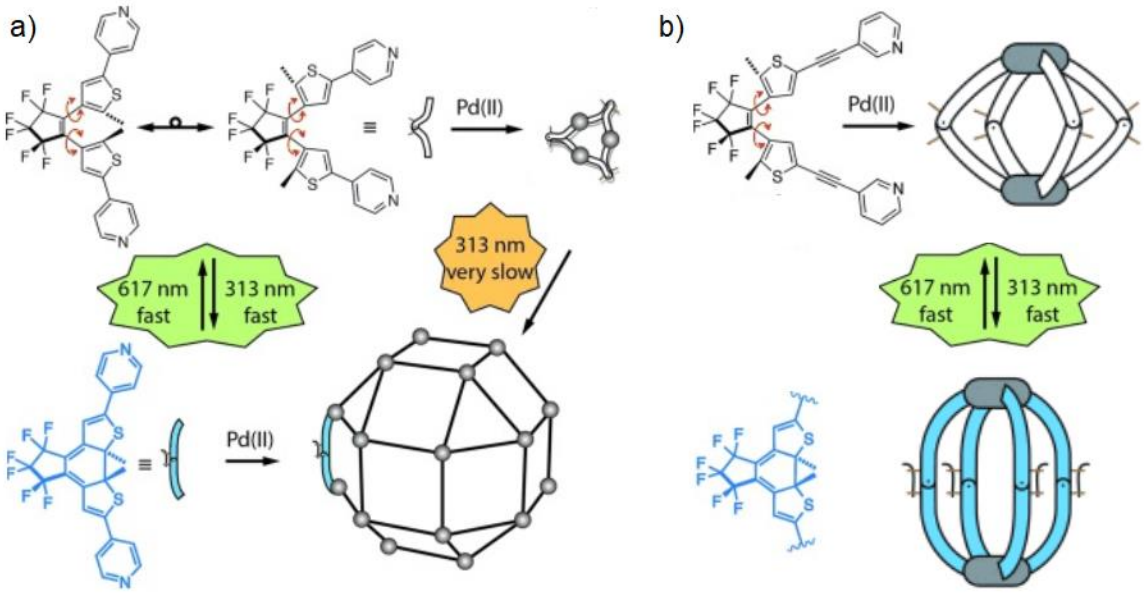

Figure 1.18. Light-controlled interconversion between a) two short ligands that form either a M_3L_6 triangle or an $M_{24}L_{48}$ rhombicuboctahedral sphere,[86] and b) two M_2L_4 complexes of different lengths.[87]

Using light as the external stimuli for PAM would be ideal, and examples of light induced modification of guest uptake have been demonstrated (Figure 1.18b).[87] One example of stoichiometric changes conferred via PAM involve unique M_3L_6 triangles. Upon irradiation of the uncomplexed ligand or M_3L_6 complex with 313 nm light (Figure 1.18a), a stoichiometric switch can be observed and a large $M_{24}L_{48}$ structure generated.[86] If this method of stoichiometric switching could be coupled with appropriate endohedral functionalization, a wealth of compounds could be created for drug delivery and stimuli responsive switches.

1.6 Endohedral Functionalization for Biomimetic Catalysis

The inclusion of reactive functionality within the cavity of self-assembled cage structures is still rare.[88] Given that the synthesis of metal ligand assemblies is dominated

by the use of rigid aromatic ligands, the resulting internal cavities remain, for the most-part, unfunctionalized. As a result, the most effective reactions of metal-ligand assemblies are unimolecular rearrangements or cycloadditions[89] driven by the close proximity of the bound reagents.[90] In some unique cases, structural characteristics such as electron rich aromatic panels,[91] localized hydroxide ions[92] or acidic CH bonds,[93] can participate in catalytic transformations, however these are not close mimics for enzymatic catalysts.

Endohedrally oriented functional groups would allow for mimicry of enzymatic selectivity and rate acceleration far more closely. Functionalized cages could also sequester reactive groups away from the bulk solution, enabling cascade reactions that were previously impossible.[94] An elegant example of this isolation is demonstrated through the use of two $Pd_{12}L_{24}$ nano-spheres (Figure 1.19), each containing a different catalyst that would normally deactivate the other in bulk solution.[95] This catalyst design allows for a two-step reaction to occur in one pot, decreasing waste and reaction time. While this reactivity is impressive, the large micro-environments of the complexes gave no acceleration to the individual reactions. This is likely a result of the large interior space of the nano-spheres, which allow catalyst, substrate and solvent to behave as in bulk solution.

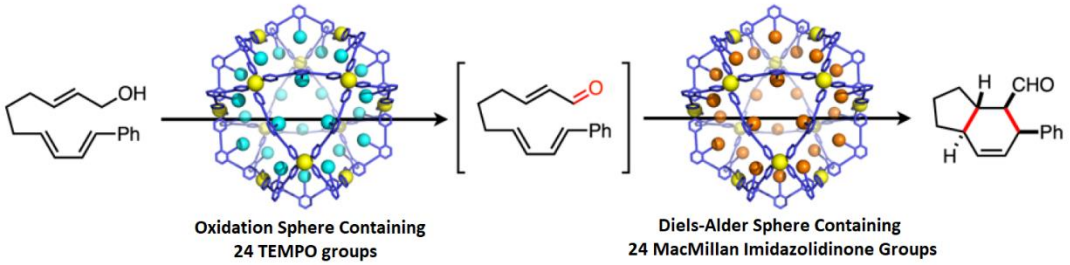

Figure 1.19. Cascade reaction scheme utilizing catalyst isolation to allow for a one pot oxidation and Diels-Alder reaction.[95]

In order to create supramolecular catalysts, modifications to the structural ligands must be made. To date, most examples of functionalized assemblies are supercontainers or nanospheres with very large internal cavities. Some of these large nano-sphere systems have been used to promote internal reactions, such as amine catalyzed Knoevenagel reactions,[96] or Au-catalyzed cyclizations controlled by cooperativity between bound substrates and internal guanidinium binding sites (Figure 1.20).[97] This example uses selective binding, in that the pendant sulfonate groups of the gold complex display higher affinities for the cage interior than the carboxylate bearing substrates. This allowed for the fixation of the gold catalyst, while the remaining binding sites pre-organize the alkyne substrate in close proximity. Here, the rate acceleration was determined to be a result of substrate preorganization rather than participation or activation by the internal functional groups.

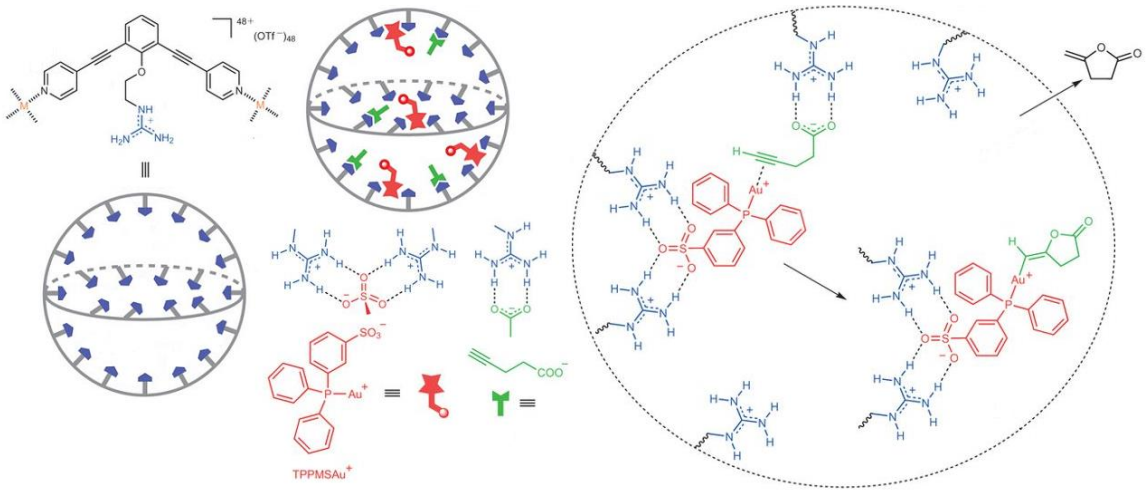

Figure 1.20. Catalyst pre-organization through the use of multiple guanidinium binding sites within a large metal-organic nanosphere.[97]

The lack of rate acceleration for reactions performed within these large supercontainers demonstrates the "goldilocks" nature of designing functionalized supramolecular hosts.[98] If the internal cavity is too large, the substrates behave as if in bulk solution and rate enhancement is not observed. But the assemblies must be large enough to accommodate both reactive functionality and the desired substrate. Future cages must find ways to combine controlled self-assembly with reactive functionality on the cage interiors while maintaining structures that can function as effective catalysts.

1.7 Conclusion

The synthesis of metal-ligand self-assembled cages is now a mature field, and many examples exist that utilize a range of metals, ligands, coordination motifs and useful functional groups to form a variety of structures. Despite this, new routes to create supramolecular cages and control the assembly process are continually being discovered. However, the focus of metal-ligand assemblies has shifted from novel structures and synthesis to the potential applications. To date, some examples of selective binding, reactant encapsulation and promotion of unusual reactivity have been demonstrated, but the vast range of potential uses for assemblies remains largely undiscovered. In order to achieve true biomimetic catalysis, inspiration must be taken from biological systems and reactive endohedral functional groups introduced to properly sized reaction cavities. Whether the endohedral functional groups are added pre- or post-assembly, reactive assemblies may eventually be able to catalyze difficult and biologically important reactions in an enzymatic manner.

1.8 References

1. Brown, C. J.; Toste, F. D.; Bergman, R. G.; Raymond, K. N. "Supra-molecular Catalysis in Metal-Ligand Cluster Hosts." *Chem. Rev*. **2015**, *115*, 3012-3035.

2. Mal, P.; Breiner, B.; Rissanen, K.; Nitschke, J. R. "White Phosphorus Is Air-Stable Within A Self-Assembled Tetrahedral Capsule." *Science* **2009**, *324*, 1697-1699.

3. Riddell, I. A.; Ronson, T. K.; Nitschke, J. R. "Mutual Stabilisation Between $M^{II}_4L_6$ Tetrahedra and $M^{II}X_4^{2-}$ Metallate Guests." *Chem. Sci.*, **2015**, *6*, 3533–3537.

4. Leenders, S. H. A. M.; Gramage-Doria, R.; de Bruin, B.; Reek, J. N. H. "Transition Metal Catalysis in Confined Spaces." *Chem. Soc. Rev*. **2015**, *44*, 433-448.

5. Tidmarsh I. S; Faust, T. B.; Adams, H.; Harding, L. P.; Russo, L.; Clegg, W.; Ward, M. D. "Octanuclear Cubic Coordination Cages." *J. Am. Chem. Soc*. **2008**, *130*, 15167-15175.

6. Mal, P.; Schultz, D.; Beyeh, K.; Rissanen, K.; Nitschke, J. R. "An Unlockable-Relockable Iron Cage by Subcomponent Self-Assembly." *Angew. Chem., Int. Ed*. **2008**, *47*, 8297-8301.

7. Kersting, B.; Meyer, M.; Powers, R. E.; Raymond, K. N. "Dinuclear Catecholate Helicates: Their Inversion Mechanism." *J. Am. Chem. Soc*. **1996**, *118*, 7221- 7222.

8. Leigh, D. A.; Pritchard, R. G.; Stephens, A. J. "A Star of David Catenane." *Nat. Chem*. **2014**, *6*, 978−982.

9. Fujita, D.; Ueda, Y.; Sato, S.; Mizuno, N.; Kumasaka, T.; Fujita, M. "Self-assembly of tetravalent Goldberg polyhedra from 144 small components." *Nature* **2016**, *540*, 563–566.

10. Riddel, I. A.; Smulders, M. M. J.; Clegg, J. K.; Hristova, Y. R.; Breiner, B.; Thoburn, J. D.; Nitschke, J. R. "Anion-induced reconstitution of a self-assembling system to express a chloride-binding $Co_{10}L_{15}$ pentagonal prism." *Nature Chem*. **2012**, *4*, 751-756.

11. Kusukawa, T.; Yoshizawa, M.; Fujita, M. "Probing Guest Geometry and Dynamics through Host–Guest Interactions." *Angew. Chem., Int. Ed*. **2001**, *40*, 1879-1884.

12. Cook, T. R.; Zheng, Y.-R.; Stang, P. J. "Metal-Organic Frameworks and Self-Assembled Supramolecular Coordination Complexes: Comparing and Contrasting

the Design, Synthesis, and Functionality of Metal-Organic Materials." *Chem. Rev.* **2013**, *113*, 734.

13. Ronson, T. K.; Meng, W.; Nitschke, J. R.; "Design Principles for the Optimization of Guest Binding in Aromatic-Paneled $Fe^{II}_4L_6$ Cages." *J. Am. Chem. Soc.* **2017**, *139*, 9698-9707.

14. Castilla, A. M.; Miller, M. A; Nitschke, J. R.; Smulders, M. M. J. "Quantification of Stereochemical Communication in Metal–Organic Assemblies." *Angew. Chem., Int. Ed.* **2016**, *55*, 10616-10620.

15. Pilgrim, B. S.; Nitschke, J. R. "That's No Moon: It's a Molecular Capsule." *Chem*, **2016**, *1*, 19-21.

16. Fiedler, D.; Bergman, R. G.; Raymond, K. N. "Stabilization of Reactive Organometallic Intermediates Inside a Self-Assembled Nanoscale Host." *Angew. Chem., Int. Ed.*, **2006**, *45*, 745-748.

17. Meng, W.; Clegg, J. K.; Thoburn, J. D.; Nitschke, J. R. "Controlling the Transmission of Stereochemical Information through Space in Terphenyl-Edged Fe_4L_6 Cages." *J. Am. Chem. Soc.* **2011**, *133*, 13652-13660.

18. Meng, W.; Ronson, T. K.; Nitschke. J. R. "Symmetry Breaking in Self-Assembled M_4L_6 Cage Complexes." *Proc. Natl. Acad. Sci.* **2013**, *110*, 10531-10535.

19. Hristova, Y. R.; Smulders, M. M. J.; Clegg, J. K.; Breiner, B.; Nitschke, J. R. "Selective anion binding by a chameleon capsule with a dynamically reconfigurable exterior." *Chem. Sci.* **2011**, *2*, 638-641.

20. Ousaka, N.; Clegg, J. K.; Nitschke, J. R. "Nonlinear Enhancement of Chiroptical Response through Subcomponent Substitution in M_4L_6 Cages." *Angew. Chem., Int. Ed.* **2012**, *51*, 1464-1468.

21. Mosquera, J.; Szyszko, B.; Ho, S. K. Y.; Nitschke, J. R. "Sequence-Selective Encapsulation and Protection of Long Peptides by a Self-Assembled $Fe^{II}_8L_6$ Cubic Cage." *Nature Communications*, **2017**, DOI:10.1038/ncomms14882.

22. Bilbeisi, R. A.; Ronson, T. K.; Nitschke, J. R. " A Self-Assembled $[Fe^{II}_{12}L_{12}]$ Capsule with an Icosahedral Framework." *Angew. Chem., Int. Ed.*, **2013**, *52*, 9027-9030.

23. Riddell, I. A.; Hristova, Y. R.; Clegg, J. K.; Wood, C. S.; Breiner, B.; Nitschke, J. R. "Five Discrete Multinuclear Metal-Organic Assemblies from One Ligand:

Deciphering the Effects of Different Templates." *J. Am. Chem. Soc*. **2013**, *135*, 2723-2733.

24. Browne, C.; Brenet, S.; Clegg, J. K.; Nitschke, J. R. "Solvent-Dependent Host-Guest Chemistry of an Fe_8L_{12} Cubic Capsule." *Angew. Chem., Int. Ed*. **2013**, *52*, 1944-1948.

25. Bolliger, J. L.; Ronson, T. K.; Ogawa, M.; Nitschke J. R. "Solvent Effects upon Guest Binding and Dynamics of a $Fe^{II}_4L_4$ Cage." *J. Am. Chem. Soc*., **2014**, *136,* 14545-14553.

26. Ronson, T. K.; Giri, C.; Beyeh, N. K.; Minkkinen, A.; Topic, F.; Holstein, J. J.; Rissanen, K.; Nitschke, J. R. "Size-Selective Encapsulation of Hydrophobic Guests by Self-Assembled M_4L_6 Cobalt and Nickel Cages." *Chem. Eur. J.* **2013**, *19*, 3374-3382.

27. Zarra, S.; Clegg, J. K.; Nitschke, J. R. "Selective Assembly and Disassembly of a Water-Soluble $Fe_{10}L_{15}$ Prism." *Angew. Chem., Int. Ed*. **2013**, *52*, 4837-4840.

28. Kieffer, M.; Pilgrim, B. S.; Ronson, T. K.; Roberts, D. A.; Aleksanyan, M.; Nitschke, J. R. "Perfluorinated Ligands Induce Meridional Metal Stereochemistry to Generate M_8L_{12}, $M_{10}L_{15}$, and $M_{12}L_{18}$ Prisms." *J. Am. Chem. Soc*. **2016**, *138*, 6813-6821.

29. Jansze, S. M.; Cecot, G.; Wise, M. D.; Zhurov, K. O.; Ronson, T. K.; Castilla, A. M.; Finelli, A.; Pattison, P.; Solari, E.; Scopelliti, R.; Zelinskii, G. E.; Vologzhanina, A. V.; Voloshin, Y. Z.; Nitschke, J. R.; Severin, K. "Ligand Aspect Ratio as a Decisive Factor for the Self-Assembly of Coordination Cages." *J. Am. Chem. Soc.* **2016**, *138*, 2046-2054.

30. Roberts, D. A.; Castilla, A. M.; Ronson, T. K.; Nitschke, J. R. "Post-assembly Modification of Kinetically Metastable $Fe^{II}_2L_3$ Triple Helicates." *J. Am. Chem. Soc*., **2014**, *136*, 8201-8204.

31. Rizzuto F. J.; Nitschke, J. R. "Stereochemical Plasticity Modulates Cooperative Binding in a $Co^{II}_{12}L_6$ Cuboctahedron." *Nature Chemistry*, **2017**, *9*, 903-908.

32. Rizzuto, F. J.; Wood, D. M.; Ronson, T. K.; Nitschke, J. R. " Tuning the Redox Properties of Fullerene Clusters within a Metal-Organic Capsule." *J. Am. Chem. Soc.* **2017**, *139*, 11008-11011.

33. Zhang, D.; Ronson, T. K.; Mosquera, J.; Martinez, A.; Nitschke, J. R. "Selective Anion Extraction and Recovery Using a $Fe^{II}_4L_4$ Cage." *Angew. Chem., Int. Ed.* **2018**, *57*, 3717-3721.

34. Ramsay, W. J.; Rizzuto, F. J.; Ronson, T. K.; Caprice, K.; Nitschke, J. R. "Subtle Ligand Modification Inverts Guest Binding Hierarchy in MII8L6 Supramolecular Cubes." *J. Am. Chem. Soc*. **2016**, *138*, 7264-7267.

35. Castilla, A. M.; Ronson, T. K.; Nitschke, J. R. "Sequence-Dependent Guest Release Triggered by Orthogonal Chemical Signals." *J. Am. Chem. Soc*. **2016**, *138*, 2342-2351.

36. Ma, S.; Smulders, M. M. J.; Hristova, Y. R.; Clegg, J. K.; Ronson, T. K.; Zarra, S.; Nitschke, J, R. "Chain-Reaction Anion Exchange between Metal-Organic Cages." *J. Am. Chem. Soc.* **2013**, *135*, 5678-5684.

37. Gromett, A. B.; Nitschke, J. R. "Directed Phase Transfer of an $Fe^{II}_4L_4$ Cage and Encapsulated Cargo." *J. Am. Chem. Soc*. **2017**, *139*, 2176-2179.

38. Percástegui, E. G.; Mosquera, J.; Nitschke, J. R. "Anion Exchange Renders Hydrophobic Capsules and Cargoes Water-Soluble." *Angew. Chem., Int. Ed.* **2017**, *56*, 9136-9140.

39. Zhang, D.: Ronson, T. K.; Mosquera, J.; Martinez, A.; Guy, L.; Nitschke, J. R. "Anion Binding in Water Drives Structural Adaptation in an Azaphosphatrane-Functionalized $Fe^{II}_4L_4$ Tetrahedron." *J. Am. Chem. Soc.* **2017**, *139*, 6574-6577.

40. Yi, S., Brega, V., Captain, B.; Kaifer, A. E. "Sulfate-Templated Self-Assembly of New M_4L_6 tetrahedral metal organic cages." *Chem. Commun.* **2012**, *48*, 10295-10297.

41. Custelcean, R., Bonnesen, P. V., Duncan, N. C., Zhang, X., Watson, L. A., Van Berkel, G., Parson, W. B; Hay, B. P. "Urea-Functionalized M_4L_6 Cage Receptors: Anion-Templated Self-Assembly and Selective Guest Exchange in Aqueous Solution." *J. Am. Chem. Soc*. **2012**, *134*, 8525-8534.

42. Heinz, T.; Rudkevich, D. M.; Rebek J. Jr. "Pairwise Selection of Guests in a Cylindrical Molecular Capsule of Nanometre Dimensions." *Nature* **1998**, *394*, 764-766.

43. Young, M. C.; Johnson, A. M.; Hooley, R. J. "Self-Promoted Post-Synthetic Modification of Metal-Ligand M_2L_3 Mesocates." *Chem. Commun.* **2014**, *50*, 1378-1380.

44. Hannon, M. J.; Painting, C. L.; Jackson, A.; Hamblin, J.; Errington, W. "An Inexpensive Approach to Supramolecular Architecture." *Chem. Commun.* **1997**, 1807-1808.

45. Young, M. C.; Holloway, L. R.; Johnson, A. M.; Hooley, R. J. "A Supramolecular Sorting Hat: Stereocontrol in Metal-Ligand Self-Assembly by Complementary Hydrogen Bonding." *Angew. Chem., Int. Ed.* **2014**, *53*, 9832-9836.

46. Lehn, J.-M. "From Supramolecular Chemistry Towards Constitutional Dynamic Chemistry and Adaptive Chemistry." *Chem. Soc. Rev*. **2007**, *36*, 151-160.

47. Schneider, H. J. "Binding Mechanisms in Supramolecular Complexes." *Angew. Chem., Int. Ed*. **2009**, *48*, 3924-3977.

48. Hof, F.; Scofield, D. M.; Schweizer, W.B.; Diederich, F. "A Weak Attractive Interaction Between Organic Fluorine and an Amide Group." *Angew. Chem., Int. Ed*. **2004**, *43*, 5056-5059.

49. Persch, E.; Dumele, O.; Diederich, F. "Molecular Recognition in Chemical and Biological Systems." *Angew. Chem., Int. Ed*. **2015**, *54*, 3290-3327.

50. Safont-Sempere, M.; Fernández, G.; Würther, F. "Self-Sorting Phenomena in Complex Supramolecular Systems." *Chem. Rev.* **2011**, *111*, 5784-5814.

51. Rizzuto, F. J.; Kieffer, M.; Nitschke, J. R. "Quantified Structural Speciation in $Co^{II}_6L_4$ Cage Systems." *Chem. Sci.* **2018**, *9*, 1925-1930.

52. Ajami, D.; Hou, J.-L.; Dale, T. J.; Barrett, E.; Rebek, J. Jr. "Disproportionation and Self-Sorting in Molecular Encapsulation." *Proc. Natl. Acad. Sci. USA* **2009**, *106*, 10430-10434.

53. Bloch, W. M.; Clever, G. H. "Integrative Self-Sorting of Coordination Cages Based on 'Naked' Metal Ions." *Chem. Commun*. **2017**, *53*, 8506-8516.

54. Smulders, M. J.; Jiménez, A.; Nitschke, J. R. "Integrative Self-Sorting Synthesis of a $Fe_8Pt_6L_{24}$ Cubic Cage." *Angew. Chem., Int. Ed.* **2012**, *51*, 6681-6685.

55. Black, S. P.; Wood, D. M.; Schwarz, F. B.; Ronson, T. K.; Holstein, J. J.; Stefankiewicz, A. R.; Schalley, C. A.; Sanders, J. K. M.; Nitschke, J. R. "Catenation and Encapsulation Induce Distinct Reconstitutions Within a Dynamic Library of Mixed-Ligand Zn_4L_6 Cages." *Chem. Sci*. **2016,** *7*, 2614-2620.

56. Johnson. A. M.; Hooley, R. J. "Steric Effects Control Self-Sorting in Self-Assembled Clusters." *Inorg. Chem*. **2011**, *50*, 4671-4673.

57. Saha, M. L.; De, S.; Pramanik, S.; Schmittel, M. "Orthogonality in Discrete Self-Assembly - Survey of Current Concepts." *Chem. Soc. Rev.* **2013**, *42*, 6860-6909.

58. Pellizzaro, M.; Houton, K. A.; Wilson, A. J. "Sequential and Phototriggered Supramolecular Self-Sorting Cascades Using Hydrogen-Bonded Motifs." *Chem. Sci.* **2013**, *4*, 1825-1829.

59. Preston, D.; Barnsley, J. E.; Gordon, K. C.; Crowley, J. D. "Controlled Formation of Heteroleptic $[Pd_2(La)_2(Lb)_2]^{4+}$ Cages." *J. Am. Chem. Soc.* **2016**, *138*, 10578-10585.

60. Suzuki, K.; Kawano, M.; Sato, S.; Fujita, M. "Endohedral Peptide Lining of a Self-Assembled Molecular Sphere to Generate Chirality-Confined Hollows." *J. Am. Chem. Soc.* **2007**, *129*, 10652-10653.

61. Bloch, W. M.; Abe, Y.; Holstein, J. J.; Wandtke, C. M.; Dittrich, B.; Clever, G. H. "Geometric Complementarity in Assembly and Guest Recognition of a Bent Heteroleptic cis-$[Pd_2La_2Lb_2]$ Coordination Cage." *J. Am. Chem. Soc*. **2016**, *138*, 13750-13755.

62. Bloch, W. M.; Holstein, J. J.; Hiller W.; Clever, G. H. "Morphological Control of Heteroleptic cis- and trans-$Pd_2L_2L'_2$ Cages." *Angew. Chem., Int. Ed*. **2017**, *56*, 8285-8289.

63. Jiménez, A.; Bilbeisi, R. A.; Ronson, T. A.; Zarra, S.; Woodhead, C.; Nitschke, J. R. "Selective Encapsulation and Sequential Release of Guests Within a Self-Sorting Mixture of Three Tetrahedral Cages." *Angew. Chem., Int. Ed*. **2014**, *53*, 4556-4560.

64. Yamanaka, M.; Yamada, Y.; Sei, Y.; Yamaguchi, K.; Kobayashi, K. "Selective Formation of a Self-Assembling Homo or Hetero Cavitand Cage Via Metal Coordination Based on Thermodynamic or Kinetic Control." *J. Am. Chem. Soc.* **2006**, *128*, 1531-1539.

65. Acharyya, K.; Mukherjee, S.; Mukherjee, P. S. "Molecular Marriage Through Partner Preferences in Covalent Cage Formation and Cage-to-Cage Transformation." *J. Am. Chem. Soc*. **2013**, *135*, 554-557.

66. Wang, W.; Zhang, Y.; Sun, B.; Chen, L.-J.; Xu, X.-D.; Wang, M.; Li, X.; Yu, Y.; Jiang W.; Yang, H.-B. "The Construction of Complex Multicomponent Supramolecular Systems Via the Combination of Orthogonal Self-Assembly and The Self-Sorting Approach." *Chem. Sci*. **2014**, *5*, 4554-4559.

67. Johnson, A. M.; Wiley, C. A.; Young, M. C.; Zhang, X.; Lyon, Y.; Julian, R. R.; Hooley, R. J. "Narcissistic Self-Sorting in Self-Assembled Cages of Rare Earth Metals and Rigid Ligands." *Angew. Chem., Int. Ed*. **2015**, *54*, 5641-5645.

68. Leung, D. H.; Fiedler, D.; Bergman, R. G.; Raymond, K. N. "Selective C-H Bond Activation by a Supramolecular Host-Guest Assembly." *Angew. Chem., Int. Ed*. **2004**, *43*, 963−966.

69. Hastings, C. J.; Pluth, M. D.; Bergman, R. G.; Raymond, K. N. "Enzyme-Like Catalysis of the Nazarov Cyclization by Supramolecular Encapsulation." *J. Am. Chem. Soc.* **2010**, *132,* 6938-6940.

70. Yoshizawa, M.; Tamura, M.; Fujita M. "Diels-Alder in Aqueous Molecular Hosts: Unusual Regioselectivity And Efficient Catalysis." *Science* **2006**, *312,* 251-254.

71. Roberts, D. A.; Pilgrim, B. S.; Nitschke, J. R. "Covalent Post-Assembly Modification in Metallosupramolecular Chemistry." *Chem. Soc. Rev*. **2017**, *47,* 626-644.

72. Tanabe, K. K.; Cohen, S. M. "Postsynthetic Modification of Metal-Organic Frameworks-A Progress Report." *Chem. Soc. Rev.* **2011**, *40,* 498-519.

73. Acharyya, K.; Mukherjee, P. S. "Post-Synthetic Exterior Decoration of An Organic Cage by Copper(I) Catalysed A3-Coupling and Detection of Nitroaromatics." *Chem. - Eur. J*. **2015**, *21,* 6823-6831.

74. Wang, M.; Lan, W.-J.; Zheng, Y.-R.; Cook, T. R.; White, H. S.; Stang, P. J. "Post-Self-Assembly Covalent Chemistry of Discrete Multicomponent Metallosupramolecular Hexagonal Prisms." *J. Am. Chem. Soc*. **2011**, *133,* 10752-10755.

75. Hiraoka, S.; Yamauchi, Y.; Arakane, R.; Shionoya, M. "Template-Directed Synthesis of a Covalent Organic Capsule Based on A 3 Nm-Sized Metallocapsule." *J. Am. Chem. Soc*. **2009**, *131*, 11646−11647.

76. Chakrabarty, R.; Stang, P. J. "Post-Assembly Functionalization of Organoplatinum(II) Metallacycles Via Copper-Free Click Chemistry." *J. Am. Chem. Soc*. **2014**, *134,* 14738-14741.

77. Brega, V.; Zeller, M.; He, Y.; Lu, P. H.; Klosterman, J. K. "Multi-Responsive Metal−Organic Lantern Cages in Solution." *Chem. Commun*. **2015**, *51*, 5077−5080.

78. Megyes, T.; Jude, H.; Grósz, T.; Bakó, I.; Radnai, T.; Tárkányi, G.; Pálinkás, G.; Stang, P. J. "X-ray Diffraction and DOSY NMR Characterization of Self-

Assembled Supramolecular Metallocyclic Species in Solution." *J. Am. Chem. Soc*. **2005**, *127*, 10731–10738.

79. Ronson, T. K.; Pilgrim, B. S.; Nitschke, J. R. "Pathway-Dependent Post-Assembly Modification of An Anthracene-Edged $M^{II}_4L_6$ Tetrahedron." *J. Am. Chem. Soc*. **2016**, *138*, 10417-10420.

80. Roberts, D. A.; Pilgrim, B. S.; Cooper, J. D.; Ronson, T. K.; Zarra, S.; Nitschke, J. R. "Post-assembly Modification of Tetrazine-Edged $Fe^{II}_4L_6$ Tetrahedra." *J. Am. Chem. Soc.* **2015**, *137*, 10068-10071.

81. Pilgrim, B. S.; Roberts, D. A.; Lohr, T. G.; Ronson, T. K.; Nitschke, J. R. "Signal Transduction in a Covalent Post-Assembly Modification Cascade." *Nat. Chem*. **2017**, *9*, 1276-1281.

82. Lifschitz, A. M.; Rosen, M. S.; McGuirk, C. M.; Mirkin C. A. "Allosteric Supramolecular Coordination Constructs." *J. Am. Chem. Soc*. **2015**, *137*, 7252-7261.

83. Ramsay, W. J.; Nitschke, J. R. "Two Distinct Allosteric Active Sites Regulate Guest Binding Within a $Fe_8Mo_{12}^{16+}$ Cubic Receptor." *J. Am. Chem. Soc.* **2014**, *136*, 7038-7043.

84. Erbas-Cakmak, S.; Leigh, D. A.; McTernan, C. T.; Nussbaumer A. L. "Artificial Molecular Machines." *Chem. Rev*. **2015**, *115*, 10081-10206.

85. McConnell, A. J.; Wood, C. S.; Neelakandan, P. P.; Nitschke, J. R. "Stimuli-Responsive Metal-Ligand Assemblies." *Chem. Rev*. **2015**, *115*, 7729-7793.

86. Han, M.; Luo, Y.; Damaschke, B.; Gomez, L.; Ribas, X.; Jose, A.; Peretzki, P.; Seibt, M.; Clever, G. H. "Light-Controlled Interconversion between a Self-Assembled Triangle and a Rhombicuboctahedral Sphere." *Angew. Chem., Int. Ed*. **2015**, *54*, 445-449.

87. Han, M.; Michel, R.; He, B.; Chen, Y.-S.; Stalke, D.; John, M.; Clever, G. H. "Light-Triggered Guest Uptake and Release by a Photochromic Coordination Cage." *Angew. Chem., Int. Ed*. **2013**, *52*, 1319-1323.

88. Cook, T. R.; Stang, P. J. "Recent Developments in the Preparation and Chemistry of Metallacycles and Metallacages via Coordination." *Chem. Rev.* **2015**, *115*, 7001-7045.

89. Nishioka, Y.; Yamaguchi, T.; Yoshizawa, M.; Fujita, M. "Unusual [2+4] and [2+2] Cycloadditions of Arenes in the Confined Cavity of Self-Assembled Cages." *J. Am. Chem. Soc.* **2007***, 129*, 7000-7001.

90. Kaphan, D. M.; Levin, M. D.; Bergman, R. G.; Raymond, K. N.; Toste, F. D. "A Supramolecular Microenvironment Strategy for Transition Metal Catalysis." *Science* **2015**, *350***,** 1235-1238.

91. Musser, A. J.; Neelakandan, P. P.; Richter, J. M.; Mori, H.; Friend, R. H.; Nitschke, J. R. "Excitation Energy Delocalization and Transfer to Guests within MII4L6 Cage Frameworks." *J. Am. Chem. Soc.* **2017**, *139*, 12050-12059.

92. Cullen, W.; Misuraca, M. C.; Hunter, C. A.; Williams, N. H.; Ward, M. D. "Highly Efficient Catalysis of the Kemp Elimination in the Cavity of a Cubic Coordination Cage." *Nat. Chem.* **2016**, *8*, 231-236.

93. Martí-Centelles, V.; Lawrence, A. L.; Lusby, P. J. "High Activity and Efficient Turnover by a Simple, Self-Assembled Artificial Diels-Alderase." *J. Am. Chem. Soc.* **2018**, *140*, 2862-2868.

94. Wasilke, J.-C.; Obrey, S. J.; Baker, R. T.; Bazan, G. C. "Conurrent Tandem Catalysis." *Chem. Rev.* **2005**, *105*, 1001-1020.

95. Ueda, Y.; Ito, H.; Fujita, D.; Fujita, M.; "Permeable Self-Assembled Molecular Containers for Catalyst Isolation Enabling Two-Step Cascade Reactions." *J. Am. Chem. Soc.* **2017**, *139*, 6090-6093

96. Qiao, Y.; Zhang, L.; Li, J.; Lin, W.; Wang, Z. "Switching on Supramolecular Catalysis via Cavity Mediation and Electrostatic Regulation." *Angew. Chem., Int. Ed.* **2016**, *55*, 12778-12782.

97. Wang, Q.-Q.; Gonell, S.; Leenders, S.H.A.M.; Dürr, M.; Ivanović-Burmazović, I.; Reek, J. N. H. "Self-Assembled Nanospheres With Multiple Endohedral Binding Sites Pre-Organize Catalysts and Substrates for Highly Efficient Reactions." *Nat. Chem.* **2016**, *8*, 225-230.

98. Bilbesi, R. A.; Clegg, J. K.; Elgrishi, N.; de Hatten, X.; Devillard, M.; Breiner, B.; Mal, P.; Nitschke, J. R. "Subcomponent Self-Assembly and Guest-Binding Properties of Face-Capped $Fe_4L_4^{8+}$ Capsules." *J. Am. Chem. Soc.* **2012**, *134*, 5110-5119.

Chapter 2: High Fidelity Sorting of Remarkably Similar Components via Metal-Mediated Assembly

2.1 Introduction

The construction of complex supramolecular structures requires a high level of control over the assembly process. As these supramolecular structures become larger and more complex, self-sorting between different ligand types becomes paramount. Variation of the metal coordinator, changing ligand length or angle, and modification of the number of donors are strategies frequently employed to control the sorting of the system. However, as the components of an assembly mixture become more similar, a greater number of undesired possibilities can result, such as aggregates, heterocomplexes, multiple stereoisomers or different stoichiometries of assembly (e.g. M_2L_3 vs M_4L_6 structures). We have previously reported that differences in pendant functional groups uninvolved in the coordination process can have drastic effects on self-sorting behavior.[1] What has yet to be investigated is whether small differences in ligand flexibility or hybridization are enough to effect narcissistic self-sorting of Fe^{II}-iminopyridine assemblies.

2.2 Dianiline Ligand Cores and Complex Synthesis

Little work has thus far been completed which focuses on minimizing the differences between ligands in narcissistic self-sorting systems. For this study, four ligands were chosen that contain minimal variations between the central ligand core, as shown in Figure 2.1. We focused on the small suberyl based M_2L_3 scaffolds as the mesocate structures are less complex than larger stoichiometries of assembly. The suberyl core can

be easily modified, and previously synthesized assemblies of 3,7-diaminodibenzosuberone **1.5** and 3,7-diaminodibenzosuberol **1.6** have been shown to form stable assemblies.[2] To test the effects of flexibility on the sorting, 3,7-diaminodibenzosuberenone **2.2** was synthesized from **1.4** in two steps: a one-pot radical bromination and elimination reaction, followed by reduction of the nitro groups. The 2,7-diaminoxanthone core **2.5** is also more rigid than cores **1.5** or **1.6** and displays a more linear coordination angle. This ligand core was synthesized from commercially available xanthone using the same nitration and reduction route.

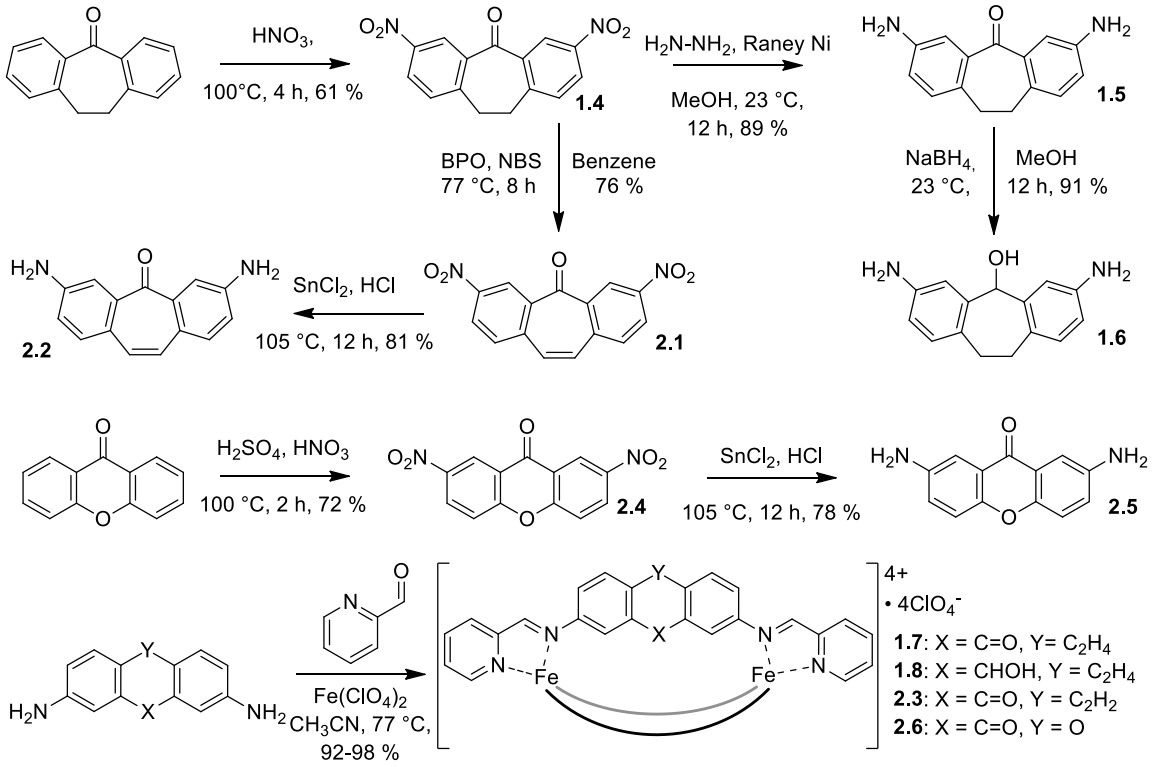

Figure 2.1. Synthetic scheme for the four dianiline ligand cores used in this study **1.5**, **1.6**, **2.2** and **2.5** and their corresponding cages **1.7**, **1.8**, **2.3** and **2.6**

The four ligand cores vary minimally in length and coordination angle, and upon multicomponent assembly will all contain identical iminopyridine coordinating groups. Each core cleanly assembles into the corresponding M_2L_3 structure upon heating with Fe^{II} salts and 2-formylpyridine (PyCHO) in acetonitrile, rather than forming complexes with larger stoichiometries.[3,4] This is evidenced by the ESI mass spectra of the assemblies, which all clearly show the presence of variably charged species arising from the sequential loss of the four ClO_4^- counterions as shown in Figure 2.2e. The M_2L_3 structures all exist in the highly symmetrical mesocate conformation, where the presence of one *fac*-Δ and one *fac*-Λ iron center are observed as opposed to the desymmetrized helicate structures with matched *fac*-ΔΔ or *fac*-ΛΛ metal centers. The major difference between the three suberyl cores lies in their flexibility, with the variance arising from the hybridization of three central carbon atoms. Dianilines **2.5** and **2.2** are nearly planar upon assembly as demonstrated in Figure 2.1c and d. Core **1.5** contains a CH_2-CH_2 backbone within the central ring, allowing for some flexibility upon assembly. Suberol core **1.6** is more flexible still, with the presence of three sp^3 carbons within the central ring and is capable of inter-ligand hydrogen bonding. This interaction may provide beneficial stabilization and drives the formation of a single isomer of the M_2L_3 product.

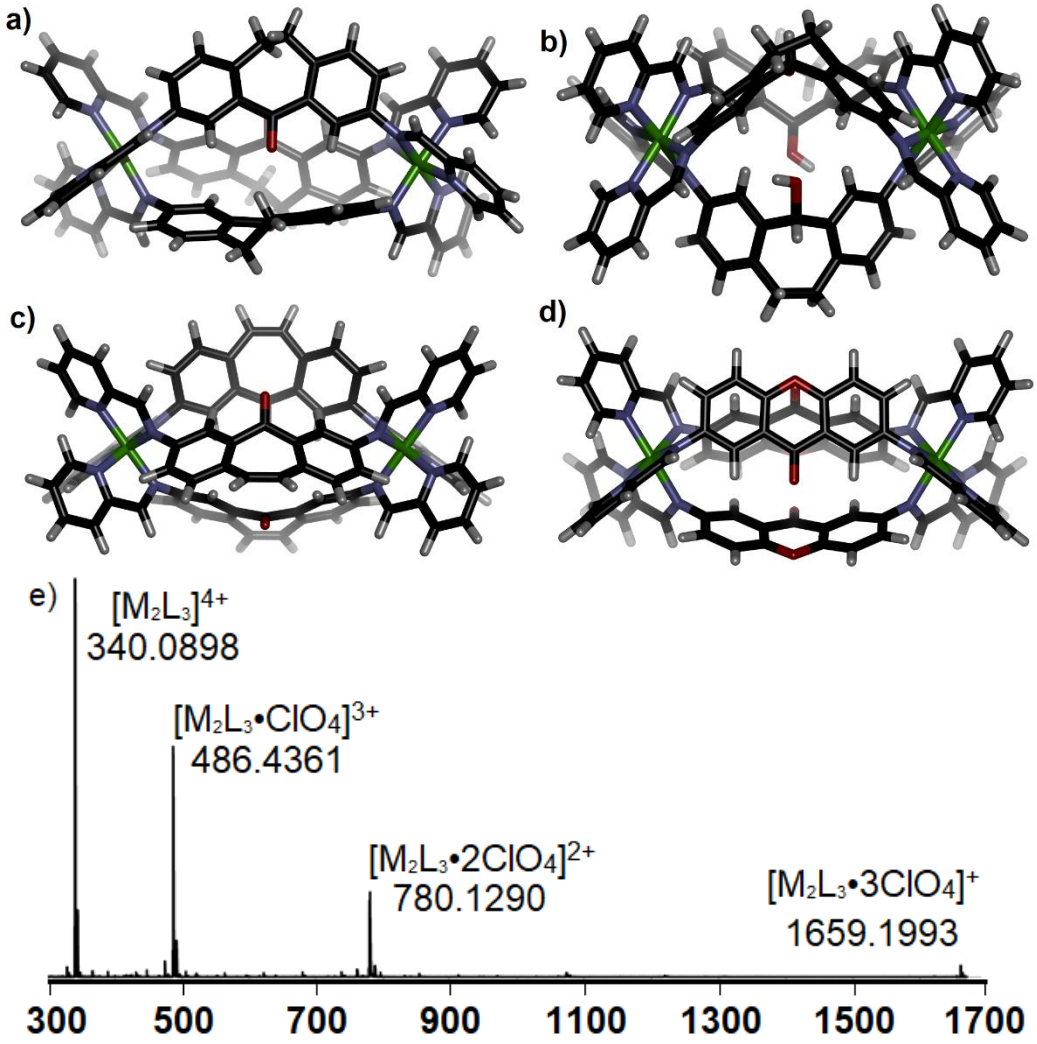

Figure 2.2. Crystal structures of cages: a) **1.7** and b) **1.8**, minimized models of: c) **2.3** and d) **2.6** and the ESI mass spectrum of cage **1.7** demonstrating the sequential loss of perchlorate anions typical of the M_2L_3 assemblies.

2.3 Ligand Displacement on Preformed Cages

Some examples of ligand displacement on pre-formed complexes exist in the literature and this method can produce interesting heterocomplex products.[5,6] While these experiments were performed on monodentate Pd-pyridyl coordinating groups, the reversible nature of the Fe^{II}-iminopyridine assembly indicated that ligand core displacement should be possible. Given that the four ligands used in this study vary

minimally, the formation of new heterocomplexes is likely, and could lead to interesting internally functionalized assemblies. Ligand displacement reactions were performed on the preformed cages **1.7**, **1.8**, **2.3** and **2.6**. One molar equivalent of isolated cage (e.g. **2.3**) was placed in an NMR tube in CD_3CN, and to this solution was added 3 equivalents of a competing dianiline core (e.g. suberone **1.5**). The samples were heated at 50 °C for 8 h and checked for evidence of ligand displacement. It was noted that under anhydrous conditions, the ligand displacement reactions were sluggish and incomplete after 8 h reaction time (Figure 2.3c). Only slight changes to the ^{1}H NMR spectrum could be observed, even after extensive heating. The ligand:PyCHO:Fe^{II} assembly process is an equilibrium that produces six equivalents of water for each M_2L_3 assembly, arising from the condensation of aniline and aldehyde. The presence of water in the displacement reactions should not have a great effect on the rate, but when the experiment was repeated with the addition of 6 eq. of water, the reaction mixtures were cleanly converted to the more favored homocomplex products after just 1 h of heating at 50 °C. The rate increase in the presence of water is interesting, especially given that PyCHO is not observed at any appreciable concentration. Under the concentrations used, water is unlikely to participate in nucleophilic displacement of the imine, and the accelerating effect is most likely due to the formation of small concentrations of Brønsted acid that aids the decomplexation of the iminopyridine ligand from the iron center and a subsequent transimination takes place. By noting which preformed complexes were resistant to displacement by specific ligands, an order of stability was determined.

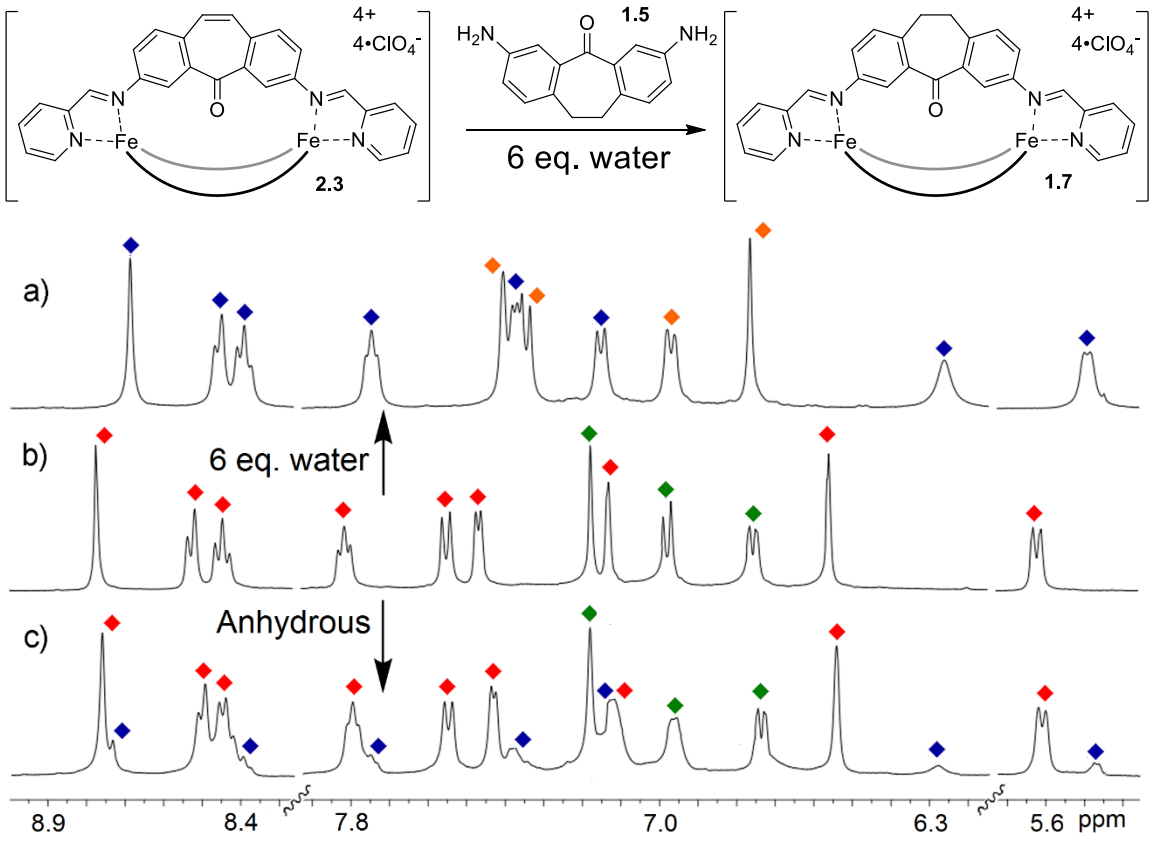

Figure 2.3. ^{1}H NMR spectra of the cage **2.3**:suberone ligand **1.5** mixture b) prior to reaction and after heating in CD_3CN with a) 6 mol.-eq. water (50 ºC, 1 h) or c) under anhydrous conditions (50 ºC, 8 h) (400 MHz, CD_3CN, 298 K). Red = cage **2.3**; blue = cage **1.7**; green = dianiline **1.5**; orange = dianiline **2.2**.

Suberone cage **1.7** was resistant to displacement by the remaining three dianiline cores, indicating that this complex is the most favorable of the four mesocate species. Conversely, when preformed cage **1.8** was mixed with dianilines **1.5** or **2.2**, the suberol assembly was rapidly replaced by the new homocomplexes. This displacement by both ligands indicates that the complex **1.8** is less favorable than complexes **1.7** and **2.3**. From these two experiments it can be determined that cage **1.7** is the most favorable and cage **1.8** is least favored between the three suberyl cores. As expected, cage **2.3** was rapidly displaced by dianiline **1.5**, and was resistant to displacement by **1.6**. When xanthone-based

2.5 was mixed with any of the pre-formed suberyl cages **1.7**, **1.8**, or **2.3**, no ligand displacement was observed, even after the use of elevated temperatures or longer reaction times.

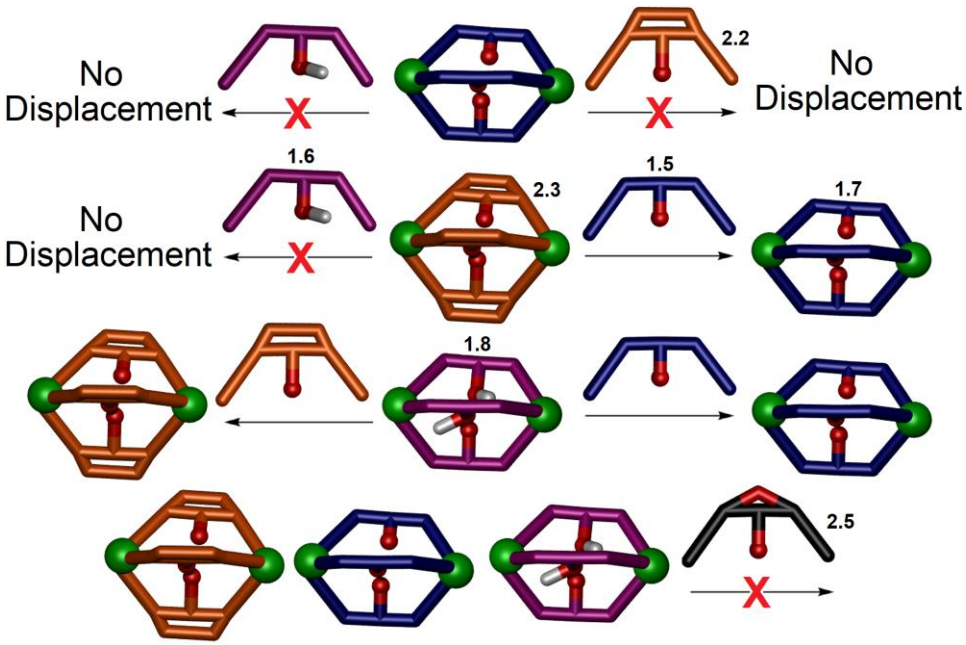

Figure 2.4. Summarized results of displacement experiments showing ligand **1.5** and corresponding cage **1.7** (blue), **1.6** and corresponding cage **1.8** (pink), ligand **2.2** and corresponding cage **2.3** (orange) and ligand **2.5** (black).

The displacement experiments were performed at elevated temperature with complete conversion observed after 8 h, but this does not provide many insights into the mechanism. Ligand displacement could occur via several pathways: dissociation of the iminopyridine coordinator from the metal centers, hydrolysis of the imine, or a transimination process. To determine how the reaction proceeds, the displacement was performed using elevated temperature NMR analysis shown in Figure 2.5.

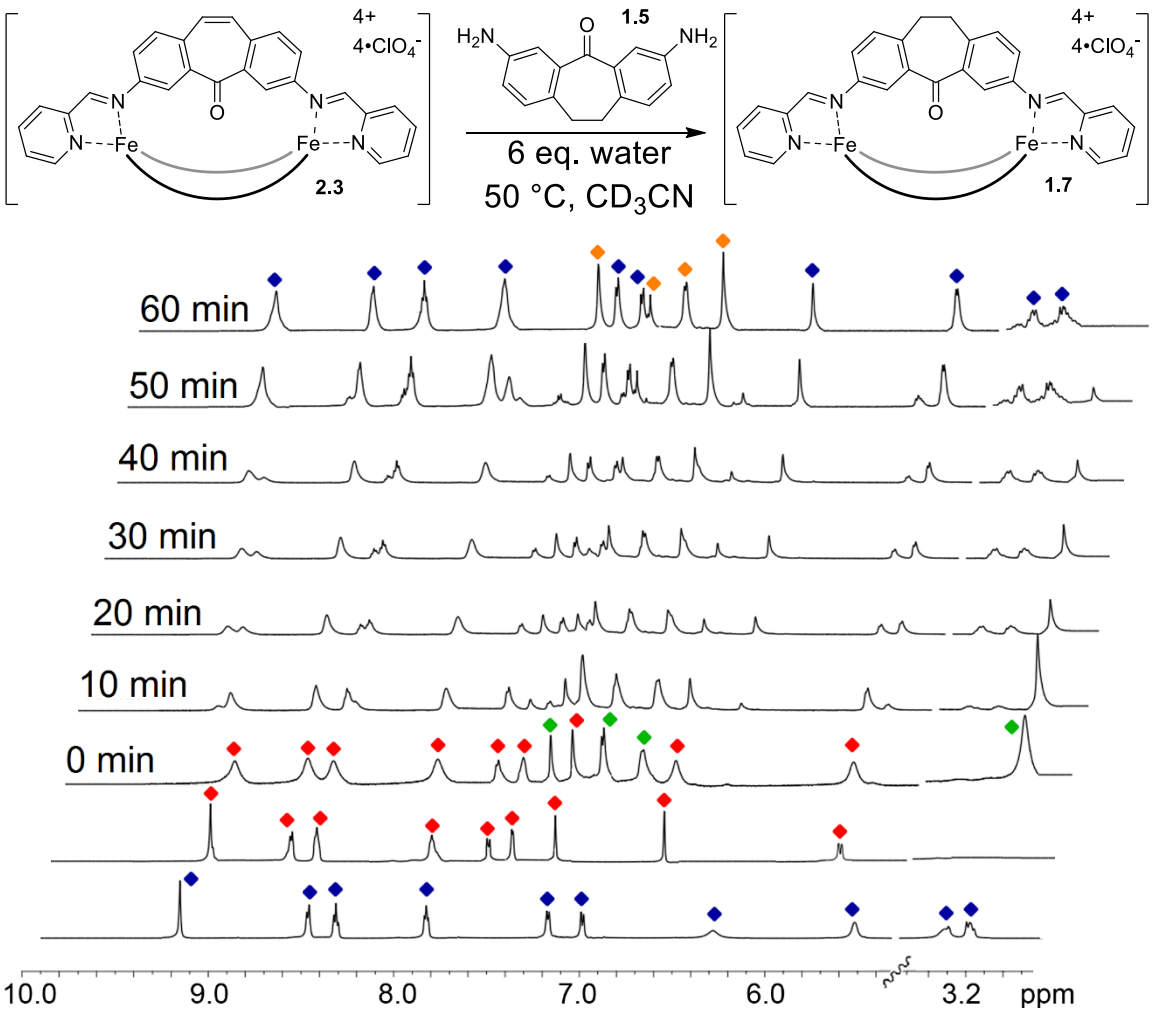

Figure 2.5. ^{1}H NMR spectra of the displacement reaction between cage **2.3** and dianiline **1.5** in the presence of 6 molar equivalents H_2O (CD_3CN, 600 MHz, 343 K). blue = cage **1.7**; red = cage **2.3**; green = dianiline **1.5**; orange = dianiline **2.2**.

Analysis of the NMR spectrum over time clearly shows the gradual loss of peaks corresponding to cage **2.3**, which are replaced with **1.7** peaks. Interestingly, no peaks for heterocomplexes or bis-iminopyridine ligands are observed at any time throughout the reaction. Heterocomplexes can occur when the ligands are complementary to each other,[7,8] but are evidently not formed in this case. Also absent from the reaction mixture are peaks for appreciable concentrations of PyCHO, which indicates that the displacement

mechanism likely involves a transimination reaction rather than hydrolysis to reform the aldehyde and subsequent attack by the more favored dianiline. The fact that heterocomplexes are not observed via NMR indicates that they exist transiently, at concentrations too low to be observed by NMR and are likely far less stable than the homocomplexes.

2.4 Competitive Cage Assembly from Mixtures of Suberone Ligand Cores

While the displacement of a dianiline core from a preformed cage does establish a hierarchy of cage favorability, no heterocomplexes were observed during the reaction. This could be due to the fact that the assemblies are pre-organized in the most stable mesocate structures. An alternative method for testing the fidelity of the sorting is to competitively form one cage over another from a mixture of dianiline cores. This experiment should be slower ad there is an entropic penalty to be paid upon supramolecular self-assembly. To test the selectivity behavior of the assembly process, and possibly observe heterocomplexes, pairs of ligands (1 equivalent each) were combined with two equivalents PyCHO and 0.67 equivalents $Fe(ClO_4)_2$ in CD_3CN. These concentrations essentially starve the reaction of iron and aldehyde components, allowing the formation of only the most favorable cage to occur. In addition, the experiments were attempted at 23 °C to determine if any reaction intermediates are observable.

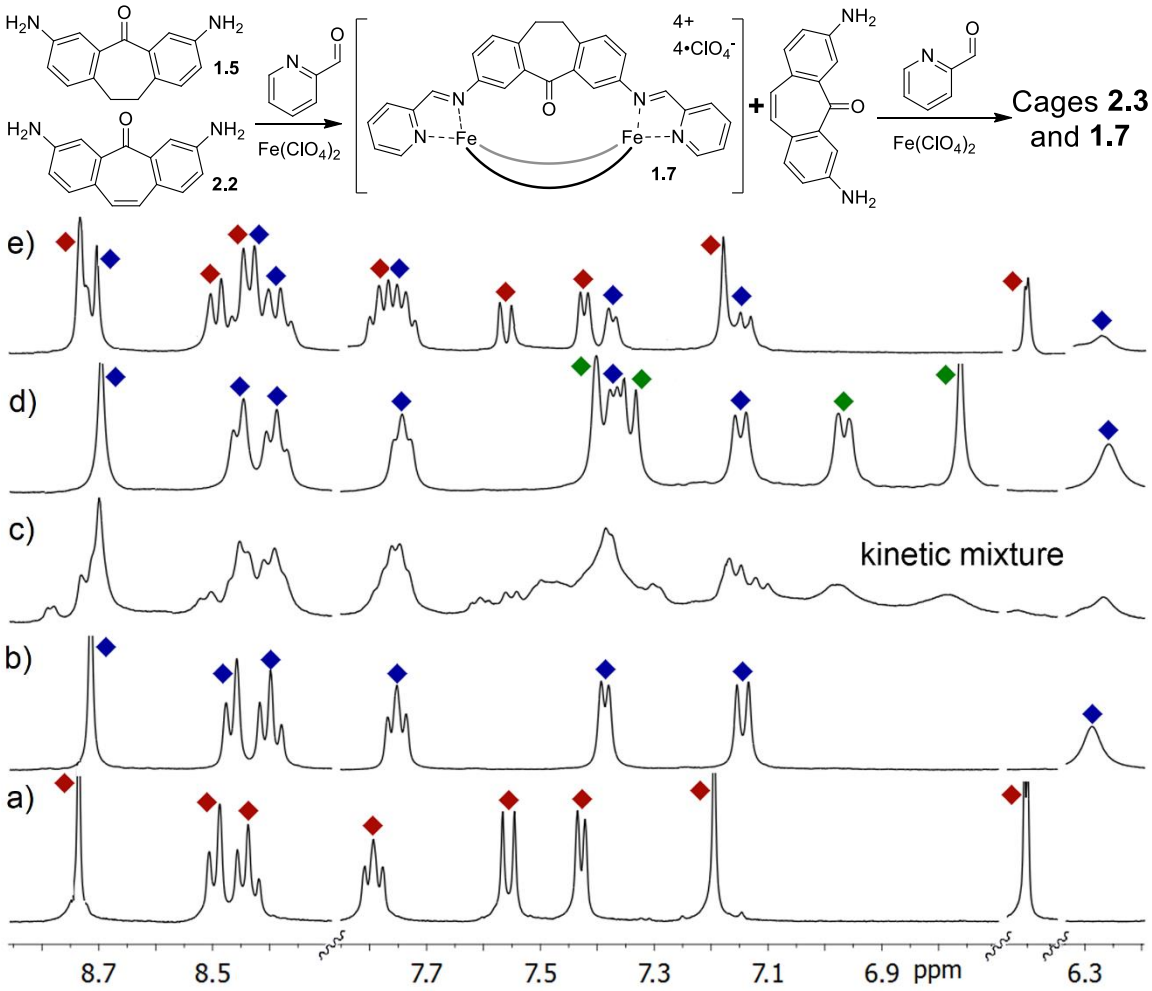

Figure 2.6. Downfield regions of the ^{1}H NMR spectra of a) cage **2.3** (red) b) cage **1.7** (blue) and the products obtained from the reaction mixture of ligands **1.5** and **2.2** (green) c) immediately after addition of 2 mol.-eq. PyCHO and 0.66 mol.-eq. $Fe(ClO_4)_2$ d) after heating (8 h @ 353 K); e) after second addition 0.67 eq. $Fe(ClO_4)_2$ + 2 eq. PyCHO and heating (8h, 353 K); (400 MHz, CD_3CN, 298 K, [**1.5**]= [**2.2**] = 36 mM).

The ^{1}H NMR spectra for the ligand competition between suberone **1.5** and core **2.2** are shown in Figure 2.6. In an attempt to observe reaction intermediates, the ^{1}H NMR was collected immediately after the first addition of $Fe(ClO_4)_2$ and PyCHO (Figure 2.6c). The characteristic purple color of an Fe^{II}-iminopyridine complex was evident at this point and the spectrum shows peaks resembling suberone cage **1.7**, but the peaks are broad and there

are other peaks present that do not correspond to either homocomplex. The reaction does not proceed without heat: the spectrum only sharpens after heating at 80 ºC for 8 h at which point discrete species can be observed (Figure 2.6d). Only two sets of peaks were visible at this first endpoint, those of cage **1.7** and core ligand **2.2**. The competitive assembly process showed clean and complete selectivity for the suberone assembly: not only was the cage **1.7** formed exclusively over cage **2.3**, no heterocomplexes or other stoichiometries of assembly are observed. In addition, no peaks for PyCHO were observed, indicating that the aldehyde component had been consumed, leaving only the homocomplex and free dianiline in solution. When a second addition of PyCHO and $Fe(ClO_4)_2$ was made, enough to form both cages, a complex NMR spectrum including cage **1.7** and broad peaks corresponding to the kinetic mixture formed. After an additional 8 h at 80 ºC, the spectrum sharpened again to give peaks for the two homocomplexes.

This competition experiment was repeated for the other combinations of ligand cores. In the case of the three suberyl ligands **1.5**, **1.6** and **2.2**, the same combination of both ligand-selective formation and narcissistic self-sorting was observed, and the order of favorability was maintained. In the presence of sufficient PyCHO and $Fe(ClO_4)_2$ to form one complex, the only peaks observable by ^{1}H NMR analysis belonged to a single cage complex and free ligand. Even though the coordinating iminopyridine motifs are the same, the coordination geometries are similar, and the size of the internal functional groups does not change significantly, clear selectivity was observed.

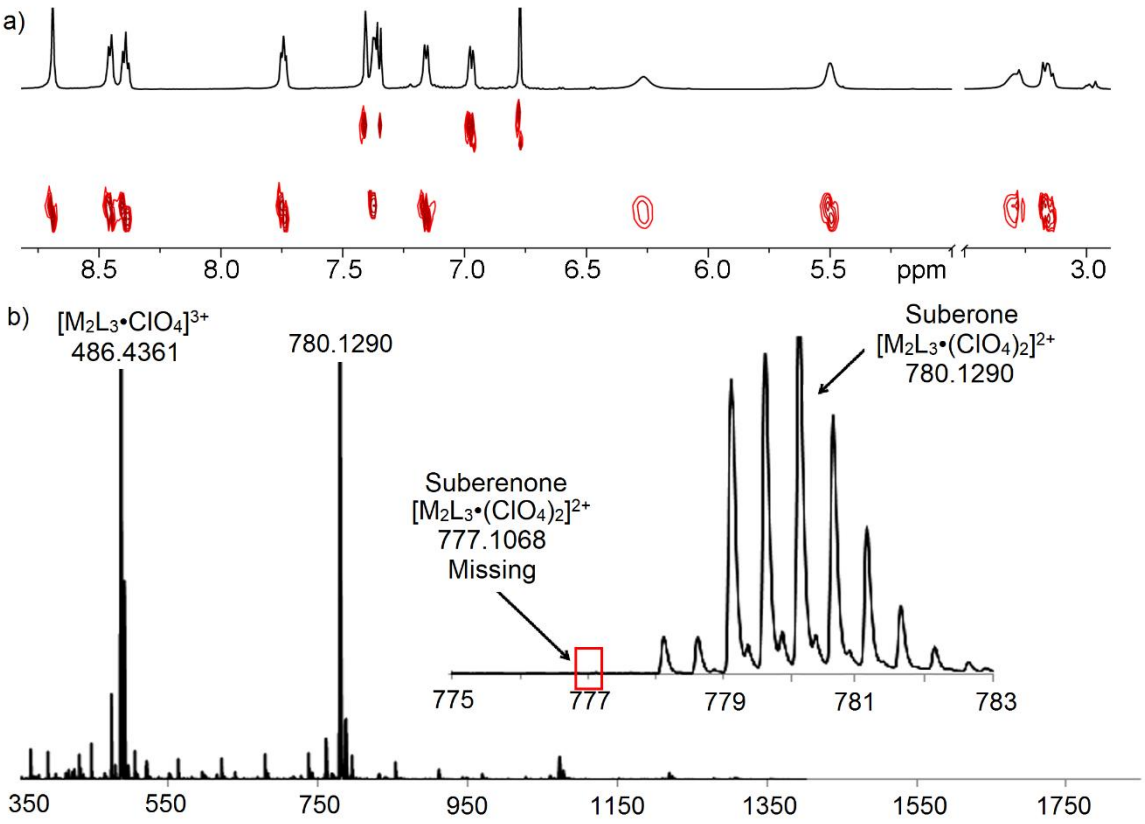

Figure 2.7. a) 2D DOSY[9] spectrum of suberone cage **1.7** and uncomplexed core **2.2** observed after addition of 0.67 eq. $Fe(ClO_4)_2$ + 2 eq. PyCHO to a ligand mixture and 8 h heating @ 353 K (600 MHz, CD_3CN, 298K); b) ESI-MS spectrum, indicating only the presence of cage **1.7** and the absence of any peaks corresponding to cage **2.3**.

The displaced ligands and the discrete complexes were easily distinguished by comparison with NMR spectra of the pure compounds, but to ensure that the peaks corresponded to discrete cage and free dianiline ligand, diffusion analysis (DOSY) NMR was performed on the mixtures after the first addition of $Fe(ClO_4)_2$ and PyCHO and heated equilibration. 2D DOSY spectra were taken of the equilibrated samples: the cages and ligands have a measurable difference in size and thus show a large difference in diffusivity as shown in Figure 2.7a. Cage **1.7** showed a diffusion constant of 8.39 $x10^{-10}$ m^2/s, whereas the uncoordinated dianiline **2.2** diffused at 2.15 $x10^{-9}$ m^2/s. ESI-MS analysis also

corroborated the completeness of the displacement reactions (Figure 2.7b). An ESI-MS spectrum of the first endpoint products was obtained, and showed only M^+ peaks for the cage **1.7** ions with cage **2.3** completely absent. The competitive assembly experiments between the three suberyl scaffolds were well controlled and followed the determined order of favorability. The kinetic mixtures observed prior to heating smoothly gave way to sharp peaks corresponding to discrete favored cage product and the remaining dianiline cores.

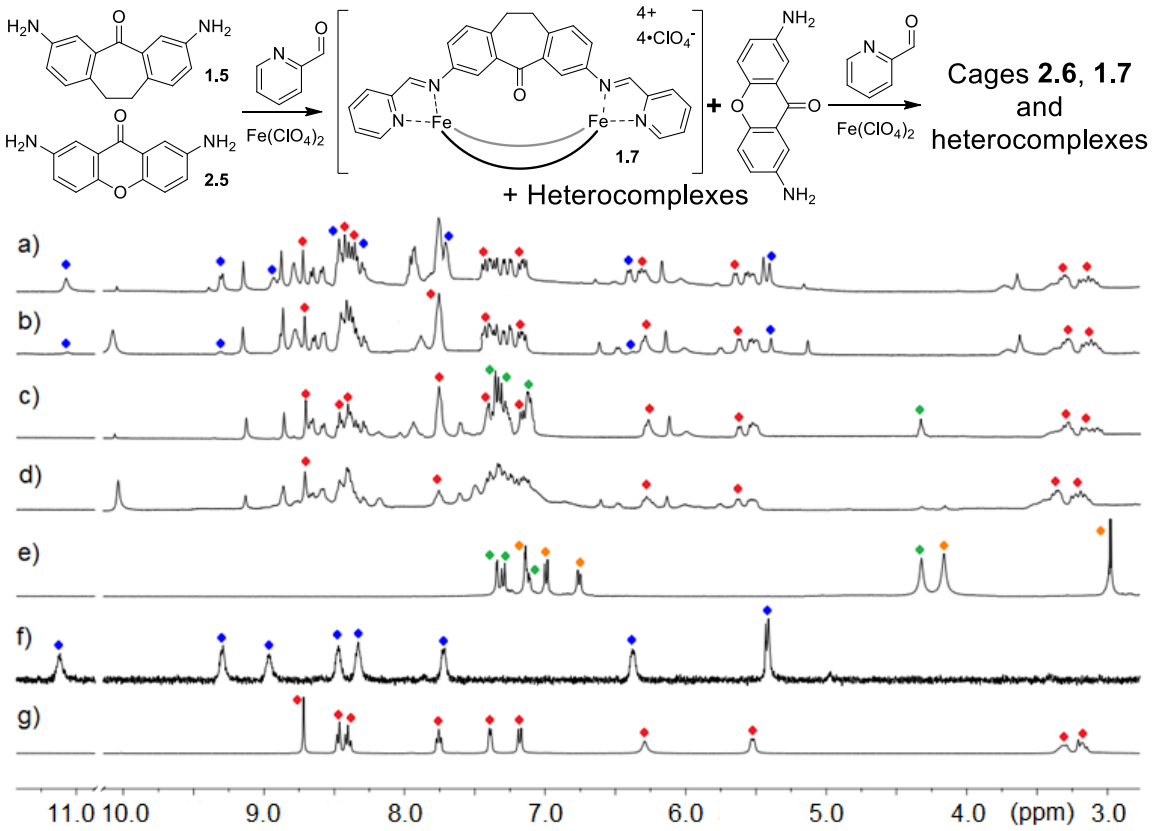

Figure 2.8. ^{1}H NMR spectra (400 MHz, CD_3CN, 298K) of a) products obtained after two additions of PyCHO and iron after final equilibration at 80 °C, b) Products obtained after two additions of PyCHO and iron prior to heating, c) Products obtained after one addition of PyCHO and iron and equilibration for 8 h at 80 °C, d) mixture obtained after first addition of PyCHO and iron prior to heating, e) starting mixture of both ligands: **1.5** (orange) and **2.5** (green), f) Cage **2.6** (blue), g) Cage **1.7** (red).

While the three suberyl cores were well controlled, clean and selective sorting was not observed when competition experiments were performed with core **2.5**. The coordination angle of xanthone is quite rigid, and closer to linear than the suberyl cores, and far less discrimination occurs upon competitive self-assembly. In experiments performed with dianiline **2.5**, complex (yet sharp) NMR spectra were observed after the addition of either stoichiometric or excess PyCHO and $Fe(ClO_4)_2$ to mixtures with either **1.5**, **1.6** or **2.2**. Peaks for heterocomplexes (sharp peaks corresponding to neither homocomplex or ligand) were clearly observable in all cases. It is unclear if these sharp peaks are heterocomplexes, full iminopyridine ligand or incomplete fragments. Also interesting was that peaks corresponding to cage **2.6** homocomplex were persistent in very small amounts for each of the tests.

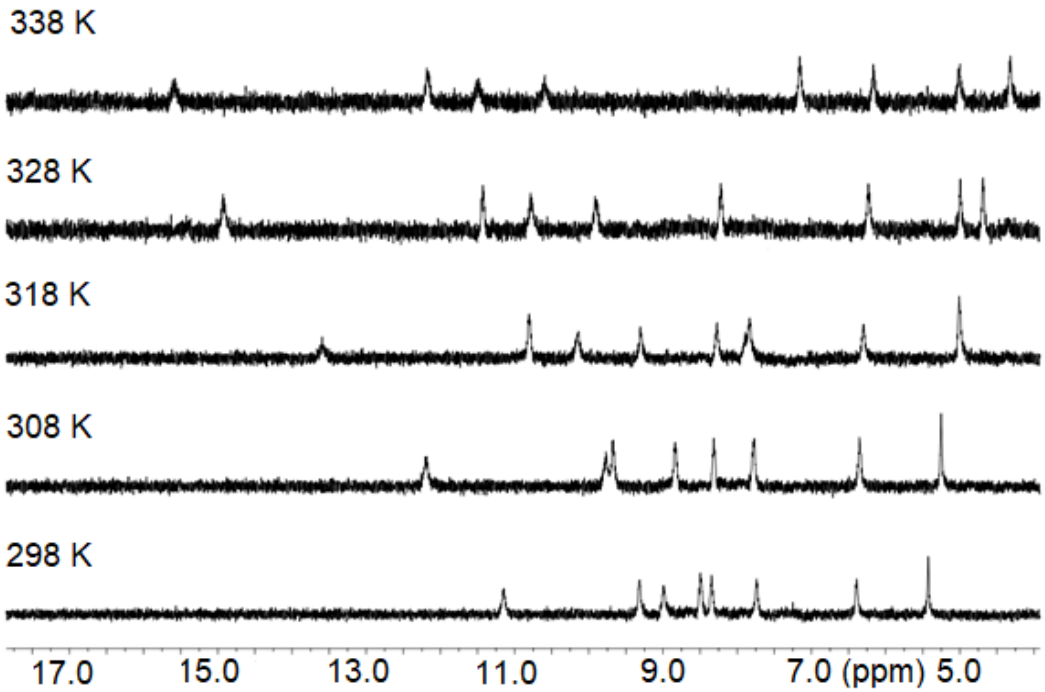

Figure 2.9. ^{1}H NMR spectra of cage **2.6** at different temperatures displaying the change in chemical shifts typical of paramagnetic species.

Complex **2.6** displays unusual magnetic characteristics that may be related to this interesting behavior. Most self-assembled Fe-iminopyridine complexes (including the suberyl cages **1.7**, **1.8** and **2.3**) are fully diamagnetic, characteristically deep purple in color and show little variation in their ^{1}H NMR spectrum upon heating. In contrast, cage **2.6** is weakly paramagnetic and shows changes in chemical shift of up to 5 ppm upon heating to 338 K, suggesting that the assembly leads to a less strongly coordinating environment around each Fe center. The unfavorability of this complex lead to further investigation of its ability to act as a "spring loaded" metastable starting material for kinetic investigations into the transimination mechanism.[10]

2.5 Sequential Cage Formation from a Mixture of 33 Components in One Pot.

The sorting fidelity between the three suberyl cores is strong and clearly follows the order of stability. While binary mixtures of ligands were well tolerated, the next question was what about more complicated reaction mixtures? While the discrimination between two different ligands in a competitive fashion is an exciting result, a far more interesting experiment would be to illustrate selectivity from a complex mixture of multiple ligands. Dianiline **2.5** was not used in this case due to its ability to form unknown species and the intrinsic paramagnetism leading to broadening of the NMR peaks. The three suberyl cores **1.5**, **1.6** and **2.2** were combined in equimolar amounts (1 equivalent each, 14 mM) in CD_3CN, followed by addition of 2 equivalents PyCHO and 0.67 equivalents $Fe(ClO_4)_2$ in CD_3CN (only enough to form one cage from the three ligands present). The progress of the competition experiment was monitored via ^{1}H NMR as shown in Figure 2.10.

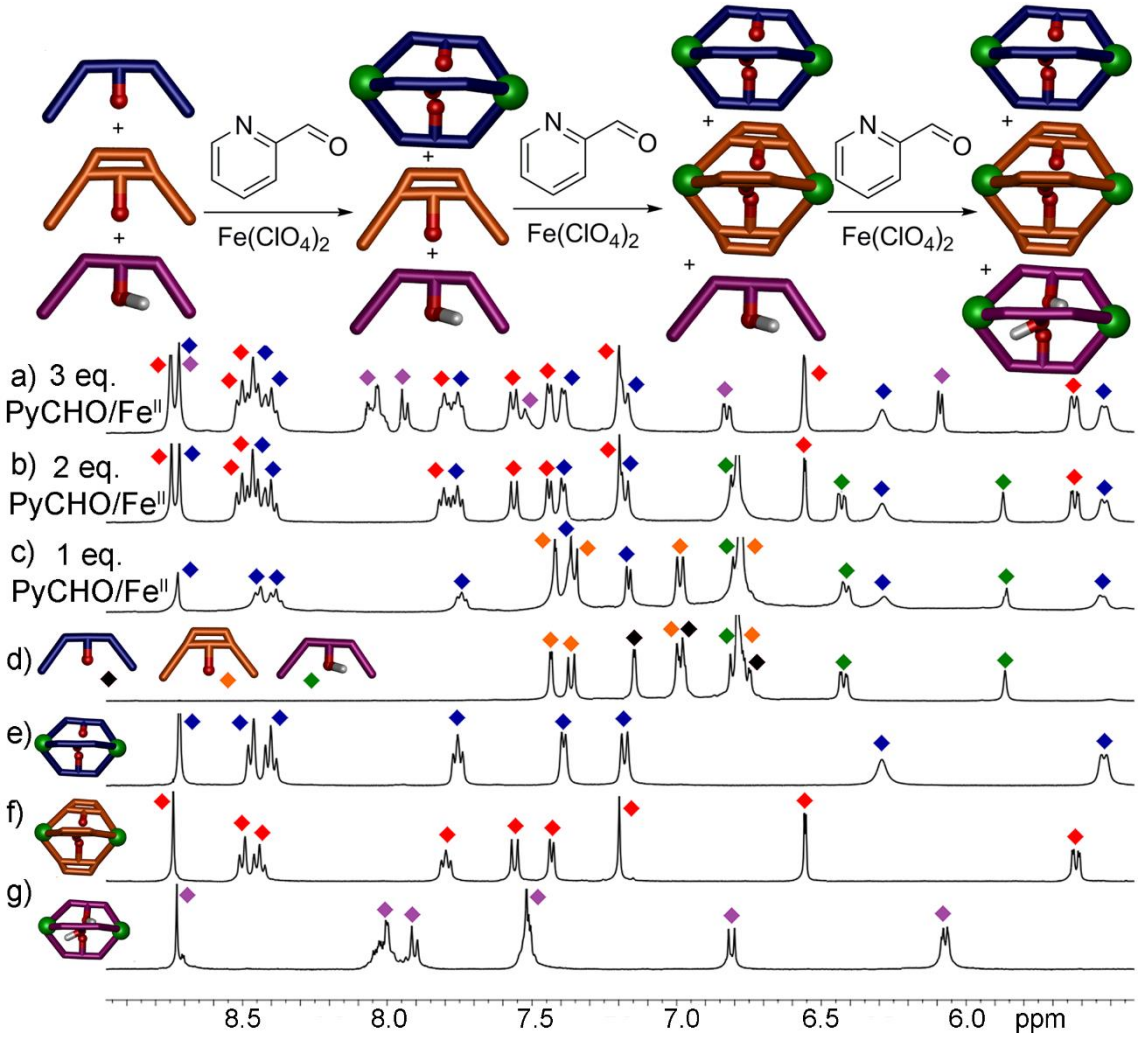

Figure 2.10. ^{1}H NMR spectra obtained after addition of 0.67 eq. $Fe(ClO_4)_2$ + 2 eq. PyCHO to a mixture of ligands: **1.5** (black), **1.6** (green) and **2.2** (orange) and 8 h heating @ 353 K; a) Cages **1.7** + **1.8** + **2.3**; b) Cages **1.7** + **2.3** and ligand **1.6**; c) Cage **1.7** and ligands **1.6** + **2.2;** d) ligands **1.5** + **1.6** + **2.2**. ^{1}H NMR spectra of independently synthesized cages: e) **1.7** (blue); f) **2.3** (red); g) **1.8** (purple) (400 MHz, CD_3CN, 298 K).

As can be seen in Figure 2.10c, suberone cage **1.7** is cleanly and selectively formed from a mixture of the three cores, while dianilines **1.6** and **2.2** remain unreacted in solution. No heterocomplexes are visible at this first endpoint. When a second aliquot of PyCHO/$Fe(ClO_4)_2$ is added (Figure 2.10b), cage **1.7** remains intact and dianiline **2.2** is converted to cage **2.3**, leaving dianiline **1.6** unreacted. Upon addition of a third equivalent

of PyCHO/$Fe(ClO_4)_2$ complete assembly is conferred upon the system, and all three assemblies are cleanly formed. Only the homocomplexes **1.7**, **2.3** and **1.8**, are formed with no trace of heterocomplexes or aggregates in the solution.

Each of the three dianiline ligands forms its corresponding homocomplex even though they all contain identical iminopyridine coordinating motifs, and display coordination geometries that vary minimally. This behavior is impressive, as the assembly process has a range of possible products including polymeric aggregates or assemblies of variable stoichiometry (e.g. M_4L_6 complexes). In addition to this, there remains the possibility of metal-based isomers, which can lead to multiple M_2L_3 species such as the mesocate or helicate structures previously discussed. Despite these possibilities, subtle modifications to the rigidity of the dianiline cores is sufficient to confer high fidelity, selective sorting. Each individual assembly is formed from 11 components (three dianiline cores, six PyCHO groups and two metal atoms must come into close proximity) from a complex mixture of three nearly identical dianilines in solution, and yet this complex system is driven to a single isomer of the favored homocomplex.

2.6 Ligand Deformation and Computational Studies

The order of cage favorability was clearly defined via ligand displacement tests: cage **1.7** is the most favorable, followed by cage **2.3** and **1.8**. Complex **2.6** can be formed and isolated, but the structure is substantially less stable than the others and displays paramagnetic properties likely due to poor coordination geometry at the metal centers. In addition, heterocomplexes from ligands **1.5**, **1.6**, and **2.2** were not observed, with the only

exception of mixing experiments utilizing dianiline **2.5**. The unanswered question is: why is this the order of favorability? No trend exists concerning ligand rigidity; if flexibility was the driving force, suberol cage **1.8** should be most favorable, with the more rigid suberenone and xanthone complexes being least favored (or vice versa). Electron donating or withdrawing nature of the aniline also appears to play no part in the favorability of the assemblies. In addition, **1.8** displays hydrogen bonding between the alcohol groups on the ligand[11] and should exhibit a stabilizing effect.

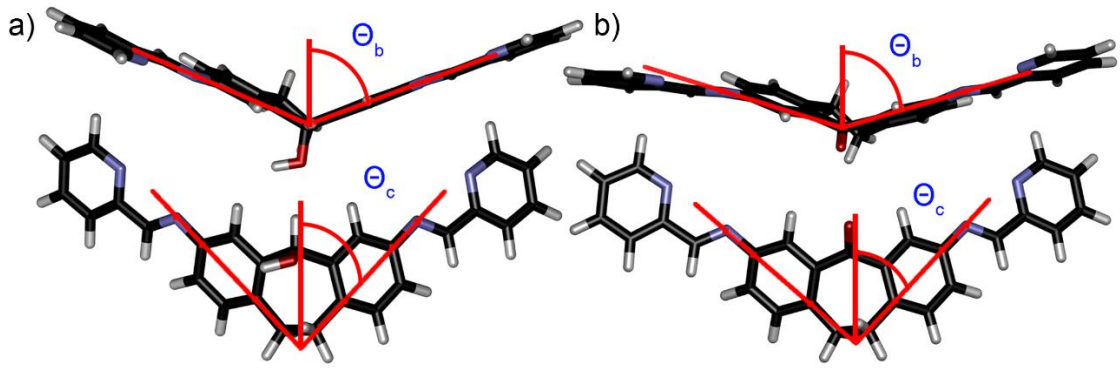

Figure 2.11. a) Coordination angle Θ_c and out of plane bending angle Θ_b for the full suberol iminopyridine ligand ($2\Theta_b$ (**1.6a**) = 130.58º) and b) for the full suberone iminopyridine ligand ($2\Theta_b$ (**1.5a**) = 106.03º).

The only remaining variation between ligands is not necessarily a property of the dianiline core itself, but the degree of deformation the ligands must undergo upon complexation. There are two relevant angles that can be measured to illustrate these changes. The coordination angle ($2\Theta_c$, Figure 2.11) of the four ligands and the corresponding cages is the major variable here. The coordination angle $2\Theta_c$ for the four uncoordinated iminopyridine ligands and the corresponding assemblies are summarized in Table 2.1. The angles for the self-assembled complexes were determined (from the crystal

structures (**1.7**, **1.8**) or energy minimized (**2.3**, **2.6**) structures. Upon complexation, changes in the coordination angle between 7 and 17 degrees are observed. Ligand **1.5a**, which forms the most favorable assembly, undergoes the least amount of distortion upon complexation, even though the suberenone and xanthone ligands are more rigid. Conversely, the more flexible suberol ligand, which contains three sp^3 centers in the central ring, undergoes the largest amount of distortion upon assembly.

Table 2.1. Values for the coordination angle $2\Theta_c$ for the four iminopyridine ligands and their corresponding complexes.

Iminopyridine Core	**Free Ligand $2\Theta_c$**	**Assembled Complex $2\Theta_c$**	**Change Upon Complexation**
Suberone **1.5a**	93.22 °	99.89 °	6.67 °
Suberol **1.6a**	87.87 °	69.96 °	17.91 °
Suberenone **2.2a**	86.75 °	95.44 °	9.27 °
Xanthone **2.5a**	125.18 °	115.08 °	10.1 °

The out-of-plane bending angle ($2\Theta_b$) also varies and was defined as the angle between the two terminal anilines and the internal carbon of the central ring. $2\Theta_b$ for iminopyridine ligands **1.5a**, **1.6a**, **2.2a** and **2.5a** were 142.81°, 130.58°, 133.20°, and 174.75°, respectively. Upon assembling into the corresponding complexes, the ligands distort out of plane to accommodate the geometry of the M_2L_3 mesocate structures. The values for the out-of-plane bend angles for the iminopyridine ligands and the assembled complexes were measured and summarized in Table 2.2. The change in bend angle sheds some light on why suberol cage **1.8** is less favored than the two other suberyl cores: it undergoes far more ligand distortion upon complexation. Suberenone and xanthone

undergo less distortion, but their rigid nature prevents a high degree of distortion from occurring.

Table 2.2. Values for the out-of-plane bend angle $2\Theta_b$ for the four iminopyridine ligands and their corresponding complexes.

Iminopyridine Core	**Free Ligand $2\Theta_b$**	**Assembled Complex $2\Theta_b$**	**Change Upon Complexation**
Suberone **1.5a**	142.81 °	160.51 °	17.7 °
Suberol **1.6a**	130.58 °	106.03 °	24.55 °
Suberenone **2.2a**	133.2 °	147.02 °	13.82 °
Xanthone **2.5a**	174.75 °	156.66 °	18.09 °

An additional variable that can be measured is the metal-metal distances of the complexes: Fe-Fe distances measured from the crystal structures of **1.7** and **1.8** are 11.65 Å and 9.70 Å, respectively (Figure 2.12). The DFT minimized Fe-Fe distances in **2.3** and **2.6** are 11.59 Å and 11.69 Å, respectively. The variance in these distances agrees with the observed angle changes: dianiline **1.6** is more flexible than the other three cores and quite distinct from the others, whereas there is little difference between the suberone/suberenone and xanthone cages **1.7**, **2.3** and **2.6**. These structural changes upon assembly provide some explanation for why narcissistic self-sorting occurs and heterocomplexes are not observed: the different ligands are variably deformed upon coordination, and mismatches are not tolerated. Even though the changes are small, the assembly process can discriminate between them effectively.

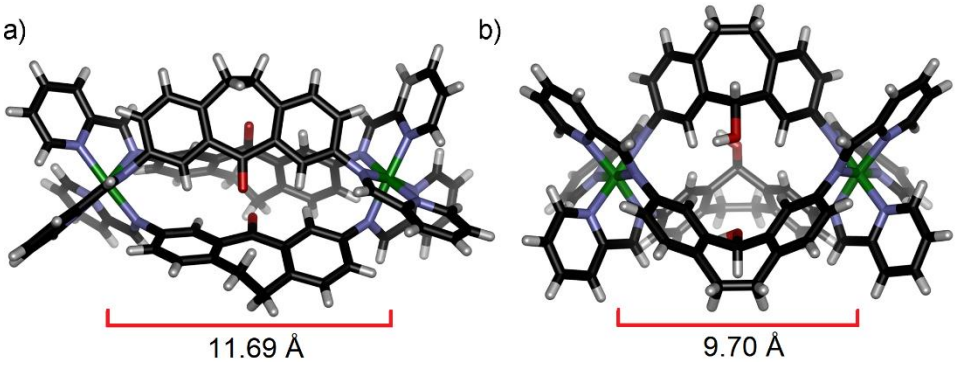

Figure 2.12. X-Ray crystal structures of cages a) **1.7** and b) **1.8** illustrating the different metal-metal distances.

To provide a more complete description of the effects of ligand deformation on assembly, computational analysis of the complexes was performed by the Beran group using the dispersion-corrected B97-D density functional. The self-assembly process between aniline, aldehyde and metal is a complex process. So, to analyze this, the reaction was broken down into several hypothetical steps, and Figure 2.13 plots the energies at each step relative to those for forming the most stable complex **1.7**. The full bis-iminopyridine derivatives of dianiline cores **1.5a**, **1.6a 2.2a** and **2.5a** were used as the starting points. The iminopyridine ligands are then deformed into their corresponding assembly conformations, at a penalty of ~50 kcal/mol per ligand. Ligand **1.6a** deforms ~2 kcal/mol more easily per ligand (~4-6 kcal/mol per cage) than the other three. This is not too surprising, given that suberol core **1.6** is the most flexible with three sp^3 centers in the central ring. Next, the ligands were brought into close proximity to form the cage complex in the absence of the coordinating iron atoms. The close packing of the ligands makes these interactions moderately repulsive. Interestingly, the inter-ligand interactions for **1.6a** proved to have the most repulsion, canceling out its more facile deformation. As such, all four clusters become

nearly degenerate energetically. Finally, the iron atoms are inserted into the clusters to form the final complexes.

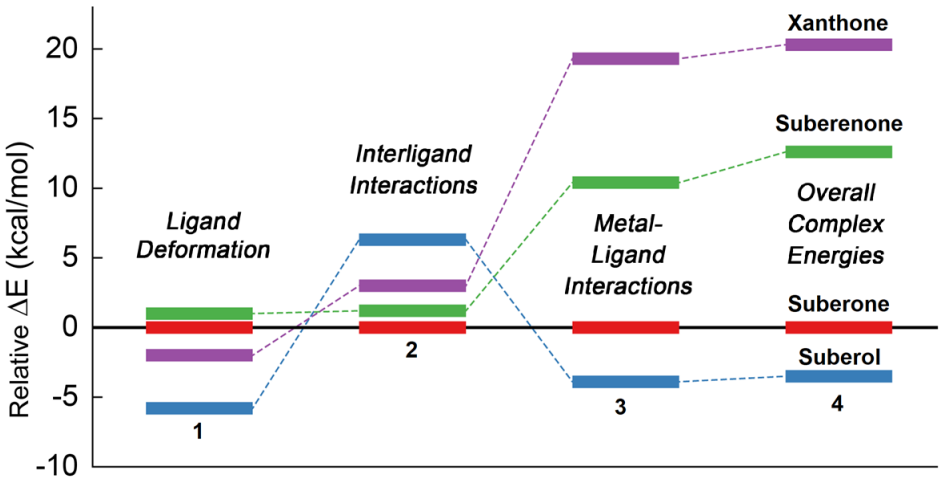

Figure 2.13. Individual contributions to the selectivity of the assembly process for cages **1.8** (blue), **2.3** (green) and **2.6** (purple) relative to cage **1.7** (red), by density functional analysis.

The strength of the iron-ligand coordination varies by ~25 kcal/mol across the four ligands, and this interaction provides the primary energetic differentiation. This makes intuitive sense: the energetic benefit of octahedral coordination around the Fe^{II} centers requires a price to be paid, and that is of ligand deformation to the required orientation. Overall, the calculations predict a relative assembly stability ordering of cage **1.8** > **1.7** > **2.3** > **2.6**. This model predicts the relative selectivity of the three ketone bearing ligands quite well: cage **2.6** is significantly less stable than the three suberyl cores. Cages **1.7**/**2.3** also show a marked difference in overall energy, consistent with the strong selectivity shown by the NMR experiments.

The one large outlier, however is that the DFT electronic energy calculations predict that alcohol ligand **1.6** will form cage **1.8** most readily, and that **1.8** is 3.5 kcal/mol more

stable than cage **1.7**. Considering that the suberol cage is much less favored than the suberone and suberenone cages, this is an unexpected discrepancy. One effect that may account for this is solvation effects upon assembly: suberol ligand **1.6** contains an alcohol group and has the potential to hydrogen bond directly to the acetonitrile solvent. The calculations performed on the iminopyridine ligands and the fully formed complexes do not take solvation effects into account, and an explicit solvent model treatment would be needed to properly differentiate between the ligand-solvent interactions. The complexity of the components in the assembly system and solvent (a mix of H_2O and CH_3CN that changes over time as the assembly proceeds) render a detailed explicit solvent model difficult and impractical.

A simpler DFT calculation was performed that combined a single acetonitrile molecule H-bonded to the hydroxyl group of iminopyridine ligand **1.6a** or coordinated to the carbonyl of iminopyridine **1.5a**. This model displayed no appreciable change in the relative stabilities of the two cages. However, alcohol cage **1.8** was destabilized relative to **1.7** by 0.4 kcal/mol upon assembly, though the simplicity of this approximation does not rule out more complicated solvent effects. From this it can be theorized that the loss of favorable hydrogen bonding between the acetonitrile solvent and the suberol -OH group upon multicomponent self-assembly causes cage **1.8** to have a much greater entropic penalty to pay in addition to the greater amount of ligand distortion that occurs upon complexation.

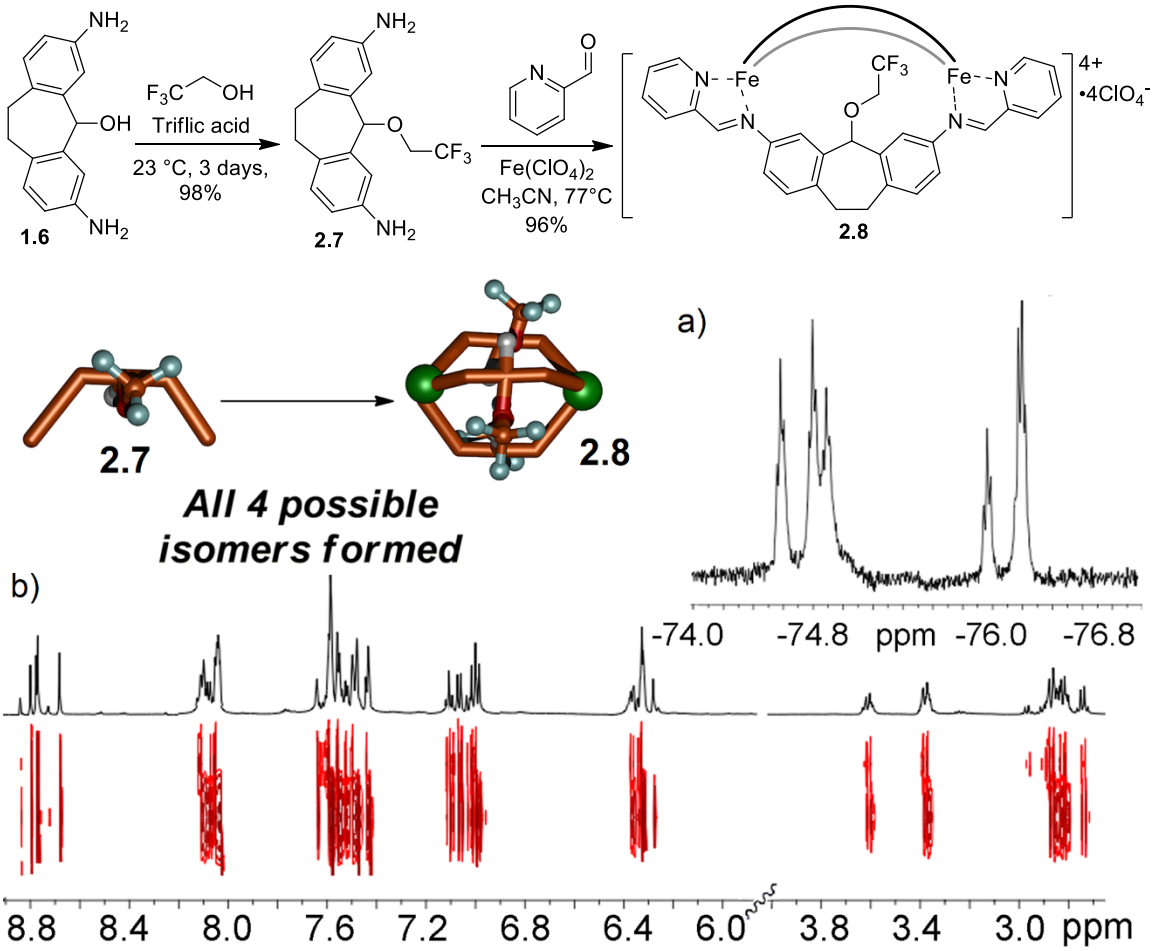

Figure 2.14. Synthesis of trifluoroethylether ligand **2.7** and cage **2.8** and a) ^{19}F NMR and b) ^{1}H NMR and DOSY NMR of trifluoroethylether cage **2.8** (600 MHz, CD_3CN, 298K).

To confirm this hypothesis, a trifluoroethylether derivative was synthesized of the diaminosuberol ligand using trifluoromethanesulfonic acid and 2,2,2-trifluoroethanol. Trifluoroethylether ligand **2.7** maintains the flexible sp^3 carbon center of ligand **1.6** but cannot form hydrogen bonds with the solvent. When assembled with PyCHO and $Fe(ClO_4)_2$ in acetonitrile, the trifluoroethylether ligand forms the discrete M_2L_3 structure **2.8**, however the ^{1}H NMR spectrum is complicated and contains far more peaks than would be expected. This arises from isomers due to the flexible nature of the trifluoroethylether

group, which can be directed towards the interior or exterior of the cage.[2] The ^{19}F NMR spectrum shows at least 5 triplet peaks, corresponding to the different combinations of three ligands directed in or out. Diffusion NMR shows that all of the peaks belong to a single complex and the diffusion coefficient is similar to that of other M_2L_3 complexes.

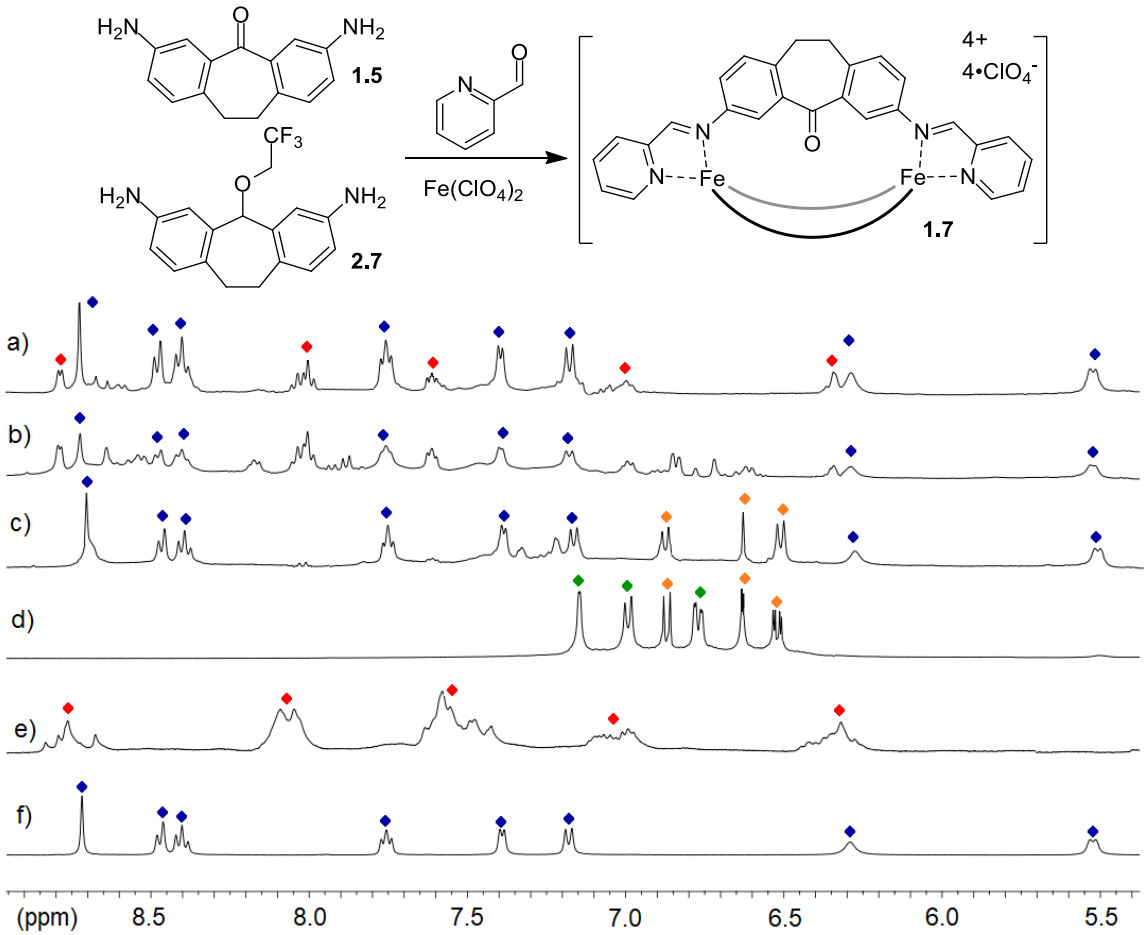

Figure 2.15. ^1H NMR spectra (CD_3CN, 400 MHz, 298K) of a) reaction mixture after two additions of PyCHO and $Fe(ClO_4)_2$ and 8 h heat at 80 °C, b) reaction mixture after second addition of 2-formylpyridine and iron prior to heating, c) reaction mixture after first addition of PyCHO and $Fe(ClO_4)_2$ after 8 h at 80 °C, d) initial dianiline mixture (**1.5** = green and **2.7** = orange), e) cage **2.8** (red), f) **1.7** (blue).

When ligand **2.7** was used in ligand competition (Figure 2.15) or displacement experiments with the preformed cages **1.7**, **1.8**, **2.2** and **2.5**, cage **2.8** was found to be more

favorable than both **2.3** and **1.8**, making this complex second in stability after **1.7**. Evidently, removal of the hydrogen bond donor has a favorable effect on the stability of the final assembly, hinting that unfavorable desolvation of the ligand -OH group in **1.6** upon cage formation contributes to the relative instability of the assembly. The complexity of both the experimental and theoretical systems in this case preclude a more accurate analysis of the solvation behavior of this system, but it is evident that solvation plays an important role.

2.7 Conclusion

Here, we have shown that high fidelity narcissistic self-sorting is possible between ligands bearing minute variances in structure. The order of complex favorability is correlated to the amount of deformation a ligand must undergo upon complexation. Small changes in ligand rigidity between species as similar as suberone, suberenone, suberol and suberyl trifluoroethylether scaffolds can be detected by the assembly process, and no heterocomplexes are observed. Here, the coordinating iminopyridine motifs are identical and the only changes to the ligand scaffold are far from the metal coordinating centers. The discrimination between ligand cores is sufficiently strong to allow sequential formation of the individual homocomplexes from a mixture of three dianiline ligands and 33 separate components in a single pot.

2.8 References

1. Johnson, A. M.; Wiley, C. A.; Young, M. C.; Zhang, X.; Lyon, Y.; Julian, R. R.; Hooley, R. J. "Narcissistic Self-Sorting in Self-Assembled Cages of Rare Earth Metals and Rigid Ligands." *Angew. Chem., Int. Ed*. **2015**, *54*, 5641-5645.

2. Young, M. C.; Johnson, A. M.; Hooley, R. J. "Self-Promoted Post-Synthetic Modification of Metal-Ligand M_2L_3 Mesocates." *Chem. Commun*. **2014**, *50*, 1378-1380.

3. Wu, A.; Isaacs, L. "Self-Sorting: The Exception or The Rule." *J. Am. Chem. Soc*. **2003**, *125*, 4831-4835.

4. Mal, P.; Schultz, D.; Beyeh, K.; Rissanen, K.; Nitschke, J. R. "An Unlockable–Relockable Iron Cage by Subcomponent Self-Assembly." *Angew. Chem., Int. Ed*. **2008**, *47*, 8297-8301.

5. Saha, M. L.; Schmittel. M. "Metal–Ligand Exchange in a Cyclic Array: The Stepwise Advancement of Supramolecular Complexity." *Inorg. Chem*. **2016**, *55*, 12366-12375.

6. Preston, D; Barnsley, J. E.; Gordon, K. C.; Crowley, J. D. "Controlled Formation of Heteroleptic $[Pd_2(L_a)_2(L_b)_2]^{4+}$ Cages." *J. Am. Chem. Soc*. **2016**, *138*, 10578-10585.

7. Johnson, A. M.; Hooley, R. J. "Steric Effects Control Self-Sorting in Self-Assembled Clusters." *Inorg. Chem*. **2011**, *50*, 4671-4673.

8. Bloch, W. M.; Abe, Y.; Holstein, J. J.; Wandtke, C. M.; Dittrich B.; Clever, G. H. "Geometric Complementarity in Assembly and Guest Recognition of a Bent Heteroleptic cis-$[Pd_2LA_2LB_2]$ Coordination Cage." *J. Am. Chem. Soc*. **2016**, *138*, 13750-13755.

9. Megyes, T.; Jude, H.; Grósz, T.; Bakó, I.; Radnai, T.; Tárkányi, G.; Pálinkás, G.; Stang, P. J. "X-ray Diffraction and DOSY NMR Characterization of Self-Assembled Supramolecular Metallocyclic Species in Solution." *J. Am. Chem. Soc*. **2005**, *127*, 10731-10738.

10. Bogie, P. M.; Holloway, L. R.; Lyon, Y.; Onishi, N. C.; Beran, G. J. O.; Julian, R. R.; Hooley, R. J. "A Springloaded Metal-Ligand Mesocate Allows Access to Trapped Intermediates of Self-Assembly" *Inorg. Chem*. **2018**, *57*, 4155-4163.

11. Johnson, A. M.; Wiley, C. A.; Young, M. C.; Zhang, X.; Lyon, Y.; Julian, R. R.; Hooley, R. J. “Narcissistic Self-Sorting in Self-Assembled Cages of Rare Earth Metals and Rigid Ligands.” *Angew. Chem., Int. Ed*. **2015**, *54*, 5641-5645.

Chapter 3: Electronic Effects of the Aldehyde Terminus on Assembly Behavior of Fe^{II}-Iminopyridine Complexes

3.1 Introduction

In Chapter 2, we investigated the possibility of controlled narcissistic self-sorting between core ligands displaying only minute differences in structure. Because these differences are so small, the individual contributions to the selectivity were difficult to determine. However, only modifications to the ligand backbone have been studied thus far, and the effects of small changes near the iminopyridine coordinating groups themselves remains unknown. In addition, there are several examples of mechanistic and kinetic analysis of assemblies in the literature[1,2] for Pt/Pd-pyridyl polygons[3,4] and polyhedra,[5] but the kinetics of iminopyridine chelating systems remains unknown. Previously, small electronic variations on the coordinators in Pd-pyridyl M_2L_4 paddlewheel assemblies were found to be ineffective in controlling assembly.[6] Fe-iminopyridine-based assemblies are far more sensitive to structural changes, however, and here we investigate the effect of small coordinator variations on the self-assembly properties of M_2L_3 mesocates.

3.2 Synthesis of New Complexes

For this study, three suberyl dianiline cores were employed: 3,7-diaminodibenzosuberone **1.5**, 3,7-diamindibenzoosuberol **1.6**, and 3,7-diaminosuberenone **2.2**. The mesocate M_2L_3 structures were chosen due to the ease of analysis, and small changes can be tracked during reaction progress. As shown in Chapters 1 and 2, each core can form the corresponding M_2L_3 mesocate **1.7**, **1.8** and **2.3** upon multicomponent self-

assembly with 2-formylpyridine (PyCHO) and $Fe(ClO_4)_2$ in CH_3CN. To determine what changes in the assembly process arise from small electronic modifications of the coordinating groups, we introduced two new formylpyridines to the system. The highly similar aldehydes (Figure 3.1) display only small electronic differences and should be useful in determining what effects arise from these differences.

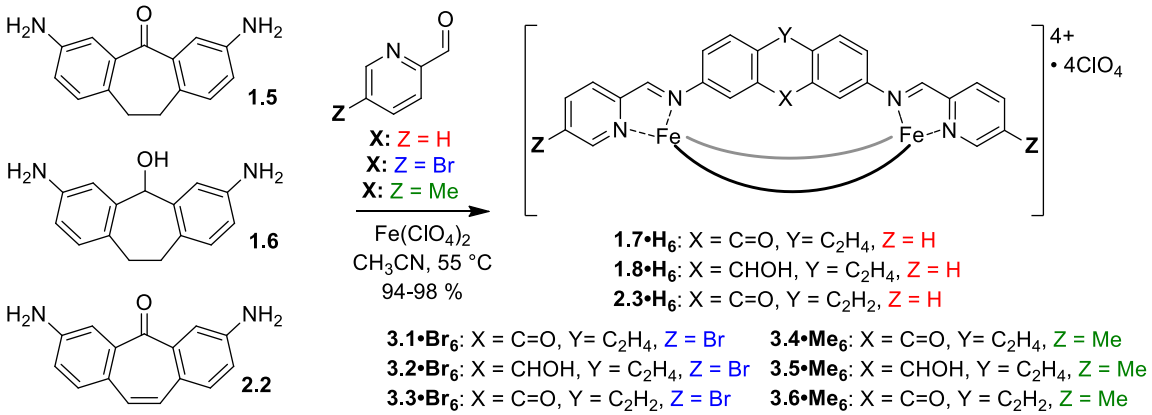

Figure 3.1. Synthesis of the nine possible mesocate assemblies from three diamine cores and three formylpyridine derivatives.

The aldehydes display no measurable steric variations around the metal center: substitution is located at the 5 position of the pyridyl ring, which should preclude any steric clashes close to the coordinating metal centers. Energy minimized molecular models of the new complexes (Figure 3.2) corroborates that no steric interactions occur between the substituents on the pyridyl groups upon self-assembly. 5-Bromo-2-formylpyridine (5-BrPyCHO) and 5-methyl-2-formyl-pyridine (5-MePyCHO) are commercially available, and provide small (and opposite) variations in both the electron-donating capacity of the pyridyl coordinator as well as changing the electrophilic nature of the aldehyde group. The

substituents (-Br, -Me) exhibit Hammett parameters of similar magnitude yet opposite sign: σ_{para} (-CH_3) = +0.23, σ_{para} (-Br) = -0.17.[7]

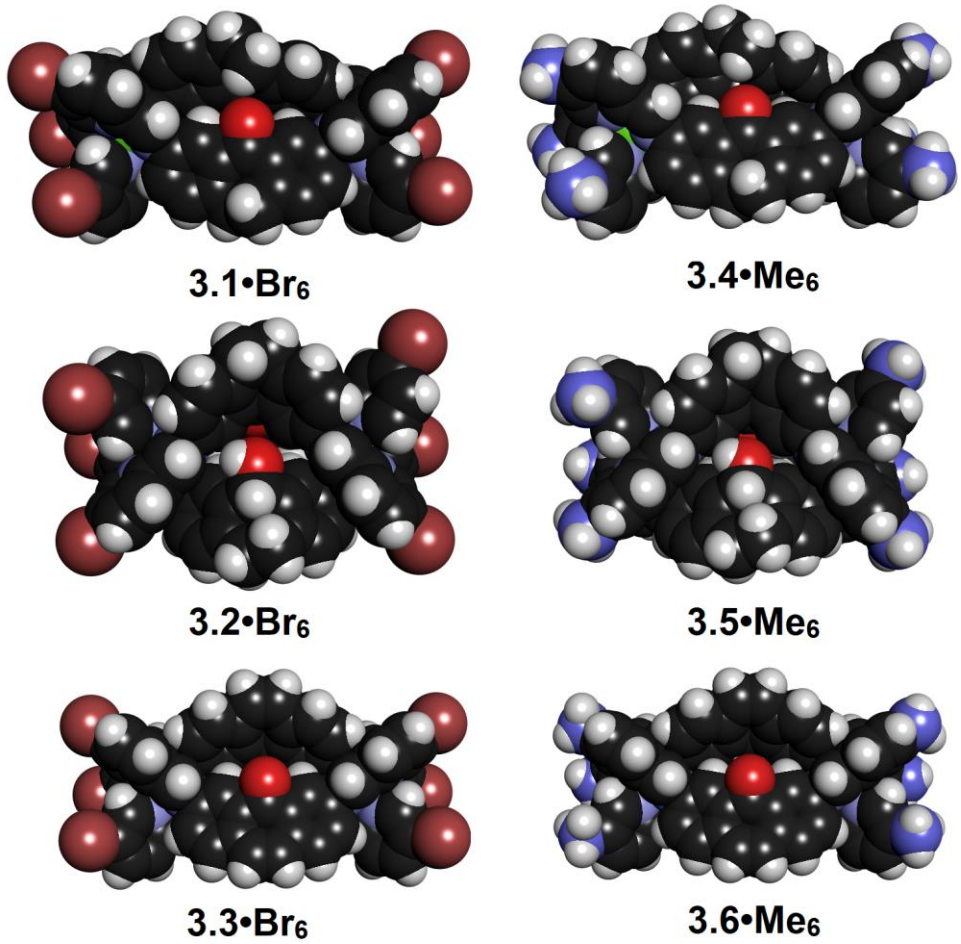

Figure 3.2. Energy minimized models of the six new complexes containing dianiline cores **1.5** (top), **1.6** (middle) and **2.2** (bottom) and the two aldehydes bearing bromo (red) or methyl (blue) substituents at the 5 position of the pyridyl ring.

The new substituted pyridyl assemblies were formed via the standard multicomponent assembly process. Dianiline precursors **1.5**, **1.6**, and **2.2** were mixed with the two new substituted formylpyridines and $Fe(ClO_4)_2$ in acetonitrile to form their respective, highly symmetrical mesocate complexes **3.1•Br6** and **3.4•Me6**, **3.2•Br6** and

3.5•Me$_6$, and **3.3•Br$_6$** and **3.6•Me$_6$**. Each new mesocate complex was highly similar to the previously formed structures **1.7**, **1.8** and **2.3**. The substitution at the 5-position of the pyridyl ring does not add any large steric constraints to the assemblies: the variation between the energy minimized structures of each mesocate complex is affected more by the dianiline core than the pyridyl coordinator (Figure 3.2).

3.3 Rates of Assembly Formation

The variation of the electronics of the aldehyde component had no effect on the stoichiometry or isomeric conformation of assembly, as all systems formed mesocate M_2L_3 complexes with full diastereocontrol at the metal centers. As shown in Chapter 2, mesocates assembled from dianiline ligands **1.5**, **1.6** or **2.2**, $Fe(ClO_4)_2$ and PyCHO showed distinct variations in the overall stability of the structure with the favorability trend determined to be **1.7** > **2.3** > **1.8**. However, the kinetics of assembly and effects of ligand variation on the rates of formation were not studied. The challenge in determining rates of formation for Fe^{II}-iminopyridine complexes is that the self-assembly reaction is a complex multicomponent equilibrium that requires heat to form the most stable thermodynamic product. Multiple ligand-based condensations between aniline and aldehyde occur along with the metal-iminopyridine coordination and assembly steps. Therefore, the accurate determination of individual rate constants is extremely challenging. Luckily, sharp, easily identifiable peaks for the fully assembled cage products as well as unreacted 2-PyCHO can be easily observed and integrated within the ^{1}H NMR spectrum throughout the assembly process. By measuring the percent conversion, unreacted aldehyde and any reaction

intermediates present at a specific time, we can get an idea of the average reaction rates and quantify how modification of ligand or aldehyde affects change the reaction in future work.

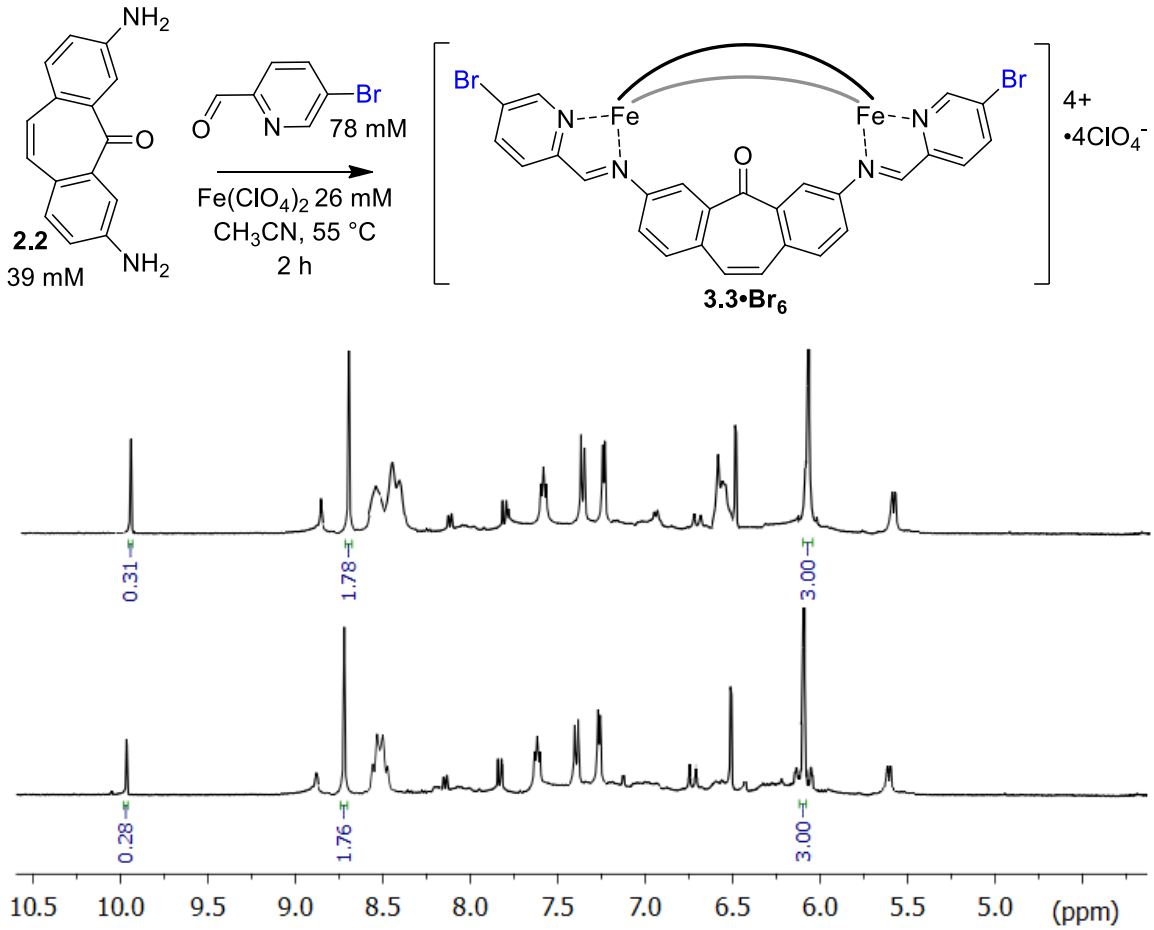

Figure 3.3. ^{1}H NMR spectra (400 MHz, CD_3CN, 298K) of duplicate mesocate formation reactions with integration of unreacted aldehyde starting material, self-assembled cage product and 1,3,5-trimethoxybenzene internal standard.

The formation of the nine mesocates was performed in NMR tubes in CD_3CN using stoichiometric 1,3,5-trimethoxybenzene as an internal standard. The concentrations of all components were kept constant, and the amounts of mesocate product and aldehyde reactant were measured via integration. All reactions were performed in triplicate, and the

errors calculated from the variations in each run. Observing the conversion at 2.0 h reaction time can provide a simple measure of the average reaction rate, with the results shown in Table 3.1 and represented visually in Figure 3.4. These numbers provide a baseline for complex formation and illustrate how ligand favorability and electron-withdrawing or donating groups on the aldehyde termini can affect the average rate of formation.

Table 3.1. Effects of varying aldehyde terminus on rate of mesocate formation.

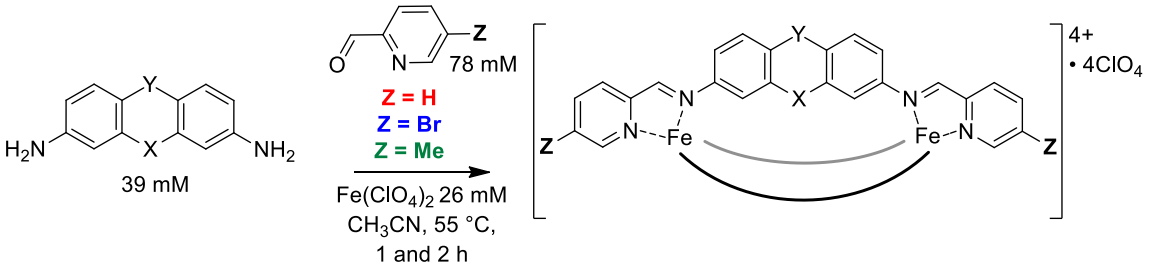

Mesocate Product	Mesocate Yield @ 1.0 h (%)	Mesocate Yield @ 2.0 h (%)	Unreacted PyCHO, @ 2.0 h (%)	Intermediates @ 2.0 h (%)	Time to full completion (approx., h)
1.7•H$_6$	38	65	29	6	3
1.8•H$_6$	25	41	40	19	5
2.3•H$_6$	30	62	32.5	5.5	3
3.1•Br$_6$	55	92	3.5	4.5	2.5
3.2•Br$_6$	32	67	15.5	17.5	3
3.3•Br$_6$	46	89	6.5	4.5	2.5
3.4•Me$_6$	23	43	15.5	41	5
3.5•Me$_6$	Not quantifiable	22	27.5	50.5	9
3.6•Me$_6$	18	37	20	43.5	5.5

As can be seen in Table 3.1 and Figure 3.4, the average rate of formation is far more dependent on the electronic nature of the aldehyde component than on the core ligands. While the reactivity of the three dianilines follows the order of final product stability, there

are only small differences in rates between ligands (e.g. after 2.0 h at 55 °C, **1.7•H$_6$** is formed in 65 % yield, whereas **2.3•H$_6$** is formed in 62 % yield). Use of the more electron-poor 5-BrPyCHO (blue in Figure 3.4) increased the rate of mesocate formation, whereas use of the more electron-rich 5-MePyCHO derivative (green in Figure 3.4) slowed the rate for formation. This is likely a kinetic effect, whereby the electron-poor nature of the Br-PyCHO increases the electrophilicity of the aldehyde and facilitates a faster condensation reaction.

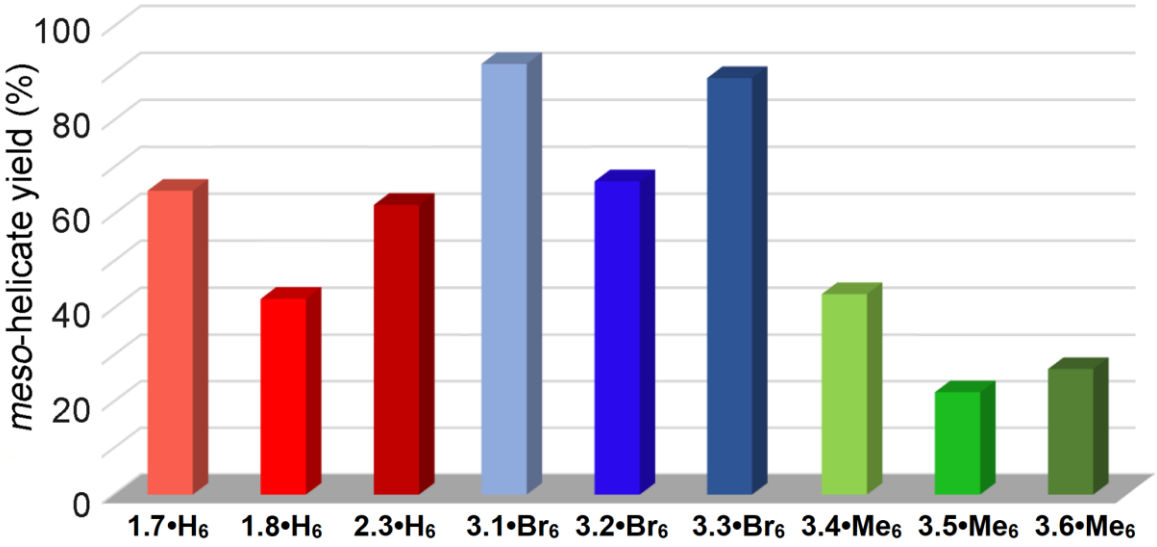

Figure 3.4. Measured percent conversion values after heating each ligand core with 2 mol.-eq. of aldehyde component and 0.66 mol.-eq. $Fe(ClO_4)_2$ in acetonitrile at 55 °C for 2 h.

After 2 h reaction time, the assembly is incomplete and peaks for the aldehyde are clearly observable in the ^{1}H NMR spectra, but the sum of aldehyde and product peaks does not equal 100 % (with respect to the standard). Table 3.1 shows this discrepancy in the sum as the percent of "intermediates" present after 2.0 h reaction. Previously, intermediates were observed during competition reactions as transient and existing in low concentrations.

Presumably, many different intermediate structures can be present in small amounts, ranging from polymeric aggregates to partial assembly structures such as incompletely formed M_2L_2 or ML_3 fragments. While in some cases, discrete ML_3 fragments can be assigned,[8] most metastable intermediates of this type have been shown to display broad, undefined ^{1}H NMR spectra.[9] The sluggish assembly formation experiments involving 5-MePyCHO contain a greater proportion of intermediates, as might be expected: initial imine formation and consumption of the aldehyde component is relatively rapid, while the full equilibration to the discrete mesocate product is slower. To investigate this, we repeated the constant time experiments, but observed the percent conversion amounts at 1.0 h with the values shown in Table 3.1. The shorter reaction time reduced the yield of formed mesocate product, as would be expected. The observed yields were approximately half of the values observed at the 2.0 h timepoint. However, a much larger proportion of intermediates were observed after 1.0 h reaction than at 2.0 h, which agrees with the observation that initial imine formation is rapid, followed by a slower equilibration to final mesocate product shown in Figure 3.5.

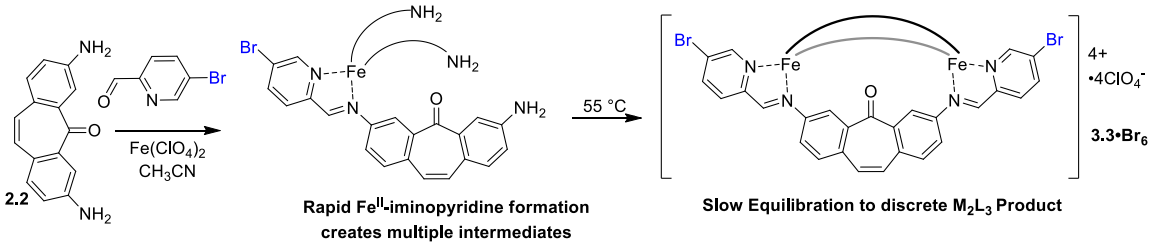

Figure 3.5. The complex multicomponent self-assembly process rapidly consumes aldehyde and aniline components to form reaction intermediates, which then slowly equilibrate to the discrete mesocate products.

It is also worth noting that complexes containing the more electron-rich 5-MePyCHO were slightly more resistant to dianiline displacement via transimination than those containing PyCHO or 5-BrPyCHO termini. The percent conversion to the 5-MePyCHO products was lower at 2 h as well, and this is likely a thermodynamic effect. The electron-rich aldehyde is less electrophilic leading to slower formation and the iminopyridine groups can better chelate to the metal centers. In this case, ligand dissociation and equilibration to the discrete assembly is slower and a higher proportion of intermediates is observed.

3.4 Aldehyde Electronic Effects on Narcissistic Self Sorting of Ligand Cores

With the average rates of formation quantified, other assembly behaviors that may be affected by modified electronics of the aldehyde termini were the next subject of focus. The three dianiline ligands were shown to exhibit impressive high fidelity narcissistic self-sorting in Chapter 2 with a well-defined order of favorability determined between the cores. The drastic variance in the average rates of formation effected by small electronic changes on the pyridyl termini lead to several new questions: does the addition of small electron-donating or withdrawing groups on the aldehyde termini affect self-sorting of the ligand cores? Will synergistic effects be observed between specific ligand and aldehyde pairs (e.g. can a previously disfavored dianiline core paired with the correct modified aldehyde form an assembly that is favored over others)? If homocomplexes remain the observed product of assembly and the narcissistic self-sorting fidelity is undisturbed, will the order of favorability be changed? Can reaction intermediates be observed under certain

circumstances? To shed more light on the complex process of multicomponent self-assembly and narcissistic self-sorting, ligand competition experiments using the three suberyl dianiline cores were carried out. The first set of experiments set out to determine if the favorability of the mesocate homocomplexes was retained.

Table 3.2. Effect of aldehyde terminus electronics on the rate of conversion under competitive self-sorting conditions. Values were determined after 2 h at 55 °C.

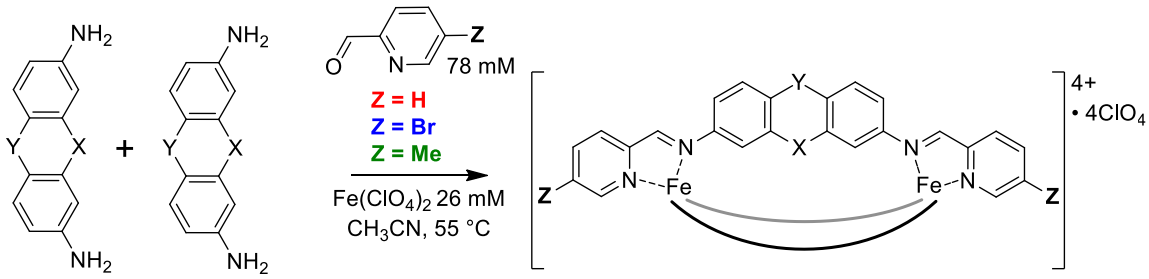

Dianilines	Aldehyde	Major Product	Major Product Yield (%)	Unreacted PyCHO (%)	Minor Product Yield (%)	Inter-mediates (%)
1.5+1.6	**PyCHO**	**1.7•H$_6$**	32	22	5	41
1.5+2.2	**PyCHO**	**1.7•H$_6$**	28	5	6	61
1.5+1.6	**BrPyCHO**	**3.1•Br$_6$**	65	12	0	23
1.5+2.2	**BrPyCHO**	**3.1•Br$_6$**	38	10	4	48
1.5+1.6	**MePyCHO**	**3.1•Me$_6$**	17	18	7	58
1.5+2.2	**MePyCHO**	**3.1•Me$_6$**	25	14	10	51

Using ligand competition experiments outlined in Chapter 2, six self-sorting experiments were performed to determine the average rates of the competitive assembly processes. In these experiments, pairs of ligand cores, aldehyde and $Fe(ClO_4)_2$ were mixed in a 1:1:2:0.66 ratio respectively, in CD_3CN and heated at 55 °C in the presence of 1,3,5-trimethoxybenzene internal standard. The concentrations of all components were kept

constant, and the reaction progress was measured after 2.0 h reaction time at 55 °C. Again, all reactions were performed in triplicate, and the results summarized in Table 3.2. Observing the reaction when partially complete allows for the percent of intermediates to be calculated and determine the effects of ligand competition on the rates of assembly.

Two observations were immediately apparent during the competitive formation experiments. First, in the presence of a second competitive ligand, the percent conversion at 2 h for the sorting experiments was significantly lower than the values observed for the single dianilines. For example, after 2.0 h at 55 °C, 65 % yield of cage **1.7•H$_6$** was formed when only ligand **1.5** is present, but when two ligands are used, only 32 % yield of cage **1.7•H$_6$** is formed under identical conditions. The favorability trend for the three ligand cores is maintained upon complexation with either 5-BrPyCHO or 5-MePyCHO, but the formation of the favored mesocate is drastically slower in the presence of a competing dianiline in each case. As before, the presence of the electron-poor 5-BrPyCHO increased the percent conversion to the favored mesocate product at 2 h compared to PyCHO, while the more electron-rich 5-MePyCHO decreased the measured percent conversion values. This is expected, as the assembly process requires multiple aldehyde condensations, and the self-sorting process is dependent on the aniline mediated transimination of the less favored complex and equilibration to form the final products.

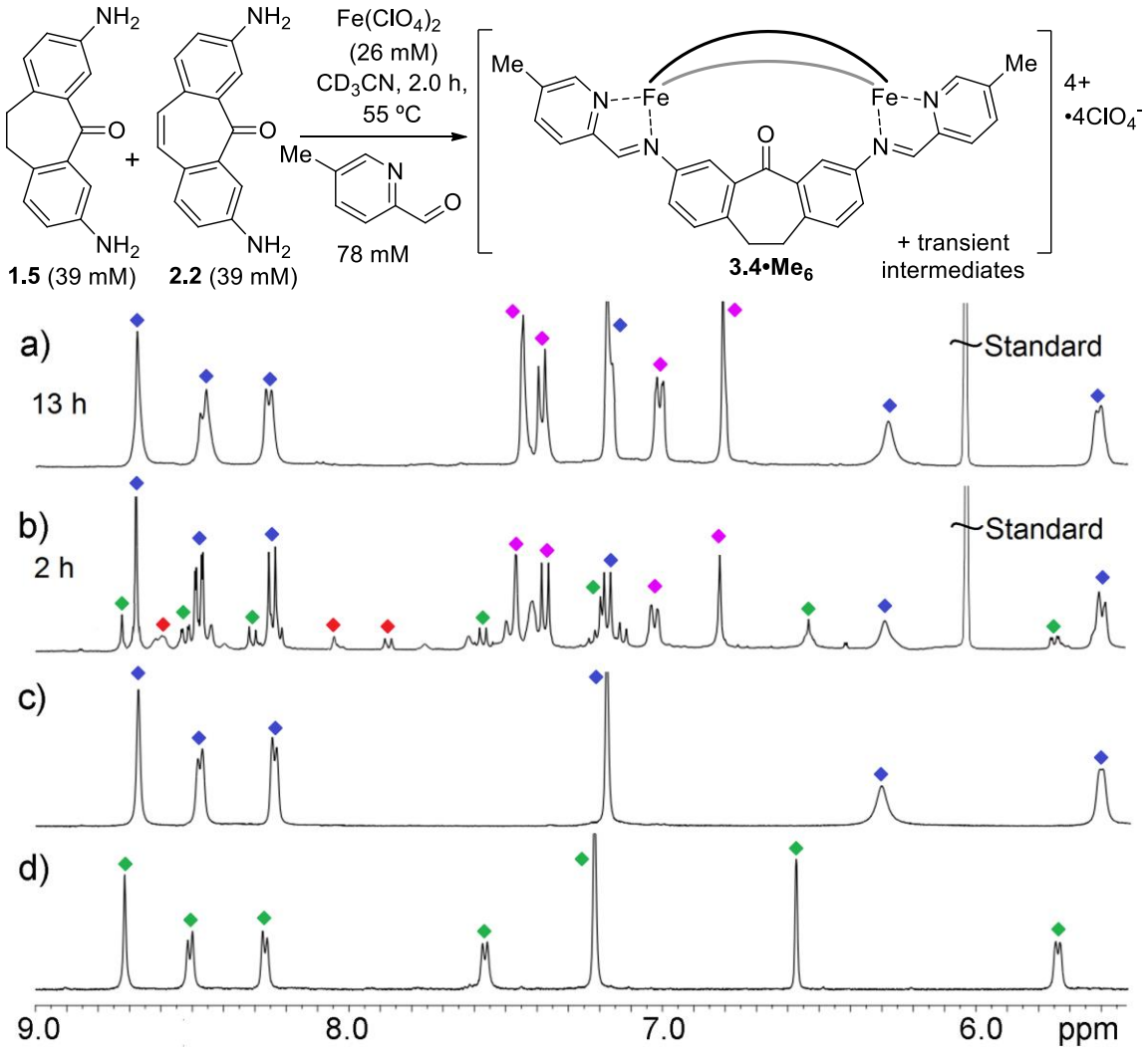

Figure 3.6. ^{1}H NMR spectra of the selective formation of mesocate **3.4•Me$_6$** (blue) in the presence of equimolar amounts of ligands **1.7** and **2.2** a) after full equilibration (13 h) and b) 2 h showing unreacted 5-MePyCHO (red) and core **2.2** (purple), compared with ^{1}H NMR spectra of cages c) **3.4•Me$_6$** (blue) and d) **3.6•Me$_6$** (green). (CD_3CN, 400 MHz, 298 K).

The second observation was that in addition to peaks in the ^{1}H NMR spectrum corresponding to the major product, peaks for the disfavored homocomplex are also present in appreciable amounts. This is an interesting result, as previously, fully formed M_2L_3 complexes were not observed as intermediates in competitive ligand experiments. The only case where disfavored homocomplex products were not observed was for the experiment

involving dianilines **1.**5 and **1.6** with 5-BrPyCHO, shown in Figure 3.7. In this trial, the electrophilic 5-BrPyCHO increases the rate of initial imine formation and the difference in favorability between the two homocomplexes is quite large; suberone ligand **1.5** is the most favored and **1.6** least favored between the three cores. This set of conditions leads to rapid formation of the favored cage with no trace of the disfavored homocomplex in solution.

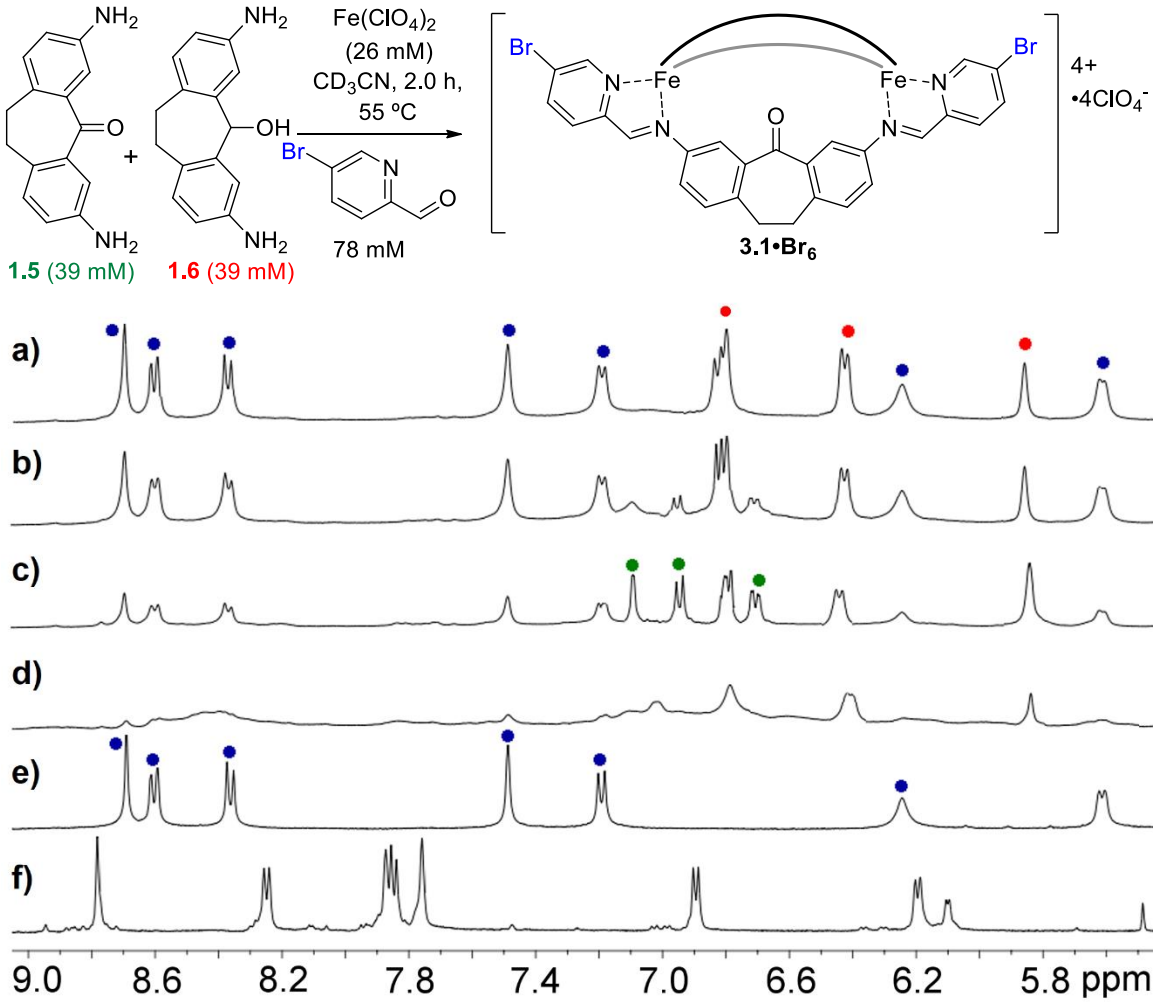

Figure 3.7. ^{1}H NMR spectra of selective formation of suberone mesocate **3.1•Br$_6$** from equimolar amounts of ligands **1.6** (red) and **1.5** (green) after a) 3 h; b) 2 h; c) 1 h; d) 0.5 h; compared to cages **3.1•Br$_6$** (blue) and f) **3.2•Br$_6$** (CD_3CN, 400 MHz, 298 K).

In all other reactions with the remaining combinations of ligand and aldehyde, peaks for the disfavored homocomplex are present throughout the reaction until just prior to completion where only the preferred homocomplex is observed. The complex multicomponent self-assembly process appears to involve all possible species in the reaction, some of which are shown in Figure 3.8. The disfavored mesocates are formed in small amounts as part of the equilibrium mixture, but only transiently, and are converted to the more favored mesocate by the reaction's end. It is not clear from the NMR spectra whether any heterocomplexes are also formed, as the remainder of the peaks in the spectra are broad and difficult to assign. However, no evidence of heterocomplex formation was observed in the ESI-MS spectra.

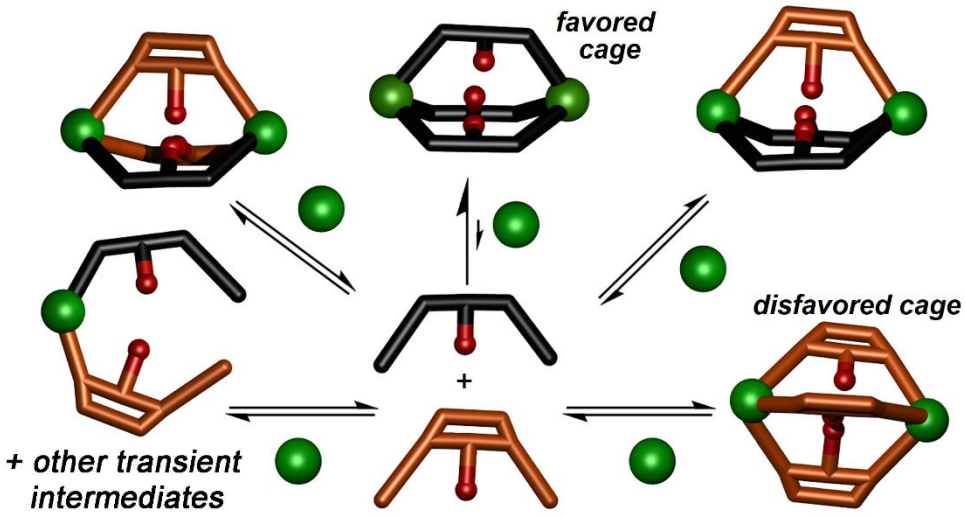

Figure 3.8. Illustration of the possible pathways to final favored product **1.7•H$_6$** after full equilibration of a mixture of ligands **1.5** (black) and **2.2** (orange).

In each case, a significant proportion of intermediates are present and quantified in Table 3.2. It is highly likely that these intermediates consist of small amounts of fully assembled heterocomplexes as well as oligomers, coordination polymers and incompletely

assembled Fe^{II}-iminopyridine fragments (e.g. M_2L_2, ML_3 etc.). This is not surprising, as the presence of transient intermediates and dead-end pathways in this type of complex multicomponent equilibrium assembly have been observed in other systems containing oligo-bipyridyl or iminopyridine units,[10,11,12] but it is interesting to observe them here, especially considering the high degree of narcissistic self-sorting seen in the assembly process after full equilibration.

3.5 Narcissistic Self-Sorting of Aldehyde Termini

Given that the system enables discrimination between ligands regardless of the electronics of the aldehyde used, the next set of trials sought to determine whether the assemblies could select for one specific aldehyde terminus over another. Furthermore, what effect will the various internal ligand cores have on the differentiation between aldehydes? To investigate the propensity for terminus-based selectivity, complex assembly with varying amounts of two different aldehyde derivatives in the reaction mixture was performed.

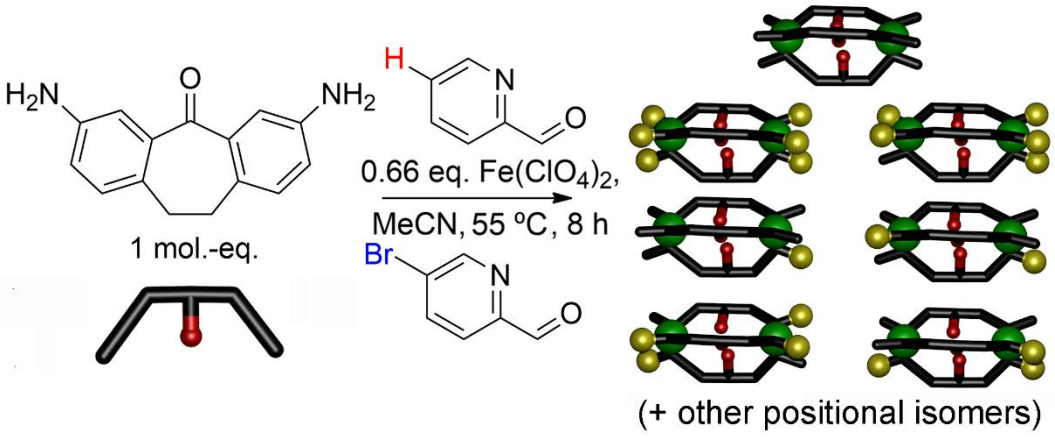

Figure 3.9. Possible products from aldehyde competition experiments showing 7 possible combinations of different aldehyde termini.

There are seven possible products that can arise from the different combinations of aldehyde groups incorporated into an M_2L_3 mesocate, not including other structures such as helicates or larger stoichiometries. These seven combinations arising from the aldehyde selectivity experiments are summarized in Figure 3.9. The figure does not include positional isomers of the **1.7•H$_4$Br$_2$**, **1.7•H$_3$Br$_3$** and **1.7•H$_2$Br$_4$** species. The ^{1}H NMR spectra for two aldehyde sorting experiments are shown in Figure 3.9. One equivalent of core **1.5** (40 mM) and 0.66 eq. $Fe(ClO_4)_2$ were dissolved in CD_3CN in the presence of either one equivalent each of PyCHO and 5-BrPyCHO (1:1, 40 mM each, Figure 3.10b) or two equivalents each of PyCHO and 5-BrPyCHO (1:1, 80 mM each, Figure 3.10a). These two variations correspond to a stoichiometric reaction where all available aldehyde is consumed and a superstoichiometric reaction whereby the system can select the most favorable terminus. These two trials were performed to investigate a) whether aldehyde homocomplexes are formed preferentially over heterocomplexes when all aldehyde must be consumed, and b) if, given the choice and excess aldehyde is present, if the assembly process will selectively incorporate one favored termini over another.

The initial NMR tests combining two different aldehydes gave spectra that were somewhat broad and difficult to analyze. While ^{1}H NMR spectra of the individual mesocates **1.7•H$_6$** and **3.1•Br$_6$**, are symmetrical and sharp, the product NMR spectra observed in the aldehyde competition experiments are significantly broader. There are numerous product possibilities from the multicomponent self-assembly of two aldehydes and one ligand, even when counting M_2L_3 stoichiometry alone. Evidently the magnetic anisotropy from the aromatic rings causes very small changes in the chemical shifts of the

protons nearby, but those shifts are not sufficient enough for obvious discrimination and analysis. What can be determined from the ^{1}H NMR however, is that both aldehydes are incorporated into the assembly in the stoichiometric reaction (Figure 3.10b). It is also clear that in the super stoichiometric reaction (Figure 3.10a), one aldehyde is predominantly incorporated: the peaks corresponding to cage **1.7•H$_6$** are significantly enhanced as compared to the stoichiometric experiment.

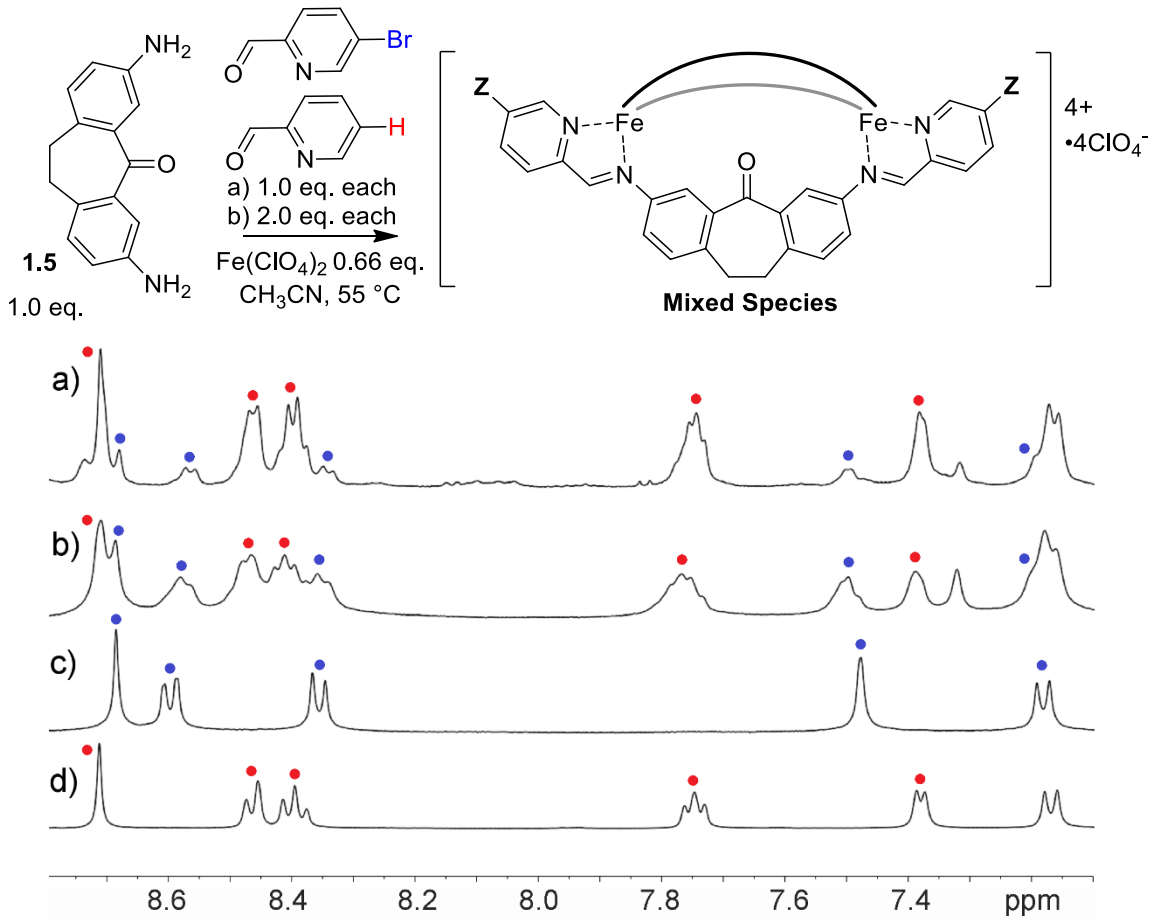

Figure 3.10. Downfield regions of the ^{1}H NMR spectra of products formed from reaction 0.66 eq. $Fe(ClO_4)_2$ and 1.0 eq. core **1.5** with a) 2.0 eq. PyCHO + 2.0 eq. 5-BrPyCHO; b) 1.0 eq. PyCHO + 1.0 eq. 5-BrPyCHO compared to c) **3.1•Br$_6$** (blue) and d) **1.7•H$_6$** (red) (500 MHz, CD_3CN, 298K).

Determining the exact amounts and compositions of the heterocomplexes formed by the incorporation of the two different aldehydes is difficult via ^{1}H NMR but can be simplified using ESI-MS. Figures 3.11 and 3.12 show the M^{4+} region of the ESI-MS gained from ionization of the two aldehyde competition experiments using ligand **1.5**. As can be seen in Figures 3.10 and 3.11, the seven possible combinations (by mass) of M_2L_3 complexes containing varying numbers of PyCHO or 5-BrPyCHO termini can be easily distinguished within the spectrum and the relative abundances can be used to qualitatively determine how much of each species is present in the product mixtures. In the stoichiometric sorting experiments (Figure 3.10) all of the available aldehyde is consumed, and the assembly must incorporate both into the products. A near-statistical mixture of all seven possibilities is observed in this case. Evidently, the small electronic differences in the aldehyde termini are not enough to allow for complete discrimination and homocomplex formation under these conditions.

The ESI data for the stoichiometric aldehyde mixing experiment with ligand **1.5** shows some selectivity between the two aldehydes in that the distribution of the observed products is not a perfect statistical mixture. There is a slight bias for the more electron-rich PyCHO in this case (Figure 3.10). However, when the superstoichiometric reaction outcome is analyzed (Figure 3.11), the self-assembly process can discriminate between the two termini if given the opportunity. Peaks corresponding to the M_2L_3 complex containing 1, 2 or 3 units of 5-BrPyCHO are present, but significantly more of the electron-rich PyCHO is incorporated. The most intense (and therefore populous) peak is that of the M_2L_3

structure containing all PyCHO units and no assemblies are present that incorporate greater than three units of 5-BrPyCHO.

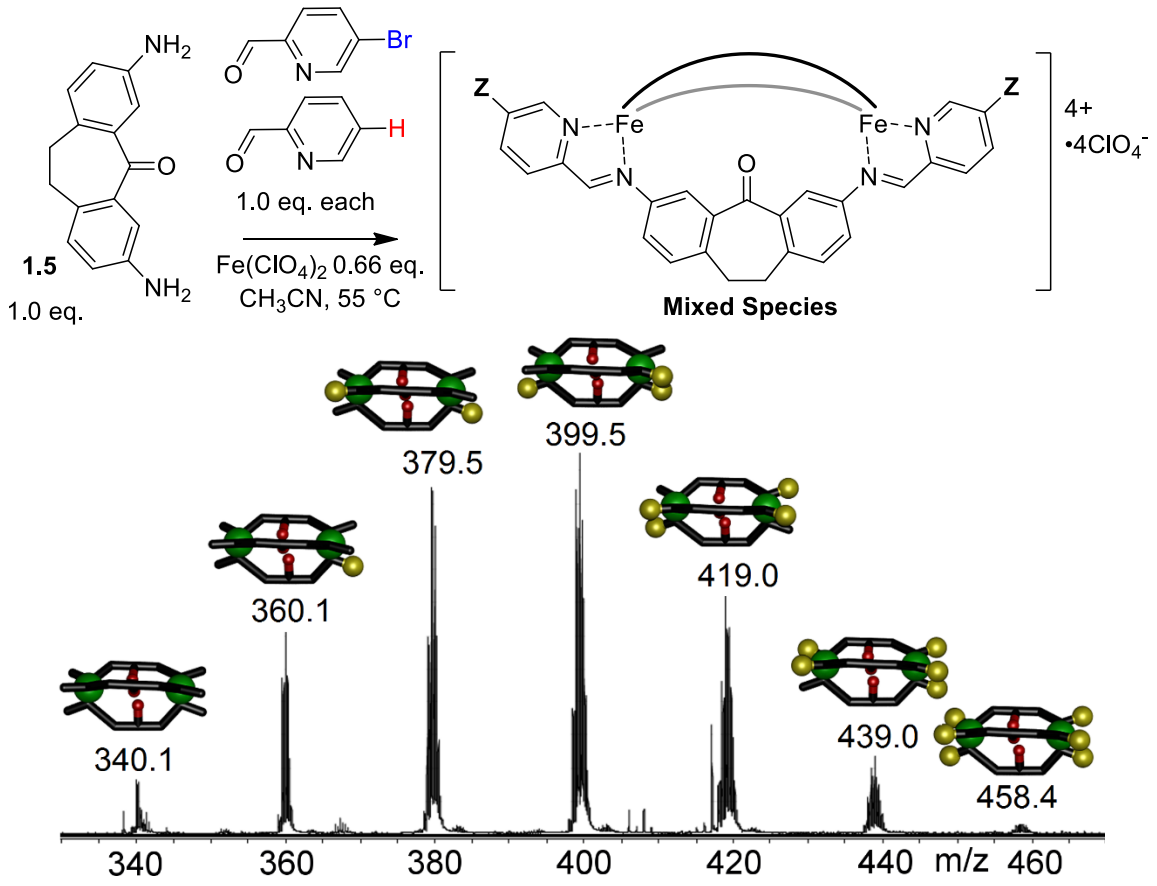

Figure 3.11. ESI Mass Spectra of the products formed from reaction of 0.66 eq. $Fe(ClO_4)_2$ and 1.0 eq. **1.5** with 1.0 eq. PyCHO + 1.0 eq. 5-BrPyCHO (in CH_3CN).

The comparison of the two ESI-MS spectra is illustrative, as it shows that the peak intensity is a somewhat quantitative method of investigating the favorability of incorporating different termini in the assembly. While there is no obvious way to discriminate between positional isomers of the different assemblies (i.e. the different positional variants in **1.7•H$_3$Br$_3$** for example), the non-selective nature of the stoichiometric reaction hints that there is likely no bias for one positional isomer over

another. It is also interesting to note that while the rate of formation of the self-assembly is increased upon the use of electron-poor aldehydes, the thermodynamic stability of the more electron-rich product is greater. The remaining combinations of aldehyde sorting were performed by Calvin Wiley and found that as the ligand cores used became less favorable, the assembly process exhibited a greater bias against the electron-poor termini. These tests, along with aldehyde displacement experiments are described in the publication.[13]

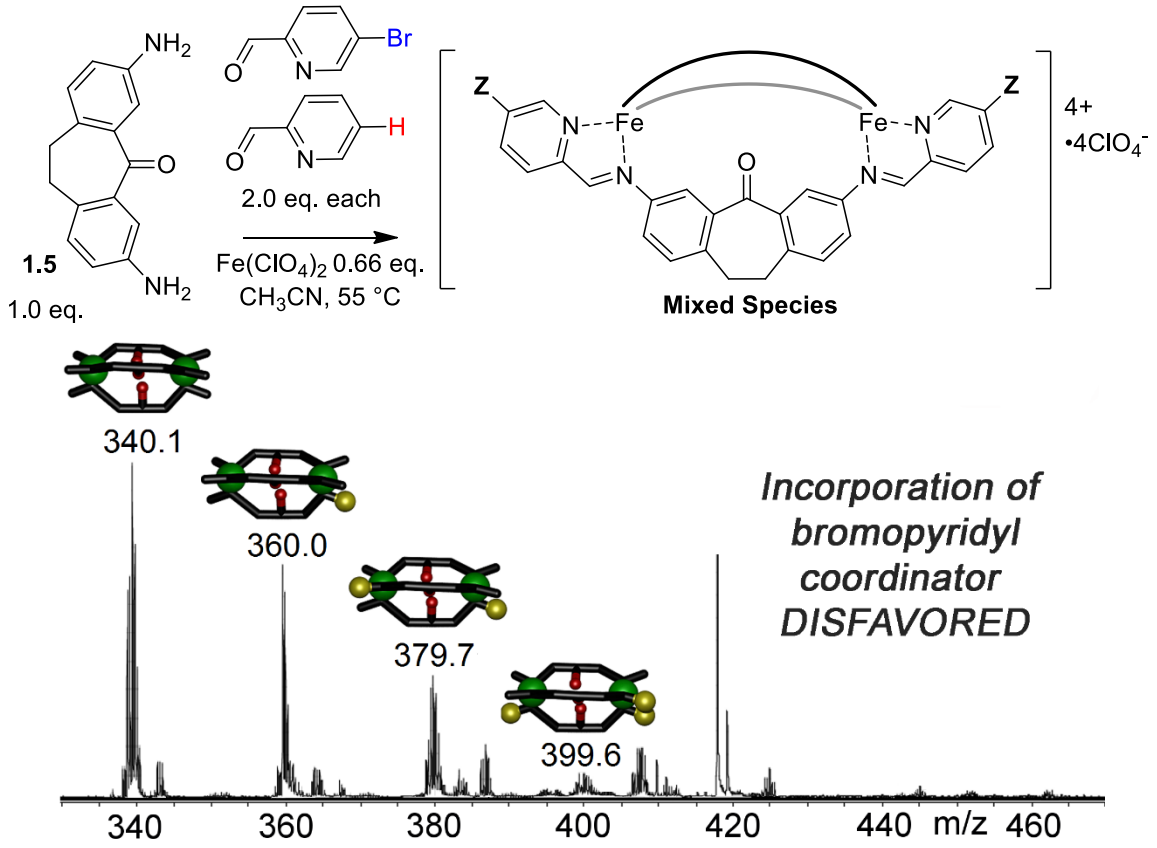

Figure 3.12. ESI Mass Spectra of the products formed from reaction of 0.66 eq. $Fe(ClO_4)_2$ and 1.0 eq. **1.5** with 2.0 eq. PyCHO + 2.0 eq. 5-BrPyCHO (in CH_3CN).

3.6 Conclusion

In conclusion, we have investigated how small changes in the electronics of the coordinating group can effect large changes on the multicomponent self-assembly process. The substitution at the 5 position of the pyridyl ring does not add steric congestion about the metal centers, and the assemblies are far more sensitive to electron-withdrawing effects than added electron-density. Selective, favorable incorporation of electron rich aldehyde termini is observed and leads to a more stable thermodynamic product overall. The rate of assembly is accelerated using electron poor aldehyde reactants likely due to kinetic effects arising from the more electrophilic nature of the aldehyde component. These experiments illustrate how significant control of self-sorting and self-assembly is possible and can be effected by extremely small variations in ligand structure and rigidity, or coordinator donor ability.

3.7 References

1. Davis, A. V.; Yeh, R. M.; Raymond K. N. "Supramolecular Assembly Dynamics." *Proc. Natl. Acad. Sci. U S A.* **2002**, *16*; 4793–4796.

2. Yan, Y.; Huanga, J.; Tang, B. Z. "Kinetic Trapping – a Strategy For Directing the Self-Assembly of Unique Functional Nanostructures." *Chem. Commun*. **2016**, *52*, 11870-11884.

3. Schalley, C.A.; Müller, T.; Linnartz, P.; Witt, M.; Schäfer, M.; Lützen, A. "Mass Spectrometric Characterization and Gas-Phase Chemistry of Self-Assembling Supramolecular Squares and Triangles." *Chem. Eur. J.* **2002**, *8*, 3538-3551.

4. Levin, M.D.; Stang, P.J. "Insights into the Mechanism of Coordination-Directed Self-Assembly." *J. Am. Chem. Soc.* **2000**, *122*, 7428–7429.

5. Tsujimoto, Y.; Kojima, T.; Hiraoka, S. "Rate-determining step in the self-assembly process of supramolecular coordination capsules." *Chem. Sci.* **2014**, *5*, 4167-4172.

6. Johnson, A. M.; Moshe, O.; Gamboa, A. S.; Langloss, B. W.; Limtiaco, J. F. K.; Larive, C. K. Hooley, R. J. "Synthesis and Properties of Metal–Ligand Complexes with Endohedral Amine Functionality." *Inorg. Chem.* **2011**, *50*, 9430-9442.

7. Hansch, C.; Leo, A.; Taft, R. W. "A Survey of Hammett Substituent Constants and Resonance and Field Parameters." *Chem. Rev*. **1991**, *91*, 165–195.

8. Bogie, P. M.; Holloway, L. R.; Lyon, Y.; Onishi, N. C.; Beran, G. J. O.; Julian, R. R.; Hooley, R. J. "A Springloaded Metal-Ligand Mesocate Allows Access to Trapped Intermediates of Self-Assembly" *Inorg. Chem*. **2018**, *57*, 4155-4163.

9. Holloway, L. R.; McGarraugh, H. H.; Young, M. C.; Sontising, W.; Beran, G. J. O.; Hooley, R. J. "Structural Switching in Self-Assembled Metal-Ligand Helicate Complexes via Ligand-Centered Reactions." *Chem. Sci.* **2016**, *7*, 4423-4427.

10. Osowska, K.; Miljanić, O. Š. "Kinetic and Thermodynamic Self-Sorting in Synthetic Systems." *Synlett.* **2011**, *12*, 1643-1648.

11. Hutin, M.; Cramer, C. J.; Gagliardi, L.; Shahi, A. R. M.; Bernardinelli, G.; Cerny R.; Nitschke, J. R. "Self-Sorting Chiral Subcomponent Rearrangement During Crystallization." *J. Am. Chem. Soc.* **2007**, *129*, 8774–8780.

12. Krämer, R.; Lehn, J-M.; Marquis-Rigault, A. “Self-Recognition in Helicate Self-Assembly: Spontaneous Formation of Helical Metal Complexes from Mixtures of Ligands and Metal Ions.” *Proc. Natl. Acad. Sci. U.S.A.* **1993**, *90*, 5394-5398.

13. Wiley, C. A.; Holloway, L. R.; Miller, T. F.; Lyon, Y.; Julian, R. R.; Hooley, R. J. "Electronic Effects on Narcissistic Self-Sorting in Multicomponent Self-Assembly of Fe-Iminopyridine meso-Helicates." *Inorg. Chem.* **2016**, *55*, 9805-9815.

Chapter 4: Post-Assembly Modification Part 1: Structural Switching from a Polymeric Aggregate to Discrete Assemblies via Ligand Centered Oxidations

4.1 Introduction

We have previously shown that ligands based on dibenzosuberone[1] or fluorenone scaffolds[2,3] can be used to control the structural and stereochemical outcomes of self-assembly. Small changes in backbone hybridization, hydrogen-bonding and the electron donating nature of the coordinating group can lead to narcissistic self-sorting between similar ligand scaffolds as shown in Chapters 2 and 3. The impressive sorting behavior and the significant stabilization of suberone mesocate **1.7** over the highly similar suberol mesocate **1.8** suggested that favorable internal functionalization could be used as a directing force for increased control over the assembly process. Precise control over the assembly process could aid in the creation of useful functionalized molecular hosts, sensors and switches. The unmet goal is the introduction of reactive groups within the cavity of the complex that can react in a predictable manner. An endohedral leaving group is ideal for this purpose, as mild post-assembly substitution reactions can be used to create a library of internally reactive products from a single parent complex.

4.2 Synthesis of A Disordered Polymeric Aggregate

The challenge in post-synthetic modification of cage structures is tailoring the reaction conditions so that the sensitive self-assembled complexes are not destroyed. We have synthesized a variety of functionalized ligand cores containing internal groups such as carbamates, secondary or tertiary amines and ethers, but many of these groups either

prevent initial self-assembly with the inclusion of steric bulk, or are unreactive under mild conditions.[4] The presence of strong nucleophiles is the greatest limitation: the cationic Fe-iminopyridine coordinators are sensitive to displacement[5] and we have found they are intolerant to species as mild as bromide or hydroxide ions, as well as primary amines or hydride reducing agents.[4] An alkyl chloride is an enticing target for post-assembly modification, as cation formation can be driven by treatment with Ag^+ salts, which additionally prevents the chloride anions from disrupting the assembly. The subsequent attack can be performed by weak, neutral nucleophiles that would not disturb the Fe-iminopyridine assembly contacts.

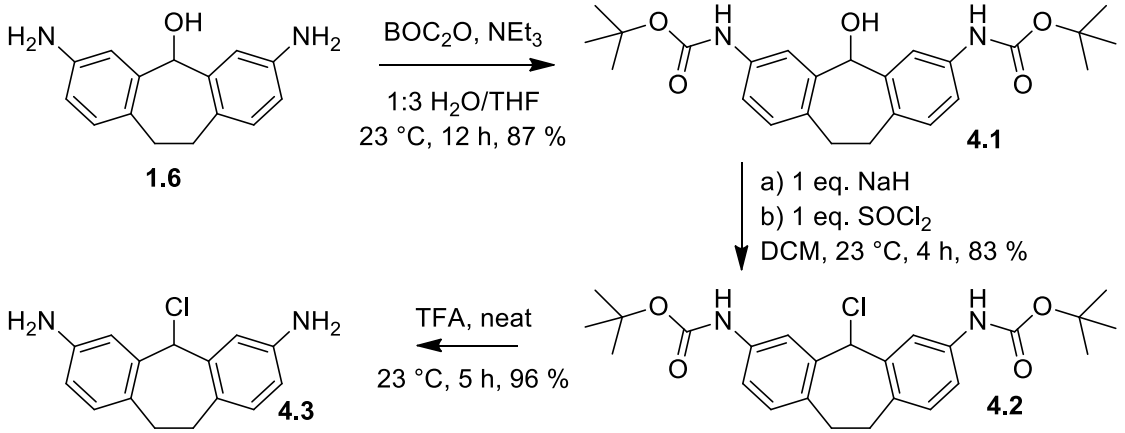

Figure 4.1. Synthesis of 3,7-diaminosuberyl chloride core **4.3** from **1.6**.

The 3,7-diaminosuberyl chloride ligand **4.3** was synthesized in 70 % yield from 3,7-diaminodibenzosuberol **1.6** by selective Boc protection of the amine groups, followed by chlorination of the alcohol, then deprotection with neat trifluoroacetic acid and subsequent neutralization to give the free dianiline. When ligand **4.3** was reacted with 0.66 eq. $Fe(ClO_4)_2$ and 2 eq. 2-formylpyridine (PyCHO) at 80 °C, the solution encouragingly

turned the characteristic purple color of an Fe^{II}-iminopyridine-based assembly. However, NMR analysis of the product formed was not representative of the expected discrete M_2L_3 mesocate (Figure 4.2b).

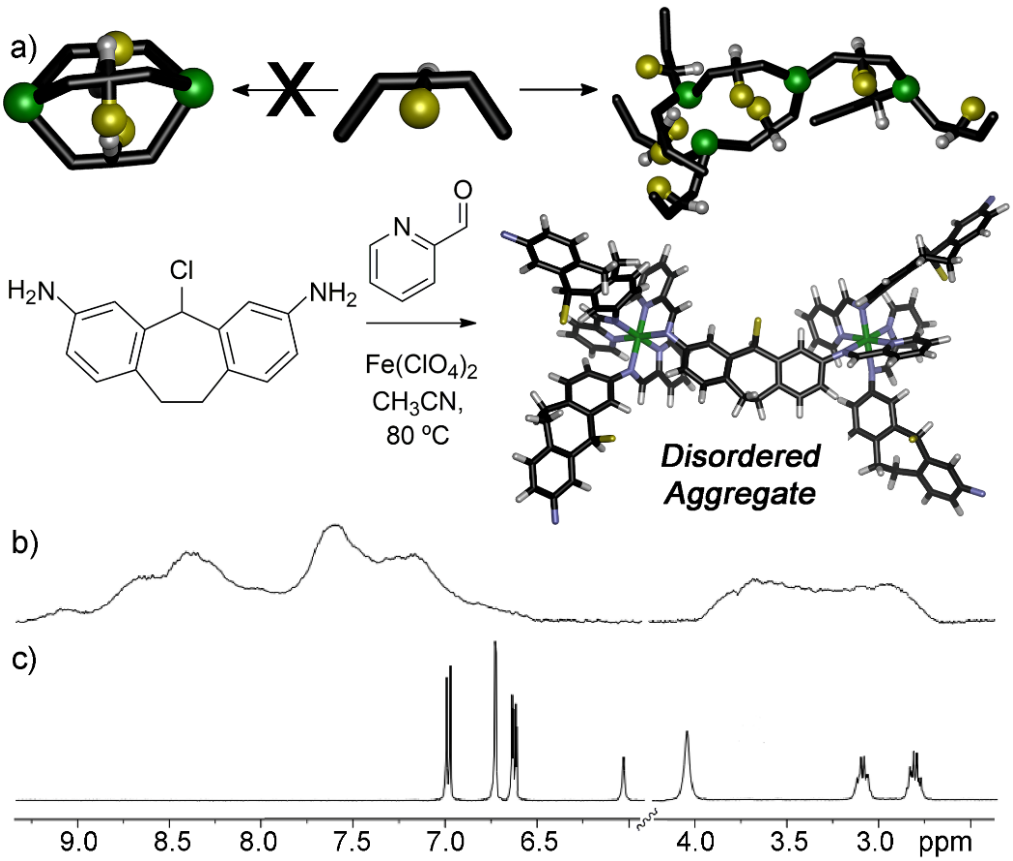

Figure 4.2. (a) Self-assembly of suberyl chloride ligand **4.3** into disordered aggregate **4.4**. ^{1}H NMR spectrum of (b) aggregate **4.4**; (c) suberyl chloride ligand **4.3** (400 MHz, CD_3CN, 298 K).

Instead of the usual sharp peaks observed in the ^{1}H spectrum of low spin Fe-iminopyridine assemblies,[6] broad mounds were observed throughout the aromatic and alkyl regions of the spectrum. Increasing the reaction time did not alter the obtained spectrum, indicating that this is not a kinetic mixture similar to those observed in Chapter 2. No significant spectral differences were observed upon acquisition at elevated

temperature, suggesting that the broad peaks in the NMR are not due to paramagnetism, but that the self-assembled product is not a discrete complex. Additionally, peaks corresponding to the diamino suberyl chloride or PyCHO starting materials were completely absent, indicating that all starting materials had been converted to product. This suggests that core **4.3** is unable to form the discrete M_2L_3 assembly, and instead forms an undefined aggregate **4.4** shown in Figure 4.2.

The lack of defined structure upon assembly of core **4.3** was odd and unexpected, and likely causes for this phenomenon are investigated further in section 4.5. Fortunately, the polymeric aggregate structure possesses an advantage for testing reactivity: the metastable assembly provides a reactive local minimum for post-synthetic modification.[7] The reactive alkyl chloride on the polymeric aggregate can be easily substituted, as the carbon center is not sterically confined within the cavity of a discrete complex. This may be useful for substitution with larger nucleophiles and may lead to the production of novel functionalized complexes.

4.3 Aggregate Oxidations and Structural Switching

To test whether the reactive alkyl chloride group is still present on aggregate **4.4**, a simple substitution reaction using water was attempted. One molar equivalent of both water and silver perchlorate were added to a solution of aggregate **4.4** in CD_3CN, and the sample was heated in an NMR tube at 45 °C for 20 h. Silver perchlorate was used to drive a dissociative substitution process, enabling the use of a weak nucleophile and preventing Cl^- anions from affecting the iminopyridine coordinators. Excitingly, after heating for 12

h at 45 °C, peaks corresponding to a discrete cage complex can be observed amongst the broad mounds. By 16 h, the NMR spectrum sharpened considerably, and a single product predominated, with full completion observed at 20 h (Figure 4.3c). However, the observed peaks did not correspond to those for the expected substitution product, suberol mesocate **1.8**, but instead, perfectly matched the spectrum of ketone mesocate **1.7**.

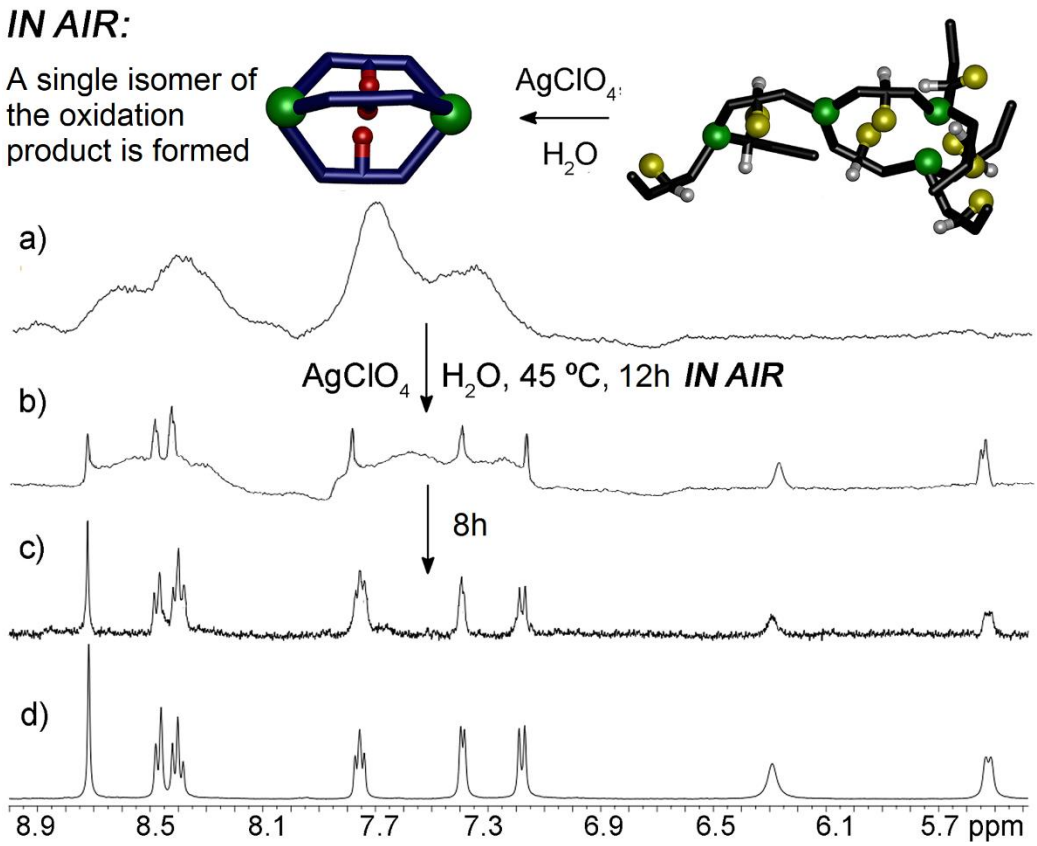

Figure 4.3. ^{1}H NMR spectra (400 MHz, CD_3CN, 298 K) of (a) aggregate **4.4**; (b) **4.4** + $AgClO_4$ + H_2O, in air, 45 °C, 12 h; (c) **4.4** + $AgClO_4$ + H_2O, in air, 45 °C, 20 h; (d) independently synthesized suberone mesocate **1.7**.

As can be seen in Figures 4.3b and 4.3c, only one product is formed as the reaction progresses, as the broad peaks for the aggregate **4.4** smoothly give way to sharp peaks for the discrete mesocate product **1.7**. There are no other visible peaks that would indicate

formation of alternate discrete cage products or multiple isomers of the ketone mesocate **1.7** (see section 4.5 below for an example of NMR spectra of stereoisomeric mixtures of mesocate assemblies). Cage **1.7** is the sole reaction product and no **1.8**, suberone/suberol/suberyl chloride mixed heterocomplexes or other varying stoichiometries (e.g. ML_3 fragments or M_4L_6 tetrahedra) are present at any time in the reaction mixture. The nature of the oxidation is surprising, as the ketone product is unexpected, and the reaction occurs in the presence of easily oxidized iron centers. The isolated product yield after oxidation is high (97 %), indicating that there is minimal degradation of the structural components. The switching reaction requires elevated temperature to occur as the reaction at 23 °C is extremely sluggish, and essentially no conversion is observed after 36 h. Although this is expected, as formation of a discrete cage would require equilibration of the Fe^{II}-Iminopyridine aggregate, which does not occur at room temperature. The specific silver salt and solvent were unimportant for the conversion: use of $AgNO_3$ or reaction in DMSO gave the same product.

Only one discrete species is observed during reaction progress, so the nature of the intermediates is unclear. What is obvious is that there is no appreciable concentration of intermediate structures (although small concentrations of reaction intermediates must be present). The metastable chloro assembly **4.4** must give way to other assemblies, presumably containing suberol and/or suberone ligands, but only after oxidation and equilibration does the final mesocate **1.7** form. ESI-MS analysis of the mixture formed after 12 h reaction (Figure 4.4) showed small traces of a mixed chloro-ketone ML_3

assembly and other intermediate fragments, but the spectrum was dominated by the fully assembled ketone cage **1.7**.

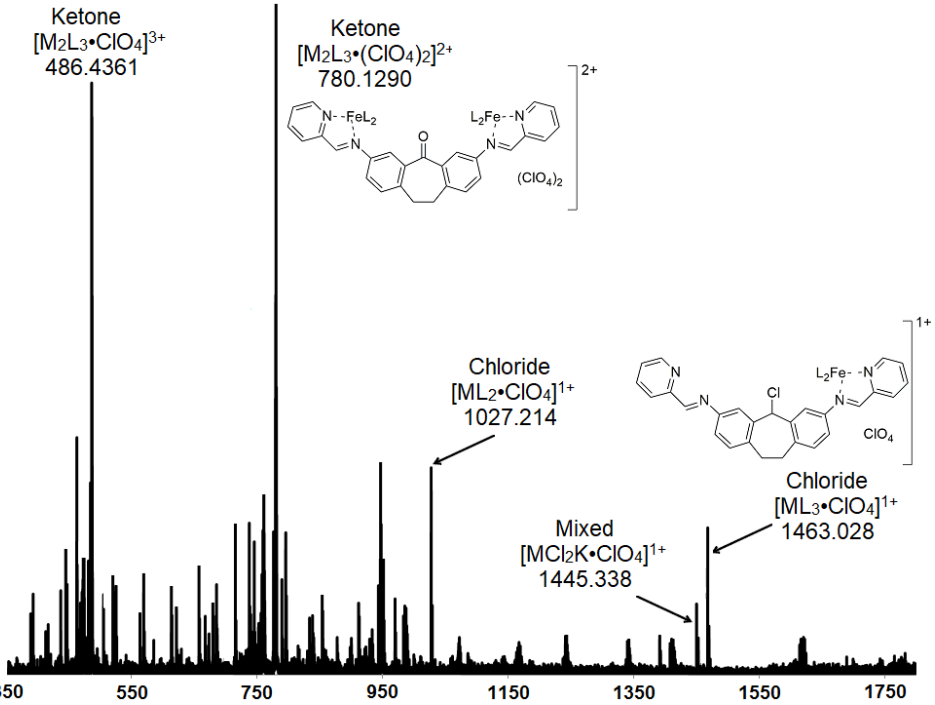

Figure 4.4. ESI-Mass Spectrum of the products observed after aggregate **4.4** was reacted with $AgClO_4$ and water for 12 h @ 45 °C (CD_3CN). Peaks corresponding to chloride ML_3 and ML_2 fragments are present. In addition, one mixed ML_3 fragment was found containing one ketone and two chloride iminopyridine ligands.

The absence of the expected alcohol product **1.8** in the presence of air is unusual: as there are only mild oxidizing agents in the system. Additionally, the Fe^{II} centers, which are easily oxidized, remain unaffected by the process. The ligand-centered oxidations on an assembly utilizing redox active iron atoms as the structural coordinating component are rare, and most examples of redox reactions on cage complexes naturally focus on metal-centered reactions.[8] To shed light on the nature of the oxidation process, we attempted the reaction in the absence of atmospheric oxygen. When aggregate **4.4** was heated at 45 °C

with $AgClO_4$ and H_2O under an oxidatively inert N_2 atmosphere, no reaction occurred after 48 h, but when the temperature was increased to 80 °C, the reaction sluggishly formed mesocate **1.8**. After 60 h at 80 °C, complete conversion was observed (Figure 4.5d).

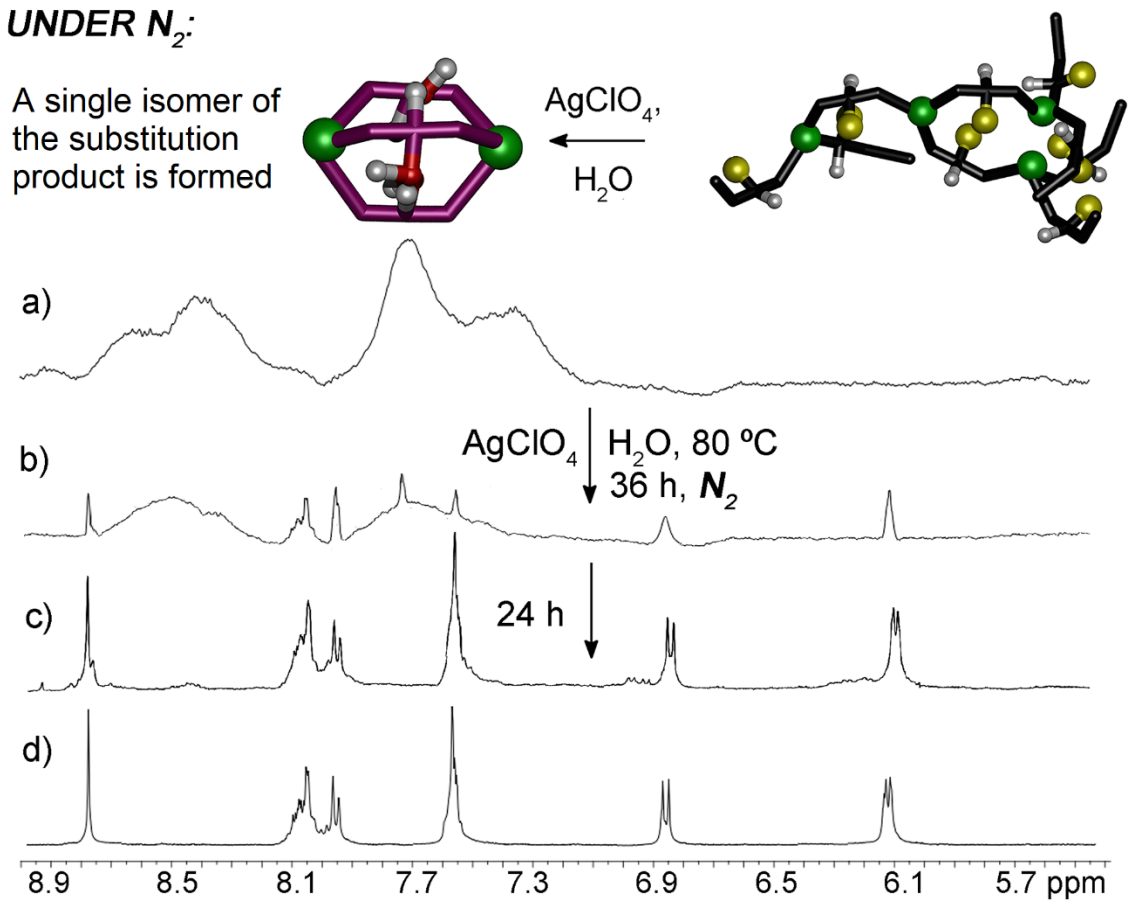

Figure 4.5. ^{1}H NMR spectra (400 MHz, CD_3CN, 298 K) of (a) aggregate **4.4**; (b) **4.4** + $AgClO_4$ + H_2O, N_2, 80 °C, 36 h; (c) **4.4** + $AgClO_4$ + H_2O, N_2, 80 °C, 60 h; (d) independently synthesized suberol mesocate **1.8**.

4.4 Control Experiments

To ensure that the ligands are not predisposed to forming the ketone products, control experiments were performed on a chloride ligand surrogate **4.7**, which was synthesized from **1.6** in 3 steps as shown in Figure 4.6. Chloride **4.7** was highly resistant

to dissolution in acetonitrile, so the control reactions were performed in DMSO-d_6, a solvent that also allowed smooth conversion of aggregate **4.4** to ketone **1.7**.

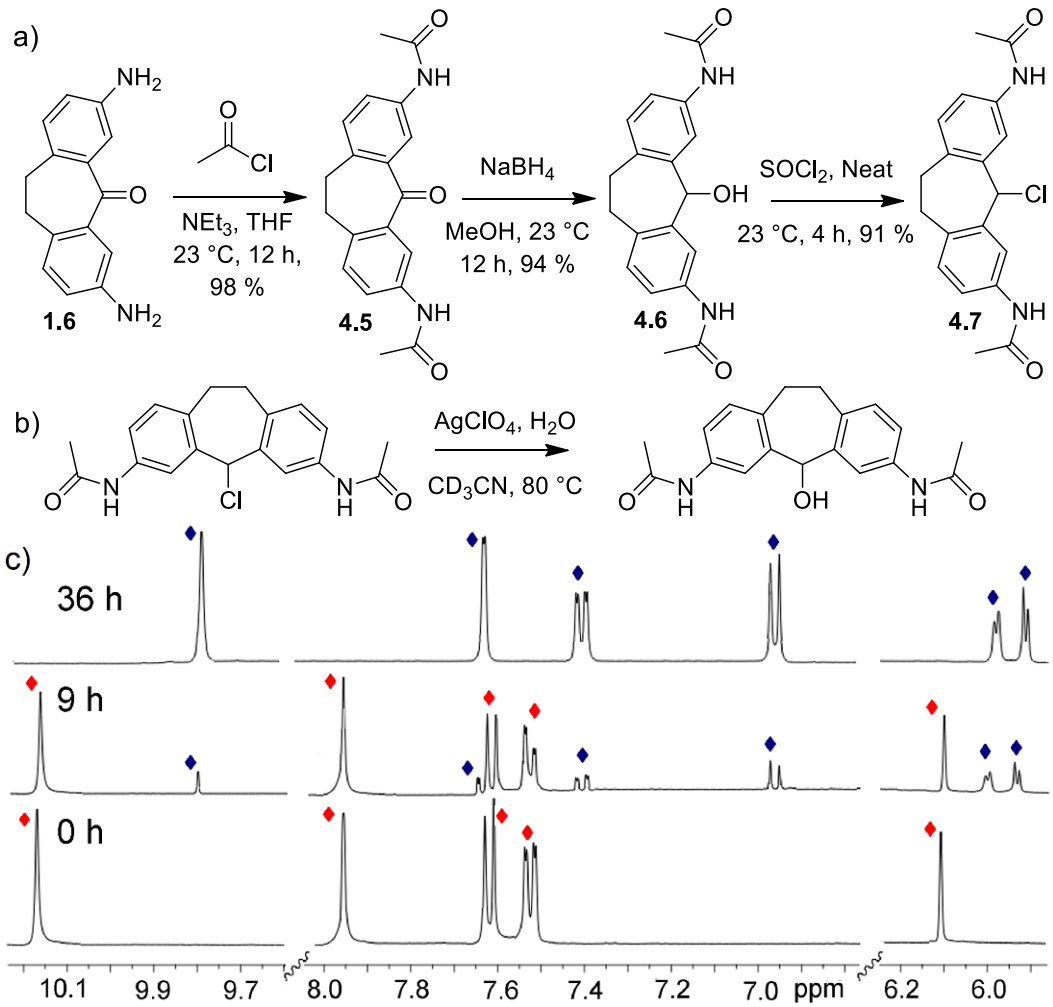

Figure 4.6. a) Synthesis of control ligand **4.7;** b) ligand substitution reaction conditions; c) ^{1}H NMR spectra of control ligand **4.7** (red), and after reaction with 1 eq. H_2O and 1 eq. $AgClO_4$ at 80 °C for 9 h and 36 h with conversion back to **4.6** (blue) (400 MHz, DMSO-d_6, 298 K).

When **4.7** was exposed to the same conditions that gave complete oxidation of **4.4** to mesocate **1.7** (i.e. 1 eq. $AgClO_4$ and 1 eq. H_2O, heating at 45 °C for 24 h), the substitution reaction was sluggish. When the temperature was increased to 80 °C and the reaction time increased to 36 h, a new product was observed, and in this case, only the alcohol

substitution product **4.6** was formed: no evidence of any oxidation to ketone was seen, even under these harsher conditions. The substitution reaction proceeds normally with or without air. These conditions are similar to those necessary for the air-free substitution reaction of aggregate **4.4**, indicating that the oxidation reaction to mesocate **1.7** in air is accelerated over the substitution. In the absence of silver (employing Bu_4NClO_4 instead), no reaction was observed after 48 h reaction time. Employing alternate counterions, such as $AgNO_3$ did not alter the outcome of the reaction. Tests performed under strictly anhydrous conditions also (unsurprisingly) gave no reaction. The only remaining variable that the control tests did not account for, is the presence of small amounts of iron that can be leached from the assembled products in solution.[9]

After isolation and purification of the assembly products, it is unlikely that any uncoordinated iron salts remain, but the reversible nature of the iminopyridine assemblies allows for ligand dissociation and small amounts of iron can become coordinatively unsaturated and act as catalysts. It is likely that trace amounts of coordinatively unsaturated iron and atmospheric oxygen catalyze the rapid conversion of the suberyl cation to the ketone product which is more favored by the assembly process than the alcohol and rapidly equilibrates to the discrete mesocate product. It is likely that this rapid oxidation requires the less hindered nature of the aggregate structure, in addition to atmospheric oxygen, catalytic iron, and the ability to form the cation via silver addition to the alkyl chloride.

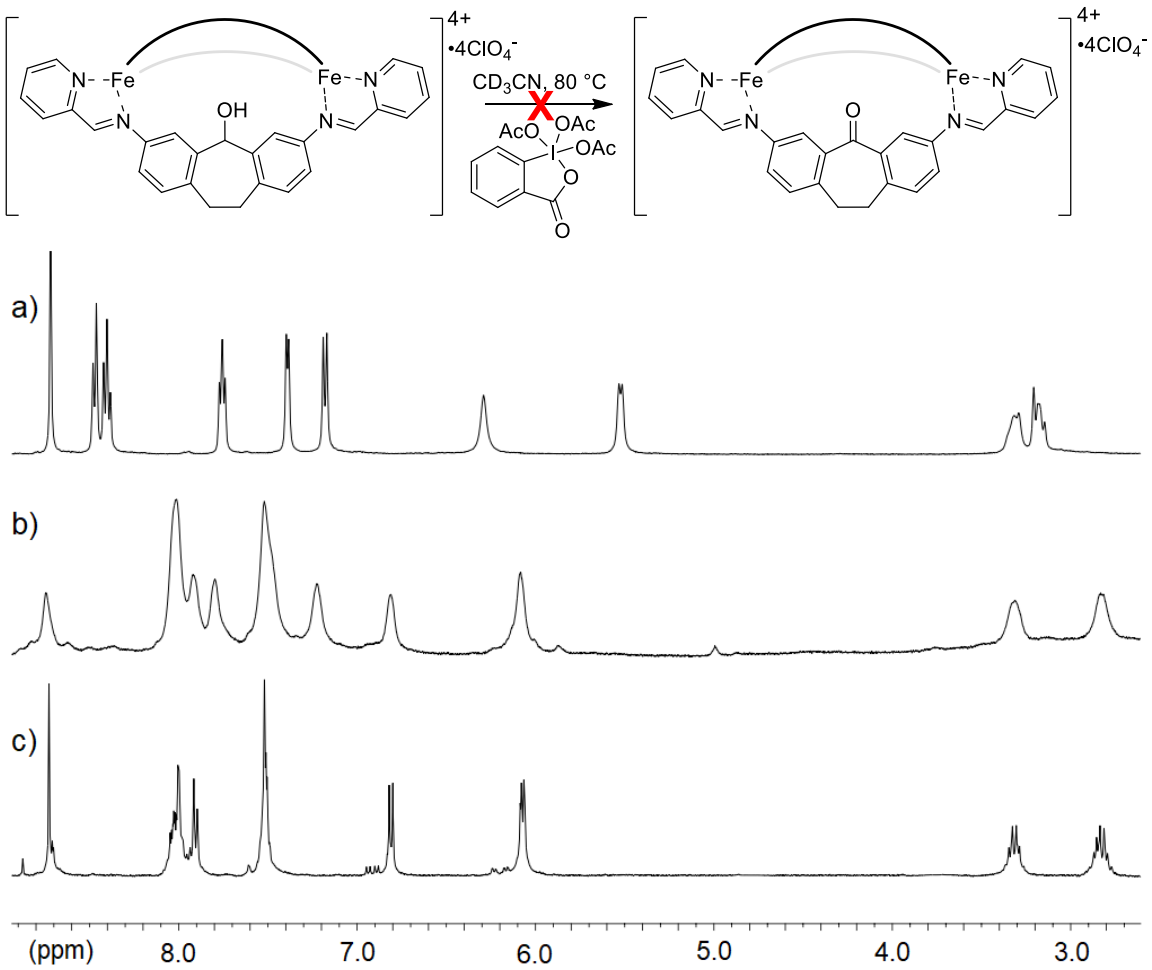

Figure 4.7. ^{1}H NMR spectra of a) ketone mesocate **1.7**, b) products obtained after alcohol cage **1.8** was reacted with Dess-Martin periodinane for 48 h at 80 °C, and c) starting cage **1.8** (400 MHz, CD_3CN, 298K).

In order to investigate the nature of the reaction and confirm that the oxidation occurs first followed by slow equilibration to the discrete cage, the conversion of preformed mesocate **1.8** to ketone **1.7** was attempted. When **1.8** was reacted with $AgClO_4$ and H_2O in air at 45 °C, unsurprisingly no reaction occurred. Heating at 80 °C for 36 h also gave no conversion to **1.7**. The alcohol mesocate was also resistant to more stringent oxidative processes: heating **1.8** at 45 °C or 80 °C with Dess-Martin periodinane did not confer oxidation to **1.7** as shown in Figure 4.7. The oxidation of **4.4** does not appear to be

acid-mediated, as addition of even catalytic amounts of acid to preformed complexes causes protonation of the iminopyridine coordinators resulting in cage decomposition. Evidently, oxidation of the aggregate is facile, but once a favorable self-assembled cage is formed, the reactive site becomes sterically blocked within the M_2L_3 interior and is resistant to further reaction. The metastable assembly **4.4** is primed for reaction, whereas the fully formed mesocate species are not.

4.5 Reactivity of Complexes Bearing Alternate Leaving Groups

The polymeric and less sterically hindered nature of aggregate **4.4** is necessary for reactivity but is also somewhat unique: we have synthesized numerous other 3,7-diaminodibenzosuberyl species that are capable of forming M_2L_3 helices upon multicomponent self-assembly. In order to understand why chloride ligand **4.3** is incapable of forming a discrete self-assembled cage, and to investigate the driving forces for the reactive behavior of **4.4**. Two substituted analogs of ligand **4.3** and their respective assemblies were compared to the reactive nature of the chloro group in **4.4**. Mesylate ligand **4.9** (Figure 4.8) was synthesized from the Boc-protected alcohol **4.1** via the same substitution/deprotection route as the chloride core **4.3**. This provides a leaving group to the central scaffold, but this leaving group should not as readily ionize to the carbocation via the application of Ag^+ ions. Trifluoroethyl ether ligand **2.7** and cage **2.8** were previously examined in Chapter 2 as a surrogate for suberol cage **1.8** which is lacking in hydrogen bonding capabilities. The assembly properties and reactivity of the two internal groups can be studied and compared to that of the aggregate **4.4**.

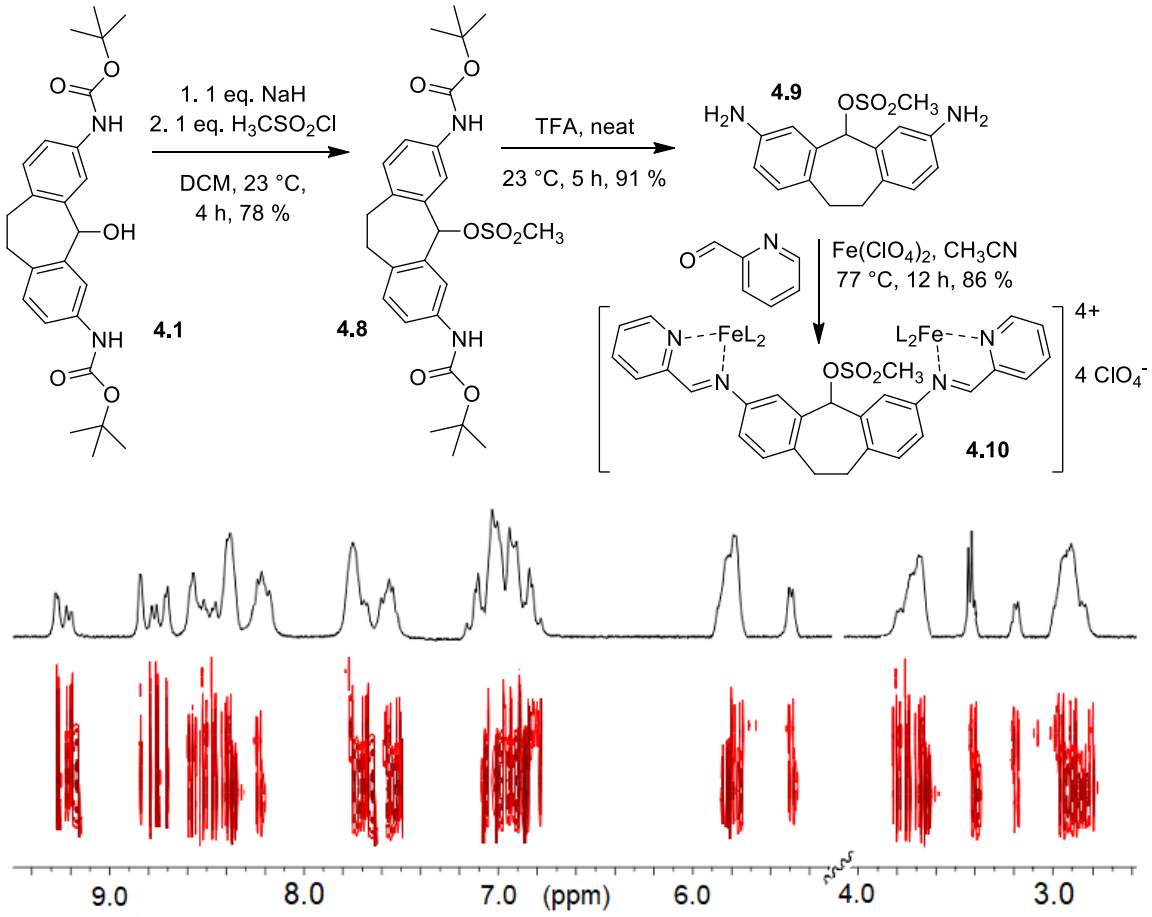

Figure 4.8. Synthesis of mesylate ligand **4.9** and ^{1}H and 2D DOSY NMR spectra of cage **4.10** displaying the typical pattern observed when multiple isomers arise from combinations of the three groups being directed towards the mesocate interior or exterior (600 MHz, CD_3CN, 298K).

One possible explanation for the uncontrolled assembly of **4.4** was the lack of hydrogen bonding groups to direct the formation of a single isomer. However, both ligands **2.7** and **4.9** have no H-bonding groups, and smoothly form discrete M_2L_3 mesocate structures. In the absence of hydrogen bonding to direct the formation of a single isomer, no stereocontrol was observed upon assembly of the two cores **2.7** and **4.9**. The ^{1}H NMR and DOSY spectra for trifluoroethyl ether cage **2.7** (Chapter 2) and mesylate cage **4.10** (Figure 4.8) illustrate the typical spectra observed for isomerically impure M_2L_3 mesocates.

More peaks were present than would be expected for a single isomer because the flexible functional groups can be oriented in or out, however the peaks are all sharp and well-defined, unlike the spectra seen for the aggregate.

The similarity in structure between ligands **4.3**, **2.7** and **4.9** is incongruous with their large differences in assembly properties. The only difference between the substituted cages and aggregate **4.4** is the ability of the large groups to flex out and away from the cage interior, thus relieving some steric congestion. Both cages **2.7** and **4.10** make use of oxygen atoms bound to the central carbon of the ligand core, which has an atomic radius that is smaller than chloride, and the C-O bond length is shorter than a C-Cl bond. Attempts to synthesize the analogous bromo- or iodo- analogs to confirm this were unsuccessful due to their increased reactivity.

To determine whether cation formation is necessary for the reactive nature of **4.4**, the reactive properties of the two substituted cages **2.8** and **4.10** were tested. Mesylate cage **4.10** contains a leaving group that should behave in a manner analogous to the alkyl chloride. However, it appears that the chloride abstraction and cation formation on the ligand is essential for the reactivity of aggregate **4.4**, as neither mesylate cage **4.10** nor trifluoroethyl ether cage **2.8** showed any reactivity.

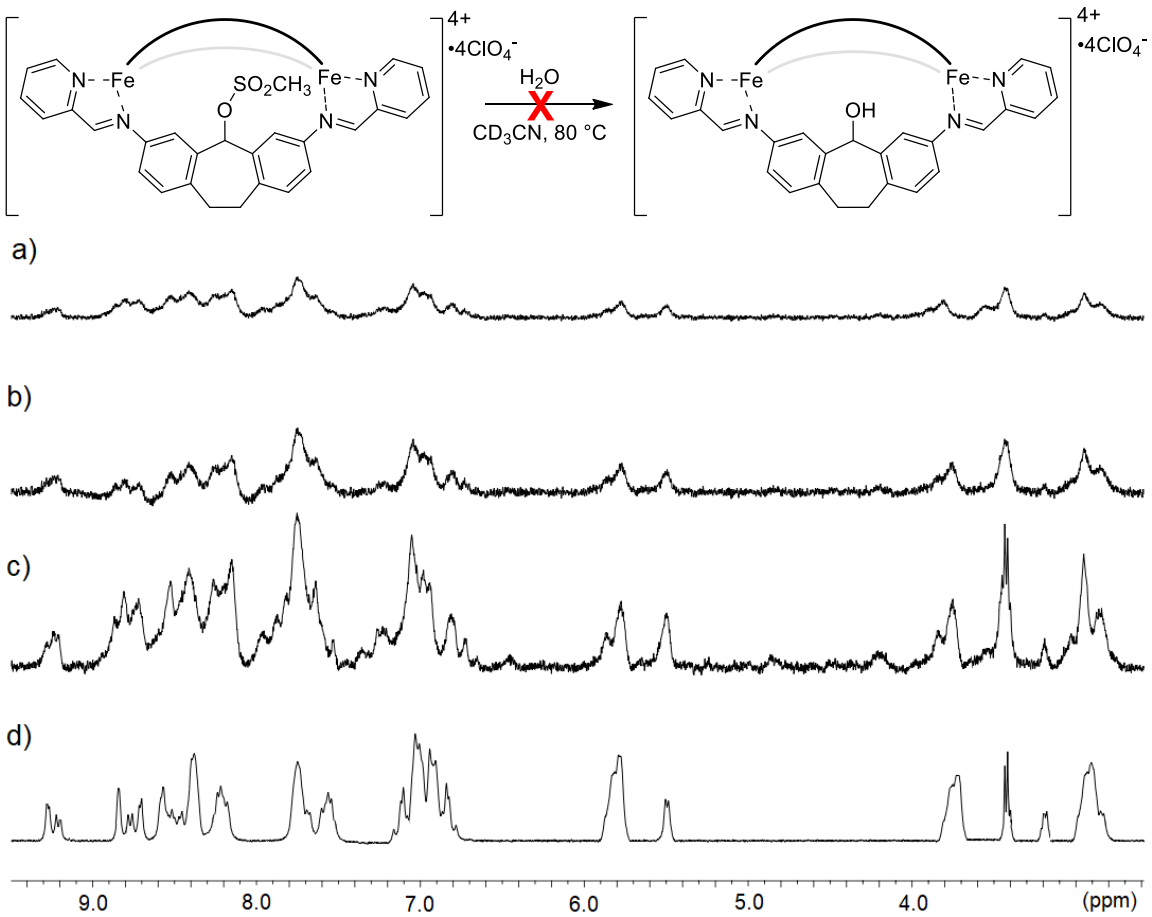

Figure 4.9. ^{1}H NMRs of attempted nucleophilic substitutions using 3 mol. eq. water and $AgClO_4$ on mesylate cage **4.10** at 80 °C after a) 48 h, b) 24 h, and c) 12 h, compared to d) cage **4.10** (400 MHz, CD_3CN, 298K).

When either **4.10** or **2.8** was heated at 45 °C or 80 °C with H_2O and $AgClO_4$, in either CD_3CN or DMSO-d_6, no change in the NMR spectra was observed after 36 h other than gradual cage decomposition (Figure 4.9). Neither the mesylate nor the trifluoroethyl ether group can be abstracted by Ag^+ ions, and so an associative reaction would be required. The hindered nature of the central carbon atom in mesocates **4.10** and **2.8** evidently limits access to weak nucleophiles, and only upon cation formation on the aggregate structure

can reaction occur. Easier access to the central carbon atom, and the metastable nature of the aggregate are responsible for its unique behavior.

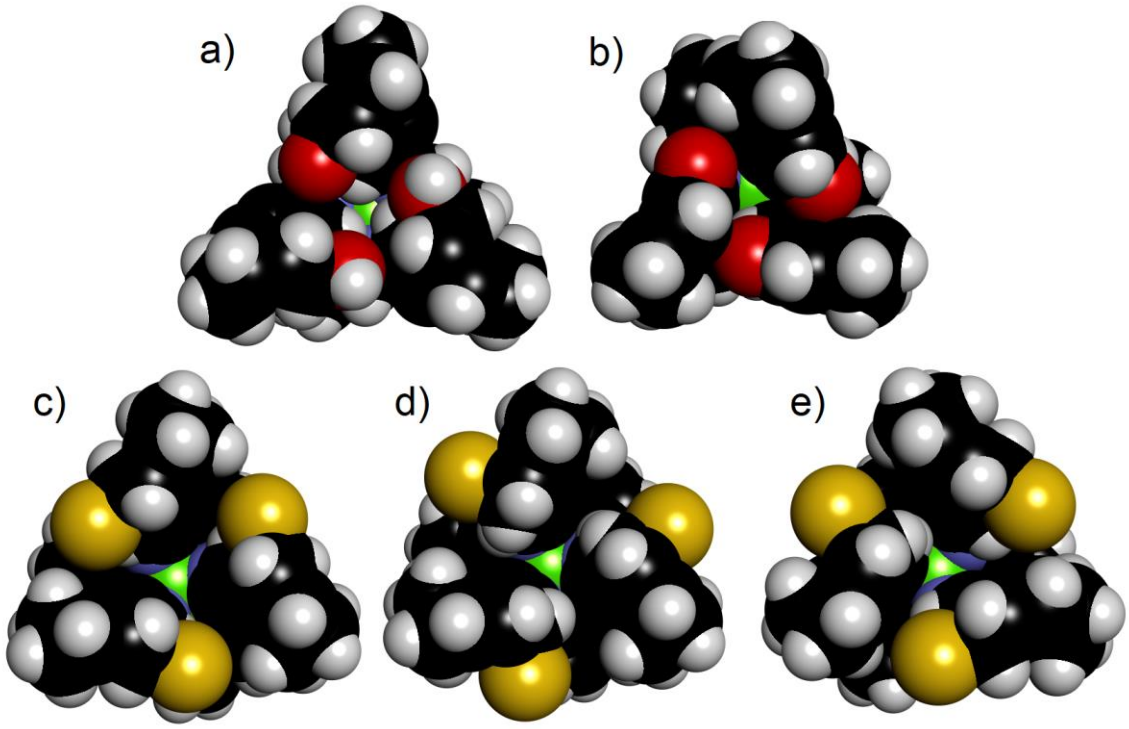

Figure 4.10. Side-on view of the X-Ray crystal structures of a) alcohol mesocate **1.8**, b) ketone mesocate **1.7** and energy minimized models of three possible chloride M_2L_3 isomers with the chloride groups directed c) all inward, b) all outward, and e) two inward, one outward.

Finally, we turned to computational analysis in an attempt to determine why chloride ligand **4.3** does not form a discrete M_2L_3 cage complex. The structure of each possible isomer of the M_2L_3 mesocate complexes that could be formed upon self-assembly of ligand **4.3**, $Fe(ClO_4)_2$ and PyCHO was optimized by the Beran group using dispersion-corrected density functional theory (at the ωB97X-D/6-31G* level), and the energies were compared to that of complex **1.7**. The calculated energy of each isomer of the chloride cage was significantly higher than that of the favorable **1.7** mesocate, ranging from

approximately +10 kcal mol^{-1} for the least hindered "all-out" isomer, to +30 kcal mol^{-1} for the sterically demanding "all-in" isomer. The M_2L_3 mesocates have very small cavities and are highly sensitive to interactions between large atoms and the other ligand backbones in the assembly (Figure 4.10). The energy minimized structures indicate that the -Cl atom is too large to allow assembly due to steric clashes with the other ligand backbones. This is somewhat confirmed by the fact that smaller atoms such as -O are known to be tolerated.

4.6 Conclusion

In conclusion, we have shown that ligand centered reactivity can confer structural switching between a metastable self-assembled aggregate species and a stable M_2L_3 mesocate. Mesocate **1.7** is formed preferentially under aerobic conditions, and the process employs atmospheric O_2 as the oxidant for ligand-centered reaction. The reaction takes place in the presence of multiple redox-active iron atoms without disrupting the metal-ligand coordination. In the absence of air, the substitution and subsequent switching are sluggish. In this case, the reaction is stereocontrolled, and one isomer of product is formed, directed by internal hydrogen bonding. The oxidation likely employs small amounts of coordinatively unsaturated metal as the catalyst, as control reactions form the substitution product. The metastable nature of the aggregate is essential for the reaction, as the chloride is less hindered, while mesocate structures are inert to both substitution and oxidation, as the M_2L_3 structure itself blocks the reactive carbon center.

4.7 References

1. Holloway, L. R.; Young, M. C.; Beran, G. J. O.; Hooley, R. J. "High Fidelity Sorting of Remarkably Similar Components Via Metal-Mediated Assembly." *Chem. Sci.* **2015**, *6*, 4801-4806.

2. Young, M. C.; Holloway, L. R.; Johnson, A. M.; Hooley, R. J. "A Supramolecular Sorting Hat: Stereocontrol in Metal–Ligand Self-Assembly by Complementary Hydrogen Bonding." *Angew. Chem., Int. Ed.* **2014**, *53*, 9832-9836.

3. Johnson, A. M.; Wiley, C. A.; Young, M. C.; Zhang, X.; Lyon, Y.; Julian, R. R.; Hooley, R. J. "Narcissistic Self-Sorting in Self-Assembled Cages of Rare Earth Metals and Rigid Ligands." *Angew. Chem., Int. Ed.* **2015**, *54*, 5641-5645.

4. Young, M. C.; Johnson, A. M.; Hooley, R. J. "Self-Promoted Post-Synthetic Modification of Metal–Ligand M_2L_3 Mesocates." *Chem. Commun.* **2014**, *50*, 1378-1380.

5. Ma, S.; Smulders, M. M. J.; Hristova, Y.; Clegg, J. K.; Ronson, T. K.; Zarra, S.; Nitschke, J. R. "Chain-Reaction Anion Exchange between Metal-Organic Cages." *J. Am. Chem. Soc.* **2013**, *135*, 5678-5684.

6. Roberts, D. A.; Castilla, A. M.; Ronson, T. K.; Nitschke, J. R. "Post-Assembly Modification of Kinetically Metastable $Fe^{II}_2L_3$ Triple Helicates." *J. Am. Chem. Soc.* **2014**, *136*, 8201-8204.

7 Roberts, D. A.; Castilla, A. M.; Roson, T. K.; Nitschke, J. R. "Post-Assembly Modification of Kinetically Metastable $Fe^{II}_2L_3$ Triple Helicates." *J. Am. Chem. Soc.* **2014**, *136*, 8201-8204.

8. Symmers, P. R.; Burke, M. J.; August, D. P..; Thomsen, P. I. T.; Nichol, G. S.; Warren, M. R.; Campbell, C. J.; Lusby, P. J. "Non-Equilibrium Cobalt(III) "Click" Capsules." *Chem. Sci.* **2015**, *6*, 756-760.

9. Holloway, L. R.; Bogie, P. M.; Lyon, Y.; Julian, R. R.; Hooley, R. J. "Stereoselective Postassembly CH Oxidation of Self-Assembled Metal-Ligand Cage Complexes." *Inorg. Chem.* **2017**, *56*, 11435-11442.

Chapter 5: Post-Assembly Modification Part 2: Stereoselective Post-Assembly CH Oxidation of Self-Assembled Cage Complexes

5.1 Introduction

Previously we demonstrated that post assembly modification could be performed on a metastable aggregate and that the oxidation induces a structural switch to produce a discrete cage in high yield. This reaction was performed under mild conditions and utilized only atmospheric oxygen and trace amounts of iron leached from the reversible iminopyridine assembly. However, the presence of the alkyl chloride prevented the formation of a discrete cage product. The remaining unmet goal is to introduce useful reactive functionality to discrete cage complexes. A C-H oxidation of unfunctionalized hydrocarbon ligands would be ideal,[1,2] and could drastically simplify the assembly process. This reaction would require careful matching of post assembly oxidation conditions to avoid disruption of the metal coordinating atoms.[3,4] In addition, new ligands must be created that allow for formation of discrete complexes, which can then be functionalized via suitable post-assembly modifications.

5.2 Synthesis of New Cage Complexes

We focused on doubly benzylic methylene units on the dianiline scaffolds, namely 2,7-diaminoxanthene **5.2** and 2,7-diaminofluorene **5.4** (Figure 5.1) as they should simplify assembly into their corresponding complexes and provide a reactive handle for mild oxidations. Ligand **5.2** was synthesized in 2 reductive steps from 2,7-dinitroxanthone: first to reduce the central carbonyl unit to an alcohol, then exhaustive reduction of the nitro

groups and the alcohol to give the dianiline core. Diaminofluorene **5.4** is easily accessed from reduction of commercially available 2,7-dinitrofluorene.

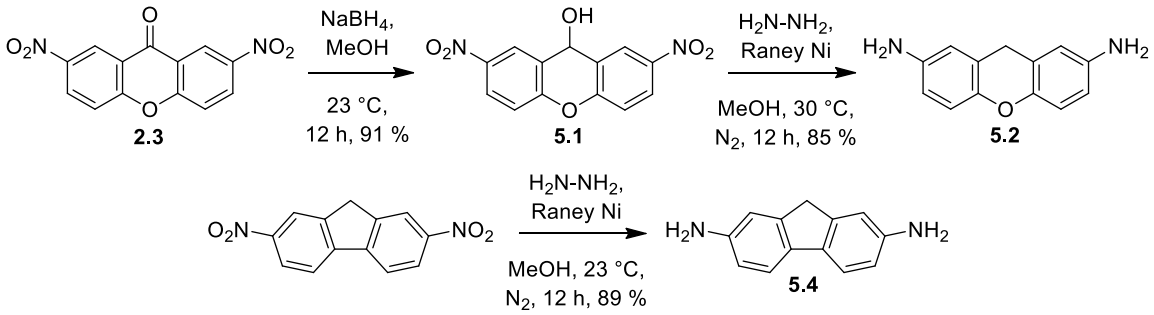

Figure 5.1. Synthesis of dianiline ligands **5.2** and **5.4**.

Core **5.2** was assembled into cage **5.3** via multicomponent self-assembly with $Fe(ClO_4)_2$ and 2-formylpyridine (PyCHO) as shown in Figure 5.2. The somewhat bent diaminoxanthene scaffold forms a stable diamagnetic M_2L_3 assembly similar to suberyl complexes **1.7**, **1.8**, and **2.3**.[5] This was surprising, as in Chapter 2 it was found that xanthone mesocate **2.6** is highly strained, and exhibits unique paramagnetic properties upon multicomponent assembly with $Fe(ClO_4)_2$ and PyCHO. Evidently the removal of the ketone and the resulting increase in flexibility relieves some of the strain and allows the formation of a favorable complex. Interestingly, competition experiments with suberone ligand **1.5** indicate that mesocates **1.7** and **5.3** are of similar favorability, as a complex mixture was observed, with no single mesocate favored over the other. Electrospray ionization mass spectrometry (ESI-MS) analysis confirms the M_2L_3 stoichiometry of **5.3**, and the mass spectrum mainly consists of variably charged perchlorate adducts. 1D and 2D NMR analysis indicates a single diastereomer of the assembly is formed, and the peaks in the ^{1}H NMR were assigned using the COSY spectrum shown in Figure 5.2. The methylene

protons of the central carbon are dissymmetric due to the chiral nature of the metal centers. A side-on view of the complex illustrating this is shown later in Figure 5.5.

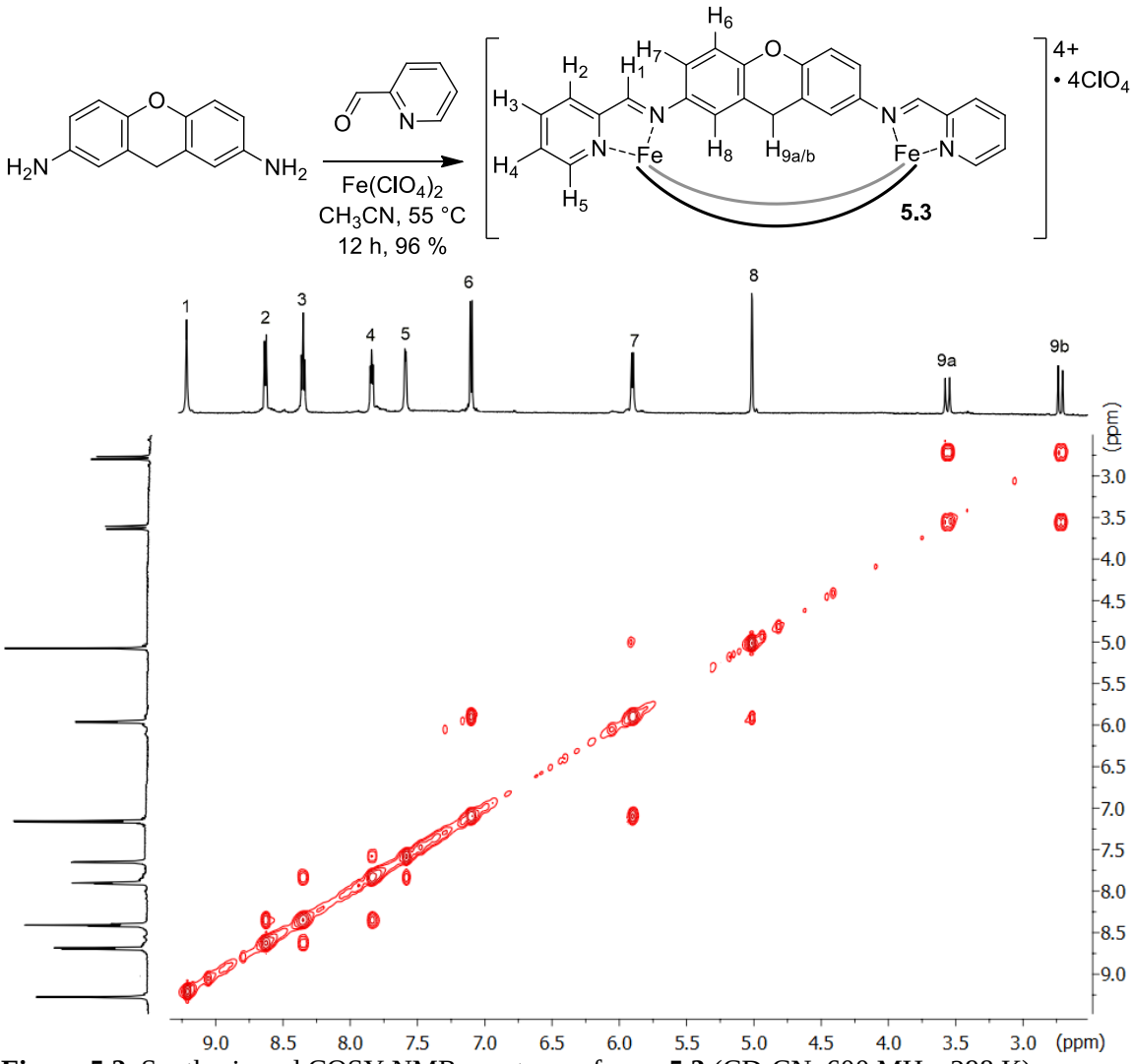

Figure 5.2. Synthesis and COSY NMR spectrum of cage **5.3** (CD_3CN, 600 MHz, 298 K).

The fluorene complex was synthesized in a similar manner: upon treatment of **5.4** with $Fe(ClO_4)_2$ and PyCHO, the characteristic purple color of a diamagnetic low spin Fe^{II}-iminopyridine assembly appeared. The ^1H NMR spectrum of the M_4L_6 assembly **5.5** was unexpectedly complex, even more so than the highly dissymmetric spectrum of **1.12**.[6]

Ligand **5.4** has no prochiral centers, therefore **5.5** should display a more symmetric NMR spectrum than **1.12**.[7] However, the assembly lacks hydrogen bonding to template the formation of a single isomer. Instead, multiple metal-centered isomers of **5.5** are formed, and the assembly is uncontrolled.

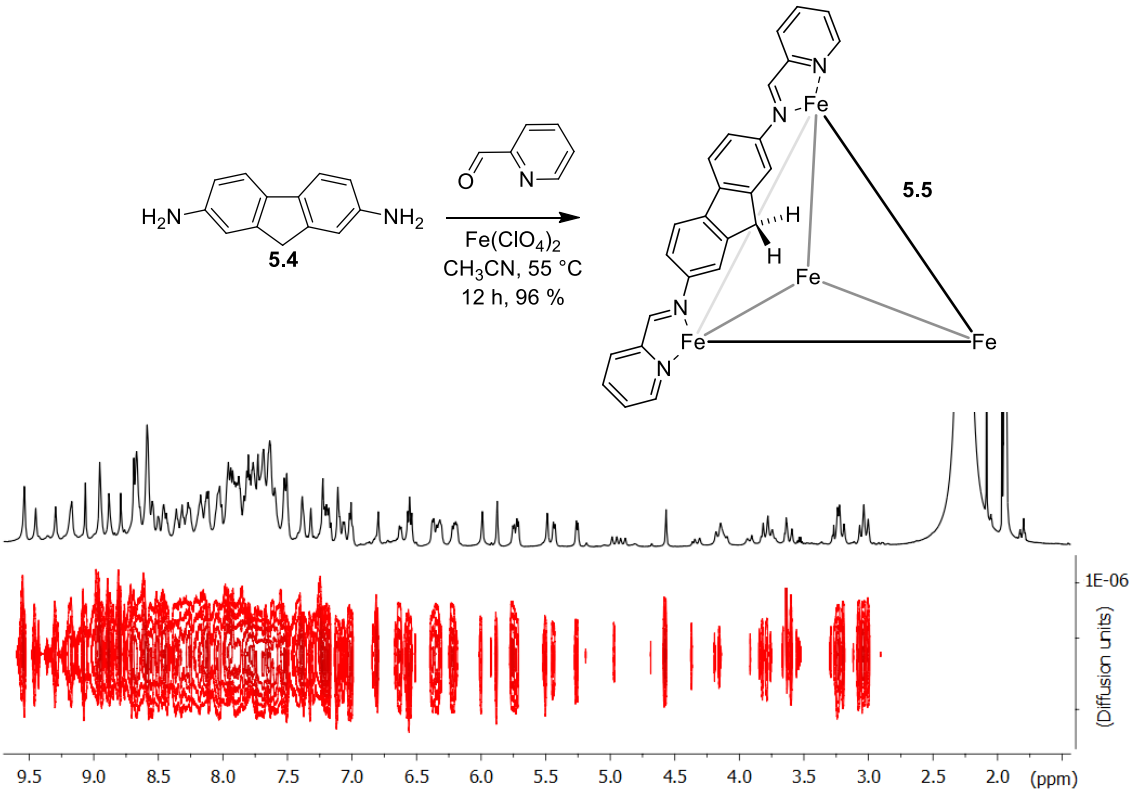

Figure 5.3. Synthesis and DOSY NMR spectrum of cage **5.5** (CD_3CN, 600 MHz, 298 K, Δ = 100 ms, δ = 2.6 μs, Diffusion constant = 9.9183 x10^{-10} m^2/s for cage **5.5** vs. 9.911 x10^{-9} m^2/s for the solvent).

2D DOSY analysis (Figure 5.3) indicates that all peaks in the ^{1}H NMR correspond to M_4L_6 structures. The diffusion coefficient of **5.5** is similar to that of complex **1.12** (diffusion constant = 9.9183 x10^{-10} m^2/s for cage **5.5** and 9.883 x10^{-10} m^2/s for cage **1.12**). Some peaks in the ^{1}H NMR spectrum of **5.5** bear a strong resemblance to those of **1.12**,

indicating that **5.5** partially exists as the *mer*$_3$•*fac* prism (red in Figure 5.4). TOCSY analysis shows the presence of at least 8 dissymmetric methylene units in the system, indicating that the other isomers are all-*fac* tetrahedra with varying symmetry (T, S_4 and C_3).[8,9] The system is complex, but this does not prevent the reactivity from being tested.

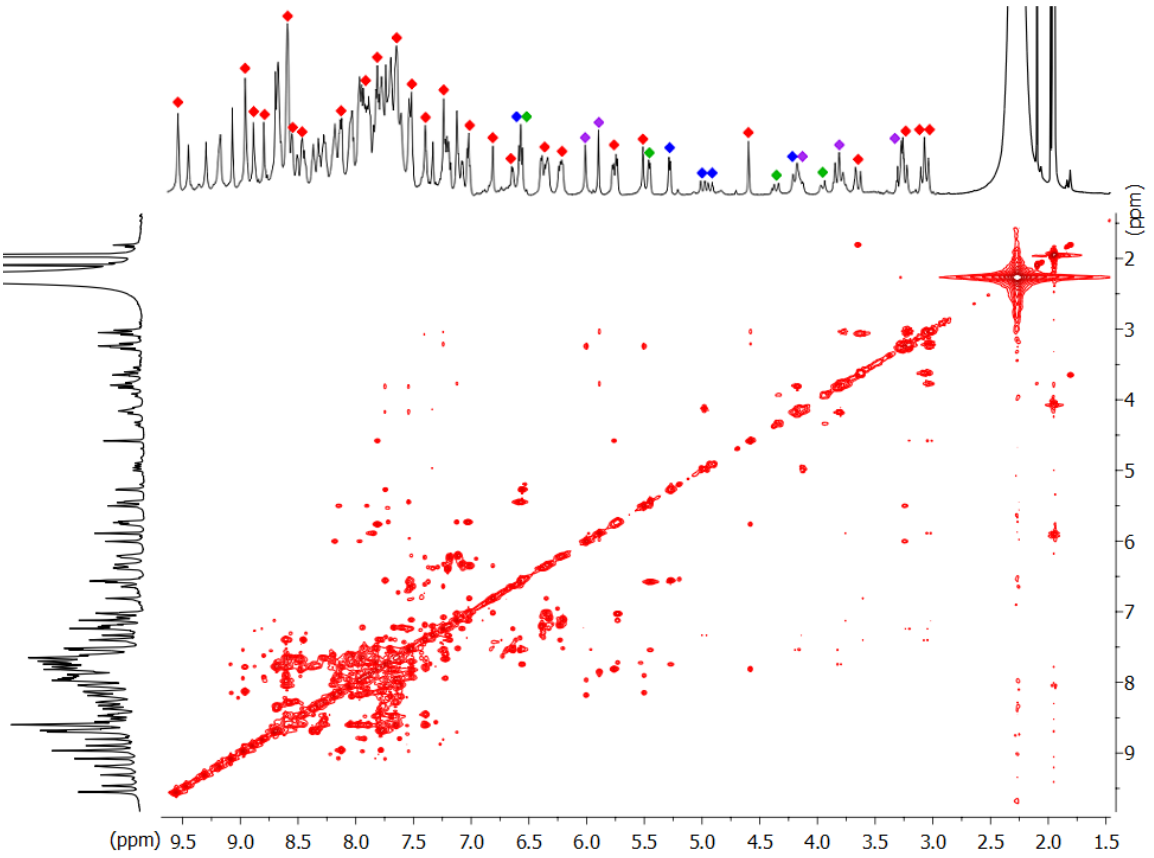

Figure 5.4. TOCSY spectrum of **5.5** (CD_3CN, 600 MHz, 298 K, mixing time = 80 ms). The *mer*$_3$•*fac* prism structure (red), and dissymmetric methylene groups from three other tetrahedral cage isomers (green, purple, and blue) with T, S_4 and C_3 symmetry are identified.

5.3 Oxidation Reactions

Mesocate **5.3** was first screened with a variety of common oxidizing agents under various conditions, including several different peroxides,[10] Dess–Martin periodinane,

potassium permanganate, sodium hypochlorite and oxone.[11] Most of these oxidizing agents yielded either no reaction, with complete recovery of intact cage **5.3** (oxone, mCPBA and Dess-Martin periodinane) or complete decomposition of the cage structure (H_2O_2, $KMnO_4$, NaOCl). However, treatment of **5.3** with ^{t}BuOOH (70 % aqueous solution) in CH_3CN at 23 ºC gave clean conversion to a new discrete complex (Figure 5.5). Monitoring of the reaction over time via NMR indicates complete conversion to product after 5 h, and the reaction maintains the deep purple color of iminopyridine complexes throughout the process, indicating that the Fe^{II} centers have not been oxidized. The ^{1}H NMR spectrum of the product **5.6** was sharp and discrete, with no appreciable shift in the peaks observed at elevated temperatures, confirming that the sample is not paramagnetic. The product was easily isolated and purified by precipitation from the reaction mixture with diethyl ether, and is stable in the solid state. Surprisingly, the spectrum of isolated product **5.6** did not correspond to that of the expected xanthone cage **2.6**. C-H oxidation of doubly benzylic methylene groups invariably forms the ketone as the major product,[12] but not in the case of **5.3**.

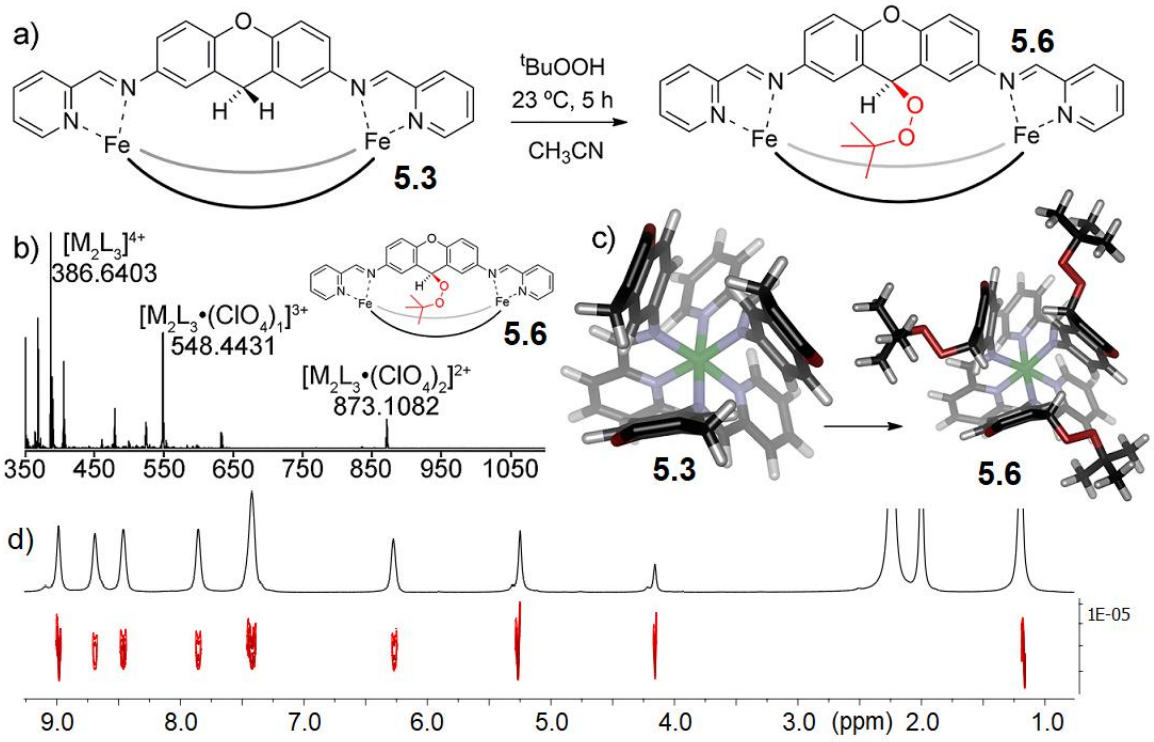

Figure 5.5. a) Synthesis of peroxide product **5.6**; b) Mass Spectrum of product **5.6** showing charged species occurring from loss of perchlorate anions; c) side-on view of the starting cage and product showing orientation of ^{t}Bu groups; d) ^{1}H NMR and DOSY spectrum of cage **5.6** (600 MHz, CD_3CN, 298 K).

Diffusion NMR analysis shows that the product has a nearly identical diffusion constant to that of the parent cage **5.3**, (D (**5.6**) = 1.859 x10^{-9} m^2/s; D (**5.3**) = 1.794 x10^{-9} m^2/s). This analysis suggests that the product maintains the M_2L_3 mesocate stoichiometry. Further analysis via NMR and ESI-MS (Figure 5.5) shows that the structure of product **5.6** is the *tris* ^{t}butyl peroxide intermediate of the oxidation process. A single, symmetric isomer of product is clearly formed, as can be seen by the simplicity of the ^{1}H NMR spectrum. The only symmetric isomeric possibilities of **5.6** place the three ^{t}BuOO- groups either all-in or all-out. Molecular modeling of **5.6** (Figure 5.5c) shows that the all-out isomer is the only realistic possibility, as significant steric clashes between inwardly facing ^{t}Bu peroxide

groups would occur in the all-in isomer. ROESY NMR corroborates the assignment of **5.6** as the all-out isomer, with NOE enhancements observed between the tert-butyl group and the distal backbone C-H (ortho to the xanthyl O atom). The *tris*-^{t}butylperoxide product **5.6** is quite stable: no conversion to other products is observed upon heating at 70 ºC for 3 days and addition of a large excess of ^{t}BuOOH to the reaction did not cause any further oxidation.

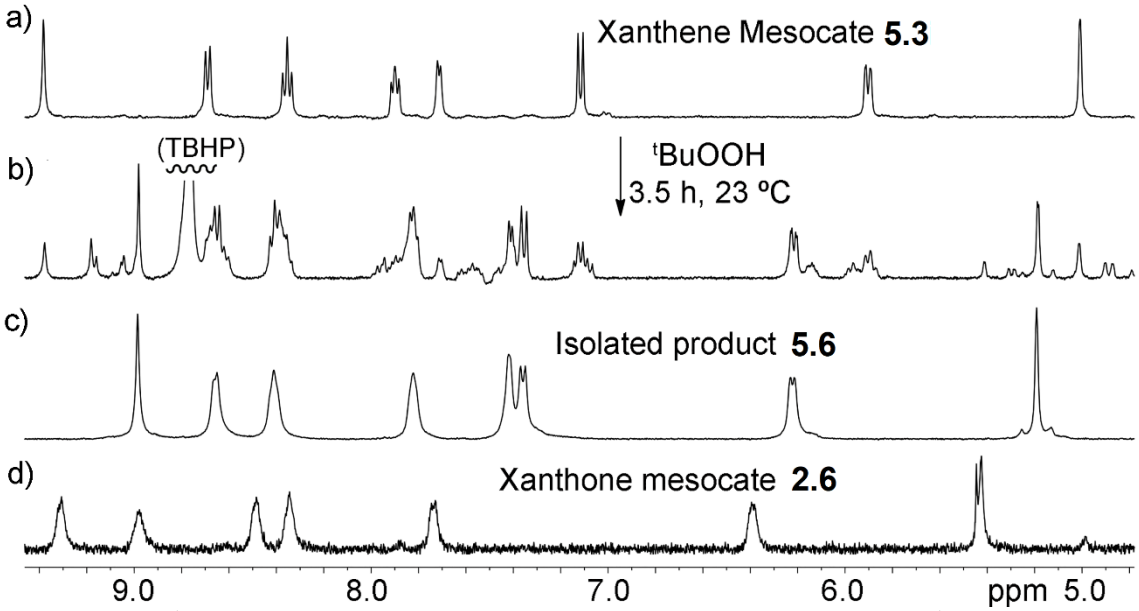

Figure 5.6. a) ^{1}H NMR spectra (400 MHz, CD_3CN, 298 K) of mesocate **5.3**; b) ^{1}H NMR spectrum of the reaction mixture of **5.3** and ^{t}BuOOH after 3.5 h at 23 ºC; c) ^{1}H NMR spectrum of the isolated product **5.6** after reacting with ^{t}BuOOH for 5 h at 23 ºC; d) ^{1}H NMR spectrum of independently prepared xanthone M_2L_3 mesocate **2.6**.

The simple spectrum of **5.3** allowed *in situ* reaction monitoring via ^{1}H NMR, and clearly shows the *mono*- and *bis*-oxidized intermediates (Figures 5.6b and 5.7), as reactant **5.3** is consumed and product **5.6** formed. The reaction proceeds cleanly, and in this case, peaks for the reaction intermediates can be clearly seen as ^{t}butyl peroxide groups are sequentially added to the complex. Three peaks for each of the imine protons in the two

desymmetrized intermediates are observed, which collapse to a single symmetric peak in product **5.6**. At no point during the reaction are any peaks observed for dissociated ligand or hydrolyzed diaminoxanthene ligand **5.2**, even in the presence of water from the ^{t}BuOOH solution. In addition, no other intermediates corresponding to ketone or hydroxyl oxidation products are seen.

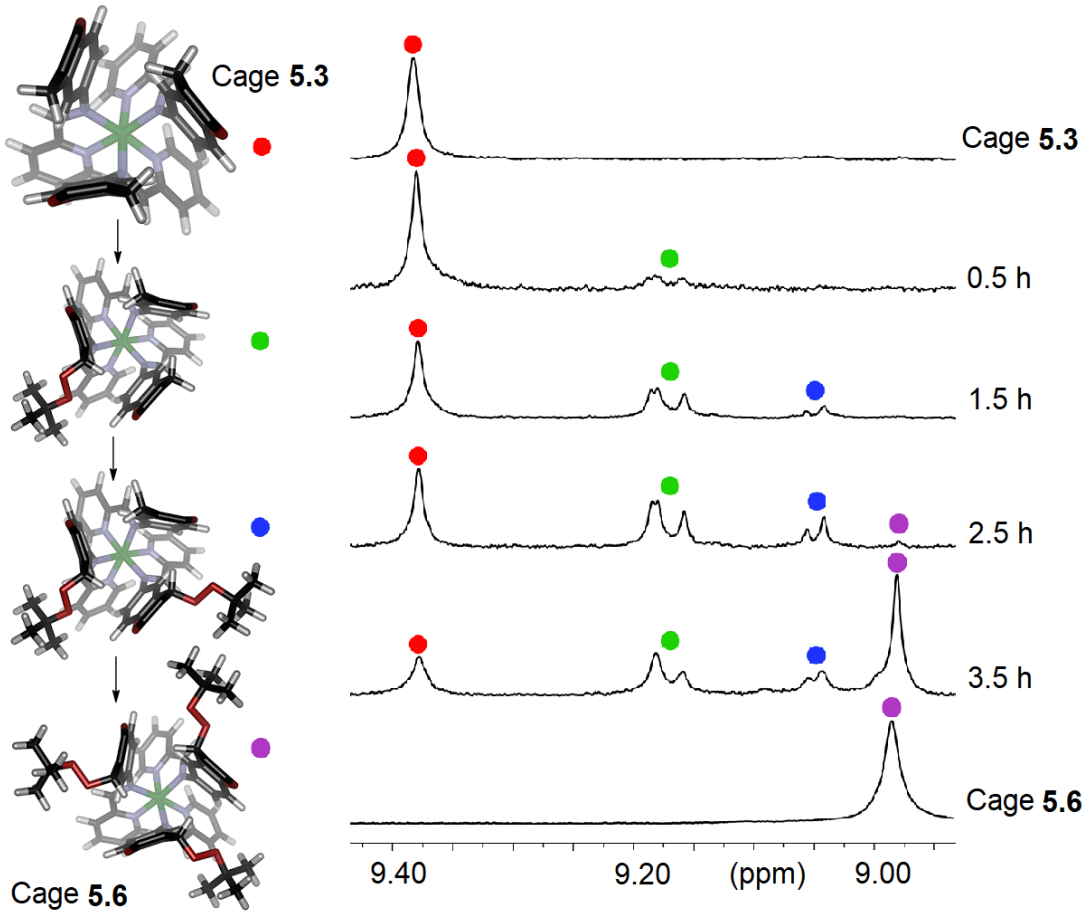

Figure 5.7. Expanded ^{1}H NMR spectra (imine CH region) of the reaction of **5.3** and ^{t}BuOOH over time, illustrating reactant **5.3** (red), *mono*-oxidized (green), and *bis*-oxidized (blue) intermediates, and the symmetrical product **5.6** (purple).

The simplicity and surprising product of the reaction of mesocate **5.5** with ^{t}BuOOH suggested the possibility that larger, more complex cages would be amenable to

derivatization. As dianiline **5.4** displays a similar backbone to 2,7-diaminofluorenol[8] and contains a similarly reactive methylene to **5.2**, we envisioned that this would be a suitable component for self-assembled cage formation and oxidation. The complexity of the ^{1}H NMR spectrum of fluorene cage **5.5** does not prevent analysis of the reactive properties of the methylene units, and we subjected **5.5** to the same conditions as cage **5.3**.

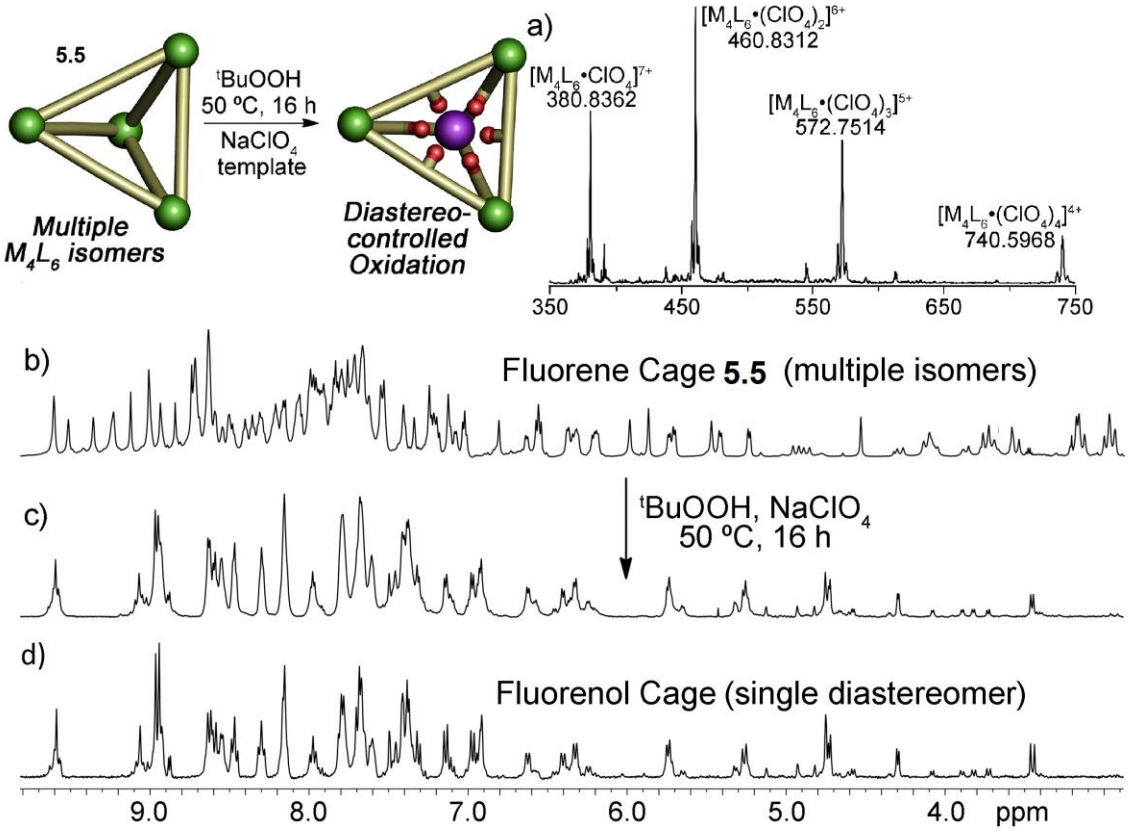

Figure 5.8. a) ESI mass spectrum of the product observed after reacting **5.5** with ^{t}BuOOH and $NaClO_4$. b) ^{1}H NMR spectrum (600 MHz, CD_3CN, 298 K) of the multiple isomers of M_4L_6 cage **5.5**; c) ^{1}H NMR spectrum of the product of reacting **5.5** with ^{t}BuOOH and $NaClO_4$; d) ^{1}H NMR spectrum of independently prepared fluorenol cage **1.12**.

When cage **5.5** was reacted with ^{t}BuOOH at 23 °C, no reaction occurred within 24 h. Evidently, the methylene group on the fluorene scaffold is less reactive than xanthene,

so the reaction was repeated at elevated temperatures until conversion to a new product was observed. Heating **5.5** with ^{t}BuOOH (70 % aqueous solution) in CH_3CN at 50 ºC for 16 h in the presence of 1 mol.-eq. $NaClO_4$ template yielded complete conversion to a new product, the ^{1}H NMR spectrum of which corresponded exactly to independently synthesized fluorenol cage **1.12** (Figure 5.8d). Again, the expected ketone product, in this case a fluorenone M_4L_6 cage **1.13** was not observed. The ESI mass spectrum of the isolated product (Figure 5.8a) is dominated by peaks corresponding to the series of ions $[M_4L_6•(ClO_4)_{1-4}]^{4-7+}$, with no obvious peaks for ketone byproducts. $NaClO_4$ was added to the reaction mixture as a template to aid formation of the analyzable single isomer of **1.12**•ClO_4. When ClO_4^- template was not added to the reaction, the product obtained is an uncontrolled mixture and the ^{1}H NMR spectrum showed only broad, unassignable mounds.

5.4 Oxidation Reactions of Control Ligands

To investigate how the oxidation proceeds and why the assemblies form rarely observed intermediates as the final products, we attempted several control experiments with diamides **5.7** and **5.8** as surrogates for the non-assembled ligands. The control ligands were each synthesized in one step by reacting the dianiline ligands with acyl chlorides (acetyl or butyryl) in the presence of triethylamine. The acetylated xanthene control ligand was highly resistant to dissolution in acetonitrile, so butyryl chloride was used to aid in the overall solubility of the control ligand.

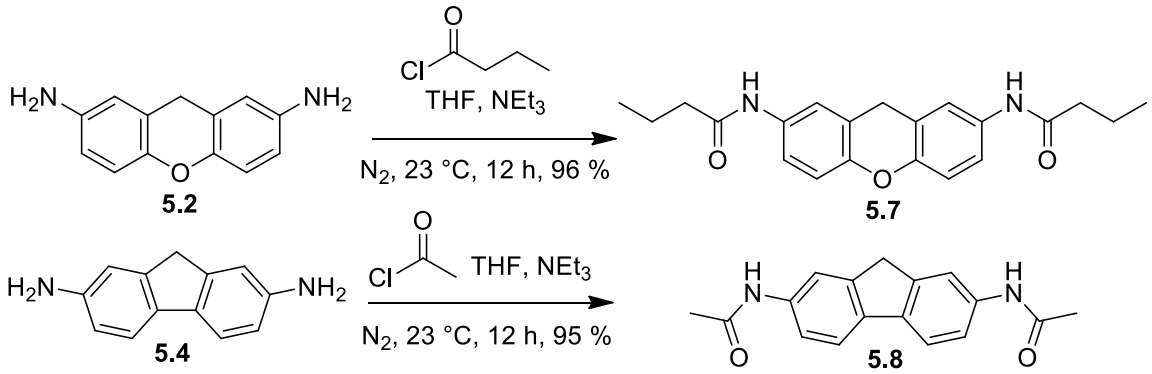

Figure 5.9. Synthesis of the two control compounds from dianiline ligands **5.2** and **5.4**. The same method was used to synthesize the expected xanthone and fluorenone derivatives **5.9** and **5.10** respectively.

Ligand surrogate **5.7** was exposed to identical conditions required for the complete conversion of **5.3** to **5.6**, i.e. 1.1 mol.-eq. ^{t}BuOOH in CH_3CN at 23 ^{o}C for 5 h. Surprisingly, under these conditions, **5.7** is completely inert, and no conversion was observed even at 50 ^{o}C or over extended periods of time. It is unlikely that the assembly itself has any drastic activating effect on the methylene units, so we attempted the reaction again with the addition of 10 % $Fe(ClO_4)_2$ as a catalyst. In the presence of metal, complete conversion of **5.7** to ketone **5.9** was observed after 3.0 h at 23 ^{o}C. As expected, the product of oxidation of **5.7** was not the peroxide adduct, but ketone **5.9**. Similarly, no reaction of **5.8** was observed in the absence of Fe^{II}, and ketone **5.10** was the major product observed upon addition of 10 % $Fe(ClO_4)_2$ (see Table 5.1) The fluorene scaffold was more sluggish towards oxidation than the xanthene, and **5.8** required 12 h reaction at 50 ^{o}C to reach completion. Neither control showed any evidence of alcohol or ^{t}BuOO- intermediates during the reaction (Figures 5.10 and 5.11).

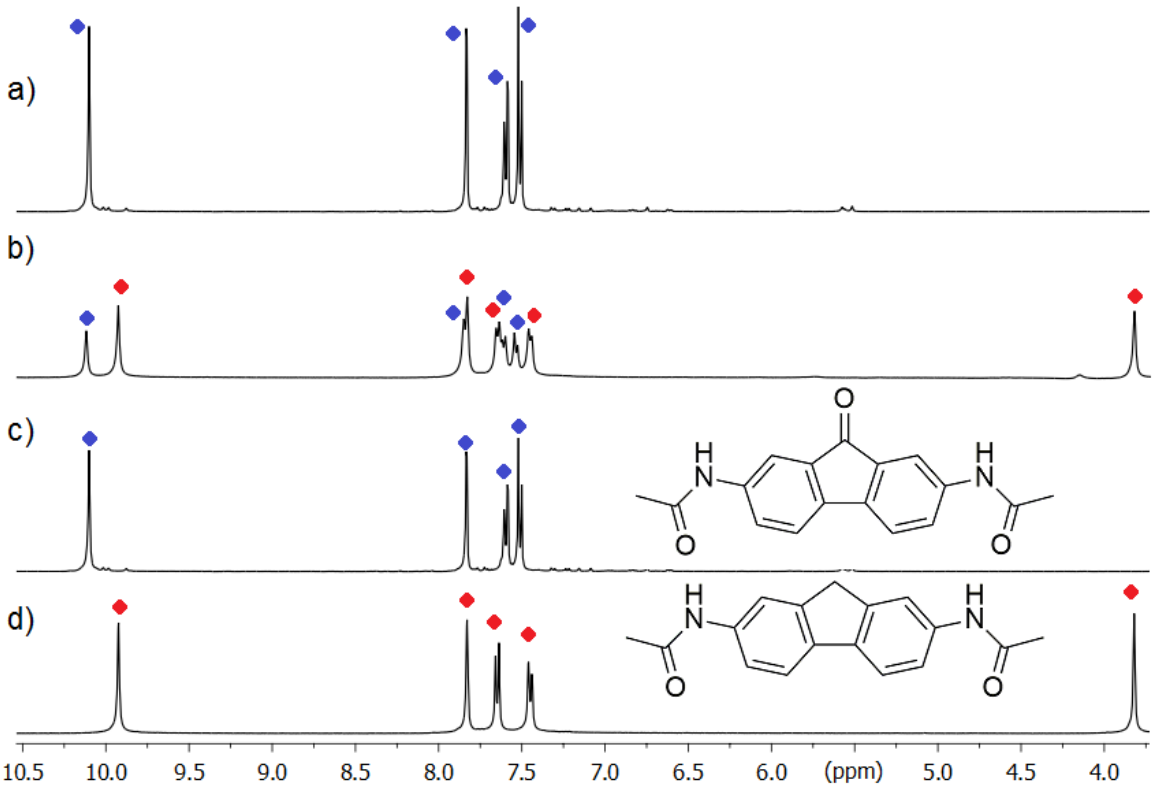

Figure 5.10. ^{1}H NMR of ligand surrogate **5.8** mixed with 1.1 mol.-eq. *tert*-butyl hydroperoxide and catalytic (0.1 mol.-eq.) $Fe(ClO_4)_2$ for a) 12 h at 50 ˚C and b) 5 h at 50 ˚C; c) expected ketone product **5.10**; d) control **5.8** (CD_3CN, 400 MHz, 298 K).

The oxidation process requires Fe^{II} as a catalyst and, as there is minimal free Fe^{II} present in **5.3**/**5.5** after isolation and purification as verified by elemental analysis, two possibilities exist. The most likely is that small amounts of iminopyridine ligand can dissociate away from the Fe^{II} vertices of the complex, allowing for catalysis of the oxidation reactions. The self-assembled systems are reversible and small amounts of water from the peroxide solutions could facilitate temporary hydrolysis of the ligands in addition to iminopyridine dissociation. The second possibility is that the cages themselves are catalytically active. However, as the intact M_2L_3 complexes have very small internal cavities for binding, it is highly unlikely that the complexes are behaving as host species.

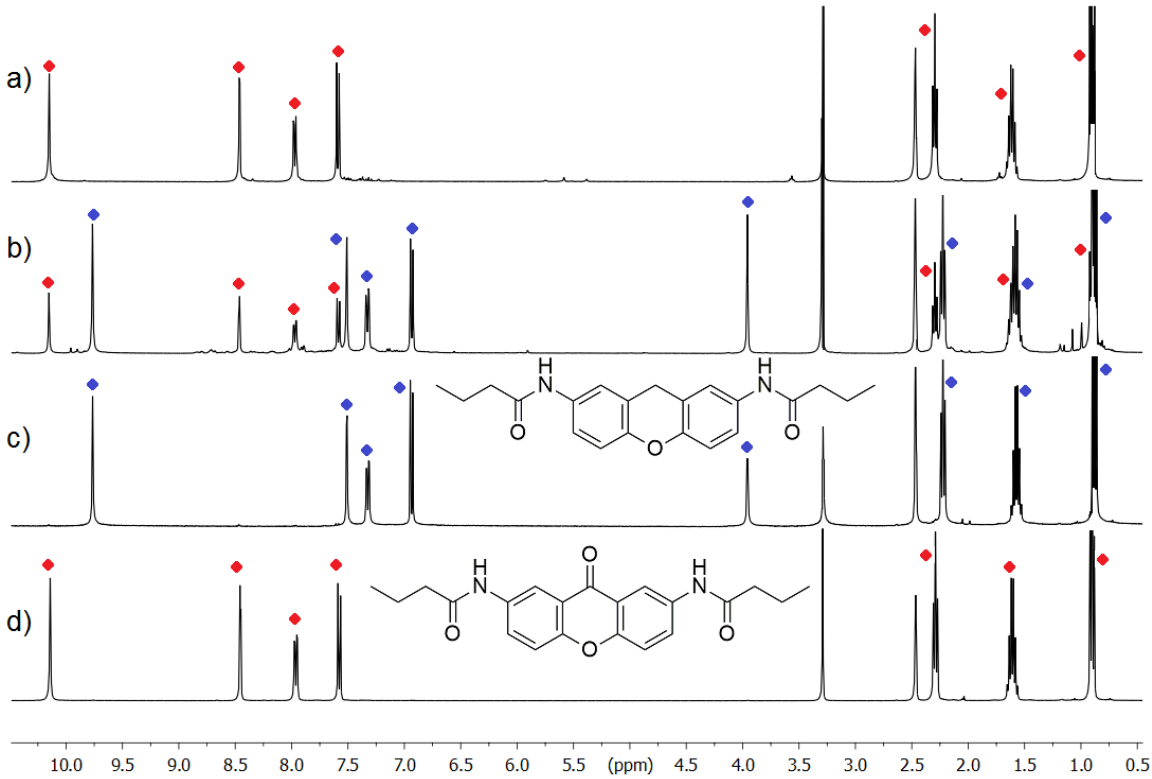

Figure 5.11. ^{1}H NMR of ligand surrogate **5.7** mixed with 1.1 mol.-eq. *tert*-butyl hydroperoxide and catalytic xanthone cage **2.6** (10 mol % iron total) for a) 2 h at 23 ˚C and b) 1 h at 23 ˚C; c) expected ketone product **5.9**; d) surrogate **5.7** (CD_3CN, 400 MHz, 298 K).

The mechanism of Fe^{II}-based hydrocarbon oxidation reactions has been carefully studied, and Fe^{II} catalysts require two free coordination sites to allow formation of the reactive Fe^{V}-oxo species,[13] so it is unlikely that the intact M_2L_3 cages themselves are the active catalysts. To test this, we used coordinatively saturated $Fe(bipy)_3(ClO_4)_2$ as catalyst, with minimal reaction occurring after 16 h at 23 °C. When 10 % xanthone cage **2.6** was used, conversion was similar to that seen in the trials utilizing free $Fe(ClO_4)_2$, giving the ketone products **5.9** and **5.10** in 58 % and 62 % conversion after 1 h and 5 h, respectively. Dissociation of an iminopyridine chelator from Fe^{II} centers does occur in solution, and could provide the two open coordination sites necessary for catalysis. The exposed Fe^{II}

then catalyzes the oxidation of the remaining, intact cage. The observed yields of oxidized cage product range from 89-95 % **5.6** (4 separate runs) and from 84-89 % (3 separate runs) **1.12**. It should be noted that no free dianiline ligand or disassembled cage was observed during the reaction of **5.3** (the complex NMR spectrum of **5.5** and **1.12** precludes accurate analysis over time). While some product is lost, the reactions are remarkably efficient. In addition, the coordinating Fe^{II} ions of the M_2L_3 product remain unaffected and oxidation occurs selectively on the ligand backbone.

Table 5.1. Oxidation outcomes for control ligand surrogates.[a]

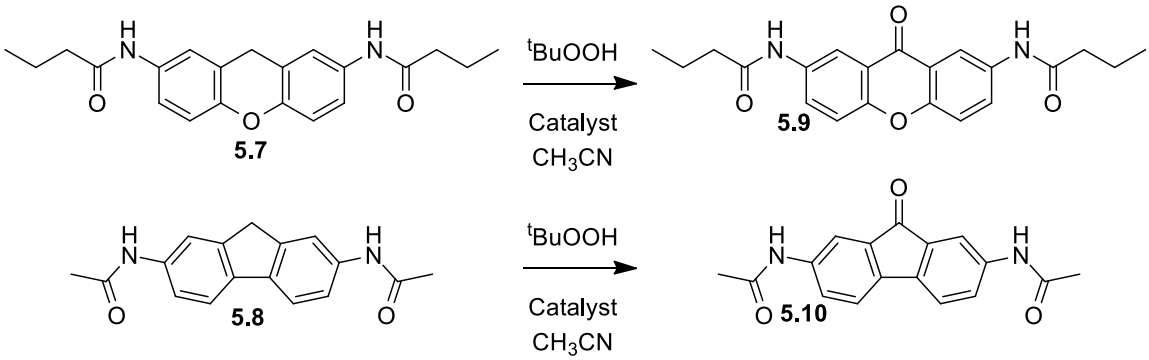

Substrate	t, h	T, ºC	Catalyst	Product, Conversion
5.7	8	50	none	no rxn
5.7	1	23	10 % $Fe(ClO_4)_2$	**5.9**, 52 %
5.7	16	23	10 % $Fe(Bipy)_3(ClO_4)_2$	**5.9**, 4 %
5.7	1	23	10 % cage **2.6**	**5.9**, 58 %
5.8	8	50	none	no rxn
5.8	5	50	10 % $Fe(ClO_4)_2$	**5.10**, 45 %
5.8	16	50	10 % $Fe(Bipy)_3(ClO_4)_2$	**5.10**, 8 %
5.8	5	50	10 % cage **2.6**	**5.10**, 62 %

[a] 1.1 mol.-eq. ^{t}BuOOH used.

5.5 Unfavorability of Ketone Cage Products

The ligand-centered oxidations of complexes **5.3** and **5.5** occur without degrading the assembly products. Considering their reversible nature and general intolerance towards nucleophiles, the overall reaction is quite impressive. In addition, the observed oxidation products are not common, and are directed by the self-assembled structure. Given the option, free and coordinated Fe^{II} salts oxidize fluorenyl and xanthenyl substrates to ketones with ^{t}BuOOH. This mechanism is well studied,[14] and occurs via formation of a reactive Fe=O species that abstracts a hydrogen atom from the CH_2, leaving a stabilized radical (Figure 5.12). Of course, Fe^{II} salts can also form $^{\bullet}$OH, $^{\bullet}$O^{t}Bu or $^{\bullet}$OO^{t}Bu radicals upon reaction with ^{t}BuOOH which can abstract hydrogen atoms as well.[15] It is likely that the final peroxide adduct is formed via reaction of an Fe-OO^{t}Bu complex with the radical intermediate and only occurs on the cage exterior.

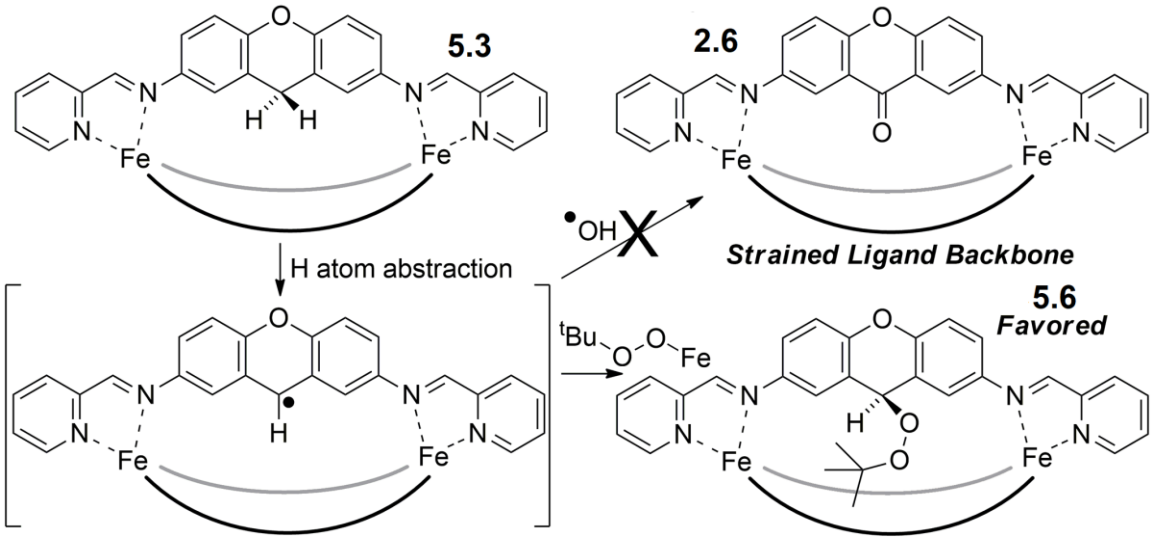

Figure 5.12. Radical abstraction and recombination to form product **5.6**.

The reason that the expected ketone products are not observed from oxidation of **5.3** and **5.5** lies in the stability of the products formed, or more precisely the unfavorability of the ketone cages. As previously discussed in Chapters 2 and 4, the unfavorability of an assembly can direct self-sorting or reaction outcomes. Xanthone cage **2.6** provides a poor coordination geometry for M_2L_3 complex formation, and the strained mesocate **2.6** is relatively unstable and paramagnetic, as discussed in Chapter 2. Mesocate **5.3** is diamagnetic and far more stable than the ketone derivative, as can be illustrated by ligand displacement from pre-formed cages (Figure 5.13). When **5.2** is added to freshly made **2.6** in CD_3CN, complete displacement of 2,7-diaminoxanthone **2.5** occurs within 4 h at 45 °C. In contrast, **5.3** is completely resistant to displacement by core **2.5**, even after 48 h at 77 °C. The peroxide-bearing complex **5.6** is also more stable than ketone **2.6**, with no displacement of peroxide ligand from **5.6** observed after reacting with core **2.5** at 70 °C for 24 h. Interestingly, unfunctionalized core **5.3** is more stable than peroxide **5.6**: ligand core **5.2** was able to cleanly displace the oxidation product ligand in situ after 8 h at 70 °C. Attempts to isolate the peroxide ligand lead to decomposition. Evidently the peroxide group is stable when complexed, but begins to decompose over time once the ligand core is displaced.

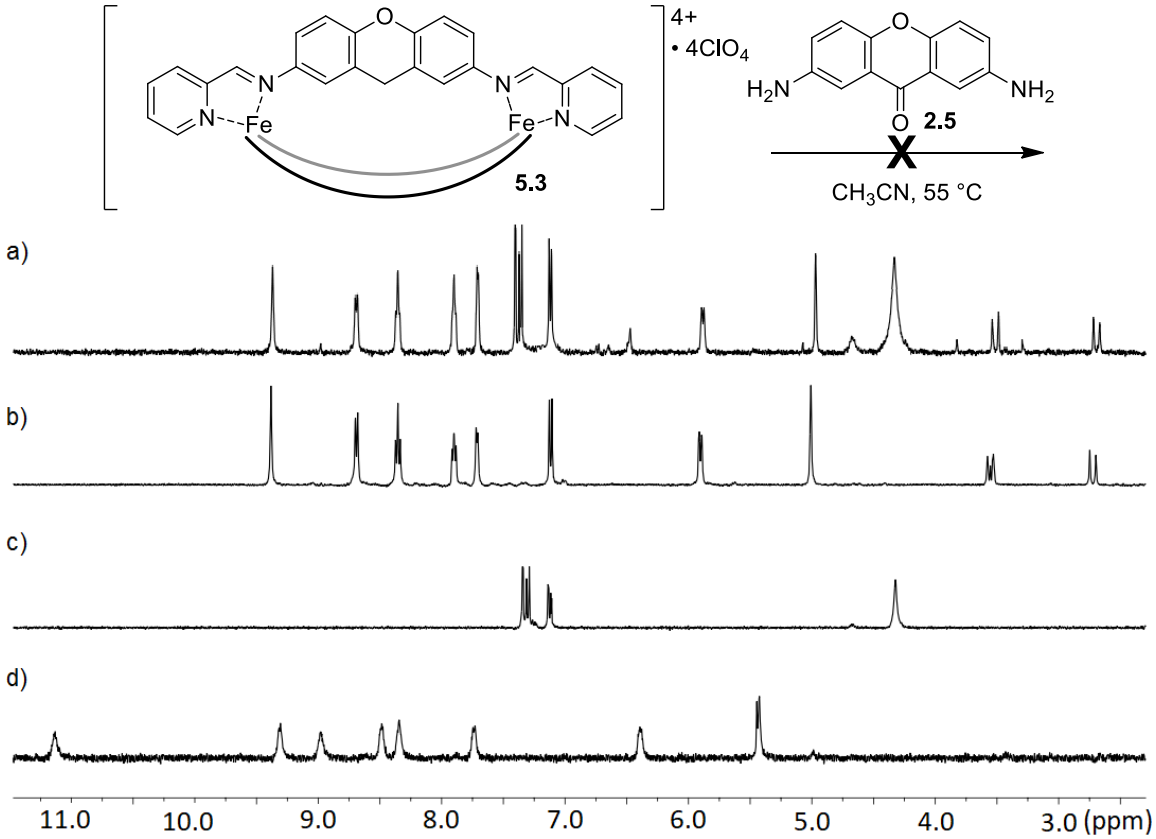

Figure 5.13. ^{1}H NMR spectra of a) mixture of cage **5.3** and 3 mol.-eq. of core **2.5** after 8 h at 55 °C, b) cage **5.3**, c) dianiline **2.5**, d) cage **2.6** (CD_3CN, 400 MHz, 298 K).

The ketone cage **2.6** is paramagnetic, strained and disfavored, but the other obvious outcome of oxidation of **5.3** would be to form the hydroxylated product. To establish why this species is not observed, the alcohol-bearing ligand 2,7-diaminoxanthol **5.11** was synthesized and assembled with $Fe(ClO_4)_2$ and PyCHO (Figure 5.14). Most surprisingly, **5.11** did not form the expected M_2L_3 mesocate upon assembly, but instead forms the M_4L_6 cage product **5.12**. The assembly is stereochemically uncontrolled, as illustrated by the highly complex ^{1}H NMR spectrum, and it is likely that ClO_4^-, while acting as a good template for fluorenol cage **1.12**, is not the proper size to template xanthol cage **5.12**. ESI-MS analysis cleanly shows the presence of $[Fe_4L_6•(ClO_4)_x]^{(8-x)+}$ ion clusters. Additionally,

there were signals corresponding to ions created by the loss of water from the ligand backbone. The xanthol -OH is evidently very easily removed via fragmentation, even more so than dissociation of the assembly.

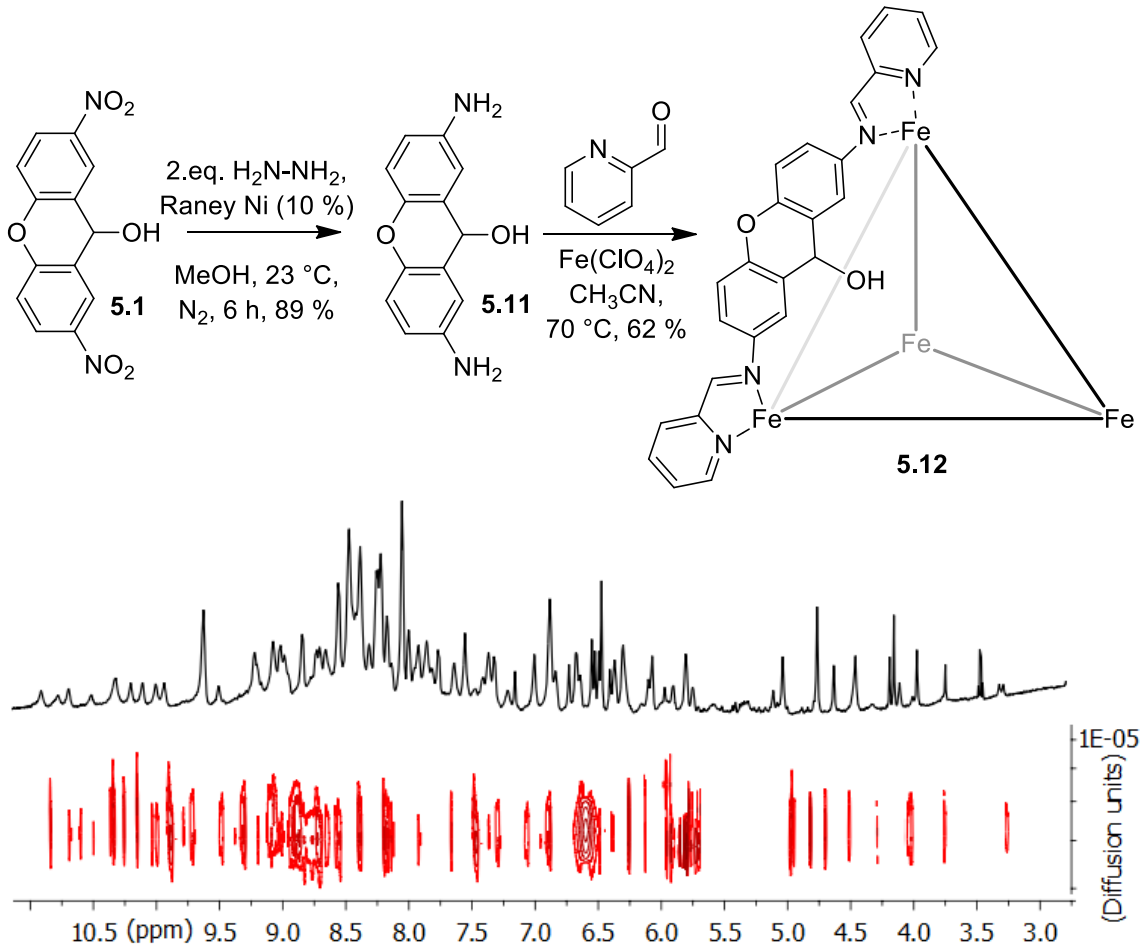

Figure 5.14. Synthesis of the unstable M_4L_6 species **5.12** and ^{1}H DOSY NMR spectrum of cage **5.12** (CD_3CN, 600 MHz, 298 K, Δ = 100 ms, δ = 2.6 µs, Diffusion constant = 8.497 x10^{-10} m^2/s for cage **5.12** vs. 9.641 x10^{-9} m^2/s for the solvent).

While the ^{1}H NMR spectrum of **5.12** is far too complex to be assigned, 2D DOSY analysis shows that all peaks have identical diffusion constants (D (**5.12**) = 8.497 x10^{-10} m^2/s), similar to those of cage **5.5** (D = 9.883 x10^{-10} m^2/s), but much smaller than that of the M_2L_3 mesocate **5.3** (D =1.794 x10^{-9} m^2/s). While it is not clear why **5.11** assembles into

an uncontrolled M_4L_6 system when all other xanthyl ligands tested form M_2L_3 structures, it is obvious that the self-assembly process is disfavored. The assembled M_4L_6 complex is stable enough to be isolated and purified but decomposes in the solid state after ~1 week. Formation of the M_4L_6 assembly **5.12** upon oxidation of **5.3** would require dissociation of the iminopyridine ligands and reorganization of the assembly into a larger, entropically disfavored assembly. Therefore, the oxidation reaction stops at the more favorable *tris*-peroxide intermediate **5.6**. Notably, 2,7-diaminoxanthol is unable to displace the peroxide ligand from tris peroxide **5.6**, xanthene **5.3** or ketone **2.6** even when heated to 70 °C overnight.

5.6 Stereoselectivity of Oxidation Reactions

The oxidation of **5.5** to fluorenol cage **1.12** is also directed by the stability of the product (Figure 5.15). Both 2,7-diaminofluorene **5.4** and 2,7-diaminofluorenone **1.10** cores form complex isomeric mixtures of M_4L_6 cages upon multicomponent self-assembly, whereas the ClO_4^- templated cage **1.12** is favored and stabilized by the presence of endohedral hydrogen-bonds. This stabilizing effect is sufficient to direct the reaction, resulting in **1.12** as the only observed reaction product. When the oxidation reaction is performed on a sample of **5.5** prepared using $Fe(OTf)_2$ with no ClO_4^- template added, multiple uncontrolled products are formed with ESI-MS analysis showing traces of ketone, peroxide and hydroxyl heterocomplexes and ligand cores. Only when $NaClO_4$ is added to the triflate-containing sample does the oxidation reaction produce a single product. This indicates that the fluorene cage oxidation process is thermodynamically controlled. The

templated fluorenol cage is the only stable assembly and thus is the favored product. The oxidation occurs via equilibration only in the presence of a suitable templating ion.

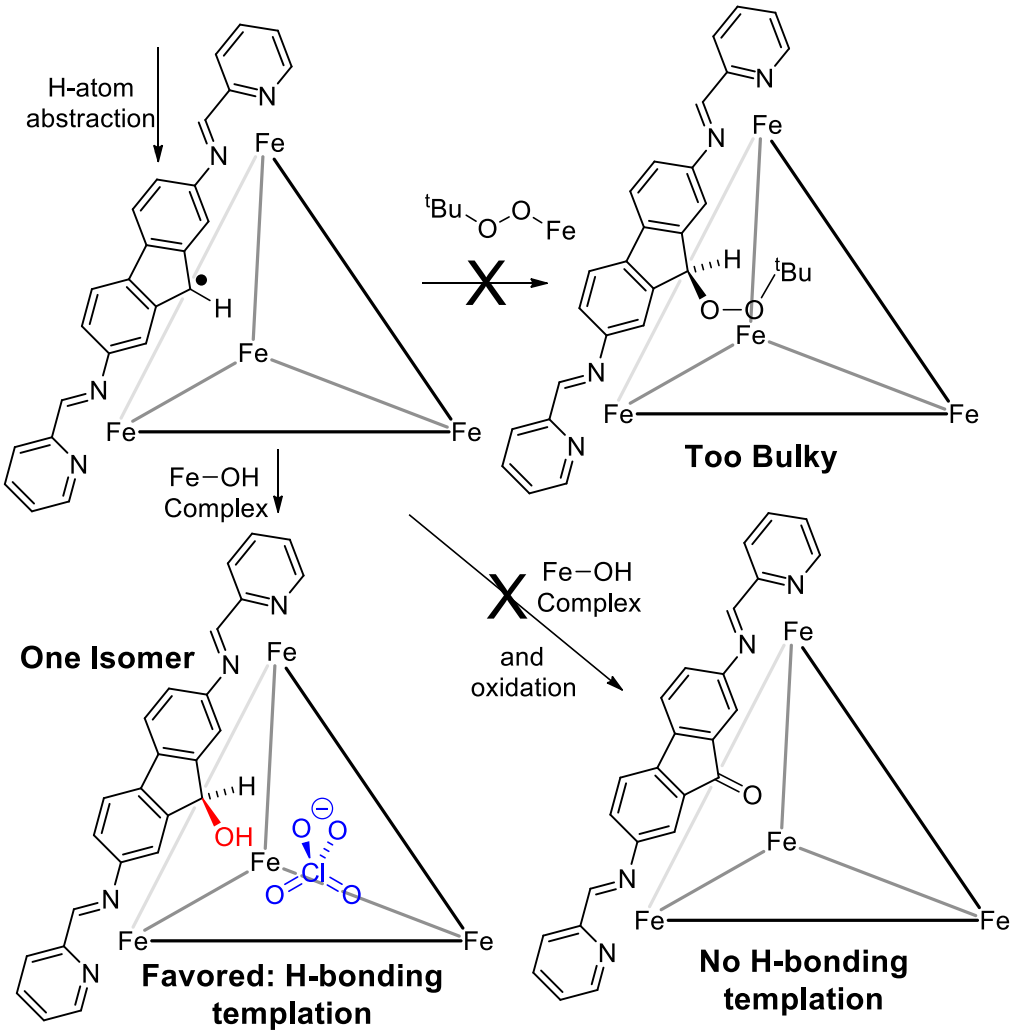

Figure 5.15. Uncontrolled assembly **5.5** exploits favorable H-bonding to form a single isomer of alcohol prism **1.12**. The ketone and peroxide assemblies are too disfavored to form.

In addition to directing the products observed after oxidation, the two methylene cage structures direct the stereochemical outcomes. The oxidation of mesocate **5.3** gives the all-out diastereomer of **5.6**, and oxidation of cage **5.5** yields a single diastereomer of

M_4L_6 prism **1.12**. In each case the stability of the product and the reversibility of the assembly controls the stereochemical outcome. The oxidation of **5.3** likely occurs only on the hydrogens pointing away from that center of the complex: the M_2L_3 assembly remains intact throughout the reaction as can be observed by the sequential addition of the ^{t}BuOO- groups. Ligand exchange in M_2L_3 mesocates can occur, but all our previous experiments involving ligand exchange indicate that some heat is required for this to occur unless the difference in energy between product and starting material is high.[16] It is likely that in this case, the kinetic and thermodynamic product are the same: there is no internal cavity to speak of and all other isomers are repulsively disfavored.

While the oxidation product of **5.5** is different from that of **5.3**, the self-assembled structure also directs the reaction stereochemistry: in this case, favorable H-bonding templation directs the oxidation away from the expected ketone and to the alcohol product. The stereochemical fidelity is even more impressive: whereas **5.6** has no cavity, and the all-out isomer is obviously most stable due to steric effects, only self-complementary H-bonding directs the formation of **1.12**.

5.7 Conclusion

Here, we have shown that post-assembly modification can be performed on reversibly formed self-assembled cage complexes and that the uncommon products observed are directed by the self-assembled structure itself. Ligand centered CH oxidation reactions can occur on Fe^{II}-containing self-assembled cages via a radical mechanism and exploit small amounts of dissociated Fe^{II} as the oxidation catalyst. Despite this, high yields

of the diastereocontrolled oxidation products can be obtained with no observed degradation of the coordinating Fe^{II} centers. The physical structure of the assemblies directs the reaction outcome: while non-assembled ligands favor complete oxidation to the ketone, the reaction of **5.3** and **5.5** forms the ^{t}Bu peroxide and alcohol-bearing products respectively. The introduction of stereocenters to the products is stereocontrolled, with excellent diastereoselectivity observed. Only single isomers are formed despite the presence of multiple new stereocenters in the final product. The self-assembled structures exploit self-complementary hydrogen bonding and geometrical constraints to direct the post-assembly reactions to outcomes not observed in free solution.

5.8 References

1. Newhouse, T.; Baran, P. S. "If C–H Bonds Could Talk – Selective C–H Bond Oxidation." *Angew. Chem., Int. Ed*. **2011**, *50*, 3362-3374.

2. Chen, M. S.; White, M. C. "A Predictably Selective Aliphatic C-H Oxidation Reaction for Complex Molecule Synthesis." *Science* **2007**, *318*, 783-787.

3. Burke, M. J.; Nichol, G. S.; Lusby, P. J. "Orthogonal Selection and Fixing of Coordination Self-Assembly Pathways for Robust Metallo-Organic Ensemble Construction." *J. Am. Chem. Soc*. **2016**, *138*, 9308-9315.

4. Symmers, P. R.; Burke, M. J.; August, D. P.; Thomson, P. I. T.; Nichol, G. S.; Warren, M. R.; Campbell, C. J.; Lusby, P. J. "Non-Equilibrium Cobalt(III) "Click" Capsules." *Chem. Sci.* **2015**, *6*, 756-760.

5. Holloway, L. R.; Young, M. C.; Beran, G. J. O.; Hooley, R. J. "High Fidelity Sorting of Remarkably Similar Components Via Metal-Mediated Assembly." *Chem. Sci*. **2015**, *6*, 4801-4806.

6. Young, M. C.; Holloway, L. R.; Johnson, A. M.; Hooley, R. J. "A Supramolecular Sorting Hat: Stereocontrol In Metal–Ligand Self-Assembly by Complementary Hydrogen Bonding." *Angew. Chem., Int. Ed*. **2014**, *53*, 9832-9836.

7. Meng, W.; Clegg, J. K.; Thoburn, J. D.; Nitschke, J. R. "Controlling the Transmission of Stereochemical Information Through Space in Terphenyl-Edged Fe_4L_6 Cages." *J. Am. Chem. Soc.* **2011**, *133*, 13652-13660.

8. Meng, W.; Ronson, T. K.; Nitschke, J. R. "Symmetry Breaking in Self-Assembled M_4L_6 Cage Complexes." *Proc. Natl. Acad. Sci. U.S.A.* **2013**, *110*, 10531-10535.

9. Clegg, J. K.; Cremers, J.; Hogben, A. J.; Breiner, B.; Smulders, M. M. J.; Thoburn, J. D.; Nitschke, J. R. "A Stimuli Responsive System of Self-Assembled Anion-Binding $Fe_4L_6^{8+}$ Cages." *Chem. Sci*. **2013**, *4*, 68-76.

10. Asahara, H.; Nishiwaki, N. "Metal-Free α-Hydroxylation of α-Unsubstituted β-Oxoesters and β-Oxoamides." *J. Org. Chem.* **2014**, *79*, 11735-11739.

11. Moriyama, K.; Takemura, M.; Togo, H. "Direct and Selective Benzylic Oxidation of Alkylarenes via C–H Abstraction Using Alkali Metal Bromides." *Org. Lett.* **2012**, *14*, 2414-2417.

12. Chen, M. S.; White, M. C. "Combined Effects on Selectivity in Fe-Catalyzed Methylene Oxidation." *Science* **2010**, *327*, 566-571.

13. Que, L.; Tolman, W. B. “Biologically Inspired Oxidation Catalysis.” *Nature* **2008**, *455*, 333-340.

14. Rabion, A.; Chen, S.; Wang, J.; Buchanan, R. M.; Seris, J.-L.; Fish, R. H. “Biomimetic Oxidation Studies. 9. Mechanistic Aspects of the Oxidation of Alcohols with Functional, Active Site Methane Monooxygenase Enzyme Models in Aqueous Solution.” *J. Am. Chem. Soc.* **1995**, *117*, 12356-12357.

15. MacFaul, P. A.; Arends, I. W. C. E.; Ingold, K. U.; Wayner, D. M. “Oxygen Activation by Metal Complexes and Alkyl Hydroperoxides. Applications of Mechanistic Probes to Explore the Role of Alkoxyl Radicals in Alkane Functionalization.” *J. Chem. Soc., Perkin Trans.* **1997**, *2*, 135-145.

16. Bogie, P. M.; Holloway, L. R.; Lyon, Y.; Onishi, N. C.; Beran, G. J. O.; Julian, R. R.; Hooley, R. J. “A Springloaded Metal-Ligand Mesocate Allows Access to Trapped Intermediates of Self-Assembly” *Inorg. Chem.* **2018**, *57*, 4155-4163.

Chapter 6: Catalytic and Tandem Reactivity of a Self-Assembled Cage Catalyst Containing Endohedral Acid Groups

6.1 Introduction

Post assembly modification is a useful tool for the creation of functional assemblies, and was performed on reactive systems containing alkyl chloride or doubly benzylic methylene units as discussed in Chapters 4 and 5. In both cases, mild oxidizing conditions were used, and the reactions were performed in the presence of redox active Fe^{II} atoms without oxidation of the metal centers. The transformations were stereoselective and gave single diastereoisomers of product in high yield. However, the isolated assemblies bearing ketone, alcohol and ^{t}Bu peroxide functionalities are quite stable and the complexes possess only small or non-existent internal cavities for host studies and catalysis.

The overarching goal is to synthesize reactive complexes, and so the focus was shifted from reactions performed on the supramolecular assemblies to potential reactions catalyzed by the complexes. To effectively synthesize useful supramolecular hosts, larger ligands must be created. The fluorene core exhibits the correct coordination angle to orient functional groups toward the interior and contains a reactive handle for functionalization. However, the cavity of fluorene cage **5.5** is too small to accommodate reactive groups, therefore, the length of the dianiline must be increased to produce a host complex. In addition, to include reactive endohedral groups to the ligand scaffold they must not interfere with the assembly process. Here the synthesis of two new extended fluorenyl cores, the creation of a large M_4L_6 complex containing twelve internalized functional groups, and the catalytic applications of the novel acid-bearing complex are described.

6.2 Synthesis of New Cage Complexes

In Chapter 5 it was demonstrated that the 2,7-diaminofluorene core self-assembles into a mixture of M_4L_6 complex isomers. Although the cavity is too small to be useful as a host, the doubly benzylic methylene group provides a handle for endohedral functionalization. An extended dianiline ligand was synthesized via Suzuki coupling of commercially available 2,7-dibromofluorene and 4-Boc-aminophenylboronic acid, followed by deprotection in neat trifluoroacetic acid (TFA) and neutralization to give dianiline **6.2** in 84 % overall yield.

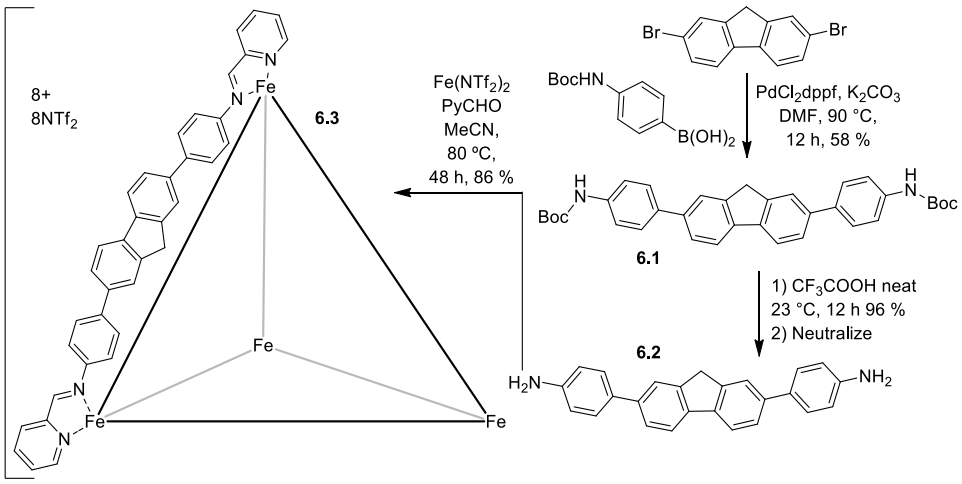

Figure 6.1. Synthesis of extended fluorene dianiline core **6.2** and assembly **6.3**.

Treatment of ligand **6.2** with 2 mol. eq. 2-formylpyridine (PyCHO) and 0.66 mol. eq. $Fe(ClO_4)_2$ was not successful. However, when $Fe(NTf_2)_2$ was utilized, a discrete and highly soluble complex was formed as shown in Figure 6.2. The ESI-MS spectrum for assembly **6.3** demonstrated the usual pattern of sequential loss of counter anions, and peaks for the $[\mathbf{6.3}]^{8+}$, $[\mathbf{6.3}\bullet NTf_2]^{7+}$ and $[\mathbf{6.3}\bullet(NTf_2)_4]^{4+}$ species were observed, as well as some

fragments corresponding to the M_2L_3 complex. This species was not observed in the ^1H NMR spectrum of **6.3**, which exhibits discrete peaks in each expected region that all correspond to the same diffusion constant. This indicates that the smaller M_2L_3 species only exists in the mass spectrum and is likely due to fragmentation of the M_4L_6 cage.

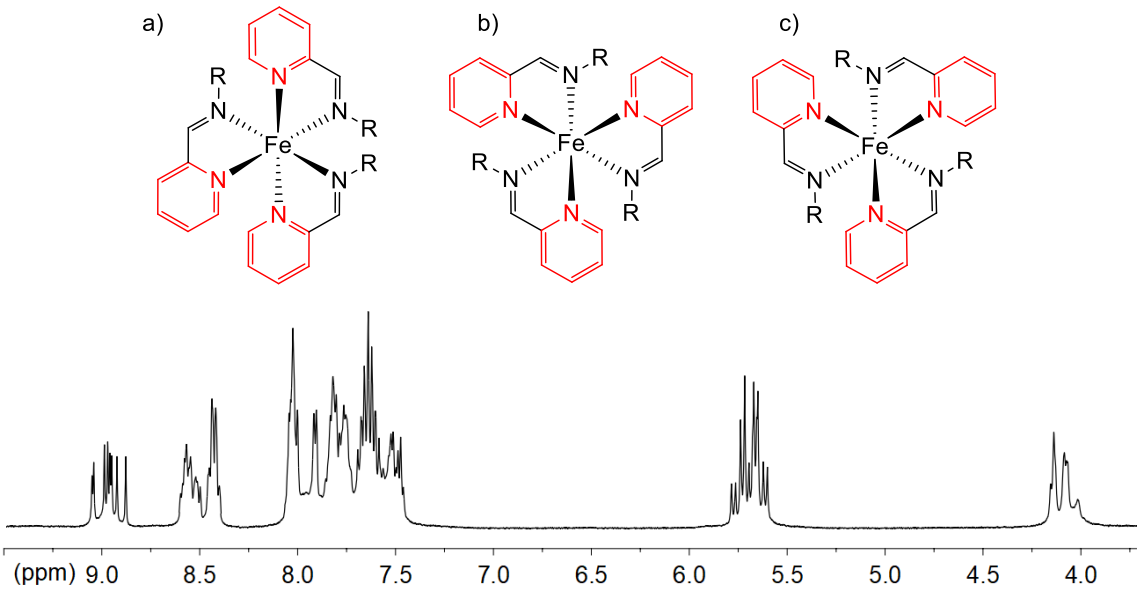

Figure 6.2. Isomeric possibilities of octahedral metal centers: a) meridional; b) facial-Λ; c) facial-Δ and ^1H NMR of the unfunctionalized fluorene cage **6.3** (600 MHz, 298 K, CD_3CN).

The complex spectrum of **6.3** is due to the multiple isomers arising from the stereochemical possibilities of the metal centers. There are a variety of isomeric possibilities for M_4L_6 assemblies.[1] The most common contains all-*fac* coordination at the metal centers, giving rise to three isomeric possibilities based on the orientation of the *fac* centers: the S_4 symmetric ΔΔΛΛ, C_3 symmetric ΔΛΛΛ, and tetrahedral ΔΔΔΔ isomers (cartoon representations are shown in Figure 6.5).[2,3] Other possibilities exist with *mer* coordination at the metal center, but these show far more complex NMR spectra.[4]

With the discrete fluorene complex **6.3** in hand, the synthesis of a cage containing endohedral functional groups was attempted. Carboxylic acids are an ideal target as Fe^{II}-iminopyridine self-assemblies are not disrupted by mild acids or structurally similar groups like sulfate anions.[5] Dianiline ligand **6.6** was synthesized using a similar method to that of **6.2** and was initially prepared by Paul Bogie, a coworker in the Hooley lab who collaborated in developing the scheme shown in Figure 6.3 along with alternate methods to obtain the ligand core **6.6**.

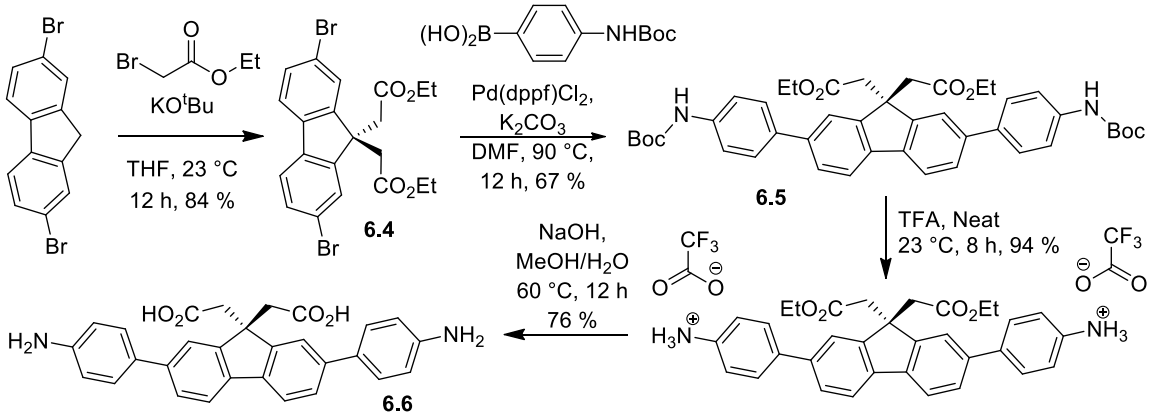

Figure 6.3. Synthesis of ligand **6.6** from commercially available 2,7-dibromofluorene.

To synthesize the functional cage, core **6.6** was mixed with PyCHO and $Fe(NTf_2)_2$ in acetonitrile at 80 °C for 48 h. The acetonitrile was filtered to remove any insoluble impurities, the solvent removed *in vacuo*, and the purple solid washed with a 1:3 solution of MeOH:Et_2O. The assembly of the acidic cage suffered from lower yields than previously synthesized iminopyridine scaffolds, but still produced a discrete structure similar to that of **6.3** (Figure 6.4). ESI-MS analysis of cage **6.7** collected by Yana Lyon in the Julian Group showed only ion peaks corresponding to an M_4L_6 stoichiometry, plus uncoordinated bis-

imine ligand. Interestingly, the observed ions are of [**6.7**-H]$^{7+}$, [**6.7**-2H]$^{6+}$ and [**6.7**•2NTf$_2$]$^{6+}$, resulting from loss of all 8 triflimide anions and deprotonation of 1-3 of the carboxylic acid groups, as opposed to the sequential loss of anions typically observed in the ESI-MS spectra of iminopyridine species.[6,7,8]

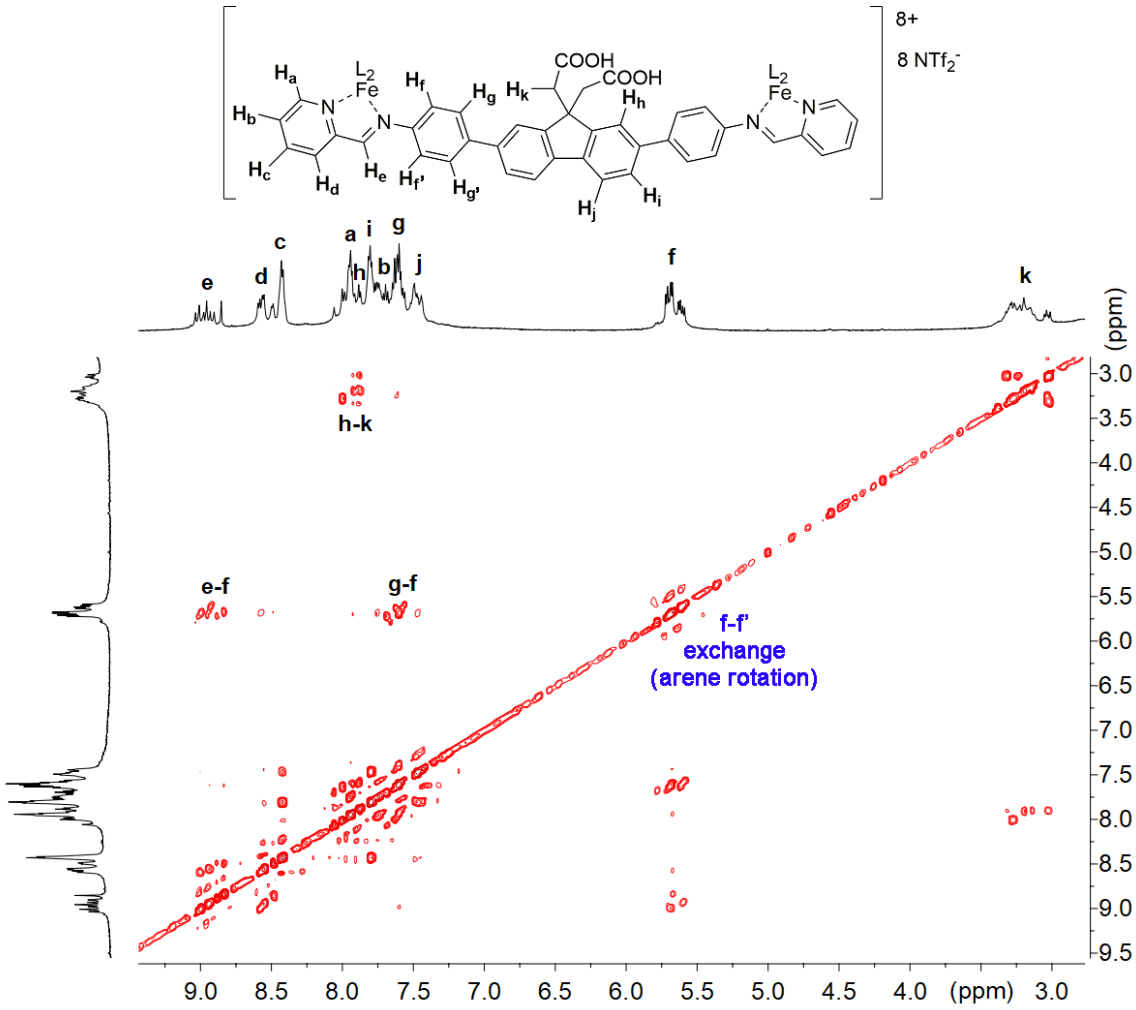

Figure 6.4. NOESY spectrum and assignment of peaks from cage **6.7**. (600 MHz, 298 K, CD_3CN).

Cages **6.3** and **6.7** displayed complex ^{1}H NMR spectra indicative of the formation of multiple cage isomers. Attempts to grow single crystals for X-ray crystallography

yielded specimens of cage **6.3**, but the quality was not high enough to collect usable data. Elemental analysis verified the purity of the two complexes, and to shed more light on the structures, 2D NMR characterization was performed, including COSY, NOESY, HMBC and HSQC spectra. From these spectra, the clustered and overlapped peaks in the ^{1}H NMR spectrum were assigned (Figure 6.4). The NOESY spectra for both complexes display intraligand NOE correlations likely arising from free rotation of the phenyl spacers. In addition, peak deconvolution (MestreNova) of the imine region of the ^{1}H NMR spectra was utilized to assign the proportions of the different cage isomers (Figure 6.5). The imine region of cage **6.3** contains 8 peaks: four from the C_3 symmetric isomer, three from the S_4 isomer, and one from the highly symmetrical tetrahedral isomer (shown in Figure 6.5). The ratio corresponds with 48 % **6.3**-C_3, 11 % **6.3**-T, and 41 % **6.3**-S_4. Acid cage **6.7** shows the presence of only two isomers: the C_3 symmetric (45 %) and the S_4 symmetric (55 %), with no observed peaks for the T-symmetric isomer.

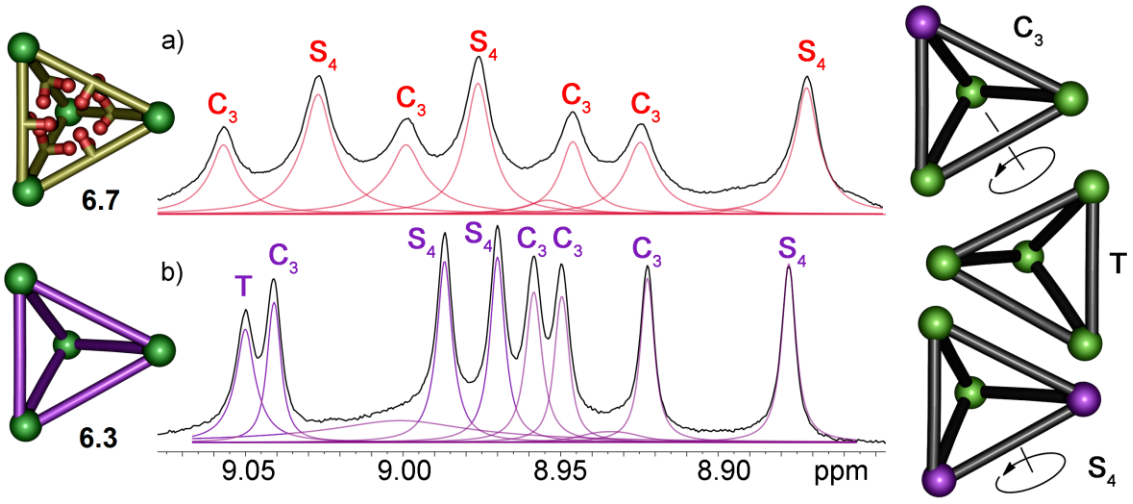

Figure 6.5. Peak deconvolutions and labeling of the imine CH regions of the ^{1}H NMR spectra of a) **6.7** and b) **6.3** (600 MHz, 298 K, CD_3CN).

Molecular modeling (semi-empirical, AM1 forcefield) of the two isomers of acid **6.7** and the three isomers of fluorene cage **6.3** (Figure 6.6) shows that in both cases, the acid groups are mostly positioned towards the internal cavity. The models also indicate that rotation of the fluorenyl groups to exohedrally orient the acids is highly unfavorable. However, this does not preclude the possibility of the flexible acid groups orienting themselves exohedrally through the cage windows. Even though the internal cavities are large, the presence of the internal acid groups in **6.7** affects the stereoisomerism at the metal centers and the T isomer is not observed.

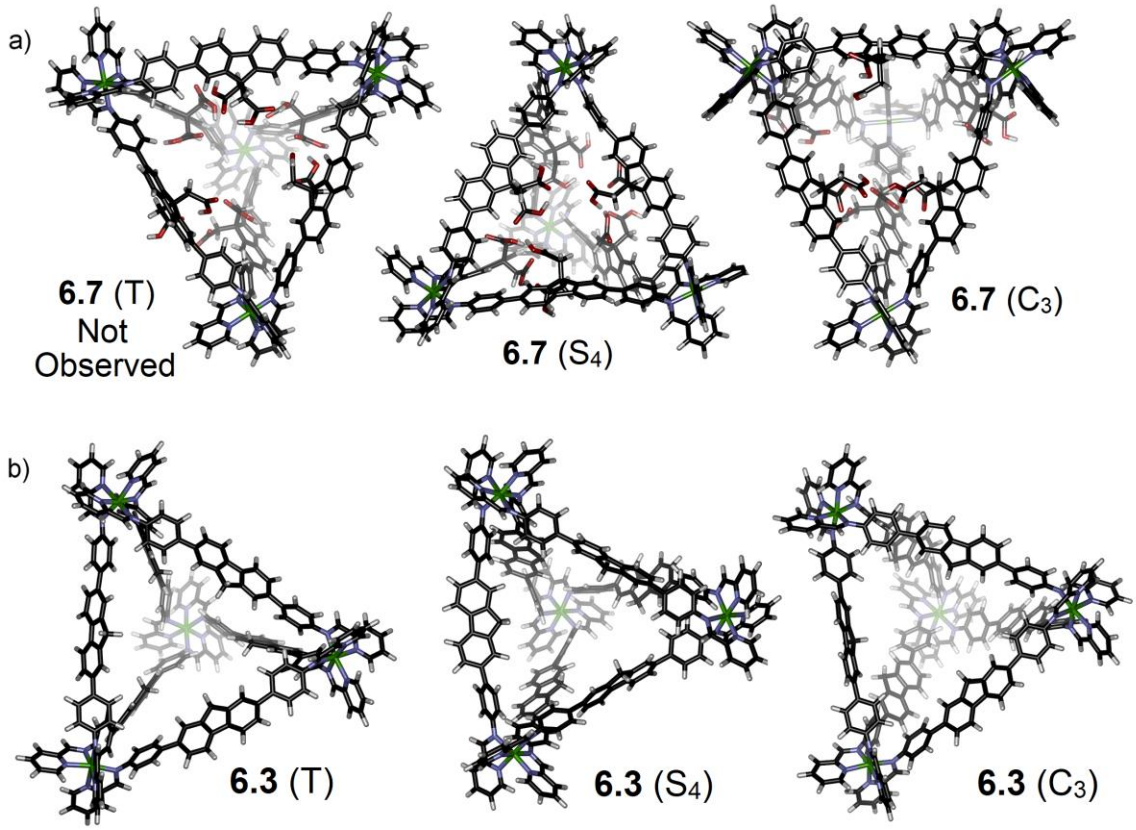

Figure 6.6. Energy minimized models of the three isomeric possibilities of all-*fac* M_4L_6 tetrahedra of a) **6.7** and b) **6.3**.

6.3 Catalytic Hydrolysis of Acetals

As complex **6.7** contains a large cavity with 12 internalized acid groups, it is a promising candidate for biomimetic catalysis. The challenge in using Fe-iminopyridine cages as catalysts is that they can be fragile. Strongly coordinating anions (e.g. Cl^-) and other strong nucleophiles are rarely tolerated, so to determine the effectiveness of acid cage **6.7** as a catalyst, acetal hydrolysis was the initial focus. This reaction can be performed under mild conditions and produces only alcohol and aldehyde products which should be tolerated by the assembly. Three acetals were chosen as substrates for the initial tests, and the hydrolysis reactions of two synthesized pyridyl acetals (**6.8** and **6.9**) and benzaldehyde dimethyl acetal ($PhCH(OMe)_2$) were optimized using a surrogate control acid to determine optimal reaction conditions (Figure 6.7).

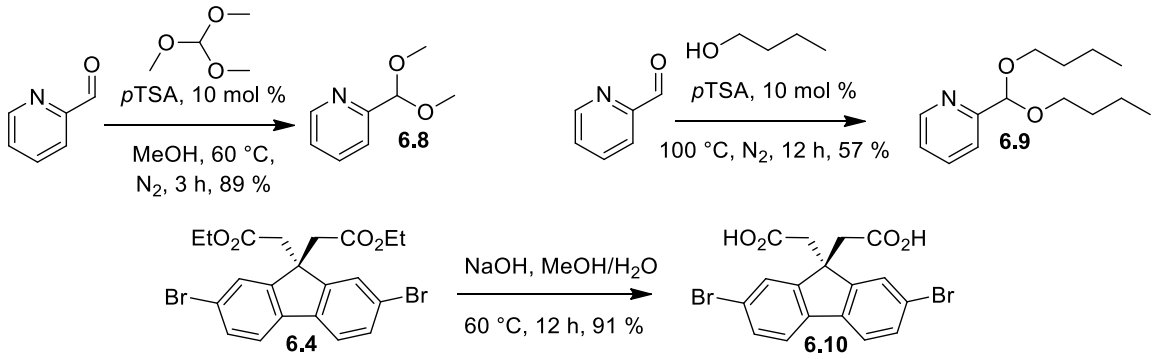

Figure 6.7. Synthesis of two pyridyl acetal substrates and control acid **6.10**.

To test the catalytic abilities of cage **6.7**, the acetals were reacted with 4 mol % cage **6.7** and 5 mol. eq. of water in CD_3CN with nitromethane as an internal standard. The reaction progress was monitored by NMR and the percent conversion and remaining unreacted acetal were calculated by integration. Hydrolysis of $PhCH(OMe)_2$ was rapid in

the presence of cage **6.7**, (shown in in Figure 6.8) with 99 % conversion observed after just 5 h at 23 °C. The pyridyl equivalent **6.8** was less reactive, and required heating to 77 °C for 14 h to effect complete conversion.

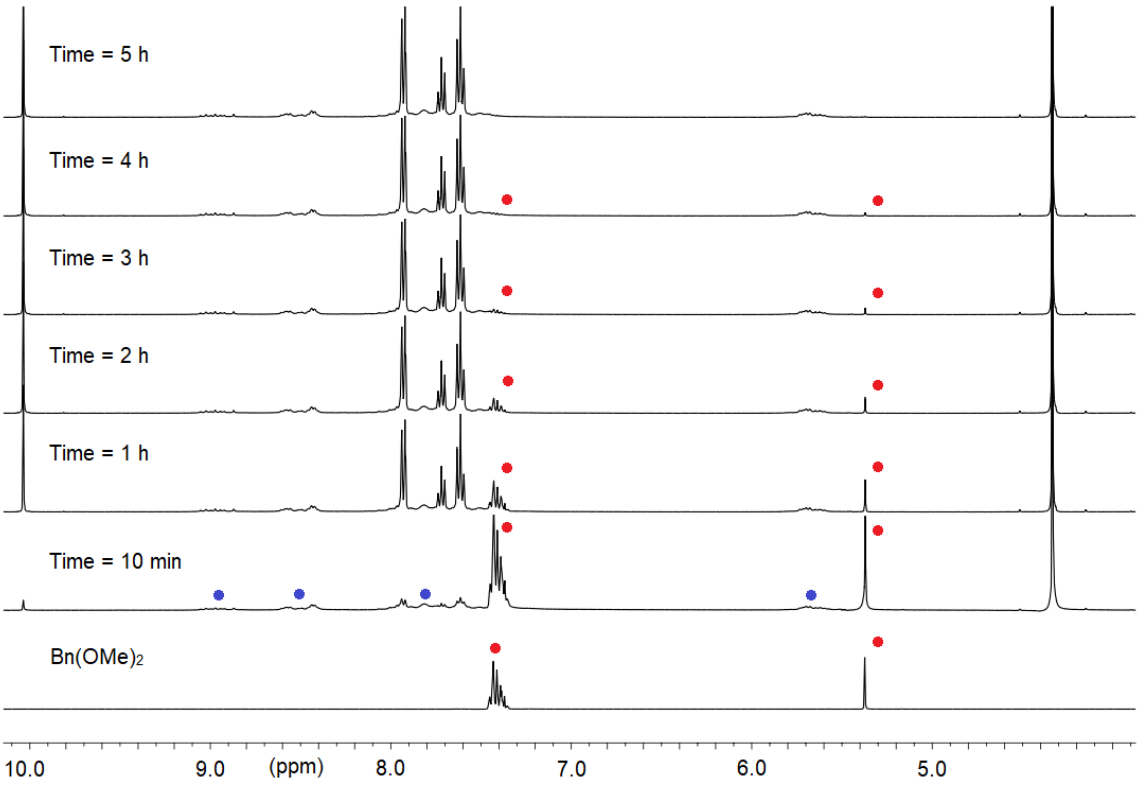

Figure 6.8. ^{1}H NMR spectra of the hydrolysis of $PhCH(OMe)_2$ (red) with 4 mol % Cage **6.7** (blue) and 5 mol. eq. water at 50 °C (400 MHz, 298 K, CD_3CN).

The reaction progress was plotted as percent conversion against time and is shown in Figure 6.9. Interestingly, acetal **6.9**, which contains two larger n-butyl chains, was hydrolyzed at essentially the same rate as the dimethyl acetal **6.8**. This indicates that cage **6.7** is not able to discriminate between the two substrates, which is somewhat expected due to the relatively large internal cavity. Molecular modeling confirms this: the butyl chains are linear and flexible and can be directed out through the cage windows. The large internal

cavity can easily accommodate the added bulk and catalyze the hydrolysis without an appreciable decrease in the reaction rate. Substantially larger substrate molecules would be necessary to test the size-based selectivity of cage catalyst **6.7**.

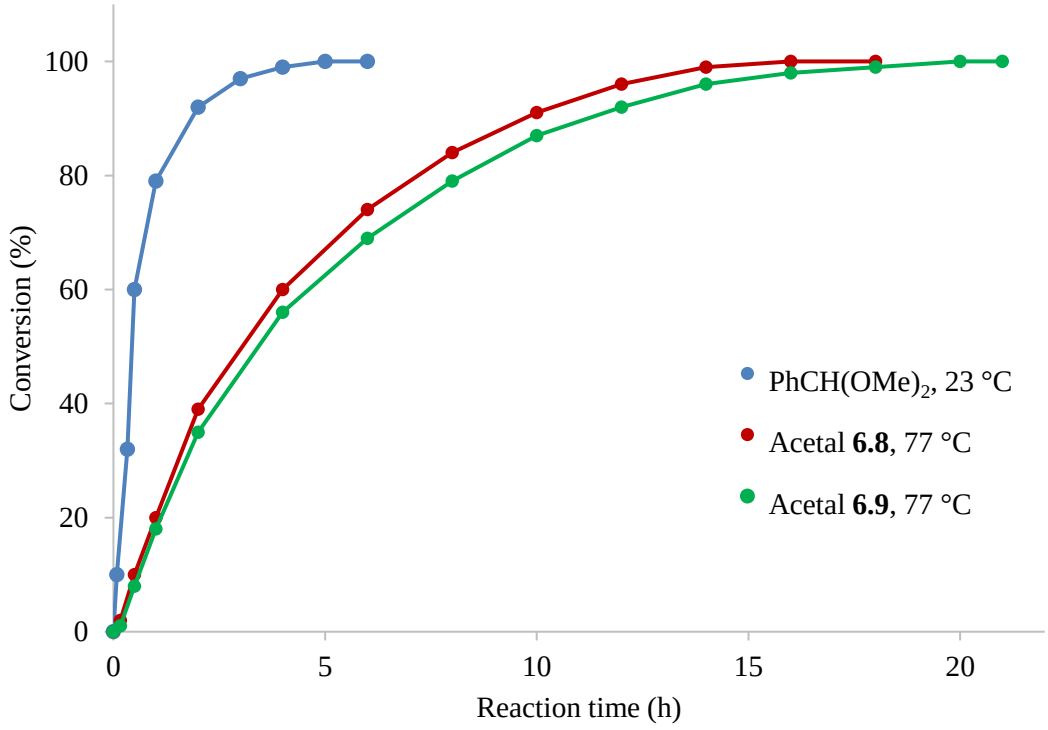

Figure 6.9. Percent conversion over time for acetal hydrolysis reactions using 5 mol. eq. water and 4 mol % acid cage **6.7**.

Control reactions were performed using varying amounts of acid surrogate **6.10** and water with nitromethane as an internal standard. Initial tests using 10 mol % or less of control acid **6.10** at 23 °C gave minimal or no conversion over 24 h for acetals **6.8** or $PhCH(OMe)_2$. When the reaction temperature was increased to 50 °C, 8 % conversion of $PhCH(OMe)_2$ was observed after 24 h, while acetal **6.8** gave no reaction. The control reaction conditions were further optimized for **6.8** and are summarized in Table 6.1. When

the amounts of water and acid surrogate were increased to 5 mol. eq. and 25 mol % respectively (conditions identical to those used for the cage catalyzed experiments) the reaction of the pyridyl acetals is sluggish, and yields just 10 % conversion after 48 h reaction time.

Table 6.1. Optimization of control hydrolysis rates for acetal substrates **6.8** and $PhCH(OMe)_2$.

Substrate	Acid	Acid Mol %	Water	Temp	Time	% Conversion
$PhCH(OMe)_2$	**6.10**	10 %	2 eq	23 °C	24 h	No rxn.
$PhCH(OMe)_2$	**6.10**	10 %	2 eq	50 °C	24 h	8 %
$PhCH(OMe)_2$	**6.10**	25 %	5 eq.	23 °C	24 h	1 %
$PhCH(OMe)_2$	**6.10**	25 %	5 eq.	50 °C	24 h	20 %
6.8	**6.10**	10 %	2 eq.	50 °C	60 h	No rxn.
6.8	**6.10**	10 %	2 eq.	77 °C	24h	1 %
6.8	**6.10**	10 %	2 eq.	77 °C	48h	3 %
6.8	**6.10**	10 %	5 eq.	77 °C	24h	2%
6.8	**6.10**	10 %	5 eq.	77 °C	48h	5 %
6.8	**6.10**	20 %	2 eq.	77 °C	24h	3 %
6.8	**6.10**	20 %	2 eq.	77 °C	48h	5 %
6.8	**6.10**	25%	5 eq.	77 °C	24h	6 %
6.8	**6.10**	25 %	5 eq.	77 °C	48h	10 %

The percent conversion values for the various control tests were plotted against reaction time and are shown in Figure 6.10. The hydrolysis control trials for all three acetal substrates display a linear trend typical of uncatalyzed reactions. Some decomposition of the samples was observed after approximately 100 h; therefore, the initial linear portion of the percent conversion plot was used to calculate an estimated time to completion of > 400

h for the pyridyl acetal substrates **6.8** and **6.9**. Under similar conditions (heating at 50 °C and 25 mol % acid surrogate **6.10**) the hydrolysis of $PhCH(OMe)_2$ reached reaction completion after 120 h.

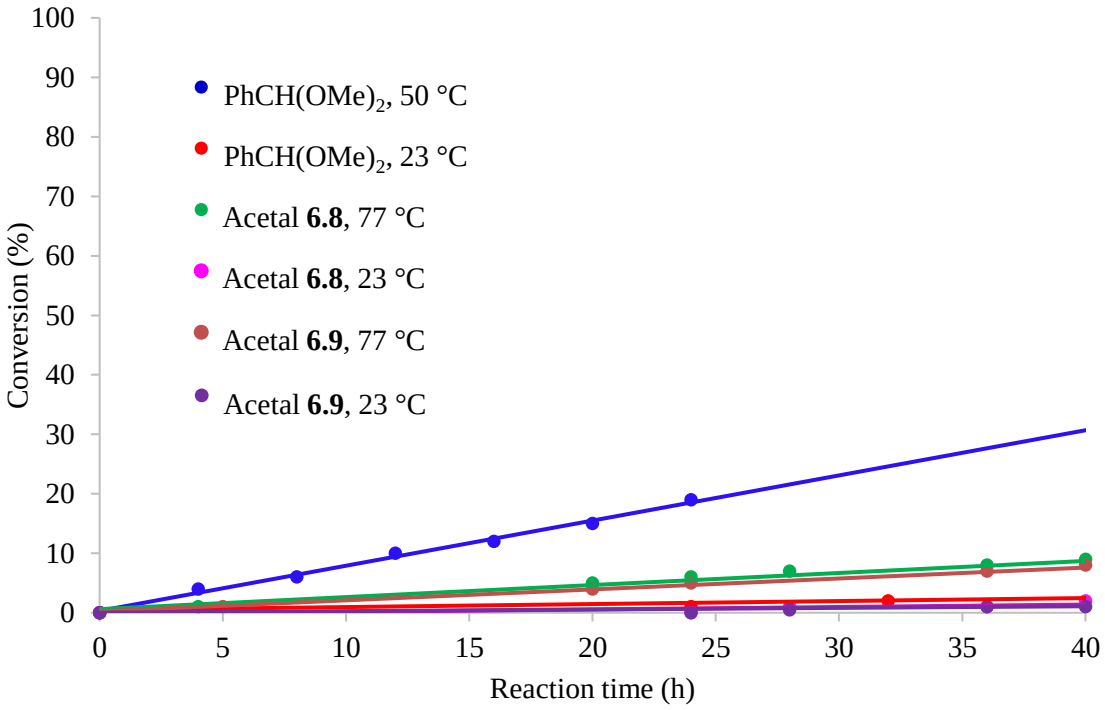

Figure 6.10. Percent conversion over time for acetal hydrolysis reactions using 5 mol.-eq. water and 25 mol % control acid **6.10**.

There is a large difference in the percent conversion values at any given time between the catalyzed experiments using **6.7** and the uncatalyzed reactions with **6.10**. In the presence of cage **6.7**, pyridyl acetal **6.8** reached 99 % completion after 14 h at 77 °C. Under identical conditions in the presence of the control ligand (25 mol % **6.10**, which maintains the same amount of carboxylic acid groups as in the catalyzed trial), the sluggish hydrolysis would require > 400 h to effect complete conversion. In addition, hydrolysis of

the benzaldehyde dimethyl acetal was complete after just 5 h at 23 °C when the acid cage **6.7** was used compared to 120 h with control acid **6.10** and heating to 50 °C.

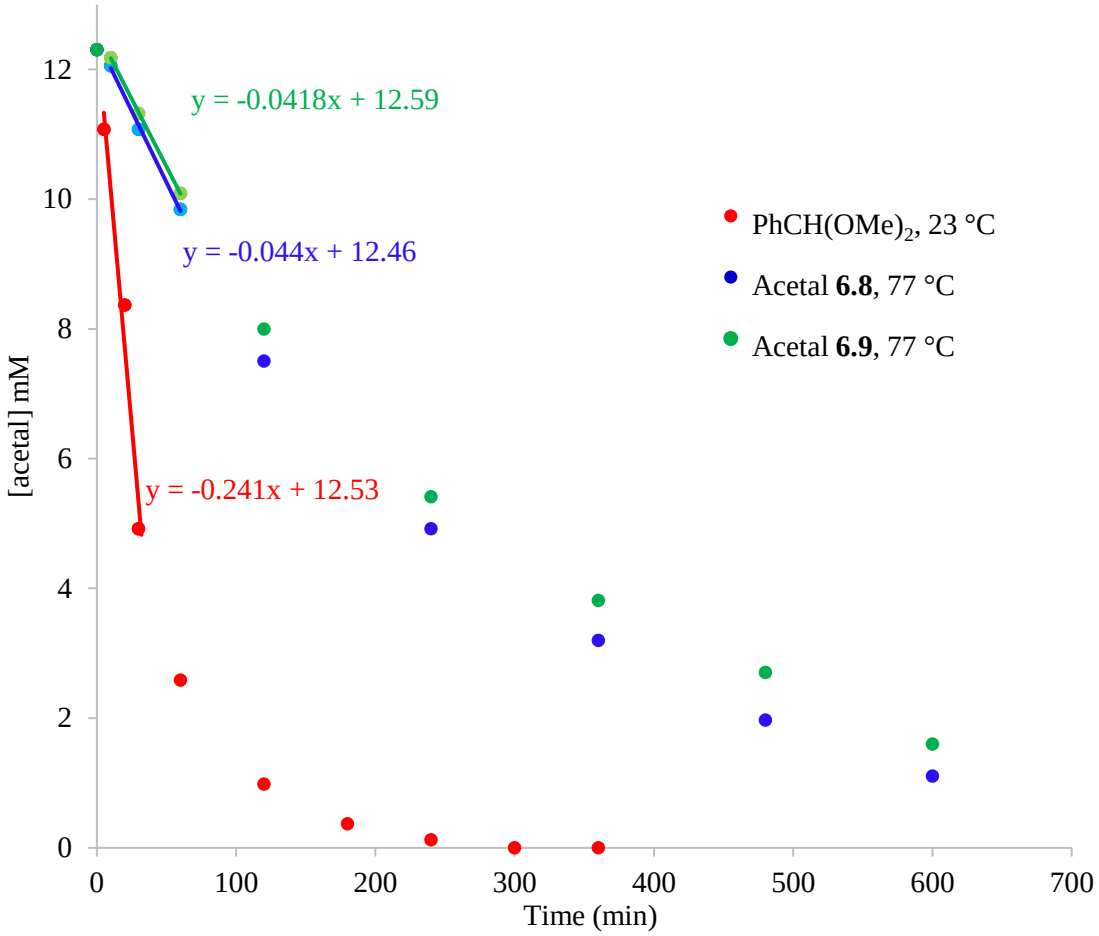

Figure 6.11. Concentration of remaining acetal reactant over time for acetal hydrolysis reactions using 5 mol. eq. water and 4 mol % cage **6.7**, and calculation of select initial reaction rates.

To more accurately quantify the rate acceleration, the initial rates of the catalyzed hydrolyses of **6.8**, **6.9** and $PhCH(OMe)_2$ using cage **6.7** were calculated (Figure 6.11). The reactions were performed in triplicate and the concentration of acetal reactant remaining in solution over time was calculated via integration against the nitromethane internal standard. Three initial linear datapoints were selected and the inverse slope of the line was

taken as the initial rate (V). These values are summarized in Table 6.2 along with the calculated initial rates for the control experiments using **6.10** (shown in Figure 6.12).

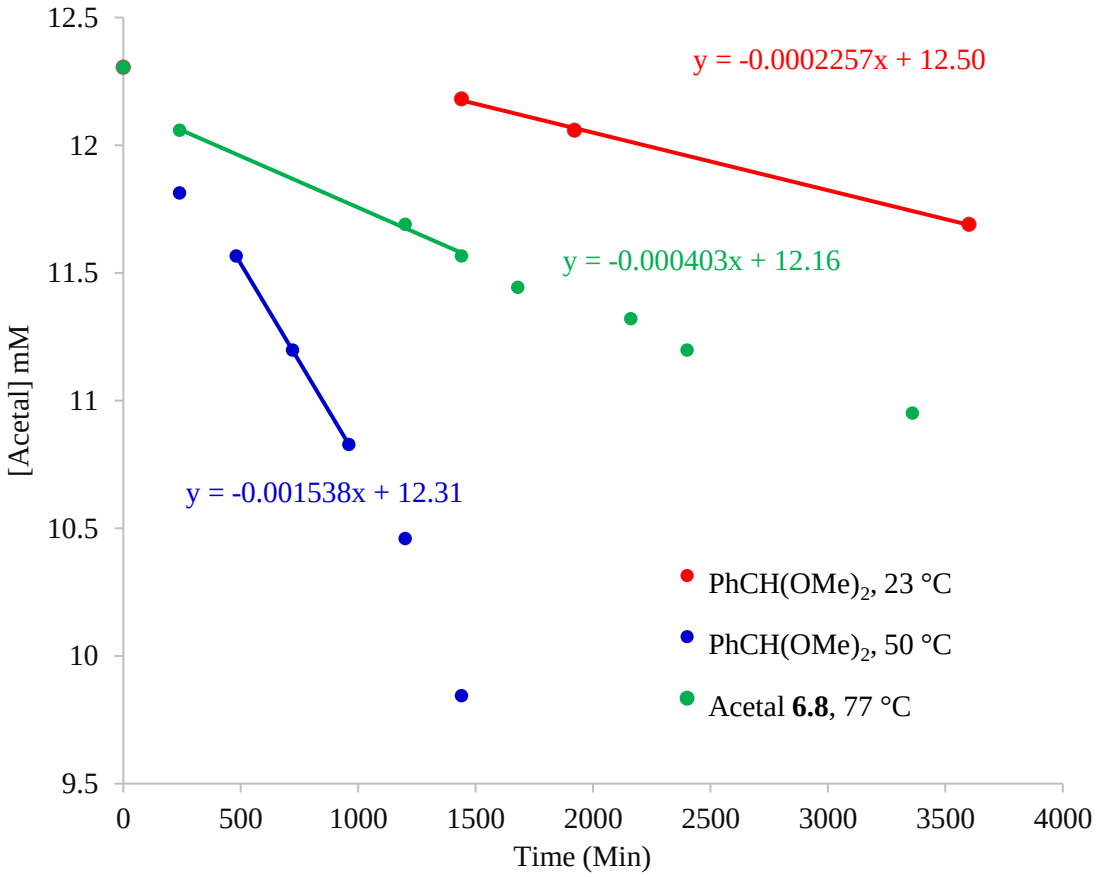

Figure 6.12. Concentration of remaining acetal reactant over time for acetal hydrolysis reactions using 5 mol. eq. water and 25 mol % surrogate **6.10**, and calculation of select initial reaction rates.

Comparing the initial rates (Table 6.2) quantifies the acceleration of the hydrolysis reactions. When the uncoordinated control acid **6.10** was used as the catalyst, very slow hydrolysis was observed, with only 1 % conversion of $PhCH(OMe)_2$ after 24 h at 23 °C. This corresponds to an initial rate of V = 2.26 $x10^{-4}$ mM/min. At elevated temperatures, only 20 % conversion was observed when $PhCH(OMe)_2$ was heated at 50 °C for 24 h (V

= 15.3 x 10^{-4} mM/min) and acetal **6.8** only yielded 6 % conversion after 24 h at 77 °C, with V = 4.03 x10^{-4} mM/min. In comparison, the initial rates for the cage catalyzed trials were calculated as V = 2410 x 10^{-4} and 440 x 10^{-4} mM/min for $PhCH(OMe)_2$ and **6.8**. This corresponds to an impressive rate enhancement of 1070-fold for $PhCH(OMe)_2$, and 100-fold for **6.8**. provided by the acidic cavity of cage **6.7**. This rate enhancement is due to sequestration of the acid functionality within the cage cavity, as both catalyzed and control reactions contain the same number of acid groups.

Table 6.2. Supramolecular catalysis of acetal solvolysis.

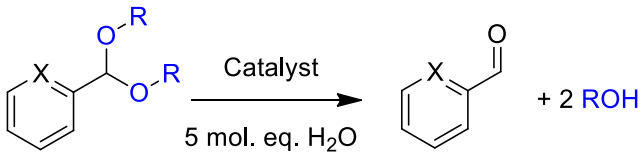

$PhCH(OMe)_2$: X = C-H, R = CH_3
6.8: X = N, R = CH_3
6.9: X = N, R = ^{n}Bu

Catalysts: **6.3**, **6.7**, **6.10**

Substrate	t, h	T, °C	Catalyst	Initial Rate V, x10^{-4} mM/min	Conversion, %
$PhCH(OMe)_2$	5	23	**6.7**	2410	99
6.8	14	77	**6.7**	440	99
6.9	14	77	**6.7**	418	96
$PhCH(OMe)_2$	24	23	**6.10**	2.26	1
$PhCH(OMe)_2$	24	23	**6.10** + **6.3**	2.87	1
$PhCH(OMe)_2$	48	23	**6.3**	n.d.	0
6.8	24	77	**6.10**	4.03	6
6.8	48	77	**6.3**	n.d.	1

In Chapters 4 and 5 it was postulated that trace amounts of iron leached from the cage samples can act as a catalyst for oxidations. To ensure that any rate acceleration

effected by catalytic cage **6.7** was not due to any leached iron acting as a possible Lewis acid, the acetals were tested for hydrolysis in the presence of unfunctionalized cage **6.3**, and 5 mol. eq. water. After 48 h reaction time, no conversion to the aldehyde products was observed, indicating that any Fe^{II} salts leached from the cage are incapable of catalyzing the hydrolysis. In addition, the hydrolysis of $PhCH(OMe)_2$ was performed with control acid **6.10** and 5 mol. eq. water in the presence of a catalytic amount of unfunctionalized cage **6.3** with no appreciable acceleration in the initial rate observed when compared to the trials with control **6.10** in the absence of cage **6.3**. This indicates that if leached Fe^{II} is present during the reaction, it does not play an appreciable role in the hydrolysis.

6.4 Tandem Reactivity

The internalized acid groups of cage **6.**7 provide a second advantage over acid surrogate **6.10**. The functional groups are compartmentalized within the cavity of the cage, which allows for size-based selectivity in reaction and isolation of the acid from large sensitive species. This functionality is crucial for a variety of catalytic processes, including tandem reactivity. It has been shown that cages can be effectively used to isolate two catalysts that would otherwise quench each other, and tandem or cascade reactions can be performed in a single flask.[9] An aldehyde displacement reaction is ideal for tandem reactions and we have previously shown that disfavored electron withdrawn aldehyde termini could be displaced from M_2L_3 mesocates in the presence of water and a more electron rich aldehyde.[10] Effecting the mesocate aldehyde exchange via specific stimuli would be a step towards the developing molecular switches, but performing the tandem

acetal deprotection and aldehyde displacement (Figure 6.13) would require careful matching of the acid catalyst and the sensitive iminopyridine complexes.

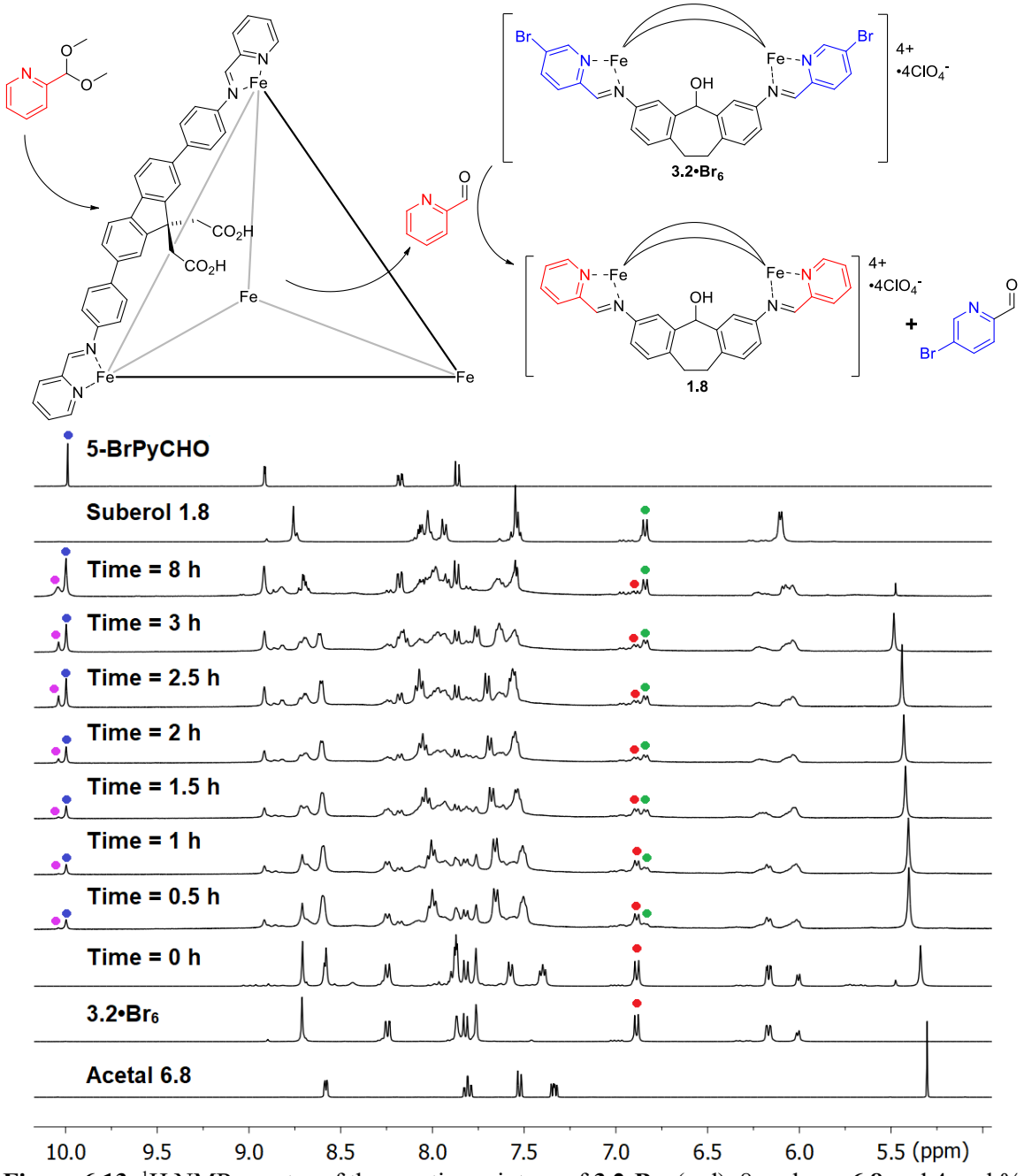

Figure 6.13. ^{1}H NMR spectra of the reaction mixture of **3.2•Br$_6$** (red), 8 mol. eq. **6.8** and 4 mol % **6.7** heated at 77 °C over time, compared to the products 5-BrPyCHO (blue), PyCHO (pink) and suberol cage **1.8•H$_6$** (green) (400 MHz, 298 K, CD_3CN).

Cage **6.7** is ideal for tandem reactivity as the acid groups are isolated from the bulk solution and should not cause degradation of the mesocate structures. In addition, the rate acceleration of the acetal hydrolysis allows for the aldehyde deprotection and termini displacement to occur within a decreased timeframe. A cascade deprotection and transformation was attempted by reacting mesocate cage **3.2•Br$_6$** with 4 % catalyst **6.7**, 8 mol. eq. acetal **6.8**, and 10 mol eq. water at 77 °C in CD_3CN. The tandem process was monitored over time and is shown below in Figure 6.13.

The hydrolysis of **3.8** and the incorporation of the resultant PyCHO into **3.2•Br$_6$** occurs rapidly: after only 30 mins, signals for **3.2•Br$_6$** have decreased while signals corresponding to displaced 5-BrPyCHO become present. Signals for PyCHO are not observed initially as any amounts produced by the hydrolysis of **6.8** are rapidly consumed by the displacement of the cage aldehyde. As an excess of the acetal is used to effect full displacement of **3.2•Br$_6$**, signals corresponding to PyCHO begin to accumulate after 3 h reaction time. After 8 h, the displacement is complete with 92 % conversion to suberol cage **1.8**. No decomposition of the mesocate or cage **6.7** occurs as no free iminopyridine ligands or dianiline cores are visible throughout the course of the reaction. Upon completion, only the products, **6.7** and excess aldehydes are present. No incorporation of Br-PyCHO into cage **6.7** is observed, as is expected: even though **6.7** is an iminopyridine cage, it is capable of catalyzing the displacement reactions of other iminopyridine assemblies.

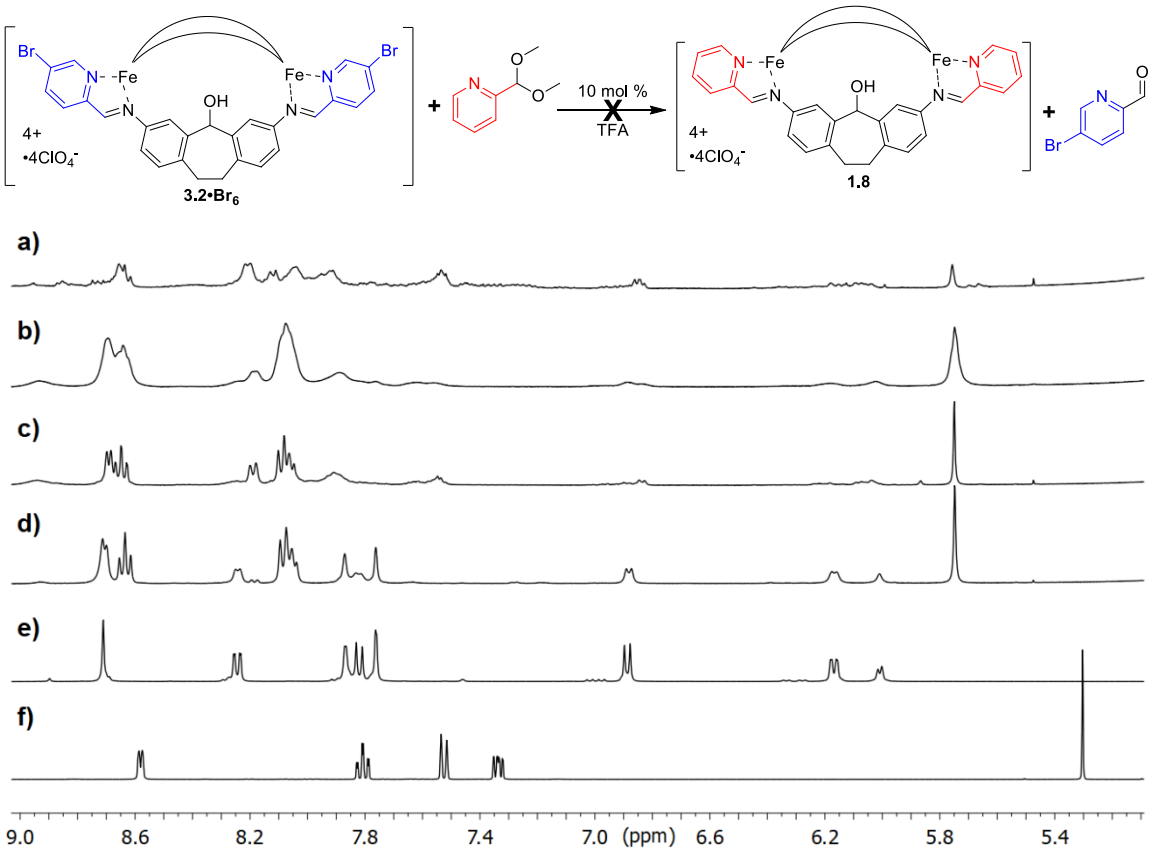

Figure 6.14. ^{1}H NMR spectra of the reaction mixture of **3.2•Br$_6$**, 8 mol. eq. **6.8** and 10 mol % TFA heated at 77 °C for a) 8 h; b) 3 h; c) 1 h and d) 10 min, compared to e) **3.2•Br$_6$** and f) acetal **6.8** (400 MHz, 298 K, CD_3CN).

Catalyst **6.7** is particularly suited for this displacement: the use of either control ligand **6.10** or stronger acid catalysts prevents the successful cascade from occurring at all. When **3.2•Br$_6$** was reacted with 8 mol. eq. of acetal **6.8** in the presence of a strong acid (10 mol % TFA), rapid acetal hydrolysis was observed in addition to near immediate cage decomposition as shown in Figure 6.14. Evidently the complexes are intolerant to even small amounts of strong acids, as rapid decomposition occurs. Conversely, when **3.2•Br$_6$** and 8 mol. eq. of acetal **6.8** were heated in the presence of 25 mol % acid surrogate **6.10**, the sluggish deprotection of the acetal at 77 °C lead to eventual decomposition of the cage

starting material and any mesocate product present after nearly 100 h reaction time. The mesocates are tolerant to the weak carboxylic acid groups but the slow hydrolysis rate and extended reaction time under elevated temperatures lead to eventual decomposition of the samples.

To control for the effects of any Fe^{II} leached from the system, the tandem reaction was repeated a final time in the presence of unfunctionalized cage **6.3** and control acid **6.10**. No acetal hydrolysis was observed even after extended reaction time and heating at 77 °C, and **3.2•Br$_6$** persisted in the reaction mixture. The tandem reaction is possible due to the combination of enhanced reactivity and compartmentalization of the acid groups in cage **6.7**. The cage is reactive enough to hydrolyze acetals at an accelerated rate and isolates the acid groups, so the overall conditions are mild enough to avoid decomposing the sensitive iminopyridine complexes.

6.5 Conclusion

In conclusion, we have successfully synthesized an extended fluorene core for the creation of new cages possessing internal cavities large enough to accommodate both reactive functional groups and small molecule substrates. We have synthesized and characterized an endohedrally functionalized cage complex that contains twelve carboxylic acid groups directed toward the cage interior that can catalyze the hydrolysis of aromatic acetals. The initial rates of hydrolysis for control and catalytic reactions were determined, with catalyst **6.7** effecting up to 1000-fold rate accelerations of acid-catalyzed reactions over non-assembled control acids. The catalytic nature of cage **6.7** allows it to be applied

to a tandem cage-to-cage interconversion reaction, which occurs cleanly without harming the sensitive iminopyridine coordinators present on both the M_2L_3 mesocates and the catalyst itself. Internalization of the functional groups allows for both rate accelerations and size selectivity in the bound substrate, and this functionalized assembly will be applied to other acid catalyzed reactions in the future.

6.6 References

1. Meng, W.; Ronson, T. K.; Nitschke. J. R. "Symmetry Breaking in Self-Assembled M_4L_6 Cage Complexes." *Proc. Natl. Acad. Sci. U.S.A.* **2013**, *110*, 10531-10535.

2. Meng, W.; Clegg, J. K.; Thoburn, J. D.; Nitschke, J. R. "Controlling the Transmission of Stereochemical Information through Space in Terphenyl-Edged Fe_4L_6 Cages." *J. Am. Chem. Soc.* **2011**, *133*, 13652-13660.

3. Ronson, T. K.; Meng, W.; Nitschke, J. R. "Design Principles for the Optimization of Guest Binding in Aromatic-Paneled $Fe^{II}_4L_6$ Cages." *J. Am. Chem. Soc.* **2017**, *139*, 9698-9707.

4. Young, M. C.; Holloway, L. R.; Johnson, A. M.; Hooley, R. J. "A Supramolecular Sorting Hat: Stereocontrol in Metal-Ligand Self-Assembly by Complementary Hydrogen Bonding." *Angew. Chem., Int. Ed.* **2014**, *53*, 9832-9836.

5. Mal, P.; Schultz, D; Beyeh, K.; Rissanen, K.; Nitschke, J. R. "An Unlockable–Relockable Iron Cage by Subcomponent Self-Assembly." *Angew. Chem., Int. Ed.* **2008**, *47*, 8297-8301.

6. Ma, S.; Smulders, M. M. J.; Hristova, Y.; Clegg, J. K.; Ronson, T. K.; Zarra, S.; Nitschke, J. R. "Chain-Reaction Anion Exchange between Metal−Organic Cages." *J. Am. Chem. Soc.* **2013**, *135*, 5678-5684.

7. Roberts, D. A.; Pilgrim, B. S.; Cooper, J. D.; Ronson, T. K.; Zarra, S.; Nitschke, J. R. "Post-assembly Modification of Tetrazine-Edged $Fe^{II}_4L_6$ Tetrahedra." *J. Am. Chem. Soc.* **2015**, *137*, 10068-10071.

8. Ronson, T. K.; Pilgrim, B. S.; Nitschke, J. R. "Pathway-Dependent Post-assembly Modification of an Anthracene-Edged $M^{II}_4L_6$ Tetrahedron." *J. Am. Chem. Soc.* **2016**, *138*, 10417-10420.

9. Ueda, Y.; Ito, H.; Fujita, D.; Fujita, M. "Permeable Self-Assembled Molecular Containers for Catalyst Isolation Enabling Two-Step Cascade Reactions." *J. Am. Chem. Soc.* **2017**, *139*, 6090-6093.

10. Wiley, C. A.; Holloway, L. R.; Miller, T. F.; Lyon, Y.; Julian, R. R.; Hooley, R. J. "Electronic Effects on Narcissistic Self-Sorting in Multicomponent Self-Assembly of Fe-Iminopyridine *meso*-Helicates." *Inorg. Chem.* **2016**, *55*, 9805-9815.

Chapter 7: Towards the Synthesis of Novel Endohedral Functionalized Cage Systems

7.1 Introduction

Supramolecular assemblies containing endohedral functional groups have the potential to act as useful catalysts and hosts. Many examples of unfunctionalized assemblies capable of host-guest chemistry exist in the literature. The task that remains is to investigate which functional groups are tolerated by the reversible multicomponent assembly process, and whether alternate metals or coordinating groups are beneficial to these systems. The iminopyridine chelator is capable of strong chelation with metals such as Fe^{II} but is sensitive reducing agents or nucleophilic attack. Modification of the coordinating motifs may provide a means to create assemblies that are tolerant to harsh reaction conditions. In addition, the use of transition metals other than Fe^{II} may be used to tune the redox or catalytic properties of the assemblies. By investigating new combinations of metal, coordinating group and functionalized ligand scaffolds, a range of potentially useful assemblies can be synthesized. Here, the efforts to create new functional complexes through modification of the internal reactive groups, coordinating motif and metal coordinating atoms are described.

7.2 Synthesis of Complexes Bearing Endohedral Functional Groups

The bulk the work shown in Chapters 2-6 work frequently made use of three central scaffolds: dibenzosuberone, fluorenone and xanthone. When selectively nitrated to form **1.4**, **1.9** and **2.4**, the bent angle of these cores allows for the ketone groups to be directed

towards the interior of the assembly, and provides a handle for endohedral functionalization. There are a great number of functional groups that can be investigated and many methods that can be used to introduce them onto the ligand scaffolds, however, functional groups capable of participating in hydrogen bonding are of the greatest interest. One simple method to transform the ketone groups would be condensation with amines to form reactive imine, oxime or hydrazone groups as shown in (Figure 7.1).

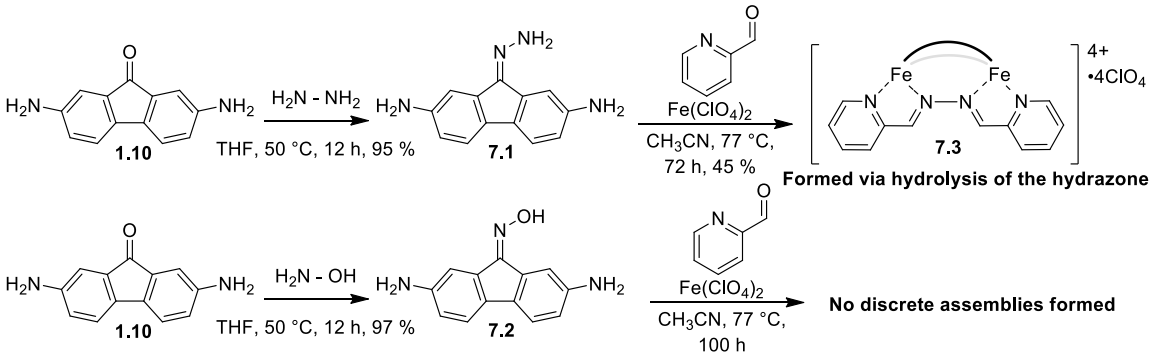

Figure 7.1. Synthesis of 2,7-diaminofluorenyl hydrazine and subsequent complex formation.

The ketone group of **1.10** is easily reacted with primary amines, and condensation with stoichiometric hydrazine or hydroxylamine cleanly forms hydrazone **7.1** or oxime **7.2** in high yield. Complexation of **7.1** with 2-formylpyridine (PyCHO) and $Fe(ClO_4)_2$ in acetonitrile at 77 °C for 24 h initially yielded a red solid and the 1H NMR spectrum of the product did not resemble that of a discrete assembly. When ligand **7.1** was refluxed in acetonitrile with PyCHO and $Fe(ClO_4)_2$ for an extended period of time, the reaction mixture began to turn purple after 48 h, with complete conversion to a blue product (**7.3**) after 72 h, which was isolated and purified in moderate yield. When the assembly was

repeated using dianiline **7.2**, no discrete products were observed at any time, even after extensive heating.

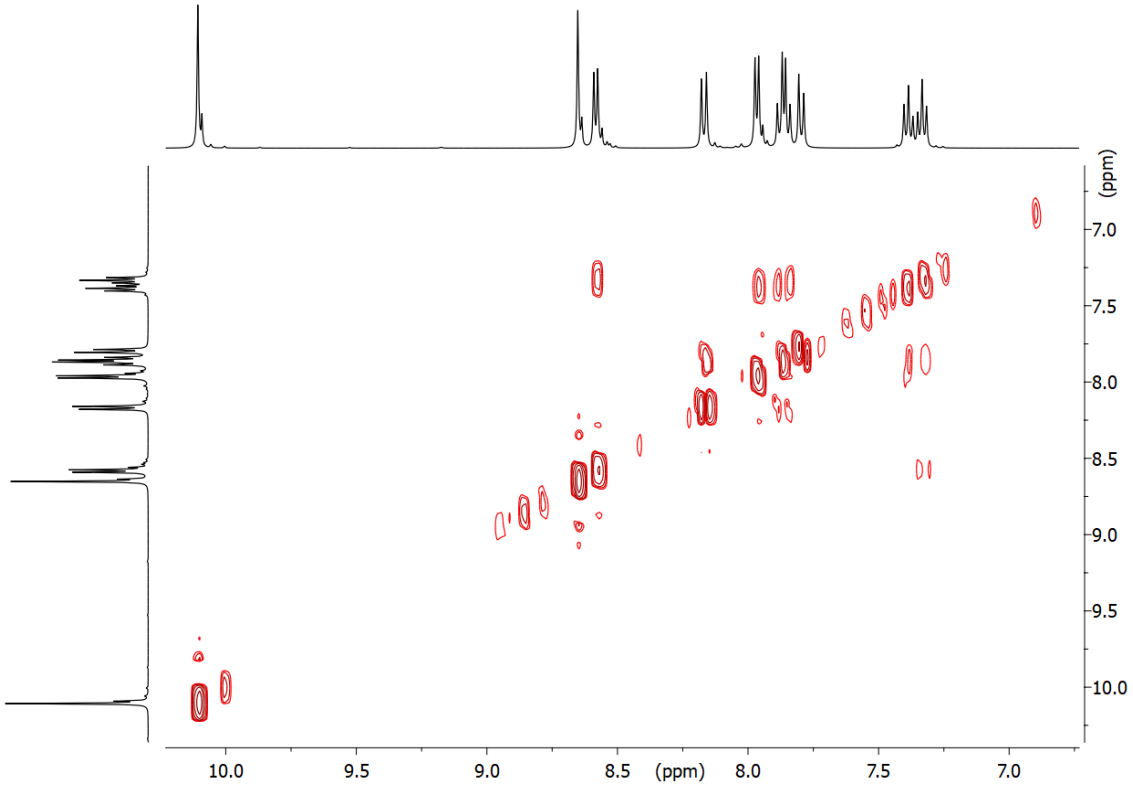

Figure 7.2. gCOSY spectrum of hydrazine M_2L_3 helicate 7.2 (CD_3CN, 600 MHz, 298 K).

^{1}H NMR, g-COSY spectra and ESI-MS analysis showed that **7.3** was not the expected fluorenyl M_4L_6, but instead a small, desymmetrized M_2L_3 helicate resulting from hydrolysis of **7.1** and complex formation with the liberated hydrazine. Monitoring of the reaction mixture over time showed the gradual appearance of peaks corresponding to **1.10** along with the discrete assembly. Product **7.3** could be independently synthesized by reacting hydrazine with 2 mol.-eq. of PyCHO and 0.66 mol.-eq. $Fe(ClO_4)_2$ with complete

conversion observed after just 4 h. Molecular modeling indicates that the internal cavities of the hypothetical M_4L_6 tetrahedra of **7.1** or **7.2** (Figure 7.3) are small and the presence of six rigid hydrazone or oxime groups creates a highly strained species. It is likely that aggregate species are formed initially. Extensive heating and the inability to form a discrete complex leads to hydrolysis of the imine groups. The liberated hydrazine is then free to form the small M_2L_3 complex.

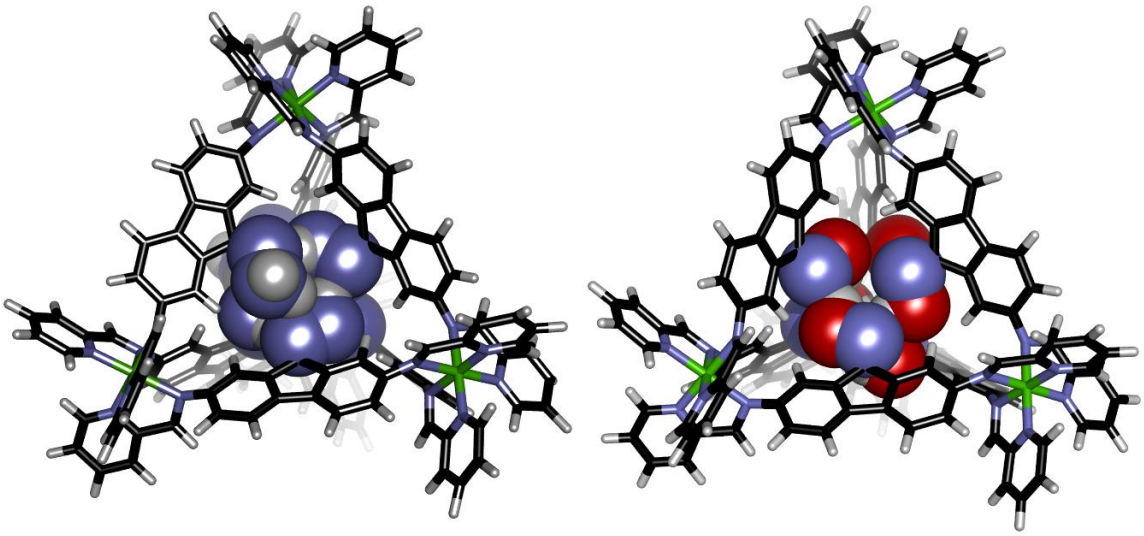

Figure 7.3. Molecular models (SPARTAN semi-empirical, AM1 forcefield) of the hypothetical M_4L_6 tetrahedral complexes of **7.1** (left) and **7.2** (right) demonstrating the high degree of steric crowding within the cavity.

While the M_4L_6 cannot accommodate discrete complexes with imine ligands, the smaller M_2L_3 complexes are more flexible and may be able to accommodate the rigid functional groups. Substitution of the ketone groups on dianilines **1.5** or **2.5** proved to be far less facile than for **1.10**. Interestingly, when condensation reactions were attempted on **2.4**, desymmetrized products were observed (Figure 7.4b). However, these proved to be

the result of a nucleophilic aromatic substitution reaction, instead of the desired condensation.

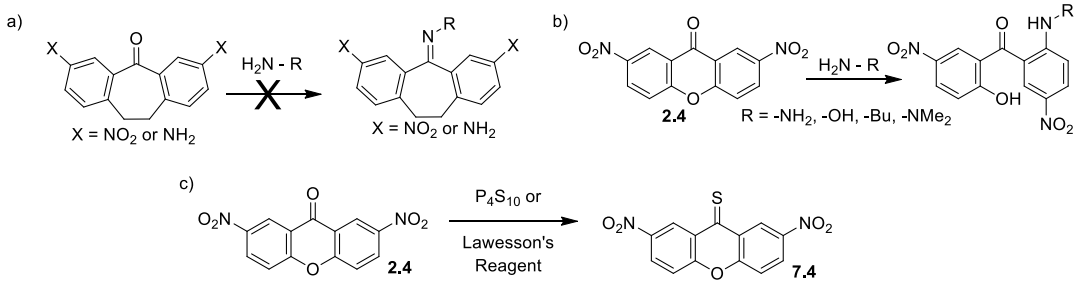

Figure 7.4. Synthetic scheme for the formation of functionalized ligand cores.

To circumvent the limited reactivity of the ketones, the corresponding thioketone compounds (Figure 7.4c) were synthesized, either using phosphorous pentasulfide or Lawesson's reagent. Compound **7.4** was cleanly isolated from the reaction mixture as a green solid in high yield. When **1.4** was reacted with Lawesson's reagent or phosphorous pentasulfide, the resulting blue solid consisted of a 50:50 mixture of thioketone product and starting material that could not be separated. Selective condensation of the more reactive thioketone in the presence of the starting material was possible, and the desired imine products were easily separated from the unreacted ketone. However, due to low yields, further trials with the dibenzosuberone core were not performed.

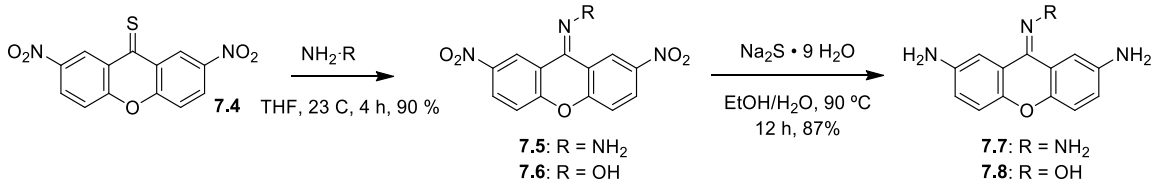

Figure 7.5. Synthesis of imine containing dianiline ligand cores.

Compound **7.4** was rapidly converted to the corresponding imine derivatives at 23 °C in anhydrous tetrahydrofuran (THF) using hydroxylamine or hydrazine. However, reduction of the nitro groups in the presence of reactive imines was far more challenging. Attempts using common reducing reagents such as tin chloride, Raney nickel and Pd on carbon failed to reduce the nitro groups without affecting the imine functionality. However, reduction using sodium sulfide produced the reduced hydrazone and oxime products **7.7** and **7.8** (See Chapter 8). When **7.7** and **7.8** were assembled with PyCHO and $Fe(ClO_4)_2$ in acetonitrile, discrete complexes were not formed. The reaction mixtures remained a red-orange color in solution and the products were isolated as brown solids. Extensive heating or prolonged reaction time failed to produce discrete products. From these trials, it remained unclear which component is not tolerated by the assembly process: the presence of the rigid substituted imines or the presence of nitrogen groups that can coordinate to the metal atoms.

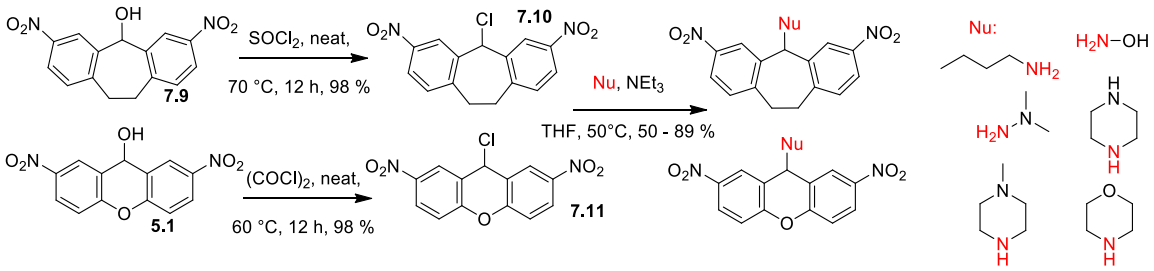

Figure 7.6. Synthesis of multiple secondary and tertiary amine bearing ligand cores.

To investigate this further, cores bearing secondary and tertiary amines with flexible sp^3 hybridization at the central carbon atoms were synthesized. The ketones on **1.4** and **2.4** were easily reduced with $NaBH_4$ to create **7.9** and **5.1** (Figure 7.6), however the reduction

of **1.9** was unsuccessful. Compounds **7.9** and **5.1** were then converted to their chloride derivatives **7.10** and **7.11** in quantitative yields. These were substituted with a variety of primary and secondary amines, and subsequently reduced to the corresponding dianilines using $SnCl_2$ and HCl. However, upon multicomponent assembly with $Fe(ClO_4)_2$ and PyCHO, no discrete products were formed for any of the amine containing ligands. The assembly products encouragingly exhibited the deep purple color of Fe^{II}-iminopyridine complexes, however the isolated products were found to exist as polymeric aggregate species. The ^{1}H NMR spectra resembled that of aggregate **4.4**, where broad mounds were observed throughout the aromatic and alkyl regions and no sharp peaks indicative of discrete assemblies were present. Increasing the reaction time or temperature did not change the ^{1}H NMR spectra, indicating that the products are not incomplete mixtures. Evidently, the short M_2L_3 scaffolds are not tolerant to the presence of endohedral amines in close proximity to the metal centers.

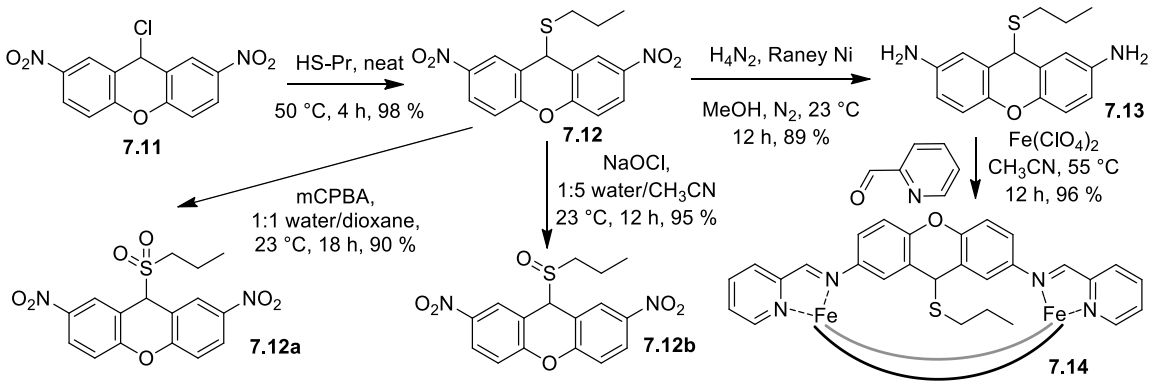

Figure 7.7. Synthesis and oxidation of xanthyl thioether cores and complex formation.

While amines are evidently not tolerated by the Fe^{II}-iminopyridine assemblies, it had been previously determined that complex **1.7** was stable to thiol groups; the ^{1}H NMR

spectrum did not show any decomposition upon refluxing a sample in acetonitrile with excess n-propyl thiol over 48 h. This tolerance lead to the investigation of sulfur-containing endohedral groups, which became the next area of focus. The reactive chloride on **7.11** was easily substituted with n-propyl thiol to create derivative **7.12** which was subsequently reduced under an inert atmosphere to produce dianiline **7.13**. In addition, **7.12** could be converted to the corresponding sulfoxide and sulfone derivatives (**7.12a** and **7.12b**) using varying oxidizing conditions, but these two cores were not amenable to clean reduction of the nitro groups. Dianiline **7.13** was assembled with PyCHO and $Fe(ClO_4)_2$ to form the M_2L_3 complex **7.14**. The signals in the NMR spectrum were broad, likely due to incomplete self-assembly, however the correct number of peaks are present. Interestingly, the broad peaks did not resemble the spectra observed when multiple isomers of product are formed, and in this case, it could be that this assembly forms the symmetrical all-out isomer.

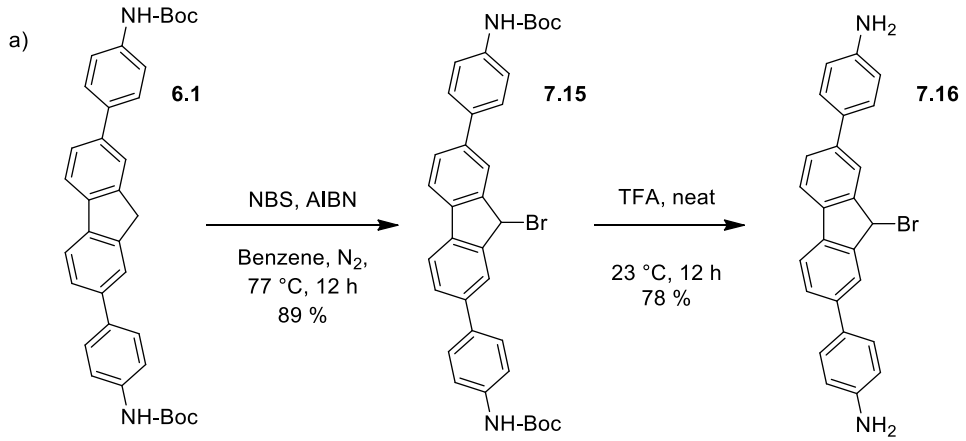

Figure 7.8. Bromination of extended ligand **6.1** and removal of the Boc protecting groups to afford aniline ligand **7.16**.

From the previous investigation, it appeared that endohedral functionalization, whether due to steric bulky or the reactive nature of the functional groups, could prevent

discrete assemblies from forming when the small dianiline ligands were used. However, larger assembly scaffolds, similar to dianiline **6.3**, may be able to accommodate functional groups. An endohedral alkyl halide is an attractive target and so radical bromination of the methylene units on **6.1** was performed. Bromination and purification of protected ligand **7.15**. was successful, and subsequent removal of the Boc groups using TFA afforded the dianiline **7.16** in good yields. Initial attempts to assemble the extended dianiline into the corresponding M_4L_6 structure have yielded promising results and further work on this system is being performed.

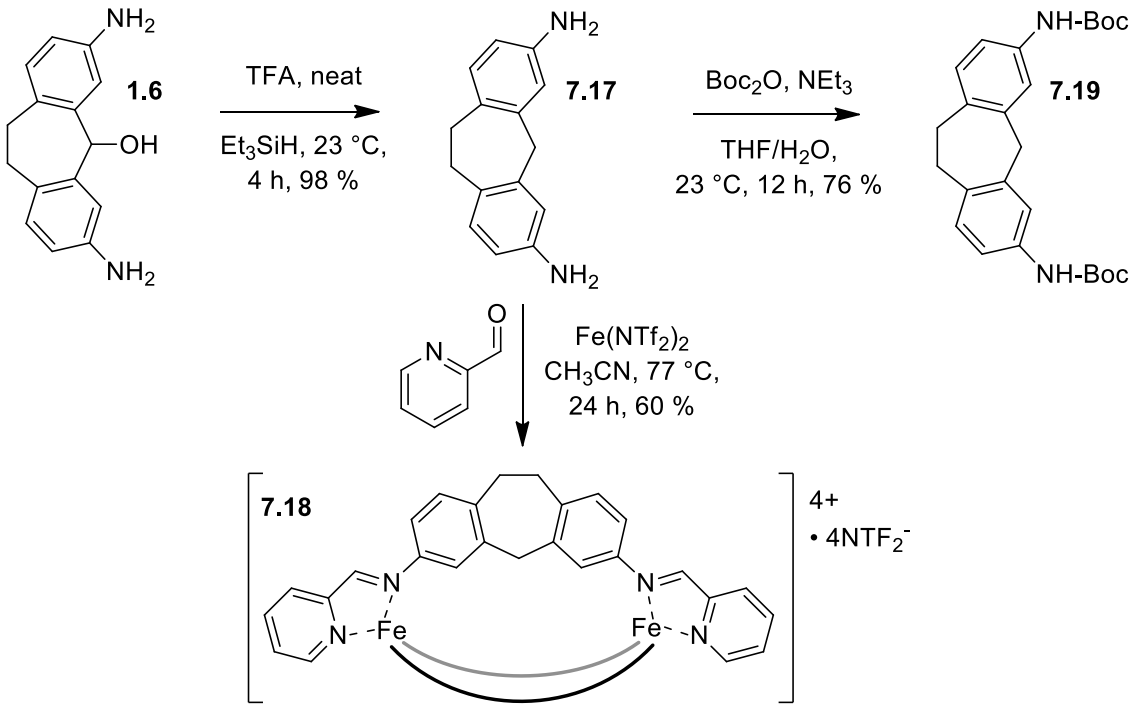

Figure 7.9. Synthesis of dianiline **7.17**, complex formation and Boc protection of the aniline groups.

The successful formation of **7.15** in the presence of Boc protected aniline groups was encouraging, and additional radical reactions were attempted on the Boc derivatives

of the previously synthesized short and extended cores. Compound **7.17** was synthesized in quantitative yield by reacting **1.6** with TFA and triethylsilane as shown in Figure 7.9, and could be converted into complex **7.18** upon self-assembly with PyCHO and $Fe(NTf_2)_2$. To test radical bromination reactions on the short cores, the amines on **7.17** were protected to form **7.19**. However, bromination of **7.19** or post-assembly bromination of **7.18** were both unsuccessful.

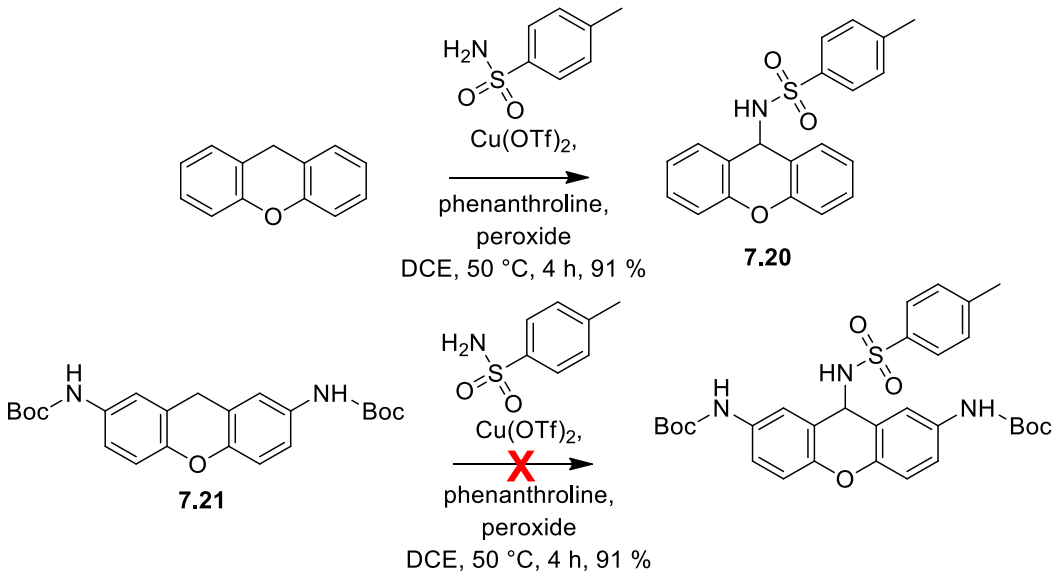

Figure 7.10. Radical additions to xanthene and substrate **7.21**.

The radical bromination of **6.1** and the radical additions to complexes **5.3** and **5.5** were encouraging, and so alternate radical addition reactions were tested on several substrates. Compound **7.20** was successfully synthesized in high yields using a literature procedure.[1] However, no reaction was observed when identical conditions were tested using commercially available fluorene, or compound **7.21** hinting at the stark differences in core reactivity. In addition, radical additions were attempted on various Boc protected

ligand scaffolds to introduce groups such as Troc-protected primary amines,[2] secondary amines,[3] and nitro groups[4] with limited success. In addition, post-assembly radical additions attempted on several preformed complexes did not yield clean products.

7.3 Alternate Metal Chelating Groups

In addition to endohedral functionalization of the ligand scaffolds, the use of novel metal chelating groups is of interest, and several new variations were investigated. These new chelating groups may be less sensitive to nucleophilic attack than the iminopyridine group. In addition, novel chelators provide opportunities for complexation with new transition metals, or for tuning the solubility of the complexes through external functionalization. A variety of bidentate N and O donors are possible, as shown in Figure 7.11 and attempts were made to synthesize new ligands containing some of these chelating groups.

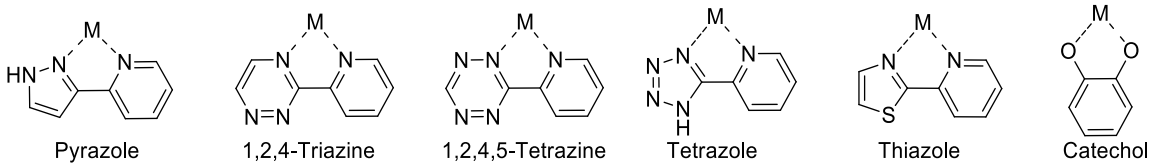

Figure 7.11. Potential bidentate chelating groups for supramolecular assembly.

Naphthyl ligand cores have been appended with pyridyl-pyrazole chelating groups and complexed to form interesting M_8L_{12} cubes.[5] To make use of this chelator, A Friedel-Crafts acylation was used to synthesize 2,7-diacetylfluorene (**7.22**) and xanthene (**7.23**) in good yields. Selective bromination of the acetyl groups was attempted first using bromine

in acetic acid. However, this reaction yielded the *bis* di-brominated fluorene and xanthene species **7.24** and **7.25** respectively.

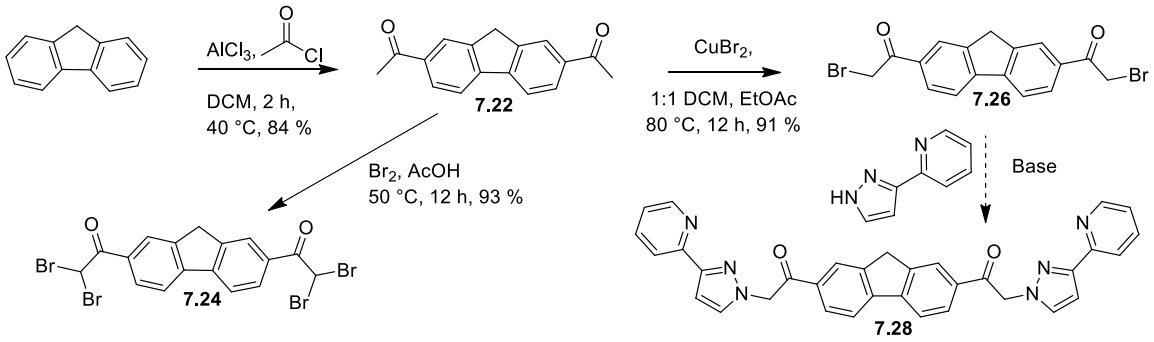

Figure 7.12. Synthetic scheme for formation of short pyridyl-pyrazole bearing ligands.

When the reaction was repeated using copper (II) bromide, the desired compounds **7.26** and **7.27** were obtained in good yields. Attempts to form the full ligand (**7.28**) using commercially available 3-(2-pyridyl)pyrazole in THF with triethylamine base were unsuccessful. The mono-substituted intermediates precipitate out of the reaction mixtures, preventing the formation of the *bis*-pyridyl pyrazole products. Varying the solvent, base or reaction temperature may lead to the synthesis of clean *bis*-pyrazole ligands.

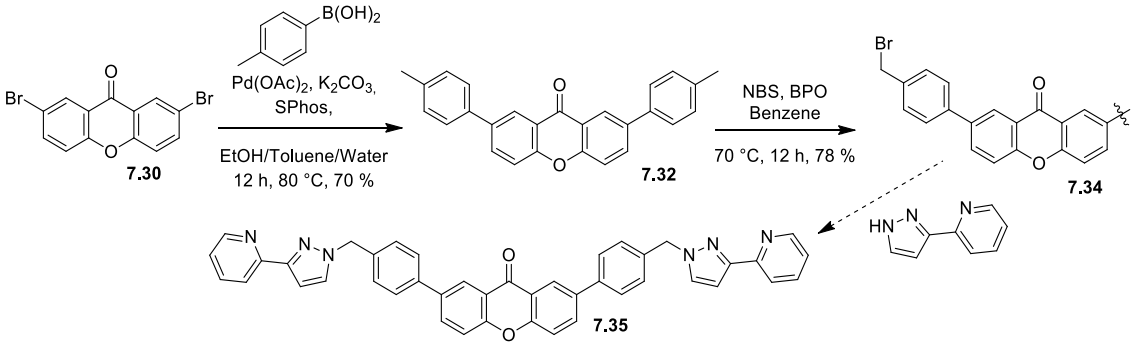

Figure 7.13. Synthesis of extended xanthone pyridyl-pyrazole ligands.

Extended cores were also synthesized for the creation of pyridyl pyrazole derivatives as shown in Figure 7.13. Brominated cores **7.29** and **7.30** were synthesized and subsequently subjected to Suzuki coupling conditions with commercially available 4-methylphenylboronic acid to produce the extended fluorenone and xanthone derivatives **7.31** and **7.32** in excellent yields, followed by radical bromination to form **7.33** and **7.34** respectively. Compound **7.34** was successfully reacted with 3-(2-pyridyl)pyrazole to form **7.35**, but the reaction suffered from very low yields and requires further optimization.

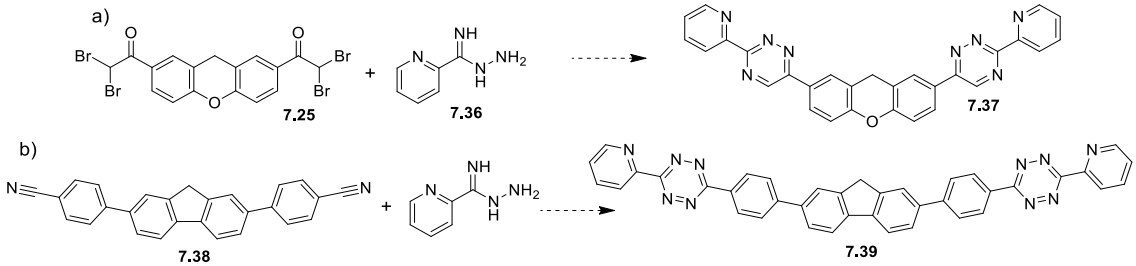

Figure 7.14. Synthesis of 1,2,4-triazine and 1,2,4,5-tetrazine derivatives based on fluorene and xanthene cores.

Compounds **7.24** and **7.25** can be used to form 1,2,4-triazine chelators. These are usually produced through the condensation of acetyl species in the presence of an oxidizing agent,[6] but in this case, condensation of **7.25** with picolinimidohydrazide (**7.36**) as shown in Figure 7.14 can also form the desired chelators. The reaction between **7.24** and **7.36** produced multiple isomers, and recrystallization in EtOH only moderately improved the purity of the product. Symmetrical ligands such as 1,2,4,5-tetrazine ligand **7.39** should simplify the ligand synthesis and analysis. To create 1,2,4,5-tetrazine chelators, *bis*-nitrile ligands such as **7.38** can be reacted with **7.36** in an appropriate solvent. Core **7.38** was

formed via Suzuki coupling between **7.29** and 4-cyanophenylboronic acid in moderate yield, and the initial reaction with **7.36** was promising.

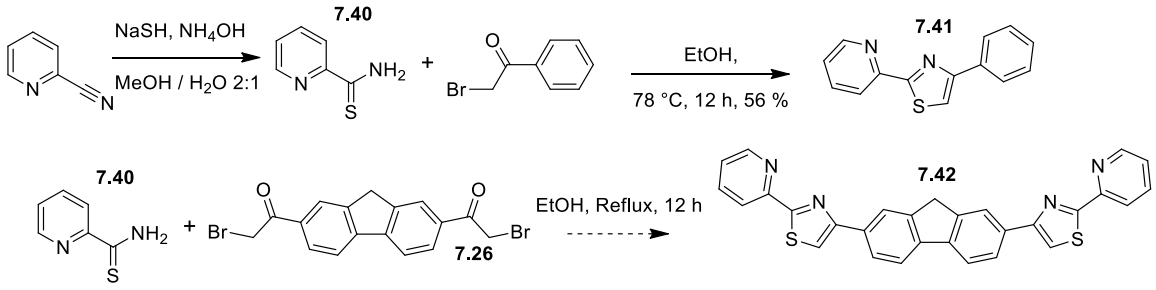

Figure 7.15. Synthetic scheme for the formation of thiazole chelators.

Pyridyl thiazole chelating groups can also be synthesized using **7.26** or **7.27** as shown in Figure 7.15. Synthesis of pyridine-2-carbothioamide **7.40** was successful and gave clean product after recrystallization in EtOH.[7] Formation of the test thiazole compound **7.41** was successful and gave pure product when commercially available 2-bromo-1-phenylethanone was reacted with **7.40** in refluxing EtOH. Attempts to form **7.42** using similar conditions suffered from poor conversion. Compound **7.26** is sparingly soluble in EtOH, and an alternate solvent will need to be used to enable the formation of the desired product.

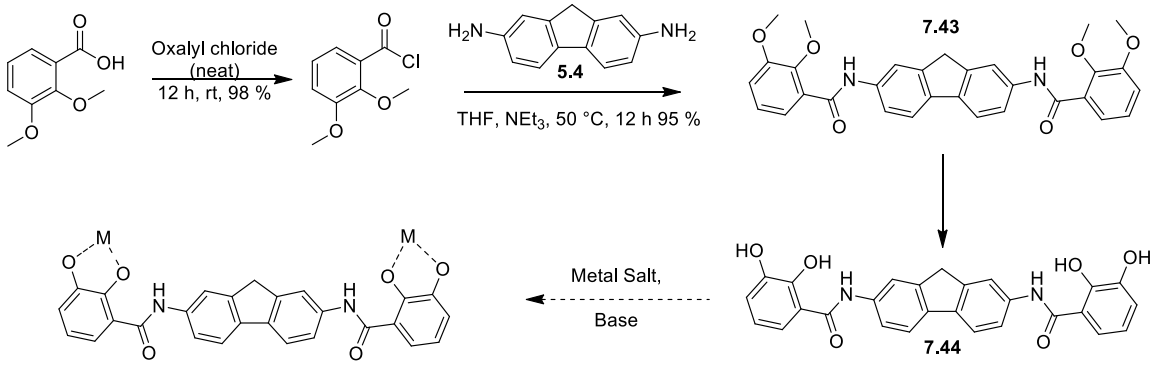

Figure 7.16. Synthetic scheme for the formation of catechol ligands from dianiline cores.

The three metal chelators investigated so far make use of bidentate N donor groups. To develop more robust complexes, O donors were also examined. Ligands containing catechol ends have been used to create novel complexes[8] and could be useful for oxophilic metals such as Ga^{III}. We previously demonstrated how iron leached from the preformed assemblies could facilitate reaction catalysis in Chapters 4 and 5, and novel metals may provide new reactivity. The catechol ligands were easily formed from pre-existing dianiline precursors as shown in Figure 7.16. The ligand was prepared by converting the commercially available benzoic acid to the acyl chloride, followed by substitution with **5.4** to form **7.43**. Compound **7.43** was then deprotected using BBr_3•Me_2S in refluxing toluene to form the catechol ligand **7.44** in good yields. Attempts to form discrete metal complexes using KOH as the base and iron or other transition metal salts were unsuccessful. In this case, it is likely that the doubly benzylic methylene unit of **7.44** is deprotonated by the strong base, and either a less reactive central core or a mild base will be necessary to form the catechol complexes.

7.4 Alternate Metal and Assembly Properties

Iminopyridine complexes in the literature frequently make use of metals such as Fe^{II}, Co^{II}, Ni^{II}, Cd^{II} and Zn^{II}. The use of new metals could provide opportunities for alternate reactivity and so assembly formation was tested with a variety of metals and ligands. Proflavine (3,6-diaminoacridine, Figure 7.17a) is commercially available as the HCl salt, and frequently used as a dye. A similar structure, 2,7-diaminoacridin-9-one is

also of interest and attempts to synthesize this ligand were made using the scheme shown in Figure 7.17b.

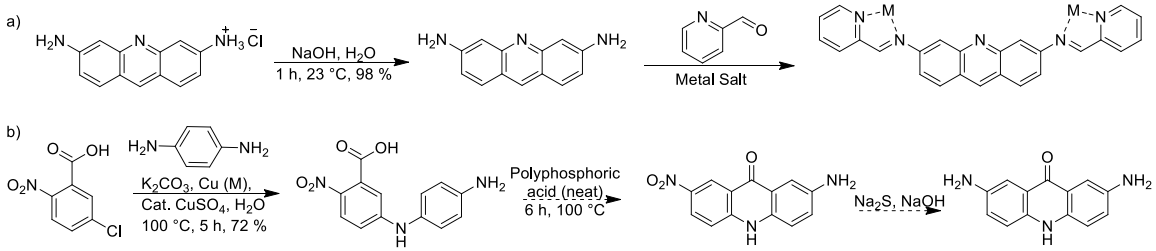

Figure 7.17. Synthesis of a) diaminoacridine complexes and b) diaminoacridone ligand.

Upon complexation of proflavine with PyCHO and metal salts, discrete complexes were synthesized and isolated when iron, cadmium and zinc were used. These complexes did not appear to display strong fluorescent properties when solutions were observed under a UV light source, although in-depth fluorescence measurements were not completed on these assemblies. Alternate metal complexes were also synthesized using dianilines **1.5**, **1.6**, **2.5**, and **5.2** with PyCHO and various metals. All ligands with the exception of suberol **1.6** were amenable to complex formation with Cd^{II} and Zn^{II} and formed complexes **7.45** – **7.50** (Chapter 8). Ligand **1.6** was capable of only partially forming a discrete assembly with $Zn(BF_4)_2$; however, the reaction was low yielding and exhibited a broad ^{1}H-NMR spectrum. Use of $Zn(ClO_4)_2$ resulted in a sharpened spectrum typical of discrete assembly formation, although it remains unclear why core **1.6** is unable to form assemblies with $Zn(BF_4)_2$,

In addition to complex formation with PyCHO, it was discovered that self-assembly of dianiline ligands, metal salts and 2-quinolinecarboxaldehyde (QnCHO) can be achieved.

When Fe^{II} is used with properly oriented ligands, paramagnetic compounds exhibiting ^1H NMR signals ranging from +190 to -100 ppm are observed. To further examine this behavior, select dianiline ligands were reacted with QnCHO and filled-shell metals. Cadmium salts cleanly formed the corresponding M_2L_3 assemblies with ligands **1.5**, **1.6**, **2.2** and **5.2**, (**7.51** – **7.54**). Interestingly, dianiline **1.5** complexed with Cd^{II} and QnCHO forms a mixture of mesocate and helicate structures, as determined through 2D DOSY and gCOSY NMR experiments. All other complexes form the highly symmetrical mesocate isomer.

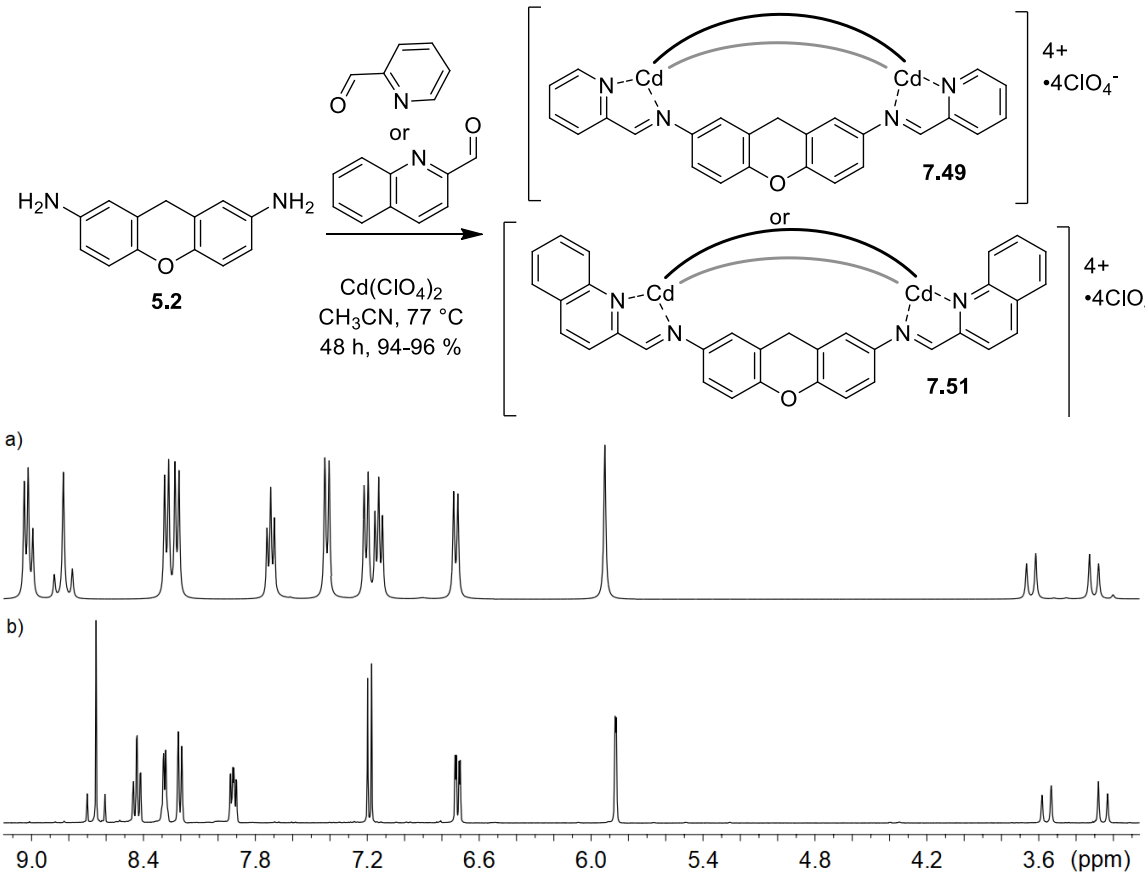

Figure 7.18. Synthesis and ^1H NMR spectra of complexes a) **7.51** and b) **7.49** displaying the diagnostic Cd coupling pattern of the imine peaks at 8.8 (a) and 8.6 (b) ppm.

The use of Cd salts provides a diagnostic tool for complexation: ^{111}Cdand ^{113}Cd, present in about 25 % natural abundance, are both NMR active with spin ½ nuclei. The ^{1}H NMR spectra of the Cd complexes display characteristic vicinal coupling between the imine H and the Cd centers, (Figure 7.18). When Zn^{II} salts and QnCHO were assembled with dianiline cores, only one discrete complex was formed (**7.55**) with dianiline **1.6**. This selectivity hints that increased steric bulk near the metal chelator can be accommodated by longer bond lengths to Cd atoms. The outlier complex using zinc and core **1.6** indicates that ligand flexibility can also accommodate the additional steric bulk.

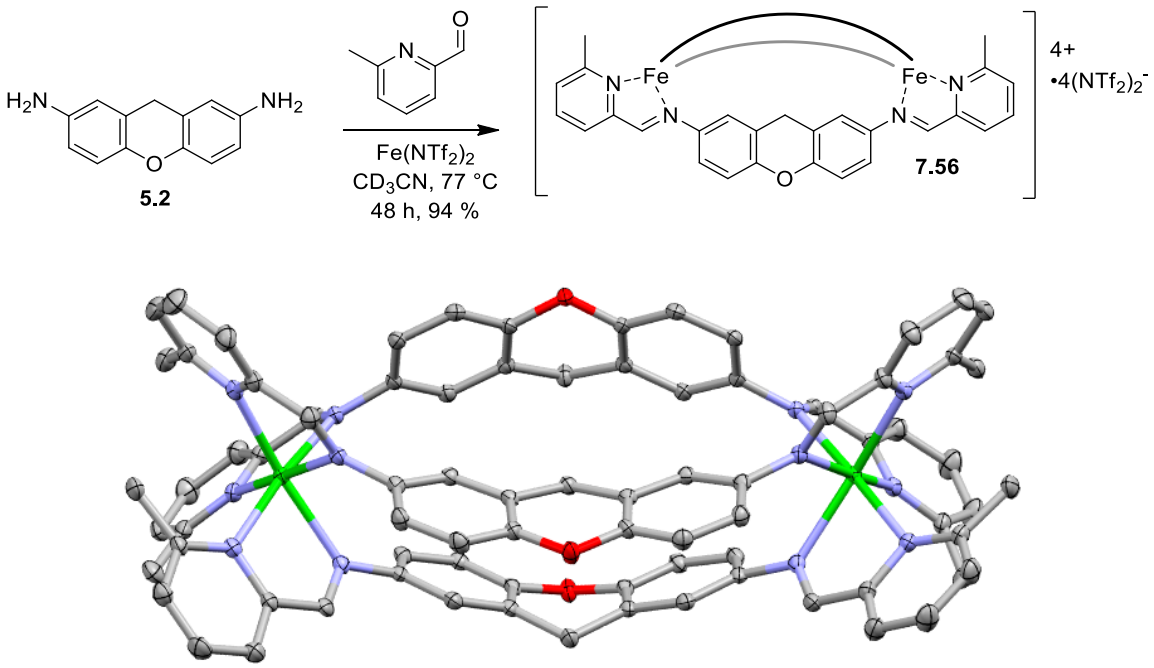

Figure 7.19. Synthesis of paramagnetic complex **7.56** and X-Ray crystal structure.

The use of QnCHO to confer paramagnetism to Fe^{II}-iminopyridine scaffolds was only successful with the highly flexible dianiline **1.6**. However, the addition of a methyl group at the 6 position of the pyridyl ring was well tolerated by more rigid cores such as

1.11 and **5.2**. The addition of steric bulk at the 6 position of the pyridyl ring causes the octahedral iron centers to adopt a distorted geometry. This behavior is accompanied by longer bond lengths and iron adopting the high spin state. The self-assembly of **1.11** with 6-MePyCHO and $Fe(NTf_2)_2$, resulted in clean formation of the desired paramagnetic product as shown in Figure 7.19. In order to fully characterize the effects of steric bulk around the metal atoms, X-Ray quality crystals were prepared via slow diffusion of diethyl ether into saturated solutions of complexes **7.56** and **7.57** in acetonitrile.

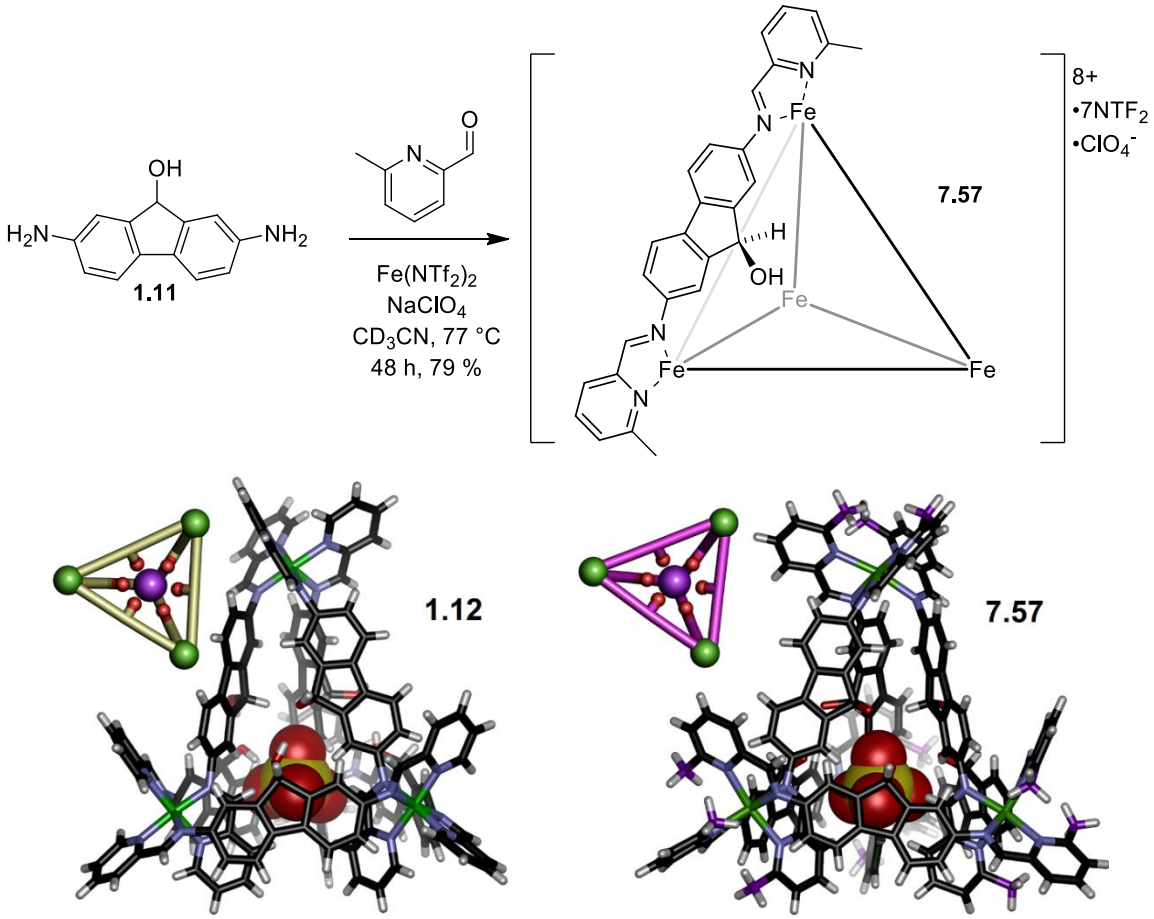

Figure 7.20. Synthesis of paramagnetic complex **7.55** and X-Ray crystal structures of **1.12** and **7.57**.

In addition to the M_2L_3 paramagnetic complex **7.56**, heating **1.11** with 6-MePyCHO, $Fe(NTf_2)_4$ with $NaClO_4$ template in CH_3CN for 72 h yielded cage **7.57** in good yield. The presence of ClO_4^- anions is vital for the formation of the templation of a single isomer of product. Dianiline **1.11** forms **1.12**, an unusual M_4L_6 complex with ClO_4^- as an internal hydrogen-bonding template, when reacted with PyCHO and Fe^{II} salts. Cage **1.12** was found to exist as one C_3-symmetric diastereoisomer with an unusual mer_3fac structure. Synthesis of a single isomer of **7.57** was possible using $Fe(ClO_4)_2$, but the resulting complex was not soluble enough to facilitate the growth of X-Ray quality crystals.

The X-ray crystal structures allow for thorough examination of the Fe^{II} coordination spheres, and when compared to the X-ray crystal structures for **1.7**, **1.8**, and **1.12**, demonstrates why **7.56** and **7.57** are paramagnetic while all previously formed Fe^{II} complexes are not. There are two measurements within the assemblies that vary drastically between the diamagnetic and paramagnetic species: the N-Fe-N bond angles and the N-Fe bond lengths. Some of these lengths and angles are shown in Figures 7.21 and 7.22.

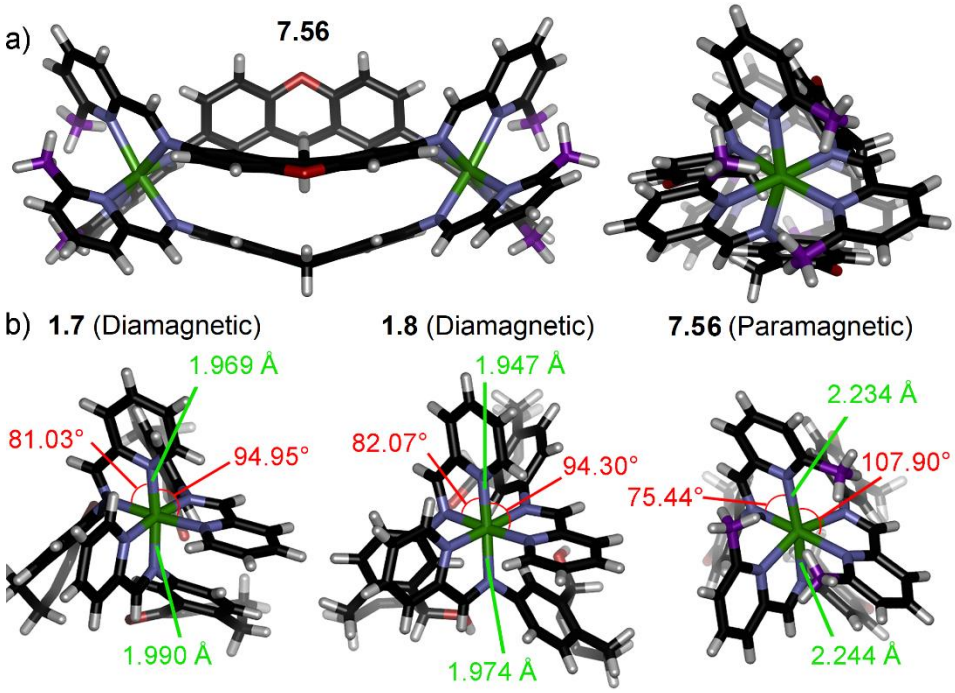

Figure 7.21. a) X-Ray crystal structure of **7.56** and b) truncated structures of a single metal center of **1.7**, **1.8** and **7.54** with highlighted angles.

The bond angles for the diamagnetic M_2L_3 assemblies **1.7** and **1.8** are very similar with both coordination geometries being nearly octahedral. When comparing the diamagnetic and paramagnetic complexes. there are two N-Fe-N angles to be considered: the internal angles (N-Fe-N in the iminopyridine 5-membered ring) and the interligand angles (N-Fe-N between two pyridyl nitrogens). The angles for the M_2L_3 complexes are shown in Figure 7.20 and summarized in Table 7.1. The coordination geometry around the Fe centers of **7.56** is far more distorted than for the diamagnetic counterparts. The internal N-Fe-N angles within the paramagnetic complex are compressed, while the interligand angles are widened. The distortion of the octahedral coordination sphere is accompanied by an average N-Fe bond length increase of almost 0.3 Å (Table 7.1). The addition of steric bulk at the 6 position of the pyridyl ring, close to the metal center results in steric clashes

at the Fe centers. In order to accommodate this, the iminopyridine ligands must adopt a distorted coordination environment in addition to increased N-Fe bond lengths. This results in the high spin, paramagnetic complexes.[9]

Table 7.1. Comparison of select bond lengths and angles taken from the X-ray crystal structures of the three M_2L_3 species, **1.7**, **1.8**, and **7.56**.

Complex	Internal angle	Interligand angle	Py N-Fe Bond length	Im N-Fe Bond length
1.7	81.03°	94.95°	1.969 Å	1.990 Å
1.8	82.07°	94.30°	1.947 Å	1.974 Å
7.56	75.44°	107.90°	2.234 Å	2.244 Å

While the synthesis and analysis of the M_2L_3 mesocates is simplified, their tolerance of extra bulk around the metal centers lies in the flexibility of the ligand backbone, which allows bending upon assembly (as discussed in Chapter 2). This flexibility allows for the distorted octahedral coordination environment observed in **7.56** to exist. Larger structures such as M_4L_6 complexes are far more challenging (Chapter 5 and 6) and require ligand cores with a coordination angle closer to 180°. However, self-assembly of ligand **1.11** with Fe^{II} salts and 6-MePyCHO was successful in producing a discrete paramagnetic complex. The remaining question is why this rigid core is able to assemble with only minimal ligand flexibility.

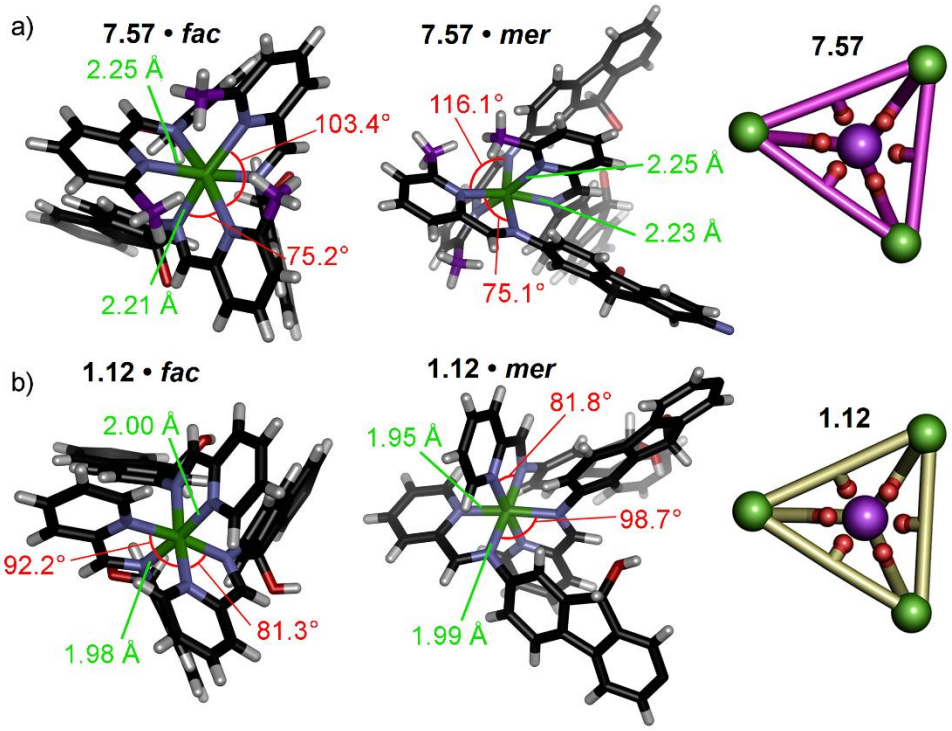

Figure 7.22. Truncated X-Ray crystal structures of a) of paramagnetic **7.57** and b) diamagnetic **1.12**, with highlighted angles.

The X-ray data for **7.57** confirms that the assembly exists as a single diastereomer with the M_4L_6 mer_3fac structure. Unfortunately, the crystals were extremely complex and cracked at low temperatures (likely the result of a spin transition at low temperature), and so the acquisition was performed at 150 K. However, the structure and connectivity of the complex was accurately determined. The solid-state structure also allowed for analysis of the coordination environment at the Fe^{II} centers. However, due to the lower resolution of the X-Ray data for **7.57**, the values for bond angles and lengths may exhibit more error. The measured internal/interligand N-Fe-N bond angles and Fe-N bond lengths for the *fac* metal centers on **7.57** are similar to those observed in **7.56**. The reason why rigid dianiline **1.11** is able to form a paramagnetic complex is due to the presence of the three *mer* centers,

which are more distorted than the *mer* centers in **1.12**. The presence of the unique *mer* centers allow for favorable distortion around the iron atoms and relieves the steric clashes introduced by the substituents.

Table 7.2. Comparison of select bond lengths and angles taken from the X-ray crystal structures of the two M_4L_6 species, **1.12**, and **7.55**.

Complex	Internal angle	Interligand angle	Py N-Fe Bond length	Im N-Fe Bond length
1.12 *fac* centers	81.3°	92.2°	2.00	1.98
1.12 *mer* centers	81.8°	98.7°	1.95	1.99
7.57 *fac* centers	75.2°	103.4°	2.25	2.21
7.57 *mer* centers	75.1°	116.1°	2.25	2.23

The solid-state structures of paramagnetic **7.56**, and **7.57** compared to diamagnetic **1.7**, **1.8** and **1.12** clearly illustrates the geometric distortion around the metal centers. However, this does not explain why some ligand cores cannot form paramagnetic species. Previously, QnCHO and $Cd(ClO_4)_2$ were successfully complexed with ligand cores **1.5**, **1.6**, **2.5** and **5.2**, and it was hypothesized that the larger radius and bond lengths of the Cd^{II} atoms can accommodate the extra steric bulk. However, when $Zn(ClO_4)_2$ was used, only the most flexible core, dianiline **1.6**, was able to form a discrete assembly. This reactivity trend was mirrored in tests with QnCHO and $Fe(ClO_4)_2$ or $Fe(NTf_2)_2$: only core **1.6** successfully forms discrete paramagnetic assemblies with the sterically demanding QnCHO. It is highly likely that the extra flexibility in **1.6** allows the extra steric bulk of QnCHO to be accommodated, while more rigid cores cannot. Further studies involving the

stability of dianiline **1.6**, the reversed hierarchy of ligand favorability (when compared to the diamagnetic complexes) and the magnetic properties of the paramagnetic complexes is underway and being completed by Tabitha Miller, a coworker in the Hooley Laboratory.

7.5 Conclusion

In conclusion, a variety of novel modifications were attempted in order to synthesize new supramolecular assemblies. Endohedral functional groups were added to ligand scaffolds through nucleophilic substitution or radical addition reactions, and it was determined that the small mesocate structures are not tolerant to amine functionalities or steric bulk. However, the Fe^{II}-iminopyridine complexes are not affected by the presence of thiol species in solution or thioether groups on the ligand scaffold. Through radical bromination and deprotection, an extended ligand bearing a reactive alkyl bromide group was successfully synthesized and initial complexation trials were promising. This may lead to the formation of a reactive parent cage that can be used to create a library of endohedrally functionalized hosts for molecular recognition and catalysis.

In addition to functionalized ligands, the synthesis of a variety of new chelating groups was attempted in order to tune the assembly properties. A library of new iminopyridine assemblies utilizing Cd^{II} and Zn^{II} metals was created and characterized. The assemblies formed using Zn^{II} and Cd^{II} provided valuable insights into the nature of the complexes utilizing the QnCHO chelator, and helped to explain the interesting ligand favorability of the paramagnetic complexes. X-Ray quality crystals were grown of two paramagnetic cages, which allowed for accurate quantification of the bond length and angle

changes between the diamagnetic and paramagnetic assemblies. From this, it was found that the paramagnetic complexes exhibit a highly distorted coordination sphere to accommodate the extra steric bulk near the metal centers. This behavior is accompanied by elongated Fe-N bonds, and the iron atoms existing in the high spin state. Continued work in this lab will focus on the potential applications for the paramagnetic complexes, in addition to further investigation into methods for creating functionalized supramolecular hosts.

7.6 References

1. Tran, B. L.; Li, B.; Driess. M.; Harwigh, J. F. "Copper-Catalyzed Intermolecular Amidation and Imidation of Unactivated Alkanes." *J. Am. Chem. Soc*. **2014**, *136*, 2555-2563.

2. Lebel, H.; Huard, K. "De Novo Synthesis of Troc-Protected Amines: Intermolecular Rhodium-Catalyzed C-H Amination with N-Tosyloxycarbamates." *Org. Lett.* **2007** *9*, 639-642.

3. Amaoka, Y.; Kamijo, S.; Hoshikawa, T.; Inoue, M. "Radical Amination of C(sp^3)-H Bonds Using N-Hydroxyphthalimide and Dialkyl Azodicarboxylate." *J. Org. Chem*. **2012**, *77*, 9959−9969.

4. Petruzziello, D.; Gualandi, A.; Grilli, S.; Cozzi, P. G. "Direct and Stereoselective Alkylation of Nitro Derivatives with Activated Alcohols In Trifluoroethanol." *Eur. J. Org. Chem*. **2012**, *34*, 6697-6701.

5. Tidmarsh I. S; Faust, T. B.; Adams, H.; Harding, L. P.; Russo, L.; Clegg, W.; Ward, M. D. "Octanuclear Cubic Coordination Cages." *J. Am. Chem. Soc*. **2008**, *130*, 15167-15175.

6. Tang, D.; Wang, J.; Wu, P.; Guo, X.; Li, J.-H.; Yangac, S. Chen, B.-H. "Synthesis of 1,2,4-Triazine Derivatives Via [4 + 2] Domino Annulation Reactions in One Pot." *RSC Adv*. **2016**, *6*, 12514–12518.

7. Habenicht, S. H.; Rohland, P.; Reichel, J.; Biver, T.; Minei, P.; Jakobi, D.; Pucci, A.Weiss, D.; Beckert, R.; Goerls, H. "Small Molecules as Long-Wavelength Fluorophores: Push-Pull Substituted 4-Alkoxy-1,3-Thiazoles." *Synthesis*, **2018**, *50*, 303-313.

8. Kersting, B.; Meyer, M.; Powers, R. E.; Raymond, K. N. "Dinuclear Catecholate Helicates: Their Inversion Mechanism." *J. Am. Chem. Soc*. **1996**, *118*, 7221- 7222.

9. Phan, H.; Hrudka, J. J.; Igimbayeva, D.; Lawson Daku, L. M.; Shatruk, M. "A Simple Approach for Predicting the Spin State of Homoleptic Fe(II) Tris-diimine Complexes." *J. Am. Chem. Soc.* **2017**, *139*, 6437-6447.

Chapter 8 - Experimental

8.1 General Information

^{1}H and ^{13}C NMR spectra were recorded on either a Varian Inova 400 MHz or 500 MHz NMR spectrometer, an Avance NEO 400 MHz spectrometer or a Bruker 600 MHz spectrometer and processed using MestReNova by Mestrelab Research S.L. gCOSY, NOESY, ROESY, TOCSY, and DOSY NMR were recorded on a Bruker 600 MHz spectrometer or a Varian Inova 400 MHz spectrometer equipped with TopSpin. HMBC and HSQC spectra were recorded on an Avance NEO 400 MHz spectrometer. Proton (^{1}H) chemical shifts are reported in parts per million (ppm) with respect to tetramethylsilane (TMS, $\delta = 0$). ^{1}H and ^{13}C spectra are referenced internally with respect to the solvent residual peak. Deuterated NMR solvents were obtained from Cambridge Isotope Laboratories, Inc., Andover, MA, and used without further purification. Mass spectra were recorded on an Agilent 6210 LC TOF mass spectrometer using electrospray ionization with fragmentation voltage set at 115 V and processed with an Agilent MassHunter Operating System for data collected in chapters 2-4. Mass spectrometric analysis for Chapter 5 was performed using a Thermo LTQ linear ion trap with a standard electrospray ionization source (Thermo Fisher Scientific, San Jose, CA, USA). Samples were directly infused at 3 µL/min in 100 % MeCN, with the source voltage set to 3 kV, tube lens at 75 kV and the capillary temperature at 270 °C. CID spectra were collected in ZoomScan mode where the isolation window = 5 m/z, normalized collision energy (nCE) = 30 and activation time = 30 ms. MS data was analyzed using Thermo XCalibur. Mass spectroscopic samples for Chapter 6 were infused into an Orbitrap Velos Pro mass spectrometer with the standard

HESI source at a flow rate of 3 μL/min. The spray voltage was 3 kV, capillary temperature was set to 170 °C and an S-lens RF level of 45% was applied. Full FTMS were acquired with a resolution of r = 30,000, and ambient ions were used as internal lock mass calibrants. CID spectra were collected in ZoomScan mode where the isolation window = 5 m/z, normalized collision energy (nCE) = 30 and activation time = 30 ms. MS data was analyzed using Thermo XCalibur. Predicted isotope patterns were prepared using ChemCalc.[1] X-Ray diffraction data was obtained and the crystal structure of **7.56** was solved at the UC Riverside ACIF facility. Data collection, solution, and refinement were routine. X-ray intensity data were collected at 100(2) K on a Bruker APEX2 platform-CCD X-ray diffractometer system (fine focus Mo-radiation, λ = 0.71073 Å, 50KV/30mA power). The structure was deposited at the CCDC (#1848253). The diffraction data for **7.57** was obtained at the UC San Diego X-ray Crystallography Facility, and the structure was solved at the UC Riverside ACIF facility. X-ray intensity data were collected at 150(2) K on a Bruker Rotating Anode generator with APEX2 platform-CCD X-ray diffractometer system (Mo-radiation, λ = 0.71073 Å, 50KV/24mA rotating anode power). The structure was deposited at the CCDC (#1848254). All other materials were obtained from Aldrich Chemical Company, St. Louis, MO and were used as received. Solvents were dried through a commercial solvent purification system (Pure Process Technologies, Inc.). Molecular modeling (semi-empirical calculations) was performed using the AM1 force field using SPARTAN.[2]

8.2 Chapter 2 Experimental

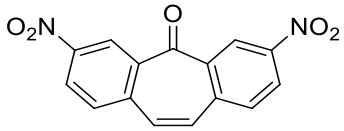

3,7-Dinitrodibenzosuberenone (**2.1**):

3,7-Dinitrodibenzosuberone[3] (**1.4**) (100 mg, 0.33 mmol) was added to a 50 mL round bottom flask, followed by the addition of benzene (25 mL). 1.1 equivalents N-bromosuccinimide (64.8 mg, 0.36 mmol) was added to the flask, followed by 0.1 eq benzoyl peroxide (8.0 mg, 0.03 mmol). The reaction was refluxed for 12 h, after which the solid was filtered and dried. The crude solid was placed into a 50 mL vial followed by acetone (25 mL). Potassium iodide (60.4 mg, 0.33mmol) was added to the flask and the mixture was stirred at room temperature for 4 h. The reaction mixture was filtered, and the product collected as a light yellow solid (47 mg, 50 %). ^{1}H NMR (400 MHz, DMSO-d_6): δ 8.70.25 (d, J = 2.5 Hz, 2H), 8.53 (dd, J = 8.5, 2.6 Hz, 2H), 7.99 (d, J = 8.5 Hz, 2H), 6.58 (s, 2H). ^{13}C NMR (150 MHz, DMSO-d_6): δ 180.2, 148.4, 140.0, 138.4, 134.6, 134.1 127.7, 126.3. HRMS (ESI) m/z calcd for $C_{15}H_8N_2O_5$ (**2.1**$^{+}$) 296.0418, found 296.0228.

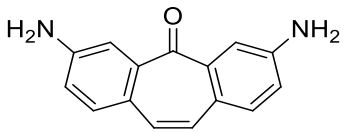

3,7-Diaminodibenzosuberenone (**2.2**):

Compound **2.1** (400 mg, 1.34 mmol) was added to a 50 mL round bottom flask with stir bar, followed by addition of Raney© 2800 Ni suspension in water (1.0 mL) and MeOH (25 mL). The flask was fixed with a septum and purged with nitrogen gas. Hydrazine monohydrate (2.0 mL, 41.2 mmol) was slowly added. After the addition, the reaction was

stirred at room temperature. After 24 h the reaction mixture was diluted with acetone (100 mL) followed by filtering through celite. After evaporating the solvent *in vacuo*, the residue was sonicated in deionized water (200 mL) before being filtered using celite. The filter was rinsed clean using MeOH (150 mL) before evaporating the solvent *in vacuo* to give an orange-yellow solid. This was recrystallized from EtOH to give product as an orange solid (162 mg, 50 %). ^{1}H NMR (400 MHz; DMSO-d_6) δ 7.33 (s, 2H), 7.31 (d, J = 5.9 Hz, 2H), 6.89 (dd, J = 5.9, 2.2 Hz, 2H), 6.69 (d, J = 2.2 Hz, 2H). ^{13}C NMR (150 MHz, DMSO-d_6): δ 191.4, 149.8, 138.7, 133.4, 127.6, 126.0, 119.7, 113.3. HRMS (ESI) m/z calcd. for $C_{15}H_{12}N_2O$ ([**2.2**•H]$^+$) 236.1178, found 236.1248.

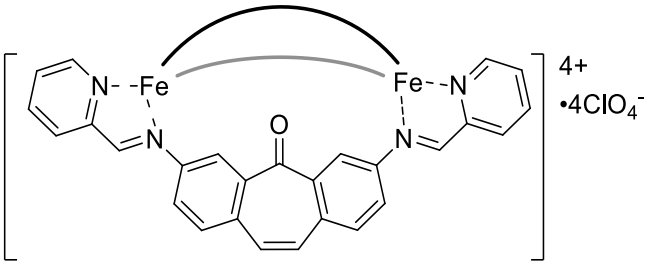

Mesocate **2.3**:

Dianiline **2.2** (38.3 mg, 0.161 mmol), 2-pyridine carboxaldehyde (27.0 μL, 0.32 mmol) and $Fe(ClO_4)_2$•xH_2O (35.1 mg) were combined in anhydrous MeCN (5 mL) in a 50 mL round-bottomed flask under a blanket of N_2 gas. The solution was then heated at 45 °C for 10 h with stirring. The purple solution was diluted with Et_2O (25 mL), cooled to -25 °C followed by filtration of the resulting precipitate. After drying, the product was isolated as a purple solid (65.0 mg, 92 %) ^{1}H NMR (400 MHz; CD_3CN) δ 8.74 (s, 2H), 8.50 (d, J = 7.4 Hz, 2H), 8.44 (t, J = 7.3 Hz, 2H), 7.8 (t, J = 5.2 Hz, 2H), 7.56 (d, J = 8.3 Hz, 2H), 7.43 (d, J = 5.3 Hz, 2H), 7.2 (s, 2H), 6.56 (d, J = 2.2 Hz, 2H), 5.62 (dd, J = 8.2, 2.2 Hz, 2H). ^{13}C NMR

(150 MHz, DMSO-d_6): δ 186.4, 176.4, 158.6, 156.4, 150.4, 140.4, 138.5, 135.8, 134.8, 132.7, 131.8, 130.4, 125.5, 122.9. HRMS (ESI) m/z calcd. for $C_{81}H_{60}Fe_2N_{12}O_3$ ([**2.3**]$^{4+}$) 339.0897, found 339.0802.

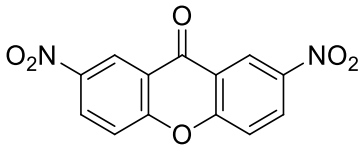

2,7-Dinitroxanthone (**2.4**):

Fuming nitric acid (15 mL) and concentrated sulfuric acid (10 mL) were combined in a 250 mL round bottom flask and cooled at 0 °C. Xanthone (2 g, 10.1 mmol) was slowly added to the solution in 200 mg portions with vigorous stirring over a period of 30 min. The yellow solution was allowed to stir for an additional h at 0 °C. The mixture was then poured into a beaker containing ice (150 g) with vigorous stirring and the precipitate was filtered. The pale-yellow crude product was washed with hexane, then recrystallized from nitromethane to yield an off white solid (1.98 g, 68 %) ^{1}H NMR (400 MHz, DMSO-d_6): δ 9.25 (d, J = 2.8 Hz, 2H), 8.65 (dd, J = 9.2, 2.8 Hz, 2H), 7.75 (d, J = 9.2 Hz, 2H). ^{13}C NMR (100 MHz, DMSO-d_6): δ 175.6, 159.5, 144.8, 131.0, 122.7, 121.8, 121.5. HRMS (ESI) m/z calcd. for $C_{13}H_6N_2O_6$ (**2.4**$^+$) 286.0257, found 286.0238.

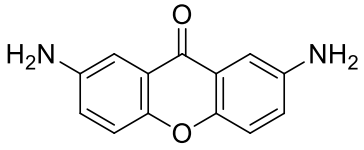

2,7-Diaminoxanthone (**2.5**):

Compound **2.4** (100 mg, 0.33 mmol) was placed in a 50 mL round bottom flask with a stir bar followed by 10 mL of concentrated hydrochloric acid. Then, 4.5 equivalents of

tin(II)chloride dihydrate was added to the flask. The reaction was refluxed for 12 h with stirring, then allowed to cool to room temperature. The reaction mixture was diluted with 50mL deionized water and brought to a pH of 8.5 using 2 M NaOH. The yellow solution was then extracted using ethyl acetate until no color was present in the aqueous layer (3 x 15 mL). The solution was dried using anhydrous $MgSO_4$, filtered and the solvent removed in vacuo to yield an orange solid (57 mg, 72 %). ^{1}H NMR (400 MHz, DMSO-d_6): δ 7.33 (d, J = 8.8 Hz, 2H), 7.22 (d, J = 2.8 Hz, 2H), 7.07 (dd, J = 9.0 Hz, 2H), 5.32 (s, 4H). ^{13}CNMR (100 MHz, DMSO-d_6): δ 176.8, 148.7, 145.1, 123.9, 122.1, 119.2, 106.8. HRMS (ESI) m/z calcd. for $C_{13}H_{10}N_2O_2$ ([**2.5**•H]$^+$) 226.0713, found 226.0628.

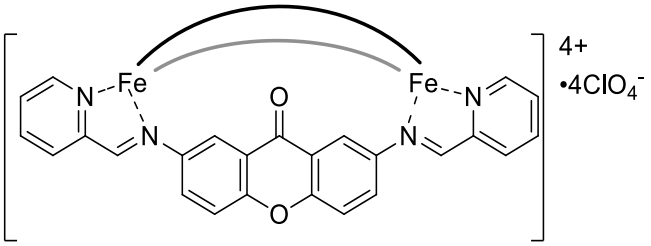

Mesocate **2.6**:

Dianiline **2.5** (100 mg, 0.44 mmol), 2-pyridine carboxaldehyde (107 μL, 0.88 mmol) and $Fe(ClO_4)_2$•xH_2O (96.3 mg) were combined in anhydrous MeCN (10 mL) in a 50 mL round-bottomed flask under a blanket of N_2, followed by heating to 45 °C for 10 h. The solution was then cooled to room temperature, diluted with Et_2O (30 mL), and cooled to -25 °C followed by filtration of the resulting precipitate. Drying product *in vacuo* gave product as a purple solid (190 mg, 96 %). ^{1}H NMR (400 MHz; CD_3CN) δ 11.13 (m, 2H), 9.31 (s, 2H), 8.98 (m, 2H), 8.48 (s, 2H), 8.34 (s, 2H), 7.33 (m, 2H), 6.39 (s, 2H), 5.44 (d, J = 8.5 Hz, 2H). Cage **4** was not soluble enough to collect a ^{13}C NMR spectrum within a reasonable

amount of time. HRMS (ESI) m/z calcd for $C_{75}H_{54}Fe_2N_{12}O_{14}Cl_2$ ([**2.6**•$(ClO_4)_2$]$^{2+}$) 761.7364, found 761.9462.

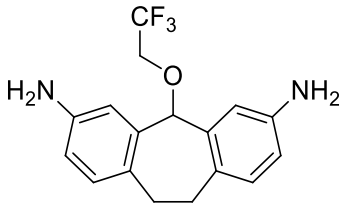

3,7-Diaminodibenzosuberyl-2,2,2-trifluoroethyl ether (**2.7**):

3,7-Diaminodibenzosuberol[3] (**1.6**) (70 mg, 0.29 mmol) was added to 2,2,2-trifluoroethanol (3 mL), followed by addition of trifluoromethanesulfonic acid (250 μL, 2.8 mmol). The reaction mixture was stirred at room temperature for 70 h, followed by neutralization of the solution using saturated sodium bicarbonate. The resulting solid was filtered to give product as a tan solid (79 mg, 84 %). ^{1}H NMR (400 MHz, DMSO-d_6): δ 6.76 (d, J = 8.0 Hz, 2H), 6.51 (d, J = 1.7 Hz, 2H), 6.40 (dd, J = 8.0, 1.7 Hz, 2H), 5.15 (s, 1H), 3.87 (q, J = 9.3 Hz, 2H), 3.11 (d, J = 6.7 Hz, 2H), 2.65 (d, J = 6.7 Hz, 2H). ^{13}C NMR (100 MHz, DMSO-d_6): δ 147.1, 138.3, 133.3, 131.5, 126.6, 123.8, 115.1, 80.1, 65.4, 31.6. HRMS (ESI) m/z calcd. for $C_{13}H_{10}N_2O_2$ ([**2.7**•H]$^+$) 322.1293, found 322.1362.

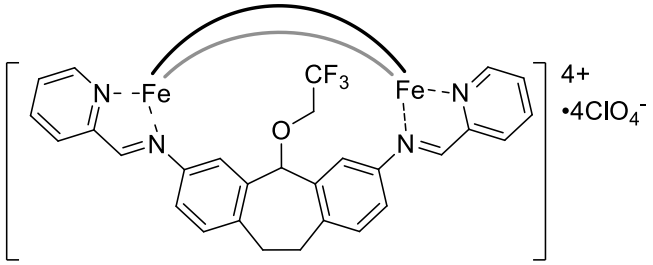

Mesocate **2.8**:

Dianiline **2.7** (100 mg, 0.31 mmol), 2-pyridine carboxaldehyde (59 μL, 0.62 mmol) and $Fe(ClO_4)_2$•xH_2O (66.8 mg, 0.20 mmol) were combined in anhydrous MeCN (10 mL) in a

50 mL round-bottomed flask under a blanket of N_2, followed by heating to 45 °C for 10 h. The solution was then cooled to room temperature, diluted with Et_2O (30 mL), and cooled to -25 °C followed by filtration of the resulting precipitate. Drying *in vacuo* gave product as a purple solid (169 mg, 98%). ^{1}H NMR and ^{13}C NMR: see publication for full spectra.[4] HRMS (ESI) m/z calcd. for $C_{58}H_{46}Fe_2N_8O_{14}F_6Cl_3$ ($[M_2L_2•(ClO_4)_3]^+$) 1409.2018, found 1409.0489.

General ligand competition procedure:

All mixing experiments were performed in an NMR tube. One equivalent of suberone dianiline **1.5** (3.5 mg, 0.015 mmol) and one equivalent of suberenone dianiline **2.2** (3.5 mg 0.015 mmol) were placed in an NMR tube. Deuterated acetonitrile (400 µL) was added to the tube and a proton spectrum of the dianiline mixture obtained. 2 equivalents of 2-formylpyridine were added (5 µL, 0.029 mmol) followed by 0.66 equivalents of iron perchlorate (100 µL of 0.098 M $Fe(ClO_4)_2$ in CD_3CN). A spectrum of the mixture was obtained. The tube was heated at 80 °C for 8 h. A second spectrum was taken after heating to determine the favored cage and the unfavored dianiline ligand. A second 2 eq. of 2-formylpyridine and 0.66 eq. of $Fe(ClO_4)_2$ were added to the tube and a proton spectrum obtained. The tube was heated to 80 °C for 8 h. A final spectrum was obtained after heating to show both cages in solution.

General ligand displacement procedure:

All displacement experiments were performed in an NMR tube. One equivalent of preformed Cage **1.7** (8.6 mg, 0.005 mmol) and three equivalents of dianiline **1.6** (3.5 mg

0.015 mmol) were placed in an NMR tube. Dry deuterated acetonitrile (400 µL) was added to the tube and a proton spectrum of the starting mixture obtained. The tube was heated at 80°C for 8 h. A second spectrum was obtained after heating to verify whether the preformed cage was displaced by the free dianiline ligand. Experiments were repeated with the addition of 6 molar equivalents of water and heated at 55°C for 1 h.

8.3 Chapter 3 Experimental

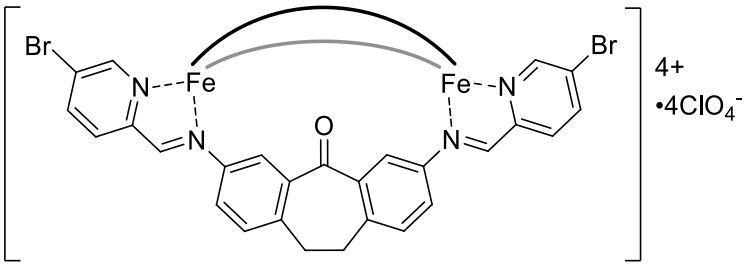

Bromopyridine mesocate (**3.1•Br$_6$**):

3,7-Diaminodibenzosuberone[3] (**1.5**) (20 mg, 0.084 mmol), 5-bromo-2-formylpyridine (31 mg, 0.17 mmol) and $Fe(ClO_4)_2$•$3H_2O$ (18 mg, 0.056 mmol) were combined in anhydrous CH_3CN (2 mL) in an 8 mL vial. The solution was then heated at 55 °C for 12 h with stirring. The purple solution was diluted with Et_2O (3 mL), placed in a freezer at 0°C for 3 h, followed by filtration of the resulting precipitate. After drying, the product was isolated as a purple solid (61.4 mg, 89 %) ^{1}H NMR (500 MHz; CD_3CN) δ 8.69 (s, 2H), 8.60 (d, *J* = 8.2 Hz, 2H), 8.36 (t, *J* = 8.2 Hz, 2H), 7.49 (s, 2H), 7.19 (d, *J* = 8.0 Hz, 2H), 6.25 (s, 2H), 5.61 (d, *J* = 6.8 Hz, 2H), 3.29 (m, 2H), 3.19 (m, 2H). ^{13}C NMR (150 MHz, CD_3CN): δ 189.0, 175.3, 157.5, 156.8, 148.1, 144.8, 143.2, 138.3, 131.6, 130.8, 126.20, 125.0, 123.4,

34.7. HRMS (ESI) m/z calcd. for $C_{81}H_{48}Fe_2N_{12}O_3Br_6$ ([**3.1•Br$_6$**]$^{4+}$) (457.9810), found 458.0136.

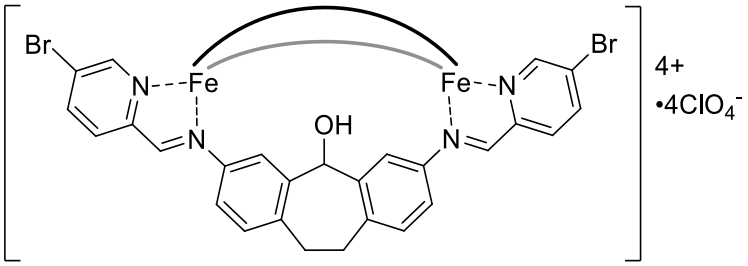

Bromopyridine mesocate (**3.2•Br$_6$**):

Dianiline **1.6** (20 mg, 0.083 mmol), 5-bromo-2-formylpyridine (29 mg, 0.16 mmol) and $Fe(ClO_4)_2$•$3H_2O$ (17 mg, 0.055 mmol) were combined in anhydrous CH_3CN (2 mL) in an 8 mL vial. The solution was then heated at 55 °C for 12 h with stirring. The purple solution was diluted with Et_2O (3 mL), and the solid collected. After drying, the product was isolated as a purple solid (60.7 mg, 92 %) ^{1}H NMR (500 MHz; CD_3CN) δ 8.78 (s, 2H), 8.25 (d, *J* = 8.2 Hz, 2H), 7.86 (m, 4H), 7.76 (s, 2H), 6.90 (d, *J* = 7.9 Hz, 2H), 6.19 (d, *J* = 7.6 Hz, 2H), 6.10 (d, *J* = 4.7 1H), 3.36 (m, 2H), 2.88 (m, 2H), 2.52 (d, *J* = 4.7, 1H). ^{13}C NMR (150 MHz, CD_3CN): δ 170.4, 157.6, 156.7, 144.8, 143.5, 141.7, 137.7, 130.6, 129.8, 125.1, 120.7, 120.2, 66.8, 30.4. HRMS (ESI) m/z calcd. for $C_{81}H_{60}Fe_2N_{12}O_3Br_6$•$Cl_2O_8$ ([**3.2•Br$_6$**]$^{2+}$) (1017.2901), found 1017.8162.

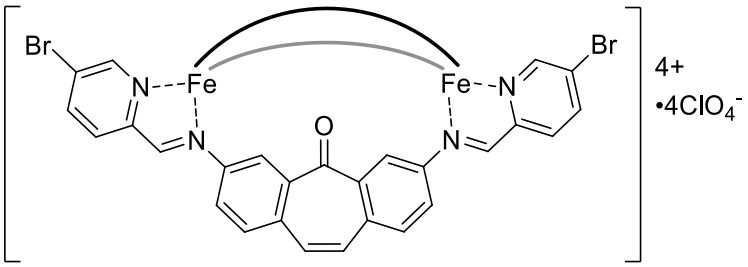

Bromopyridine mesocate (**3.3•Br$_6$**):

Dianiline **2.3** (20 mg, 0.085 mmol), 5-bromo-2-formylpyridine (31 mg, 0.17 mmol) and $Fe(ClO_4)_2•3H_2O$ (18 mg, 0.056 mmol) were combined in anhydrous CH_3CN (2 mL) in an 8 mL vial. The solution was then heated at 55 °C for 12 h with stirring. The purple solution was diluted with Et_2O (3 mL), placed in a freezer at 0°C for 3 h, followed by filtration of the resulting precipitate. After drying, the product was isolated as a purple solid (64.1 mg, 93 %) ^{1}H NMR (500 MHz; CD_3CN) δ 8.74 (s, 2H), 8.68 (d, *J* = 7.6 Hz, 2H), 8.43 (d, *J* = 7.9 Hz, 2H), 7.61 (d, *J* = 8.1 Hz, 2H), 7.55 (s, 2H), 7.24 (s, 2H), 6.56 (s, 2H), 5.77 (d, *J* = 7.5 Hz, 2H). ^{13}C NMR (150 MHz, CD_3CN): δ 185.9, 176.1, 157.7, 156.7, 149.7, 143.5, 138.0, 135.5, 134.5, 132.4, 131.6, 126.5, 125.3, 122.6. HRMS (ESI) m/z calcd. for $C_{81}H_{48}Fe_2N_{12}O_3Br_6$ ([**3.3•Br$_6$**]$^{4+}$) (456.6315), found 456.7847.

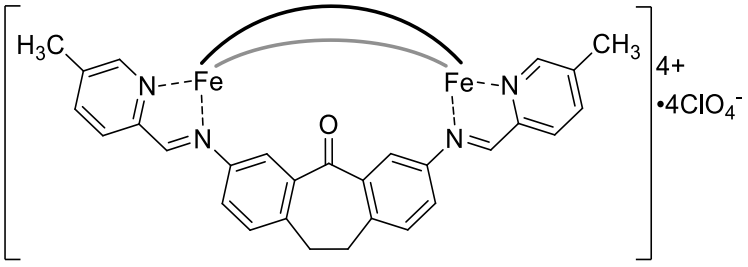

Methylpyridine mesocate (**3.4•Me$_6$**):

Dianiline **1.5** (20 mg, 0.084 mmol), 5-methyl-2-formylpyridine (21 mg, 0.17 mmol) and $Fe(ClO_4)_2•3H_2O$ (18 mg, 0.056 mmol) were combined in anhydrous CH_3CN (2 mL) in an 8 mL vial. The solution was then heated at 55 °C for 12 h with stirring. The purple solution was diluted with Et_2O (3 mL), placed in a freezer at 0°C for 3 h, followed by filtration of the resulting precipitate. After drying, the product was isolated as a purple solid (51.3 mg, 87 %) ^{1}H NMR (500 MHz; CD_3CN) δ 8.67 (s, 2H), 8.36 (d, *J* = 7.0 Hz, 2H), 8.21 (d, *J* = 6.9 Hz, 2H), 7.19 (d, *J* = 7.5 Hz, 4H), 6.3 (s, 2H), 5.56 (s, 2H), 3.33 (m, 2H), 3.20 (m, 2H),

2.43 (s, 6H). ^{13}C NMR (150 MHz, CD_3CN): δ 189.7, 174.8, 174.2, 155.6, 148.5, 144.2, 141.5, 139.8, 138.2, 130.7, 130.2, 125.1, 123.3, 34.7, 18.6. HRMS (ESI) m/z calcd. for $C_{87}H_{72}Fe_2N_{12}O_3$ ([**3.4•Me$_6$**]$^{4+}$) (361.0688), found 361.1037.

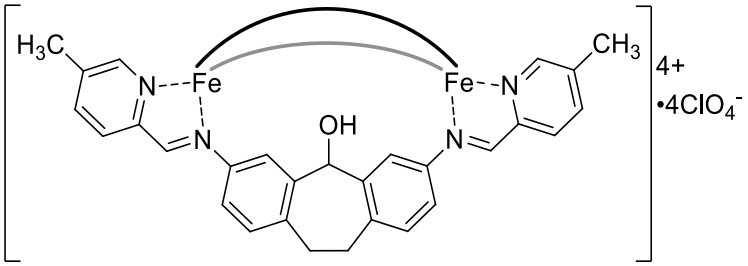

Methylpyridine mesocate (**3.5•Me$_6$**):

Dianiline **1.6** (20 mg, 0.083 mmol), 5-methyl-2-formylpyridine (19 mg, 0.16 mmol) and $Fe(ClO_4)_2$•$3H_2O$ (17 mg, 0.055 mmol) were combined in CH_3CN (2 mL) in an 8 mL vial. The solution was heated at 55 °C for 12 h. The purple solution was diluted with Et_2O (3 mL), and the solid collected. After drying, the product was isolated as a purple solid (49.8 mg, 89 %) ^{1}H NMR (500 MHz; CD_3CN) δ 8.7 (s, 2H), 7.98 (s, 2H), 7.83 (m, 4H), 7.35 (s, 2H), 6.83 (d, J = 5.9 Hz, 2H), 6.13 (d, J = 6.9 Hz, 2H), 6.09 (s, 1H), 3.34 (m, 2H), 2.85 (m, 2H), 2.43 (s, 1H), 2.33 (s, 6H). ^{13}C NMR (150 MHz, CD_3CN): δ 189.2, 174.7, 156.3, 155.7, 148.5, 144.3, 141.5, 139.9, 138.2, 130.6, 130.0, 125.0, 123.3, 34.6, 18.7. HRMS (ESI) m/z calcd. for $C_{87}H_{78}Fe_2N_{12}O_3$ ([**3.5•Me$_6$**]$^{4+}$) (362.5906), found 362.6257.

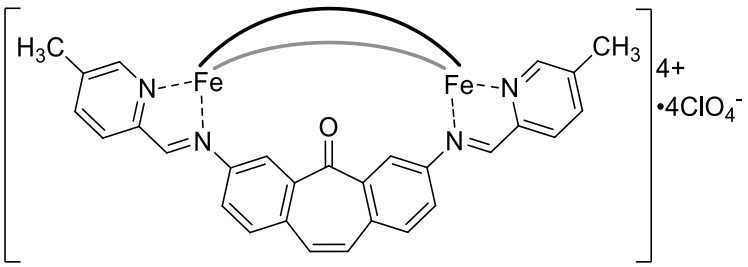

Methylpyridine mesocate (**3.6•Me$_6$**):

Dianiline **2.3** (20 mg, 0.085 mmol), 5-methyl-2-formylpyridine (21 mg, 0.17 mmol) and $Fe(ClO_4)_2 \bullet 3H_2O$ (18 mg, 0.056 mmol) were combined in anhydrous CH_3CN (2 mL) in an 8 mL vial. The solution was then heated at 55 °C for 12 h with stirring. The purple solution was diluted with Et_2O (3 mL), placed in a freezer at 0°C for 3 h, followed by filtration of the resulting precipitate. After drying, the product was isolated as a purple solid (53.1 mg, 91 %) ^{1}H NMR (500 MHz; CD_3CN) δ 8.77 (s, 2H), 8.53 (s, 2H), 8.47 (s, 2H), 7.59 (d, J = 7.8 Hz, 2H), 7.47 (d, J = 4.3 Hz, 2H), 7.23 (s, 2H), 6.58 (s, 2H), 5.65 (d, J = 7.2 Hz, 2H), 2.16 (s, 6H). ^{13}C NMR (150 MHz, CD_3CN): δ 186.2, 175.5, 156.7, 156.4, 155.7, 150.2, 141.8, 140.0, 138.1, 135.3, 134.2, 130.5, 125.3, 122.8, 18.6. HRMS (ESI) m/z calcd. for $C_{87}H_{66}Fe_2N_{12}O_3$ ([**3.6•Me$_6$**]$^{4+}$) (359.8059), found 359.3785.

8.4 Chapter 4 Experimental

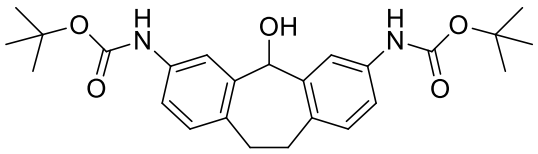

Dibenzosuberol-3,7-di-tert-butylcarbamate (**4.1**):

Dianiline **1.6** (350 mg, 1.46 mmol) was added to a 50 mL round bottom flask with a stir bar, followed by the addition of DMA (10 mL) and trimethylamine (0.61 mL). Di-tert-butyl dicarbonate (954 mg, 4.37 mmol) was slowly added to the flask. The reaction mixture was stirred at room temperature for 36 h, after which the reaction mixture was poured into a separatory funnel and washed with 3 x 10 mL portions of hexane. The reaction layer was then slowly dropped into a flask containing 100 mL of ice water with rapid stirring. The precipitate that formed was filtered, dried and collected as a tan solid (604 mg, 95 %). ^{1}H

NMR (400 MHz; DMSO-d_6) δ 9.36 (s, 2H), 7.69 (s, 2H), 7.23 (d, 2.1 Hz, 2H), 6.88 (d, J = 2.1 Hz, 2H), 5.92 (d, J = 1.9 Hz, 1H), 5.83 (d, J = 1.9 Hz, 1H), 3.31 (m, 2H), 2.91 (m, 2H) 1.45 (s, 18H). ^{13}C NMR (100 MHz, DMSO-d_6): δ 168.6, 144.2, 137.72, 131.9, 130.18, 117.9, 115.8, 79.8, 69.9, 31.5, 24.6. HRMS (ESI) m/z calcd. for $C_{25}H_{31}N_2O_5$ ($[M-H]^-$) 439.2238, found 439.1937.

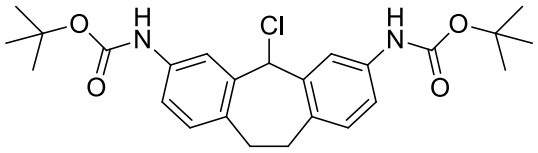

Dibenzosuberylchloride-3,7-ditertbutylcarbamate (**4.2**):

Compound **4.1** (100 mg, 0.23 mmol) was placed in a 25 mL round bottomed flask followed by 5 mL of dry DCM. One equivalent of sodium hydride (9 mg, 0.22 mmol) was slowly added to the flask and allowed to stir for 4 h. Thionyl chloride (0.016 mL, 0.22 mmol) was slowly added and the reaction was stirred for 24 h at 45 °C. The mixture was then filtered, and the solvent removed *in vacuo* to yield a pale orange solid (77 mg, 74%). The product was purified by column chromatography using 15:85 ethyl acetate/hexane as the eluent. ^{1}H NMR (400 MHz; DMSO-d_6) δ 9.3 (s, 2H), 7.94 (d, 2.2Hz, 2H), 7.22 (dd, 8.3, 2.2 Hz, 2H), 7.18 (d, *J* = 8.3 Hz, 2H), 6.22 (s, 1H), 3.49 (m, 2H), 2.77 (m, 2H), 1.44 (s, 18H). ^{13}C NMR (100 MHz, DMSO-d_6): δ 167.8, 144.8, 140.12, 137.74, 130.9, 118.13, 115.61, 78.3, 60.7, 29.8, 24.2. HRMS (ESI) m/z calcd. for $C_{25}H_{31}N_2O_4Cl$ ($[M]^+$) 458.1993, found 458.1972.

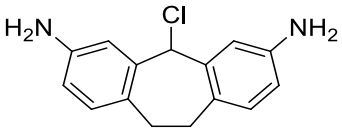

3,7- Diaminodibenzosuberylchloride (dianiline **4.3**):

Compound **4.2** (100 mg, 0.22 mmol) was placed in a 25 mL round bottom flask with a stir bar followed by 4 mL of 2M HCl in THF. The reaction was stirred for 12 h at room temperature, then poured over 5g ice. The pH was brought to 7.5 using saturated sodium bicarbonate and the solid quickly filtered to yield product (49 mg, 86%). ^{1}H NMR (400 MHz, DMSO-d_6): δ 6.89 (d, J = 8.0 Hz, 2H), 6.63 (d, J = 2.5 Hz, 2H), 6.53 (dd, J = 8.0, 2.5 Hz, 2H), 5.96 (dd, 1H), 4,53 (s, 4H), 3.03 (m, 2H), 2.77 (m, 2H). ^{13}CNMR (100 MHz, DMSO-d_6): δ 142.6, 137.8, 131.7, 126.4, 124.3, 114.2, 67.1, 31.3. HRMS (ESI) m/z calcd. for $C_{15}H_{15}N_2Cl$ ([M+H]$^+$) 259.0124, found 259.0097.

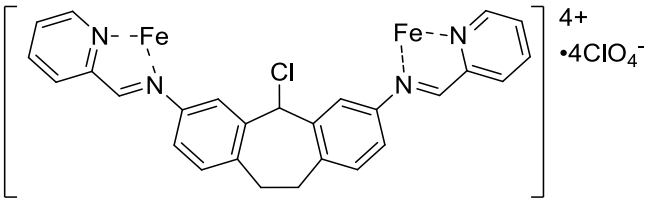

Metastable Aggregate **4.4**:

Dianiline **4.3** (100 mg, 0.39 mmol), 2-pyridine carboxaldehyde (74 μL, 0.78 mmol) and $Fe(ClO_4)_2$•H_2O (71.6 mg, 0.26 mmol) were combined in anhydrous MeCN (10 mL) in a 50 mL round-bottomed flask under a blanket of N_2, followed by heating to 45 °C for 24 h. The solution was then cooled to room temperature, diluted with Et_2O (30 mL), and cooled to -25 °C followed by filtration of the resulting precipitate. Drying product *in vacuo* gave product as a purple solid (169 mg, 98%). Forms an undefined polymeric aggregate.

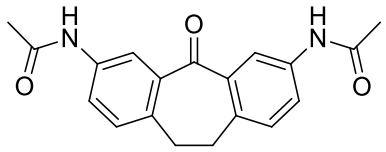

3,7-Diacetamidedibenzosuberone (**4.5**):

Dianiline **1.5** (200 mg, 0.84 mmol) was added to a 50 mL round bottom flask with stir bar, followed by the addition of THF (10 mL). Triethylamine (0.30 mL, 2.09 mmol) and 2.1 equivalents acetic anhydride (0.18 mL, 1.76 mmol) were added to the flask. The mixture was stirred at room temperature for 14 h, followed by pouring the resulting solution over 10 g ice. The resulting precipitate was filtered to give product as a pale yellow solid (270 mg, 89%). ^{1}H NMR (400 MHz, DMSO-d_6): δ 10.04 (s, 2H), 8.01 (d, J = 2.0 Hz, 2H), 7.73 (dd, J = 8.2, 2.1 Hz, 2H), 7.22 (d, J = 8.3 Hz, 2H), 3.03 (s, 4H), 2.01 (s, 6H). ^{13}CNMR (100 MHz, DMSO-d_6): δ 194.6, 169.0, 138.6, 138.4, 137.4, 130.7, 123.9, 120.8, 34.4, 24.6. HRMS (ESI) m/z calcd. for $C_{19}H_{18}N_2O_3$ ([M+H]$^+$) 323.1317, found 323.1362.

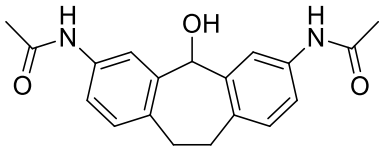

3,7-Diacetamidedibenzosuberol (**4.6**):

Compound **4.5** (200 mg, 0.62 mmol) was added to a 50 mL round bottom flask with a stir bar, followed by addition of MeOH (10 mL). Sodium borohydride (23 mg, 0.62 mmol) was slowly added. The reaction was stirred at room temperature overnight. After 14 h the reaction mixture was poured over 15g of ice, neutralized with 1M HCl and allowed to stir for 1h. The solid was filtered, dried and collected as a tan solid (185 mg, 92 %). ^{1}H NMR (400 MHz; CD_3CN) δ 9.78 (s, 2H), 7.62 (d, J = 1.8 Hz, 2H), 7.39 (dd, J = 8.1, 2.0 Hz, 2H), 6.94 (d, J = 8.2 Hz, 2H), 6.0 (d, J = 4.0 Hz, 1H), 5.93 (d, J = 4.2 Hz, 1H), 3.15 (m, 2H), 2.90 (m, 2H), 1.96 (s, 6H). ^{13}C NMR (100 MHz, DMSO-d_6): δ 168.58, 144.20, 137.72, 131.90, 130.18, 117.97, 115.76, 69.96, 31.54, 24.58. HRMS (ESI) m/z calcd. for $C_{19}H_{19}N_2O_3$ ([M-H]$^-$) 323.1474, found 323.1501

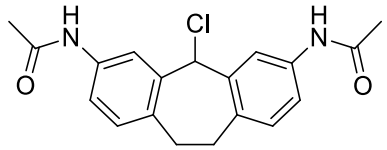

3,7-Diacetamidedibenzosuberylchloride (**4.7**):

Compound **4.6** (200 mg, 0.61 mmol) was placed in a 25 mL round bottomed flask with a stir bar followed by 5 mL of dry THF. One equivalent of sodium hydride (24 mg, 0.61 mmol) was slowly added to the flask and allowed to stir for 2 h. Thionyl chloride (0.045 mL, 0.22 mmol) was slowly added to the flask and the reaction was allowed to stir for 24 h. The reaction mixture was then poured over 20 mL of ice water and the tan solid filtered (163 mg, 78 %). ^{1}H NMR (400 MHz; CD_3CN) δ 10.16 (s, 2H), 7.94 (s, 2H), 7.61 (d, *J* = 8.3 Hz, 2H), 7.54 (d, *J* = 8.3 Hz, 2H), 6.11 (s, 1H), 3.17 (m, 2H) 2.9 (m, 2H), 2.02 (s, 6H). ^{13}C NMR (100 MHz, DMSO-d_6): δ 166.58, 136.20, 134.72, 131.50, 130.08, 117.77, 114.99, 57.86, 29.54, 24.38. HRMS (ESI) m/z calcd. for $C_{19}H_{19}N_2O_2Cl$ ($[M]^+$) 342.1135, found 342.1096.

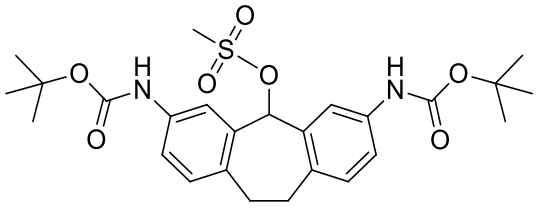

Dibenzosuberylmesylate-3,7-ditertbutylcarbamate (**4.8**):

Compound **4.1** (100 mg, 0.22 mmol) was placed in a 25 mL round bottomed flask with a stir bar followed by 5 mL of dry dichloromethane. One equivalent of sodium hydride 60% in mineral oil (9 mg, 0.22 mmol) was slowly added to the flask and allowed to stir for 6 h. Mesyl chloride (0.018 mL, 0.22 mmol) was slowly added to the mixture and the reaction was allowed to stir at room temperature for an additional 6 h. The reaction mixture was

placed in a separatory funnel and washed with water (2 x 5 mL) and the organic layer dried over $MgSO_4$. The solvent was removed *in vacuo* to yield product as a pale yellow solid (110 mg, 96 %). ^{1}H NMR (400 MHz; DMSO-d_6) δ 9.12 (s, 2H), 7.61 (s, 2H), 7.09 (d, 2.1 Hz, 2H), 6.9 (d, J = 2.1 Hz, 2H), 6.02 (s, 1H), 3.16 (m, 2H), 2.88 (m, 2H) 2.28 (s, 3H) 1.42 (s, 18H). ^{13}C NMR (100 MHz, DMSO-d_6): δ 168.6, 143.9, 135.32, 132.2, 129.8, 117.9, 115.8, 80.1, 70.1, 52.3, 32.5, 25.1. HRMS (ESI) m/z calcd. for $C_{26}H_{34}N_2O_7S$ ($[M]^+$) 518.2087, found 518.1994.

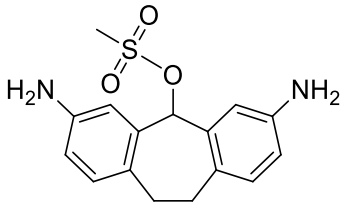

3,7- Diaminodibenzosuberylmesylate (dianiline **4.9**):

Compound **4.8** (100 mg, 0.19 mmol) was placed in a 25 mL round bottom flask with a stir bar followed by 2 mL of trifluoroacetic acid. The reaction was stirred for 12 h at room temperature, then poured over 5g ice. The pH was brought to 7.5 using saturated sodium bicarbonate and the solid filtered to yield product (52 mg, 85 %). ^{1}H NMR (400 MHz, DMSO-d_6): δ 7.05 (d, J = 8.0 Hz, 2H), 6.64 (d, J = 2.5 Hz, 2H), 6.48 (dd, J = 8.0, 2.5 Hz, 2H), 6.24 (dd, 1H), 4.59 (s, 4H), 3.24 (s, 3H) 3.01 (m, 2H), 2.71 (m, 2H). ^{13}CNMR (100 MHz, DMSO-d_6): δ 142.6, 137.5, 127.1, 126.8, 116.3, 114.9, 78.1, 43.1, 34.9. HRMS (ESI) m/z calcd. for $C_{16}H_{19}N_2O_3S$ ($[M+H]^+$) 319.1012, found 319.0914.

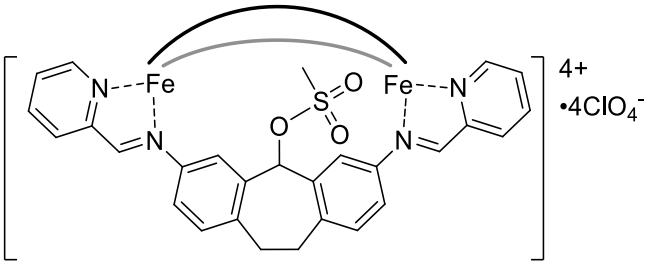

Mesocate **4.10**:

Dianiline **4.9** (50 mg, 0.19 mmol), 2-pyridine carboxaldehyde (37 µL, 0.39 mmol) and $Fe(ClO_4)_2•XH_2O$ (42 mg, 0.13 mmol) were combined in anhydrous MeCN (10 mL) in a 50 mL round-bottomed flask under a blanket of N_2, followed by heating to 45 °C for 24 h. The solution was then cooled to room temperature, diluted with Et_2O (30 mL), and cooled to -25 °C followed by filtration of the resulting precipitate. Drying product *in vacuo* gave product as a purple solid (84.5 mg, 98%). ^{1}H NMR and ^{13}C NMR: see Publication for full characterization.[4] HRMS (ESI) m/z calcd. for $C_{84}H_{72}Fe_2N_{12}O_{21}S_3Cl_3$ ($[Fe_2L_3•(ClO_4)_3]^+$) 1899.9137, found 1900.2734.

General oxidation procedure:

All mixing experiments were performed in an NMR tube. Aggregate **4.4** was formed *in situ* in an NMR tube: Dianiline **4.3** (10 mg, 0.039 mmol) was placed in an NMR tube along with 2 molar equivalents of 2-formylpyridine (7.4 µL, 0.077 mmol) and 0.66 molar equivalents of Iron (II) perchlorate (0.026 mmol, 8.3 mg). The tube contents were quickly mixed in an ultrasonication bath and allowed to heat at 45°C for 18 h to form the aggregate. One molar equivalent of silver perchlorate relative to chloride ligand (0.039 mmol, 8 mg) and 1 equivalent water (0.039 mmol, 5 µl of a 7.8 M H_2O solution in CD_3CN). The tube

contents were quickly mixed and heated at 45 or 80°C. The NMR spectra of the reaction mixture were taken at regular intervals to monitor oxidation progress.

General control procedure:

Control ligand **4.7** (7 mg, 0.02 mmol) and 400 µL of DMSO-d_6 were placed in an NMR tube. The DMSO-d_6 was degassed with N_2 for 1h prior to attempting air free trials. Depending on the trial, 1 molar eq. of silver perchlorate (4.2 mg, 0.02 mmol), tetrabutyl ammonium perchlorate (6.98 mg, 0.02 mmol), or silver nitrate (3.4 mg, 0.02 mmol) were added to the tube. A solution of water in DMSO-d_6 (0.02 mmol, 6.4 µL of 3.17 M water in DMSO-d_6) was added to the appropriate trials. The NMR tubes were heated at 80 °C and the spectra of the reactions were taken at regular intervals.

Structure optimizations:

Structures of the suberone complex **1.7** formed from ligand **1.5** and four possible isomers of the M_2L_3 helicate involving ligand **4.3** (with zero, one, two, or three chlorides pointed toward the center of the helicate) were optimized using wB97X-D/6-31G(d).[3,4] The structures of the uncomplexed ligands were optimized at the same level of theory. The relative stability of the complexes was then assessed by computing the reaction energy for the hypothetical dianiline exchange. The results indicate that all chloride complexes are less stable than suberone complex **1.7**. Among the chloride complexes, the isomer with all chlorides facing outward is the most stable. Each inward-facing chloride destabilizes the helicate by ~5-8 kcal/mol.

8.5 Chapter 5 Experimental

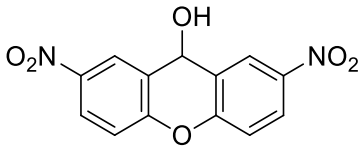

2,7-Dinitroxanthol (**5.1**):

One gram of 2,7-dinitroxanthone **2.3** (3.49 mmol) was placed in a 250 mL round bottomed flask and dissolved in 100 mL of dry tetrahydrofuran and 25 mL of dry methanol. Sodium borohydride (150 mg, 3.97 mmol, 1.2 mol.-eq.) was slowly added to the flask and the reaction was allowed to stir at room temperature. After 12 h, a second portion of sodium borohydride (30 mg) was added to the flask and the reaction stirred for 1 h. The reaction mixture was then poured into a beaker containing 500 mL of ice water. The mixture was rapidly stirred and brought to a pH of 3 with 1M hydrochloric acid. The product was then filtered and collected as a powdery tan solid (942 mg, 94 %). ^{1}H NMR (400 MHz, DMSO-d_6): δ 8.46 (d, J = 2.7 Hz, 2H), 8.23 (dd, J = 9.0, 2.7 Hz, 2H), 7.46 (d, J = 9.1 Hz, 2H), 6.84 (d, J = 6.8 Hz, 1H), 5.90 (d, J = 6.5 Hz, 1H). ^{13}C NMR (100 MHz, DMSO-d_6): δ 154.2, 144.2, 126.1, 125.4, 124.7, 118.5, 60.7. HRMS (ESI) m/z calcd. for $C_{13}H_9N_2O_6$ ([**5.1**•H]$^+$) 289.0234, found 289.0259.

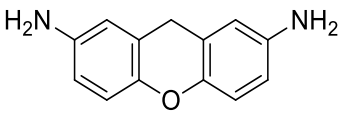

2,7-Diaminoxanthene (dianiline **5.2**):

Dinitroxanthol **5.1** (300 mg, 1.1 mmol) was placed in a long-necked Schlenk flask with a septum and stir bar and the flask was purged several times with nitrogen. Methanol (15 mL) and a large excess of Raney nickel slurry in water (5 mL) were injected into the flask

and the system was quickly purged with nitrogen a second time. Hydrazine monohydrate (1 mL) was slowly injected into the flask. The mixture was allowed to stir overnight at room temperature. The mixture was diluted with additional methanol (25 mL) and the solid catalyst was carefully removed via filtration through a Celite plug. The filtrate solvent was removed *in vacuo* to afford clean product as a pale yellow solid (291 mg, 94 %). ^{1}H NMR (400 MHz, DMSO-d_6): δ 6.65 (d, J = 8.1 Hz, 2H), 6.37 (m, 4H), 4.67 (s, 4H), 3.71 (s, 2H). ^{13}C NMR (100 MHz, DMSO-d_6): δ 144.4, 143.8, 121.0, 116.7, 114.2, 113.9, 28.4. HRMS (ESI) m/z calcd. for $C_{13}H_{13}N_2O_1$ ([dianiline **5.2**•H]$^+$) 213.0493, found 213.1062.

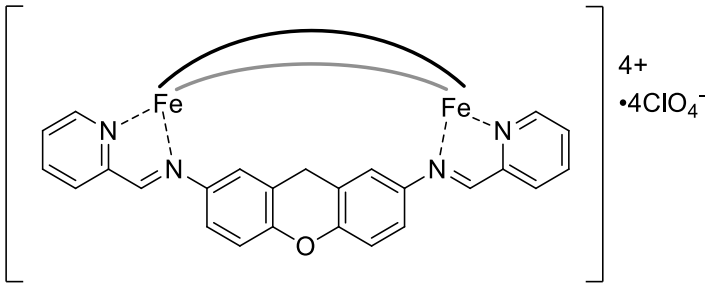

Mesocate **5.3**:

Dianiline **5.2** (100 mg, 0.47 mmol), 2-pyridine carboxaldehyde (90 μL, 0.94 mmol) and $Fe(ClO_4)_2$•$4H_2O$ (103 mg, 0.31 mmol) were combined in anhydrous acetonitrile (10 mL) in a 25 mL round-bottomed flask under a blanket of nitrogen gas. The solution was then heated at 45 °C for 10 h with stirring. The solution was diluted with diethyl ether (25 mL), and the resulting precipitate was filtered. After drying, the product was isolated as a purple solid (201 mg, 93 %). ^{1}H NMR (400 MHz; CD_3CN) δ 9.38 (s, 2H), 8.69 (d, J = 7.5 Hz, 2H), 8.35 (t, J = 7.3 Hz, 2H), 7.9 (t, J = 5.4 Hz, 2H), 7.71 (d, J = 5.1 Hz, 2H), 7.12 (d, J = 8.1 Hz, 2H), 5.9 (d, J = 6.9 Hz, 2H), 5.01 (s, 2H), 3.55 (d, J = 19.9 Hz, 1H) 2.72 (d, J = 19.9 Hz, 1H). ^{13}C NMR (125 MHz, CD_3CN): δ 173.6, 157.1, 156.1, 151.4, 148.2, 139.6,

132.2, 131.4, 124.1, 121.7, 121.0, 27.5. HRMS (ESI) m/z calcd. for $C_{75}H_{54}Cl_3Fe_2N_{12}O_{15}$ ([**5.3**•$(ClO_4)_3$]$^+$) 1581.3561, found 1581.3427. Elemental Analysis: Calc. for $C_{75}H_{54}Cl_4Fe_2N_{12}O_{19}$ C: 53.59; H: 3.24; N: 10.01; Found: C: 53.46; H: 3.35; N: 9.97.

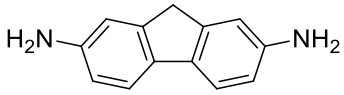

2,7-Diaminofluorene (Dianiline **5.4**):

2,7-Dinitrofluorene (500 mg, 2.0 mmol) was placed in a round-bottomed flask with stir bar and dissolved in methanol (35 mL). Raney nickel slurry in water (0.5 mL) and hydrazine monohydrate (0.5 mL) were slowly added to the flask. The mixture was allowed to stir overnight at room temperature. The mixture was diluted with additional methanol (25 mL) and the solid catalyst was carefully filtered off over a firmly packed celite plug. The solvent was removed *in vacuo* to afford clean product as a tan solid (368 mg, 96 %). ^{1}H NMR (400 MHz, DMSO-d_6): δ 7.22 (d, J = 8.0 Hz, 2H), 6.65 (d, J = 1.4 Hz, 2H), 6.46 (dd, J = 8.0, 2.0 Hz, 2H), 4.86 (s, 4H), 3.54 (s, 2H). ^{13}C NMR (125 MHz, DMSO-d_6): δ 146.8, 143.4, 131.5, 118.9, 113.1, 111.4, 36.6. HRMS (ESI) m/z calcd. for $C_{13}H_{13}N_2$ ([dianiline **5.4**•H]$^+$) 196.1012, found 196.4271.

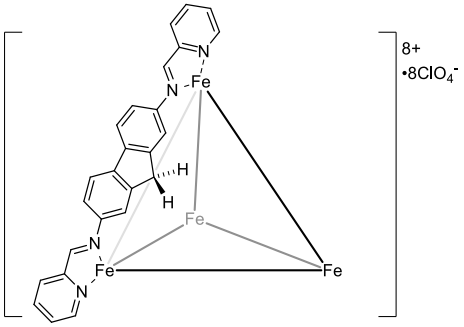

M_4L_6 complex **5.5**:

Dianiline **5.4** (100 mg, 0.51 mmol), 2-pyridine carboxaldehyde (96.9 μL, 1.02 mmol) and $Fe(ClO_4)_2 \bullet 4H_2O$ (111 mg, 0.34 mmol) were combined in anhydrous acetonitrile (10 mL) in a 50 mL Schlenk flask under a nitrogen atmosphere, followed by heating to 60 °C for 10 h. The solution was then cooled to room temperature, diluted with diethyl ether (30 mL), and the resulting precipitate was filtered. Drying product *in vacuo* gave product as a purple solid (187 mg, 94 %). ^{1}H NMR and ^{13}C NMR: see Publication for full characterization.[5] HRMS (ESI) m/z calcd for $C_{150}H_{108}Cl_2Fe_4N_{24}O_8$ ([**5.5**•$(ClO_4)_2$]$^{6+}$) 444.5932, found 444.8816. Elemental Analysis: Calc. for $C_{150}H_{108}Cl_8Fe_4N_{24}O_{32}$ C: 55.17; H: 3.33; N: 10.29; Found: C: 55.25; H: 3.37; N: 10.39.

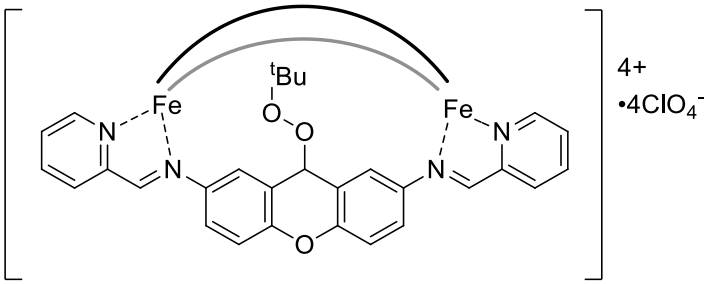

Mesocate **5.6**:

One equivalent of xanthene cage **5.3** (30 mg, 0.018 mmol) was dissolved in 2 mL of acetonitrile in a 10 mL round bottomed flask. 3.3 mol.-eq. of *tert*-butyl hydroperoxide 70 % solution in water (7.6 μL 0.059 mmol) was then added, and the reaction mixture was allowed to stir at room temperature for 8 h. Diethyl ether (10 mL) was then added to the solution, and xanthyl peroxide cage **3** precipitated as a purple solid that was filtered and dried (29 mg, 88 %). ^{1}H NMR (500 MHz; CD_3CN) δ 8.99 (s, 2H), 8.65 (d, *J* = 6.7 Hz, 2H), 8.41 (s, 2H), 7.82 (s, 2H), 7.39 (d, *J* = 8.2 Hz, 2H), 7.36 (d, *J* = 7.1 Hz, 2H), 6.22 (d, *J* = 6.1 Hz, 2H), 5.19 (s, 1H), 4.11 (s, 1H), 1.14 (s, 9H).^{13}C NMR (125 MHz, CD_3CN) δ 175.4,

157.5, 156.1, 151.7, 147.4, 139.7, 132.1, 130.5, 124.7, 124.5, 119.1, 117.8, 80.7, 72.9, 25.6. HRMS (ESI) m/z calcd. for $C_{87}H_{78}Fe_2N_{12}O_9$ (**5.6**$^{4+}$) 386.5788, found 386.6403. Elemental Analysis: Calc. for $C_{87}H_{78}Cl_4Fe_2N_{12}O_{25}$ C: 53.72; H: 4.04; N: 8.64; Found: C: 53.67; H: 4.10; N: 8.58.

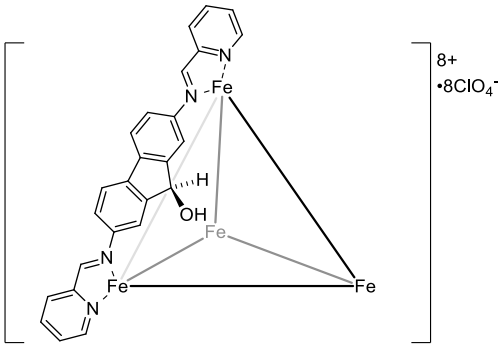

M_4L_6 complex **1.12**:

One equivalent of fluorene cage **5.5** (30 mg, 0.009 mmol) was dissolved in 2 mL of acetonitrile in a 10 mL round bottomed flask. 6.6 mol.-eq. of tert-butyl hydroperoxide 70 % solution in water (7.6 μL 0.055 mmol) was added, followed by 1 mg of sodium perchlorate template source, and the reaction mixture was allowed to stir at 50˚C for 24 h. Diethyl ether (10 mL) was then added to the solution, and fluorenol cage 5 precipitated as a purple solid that was filtered and dried (28 mg, 87 %). ^{1}H NMR and ^{13}C NMR: see Publication for full characterization.[5] HRMS (ESI) m/z calcd for $C_{150}H_{108}Cl_2Fe_4N_{24}O_{14}$ ([1.12•$(ClO_4)_2$]$^{6+}$) 460.5881, found 460.8312.

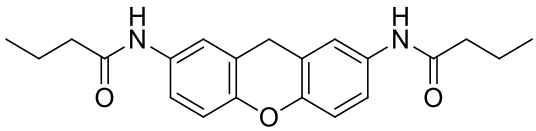

N,N'-(9H-xanthene-2,7-diyl)dibutyramide (control ligand **5.7**):

Dianiline **5.2** (212 mg, 1 mmol) was placed in a two-necked flask outfitted with a septum. The flask was purged with nitrogen, and 10 mL of anhydrous tetrahydrofuran was added to the flask. Acetic anhydride (236 μL, 2.5 mmol) and triethylamine (350 mL, 2.5 mmol) were added and the flask was quickly purged with nitrogen a second time. The mixture was allowed to stir at room temperature overnight before being poured into ice water and filtered as a tan solid (338 mg, 96 %). ^{1}H NMR (400 MHz, DMSO-d_6) δ 9.77 (s, 2H), 7.51 (s, 2H), 7.33 (d, J = 8.6 Hz, 2H), 6.94 (dd, J = 8.8, 3.5 Hz, 2H), 3.96 (s, 2H), 2.23 (t, J = 7.4 Hz, 4H), 1.59 (m, 4H), 0.89 (t, J = 7.3 Hz, 6H). ^{13}C NMR (100 MHz, DMSO-d_6): δ 171.2, 147.3, 135.1, 120.6, 119.7, 119.1, 116.4, 38.7, 27.7, 19.2, 14.1. HRMS (ESI) m/z calcd. for $C_{21}H_{25}N_2O_3$ ([**5.7**•H]$^+$) 353.1843, found 353.1692.

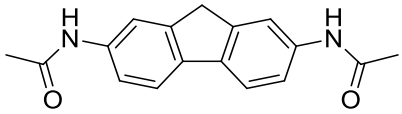

N,N'-(9H-fluorene-2,7-diyl)diacetamide (control ligand **5.8**):

Dianiline **5.4** (196 mg, 1 mmol) was placed in a two-necked flask outfitted with a septum. The flask was purged with nitrogen, and 10 mL of anhydrous tetrahydrofuran was added to the flask. Acetic anhydride (236 μL, 2.5 mmol) and triethylamine (350 mL, 2.5 mmol) were added and the flask was quickly purged with nitrogen a second time. The mixture was allowed to stir at room temperature overnight before being poured into ice water and filtered as a tan solid (255 mg, 91 %). ^{1}H NMR (400 MHz, DMSO-d_6): δ 9.92 (s, 2H), 7.83 (s, 2H), 7.65 (d, J = 8.2 Hz, 2H), 7.45 (d, J = 8.1 Hz, 2H), 3.82 (s, 2H), 2.18 (s, 1H), 2.02 (s, 6H). ^{13}C NMR (100 MHz, DMSO-d_6): δ 168.8, 144.0, 138.5, 136.7, 120.1, 118.3, 116.4, 37.2, 24.6. HRMS (ESI) m/z calcd. for $C_{17}H_{17}N_2O_2$ ([**5.8**•H]$^+$) 280.1248, found 281.0285.

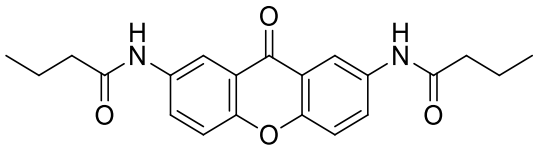

N,N'-(9-oxo-9H-xanthene-2,7-diyl)dibutyramide (**5.9**):

Dianiline **2.5** (0.5 mmol, 113 mg) was placed in a round bottomed flask and dissolved in 10 mL of dry tetrahydrofuran, followed by addition of *n*-butyric anhydride (1.25 mmol, 205 μL) and triethylamine (1.25 mmol, 174 μL). The reaction mixture was stirred at room temperature overnight, then slowly added to a beaker containing 50 mL of water. The product was filtered and collected as a yellow solid (162 mg, 89 %). ^{1}H NMR (400 MHz, DMSO-d_6): δ 10.15 (s, 2H), 8.46 (d, J = 2.6 Hz, 2H), 7.97 (dd, J = 9.1, 2.6 Hz, 2H), 7.59 (d, J = 9.1 Hz, 2H), 2.30 (t, J = 7.3 Hz, 4H), 1.61 (m, 4H), 0.91 (t, J = 7.4 Hz, 6H). ^{13}C NMR (100 MHz, DMSO-d_6): δ 183.1, 172.0, 152.0, 136.3, 127.6, 121.3, 119.2, 114.8, 38.9, 19.2, 14.3. HRMS (ESI) m/z calcd. for $C_{21}H_{23}N_2O_4$ ([**5.9**•H]$^+$) 367.1793, found 367.1897.

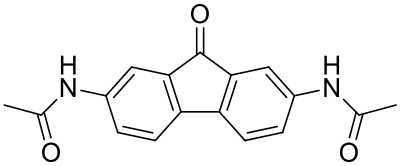

N,N'-(9-oxo-9H-fluorene-2,7-diyl)diacetamide (**5.10**):

2,7-Diaminofluorenone[6] (300 mg, 1.43 mmol) was placed in a round bottomed flask with 15 mL of dry tetrahydrofuran. Acetic anhydride (296 μL, 3.1 mmol) and triethylamine (1 mL) were added to the flask. The mixture was stirred overnight at room temperature, then poured into a beaker containing 60 mL of ice water. The product was filtered as a dark red solid (394 mg, 93 %). ^{1}H NMR (400 MHz, DMSO-d_6): δ 10.10 (s, 2H), 7.83 (d, J = 1.7

Hz, 2H), 7.59 (dd, J = 8.1, 1.9 Hz, 2H), 7.51 (d, J = 8.1 Hz, 1H), 2.00 (s, 6H). ^{13}C NMR (100 MHz, DMSO-d_6): δ 193.5, 169.4, 140.3, 138.9, 134.6, 125.2, 121.6, 115.1, 24.6. HRMS (ESI) m/z calcd. for $C_{17}H_{14}N_2O_3$ ([**5.10**•2H]$^{2+}$) 148.0551, found 148.0872.

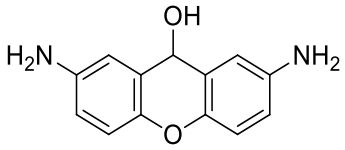

2,7-Diaminoxanthol (dianiline **5.11**):

Dinitroxanthol **5.1** (600 mg, 2.1 mmol) was placed in a long-necked Schlenk flask with a septum and stir bar and the flask was purged several times with nitrogen. Methanol (10 mL) and Raney nickel slurry in water (0.2 mL) were injected into the flask and the system was quickly purged with nitrogen a second time. Hydrazine monohydrate (0.4 mL) was slowly injected into the flask. The mixture was allowed to stir for 6 h at room temperature. The solid catalyst was carefully filtered off over a firmly packed celite plug. Dichloromethane (20 mL) was added to the filtrate and the solution was washed with brine (2 x 15 mL). The solvent was removed *in vacuo* to afford crude product as an orange solid (393 mg, 82 %). The product was purified via selective Boc-protection of the amines (2.1 mol.-eq. Boc_2O, 2.1 mol.-eq. triethylamine in tetrahydrofuran overnight[1]) followed by column chromatography (5 % ethyl acetate in hexanes as eluent), and deprotection with hydrochloric acid in diethyl ether followed by neutralization. ^{1}H NMR (400 MHz, DMSO-d_6): δ 6.73 (d, J = 8.6 Hz, 2H), 6.68 (d, J = 1.8 Hz, 2H), 6.49 (dd, J = 8.6, 2.7 Hz, 1H), 5.60 (d, J = 7.7 Hz, 1H), 5.33 (d, J = 7.7 Hz, 1H). ^{13}C NMR (125 MHz, CD_3CN): δ 143.5, 143.2, 123.7, 116.5, 116.2, 114.1, 63.2. HRMS (ESI) m/z calcd. for $C_{13}H_{13}N_2O_1$ ([dianiline **5.11**•H]$^+$) 213.0493, found 213.1062.

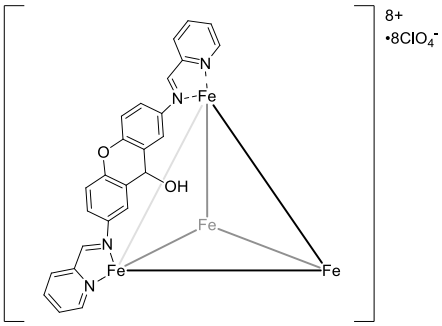

M_4L_6 complex **5.12**:

Dianiline **5.11** (25 mg, 0.11 mmol), 2-pyridine carboxaldehyde (21 μL, 0.22 mmol) and $Fe(ClO_4)_2$•$4H_2O$ (24 mg, 0.08 mmol) were combined in anhydrous acetonitrile (5 mL) in a 10 mL round-bottomed flask under a blanket of nitrogen, followed by heating to 45 °C for 10 h. The solution was then cooled to room temperature, diluted with diethyl ether (30 mL), and the resulting precipitate was filtered. Drying product *in vacuo* gave product as a purple solid (49 mg, 98 %). ^{1}H NMR and ^{13}C NMR: see Publication for full characterization.[5] HRMS (ESI) m/z calcd for $C_{150}H_{108}Cl_5Fe_4N_{24}O_{32}$ ([**5.12**•$(ClO_4)_5$]$^{3+}$) 1053.0846, found 1053.0830. Elemental Analysis: Calc. for $C_{150}H_{105}Cl_8Fe_4N_{24}O_{41}$ (loss of 3 x H_2O) C: 52.89; H: 3.11; N: 9.87 and $C_{150}H_{106}Cl_8Fe_4N_{24}O_{42}$ (loss of 2 x H_2O) C: 52.62; H: 3.12; N: 9.81; Found: C: 52.73; H: 3.13; N: 9.85.

8.6 Chapter 6 Experimental

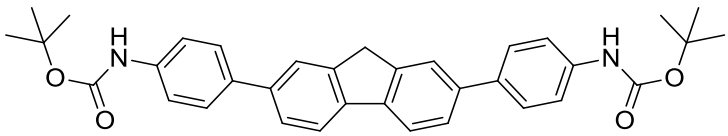

Di-tert-butyl ((9H-fluorene-2,7-diyl)bis(4,1-phenylene))dicarbamate (**6.1**):

To a Schlenk flask was added 2,7-dibromo-9H-fluorene (259 mg, 0.8 mmol), 4-BOCaminophenylboronic acid (474 mg, 2 mmol), cesium carbonate (1.56 g, 4.8 mmol), and Pd(dppf)Cl_2 (59 mg, 0.08 mmol). The flask was purged with N_2, 2 mL of DMF was added and the flask quickly purged a second time. The mixture was stirred at 90 °C for 16 h, then the reaction was cooled to room temperature and diluted with 100 mL of water. The product was extracted with diethyl ether (4 x 60 mL) and the organic layer washed with a solution of 1 M $NaCO_3$ and 1 M sorbitol in water (30 mL) followed by washings with saturated sodium bicarbonate and brine (2 x 20 mL each). The cloudy organic layer was dried with magnesium sulfate, filtered through a celite plug and the solvent removed in vacuo to give the product as a tan solid (420 mg, 90 %). ^{1}H NMR (400 MHz, $CDCl_3$) δ 7.85 (d, *J* = 7.9 Hz, 2H), 7.78 (s, 2H), 7.65 – 7.60 (m, 6H), 7.48 (d, *J* = 8.3 Hz, 4H), 6.55 (s, 2H), 4.03 (s, 2H), 1.57 (s, 18H). ^{13}C NMR (101 MHz, DMSO-d_6) δ 153.24, 144.53, 140.10, 139.39, 138.87, 134.45, 127.31, 125.52, 123.32, 120.84, 118.93, 79.59, 37.08, 28.61. HRMS (ESI) m/z calcd for $C_{35}H_{35}N_2O_4$ 547.27, found 547.3401 (**6.1**-H)$^-$.

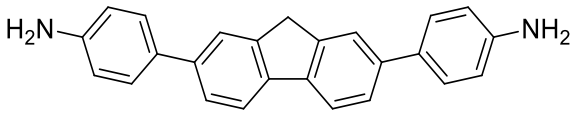

4,4'-(9H-fluorene-2,7-diyl)dianiline (Dianiline **6.2**):

6.1 (250 mg, 0.456 mmol) was placed in a round-bottomed flask with a stir bar. Trifluoroacetic acid (5 mL, neat) was added to the flask and the mixture was stirred overnight at room temperature. The mixture was slowly added to a beaker containing 100 mL of ice water. The solution was brought to pH 9 using 1 M NaOH, and the precipitate filtered and washed with hexane to yield product as a tan powder (154 mg, 94 %). ^{1}H NMR

(400 MHz, DMSO-d_6) δ 7.84 (d, J = 8.0 Hz, 2H), 7.74 (s, 2H), 7.56 (dd, J = 8.0, 1.4 Hz, 2H), 7.43 (d, J = 8.5 Hz, 4H), 6.67 (d, J = 8.5 Hz, 4H), 5.23 (s, 4H), 3.97 (s, 2H). ^{13}C NMR (101 MHz, DMSO-d_6) δ 148.71, 144.26, 139.58, 139.25, 128.22, 127.64, 124.65, 122.46, 120.45, 114.75, 37.04. HRMS (ESI) m/z calcd for $C_{25}H_{21}N_2$: 349.1626, found 349.1488 (**6.2**+H)$^+$.

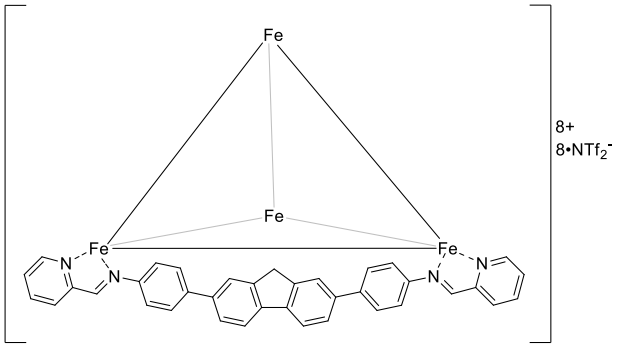

M_4L_6 complex **6.3**:

Ligand **6.2** (35 mg, 0.08 mmol) was placed in a round bottomed flask with a stir bar and acetonitrile (9 mL) was added to the flask followed by 2-formylpyridine (14.4 μL, 0.16 mmol). Iron (II) triflimide (33 mg, 0.05 mmol) was added, and the solution stirred at reflux for 24 h. The solution was allowed to cool and was filtered to remove any undissolved solids. The acetonitrile was removed in vacuo and the solid residue sonicated for 10 min with 20 mL of a 1:3 mixture of MeOH/Et_2O followed by additional Et_2O to remove any remaining ligand or metal. The solid product was filtered and collected as a dark purple solid (57 mg, 82 %). See Publication for full characterization.[7]

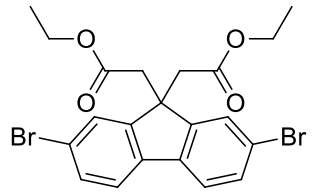

Diethyl 2,2'-(2,7-dibromo-9H-fluorene-9,9-diyl)diacetate (**6.4**):

2,7-Dibromo-9H-fluorene (500 mg, 1.54 mmol) and KO^{t}Bu (865 mg, 7.71 mmol) were added to a two-neck round bottom flask equipped with a stir bar and a septum. The flask was purged with N_2, and anhydrous THF (15 mL) was then added via syringe. To the flask was then added α-bromoethylacetate (510 µL, 4.62 mmol) dropwise over 5 min. The solution was then stirred for 16 h at 23 °C. The reaction was diluted with 20 mL Et_2O and filtered. The resulting solution was then extracted with saturated $NaHCO_3$ (3 x 20 mL) and brine (2 x 20 mL) and dried over Na_2SO_4. The reaction mixture was filtered, transferred to a round bottom flask and concentrated in vacuo to afford an orange crystalline solid (614 mg, 85 %). ^{1}H NMR: (500 MHz, $CDCl_3$) δ 7.68 (d, *J* = 1.4 Hz, 2H), 7.55 (d, *J* = 8.1 Hz, 2H), 7.51 (dd, *J* = 8.1, 1.6 Hz, 2H), 3.97 (q, *J* = 7.1 Hz, 4H), 3.03 (s, 4H), 1.06 (t, *J* = 7.1 Hz, 6H). ^{13}C NMR (101 MHz, $CDCl_3$) δ 169.99, 150.38, 138.17, 131.26, 127.34, 121.55, 121.38, 60.47, 50.01, 41.73, 13.95. HRMS (ESI) m/z calcd for $C_{21}H_{20}Br_2O_4$: 493.9728, found 494.0067 (**6.4**)$^+$.

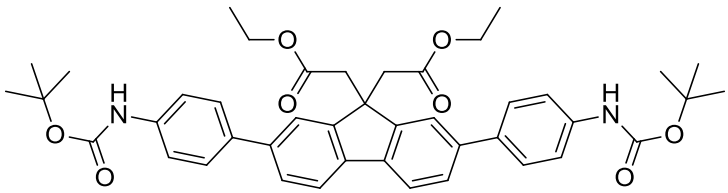

Diethyl 2,2'-(2,7-bis(4-nitrophenyl)-9H-fluorene-9,9-diyl)diacetate (**6.5**):

To a Schlenk flask was added **6.4** (397 mg, 0.8 mmol), 4-BOCaminophenylboronic acid (474 mg, 2 mmol), cesium carbonate (1.56 g, 4.8 mmol), and Pd(dppf)Cl_2 (59 mg, 0.08 mmol). The flask was then purged with N_2, 2 mL of DMF was added and the flask quickly purged a second time. The mixture was stirred at 90 °C for 16 h, then the reaction was cooled to room temperature and diluted with 100 mL of water. The product was extracted with diethyl ether (2 x 60 mL) and the organic layer washed with a solution of 1 M $NaCO_3$ and 1 M sorbitol in water (30 mL) followed by washings with saturated sodium bicarbonate and brine. The organic layer was dried with magnesium sulfate, filtered through a celite plug and the solvent removed in vacuo to give the product as an orange solid (403 mg, 70 %). ^{1}H NMR (500 MHz, $CDCl_3$) δ 7.78 – 7.75 (m, 4H), 7.61 – 7.57 (m, 6H), 7.46 (d, *J* = 8.0 Hz, 4H), 6.58 (s, 2H), 3.96 (q, *J* = 7.1 Hz, 4H), 3.16 (s, 4H), 1.56 (s, 18H), 1.00 (t, *J* = 7.1 Hz, 6H). ^{13}C NMR (101 MHz, $CDCl_3$) δ 170.74, 152.77, 149.61, 139.79, 138.64, 137.68, 136.02, 127.60, 126.70, 122.26, 120.25, 118.83, 80.65, 60.26, 49.92, 42.17, 28.39, 13.92. HRMS (ESI) m/z calcd for $C_{43}H_{48}N_2O_8$: 721.3406, found 721.2795 (**6.5**+H)$^+$.

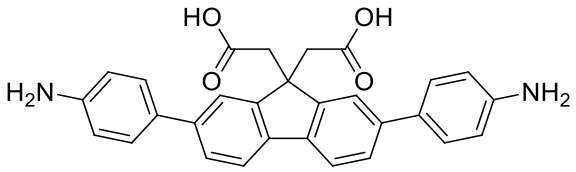

2,2'-(2,7-Bis(4-aminophenyl)-9H-fluorene-9,9-diyl)diacetic acid (**6.6**):

Compound **6.5** (300 mg, 0.4 mmol) was added to a 5 mL round bottom flask and dissolved in 5 mL neat trifluoroacetic acid (TFA) and stirred at room temperature overnight. The TFA was then removed in vacuo to give the deprotected amine as the TFA salt. 30 mL of MeOH was added to the flask and the mixture heated to 50 °C to dissolve the solid. To this

solution was added 5 mL concentrated NaOH in water. The reaction was stirred overnight at 65 °C and then allowed to cool. The reaction was then filtered through a celite plug to remove any solid impurities and the pH brought to 7 using 1 M HCl. The product was then extracted from the aqueous mixture using DCM (3 x 50 mL), the organic portion was dried using magnesium sulfate, and the solvent removed in vacuo to give a tan powder (137 mg, 71 %). ^{1}H NMR (400 MHz, DMSO-d_6) δ 11.90 (s, 2H), 7.78 – 7.72 (m, 4H), 7.51 (d, J = 8.0 Hz, 2H), 7.39 (d, J = 8.3 Hz, 4H), 6.67 (d, J = 8.3 Hz, 4H), 5.24 (s, 4H), 3.33 (s, 4H). ^{13}C NMR (101 MHz, DMSO-d_6) δ 172.37, 150.59, 148.73, 139.82, 137.78, 128.37, 127.68, 125.17, 121.20, 120.44, 114.69, 49.79, 42.63. HRMS (ESI) m/z calcd for $C_{29}H_{23}N_2O_4$: 463.1701, found 463.2344 (**6.6**-H)$^-$.

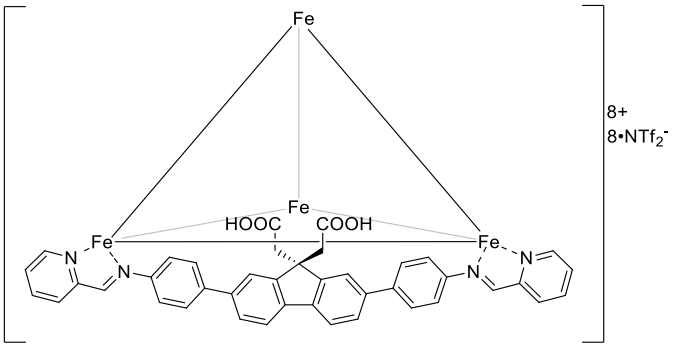

<u>M_4L_6 complex **6.7**</u>:

Dianiline **6.6** (35 mg, 0.08 mmol) was placed in a Schlenk flask with a stir bar and the flask purged with N_2 gas. Anhydrous acetonitrile (9 mL) was added to the flask along with 2-formylpyridine (14.4 μL, 0.16 mmol). Iron (II) triflimide (33 mg, 0.05 mmol) was dissolved in a vial with 1 mL of anhydrous acetonitrile, and the solution added to the flask via cannula transfer. The reaction mixture immediately turned a burgundy color and was allowed to stir at reflux for 24 h. The solution was allowed to cool and was filtered to

remove any undissolved solids. The acetonitrile was removed in vacuo and the solid residue sonicated for 30 min with 20 mL of a 1:3 mixture of MeOH/Et_2O followed by 15 mL of THF to remove any remaining ligand or metal. The solid product was filtered and collected as a dark purple solid (57 mg, 82 %). See publication for full characterization.[7]

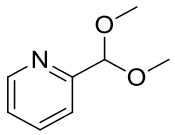

2-(Dimethoxymethyl)pyridine (acetal **6.8**):

2-Formylpyridine (1 mL, 0.011 mol) was placed in a 100 mL round bottomed flask along with 10 mL of methanol. *p*-Toluenesulfonic acid monohydrate (10 mol %, 0.001 mol, 627 mg) was added to the flask along with methylorthoformate (0.022 mol, 2.41 mL). The reaction mixture was refluxed overnight under N_2, then allowed to cool. The reaction mixture was slowly poured into a beaker containing 50 mL of saturated sodium bicarbonate solution. The pH was tested, and more sodium bicarbonate solution was added as needed to bring the pH to between 7 and 8. The product was extracted using 15 mL of DCM and washed extensively with brine (5 x 20 mL) to remove any remaining starting material. The organic layer was dried with magnesium sulfate and the solvent removed *in vacuo* to give product as a red-brown oil (1.08 g, 64 %). ^{1}H NMR (400 MHz, CD_3CN) δ 8.58 (d, *J* = 4.7 Hz, 1H), 7.81 (td, *J* = 7.7, 1.7 Hz, 1H), 7.53 (d, *J* = 7.9 Hz, 1H), 7.34 (ddd, *J* = 7.5, 4.8, 1.0 Hz, 1H), 5.30 (s, 1H), 3.37 (s, 6H). ^{13}C NMR (101 MHz, $CDCl_3$) δ 157.13, 149.12, 136.66, 123.49, 121.24, 103.94, 53.64. HRMS (ESI) m/z calcd for $C_8H_{12}NO_2$: 154.0717, found 154.0786 (**6.8**+H)$^+$.

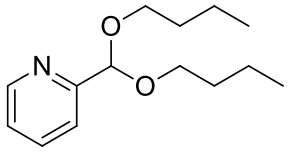

2-(Dibutoxymethyl)pyridine (acetal **6.9**):

2-Formylpyridine (1 mL, 0.011 mol) was placed in a 100 mL round bottomed flask along with 10 mL of n-butanol. *p*-Toluenesulfonic acid monohydrate (30 mol %, 0.003 mol, 627 mg) was added to the flask. The reaction mixture was heated to 80 °C overnight under N_2, then the reaction mixture was allowed to cool. The solution was slowly poured into a beaker containing 50 mL of saturated sodium bicarbonate solution. The pH was tested, and more sodium bicarbonate solution was added as needed to bring the pH to between 7 and 8. The product was extracted using 15 mL of hexane and washed extensively with brine (5 x 20 mL) to remove any remaining starting material. The organic layer was dried with magnesium sulfate and the solvent removed *in vacuo* to give product as a red-brown oil (1.28 g, 49 %). ^{1}H NMR (400 MHz, CD_3CN) δ 8.56 (dd, *J* = 4.1, 0.7 Hz, 1H), 7.80 (ddd, *J* = 9.5, 6.6, 2.7 Hz, 1H), 7.56 (dd, *J* = 9.6, 4.6 Hz, 1H), 7.33 – 7.27 (ddd, 9.5, 6.6, 4.1 1H), 5.40 (s, 1H), 3.67 – 3.48 (m, 4H), 1.61 – 1.32 (m, 8H), 0.92 (t, *J* = 5.5 Hz, 6H). ^{13}C NMR (101 MHz, $CDCl_3$) δ 158.35, 148.89, 136.58, 123.28, 121.07, 102.86, 66.40, 31.80, 19.35, 13.86. HRMS (ESI) m/z calcd for $C_{14}H_{24}NO_2$: 238.1721, found 238.1667 (**6.9**+H)$^+$.

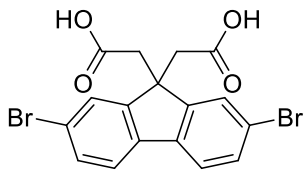

2,2'-(2,7-Dibromo-9H-fluorene-9,9-diyl)diacetic acid (**6.10**):

Compound **6.4** (100 mg, 0.2 mmol), was placed in a 10 mL round bottomed flask. Methanol (3 mL) was added along with excess aqueous 2 M NaOH solution **(**1.5 mL). The reaction was refluxed for 7 h. The mixture was allowed to cool, and the pH brought to 4 using 1 M HCl. The product was extracted using Et_2O (10 mL) and washed with brine (2 x 15 mL). The organic layer was dried with magnesium sulfate, and the solvent removed *in vacuo* to give product as a pale yellow solid (84 mg, 95 %). ^{1}H NMR: (400 MHz, CD_3CN) δ 8.88 (s, 2H), 7.78 (d, *J* = 1.7 Hz, 2H), 7.71 (d, *J* = 8.1 Hz, 2H), 7.57 (dd, *J* = 8.1, 1.8 Hz, 2H), 3.09 (s, 4H).^{13}C NMR (101 MHz, CD_3CN) δ 170.28, 150.90, 138.92, 130.92, 126.98, 121.77, 120.81, 49.77, 41.06. HRMS (ESI) m/z calcd for $C_{17}H_{12}Br_2O_4$: 437.91, found 496.9241 (**6.10**+$CH_3COO)^-$.

8.7 Chapter 7 Experimental

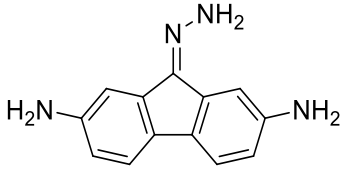

2,7-diaminofluorenylhydrazone (**7.1**):

Ligand **1.10** (200 mg, 0.95 mmol) was placed in a round-bottom flask and dissolved in 5 mL of THF. To this solution was added 1 mL hydrazine monohydrate. The reaction mixture was heated to reflux for 12 h, before being cooled to room temperature. Water (50 mL) was added to the mixture, and the precipitate was collected via filtration. After drying, the product was obtained as a red solid (209 mg, 98 %). ^{1}H NMR (400 MHz, DMSO-d_6) δ 7.31 (s, 2H), 7.26 (s, 1H), 7.22 (d, *J* = 8.0 Hz, 1H), 7.13 (d, *J* = 7.9 Hz, 1H), 6.75 (s, 1H), 6.51

(d, *J* = 7.9 Hz, 1H), 6.40 (d, *J* = 7.9 Hz, 1H), 4.91 (s, 4H). ^{13}C NMR (101 MHz, DMSO-d_6) δ 147.54, 147.47, 142.69, 139.26, 135.81, 131.27, 130.72, 128.53, 119.53, 119.08, 114.59, 114.12, 112.75, 106.26.

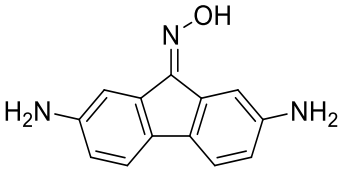

2,7-diaminofluorenylhydrazone (**7.2**):

Ligand **1.10** (200 mg, 0.95 mmol) was placed in a round-bottom flask and dissolved in 5 mL of THF. To this solution was added 1 mL hydrazine monohydrate. The reaction mixture was heated to reflux for 12 h, before being cooled to room temperature. Water (50 mL) was added to the mixture, and the precipitate was collected via filtration. After drying, the product was obtained as a red solid (209 mg, 98 %). ^{1}H NMR (400 MHz, DMSO-d_6) δ 7.31 (s, 2H), 7.26 (s, 1H), 7.22 (d, *J* = 8.0 Hz, 1H), 7.13 (d, *J* = 7.9 Hz, 1H), 6.75 (s, 1H), 6.51 (d, *J* = 7.9 Hz, 1H), 6.40 (d, *J* = 7.9 Hz, 1H), 4.91 (s, 4H). ^{13}C NMR (101 MHz, DMSO-d_6) δ 147.54, 147.47, 142.69, 139.26, 135.81, 131.27, 130.72, 128.53, 119.53, 119.08, 114.59, 114.12, 112.75, 106.26.

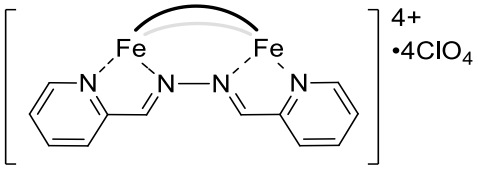

Mesocate (**7.3**):

Dianiline **7.1** (50 mg, 0.22 mmol) was placed in a round bottom flask with a stir bar. Acetonitrile (5 mL) was added to the flask along with 2-formylpyridine (42.4 μL, 0.45

mmol). Iron (II) perchlorate (49 mg, 0.15 mmol) was then added to the flask. The reaction mixture immediately turned a burgundy color and was allowed to stir at reflux for 72 h. The solution was allowed to cool and was filtered to remove any undissolved solids. The acetonitrile was removed in vacuo and the solid residue sonicated for 30 min with 20 mL Et_2O. The solid product was filtered and collected as a dark blue solid (21 mg, 42 %). The identical product was obtained by reacting hydrazine monohydrate (11 µL, 0.22 mmol) with 2-formylpyridine (42.4 µL, 0.45 mmol) and iron (II) perchlorate (49 mg, 0.15 mmol) and heating at 77 °C for 12 h. The acetonitrile was evaporated and the solid was sonicated with 20 mL Et_2O and collected via filtration (40 mg, 81 %). ^{1}H NMR (400 MHz, CD_3CN) δ 10.11 (s, 1H), 8.65 (s, 1H), 8.58 (d, *J* = 6.0 Hz, 1H), 8.17 (d, *J* = 7.8 Hz, 1H), 7.97 (d, *J* = 5.6 Hz, 1H), 7.86 (dd, *J* = 12.3, 7.2 Hz, 2H), 7.80 (d, *J* = 7.6 Hz, 1H), 7.39 (t, *J* = 6.8 Hz, 1H), 7.33 (t, *J* = 6.7 Hz, 1H).

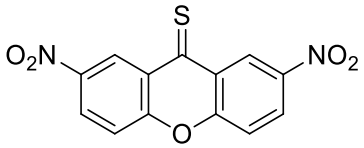

2,7-Dinitro-9H-xanthene-9-thione (**7.4**):

Compound **2.4** (400 mg, 1.3 mmol) was placed in a 100 mL round bottom flask with a stir bar. To the flask was added phosphorous pentasulfide (1.3 g, 2.9 mmol) and toluene (30 mL). The reaction mixture was heated to reflux for 16 h, then cooled to room temperature. The toluene was removed *in vacuo* and the solid redissolved in ethyl acetate. The solution was passed through a plug of neutral alumina, the solution was dried using $MgSO_4$ and the solvent removed *in vacuo* to give the product as a green solid (297 mg, 82 %). ^{1}H NMR

(400 MHz, DMSO-d_6) δ 9.13 (d, J = 2.7 Hz, 2H), 8.65 (dd, J = 9.2, 2.6 Hz, 2H), 7.93 (d, J = 9.2 Hz, 2H).

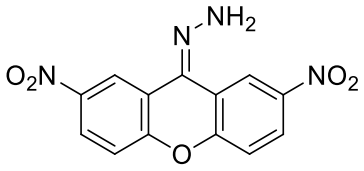

(2,7-dinitro-9H-xanthen-9-ylidene)hydrazine (**7.5**):

Compound **7.4** (400 mg, 1.3 mmol) was placed in a 100 mL round bottom flask with a stir bar. To the flask was added anhydrous THF (10mL) and hydrazine hydrate solution (50% solution w/w, 0.2 mL). The reaction mixture was stirred at room temperature for 4 h, during which time the solution color changed from green to red. The reaction mixture was slowly poured into a beaker containing 50 mL of cold saturated ammonium chloride solution. The solid was collected via filtration, washed with 30 mL deionized water and dried to give the product as a red solid (374 mg, 94 %). ^{1}H NMR (400 MHz, DMSO-d_6) δ 9.19 (s, 1H), 8.43 (dd, J = 3.1, 1.1 Hz, 1H), 8.10 – 8.03 (m, 1H), 7.82 (ddd, J = 9.4, 3.1, 1.1 Hz, 1H), 7.62 (d, J = 9.2 Hz, 1H), 6.28 (dd, J = 9.5, 1.0 Hz, 1H).

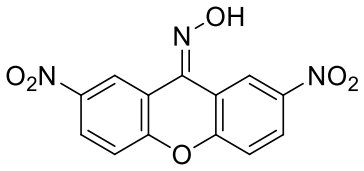

2,7-dinitro-9H-xanthen-9-one oxime (**7.6**):

Compound **7.4** (400 mg, 1.3 mmol) was placed in a 100 mL round bottom flask with a stir bar. To the flask was added anhydrous THF (10mL) and hydroxylamine solution (50% solution w/w, 0.3 mL). The reaction mixture was stirred at room temperature for 4 h, during

which time the solution color changed from green to red. The reaction mixture was slowly poured into a beaker containing 50 mL of cold saturated ammonium chloride solution. The solid was collected via filtration, washed with 30 mL deionized water and dried to give the product as a red solid (381 mg, 95 %). ^{1}H NMR (400 MHz, DMSO-d_6) δ 12.86 (s, 1H), 9.80 (d, J = 2.8 Hz, 1H), 8.63 (d, J = 2.7 Hz, 1H), 8.41 (dd, J = 8.2, 2.7 Hz 1H), 8.24 (m, J = 8.0, 2.7 Hz 1H), 7.55 (d, J = 9.1 Hz, 1H), 7.51 (d, J = 9.0 Hz, 1H).

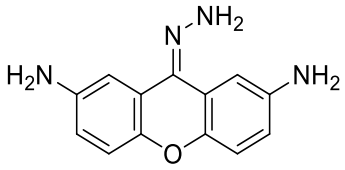

9-Hydrazono-9H-xanthene-2,7-diamine (**7.7**):

Compound **7.5** (200 mg, 0.67 mmol) was placed in a 100 mL round bottom flask with a stir bar. To the flask was added EtOH (5 mL) and the solution was warmed to 50 °C. Sodium sulfide nonahydrate (900 mg) was dissolved in 15 mL deionized water and this solution was slowly added to the reaction flask. The mixture was heated to reflux for 4 h, then cooled to room temperature and allowed to stir overnight. The product precipitated as an orange solid and was collected via filtration and washed with 30 mL cool deionized water. The solid was dried to give the product as an orange solid (137 mg, 73 %). ^{1}H NMR (400 MHz, DMSO-d_6) δ 7.50 (d, J = 2.5 Hz, 1H), 6.96 (d, J = 2.7 Hz, 1H), 6.93 (d, J = 8.7 Hz, 1H), 6.78 (d, J = 8.6 Hz, 1H), 6.63 (dd, J = 8.7, 2.6 Hz, 1H), 6.54 – 6.46 (m, 3H), 4.91 (s, 2H), 4.81 (s, 2H).

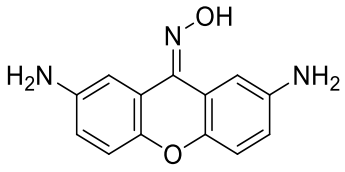

2,7-Diamino-9H-xanthen-9-one oxime (**7.8**):

Compound **7.6** (200 mg, 0.67 mmol) was placed in a 100 mL round bottom flask with a stir bar. To the flask was added EtOH (5 mL) and the solution was warmed to 50 °C. Sodium sulfide nonahydrate (900 mg) was dissolved in 15 mL deionized water and this solution was slowly added to the reaction flask. The mixture was heated to reflux for 4 h, then cooled to room temperature and allowed to stir overnight. The product precipitated as an orange solid and was collected via filtration and washed with 30 mL cool deionized water. The solid was dried to give the product as an orange solid (146 mg, 80 %). ^{1}H NMR (400 MHz, DMSO-d_6) δ 11.36 (s, 1H), 8.18 (d, J = 2.7 Hz, 1H), 7.06 (d, J = 2.7 Hz, 1H), 6.93 (d, J = 8.7 Hz, 1H), 6.87 (d, J = 8.7 Hz, 1H), 6.71 (dd, J = 8.7, 2.8 Hz, 1H), 6.64 (dd, J = 8.7, 2.8 Hz, 1H), 4.92 (s, 2H), 4.90 (s, 2H).

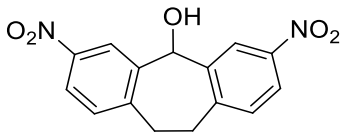

3,7-Dinitrosuberol (**7.9**):

Compound **1.5** (250 mg, 0.84 mmol) was placed in a round bottomed flask with a stir bar. Methanol (10 mL) was added to the flask along with $NaBH_4$ (38 mg , 1.01 mmol). The reaction was stirred at room temperature overnight, then poured into a beaker containing 50 mL deionized water. The pH was brought to 6 and the solid tan precipitate was collected via filtration. (221 mg, 88 %). ^{1}H NMR (400 MHz, DMSO-d_6) δ 8.39 (d, J = 2.0 Hz, 2H),

7.99 (dd, *J* = 8.3, 2.4 Hz, 2H), 7.40 (d, *J* = 8.4 Hz, 2H), 6.78 (d, *J* = 4.8 Hz, 1H), 6.42 (d, *J* = 4.4 Hz, 1H), 3.49 (m, 2H), 3.10 (m, 2H). ^{13}C NMR (101 MHz, DMSO-d_6) δ 146.59, 145.49, 144.79, 131.72, 122.62, 119.40, 67.73, 31.35.

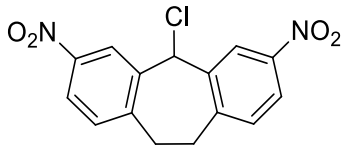

3,7-Dinitrosuberyl chloride (**7.10**):

Compound **7.9** (200 mg, 0.66 mmol) was placed in a round bottomed flask along with a stir bar. Thionyl chloride (3 mL) was slowly added to the flask, and the solution was heated to 50 °C overnight. The reaction was allowed to cool, and the volatiles were removed in vacuo to yield product as a tan solid (208 mg, 98 %). ^{1}H NMR (400 MHz, DMSO-d_6) δ 8.41 (s, 2H), 8.16 (d, *J* = 7.9 Hz, 2H), 7.59 – 7.53 (dd, *J* = 8.1, 2.8 Hz, 2H), 7.08 (s, 1H), 3.79 (m, 2H), 3.10 (m, 2H).

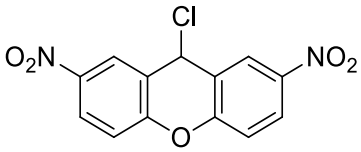

2,7-Dinitroxanthol (**7.11**):

Compound **5.1** (200 mg, 0.69 mmol) was placed in a 25 mL round bottomed flask with a stir bar. To the flask was added neat oxalyl chloride (2 mL). The solution was heated to 40 C for 12 h before being allowed to cool. The volatile components were removed *in vacuo* and the solid product was collected as a tan solid and dried (208 mg, 98 %). ^{1}H NMR (400 MHz, DMSO-d_6) δ 8.58 (d, *J* = 2.7 Hz, 2H), 8.32 (dd, *J* = 9.1, 2.8 Hz, 2H), 7.60 (d, *J* = 9.1 Hz, 2H), 7.23 (s, 1H).

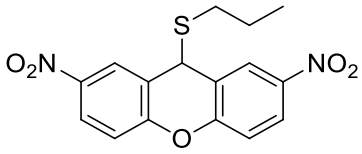

2,7-Dinitro-9-(propylthio)-9H-xanthene (**7.12**):

Compound **7.11** (200 mg, 0.65 mmol) was placed in a round bottomed flask along with a stir bar. To the flask was added neat n-propyl thiol (3 mL) and the reaction heated to 40 °C for 12 h. The reaction was cooled and poured into a beaker containing 50 mL of ice water. The solid product precipitated as a tan solid and was collected via filtration (214 mg, 95 %). ^{1}H NMR (400 MHz, DMSO-d_6) δ 8.36 (s, 2H), 8.18 (d, J = 9.0 Hz, 2H), 7.43 (d, J = 9.0 Hz, 2H), 5.79 (s, 1H), 2.26 (t, J = 7.2 Hz, 2H), 1.37 – 1.24 (m, 2H), 0.73 (t, J = 7.3 Hz, 3H).

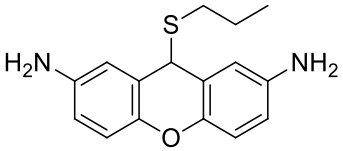

2,7-Diamino-9-(propylthio)-9H-xanthene (**7.13**):

Compound **7.12** (200 mg, 0.57 mmol) was placed in a Schlenk flask with a stir bar and the system was purged with N_2. Methanol (2 mL) and Raney Ni in water slurry (0.25 mL) was injected into the flask, followed by 0.5 mL of hydrazine monohydrate. The reaction was allowed to stir at 23 °C overnight. The solid catalyst was carefully removed via filtration through a plug of celite, and the solvent was removed *in vacuo*. The product was collected and dried to yield a pale yellow solid (144 mg, 87 %) ^{1}H NMR (400 MHz, DMSO-d_6) δ 6.63 (d, J = 7.8 Hz, 2H), 6.44 (s, 2H), 6.37 (d, J = 7.6 Hz, 2H), 4.97 (s, 1H), 4.70 (s, 4H), 2.12 (t, J = 7.2 Hz, 2H), 1.24 (m, 2H), 0.68 (t, J = 7.3 Hz, 3H).

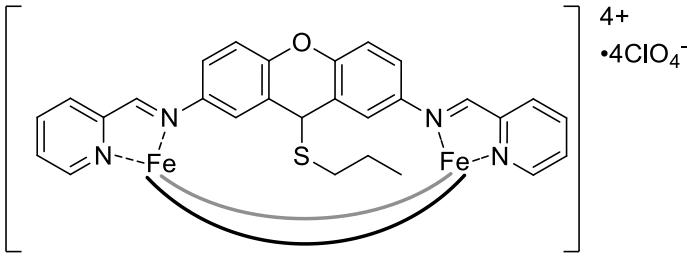

Complex (**7.14**):

Compound **7.13** (100 mg, 0.35 mmol) was placed in a Schlenk flask with a stir bar and the system was purged with N_2. Acetonitrile (2 mL)was injected into the flask, followed by 2-PyCHO (67 μL, 0.7 mmol). $Fe(ClO_4)_2$ (76 mg, 0.23 mmol) was dissolved with 1 mL anhydrous acetonitrile in a vial and transferred to the Schlenk flask via cannula. The reaction was allowed to stir at 50 °C overnight. The reaction mixture was diluted with Et_2O and the solid collected via filtration. The product was collected and dried to yield a purple solid (164 mg, 89 %) ^{1}H NMR See Figure 8.80 for full spectrum.

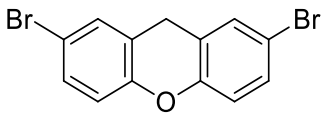

2,7-Dibromo Xanthene

Xanthene (729 mg, 4 mmol) was placed in a round bottom flask with a stir bar. Acetic anhydride (10 mL) was added and the flask placed in an ice bath with rapid stirring. A solution of bromine in acetic acid was prepared by mixing 0.51 mL bromine with 1 mL glacial acetic acid in a separate round bottom flask. The bromine solution was slowly added to the reaction mixture via dropwise addition over 10 min. The flask was then removed from the ice bath, allowed to warm to room temperature, and stirred for an additional 2 h. The reaction mixture was then poured into a beaker containing 100 mL of ice water, and

the excess bromine quenched with saturated sodium bisulfite solution. The white precipitate was collected via filtration and dried (1.28 g, 94 %). ^{1}H NMR (400 MHz, $CDCl_3$) δ 7.31 (m, 4H), 6.94 (d, *J* = 9.2 Hz, 2H), 4.04 (d, *J* = 11.3 Hz, 2H).

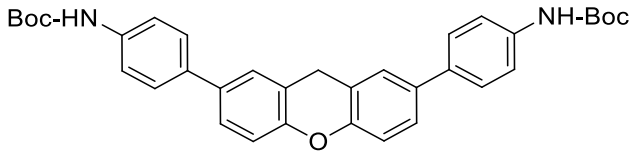

Di-tert-butyl ((9-bromo-9H-xanthene-2,7-diyl)bis(4,1-phenylene))dicarbamate:

2,7-Dibromo Xanthene (272 mg, 0.8 mmol), 4-BOCaminophenylboronic acid (474 mg, 2 mmol), cesium carbonate (1.56 g, 4.8 mmol), and Pd(dppf)Cl_2 (59 mg, 0.08 mmol) were placed in a Schlenk flask with a stir bar. The flask was purged with N_2, 1.8 mL of DMF was added and the flask quickly purged a second time. The mixture was stirred at 90 °C for 16 h, then the reaction was cooled to room temperature and diluted with 100 mL of water. The product was extracted with diethyl ether (4 x 60 mL) and the organic layer washed with a solution of 1 M $NaCO_3$ and 1 M sorbitol in water (30 mL) followed by washings with saturated sodium bicarbonate and brine (2 x 20 mL each). The cloudy organic layer was dried with magnesium sulfate, filtered through a celite plug and the solvent removed in vacuo to give the product as a tan solid (420 mg, 90 %). ^{1}H NMR (400 MHz, $CDCl_3$) δ 7.53 (d, J = 8.2 Hz, 4H), 7.47 – 7.38 (m, 8H), 7.13 (d, J = 8.2 Hz, 2H), 6.57 (s, 2H), 4.18 (s, 2H), 1.58 – 1.52 (m, 18H).

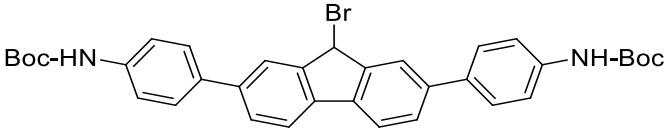

Di-tert-butyl ((9-bromo-9H-fluorene-2,7-diyl)bis(4,1-phenylene))dicarbamate (**7.15**):

Compound **6.1** (300 mg) was dissolved in minimal DCM and passed through a 2-inch plug of neutral alumina in order to remove any trace palladium catalyst remaining from the Suzuki coupling reaction. The purified material was dried and obtained as a white or pale yellow solid. The purified solid (200 mg, 0.36 mmol) was placed in a Schlenk flask along with N-bromosuccinimide (NBS, 110 mg, 0.61 mmol) and azo-bis-isobutyronitrile (AIBN) (60 mg, 0.36 mmol). The flask was purged with N_2 and benzene (10 mL) was added via syringe. The solution was heated to 80 °C for 18 h and then allowed to cool. The reaction mixture was diluted with 10 mL diethyl ether and washed with saturated sodium bicarbonate solution (3 x 10 mL) and brine (2 x 10 mL). The organic layer was dried using $MgSO_4$ and the solvent removed *in vacuo* to yield an orange solid (203 mg, 90 %). ^{1}H NMR (400 MHz, $CDCl_3$) δ 7.87 (s, 2H), 7.74 (d, *J* = 7.9 Hz, 2H), 7.64 – 7.58 (m, 6H), 7.49 (d, *J* = 8.6 Hz, 4H), 6.57 (s, 2H), 6.11 (s, 2H), 1.57 (s, 18H).

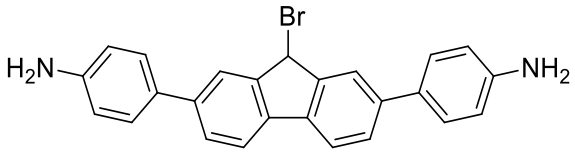

4,4'-(9-Bromo-9H-fluorene-2,7-diyl)dianiline (**7.16**):

Compound **7.15** (200 mg, 0.32 mmol) was placed in a round bottomed flask with a stir bar. Neat TFA (5 mL) was added to the flask and the reaction mixture was allowed to stir at room temperature for 6 h. Diethyl ether (20 mL) was added to the flask and the acid was neutralized using saturated sodium bicarbonate solution until the pH reached 8. The organic layer was washed with brine (3 x 10 mL) and dried using $MgSO_4$. The solvent was removed *in vacuo* and the product collected as an orange-brown solid (117 mg, 87 %). ^{1}H NMR

(400 MHz, DMSO-d_6) δ 7.83 (d, J = 8.0 Hz, 2H), 7.78 (s, 2H), 7.63 (dd, J = 8.0, 1.6 Hz, 2H), 7.45 (d, J = 8.3 Hz, 4H), 6.72 (d, J = 8.5 Hz, 4H), 6.44 (s, 1H).

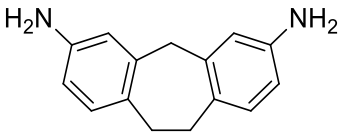

3,7-Diaminosuberene (**7.17**):

Dianiline **1.6** (50 mg, 0.21 mmol) was placed in a 10 mL glass vial, and 2 mL of neat TFA was added. The solution was stirred until all solids had dissolved. Triethyl silane (0.25 mL) was slowly added dropwise to the vial. The reaction was allowed to stir at room temperature for 3 h. The reaction mixture was neutralized via dropwise addition of saturated sodium bicarbonate solution until the pH reacted 8. The solid precipitate was collected via filtration and dried (39 mg, 84 %). ^{1}H NMR (400 MHz, DMSO-d_6) δ 6.73 (d, J = 7.9 Hz, 2H), 6.37 (s, 2H), 6.32 (d, J = 8.0 Hz, 2H), 4.74 (s, 4H), 3.72 (s, 2H), 2.86 (s, 4H).

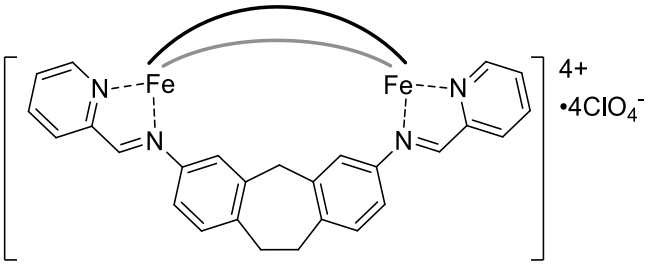

Mesocate (**7.18**):

Dianiline **7.17** (50 mg, 0.076 mmol) was placed in a round bottomed flask with a stir bar and 5 mL of acetonitrile. 2-Formylpyridine (42 µL, 0.15 mmol) and iron triflimide (101 mg, 0.051 mmol) were added to the flask, and the reaction was stirred at 60 °C for 24 h. The product was precipitated with 30 mL Et_2O, and the dark purple solid was collected via filtration (132 mg, 88 %). ^{1}H NMR (400 MHz, CD_3CN) δ 8.88 (s, 2H), 8.37 (s, 2H), 8.31

(s, 2H), 7.73 (s, 2H), 7.46 (s, 2H), 6.97 (d, *J* = 7.0 Hz, 2H), 6.44 (s, 2H), 5.55 (d, *J* = 6.3 Hz, 2H), 4.38 (d, *J* = 15.3 Hz, 1H), 3.98 (d, *J* = 15.3 Hz, 1H), 3.09 (s, 4H).

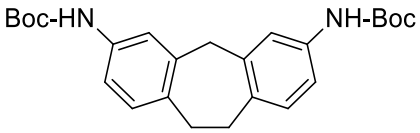

3,7-Boc-Diaminosuberene (**7.19**):

Compound **7.17** (100 mg, 0.44 mmol) was placed in a round bottomed flask along with a stir bar. To the flask was added 5 mL of a 1:1 mixture of THF and water. Sodium carbonate (140 mg, 1.32 mmol) and di-tert-butyl dicarbonate (288 mg, 1.32 mmol) were added to the flask. The reaction was stirred at 23 °C for 18 h followed by precipitation of the product with water and filtration. The solid tan product was washed with hexane and dried (135 mg 72 %) ^{1}H NMR (400 MHz, DMSO-d_6) δ 9.17 (s, 2H), 7.37 – 7.30 (m, 2H), 7.14 (dd, *J* = 8.2, 2.0 Hz, 2H), 6.96 (t, *J* = 9.6 Hz, 2H), 3.92 (s, 2H), 2.99 (s, 4H), 1.44 (s, 9H).

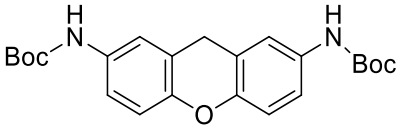

2,7-Boc-Diaminoxanthene (**7.21**):

Compound **5.2** (93 mg, 0.44 mmol) was placed in a round bottomed flask along with a stir bar. To the flask was added 5 mL of a 1:1 mixture of THF and water. Sodium carbonate (140 mg, 1.32 mmol) and di-tert-butyl dicarbonate (288 mg, 1.32 mmol) were added to the flask. The reaction was stirred at 23 °C for 18 h followed by precipitation of the product with water and filtration. The solid tan product was washed with hexane and dried (135 mg 72 %) ^{1}H NMR (400 MHz, DMSO-d_6) δ 9.26 (s, 2H), 7.40 (s, 2H), 7.19 (dd, J = 8.1, 2.1 Hz, 2H), 6.93 (d, J = 8.8 Hz, 2H), 3.96 (s, 2H), 1.50 (s, 18H),

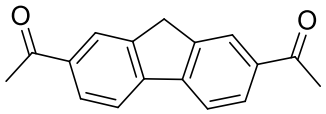

2,7-Diacetylfluorene (**7.22**):

Acetyl chloride (15.04 mL of a 1M solution) was placed in a 100 mL round bottom flask with a stir bar, 5 mL dry DCM was added, and the flask was lowered into an ice bath. Aluminum chloride (4 mol.-eq., 3.21 g, 24 mmol) was added to the flask. Fluorene (1 g, 6 mmol) was dissolved in 5 mL DCM, and this solution was added to the flask dropwise over approximately 15 min. Once the addition was complete, the flask was transferred from the ice bath and heated at reflux for 2 h. The reaction was monitored via TLC and allowed to continue until all starting material and mono-acylated intermediate was consumed. The reaction was washed with brine (4 x 20 mL), dried with $MgSO_4$ and the solvent removed *in vacuo*. The product was obtained as a yellow solid (1.21, 90 %). ^{1}H NMR (400 MHz, $CDCl_3$) δ 8.16 (s, 2H), 8.02 (d, *J* = 8.0 Hz, 2H), 7.89 (dd, *J* = 8.0, 1.7 Hz, 2H), 4.00 (s, 2H), 2.65 (dd, *J* = 4.6, 1.1 Hz, 6H).

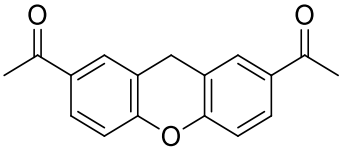

2,7-Diacetylxanthene (**7.23**):

Acetyl chloride (15.04 mL of 1M solution) was placed in a 100 mL round bottom flask with a stir bar, 5 mL dry DCM was added, and the flask was laced in an ice bath. Aluminum chloride (4 mol.-eq., 3.21 g, 24 mmol) was added to the flask. Xanthene (1.09 g, 6 mmol) was dissolved in 10 mL DCM, and slowly added to the flask dropwise over approximately 15 min. Once the addition was complete, the flask was transferred from the ice bath and

allowed to stir at 23 °C for 2 h. The reaction was monitored via TLC and allowed to continue until all starting material and mono-acylated intermediate was consumed. The reaction was washed with brine (4 x 20 mL), dried with $MgSO_4$ and the solvent removed *in vacuo*. The product was obtained as a tan solid (1.41 g, 94 %). ^{1}H NMR (400 MHz, $CDCl_3$) δ 7.85 (m, 2H), 7.13 (dd, *J* = 7.2, 2.0 Hz, 2H), 4.17 (s, 2H), 2.61 (s, 6H).

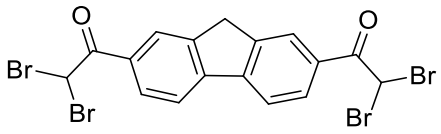

1,1'-(9H-Fluorene-2,7-diyl)bis(2,2-dibromoethanone) (**7.24**):

Compound **7.22** (1 g, 4 mmol) was placed in a 50 mL round bottom flask. Acetic acid (30 mL) was added to the flask followed by the slow addition of bromine (1.5 mL). The mixture was heated to 50 °C overnight, then allowed to cool. The reaction mixture was poured into a beaker containing 150 mL of ice water and the beige precipitate was filtered and collected (1.97 g, 87 %). ^{1}H NMR (400 MHz, $CDCl_3$) δ 8.31 (s, 2H), 8.17 (dd, *J* = 8.1, 0.8 Hz, 2H), 7.95 (dd, *J* = 7.8, 3.9 Hz, 2H), 6.75 (d, *J* = 7.3 Hz, 2H), 4.09 (s, 2H).

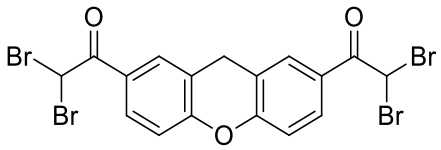

1,1'-(9H-Xanthene-2,7-diyl)bis(2,2-dibromoethanone) (**7.25**):

Compound **7.23** (1.06 g, 4 mmol) was placed in a 50 mL round bottom flask along with a stir bar. Acetic acid (30 mL) was added to the flask followed by the slow addition of bromine (1.5 mL). The mixture was heated to 50 °C overnight, then allowed to cool. The reaction mixture was poured into a beaker containing 150 mL of ice water and the beige

precipitate was filtered and collected (1.83 g, 82 %). ^{1}H NMR (400 MHz, $CDCl_3$) δ 7.60 (s, 2H), 7.55 (m, 4H), 7.05 (d, *J* = 7.8, 3.9 Hz, 2H), 6.85 (d, *J* = 7.3 Hz, 2H), 3.95 (s, 2H).

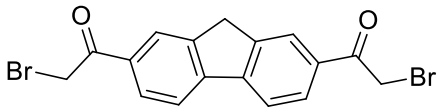

1,1'-(9H-Fluorene-2,7-diyl)bis(2-bromoethanone) (**7.26**):

Compound **7.22** (500 mg, 2 mmol) was placed in a round bottom flask with a stir bar and 10 mL of DCM and 10 mL EtOAc. To this solution was added 6 eq. CuBr (1.72 g, 12 mmol). The reaction was heated to reflux for 18 h, before being cooled to room temperature and any solid impurities removed via filtration. 10 mL DCM was added to the mixture, and the organic layer was extracted with brine (3 x 20 mL). The solution was dried with $MgSO_4$ and the solvent removed *in vacuo*. The product was collected as a beige solid (686 mg, 84 %). ^{1}H NMR (400 MHz, DMSO-d_6) δ 8.20 (s, 2H), 8.08 (dd, *J* = 8.4, 1.8 Hz, 2H), 7.96 (dd, *J* = 8.6, 3.6 Hz, 2H), 4.51 (s, 4H), 4.04 (s, 2H).

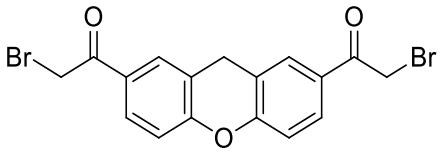

1,1'-(9H-Xanthene-2,7-diyl)bis(2-bromoethanone) (**7.27**):

Compound **7.23** (100 mg, 0.38 mmol) was placed in a round bottom flask with a stir bar and 2 mL of DCM and 2 mL EtOAc. To this solution was added 4.5 eq. CuBr (242 mg, 1.69 mmol). The reaction was heated to reflux for 18 h, before being cooled to room temperature. 5 mL DCM was added to the mixture, and the organic layer was extracted with brine (3 x 10 mL). The solution was dried with $MgSO_4$ and the solvent removed *in vacuo*. The product was collected as a tan solid (140 mg, 87 %). ^{1}H NMR (400 MHz,

DMSO-d_6) δ 8.00 (s, 2H), 7.93 (dd, J = 8.4, 1.8 Hz, 2H), 7.27 (dd, J = 8.6, 3.6 Hz, 2H), 4.91 (s, 4H), 4.23 (s, 2H).

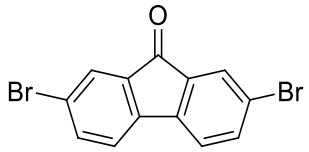

2,7-Dibromofluorenone (**7.29**):

Fluorenone (12 g, 0.066 mol) was placed in a 100 mL round bottom flask and 100 mL of water was added. The mixture was heated to 80 °C. Bromine (4.8 mL) was slowly added to the reaction mixture over 10 min. The reaction was allowed to stir for 5 h before a second portion of bromine (2 mL) was added. The pH of the mixture was checked and if the pH is > 4, 2M NaOH was added dropwise until the pH reacted 7. The reaction was allowed to stir at 80 °C for 12 h. The reaction mixture was cooled and poured into a beaker containing 150 mL of ice water and the excess bromine was quenched with saturated sodium bisulfite solution. The yellow solid was filtered, and dried (20.48g, 91 %) ^{1}H NMR (400 MHz, $CDCl_3$) δ 7.75 (d, J = 1.7 Hz, 2H), 7.61 (dd, J = 7.9, 1.8 Hz, 2H), 7.37 (d, J = 7.9 Hz, 2H).

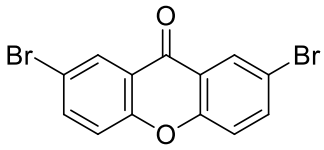

2,7-Dibromoxanthone (**7.30**):

Xanthone (2 g, 0.01 mol) was placed in a round bottom flask with 10 mL acetic acid. Bromine (4 mL) was added to the solution dropwise over the course of 30 min. The solution was heated to reflux and allowed to stir for 20 h. The reaction mixture was allowed to cool and poured into a beaker containing 50 mL of ice water and the excess bromine was

quenched with saturated sodium bisulfite solution. The solid product was collected via filtration and dried to yield tan product (3.39 g, 94 %). The product can be recrystallized from toluene if necessary ^{1}H NMR (400 MHz, $CDCl_3$) δ 8.40 (d, *J* = 2.4 Hz, 1H), 7.80 – 7.77 (dd, *J* = 7.6, 2.4 Hz, 1H), 7.37 (d, *J* = 7.5 Hz, 2H).

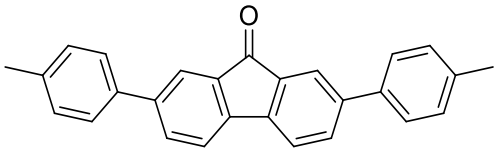

2,7-di-p-tolyl-9H-fluoren-9-one (**7.31**):

Compound **7.29** (338 mg, 1 mmol) was placed in a Schlenk flask along with *p*-Tolylboronic acid (272 mg, 2 mmol), potassium carbonate (553 mg, 4 mmol), $Pd(OAc)_2$ (10 mg, 0.05 mmol) and SPhos ligand (41 mg, 0.1 mmol). The flask was purged with N_2 and 4 mL ethanol, 1 mL deionized water and 1.5 mL toluene were added via syringe. The mixture was heated at 85 °C for 16 h and then allowed to cool. The reaction mixture was diluted with 25 mL diethyl ether and the organic layer washed with saturated sodium bicarbonate solution (4 x 15 mL) and brine (3 x 15 mL). The organic layer was dried using $MgSO_4$ and the solvent removed *in vacuo* to yield product as a bright yellow solid (266 mg, 74 %). ^{1}H NMR (400 MHz, $CDCl_3$) δ 7.89 (s, 2H), 7.69 (d, *J* = 7.7 Hz, 2H), 7.55 (d, *J* = 7.7 Hz, 2H), 7.51 (d, *J* = 8.0 Hz, 4H), 7.26 (d, *J* = 8.2 Hz, 4H), 2.42 (s, 6H).

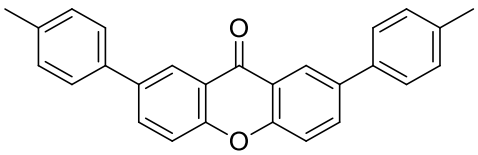

2,7-Di-p-tolyl-9H-xanthen-9-one (**7.32**):

Compound **7.30** (354 mg, 1 mmol) was placed in a Schlenk flask along with *p*-Tolylboronic acid (272 mg, 2 mmol), potassium carbonate (553 mg, 4 mmol), $Pd(OAc)_2$ (10 mg, 0.05 mmol) and SPhos ligand (41 mg, 0.1 mmol). The flask was purged with N_2 and 4 mL ethanol, 1 mL deionized water and 1.5 mL toluene were added via syringe. The mixture was heated at 85 °C for 16 h and then allowed to cool. The reaction mixture was diluted with 25 mL diethyl ether and the organic layer washed with saturated sodium bicarbonate solution (4 x 15 mL) and brine (3 x 15 mL). The organic layer was dried using $MgSO_4$ and the solvent removed *in vacuo* to yield product as a beige solid (263 mg, 70 %). ^{1}H NMR (400 MHz, $CDCl_3$) δ 8.55 (d, *J* = 2.2 Hz, 2H), 7.95 (dd, *J* = 8.7, 2.3 Hz, 2H), 7.58 (d, *J* = 8.5 Hz, 4H), 7.55 (d, *J* = 2.9 Hz, 2H), 7.28 (d, *J* = 7.9 Hz, 4H), 2.40 (s, 6H).

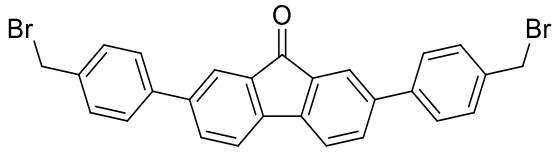

2,7-Bis(4-(bromomethyl)phenyl)-9H-fluoren-9-one (**7.33**):

Compound **7.31** (50 mg, 0.14 mmol) was placed in a Schlenk flask with a stir bar, To the flask was added NBS (49.6 mg, 0.28 mmol) and benzoyl peroxide (3.21 mg, 0.013 mmol). The flask was purged with N_2 and benzene (3 mL) was added via syringe. The solution was heated at 77 °C for 14 h, then the reaction mixture was allowed to cool. The product precipitated from the reaction mixture as a yellow orange solid and was collected via filtration and washed with hexane (56 mg, 81 %.) ^{1}H NMR (500 MHz, DMSO-d_6) δ 8.24 (d, *J* = 2.0 Hz, 2H), 7.97 (dd, *J* = 7.1, 2.1 Hz, 2H), 7.81 (d, *J* = 7.3 Hz, 2H), 7.71 (d, *J* = 8.2 Hz, 4H), 7.43 (d, *J* = 8.1 Hz, 4H), 4.69 (s, 2H).

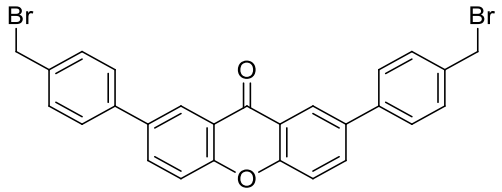

2,7-Bis(4-(bromomethyl)phenyl)-9H-xanthen-9-one (**7.34**):

Compound **7.32** (52 mg, 0.14 mmol) was placed in a Schlenk flask with a stir bar, To the flask was added NBS (49.6 mg, 0.28 mmol) and benzoyl peroxide (3.21 mg, 0.013 mmol). The flask was purged with N_2 and benzene (3 mL) was added via syringe. The solution was heated at 77 °C for 14 h, then the reaction mixture was allowed to cool. The product precipitated from the reaction mixture as a yellow orange solid and was collected via filtration and washed with hexane (64 mg, 85 %.) ^{1}H NMR (500 MHz, DMSO-d_6) δ 8.15 (s, 2H), 7.71 (d, J = 7.3 Hz, 2H), 7.54 (d, J = 8.1 Hz 4H), 7.41 (d, J = 8.3 Hz, 4H), 7.28 (d, J = 7.1 Hz 2H), 4.64 (s, 4H).

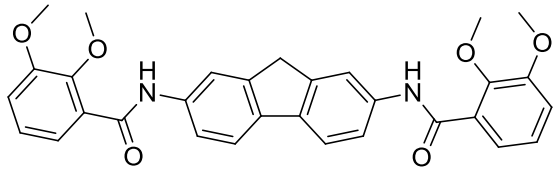

N,N'-(9H-Fluorene-2,7-diyl)bis(2,3-dimethoxybenzamide) (**7.43**):

Dianiline **5.4** (50 mg, 0.25 mmol) was placed in a round bottomed flask along with a stir bar and 3 ml anhydrous THF. 2,3-Dimethoxybenzoylchloride (107.3 mg, 0.53 mmol) was added to the flask along with triethylamine (75 µL, 0.53 mmol). The reaction was allowed to stir overnight at 23 °C, and the product was precipitated from the reaction mixture with 15 mL water. The product was isolated as a tan solid via filtration and dried (124 mg, 95 %) ^{1}H NMR (400 MHz, DMSO-d_6) δ 10.32 (s, 2H), 8.04 (s, 2H), 7.78 (d, J = 8.3 Hz, 2H), 7.69 (d, J = 8.2 Hz, 2H), 7.24 – 7.11 (m, 6H), 3.95 (s, 2H), 3.88 (s, 6H), 3.84 (s, 6H).

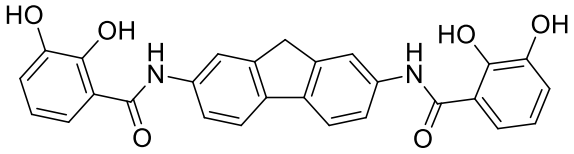

N,N'-(9H-Fluorene-2,7-diyl)bis(2,3-dihydroxybenzamide) (**7.44**):

Compound **7.43** (50 mg, 0.09 mmol) was placed in a Schlenk flask with a stir bar. BBr_3•Me_2S (476 mg, 1.52 mmol) was added to the flask, and the system was purged with N_2. Toluene (5 mL) was added, and the reaction mixture was refluxed for 18 h. The volatiles were removed *in vacuo* and the solids were suspended in water and refluxed for 4 h. The reaction was cooled, the tan solid product was collected via filtration and the solid quickly placed in a vial and dried *in vacuo*. The tan solid is stable while stored at 23 °C under an inert atmosphere (35 mg, 82 %). ^{1}H NMR (400 MHz, DMSO-d_6) δ 11.75 (s, 2H), 10.44 (s, 2H), 9.41 (s, 2H), 8.00 (s, 2H), 7.85 (d, *J* = 8.3 Hz, 2H), 7.70 – 7.65 (d, *J* = 7.1 Hz, 2H), 7.49 (d, *J* = 7.1 Hz, 2H), 7.00 (dd, *J* = 7.8, 1.1 Hz, 2H), 6.80 (t, *J* = 7.9 Hz, 2H), 3.97 (d, *J* = 11.9 Hz, 2H).

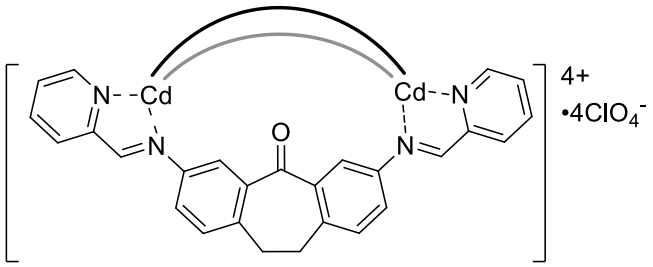

Suberone Cd Mesocate (**7.45**):

Dianiline **1.5** (20 mg, 0.084 mmol), PyCHO (16 μL, 0.17 mmol) and $Cd(ClO_4)_2$•$2H_2O$ (19 mg, 0.055 mmol) were combined in anhydrous MeCN (2.5 mL) in a 25 mL flask under a blanket of N_2. The solution was heated at 70 °C for 16 h with stirring. The orange solution

was diluted with Et_2O (10 mL), and the resulting precipitate was filtered. After drying, the product was isolated as a yellow solid (31 mg, 73.7 % yield). ^{1}H NMR (400 MHz, CD_3CN) δ 8.95 (m, 1H), 8.53 (d, *J* = 6.3 Hz, 1H), 8.36 (dd, *J* = 17.1, 9.3 Hz, 1H), 8.15 (t, *J* = 7.0 Hz, 1H), 7.85 (q, *J* = 6.4 Hz, 1H), 7.75 (t, *J* = 3.8 Hz, 1H), 7.04 (t, *J* = 7.3 Hz, 1H), 6.78 (dt, *J* = 7.7, 3.8 Hz, 1H), 2.84 (m, 2H).

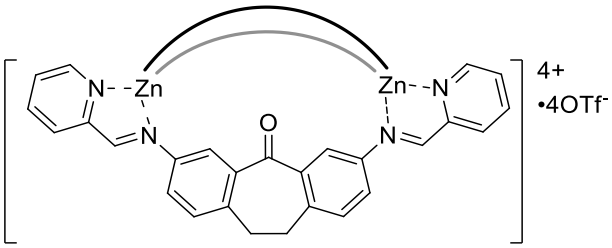

Suberone Zn Mesocate (**7.46**):

Dianiline **1.5** (50 mg, 0.21 mmol), PyCHO (40 μL, 0.42 mmol) and $Zn(OTf)_2$•$2H_2O$ (56 mg, 0.14 mmol) were combined in anhydrous MeCN (3 mL) in a 25 mL flask under a blanket of N_2. The solution was then heated at 70 °C for 16 h with stirring. The orange-red solution was diluted with Et_2O (10 mL), and the precipitate was filtered. After drying, the product was isolated as a yellow solid (51 mg, 89.5 % yield). ^{1}H NMR (400 MHz, CD_3CN) δ 8.49 (td, *J* = 7.8, 1.6 Hz, 1H), 8.44 (s, 1H), 8.21 (dt, *J* = 7.9, 1.0 Hz, 1H), 8.14 (d, *J* = 4.8 Hz, 1H), 7.94 (ddd, *J* = 7.8, 5.1, 1.2 Hz, 1H), 7.21 (d, *J* = 8.1 Hz, 1H), 6.57 (s, 1H), 5.98 (dd, *J* = 7.9, 2.5 Hz, 1H), 3.22 (m, 2H).

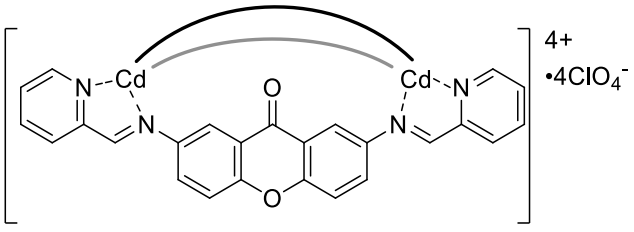

Xanthone Cd Mesocate (**7.47**):

Ligand **2.5** (104 mg, 0.47 mmol), PyCHO (89.4 µL, 0.94 mmol) and $Cd(ClO_4)_2 \bullet 2H_2O$ (114 mg, 0.31 mmol) were combined in acetonitrile (10 mL) in a round bottom flask. The solution was then heated at 70 °C for 16 h. After the reaction was complete, Et_2O was added (30 mL) and the product collected as an orange solid (227 mg, 93 %). ^{1}H NMR (400 MHz, CD_3CN) δ 8.71 – 8.59 (m, 2H), 8.44 (td, *J* = 7.8, 1.5 Hz, 2H), 8.29 (d, *J* = 4.5 Hz, 2H), 8.20 (d, *J* = 7.6 Hz, 2H), 7.95 – 7.88 (m, 2H), 7.19 (d, *J* = 8.6 Hz, 2H), 6.72 (dd, *J* = 8.6, 2.6 Hz, 2H), 5.87 (d, *J* = 2.4 Hz, 2H), 3.56 (d, *J* = 19.7 Hz, 1H), 3.26 (d, *J* = 19.7 Hz, 1H).

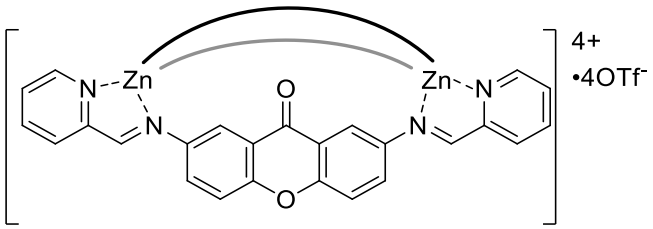

Xanthone Zn Mesocate (**7.48**):

Dianiline **2.5** (51 mg, .24 mmol) was placed in a 25 mL round bottom flask along with a stir bar and 5 mL acetonitrile. 2-Formylpyridine (44.8 µL, 0.46 mmol) was added along with zinc salt (0.15 mmol, 42.1 mg $Zn(BF_4)_2$ or 44.9 mg $Zn(ClO_4)_2$) and the reaction mixture was heated at 45 °C for 12 h. The yellow product was precipitated with Et_2O (20 mL) and collected via filtration (85 mg BF_4 salt, 94 %, 91 mg, ClO_4 salt, 97 %). The ^{1}H NMR spectra did not change appreciably when different counter anions were used. ^{1}H NMR (400 MHz, CD_3CN) δ 8.59 (s, 2H), 8.48 – 8.42 (m, 2H), 8.25 (d, *J* = 7.3 Hz, 2H), 7.87 (m, 4H), 7.13 (dd, *J* = 8.6, 1.7 Hz, 2H), 6.55 – 6.48 (m, 2H), 5.65 (d, *J* = 1.6 Hz, 2H), 3.47 (d, *J* = 14.6 Hz, 1H), 3.14 (d, *J* = 18.3 Hz, 1H).

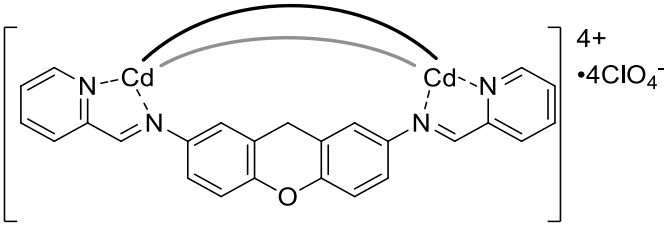

Xanthene Cd Mesocate (**7.49**):

Ligand **5.2** (100 mg, 0.47 mmol), QnCHO (89.4 µL, 0.94 mmol) and $Cd(ClO_4)_2$•$2H_2O$ (114 mg, 0.31 mmol) were combined in acetonitrile (10 mL) in a round bottom flask. The solution was then heated at 70 °C for 16 h. After the reaction was complete, Et_2O was added (30 mL) and the product collected as an orange solid (227 mg, 93 %). ^{1}H NMR (400 MHz, CD_3CN) δ 8.71 – 8.59 (m, 2H), 8.44 (td, *J* = 7.8, 1.5 Hz, 2H), 8.29 (d, *J* = 4.5 Hz, 2H), 8.20 (d, *J* = 7.6 Hz, 2H), 7.95 – 7.88 (m, 2H), 7.19 (d, *J* = 8.6 Hz, 2H), 6.72 (dd, *J* = 8.6, 2.6 Hz, 2H), 5.87 (d, *J* = 2.4 Hz, 2H), 3.56 (d, *J* = 19.7 Hz, 1H), 3.26 (d, *J* = 19.7 Hz, 1H).

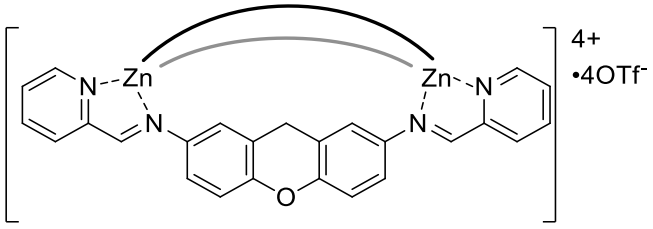

Xanthene Zn Mesocate (**7.50**):

Dianiline **5.2** (50 mg, .24 mmol) was placed in a 25 mL round bottom flask along with a stir bar and 5 mL acetonitrile. 2-Formylpyridine (44.8 µL, 0.46 mmol) was added along with zinc salt (0.15 mmol, 42.1 mg $Zn(BF_4)_2$ or 44.9 mg $Zn(ClO_4)_2$) and the reaction mixture was heated at 45 °C for 12 h. The yellow product was precipitated with Et_2O (20 mL) and collected via filtration (85 mg BF_4 salt, 94 %, 91 mg, ClO_4 salt, 97 %). The ^{1}H

NMR spectra did not change appreciably when different counter anions were used. ^{1}H NMR (400 MHz, CD_3CN) δ 8.59 (s, 2H), 8.48 – 8.42 (m, 2H), 8.25 (d, *J* = 7.3 Hz, 2H), 7.87 (m, 4H), 7.13 (dd, *J* = 8.6, 1.7 Hz, 2H), 6.55 – 6.48 (m, 2H), 5.65 (d, *J* = 1.6 Hz, 2H), 3.47 (d, *J* = 14.6 Hz, 1H), 3.14 (d, *J* = 18.3 Hz, 1H).

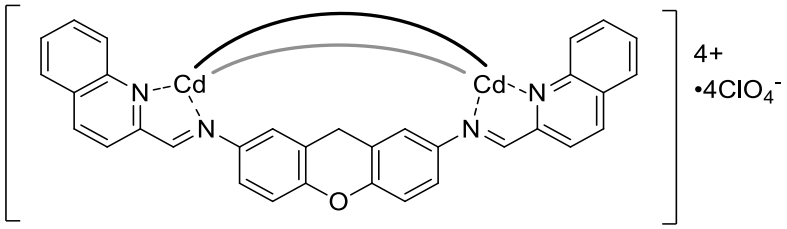

Mesocate (**7.51**):

Ligand **5.2** (100 mg, 0.47 mmol), QnCHO (148 mg, 0.94 mmol) and $Cd(ClO_4)_2$•$2H_2O$ (114 mg, 0.31 mmol) were combined in acetonitrile (10 mL) in a round bottom flask. The solution was then heated at 70 °C for 16 h. After the reaction was complete, Et_2O was added (30 mL) and the product collected as an orange solid (225 mg, 91 %). ^{1}H NMR (400 MHz, CD_3CN) δ 9.07 – 8.96 (m, 2H), 8.90 – 8.76 (m, 2H), 8.25 (dd, *J* = 22.3, 8.5 Hz, 4H), 7.75 – 7.68 (m, 2H), 7.42 (d, *J* = 9.1 Hz, 2H), 7.21 (d, *J* = 8.8 Hz, 2H), 7.17 – 7.10 (m, 2H), 6.73 (d, *J* = 9.1 Hz, 2H), 5.93 (s, 2H), 3.64 (d, *J* = 19.8 Hz, 1H), 3.30 (d, *J* = 19.5 Hz, 1H).

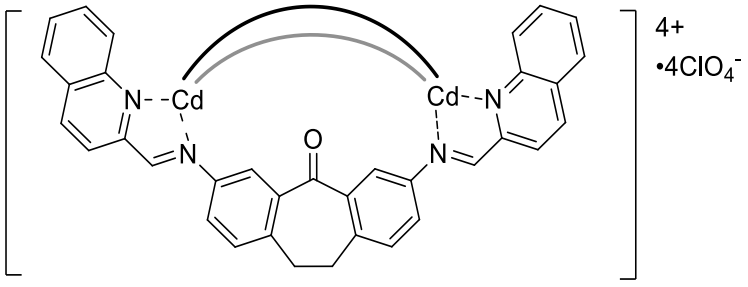

Mesocate (**7.52**):

Ligand **1.5** (30 mg, 0.13 mmol), QnCHO (40 mg, 0.25 mmol) and $Cd(ClO_4)_2 \bullet 2H_2O$ (28 mg, 0.083 mmol) were combined in anhydrous MeCN (2.5 mL) in a 25 mL round-bottomed flask under a blanket of N_2. The solution was heated at 70 °C for 16 h with stirring. The light brown-red solution was diluted with Et_2O (10 mL), and the resulting yellow precipitate was filtered. After drying, the product was isolated as a yellow solid (52 mg, 61.9 % yield). ^{1}H NMR: (400 MHz, CD_3CN) δ 9.10 (d, *J* = 8.2 Hz, 2H), 8.86 (m, 4H), 8.55 (m, 2H), 8.36 (d, *J* = 8.3 Hz, 2H), 8.20 (m, 4H), 8.01 (d, *J* = 8.4 Hz, 2H), 7.96 (d, *J* = 8.6 Hz, 2H), 7.80 (m, 8H), 7.45 (t, *J* = 7.9 Hz, 2H), 7.39 (t, *J* = 7.8 Hz, 2H), 7.19 (d, *J* = 8.0 Hz, 2H), 6.96 (d, *J* = 8.1 Hz, 2H), 6.72 (d, *J* = 2.4 Hz, 2H), 6.39 (dd, *J* = 8.1, 2.4 Hz, 2H), 5.92 (dd, *J* = 8.1, 2.5 Hz, 2H), 3.43 (dd, *J* = 15.8, 9.8 Hz, 2H), 3.19 (dd, *J* = 15.5, 9.5 Hz, 2H), 2.88 (m, 2H), 2.79 (t, *J* = 14.5 Hz, 2H).

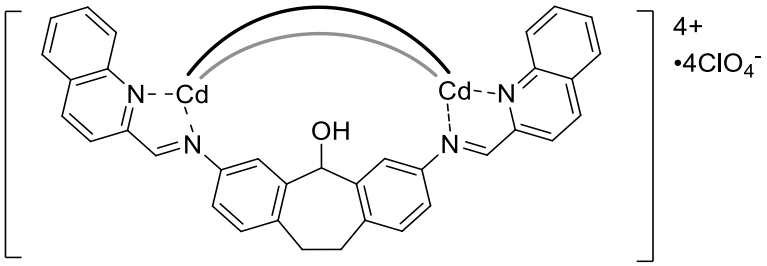

Mesocate (**7.53**):

Ligand **1.6** (200 mg, 0.84 mmol), QnCHO (263 mg, 1.67 mmol) and $Cd(ClO_4)_2 \bullet 2H_2O$ (192 mg, 0.55 mmol) were combined in anhydrous MeCN (4 mL) in a 25 mL round-bottomed flask under a blanket of N_2. The solution was heated at 65 °C for 16 h with stirring. The orange solution was diluted with Et_2O (10 mL), and the resulting yellow precipitate was filtered. After drying, the product was isolated as a yellow solid (457 mg, 93.3 % yield). ^{1}H NMR (400 MHz, CD_3CN) δ 8.62 (d, *J* = 8.3 Hz, 2H), 8.27 (m, 2H), 8.18 (d, *J* = 8.3 Hz,

2H), 8.06 (d, *J* = 8.6 Hz, 2H), 7.95 (d, *J* = 2.4 Hz, 2H), 7.78 (dd, *J* = 8.2, 6.9 Hz, 2H), 7.56 (m, 4H), 6.55 (d, *J* = 8.0 Hz, 2H), 6.01 (d, *J* = 5.3 Hz, 2H), 5.24 (dd, *J* = 8.0, 2.4 Hz, 2H), 3.24 (s, 1H), 2.74 (m, 4H).

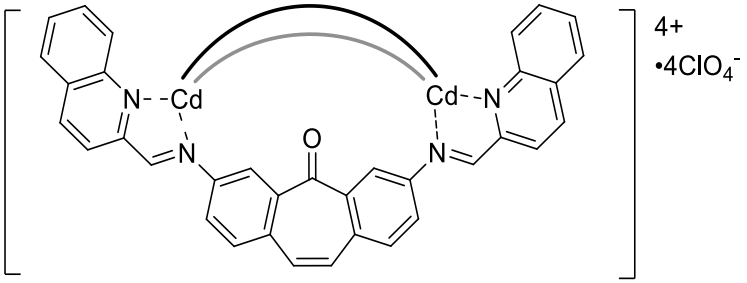

Mesocate (**7.54**):

Ligand **2.2** (10 mg, 0.042 mmol), 2-quinolinecarboxaldehyde (13 mg, 0.085 mmol) and $Cd(ClO_4)_2$•$2H_2O$ (8 mg, 0.028 mmol) were combined in CD_3CN (0.3 mL) in an NMR tube. The solution was sonicated for 5 min, then heated at 70 °C for 16 h. Upon reaction completion the sample displayed a red color. ^{1}H NMR (400 MHz, CD_3CN) δ 8.86 (d, *J* = 8.6 Hz, 2H), 8.80 (s, 2H), 8.28 (d, *J* = 2.5 Hz, 2H), 8.24 (d, *J* = 8.4 Hz, 2H), 8.00 (m, 4H), 7.81 (t, *J* = 7.6 Hz, 2H), 7.53 (t, *J* = 7.8 Hz, 2H), 7.29 (d, *J* = 8.4 Hz, 2H), 6.96 (s, 2H), 6.36 (dd, *J* = 8.4, 2.5 Hz, 2H).

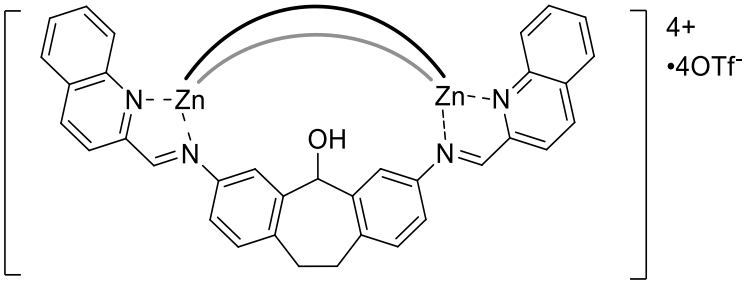

Mesocate (**7.55**):

Ligand **1.6** (40 mg, 0.17 mmol), QnCHO (53 mg, 0.34 mmol) and $Zn(OTf)_2 \cdot 2H_2O$ (44 mg, 0.11 mmol) were combined in anhydrous MeCN (2.5 mL) in a 25 mL round-bottomed flask under a blanket of N_2. The solution was then heated at 70 °C for 16 h with stirring. The dark red solution was diluted with Et_2O (10 mL), and the resulting brown precipitate was filtered. After drying, the product was isolated as a dark solid (87 mg, 93 % yield). ^{1}H NMR (400 MHz, CD_3CN) δ 8.61 (d, *J* = 8.4 Hz, 1H), 8.17 (m, 2H), 8.02 (d, *J* = 2.6 Hz, 1H), 7.77 (t, *J* = 7.6 Hz, 1H), 7.48 (dd, *J* = 8.2, 4.0 Hz, 1H), 6.62 (d, *J* = 7.9 Hz, 1H), 6.06 (d, *J* = 5.1 Hz, 1H), 5.21 (dd, *J* = 8.1, 2.5 Hz, 1H), 3.54 (q, *J* = 7.0 Hz, 1H), 3.31 (t, *J* = 8.2 Hz, 1H), 2.78 (h, *J* = 10.6, 10.1 Hz, 1H), 2.66 (d, *J* = 5.2 Hz, 1H).

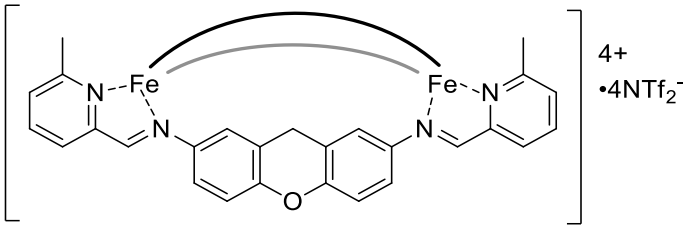

Mesocate (**7.56**):

Ligand **5.2** (150 mg, 0.71 mmol), 6-methylpyridine-2-carboxaldehyde (171 mg, 1.41 mmol) and $Fe(NTf_2)_4$ (310 mg, 0.47 mmol) were combined in MeCN (10 mL) in a 25 mL round-bottom flask. The solution was then heated at 77 °C for 48 h with stirring. The reaction mixture was cooled, and the acetonitrile removed *in vacuo*. The red solid was sonicated with 20 mL of 3:1 Et_2O/MeOH solution and the red solid was removed via vacuum filtration. After drying, the product was isolated as a red powder (592 mg, 94 % yield). ^{1}H NMR (400 MHz; CD_3CN) δ 184.25, 54.01 (s), 52.89 (s), 13.56 (s), 8.41 (s), 6.87 (s), -25.49 (s), -30.94 (s), -33.24 (s), -48.88 (s).

Mesocate **7.56** (CCDC #1848253).

150 mg of cage **7.56** was dissolved in a minimal amount of acetonitrile and 0.5 mL of the resulting solution was pipetted into an NMR tube. The tube was placed into an 8 oz. glass jar containing 25 mL of diethyl ether. The jar was capped tightly, and the sample was allowed to sit for 5 days, until solvent diffusion was complete and the solution inside the NMR tube was colorless. Red prisms and needles were both observed within the NMR tube.

A red prism fragment (0.488 x 0.136 x 0.030 mm^3) was used for the single crystal X-ray diffraction study of $[C_{81}H_{66}Fe_2N_{12}O_3]^{4+}.[C_2F_6NO_4S_2]^{-}{}_4.[CH_3CN]_3$. The crystal was coated with paratone oil and mounted on to a cryo-loop glass fiber. X-ray intensity data were collected at 100(2) K on a Bruker APEX2 platform-CCD x-ray diffractometer system (fine focus Mo-radiation, λ = 0.71073 Å, 50KV/30mA power).[8] The CCD detector was placed at a distance of 5.0600 cm from the crystal.

A total of 3600 frames were collected for a sphere of reflections (with scan width of 0.3º in ω, starting ω and 2θ angles of –30º, and φ angles of 0º, 90º, 120º, 180º, 240º, and 270º for every 600 frames, 60 sec/frame exposure time). The frames were integrated using the Bruker SAINT software package[9] and using a narrow-frame integration algorithm. Based on a triclinic crystal system, the integrated frames yielded a total of 109946 reflections at a maximum 2θ angle of 56.564º (0.75 Å resolution), of which 26638 were independent reflections (R_{int} = 0.0396, R_{sig} = 0.0366, redundancy = 4.1, completeness = 99.9%) and 20391 (76.5%) reflections were greater than 2σ(I). The unit cell parameters were, **a** = 14.5840(5) Å, **b** = 18.9278(7) Å, **c** = 19.8975(7) Å, **α** =80.8140(6)**, β** =

82.2801(6)°, γ = 89.9495(6) V = 5371.8(3) Å^3, Z = 2, calculated density D_c = 1.614 g/cm^3. Absorption corrections were applied (absorption coefficient μ = 0.544 mm^{-1}; max/min transmission = 0.984/0.777) to the raw intensity data using the SADABS program.[10]

The Bruker SHELXTL software package[11] (was used for phase determination and structure refinement. The distribution of intensities (E^2-1 = 0.933) and no systematic absent reflections indicated two possible space groups, P-1 and P1. The space group P-1 (#2) was later determined to be correct. Direct methods of phase determination followed by two Fourier cycles of refinement led to an electron density map from which most of the non-hydrogen atoms were identified in the asymmetric unit of the unit cell. With subsequent isotropic refinement, all of the non-hydrogen atoms were identified. There was one cation of $[C_{81}H_{66}Fe_2N_{12}O_3]^{4+}$, four anions of $[C_2F_6NO_4S_2]^-$, and three solvent molecules of CH_3CN present in the asymmetric unit of the unit cell. Three of the four anions of $[C_2F_6NO_4S_2]^-$ were modeled with disorder (disordered site occupancy ratios were 93 % / 7 %, 62 % / 38 %, and 46 % / 44 % / 10 %). The alert level B of the short non-bonding inter halogen contact of F2F...F1L is probably due to the disordered anions.

Atomic coordinates, isotropic and anisotropic displacement parameters of all the non-hydrogen atoms were refined by means of a full matrix least-squares procedure on F^2. The H-atoms were included in the refinement in calculated positions riding on the atoms to which they were attached. The refinement converged at R_1 = 0.0443, wR_2 = 0.1000, with intensity I > 2σ (I). The largest peak/hole in the final difference map was 0.953 / -0.737 e/Å^3.

Table 8.1: Crystal data and structure refinement for mesocate **3.56**.

Empirical formula	$C_{95}H_{75}F_{24}Fe_2N_{19}O_{19}S_8$	
Formula weight	2610.92	
Temperature	100(2) K	
Wavelength	0.71073 Å	
Crystal system	Triclinic	
Space group	P -1	
Unit cell dimensions	a = 14.5840(5) Å	α= 80.8140(6)°
	b = 18.9278(7) Å	β= 82.2801(6)°
	c = 19.8975(7) Å	γ = 89.9495(6)°
Volume	5371.8(3) $Å^3$	
Z	2	
Density (calculated)	1.614 Mg/m^3	
Absorption coefficient	0.544 mm^{-1}	
F(000)	2652	
Crystal size	0.488 x 0.136 x 0.030 mm^3	
Theta range for data collection	1.384 to 28.282°.	
Index ranges	-19<=h<=19, -25<=k<=25, -26<=l<=26	
Reflections collected	109946	
Independent reflections	26638 [R(int) = 0.0396]	
Completeness to θ = 25.242°	100.0 %	
Absorption correction	Semi-empirical from equivalents	
Refinement method	Full-matrix least-squares on F^2	
Data / restraints / parameters	26638 / 1777 / 2028	
Goodness-of-fit on F^2	1.017	
Final R indices [I>2σ(I)]	R_1 = 0.0443, wR_2 = 0.1000	
R indices (all data)	R_1 = 0.0662, wR_2 = 0.1099	
Extinction coefficient	n/a	
Largest diff. peak and hole	0.953 and -0.737 $e.Å^{-3}$	

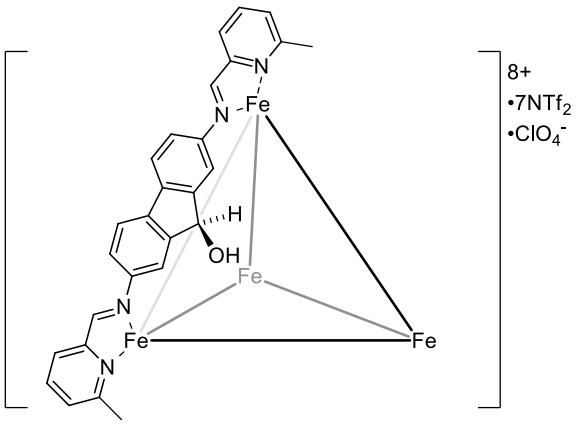

M$_4$L$_6$ Prism (**7.57**):

Ligand **1.11** (200 mg, 0.94 mmol), 6-methylpyridine-2-carboxaldehyde (228.29 mg, 1.88 mmol), $Fe(NTf_2)_2$ (412.82 mg, 0.63 mmol) and $NaClO_4$ (24.99 mg, 0.20 mmol) were combined in MeCN (15 mL) in a 25 mL round-bottom flask. The solution was heated at 77 °C for 72 h. The red solid was sonicated with 20 mL of 3:1 Et_2O/MeOH solution and collected via vacuum filtration. After drying, the product was isolated as a red solid (570 mg, 79 % yield). ^1H NMR (400 MHz; CD_3CN) : δ 198.17 (s), 194.84 (s), 186.44 (s), 185.28 (s), 72.77 (s), 62.18 (s), 60.26 (s), 57.38 (s), 55.50 (s), 55.41 (s), 54.81 (s), 53.05 (s), 36.65 (s), 27.89 (s), 23.98 (s), 19.40 (s), 17.15 (s), 11.32 (s), 9.17 (s) (s), 8.99 (s), 8.55 (s), 7.96 (s), 3.47 (s), 3.02 (s), 2.60 (s), 1.14 (s), -0.18 (s), -1.54 (s), -3.55 (s), -7.10 (s), -7.57 (s), -7.72 (s), -21.24 (s), -32.07 (s), -33.02 (s), -40.82 (s), -47.73 (s), -88.59 (s), -106.85 (s), -112.94 (s), -324.92 (s).

M_4L_6 Prism **7.57** (CCDC #1848254)

100 mg of cage **7.57** was dissolved in a minimal amount of acetonitrile and 0.5 mL of the resulting solution was pipetted into an NMR tube. The tube was placed into an 8 oz. glass jar containing 25 mL of diethyl ether. The jar was capped tightly, and the sample was allowed to sit for 5 days, until solvent diffusion was complete and the solution inside the NMR tube was colorless. Red prisms and needles were both observed within the NMR tube.

A dark red prism fragment (0.150 x 0.125 x 0.125 mm^3) was used for the single crystal X-ray diffraction study of $[C_{162}H_{132}Fe_4N_{24}O_6]^{8+}.[C_2F_6NO_4S_2]^-_7.[ClO_4]^-$. The crystal was coated with paratone oil and mounted on to a cryo-loop glass fiber. X-ray intensity data were collected at 150(2) K on a Bruker Rotating Anode generator with APEX2

platform-CCD X-ray diffractometer system (Mo-radiation, λ = 0.71073 Å, 50KV/24mA rotating anode power).[8] The CCD detector was placed at a distance of 7.0000 cm from the crystal.

A total of 2188 frames were collected for a sphere of reflections (with scan width of 0.5° in ω and ϕ, for ω-scan starting ω angle at -15.19°, starting 2θ angle at 11.88°, ϕ angles of 0°, 51°, 153°, and 225° for every 332 frames, for one ϕ scan starting ϕ angle at 266.77°, starting 2θ angle of 11.88°, ω angle of -35.92° for every 760 frames, 60 sec/frame exposure time). The frames were integrated using the Bruker SAINT software package[9] and using a narrow-frame integration algorithm. Based on a monoclinic crystal system, the integrated frames yielded a total of 513139 reflections at a maximum 2θ angle of 33.586° (1.23 Å resolution), of which 49262 were independent reflections (R_{int} = 0.0559, R_{sig} = 0.0332, redundancy = 10.4, completeness = 100 %) and 34050 (69.1 %) reflections were greater than 2σ(I). The unit cell parameters were, **a** = 45.686(2) Å, **b** = 31.2027(14) Å, **c** = 61.452(3) Å, **β** = 91.4112(10)°**,** V = 87576(7) Å^3, Z = 16, calculated density D_c = 1.128 g/cm^3 [Note that the calculated density is based on the Empirical Formula and unit cell volume used and it's not the true density of the crystal because of unresolved anions and solvents that are missing]. Absorption corrections were applied (absorption coefficient μ = 0.395 mm^{-1}; max/min transmission = 0.952/0.943) to the raw intensity data using the SADABS program.[10]

The Bruker SHELXTL software package[11] was used for phase determination and structure refinement. The distribution of intensities (E^2-1 = 0.934) and systematic absent reflections indicated one possible space group, P2(1)/c. The space group P2(1)/c (#14) was

later determined to be correct. Direct methods of phase determination followed by two Fourier cycles of refinement led to an electron density map from which most of the non-hydrogen atoms were identified in the asymmetric unit of the unit cell. With subsequent isotropic refinement, all 4 cations, 21 anions and 15 molecules of ether were identified. There were four cations of $[C_{162}H_{132}Fe_4N_{24}O_6]^{8+}$, 16 anions of $[C_2F_6NO_4S_2]^-$, 5 anions of $[ClO_4]^-$ and 15 solvent molecules of $C_4H_{10}O$ present in the asymmetric unit of the unit cell. There are a total of 11 anions and possible solvents of ether/acetonitrile that can't be identified. SQUEEZE for removing unresolved solvent disorder could not be applied because of the missing anions. All the alert levels A through G for the checkcif are due to the poor resolution data, poor crystal quality, and unresolved electron density peaks in the final difference map. The connectivity of all the four cations are clearly resolved.

Atomic coordinates, isotropic and anisotropic displacement parameters of all the non-hydrogen atoms were refined by means of a full matrix least-squares procedure on F^2. The H-atoms were included in the refinement in calculated positions riding on the atoms to which they were attached. The refinement converged at $R_1 = 0.2213$, $wR_2 = 0.5334$, with intensity $I>2\sigma$ (I). The largest peak/hole in the final difference map was 2.584/-0.913 e/Å^3. The high difference electron density peak/hole is mainly due to the unresolved anions and solvents of crystallization.

Table 8.2: Crystal data and structure refinement for **7.57**.

Empirical formula	$C_{175.56}H_{153.43}Cl_{1.22}F_{14.96}Fe_4N_{26.49}O_{23.22}S_{4.99}$
Formula weight	3716.73
Temperature	150(2) K
Wavelength	0.71073 Å
Crystal system	Monoclinic

Space group	P2(1)/c	
Unit cell dimensions	a = 45.686(2) Å	α = 90°.
	b = 31.2027(14) Å	β = 91.4112(10)°.
	c = 61.452(3) Å	γ = 90°.
Volume	87576(7) $Å^3$	
Z	16	
Density (calculated)	1.128 Mg/m^3	
Absorption coefficient	0.395 mm^{-1}	
F(000)	30676	
Crystal size	0.150 x 0.125 x 0.125 mm^3	
Theta range for data collection	0.663 to 16.793°.	
Index ranges	-37<=*h*<=36, -25<=*k*<=25, -49<=*l*<=49	
Reflections collected	513139	
Independent reflections	49262 [*R*(int) = 0.0559]	
Completeness to theta = 25.242°	31.1 %	
Absorption correction	Semi-empirical from equivalents	
Refinement method	Full-matrix least-squares on F^2	
Data / restraints / parameters	49262 / 17672 / 10141	
Goodness-of-fit on F^2	2.758	
Final R indices [I>2sigma(I)]	R_1 = 0.2213, wR_2 = 0.5334	
R indices (all data)	R_1 = 0.2663, wR_2 = 0.5687	
Extinction coefficient	n/a	
Largest diff. peak and hole	2.584 and -0.913 $e.Å^{-3}$	

8.8 Selected Spectra from Chapter 2

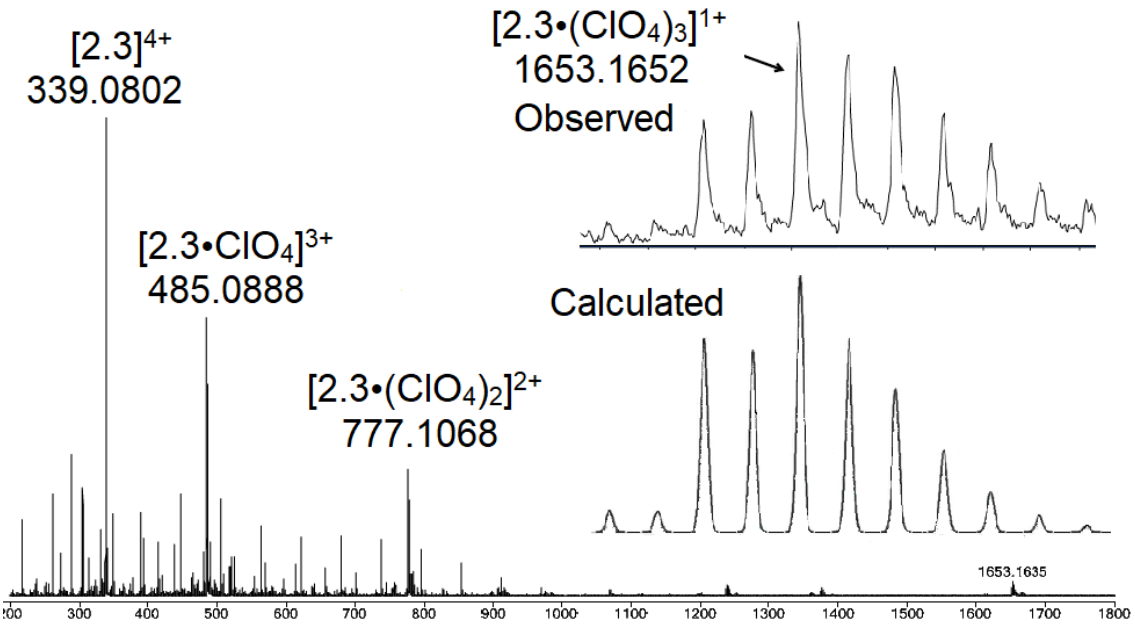

Figure 8.1. ESI-MS of suberenone cage **2.3** (CH_3CN).

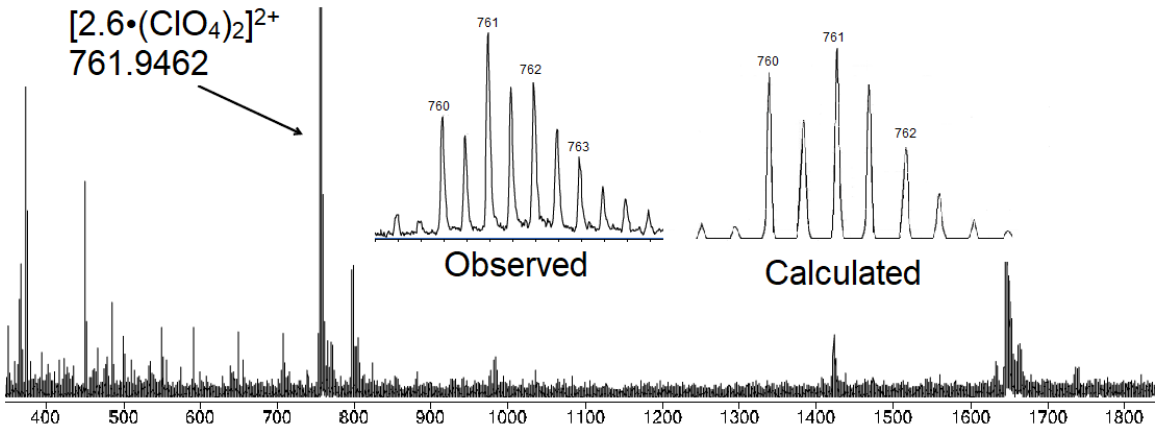

Figure 8.2. ESI-MS of xanthone cage **2.6** (CH_3CN).

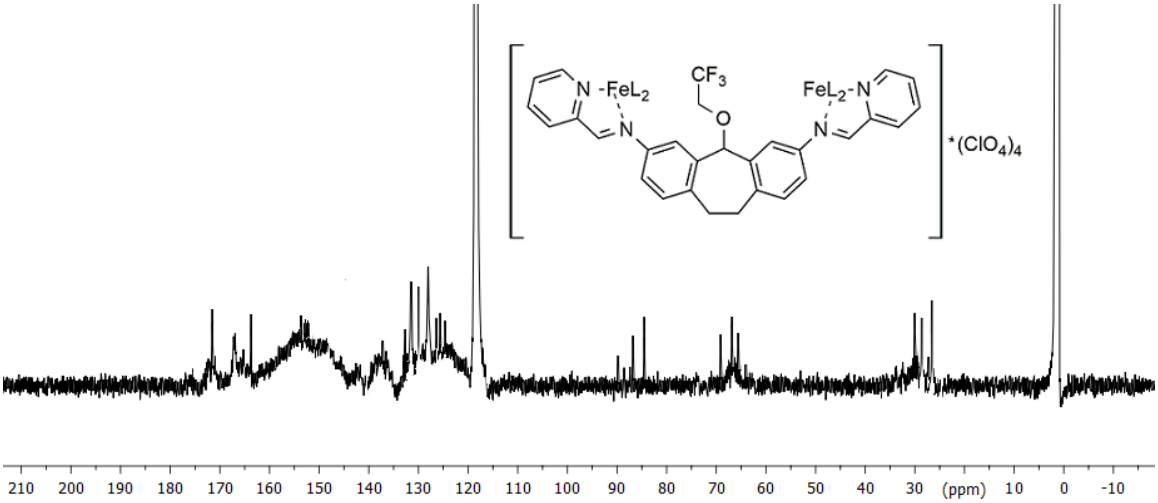

Figure 8.3 .^{13}C NMR spectrum of trifluoroethylether cage **2.8** (CD_3CN, 150 MHz, 298 K).

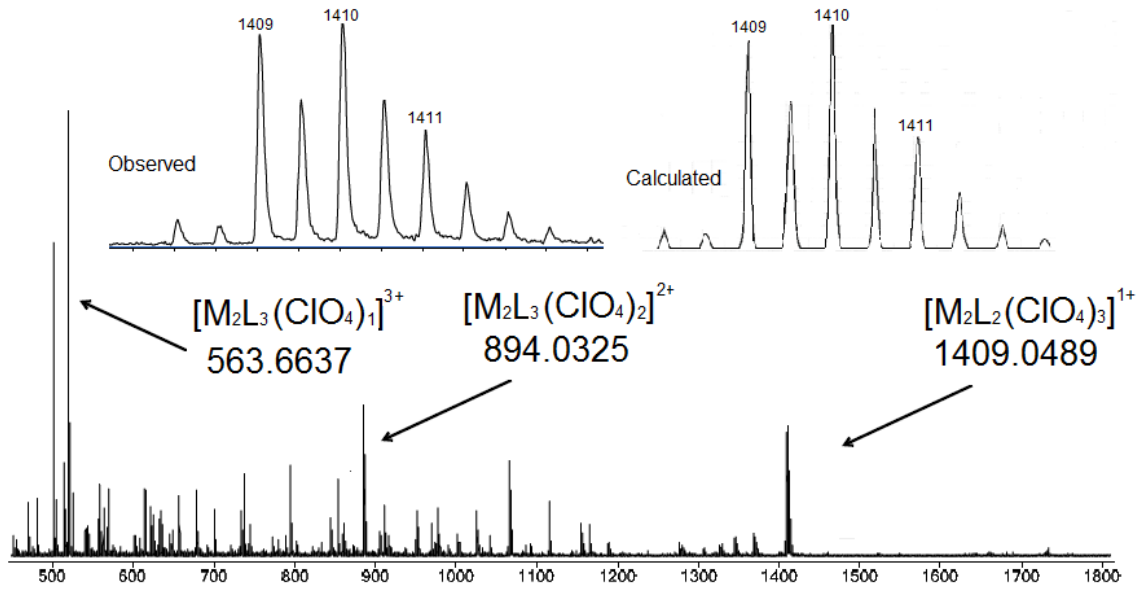

Figure 8.4 .ESI-MS of cage **2.8** (CH_3CN).

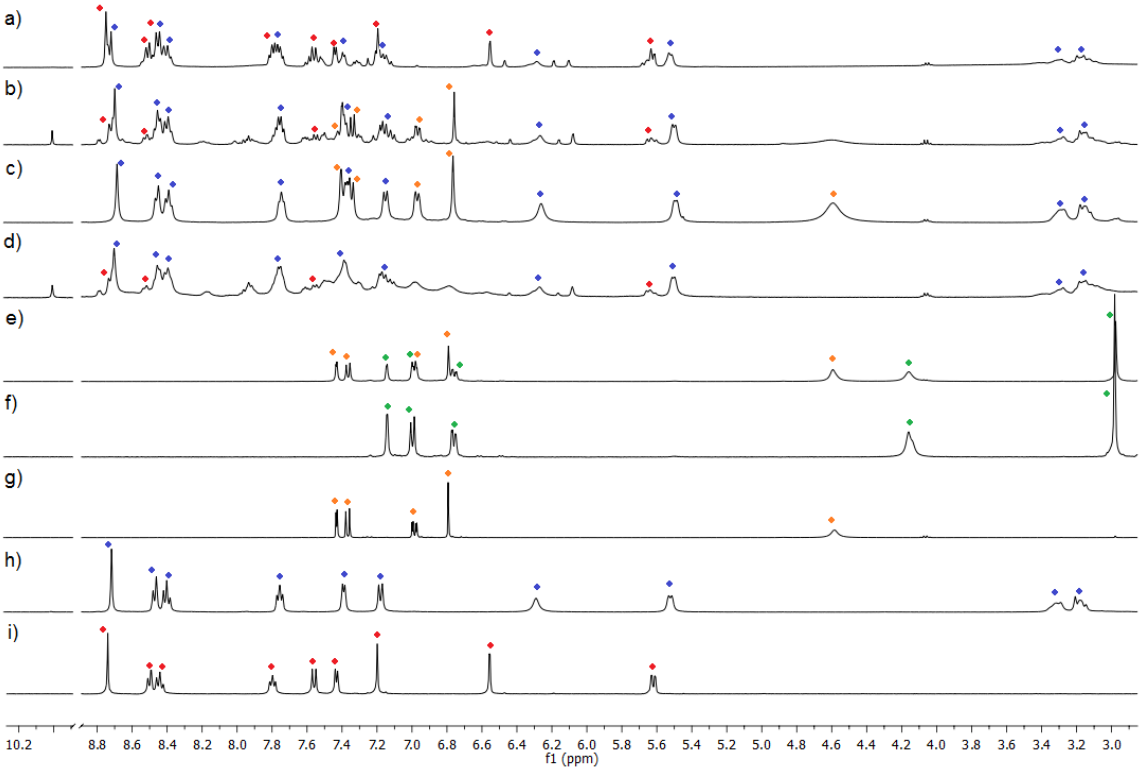

Figure 8.5. ^{1}H NMR spectra of mixing experiment between ligands **1.5** and **2.2** (CD_3CN, 400 MHz, 298K). i) cage **2.3** (red), h) cage **2.3** (blue), g) dianiline **2.2** (orange), f) dianiline **1.5** (green), e) dianiline mixture, d) mixture after first addition of 2-formylpyridine and iron prior to heating, c) mixture with first addition after 8 h at 80 °C, b) mixture after second addition of 2-formylpyridine and iron with no heat, a) mixture after second addition and 8 h heat at 80 °C.

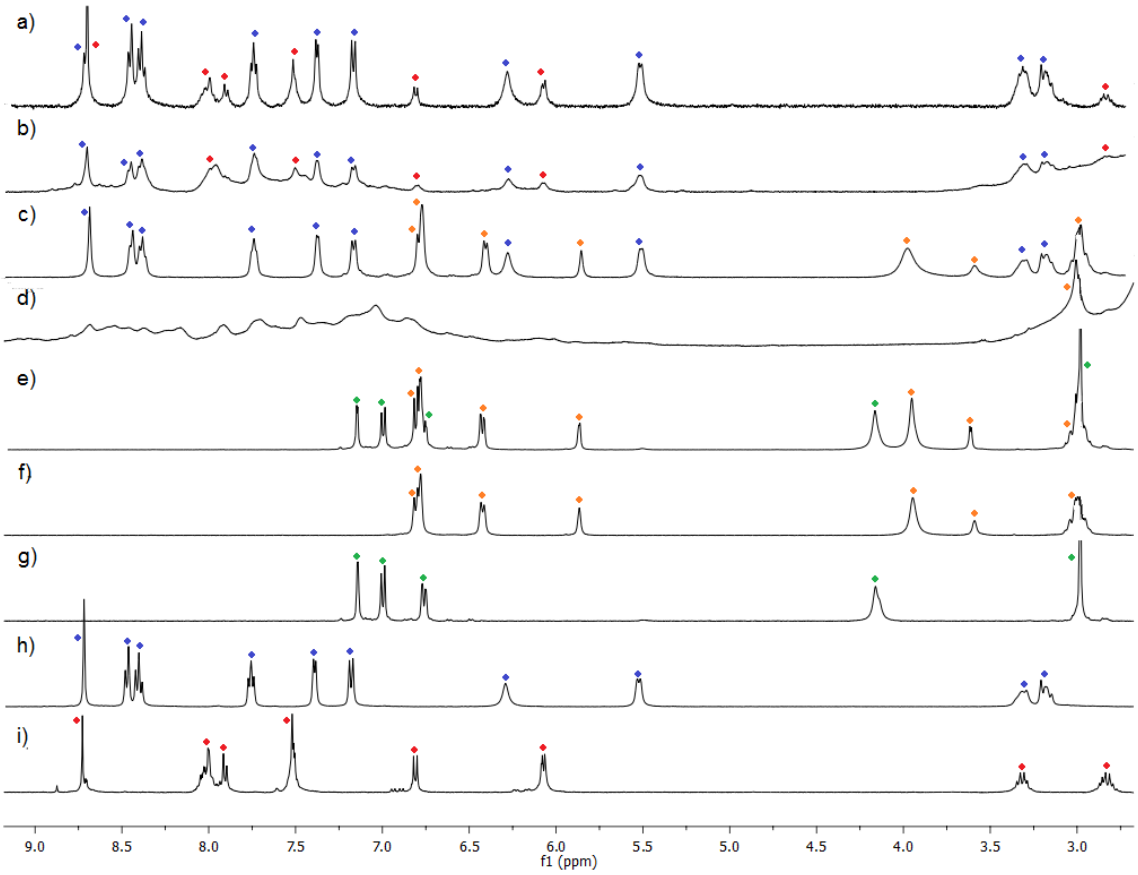

Figure 8.6. ^{1}H NMR spectra of mixing experiment between suberone ligand **1.5** and suberol **1.6** (CD_3CN, 400 MHz, 298K). i) cage **1.8** (red), h) suberone cage **1.7** (blue), g) **1.5** (green), f) **1.6** (orange), e) dianiline mixture, d) mixture after first addition of 2-formylpyridine and iron prior to heating, c) mixture of first addition after 8 h at 80 °C, b) mixture after second addition of 2-formylpyridine and iron, a) mixture after second addition and 8 h heat at 80 °C.

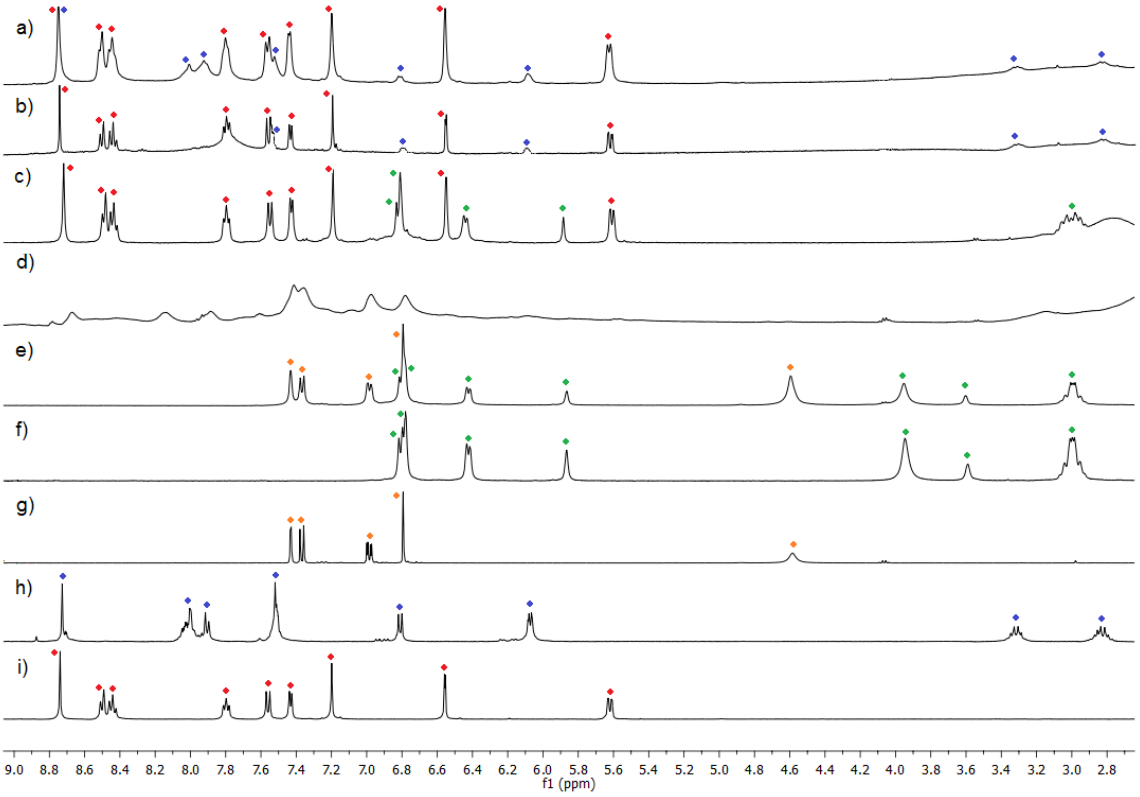

Figure 8.7. ^{1}H NMR spectra of mixing experiment between suberol and suberenone ligands **1.6** and **2.2** (CD_3CN, 400 MHz, 298K). i) cage **2.3** (red), h) cage **1.8** (blue), g) **2.2** (orange), f) **1.6** (green), e) dianiline mixture, d) mixture after first addition of 2-formylpyridine and iron prior to heating, c) mixture of first addition after 8 h at 80 °C, b) mixture after second addition of 2-formylpyridine, a) mixture after second addition and 8 h heat at 80 °C.

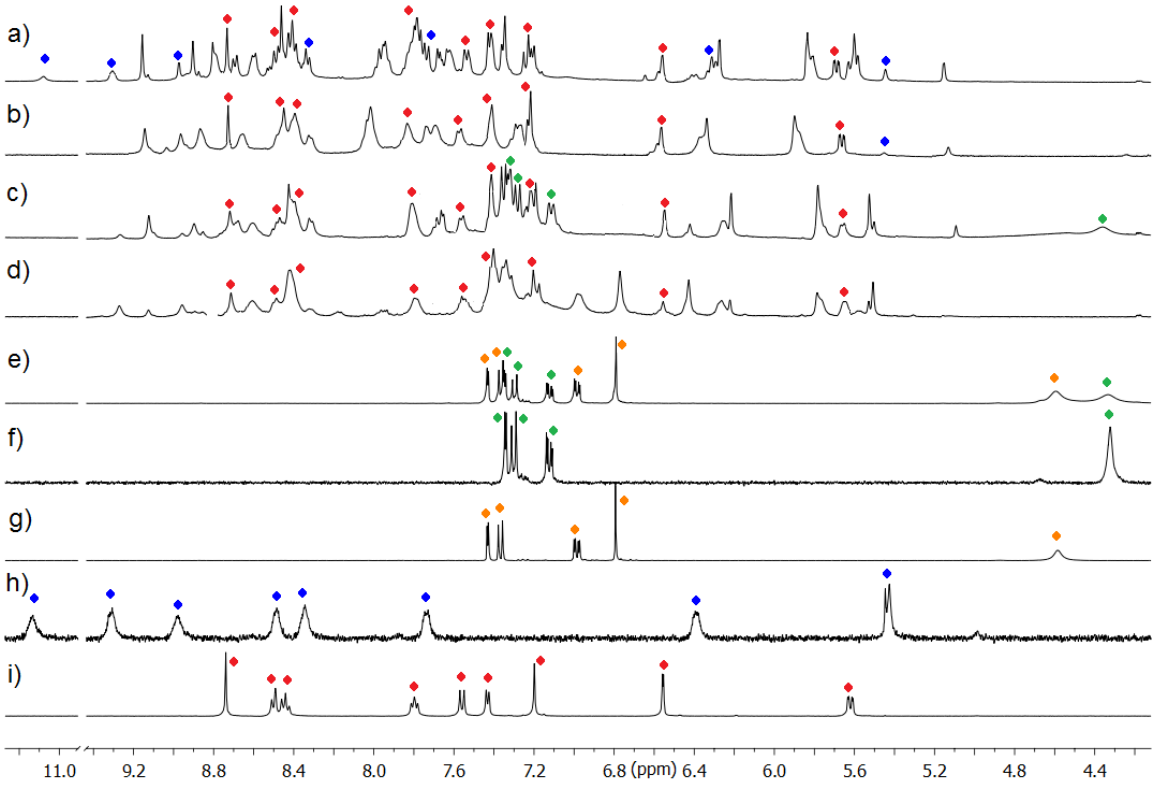

Figure 8.8. 1H NMR spectra of mixing experiment between suberenone and xanthone ligands **2.2** and **2.5** (CD_3CN, 400 MHz, 298K). i) cage **2.3** (red), h) cage **2.6** (blue), g) **2.2** (orange), f) **2.5** (green), e) dianiline mixture, d) mixture after first addition of 2-formylpyridine and iron prior to heating, c) mixture of first addition after 8 h at 80 °C, b) mixture after second addition of 2-formylpyridine and iron with no heat, a) mixture after second addition and 8 h heat at 80 °C.

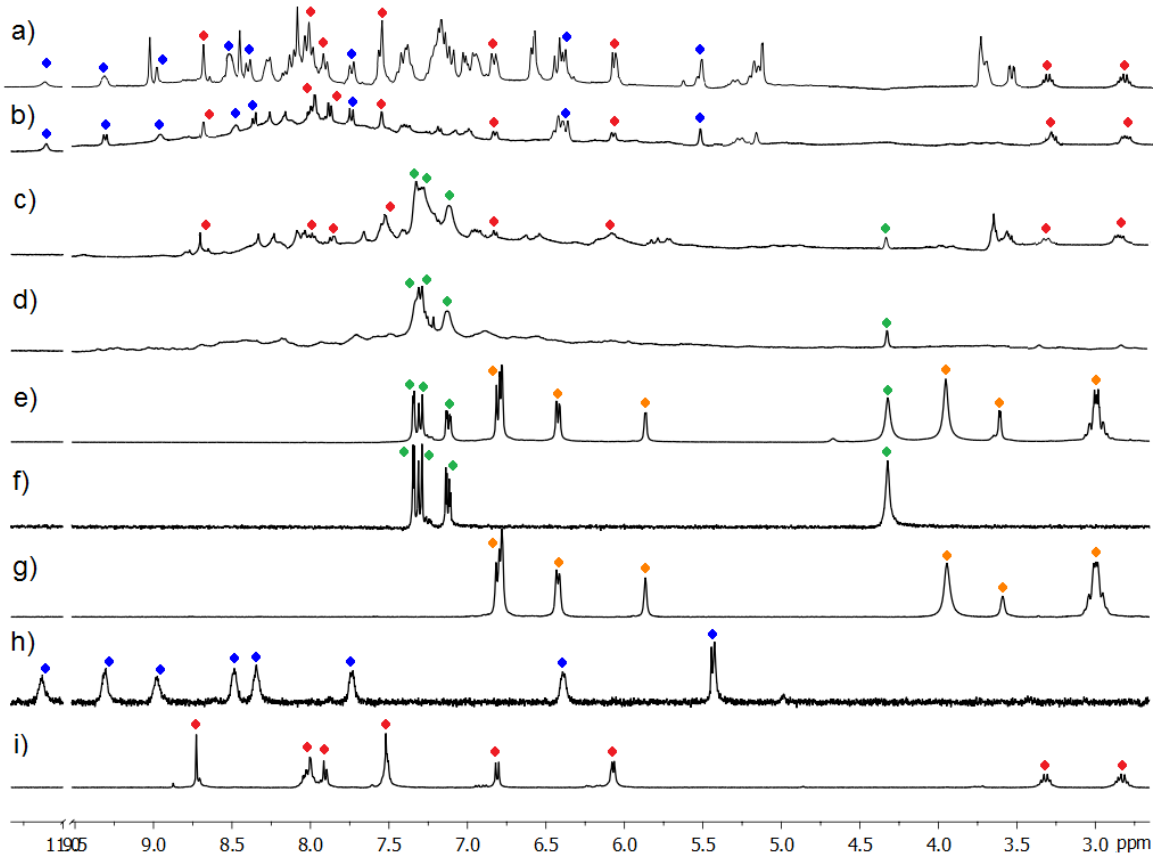

Figure 8.9. ^{1}H NMR spectra of mixing between **1.6** and **2.5** (CD_3CN, 400 MHz, 298K). i) **1.8** (red), h) **2.6** (blue), g) **1.6** (orange), f) **2.5** (green), e) dianiline mixture, d) mixture of first addition of PyCHO and iron prior to heating, c) mixture of first addition after 8 h at 80 °C, b) mixture after second addition of PyCHO and iron with no heat, a) mixture after second addition and 8 h at 80 °C.

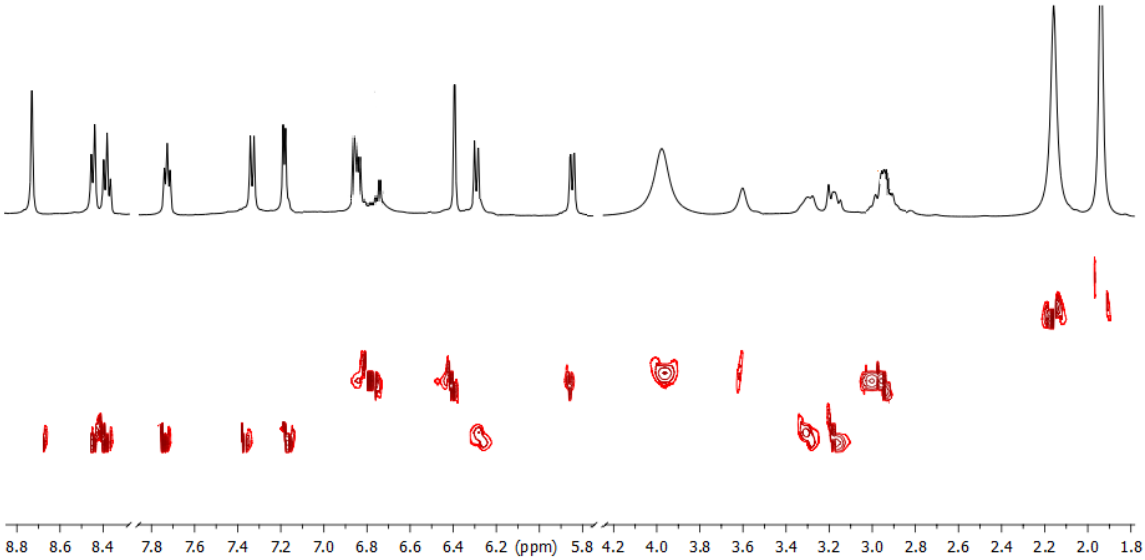

Figure 8.10. ^{1}H DOSY NMR of mixing between **1.5** and **1.6** after 1 addition of $Fe(ClO_4)_2$ and PyCHO and 8 h at 80°C (CD_3CN, 600 MHz, 298 K, Δ = 100 ms, δ = 2.6 μs, Diffusion Coefficient = 7.21 x10^{-10} m^2/s for cage **1.7** vs. 1.91 x10^{-9} m^2/s for uncomplexed **1.6** vs. 4.16 x10^{-9} m^2/s for solvent).

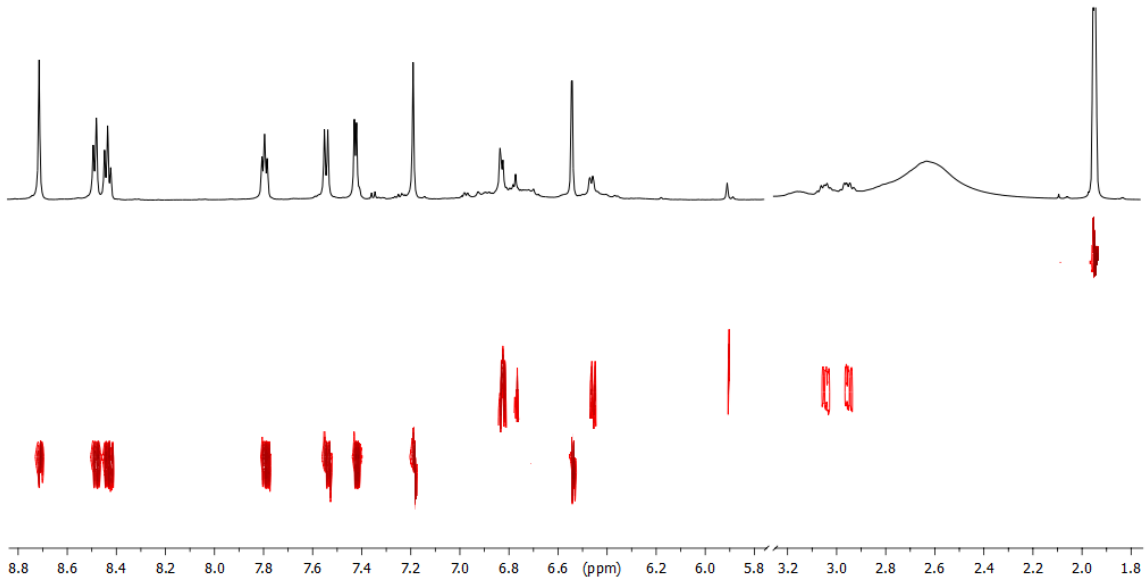

Figure 8.11. ^{1}H-DOSY NMR of mixing between **1.6** and **2.2** after 1 addition of $Fe(ClO_4)_2$ and 2-formylpyridine and 8 h heat at 80°C (CD_3CN, 600 MHz, 298 K, Δ = 100 ms, δ = 2.6 μs, Diffusion Coefficient = 9.23 x10^{-10} m^2/s for cage **2.3** vs. 1.66 x10^{-9} m^2/s for **1.6** vs. 5.57 x10^{-9} m^2/s for solvent).

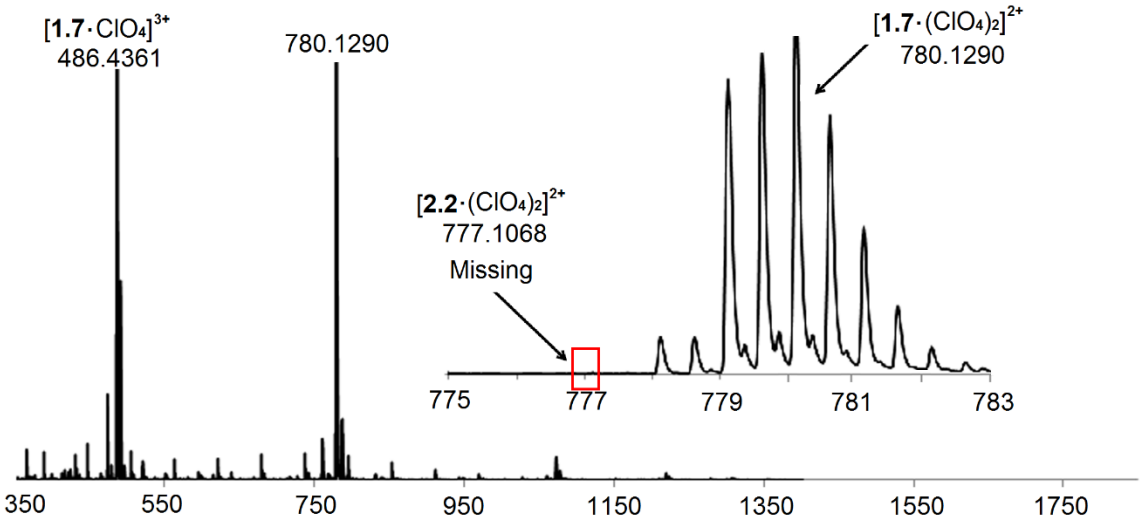

Figure 8.12. ESI-MS of mixing experiment between **1.5** and **2.2** after 1 addition of $Fe(ClO_4)_2$ and 2-formylpyridine and 8 h heat at 80°C. Only cage **1.7** and ligand **2.2** were detected.

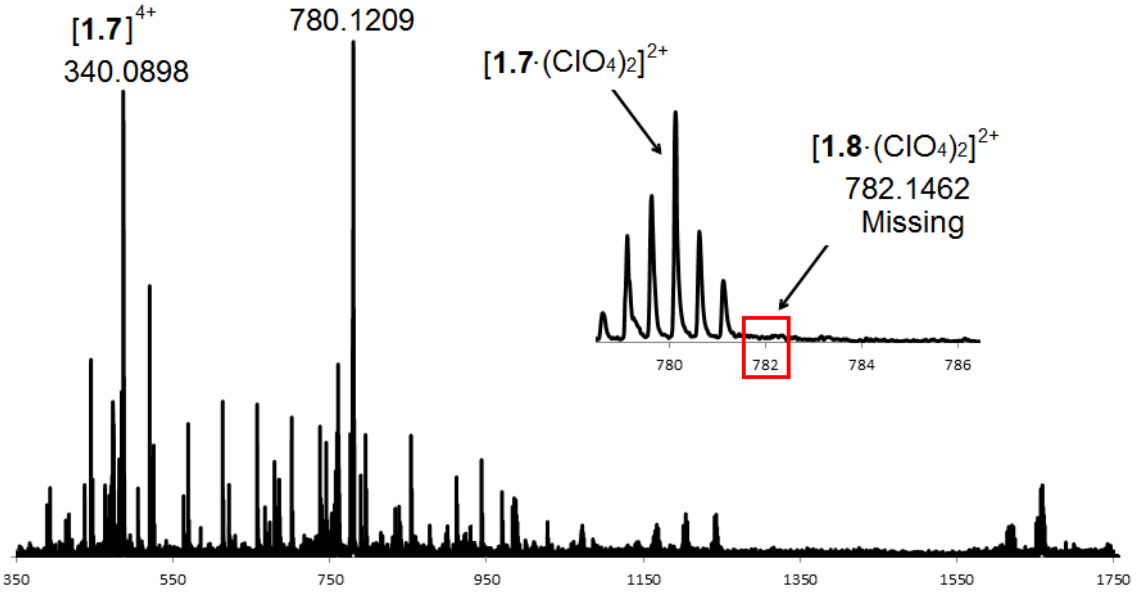

Figure 8.13. ESI-MS of mixing experiment between **1.5** and **1.6** after 1 addition of $Fe(ClO_4)_2$ and 2-formylpyridine and 8h heat at 80°C. Only suberone cage **1.7** and suberol ligand 1.6 are present.

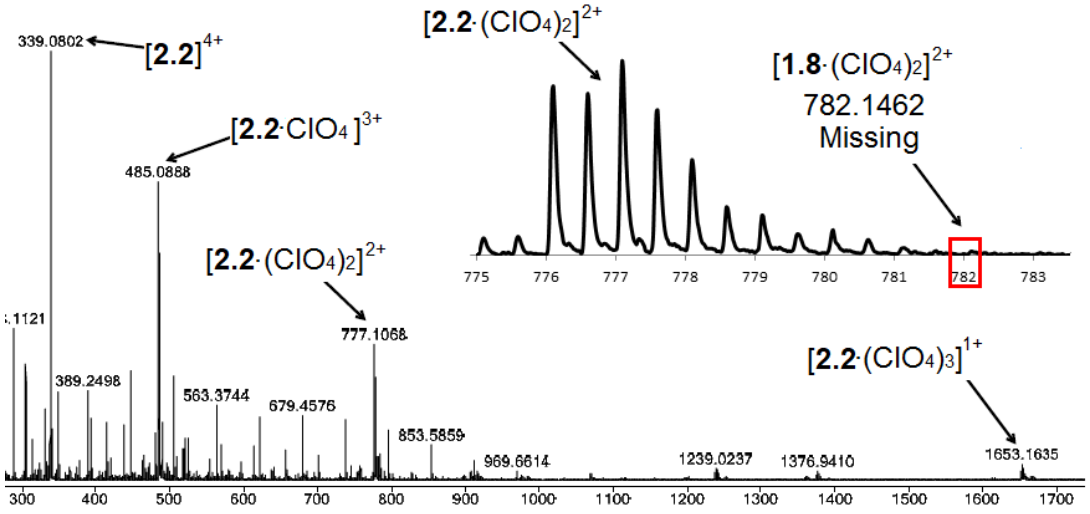

Figure 8.14. ESI-MS of mixing experiment between **1.6** and **2.2** after 1 addition of $Fe(ClO_4)_2$ and 2-formylpyridine and 8 h heat at 80°C. Only cage **2.3** and ligand **1.6** were detected.

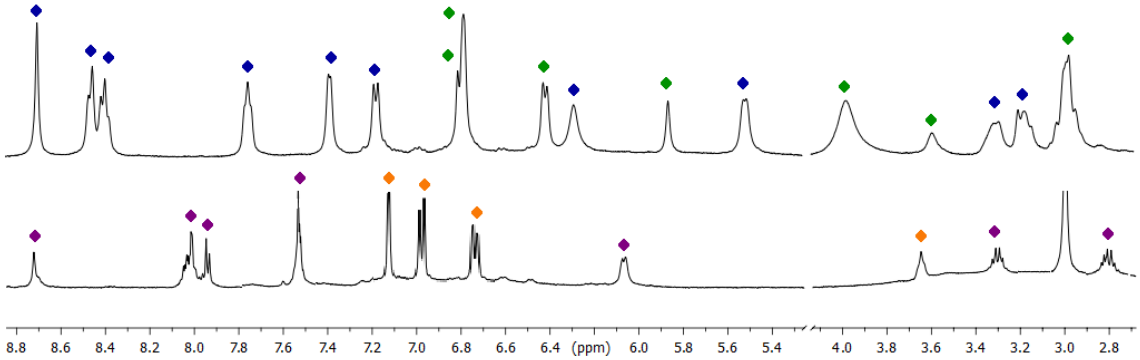

Figure 8.15. ^{1}H NMR spectra of displacement between suberol cage **1.8** and suberone dianiline **1.5** (CD_3CN, 400 MHz, 298K). Top: cage **1.7** and displaced dianiline **1.6** after heating at 80 °C for 8 h. Bottom: cage **1.8** and dianiline **1.5** prior to heating. The reverse experiment (cage **1.7** ligand displacement by dianiline **1.6**) showed no change in the spectrum even after heating for 24 h.

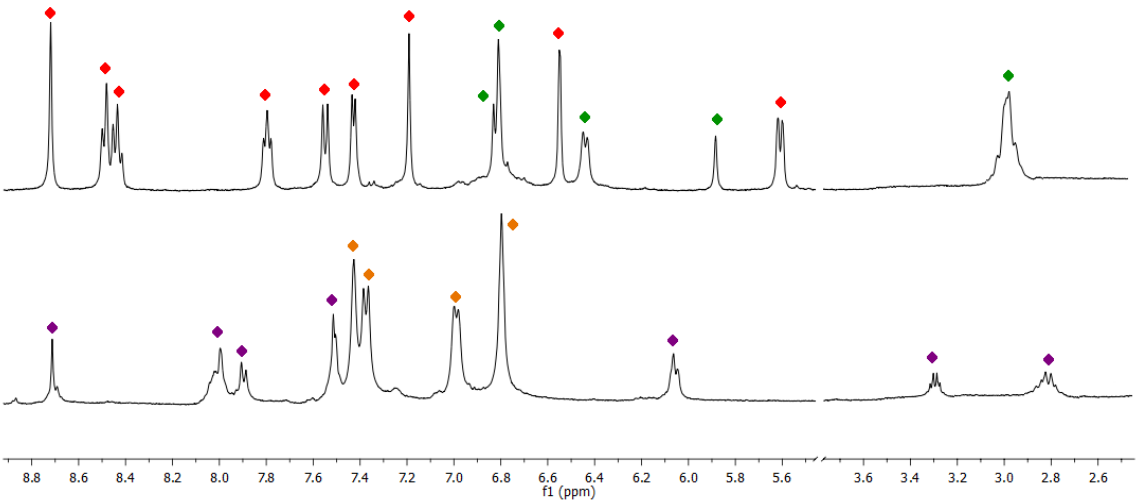

Figure 8.16. ^{1}H NMR spectra of anhydrous displacement experiment between cage **1.8** and dianiline **2.2** (CD_3CN, 400 MHz, 298K). Top: cage **2.3** and displaced dianiline **1.6** after heating at 80 °C for 8 h. Bottom: cage **1.8** and dianiline **2.2** prior to heating. The reverse experiment (cage **2.3** displacement by dianiline **1.6**) showed no change in the spectrum even after heating for 24 h.

8.9 Selected Spectra from Chapter 3

Table 8.3. Calculated values for kinetic 2 h formation experiments.

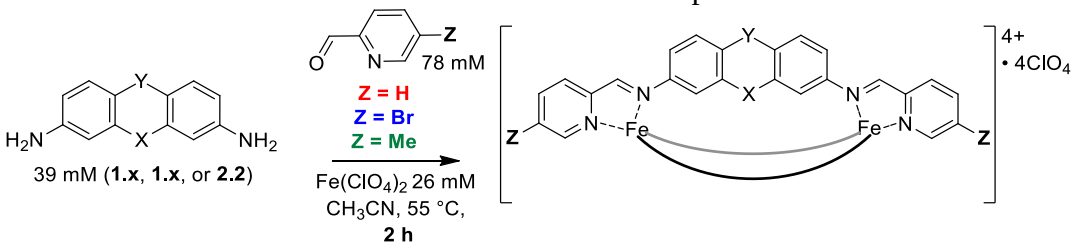

Cage	% Cage Formed at 2h	[Cage] (mM) at 2 h	% Unreacted PyCHO at 2h	% Intermediates at 2 h	Time to Completion
1.7•H_6	65.1 ± 0.5	8.5 ± 0.03	29.1 ± 0.5	5.8	3 h
3.1•Br_6	92.1 ± 0.5	11.9 ± 0.04	3.51 ± 0.5	4.39	2.5 h
3.4•Me_6	43.4 ± 0.5	5.7 ± 0.03	15.5 ± 0.5	41.1	5 h
1.8•H_6	41.5 ± 0.5	5.4 ± 0.07	39.8 ± 0.5	18.7	5 h
3.2•Br_6	66.7 ± 0.5	8.3 ± 0.05	15.6 ± 0.5	17.7	3 h
3.5•Me_6	21.5 ± 0.5	2.8 ± 0.03	27.7 ± 0.5	50.8	9 h
2.3•H_6	62.1 ± 0.5	8.2 ± 0.04	32.5 ± 0.5	5.4	3 h
3.3•Br_6	89.1 ± 0.5	11.6 ± 0.03	6.5 ± 0.5	4.4	2.5 h
3.6•Me_6	36.7 ± 0.5	4.8 ± 0.04	19.8 ± 0.5	43.5	5.5 h

Table 8.4. Calculated values for kinetic 1 h formation experiments.

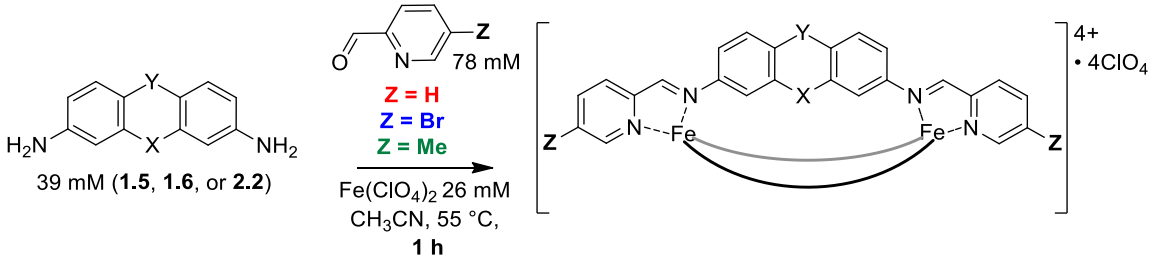

Cage	% Cage Formed at 1 h	[Cage] (mM) at 1 h	% Unreacted PyCHO at 1 h	% Intermediates at 1 h
1.7•H_6	38.2 ± 0.5	4.3 ± 0.04	49.1 ± 0.5	12.7
3.1•Br_6	54.6 ± 0.5	6.3 ± 0.05	20.3 ± 0.5	25.1
3.4•Me_6	22.8 ± 0.5	2.9 ± 0.04	30.2 ± 0.6	47
1.8•H_6	24.5 ± 0.5	3.2 ± 0.08	53.1 ± 0.5	22.4
3.2•Br_6	32.1 ± 0.6	4.2 ± 0.08	37.3 ± 0.6	30.6
3.5•Me_6	-	--	62.1 ± 0.5	-
2.3•H_6	30.2 ± 0.5	3.9 ± 0.05	57.3 ± 0.5	12.5
3.3•Br_6	45.8 ± 0.5	5.9 ± 0.04	26.1 ± 0.5	28.1
3.6•Me_6	17.5 ± 0.5	2.3 ± 0.05	31.8 ± 0.7	50.7

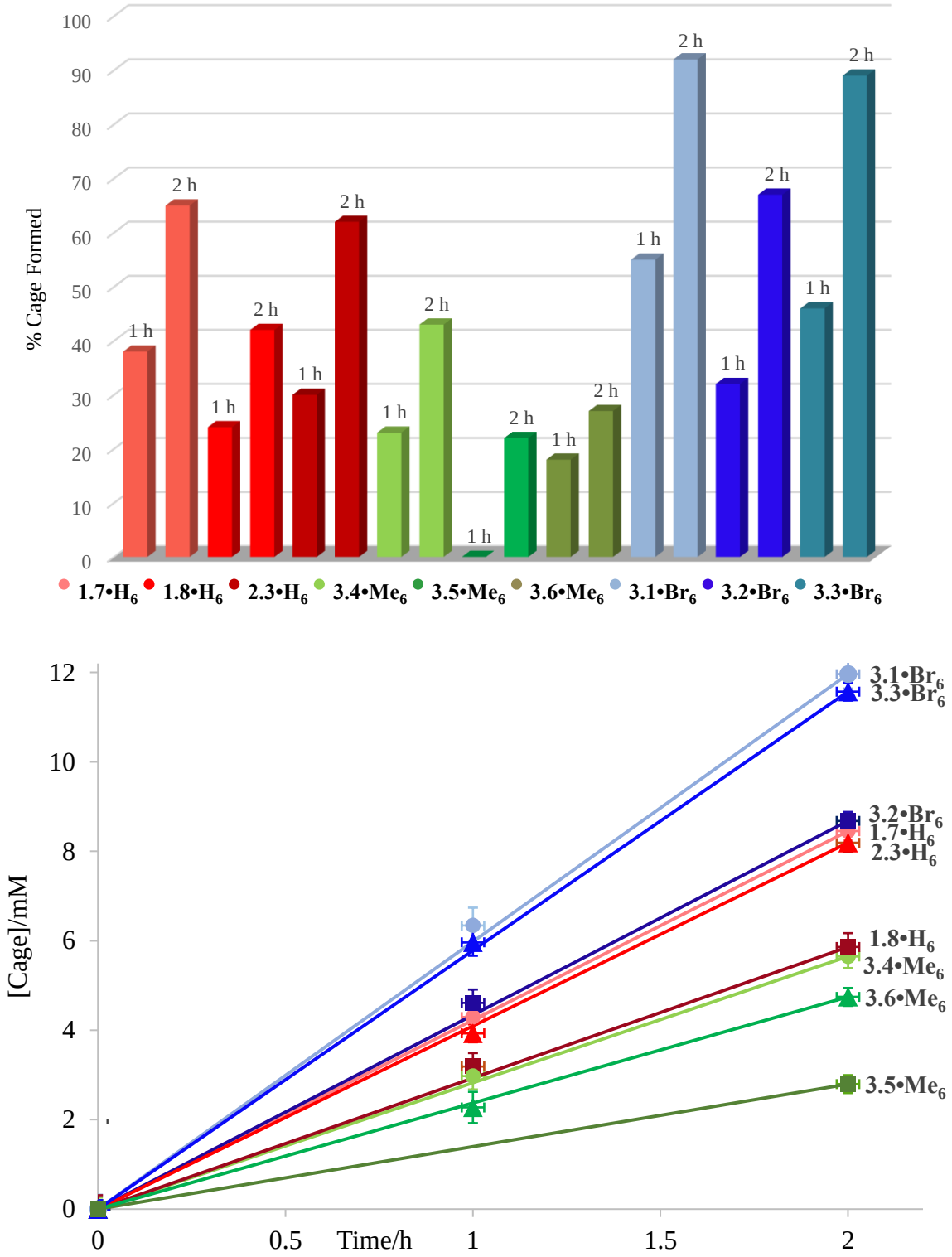

Figure 8.17. Plotted summary of 2 h and 1 h kinetic formation experiments (top) and comparison of linearity between 1 h and 2 h concentrations of cage product (bottom).

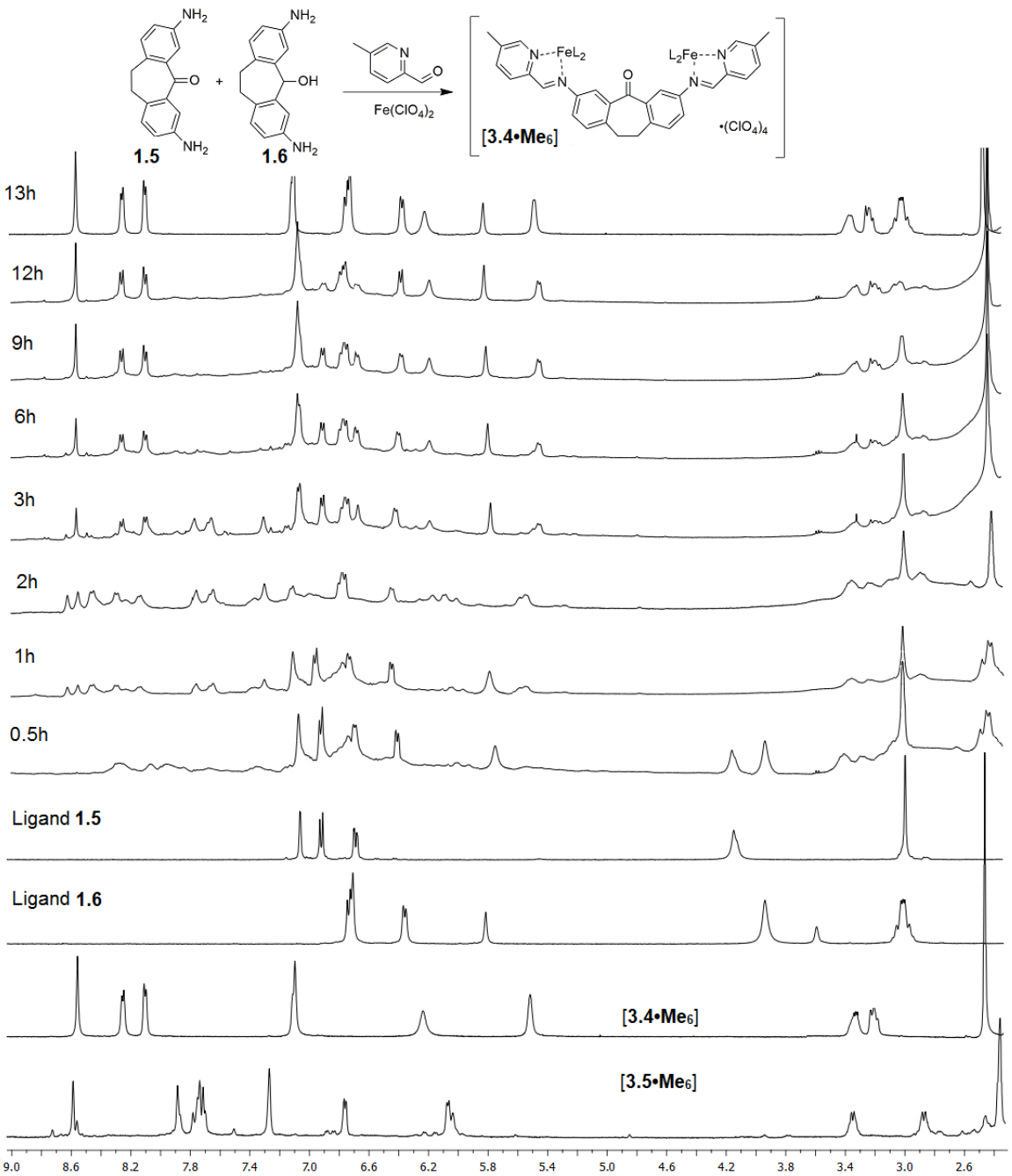

Figure 8.18. ^{1}H NMR spectra of products formed upon mixing ligands **1.5** and **1.6**, and 5-MePyCHO with $Fe(ClO_4)_2$ in an NMR tube at 55 °C over time (CD_3CN, 400 MHz, 298 K).

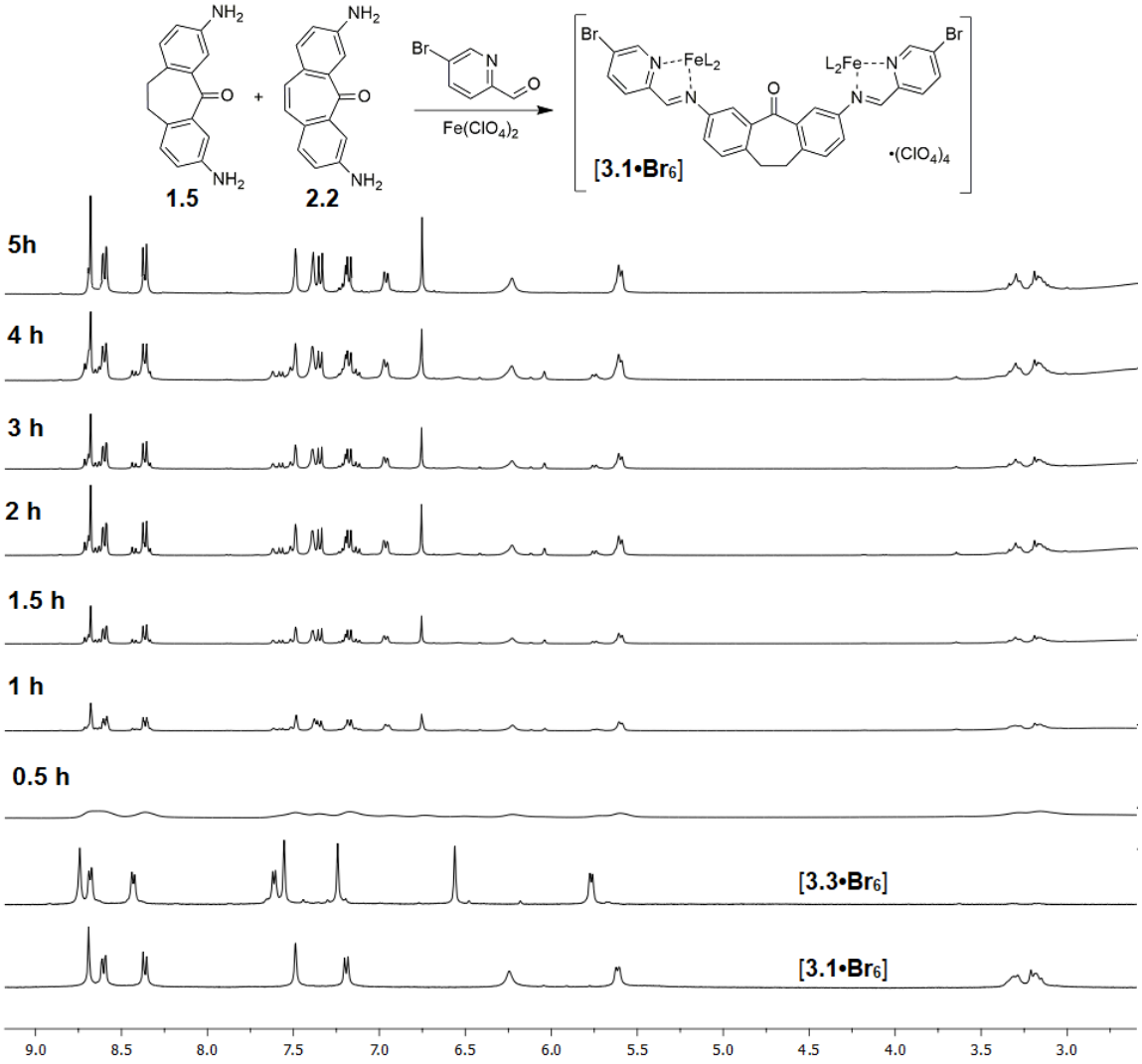

Figure 8.19. ^{1}H NMR spectra of products formed upon mixing ligands **1.5** and **2.2**, and 5-BrPyCHO with $Fe(ClO_4)_2$ in an NMR tube at 55 °C over time (CD_3CN, 400 MHz, 298 K).

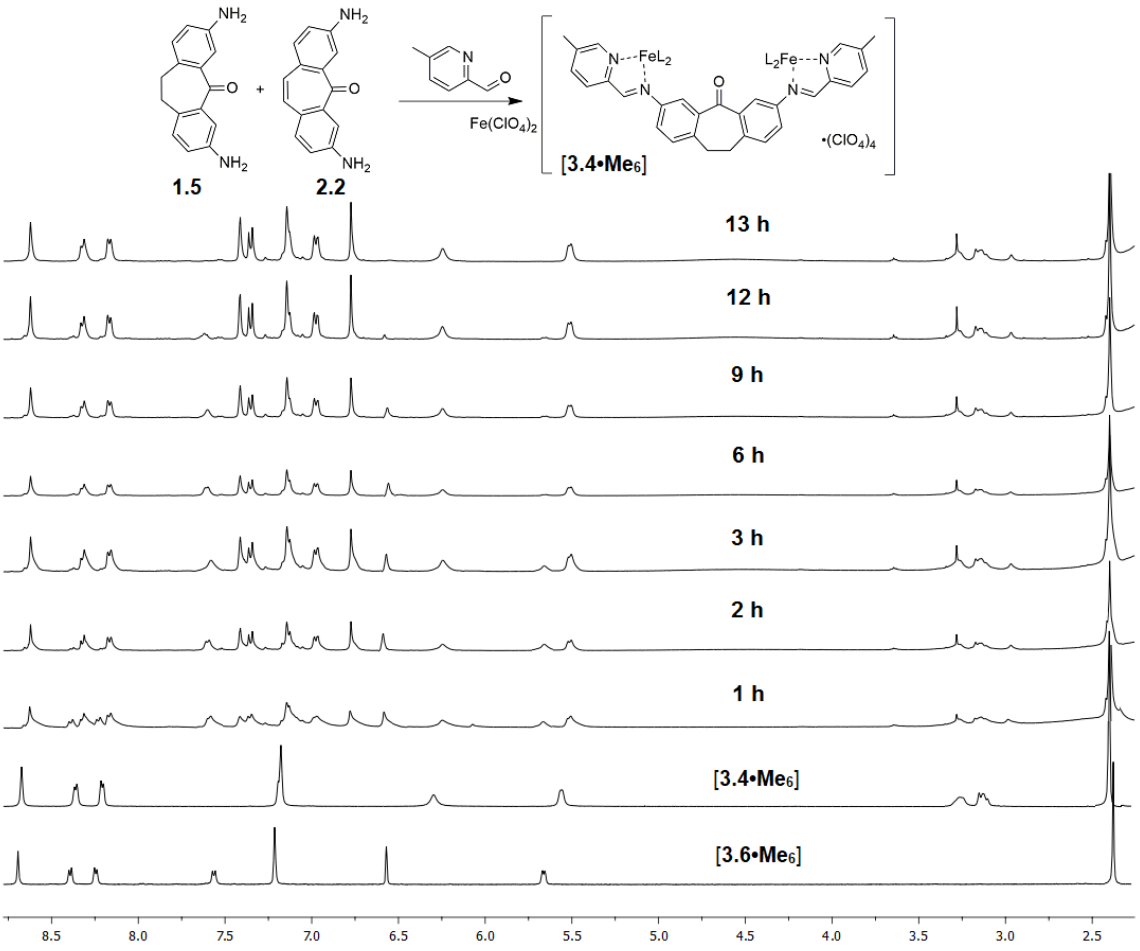

Figure 8.20. ^{1}H NMR spectra of products formed upon mixing ligands **1.5** and **2.2**, and 5-MePyCHO with $Fe(ClO_4)_2$ in an NMR tube at 55 °C over time (CD_3CN, 400 MHz, 298 K).

Table 8.5. Results of timed and standardized self-sorting experiments.

Cores	Aldehyde	Sorting Completion	% Favored Cage at 2 h	% Less Favored Cage at 2 h	% Unreacted PyCHO at 2 h	% Intermediates at 2h
1.5+1.6	**PyCHO**	8 h	30.7 ± 0.5 **1.7**•H_6	4.5 ± 0.5 **1.8**•H_6	22 ± 0.5	42
1.5+2.2	**PyCHO**	8 h	29.2 ± 0.5 **1.7**•H_6	6.4 ± 0.5 **2.3**•H_6	5.1 ± 0.5	61
1.5+1.6	**BrPyCHO**	3 h	63.1 ± 0.5 **3.1**•Br_6	0 **3.2**•Br_6	12.1 ± 0.6	24
1.7+2.2	**BrPyCHO**	5 h	34.6 ± 0.5 **3.1**•Br_6	4.1 ± 0.5 **3.3**•Br_6	10.2 ± 0.5	52
1.5+1.6	**MePyCHO**	13 h	16.9 ± 0.5 **3.4**•Me_6	7.4 ± 0.5 **3.5**•Me_6	18 ± 0.6	58
1.5+2.2	**MePyCHO**	13 h	27.1 ± 0.5 **3.4**•Me_6	9.6 ± 0.5 **3.6**•Me_6	14.2 ± 0.5	49

8.10 Selected Spectra from Chapter 4

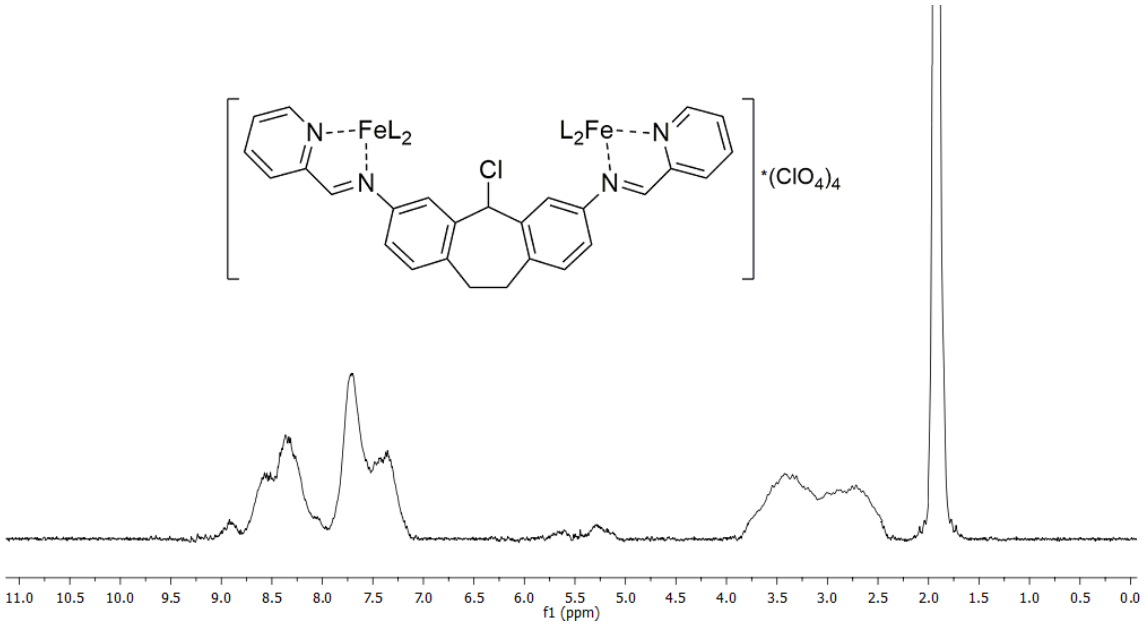

Figure 8.21. ^{1}H NMR spectrum of aggregate **4.4** (CD_3CN, 600 MHz, 298 K).

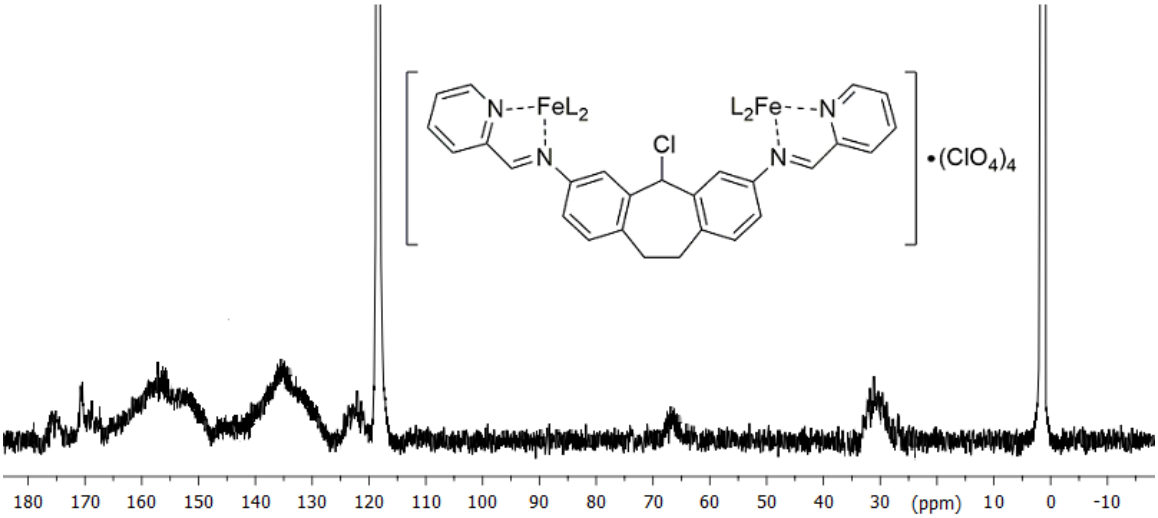

Figure 8.22. ^{13}C NMR spectrum of aggregate **4.4** (CD_3CN, 150 MHz, 298 K).

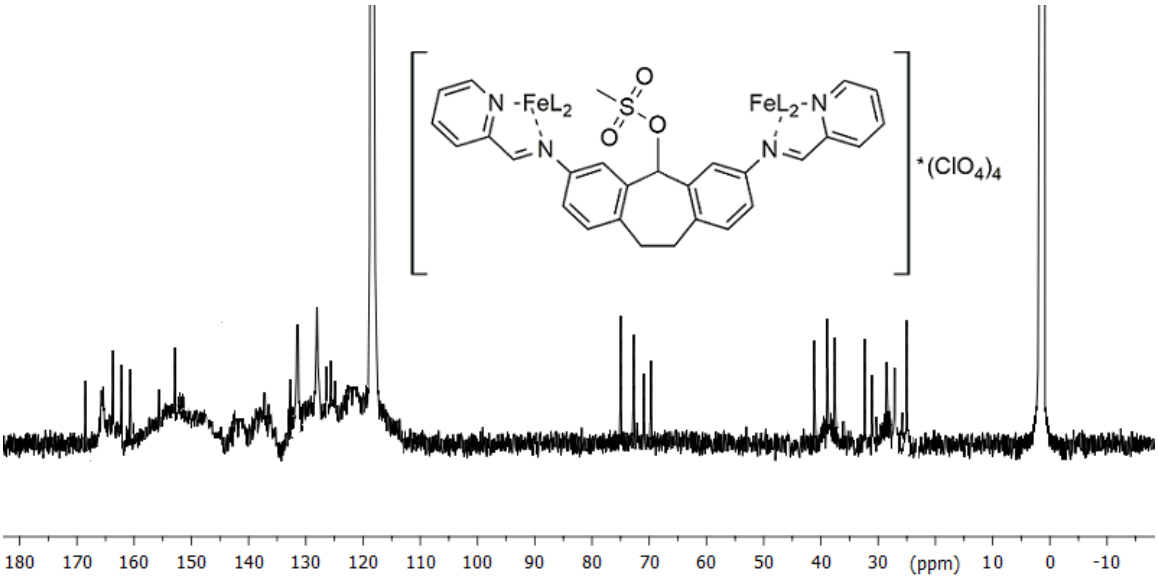

Figure 8.23. ^{13}C NMR spectrum of cage **4.10** (CD_3CN, 150 MHz, 298 K).

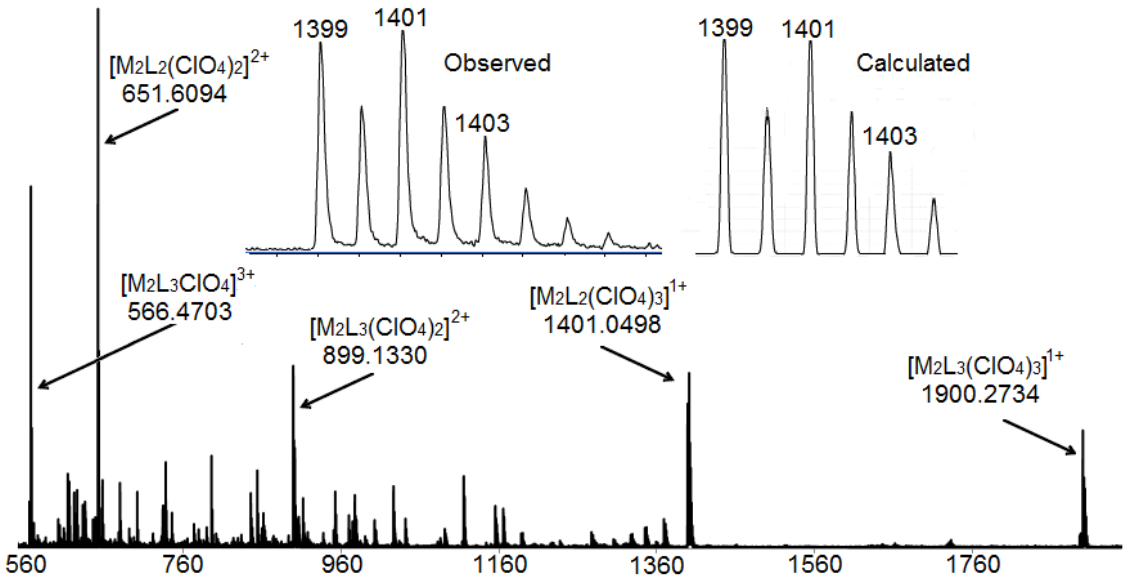

Figure 8.24. ESI-MS of cage **4.10** (CH_3CN).

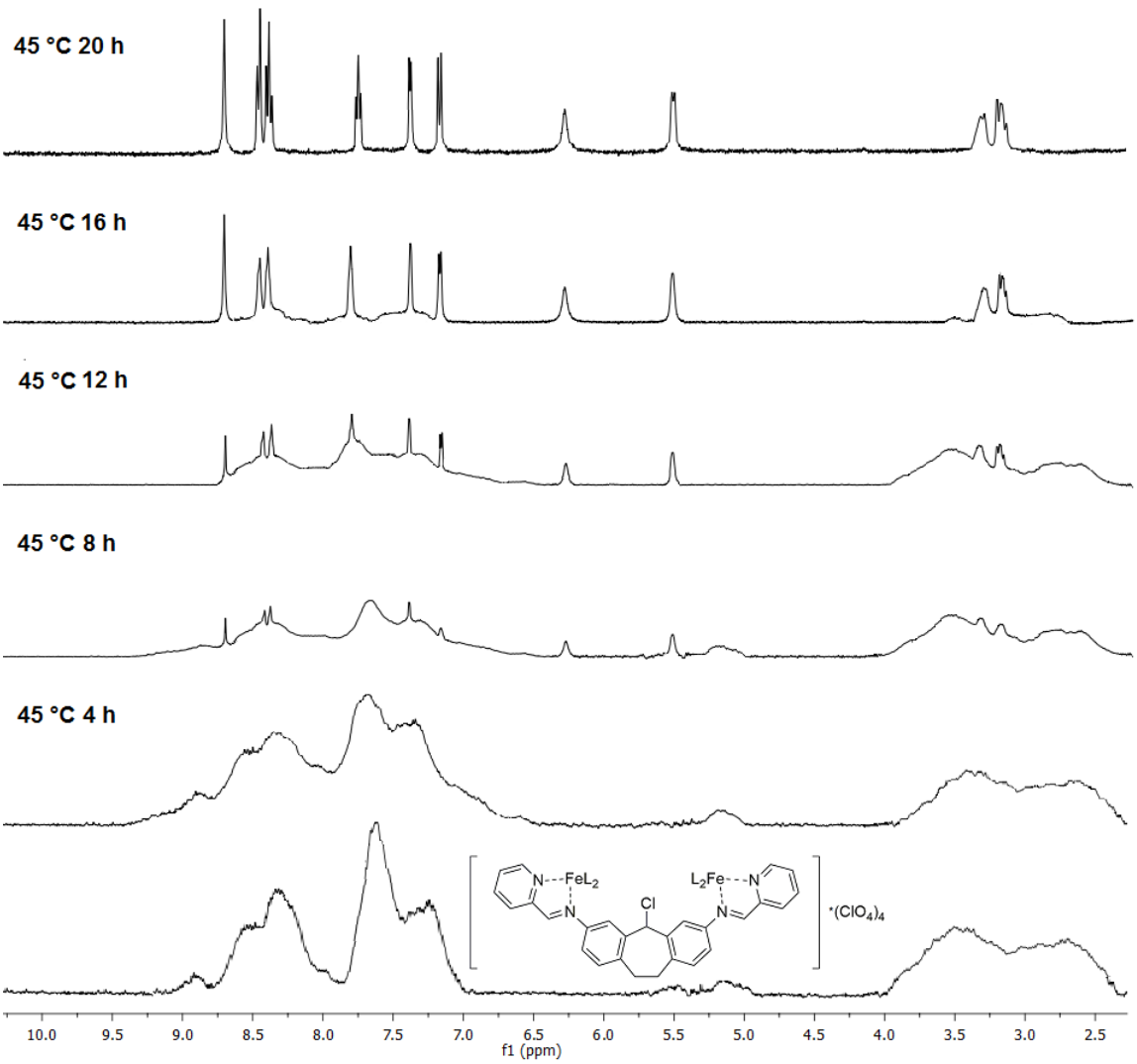

Figure 8.25. ^{1}H NMR spectrum of oxidation products obtained after aggregate **4.4** was heated at 45 °C for 20 h with 1 eq. silver perchlorate and water (CD_3CN, 400 MHz, 298 K). The aggregate was cleanly converted to suberone cage **1.7** within 20 h in acetonitrile or DMSO solvent.

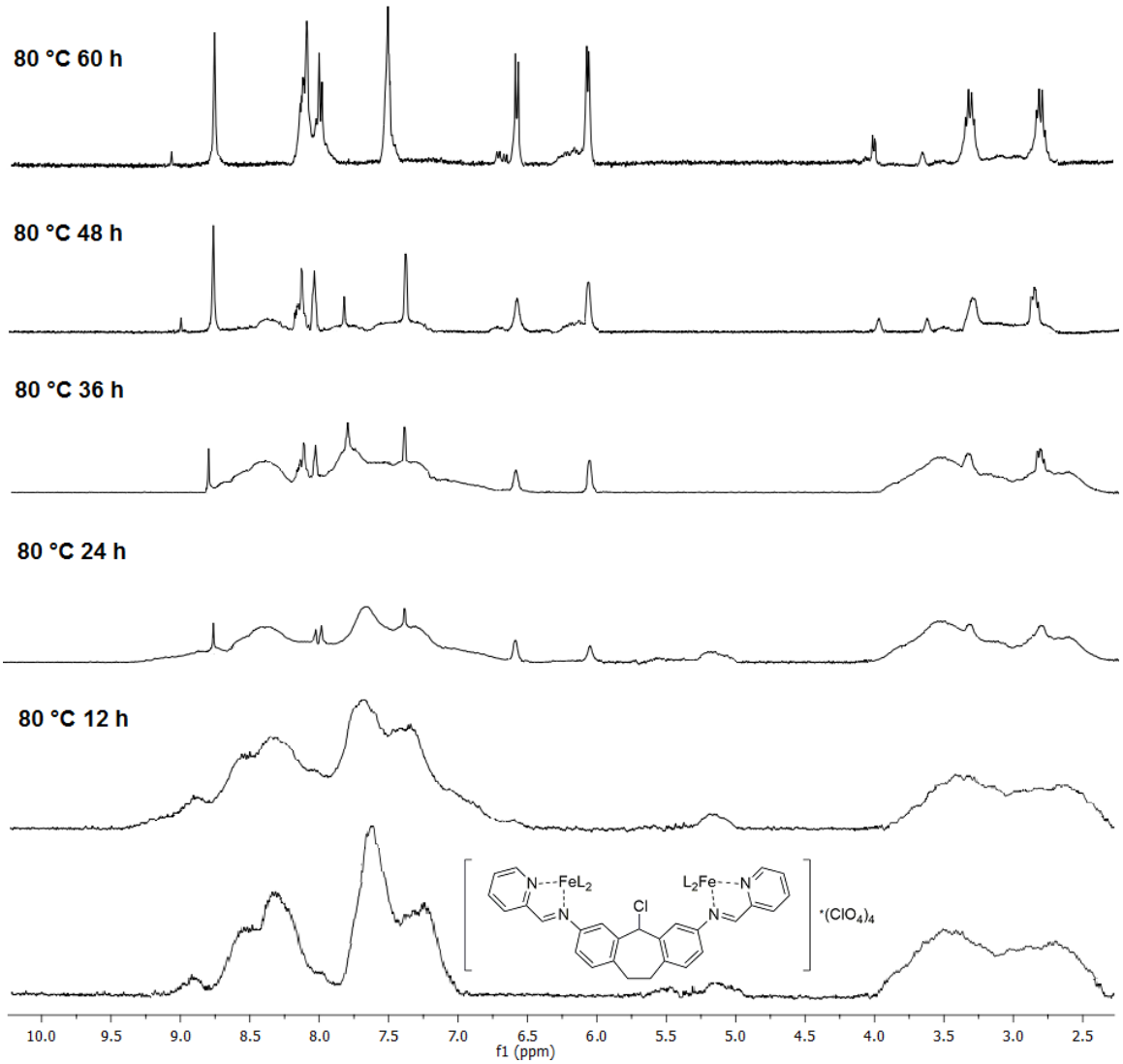

Figure 8.26. ^{1}H NMR spectrum of oxidation products obtained after aggregate **4.4** was heated at 80 °C for 60 h with 1 eq. silver perchlorate and water in the absence of O_2 (CD_3CN, 400 MHz, 298 K). Chloride aggregate **4.4** proceeds to the alcohol cage **1.8** with some thermal decomposition.

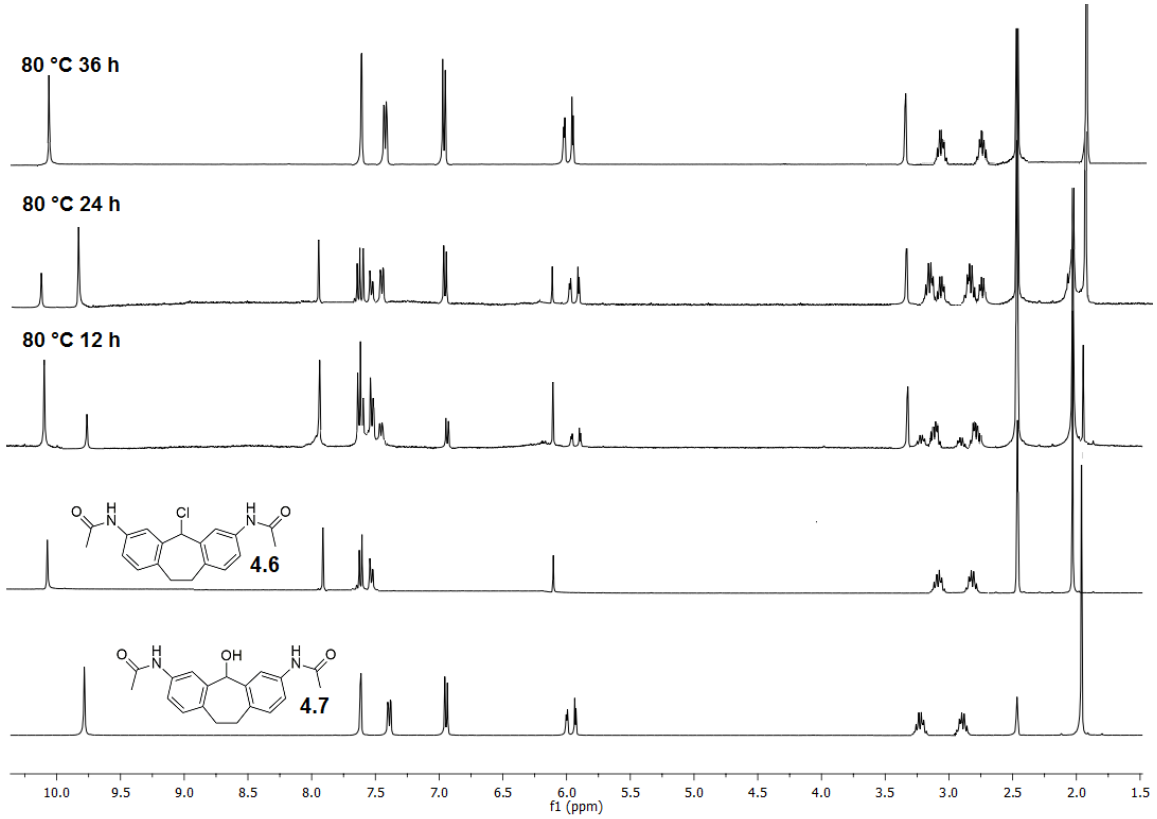

Figure 8.27. ^{1}H NMR spectrum of oxidation products obtained after **4.7** was heated at 80 °C with 1 eq. silver perchlorate and water under a nitrogen atmosphere for 12, 24 and 36 h (DMSO-d_6, 400 MHz, 298 K).

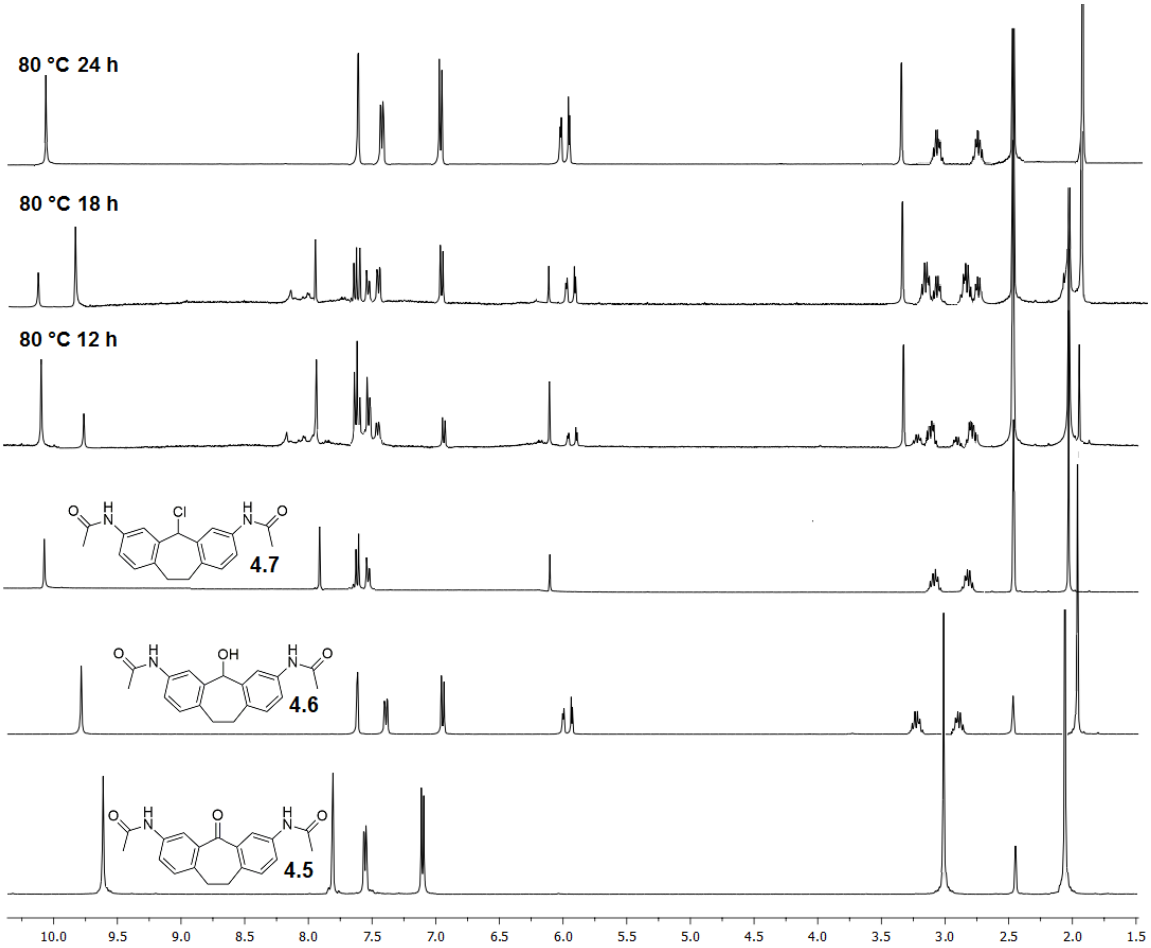

Figure 8.28. ^{1}H NMR spectrum of oxidation products obtained after **4.7** was heated at 80 °C with 1 eq. silver perchlorate, 1 eq. water, and 0.66 eq. iron perchlorate for 12, 24 and 36 h (DMSO-d_6, 400 MHz, 298 K).

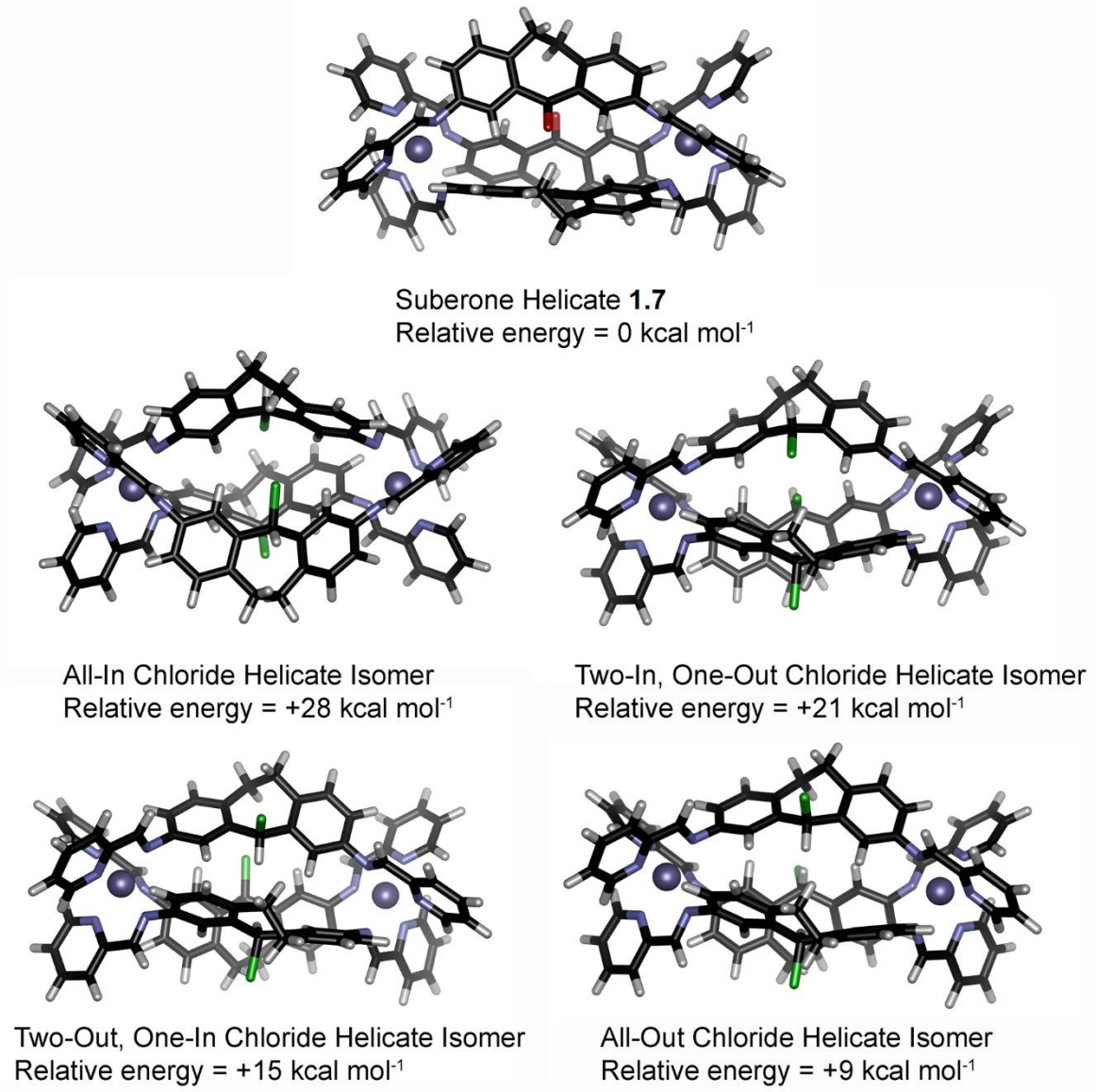

Figure 8.29. Optimized structures (and calculated relative energies) of suberone cage **1.7** and the four possible isomers of M_2L_3 cages that could be formed from assembly of core **4.3**, $Fe(ClO_4)_2$ and 2-formylpyridine.

8.11 Selected Spectra from Chapter 5

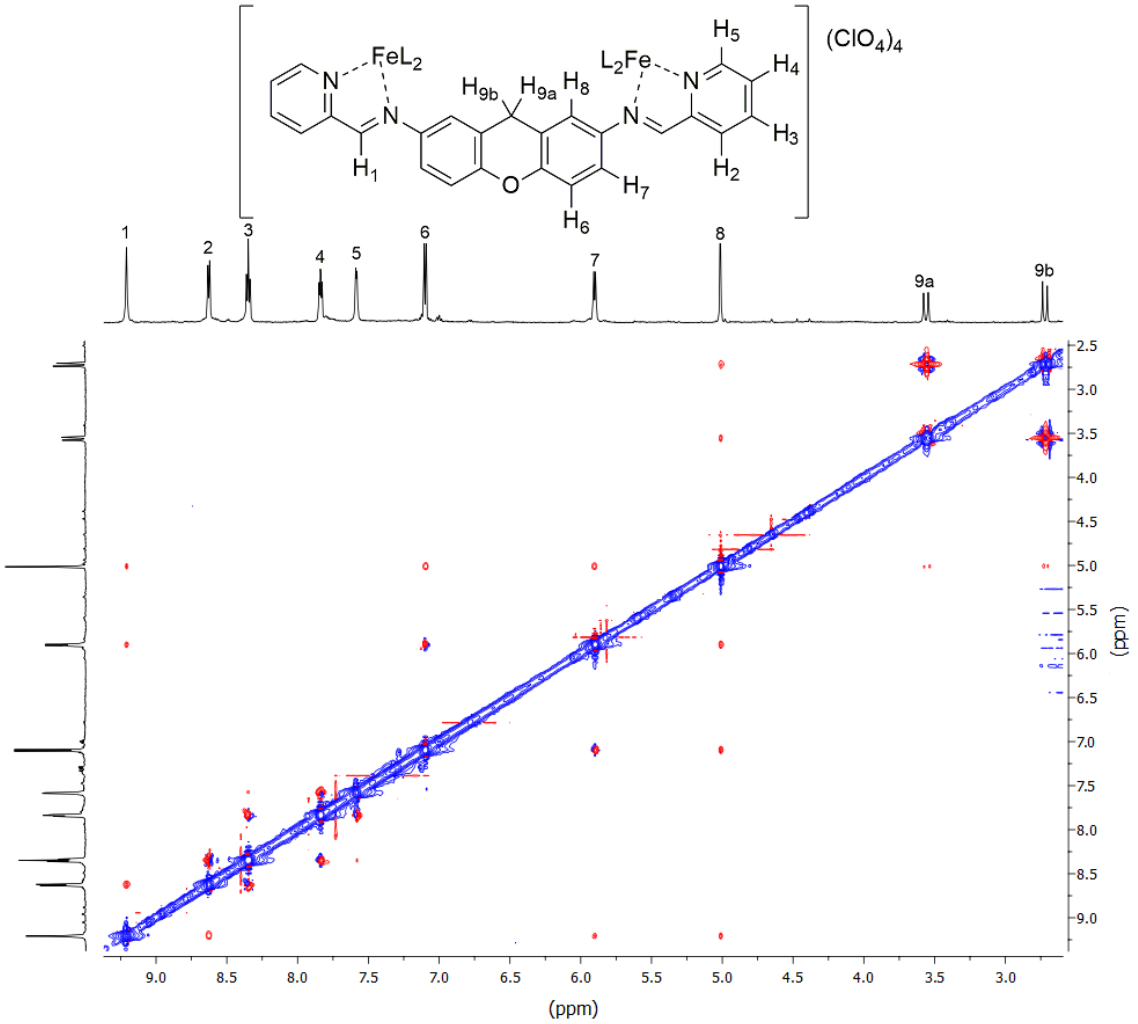

Figure 8.30. NOESY spectrum of cage **5.3** (CD_3CN, 600 MHz, 298 K, mixing time = 300 ms).

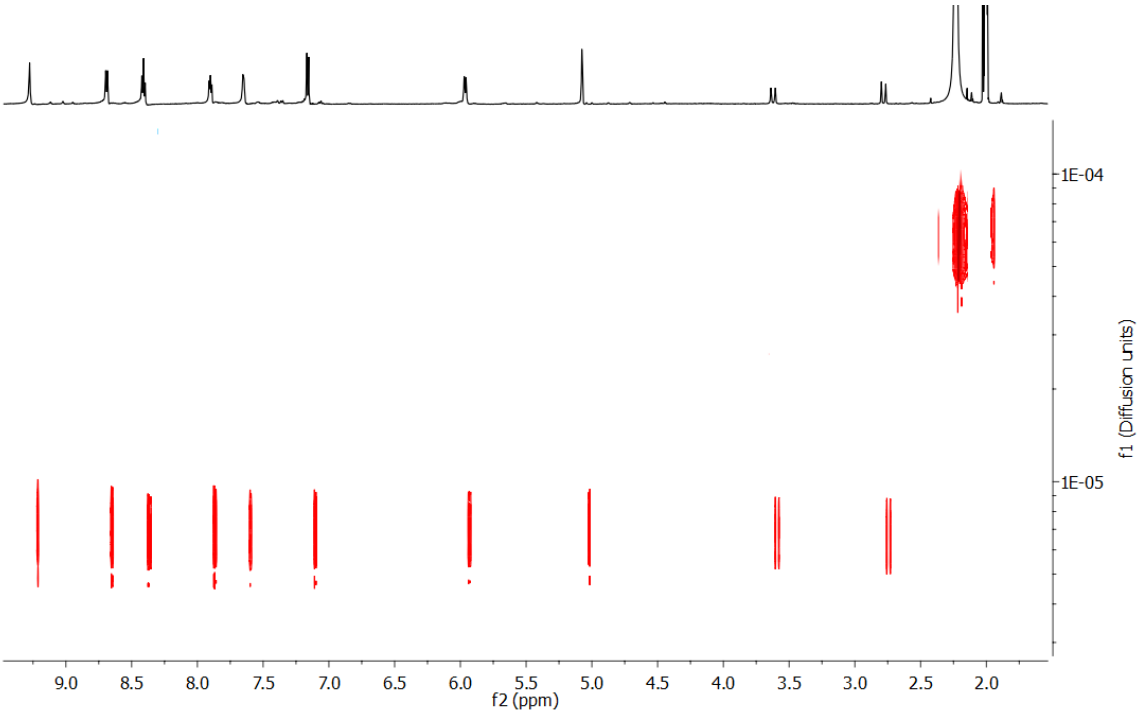

Figure 8.31. ^{1}H-DOSY NMR spectrum of cage **5.3** (CD_3CN, 600 MHz, 298 K, Δ = 100 ms, δ = 1.8 µs, Diffusion constant = 1.794 x10^{-9} m^2/s for cage **5.3** vs. 9.908 x10^{-9} m^2/s for the solvent).

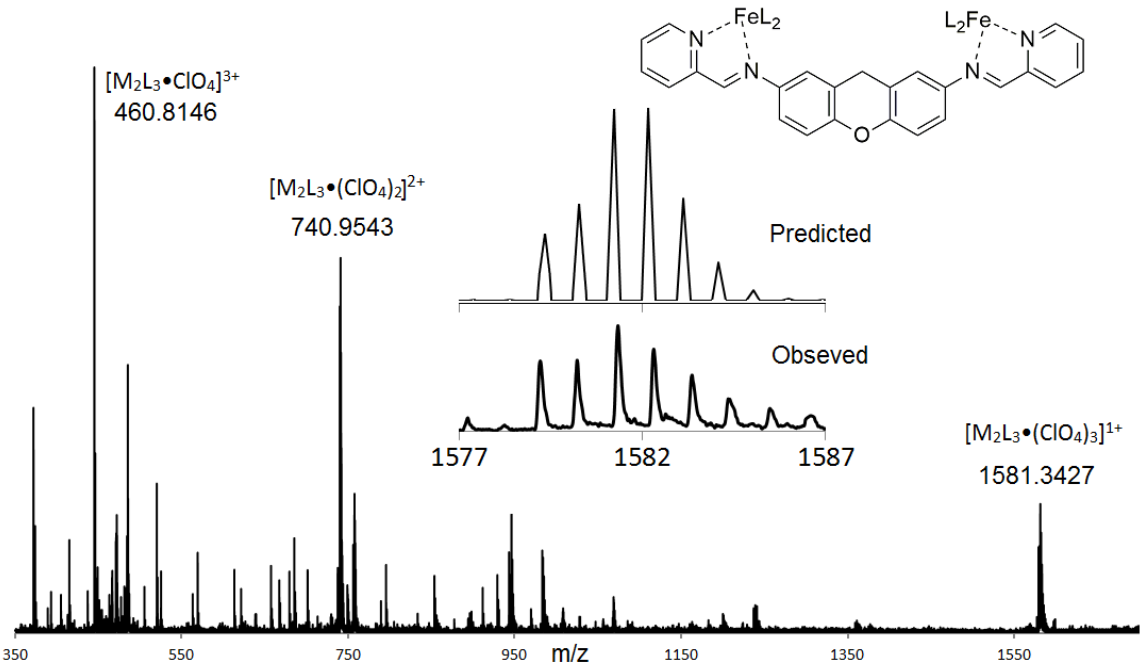

Figure 8.32. Full ESI-MS of cage **5.3** (CH_3CN).

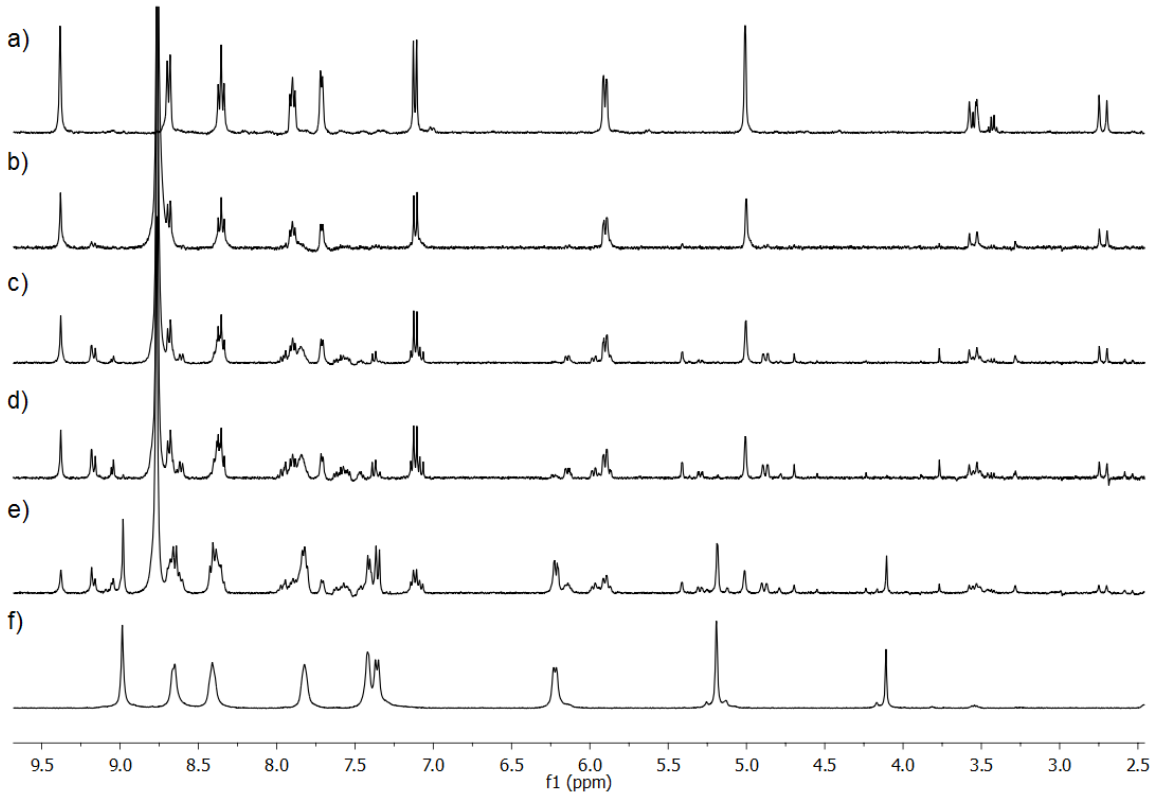

Figure 8.33. ^{1}H NMR spectra of a) xanthene cage **5.3**; b-e) xanthene cage **5.3** reacted with 3.1 mol.-eq. *tert*-butyl hydroperoxide at room temperature over a time period of: b) 30 min; c) 1.5 h; d) 2.5 h; e) 3.5 h; f) isolated xanthyl peroxide cage **5.6** product (CD_3CN, 400 MHz, 298 K).

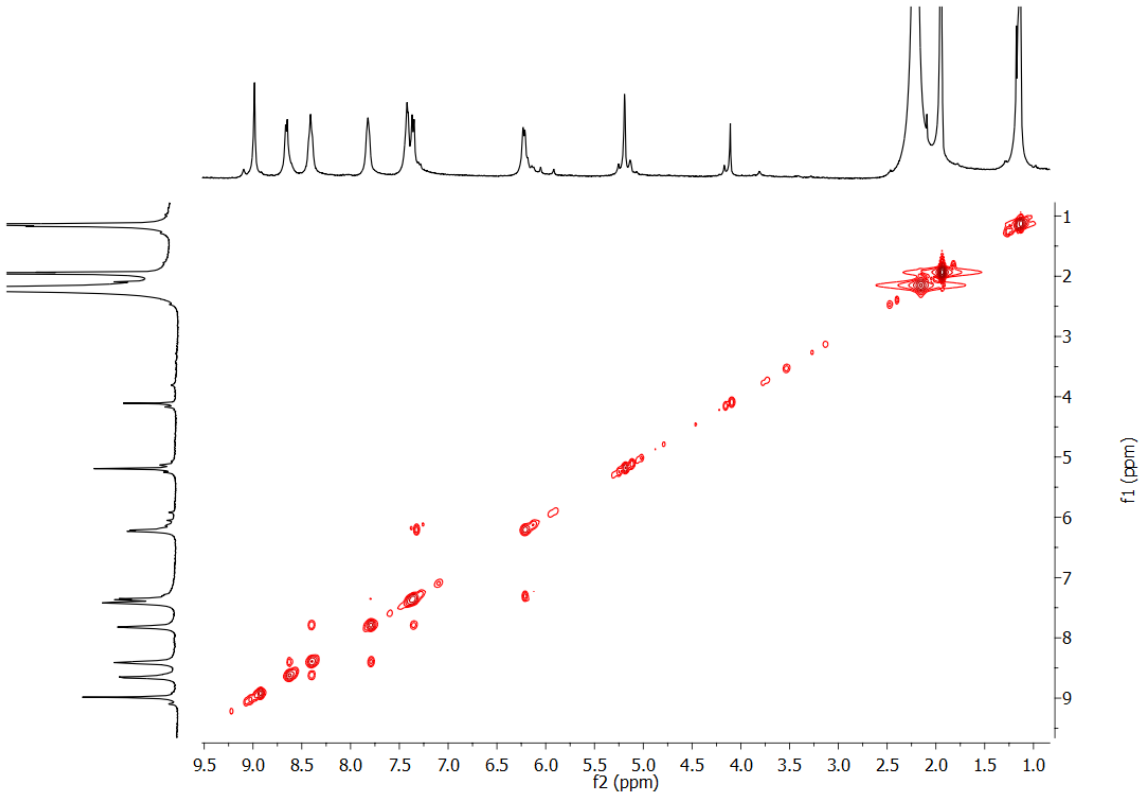

Figure 8.34. Full COSY spectrum of cage **5.6** (CD_3CN, 600 MHz, 298 K).

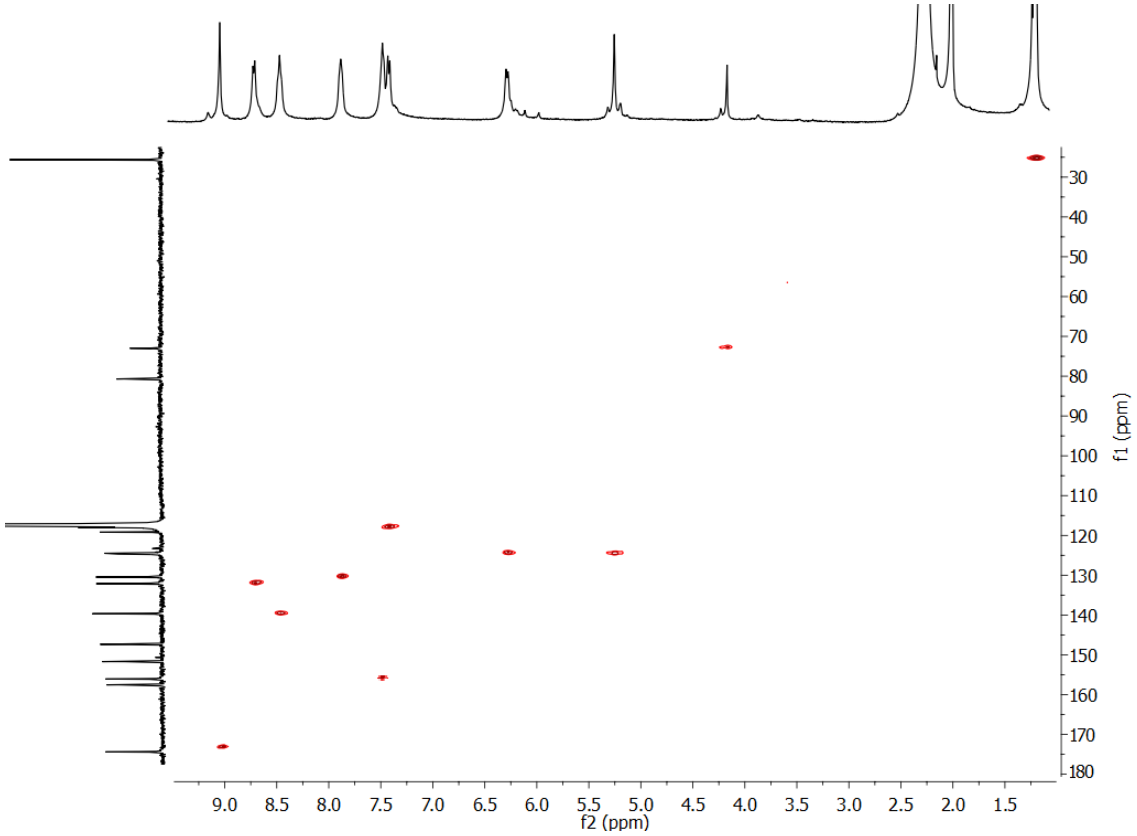

Figure 8.35. Full HSQC spectrum of cage **5.6** (CD_3CN, 600 MHz, 298 K).

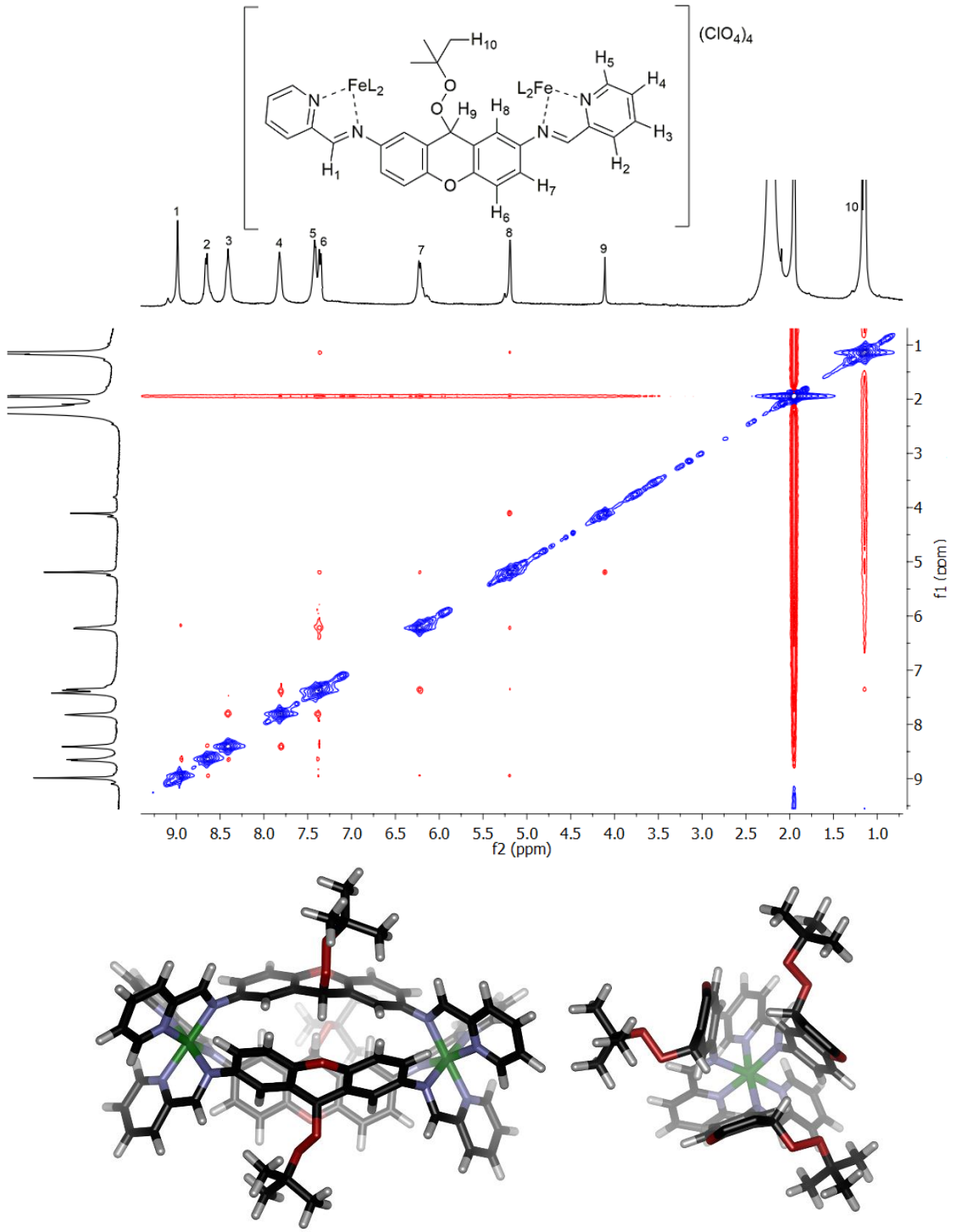

Figure 8.36. ROESY spectrum of xanthyl peroxide cage **5.6** (CD_3CN, 600 MHz, 298 K, mixing time = 200 ms) and molecular minimized structure of **5.6** (SPARTAN semi-empirical, AM1 forcefield).

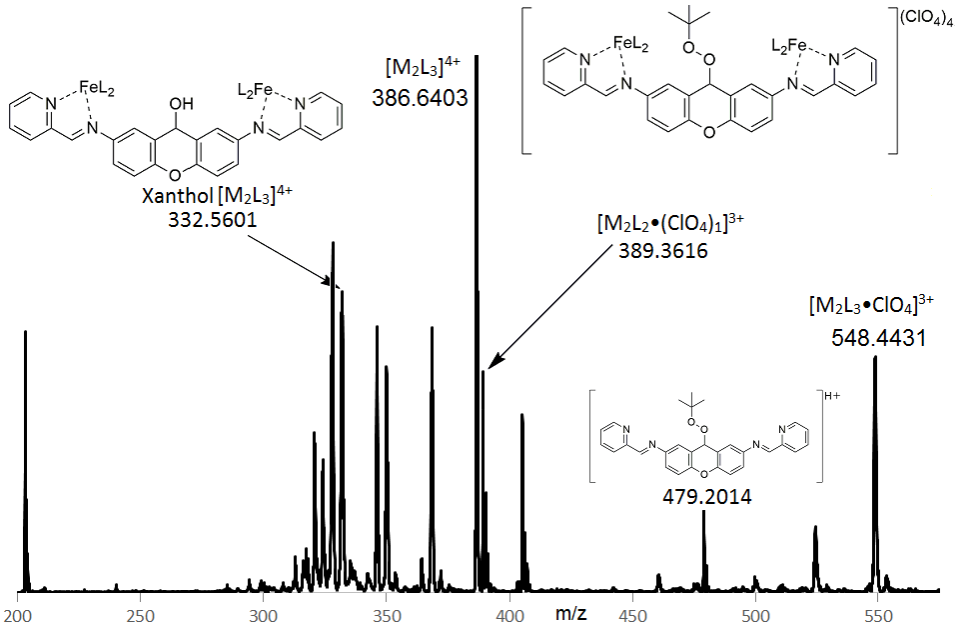

Figure 8.37. Expanded ESI-MS of xanthyl peroxide cage **5.6** (CH_3CN). One peak corresponding to the xanthol M_2L_3 cage **5.12** was observed in the spectrum due to cleavage of the peroxide groups, while the remaining peaks are attributed to the xanthyl peroxide cage **5.6**, iminopyridine ligand and cage fragments.

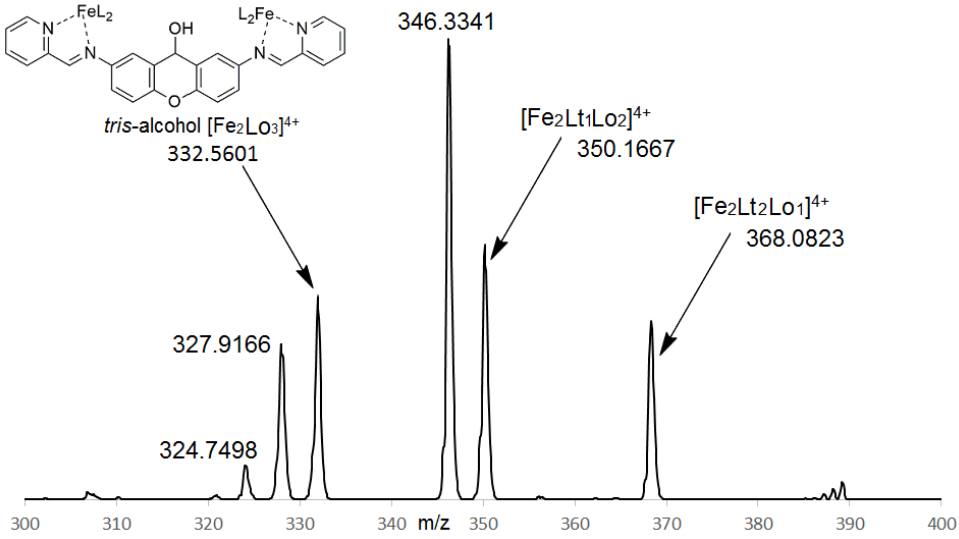

Figure 8.38. Collision induced dissociation of the **5.6** cage $[M_2L_3]^{4+}$ peak at 386.64 (CH_3CN). Peaks corresponding to heterocomplexes (where Lt = peroxide ligand and Lo = alcohol bearing ligand) are clearly present. The spectrum shows $[M_2L_3]^{4+}$ complexes arising from the loss of ^{t}BuO- on 1, 2 and 3 ligands of the parent complex **5.6**. Peaks arising from dehydration of one of the alcohol bearing ligands of the $[Fe_2Lt_1Lo_2]^{4+}$ complex (346.3314), and dehydration of one and two alcohol ligands (327.9166 and 324.7498 respectively) from the *tris*-alcohol $[Fe_2L_3]^{4+}$ complex are also present.

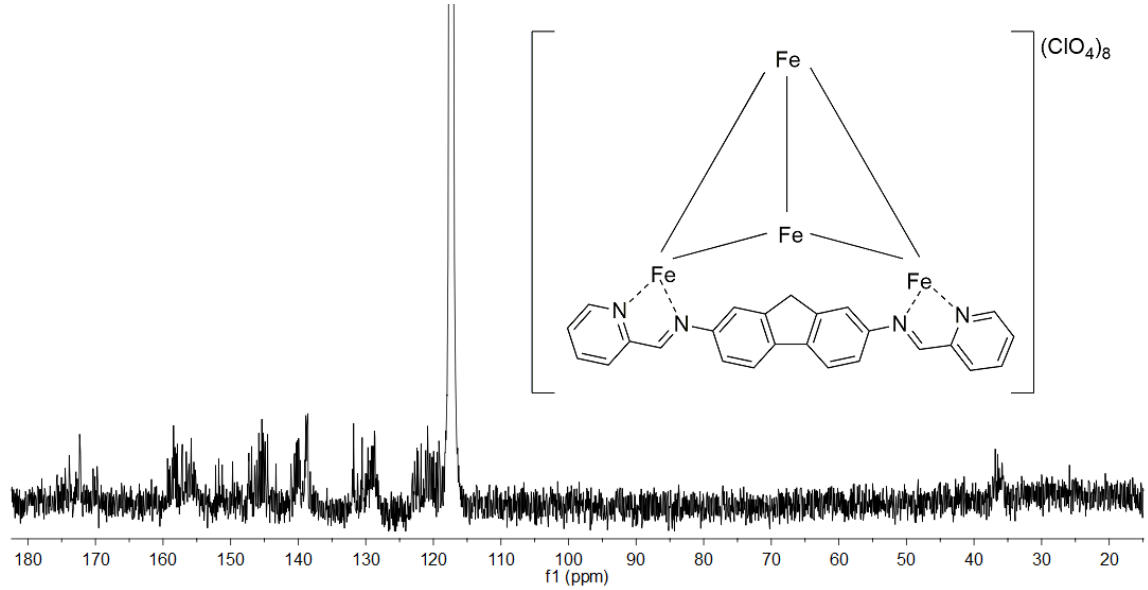

Figure 8.39. ^{13}C NMR spectrum of fluorene cage **5.5** (CD_3CN, 500 MHz, 298 K).

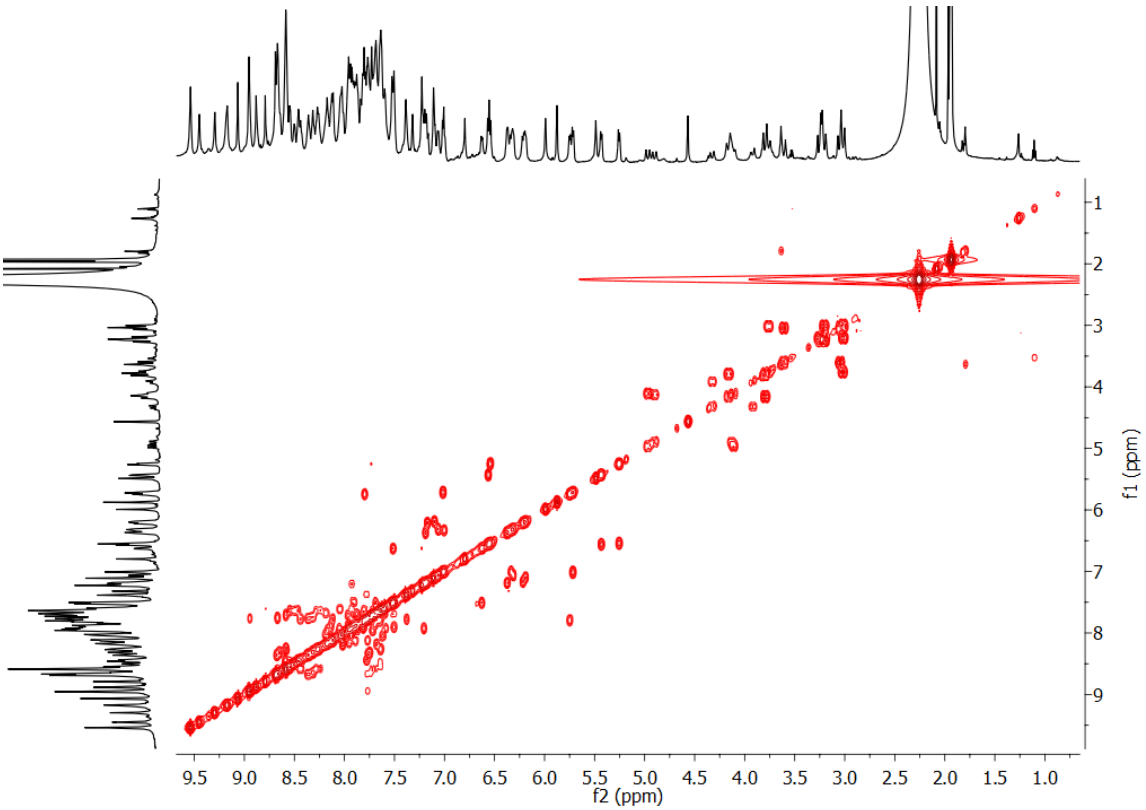

Figure 8.40. Full COSY spectrum of fluorene cage **5.5** (CD_3CN, 600 MHz, 298 K).

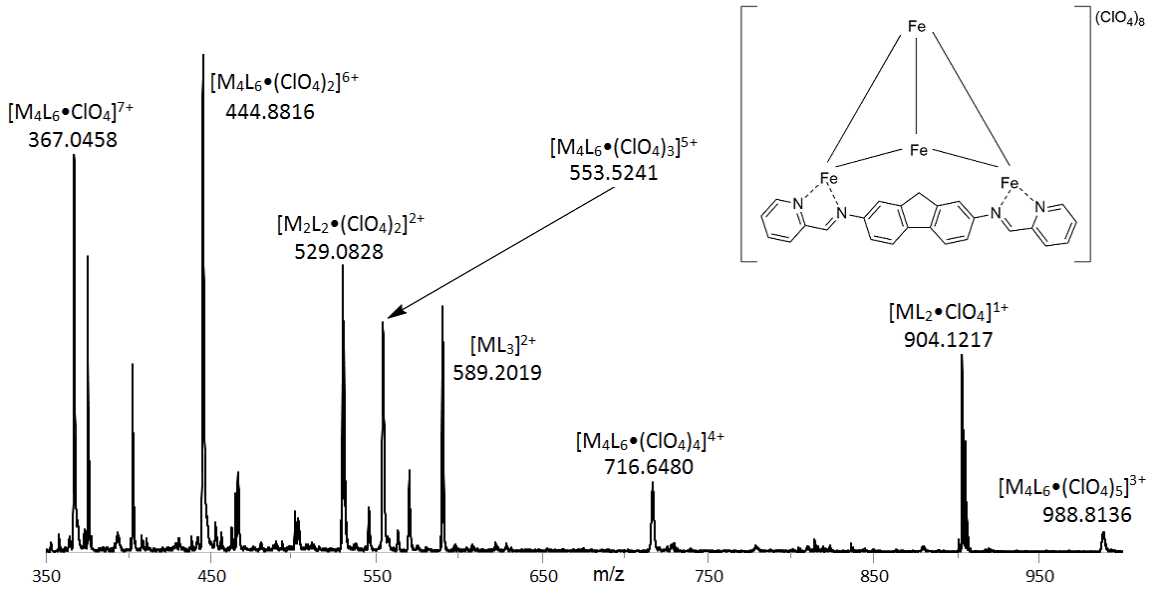

Figure 8.41. ESI-MS Expansion of fluorene cage **5.5** (CH_3CN).

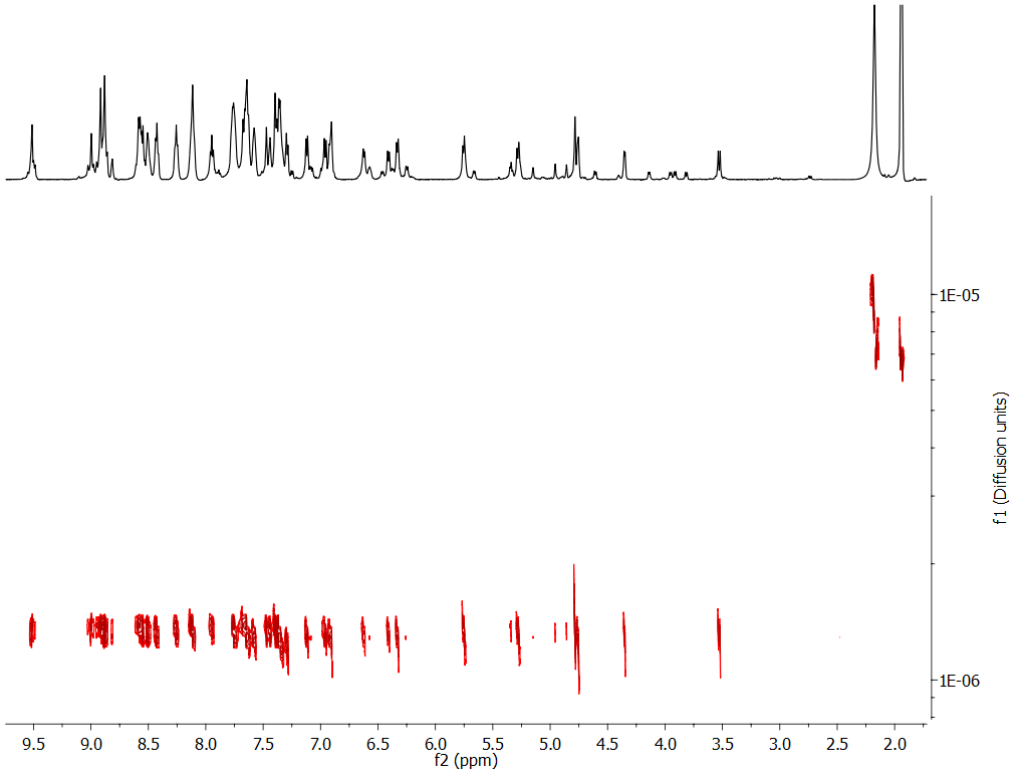

Figure 8.42. ^1H DOSY NMR spectrum of fluorenol cage **1.12** formed via oxidation of fluorene cage **5.5** (CD_3CN, 600 MHz, 298 K, Δ = 100 ms, δ = 2.6 µs, Diffusion constant= 9.883 x10^{-10} m^2/s for cage **1.12** vs. 9.893 x10^{-9} m^2/s for the solvent).

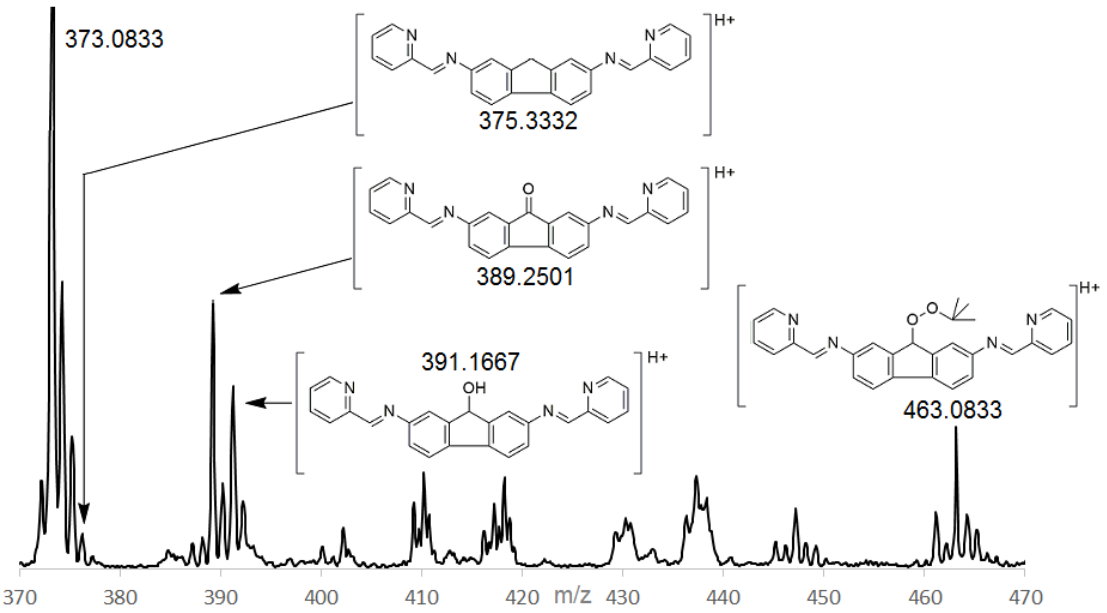

Figure 8.43. Expanded ESI-MS spectrum of oxidation products from the reaction between fluorene cage **5.5** containing non-directing triflate counterions and *tert*-butyl hydroperoxide (CH_3CN). The spectrum shows the presence of protonated alkane, ketone, alcohol and peroxide iminopyridine ligands as well as the product of dehydration of the alcohol bearing ligand (373.0833).

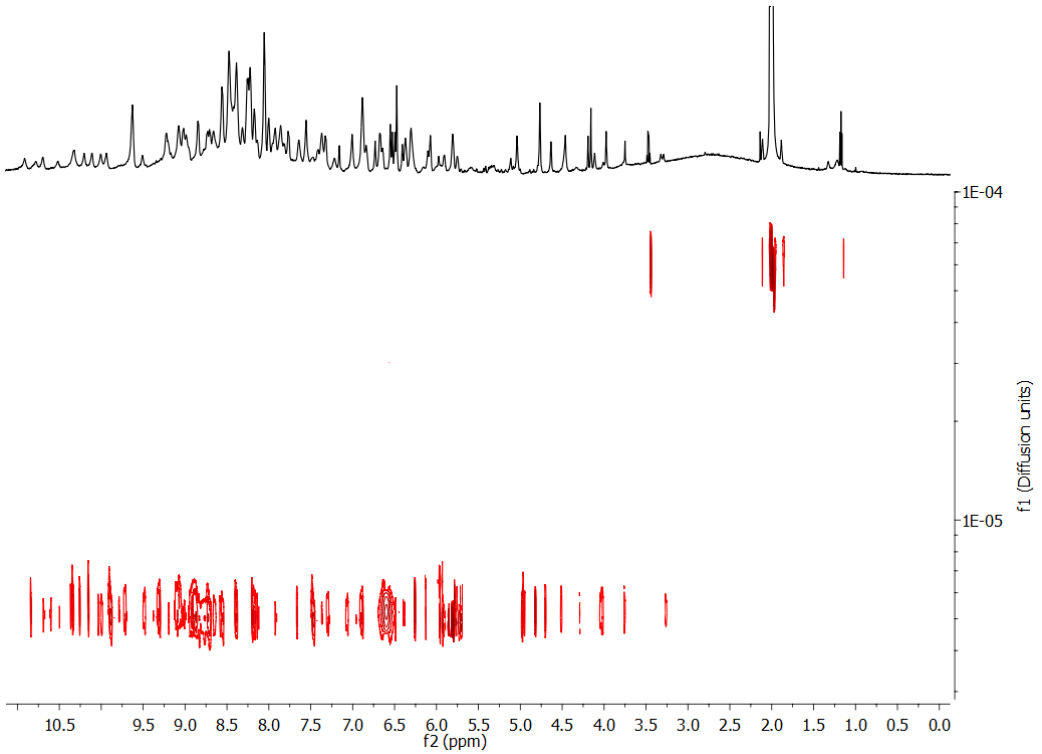

Figure 8.44. ^{1}H DOSY NMR spectrum of xanthol cage **5.12** (CD_3CN, 600 MHz, 298 K, Δ = 100 ms, δ = 2.6 μs, Diffusion constant = 8.497 x10^{-10} m^2/s for cage **5.12** vs. 9.641 x10^{-9} m^2/s for the solvent).

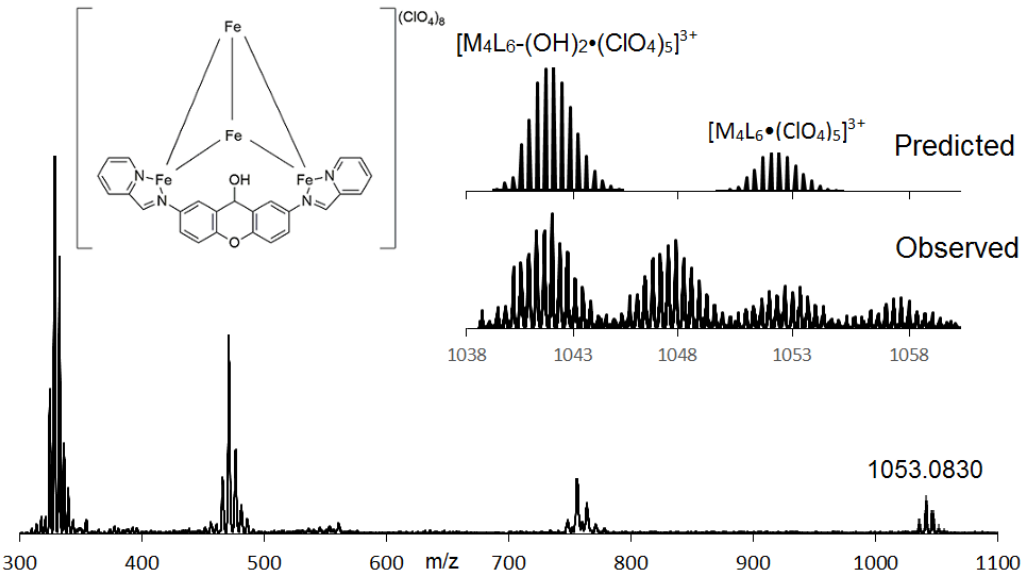

Figure 8.45. Full ESI-MS of cage **5.12** (CH_3CN). Predicted splitting patterns for the $[M_4L_6•(ClO_4)_5]^{3+}$ peaks, which cannot arise from a $M_2L_3•(ClO_4)_4$ complex, are shown.

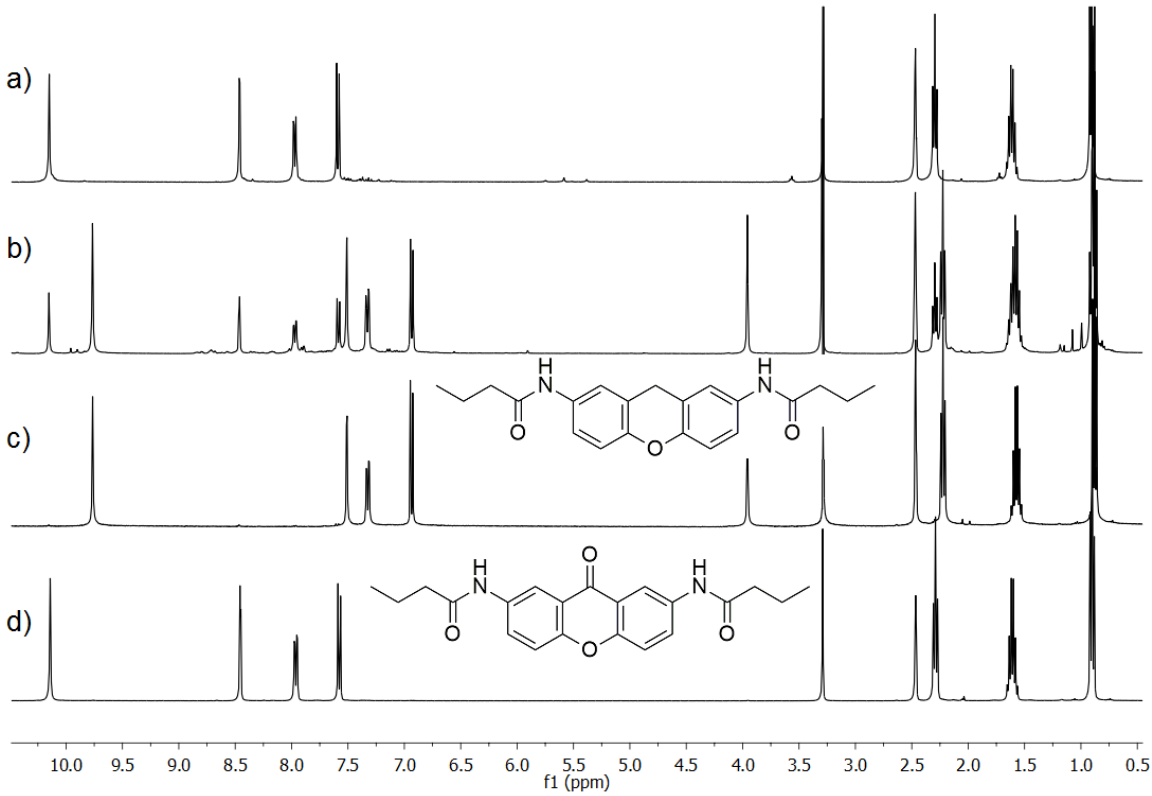

Figure 8.46. ^{1}H NMR stack of a) xanthene control ligand **5.7** mixed with 1.1 mol.-eq. *tert*-butyl hydroperoxide oxidant and catalytic xanthone cage **2.6** (10 % metal total) for 2 h at room temperature; b) xanthene control ligand **5.7** mixed with 1.1 mol.-eq. *tert*-butyl hydroperoxide oxidant and catalytic xanthone cage **2.6** (10 % metal total) for 1 h at room temperature; c) Xanthene control **5.7**; d) expected xanthone oxidation product **5.9** (CD_3CN, 400 MHz, 298 K).

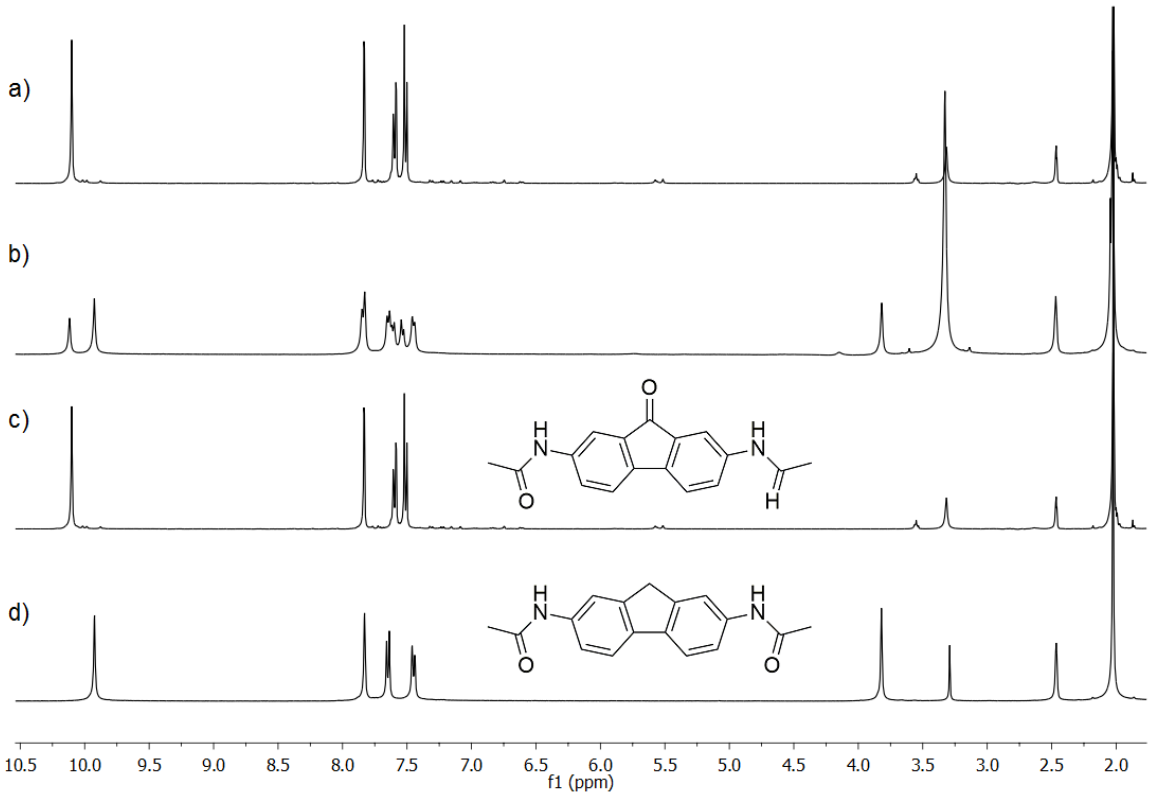

Figure 8.47. ^{1}H NMR stack of a) fluorene control ligand **5.8** mixed with 1.1 mol.-eq. *tert*-butyl hydroperoxide oxidant and catalytic (0.1 mol.-eq.) $Fe(ClO_4)_2$ for 12 h at 50 ˚C; b) fluorene control ligand **5.8** mixed with 1.1 mol.-eq. *tert*-butyl hydroperoxide oxidant and catalytic (0.1 mol.-eq.) $Fe(ClO_4)_2$ for 5 h at 50 ˚C; c) expected fluorenone oxidation product **5.10**; d) fluorene control **5.8** (CD_3CN, 400 MHz, 298 K).

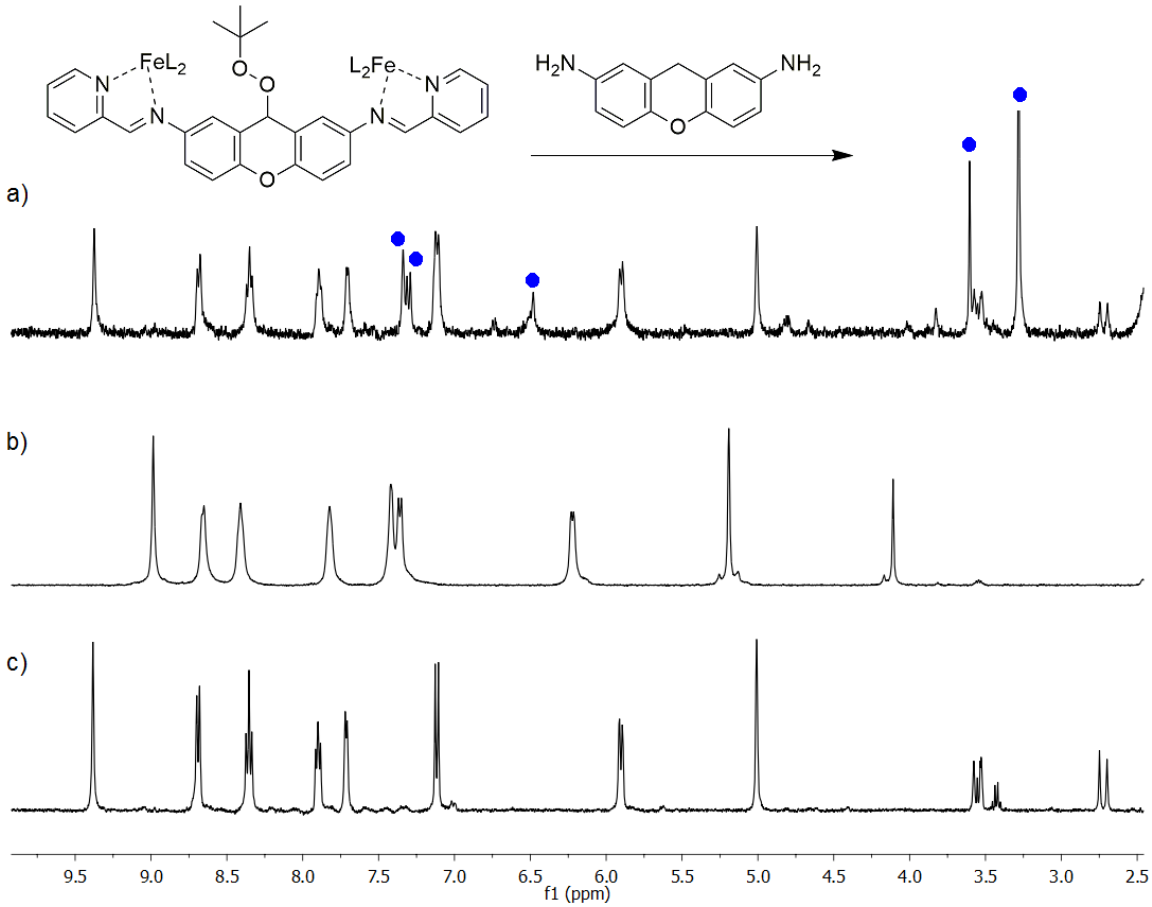

Figure 8.48. ^{1}H NMR stack of a) xanthyl peroxide cage **5.6** when mixed with 3 mol.-eq. diaminoxanthene **5.2** at 70 ˚C for 8 h; b) xanthyl peroxide cage **5.6**; c) xanthene cage **5.3** (CD_3CN, 400 MHz, 298 K). The spectrum shows complete displacement of xanthyl *tert*-butyl peroxide ligand (blue) and formation of xanthene cage **5.3**.

8.12 Selected Spectra from Chapter 6

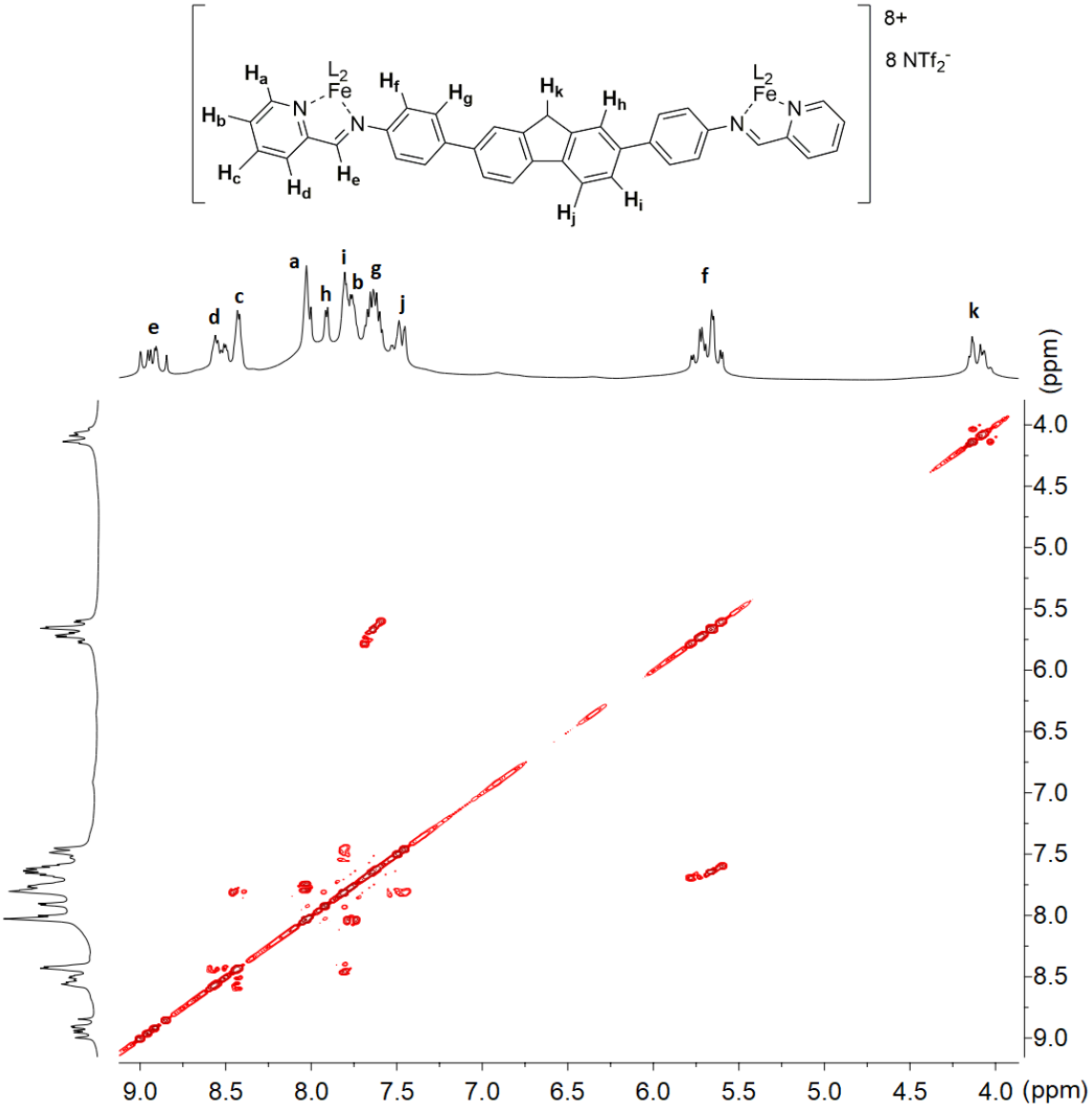

Figure 8.49. gCOSY NMR spectrum of fluorene cage **6.3** (CD_3CN, 600 MHz, 298 K).

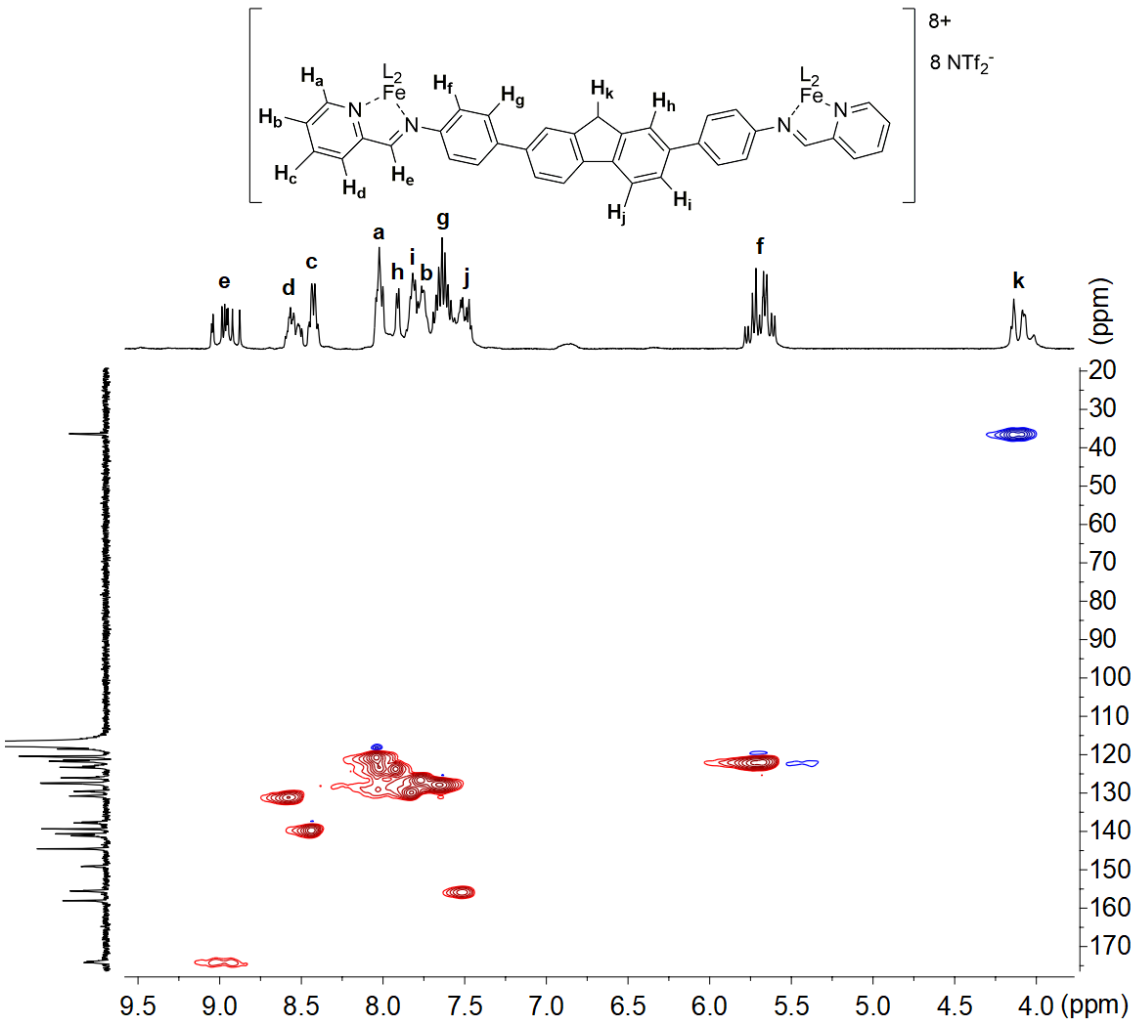

Figure 8.50. DEPT-HSQC NMR spectrum of fluorene cage **6.3** (CD_3CN, 400 MHz, 298 K).

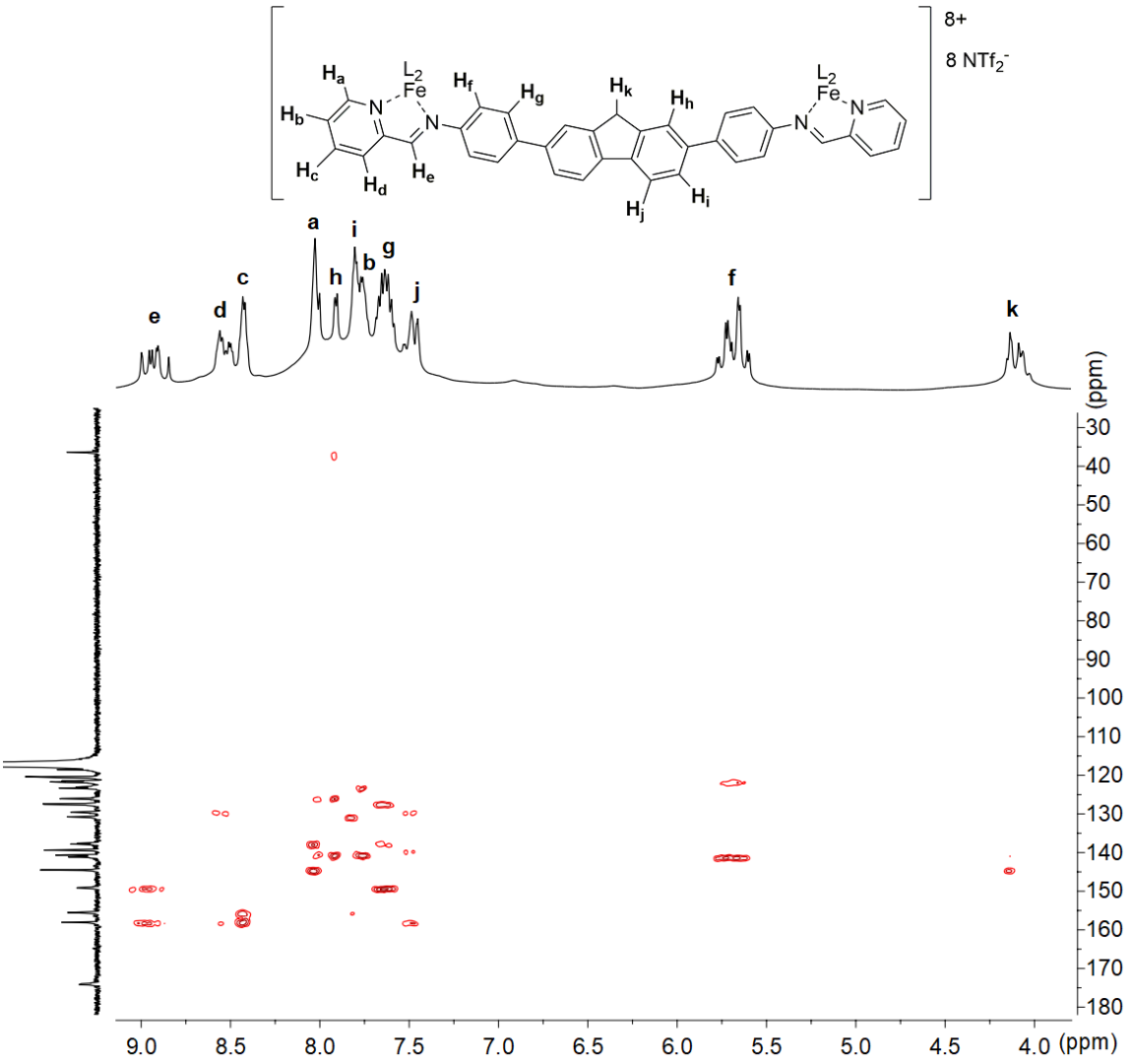

Figure 8.51. HMBC NMR spectrum of fluorene cage **6.3** (CD_3CN, 400 MHz, 298 K).

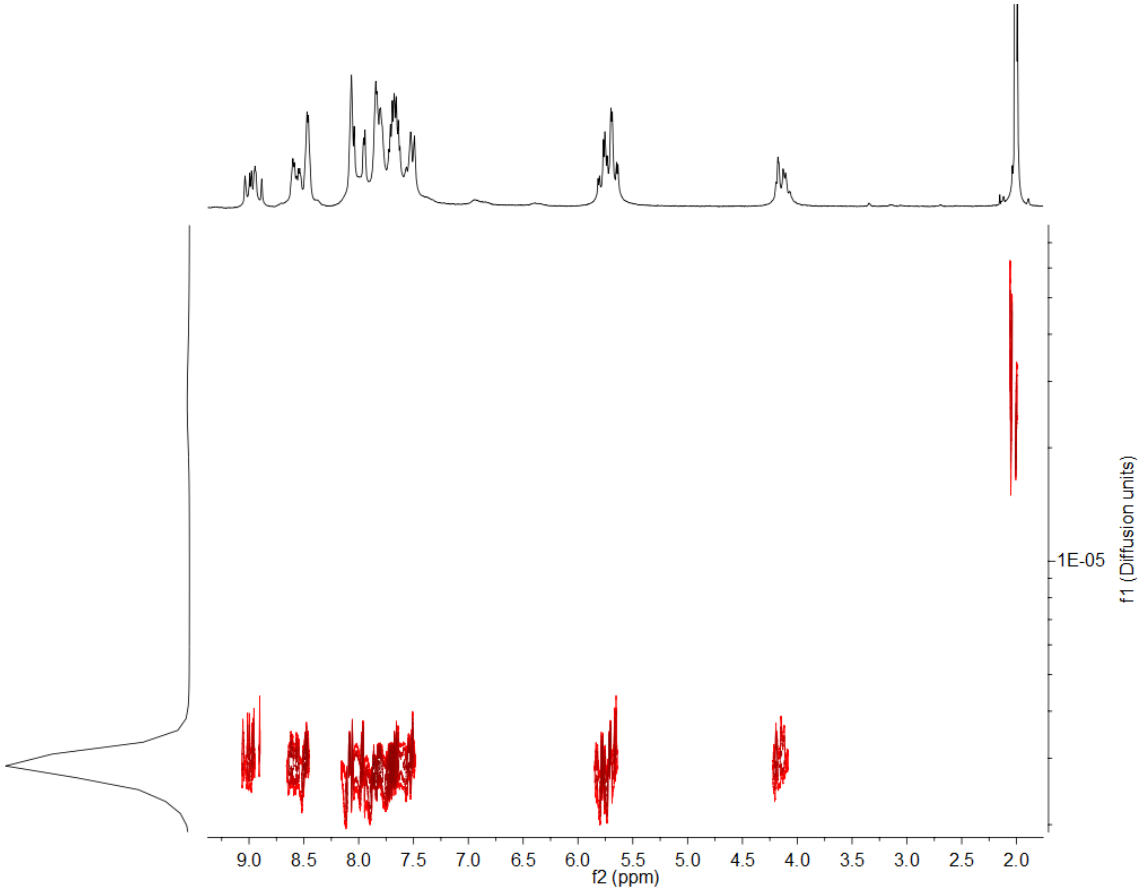

Figure 8.52. ^{1}H DOSY NMR spectrum of fluorene cage **6.3** (CD_3CN, 600 MHz, 298 K, Δ = 100 ms, δ = 1.8 μs, Diffusion constant = 3.020 x10^{-10} m^2/s for cage **6.3** vs. 3.890 x10^{-9} m^2/s for the solvent).

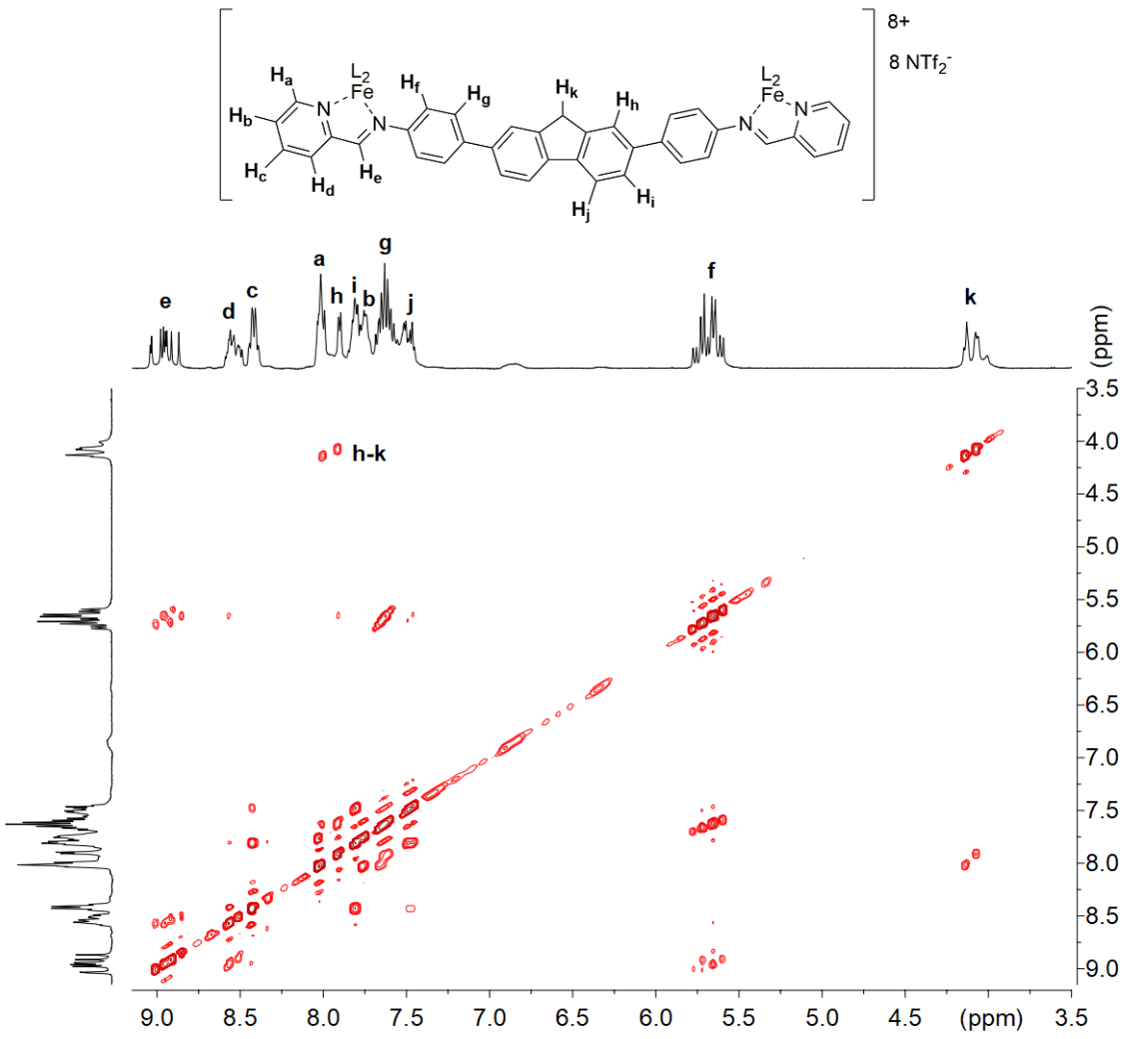

Figure 8.53. gNOESY NMR spectrum of fluorene cage **6.3** (CD_3CN, 600 MHz, 298 K, mixing time = 300 ms).

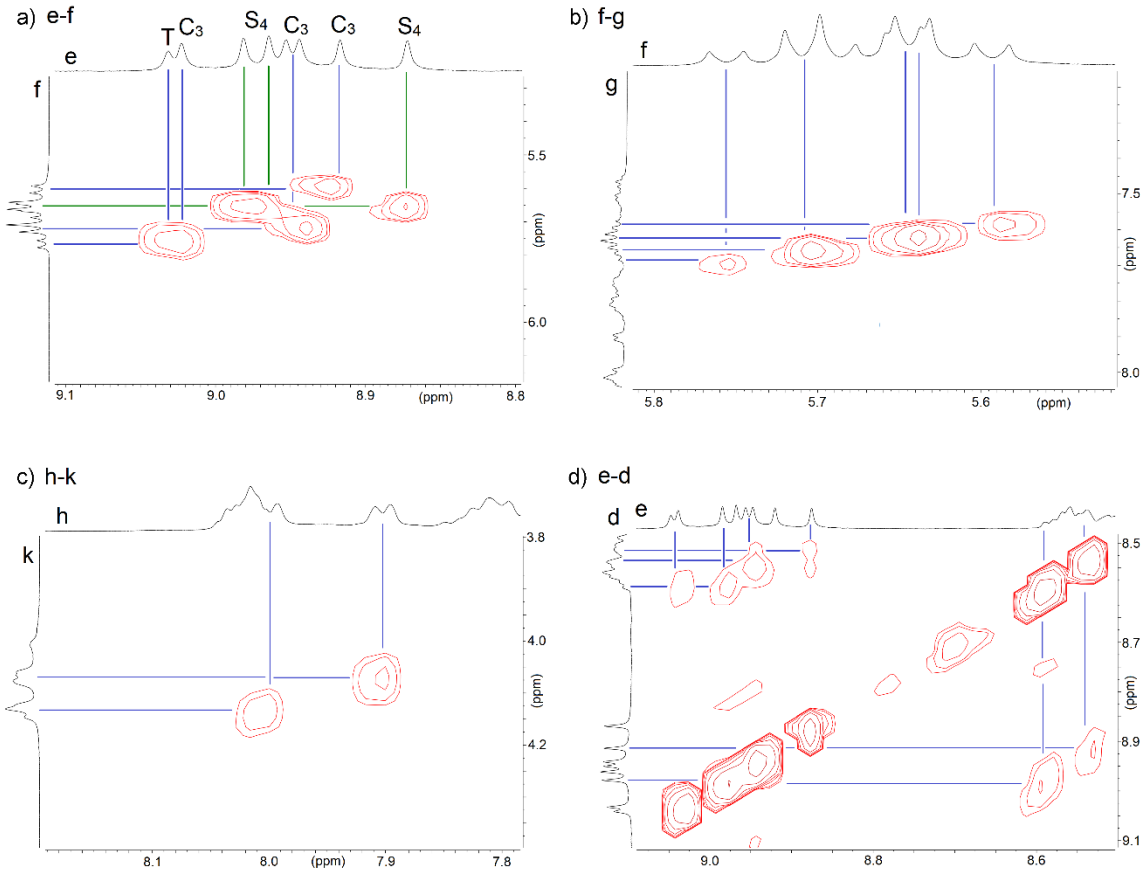

Figure 8.54. Expanded aromatic regions of the gNOESY NMR spectrum of fluorene cage **6.3** illustrating the presence of three different isomers through correlations of protons a) e and f, b) f and g, c) h and k, and d) e and d. (CD_3CN, 600 MHz, 298 K, mixing time = 300 ms).

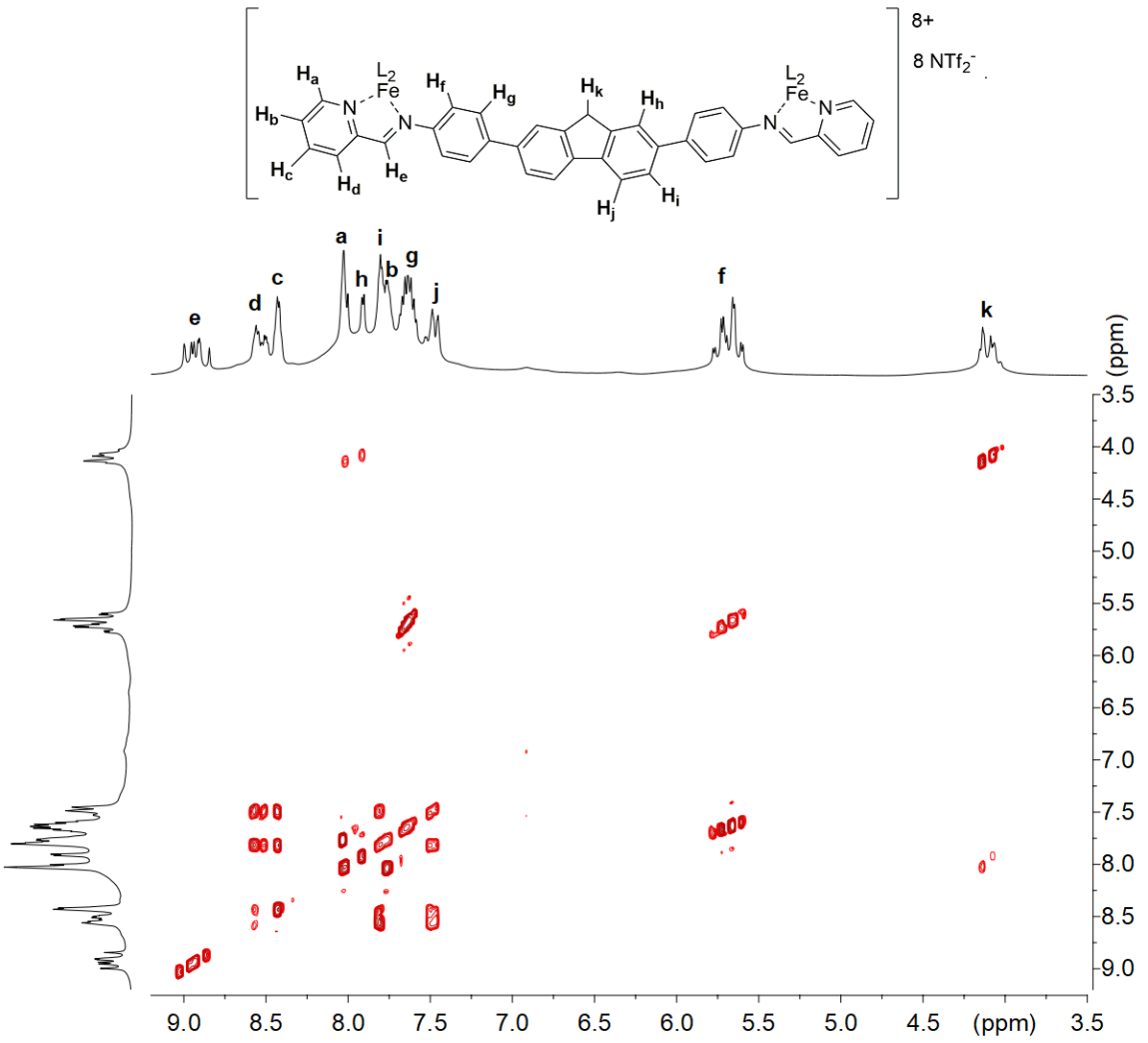

Figure 8.55. TOCSY NMR spectrum of cage **6.3** (CD_3CN, 600 MHz, 298 K, mixing time = 80 ms).

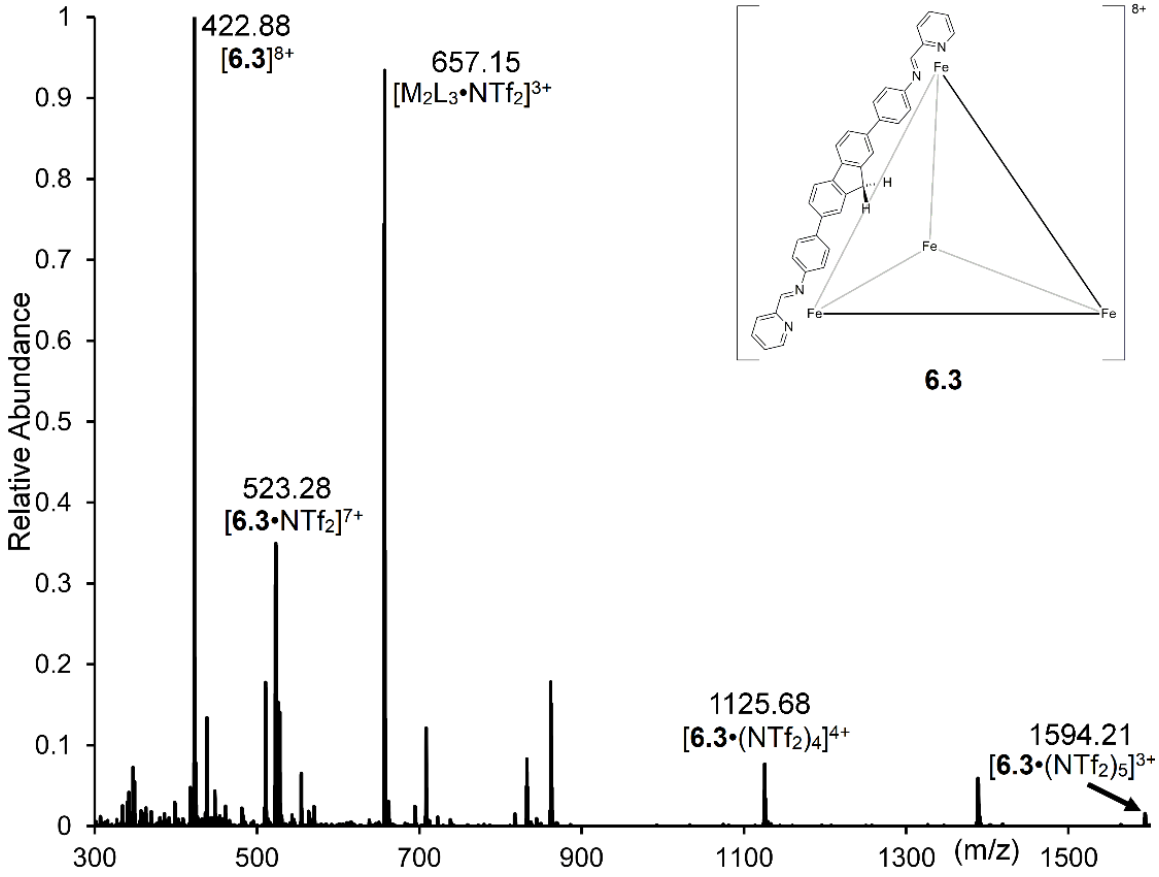

Figure 8.56. Full Mass Spectrum of fluorene cage **6.3** (CH_3CN).

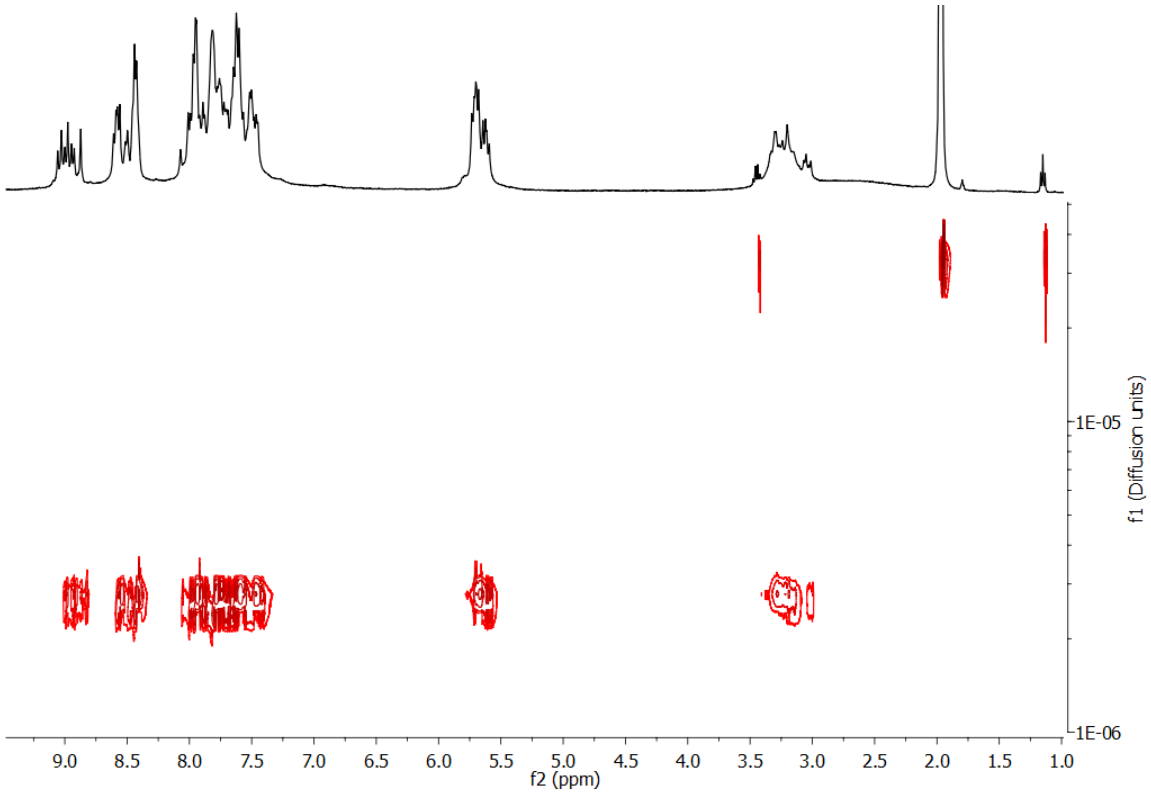

Figure 8.57. ^{1}H DOSY NMR spectrum of acid cage **6.7** (CD_3CN, 600 MHz, 298 K, Δ = 100 ms, δ = 1.8 μs, Diffusion constant = 3.090 x10^{-10} m^2/s for cage **6.7** vs. 3.467 x10^{-9} m^2/s for the solvent).

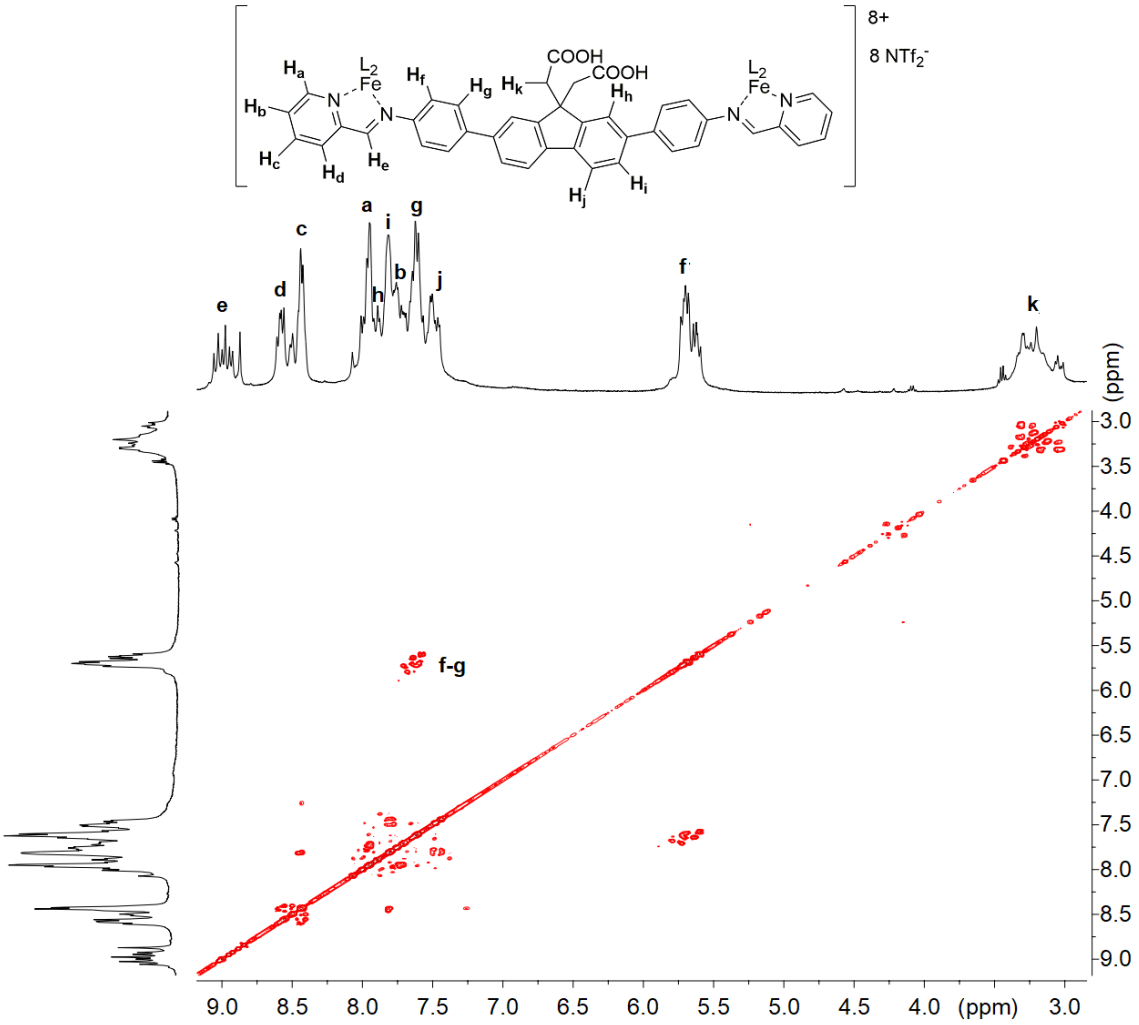

Figure 8.58. gCOSY NMR spectrum of acid cage **6.7** (CD_3CN, 600 MHz, 298 K).

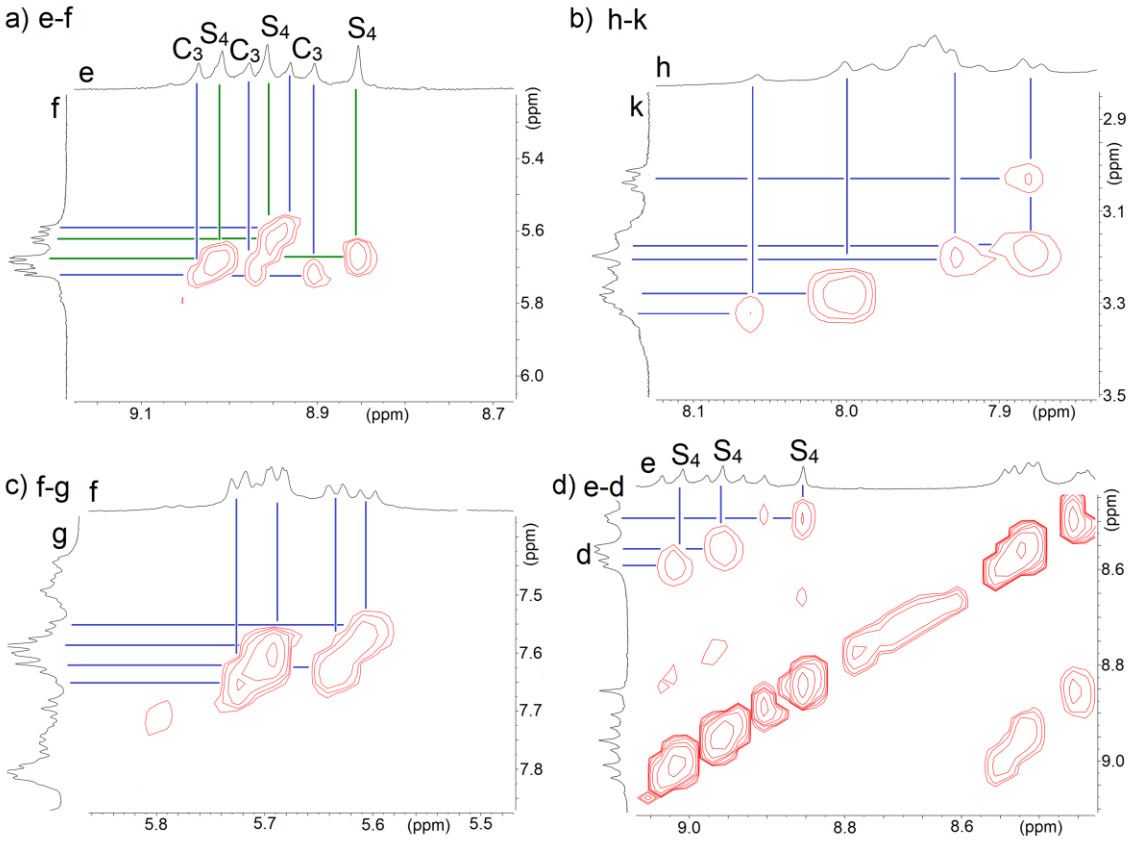

Figure 8.59. Expanded aromatic regions of the gNOESY NMR spectrum of acid cage **6.7** illustrating the presence of three different isomers through correlations of protons a) e and f, b) h and k, c) f and g, and d) e and d. (CD_3CN, 600 MHz, 298 K, mixing time = 300 ms).

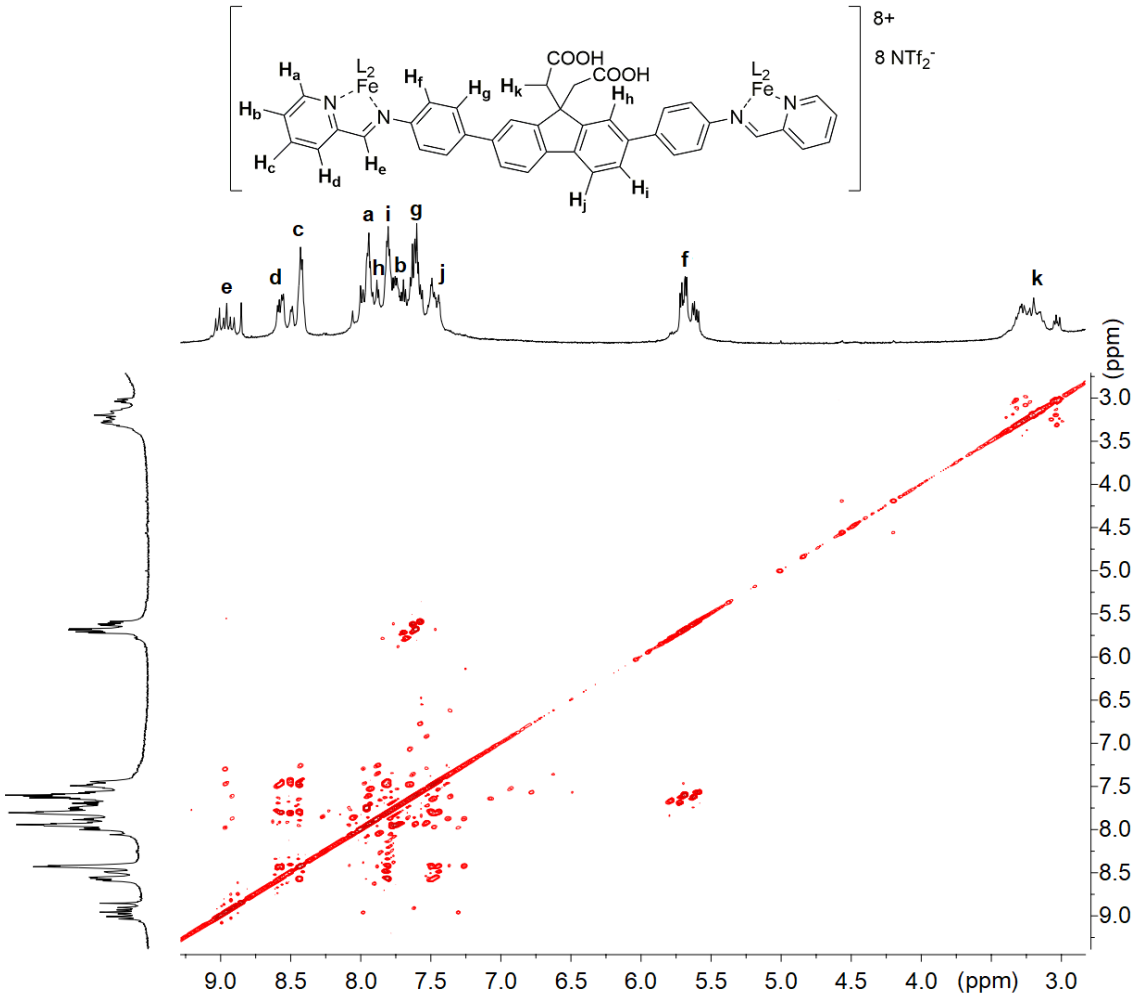

Figure 8.60. TOCSY NMR spectrum of **6.7** (CD_3CN, 600 MHz, 298 K, mixing time = 60 ms).

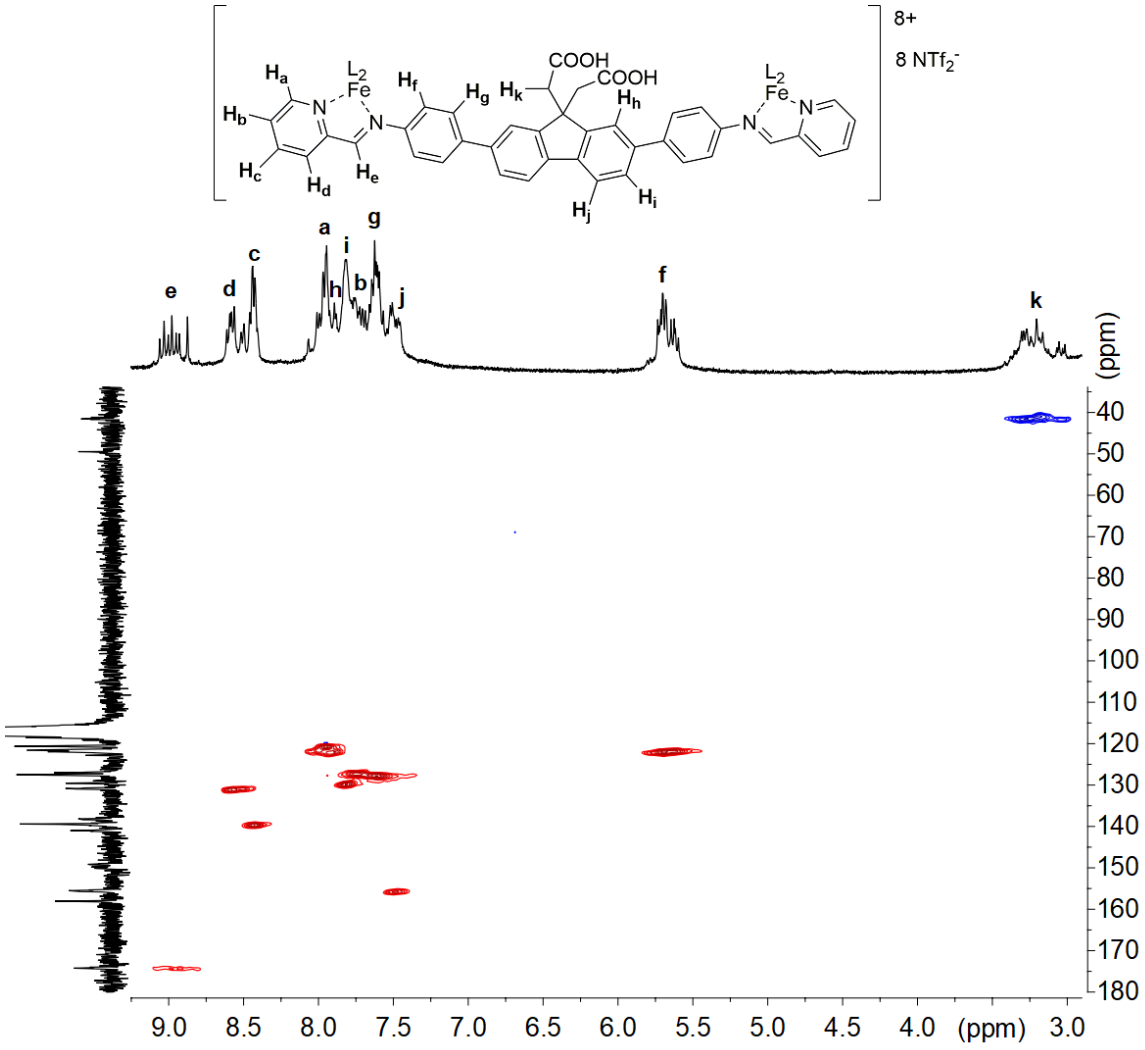

Figure 8.61. DEPT-HSQC NMR spectrum of acid cage **6.7** (CD_3CN, 400 MHz, 298 K).

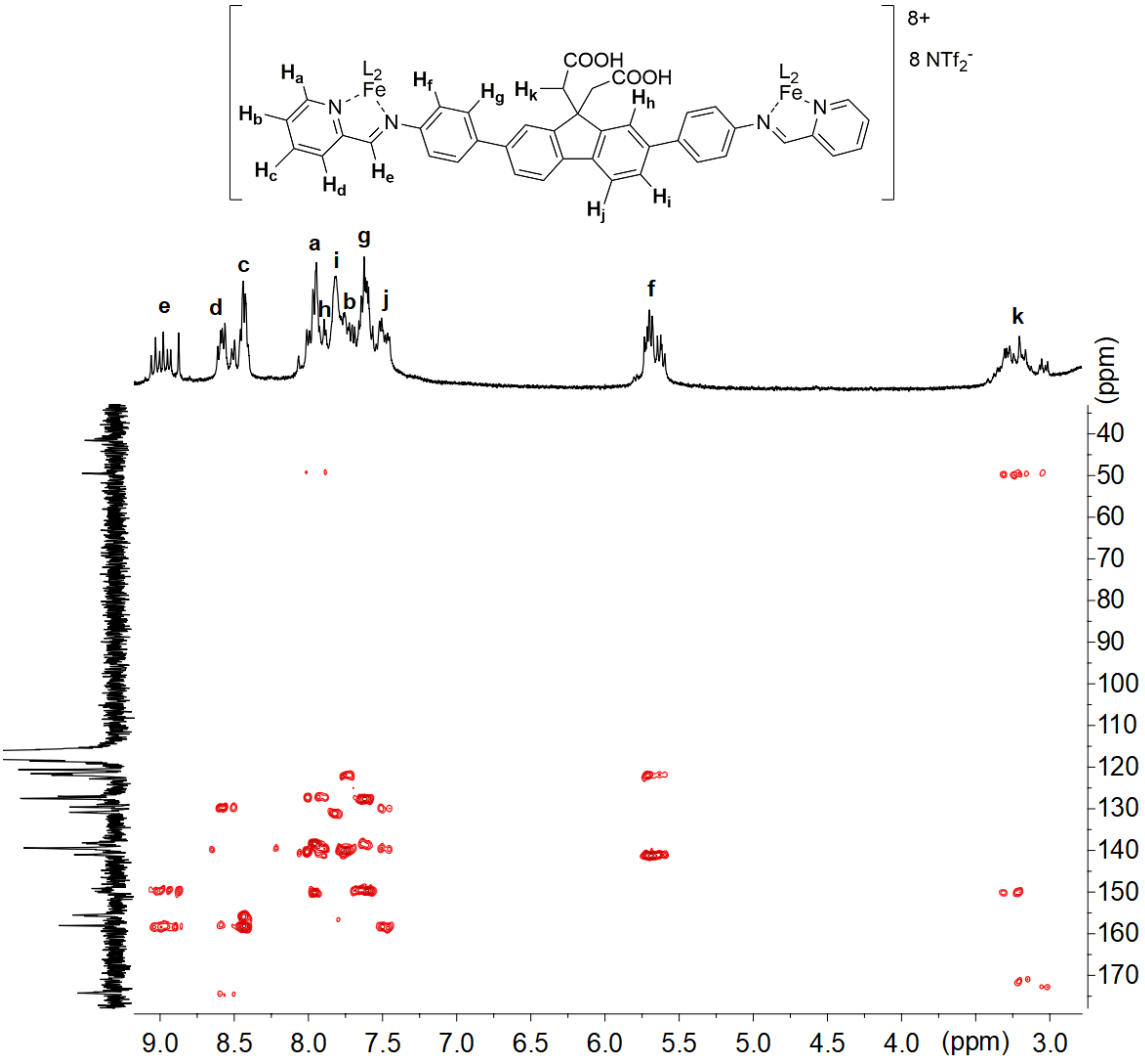

Figure 8.62. HMBC NMR spectrum of acid cage **6.7** (CD_3CN, 400 MHz, 298 K).

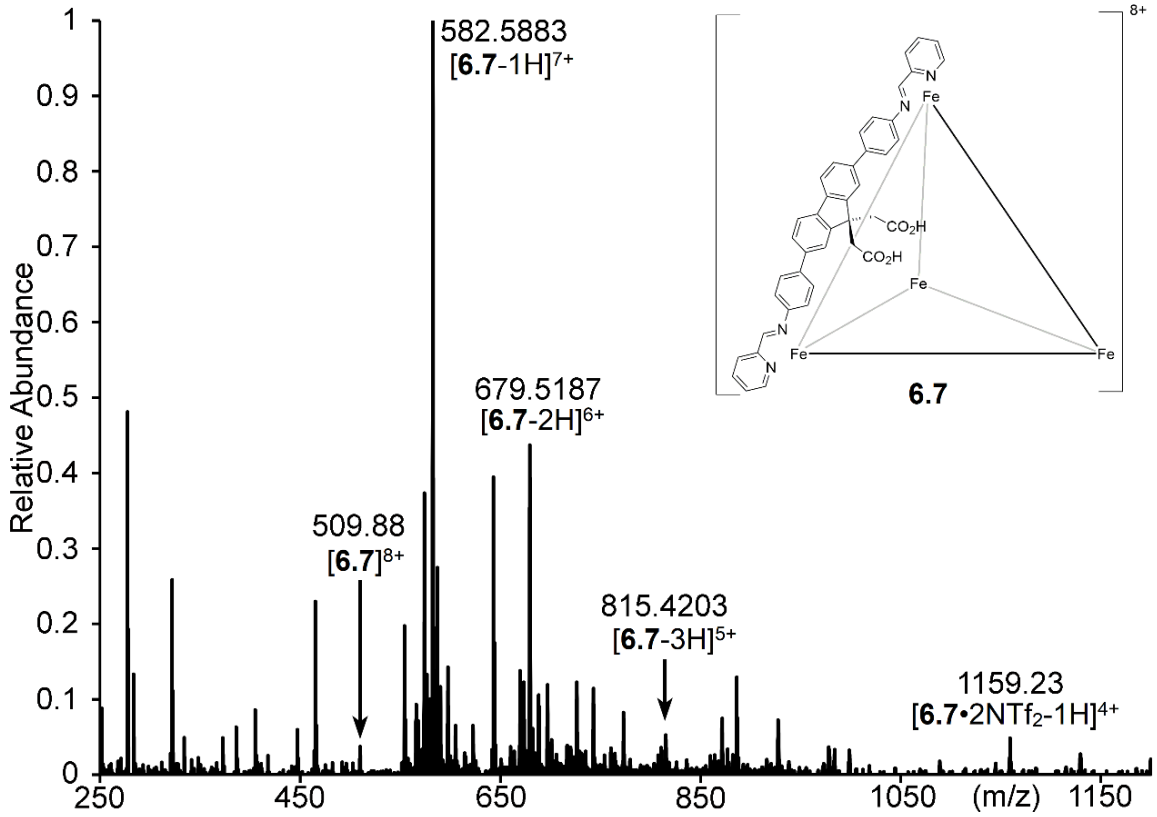

Figure 8.63. Full positive mode ESI-mass spectrum of acid cage **6.7** in 100 % CH_3CN.

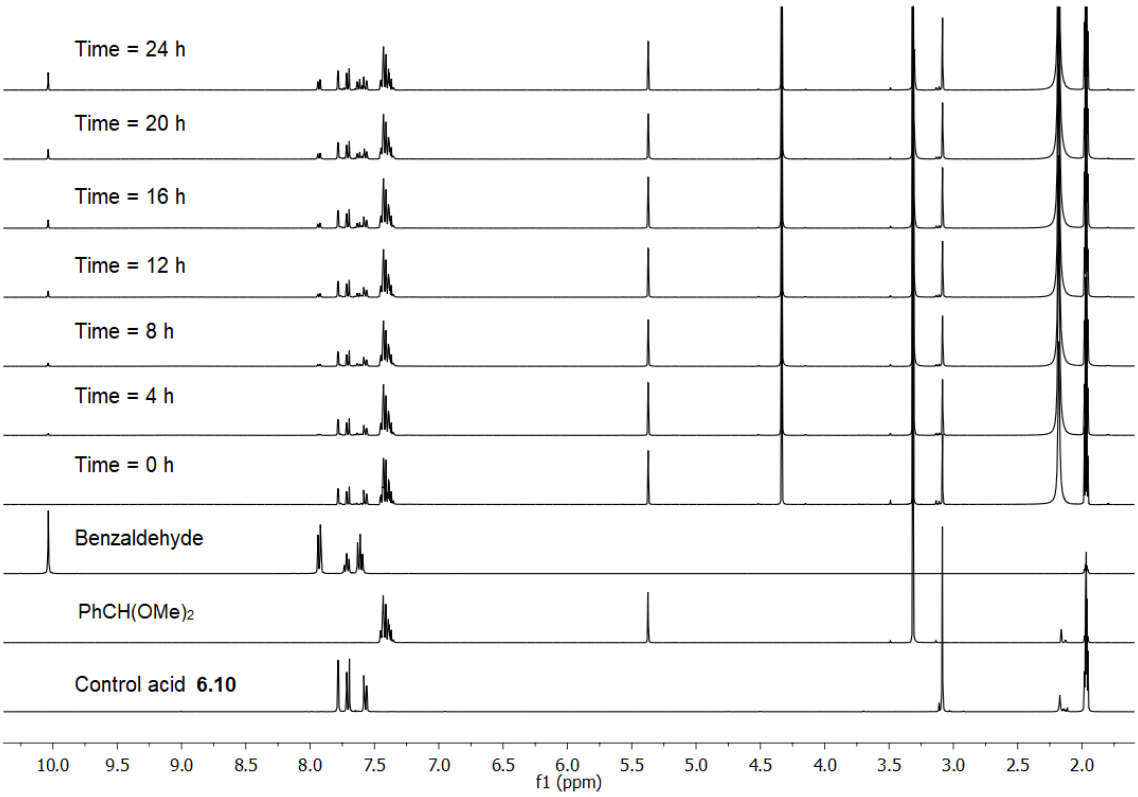

Figure 8.64. ^{1}H NMR spectrum of $PhCH(OMe)_2$ hydrolysis over time using 0.25 mol.-eq. 2,7-dibromofluorenyl diacid catalyst **6.10** at 50 °C (CD_3CN, 400 MHz, 298 K).

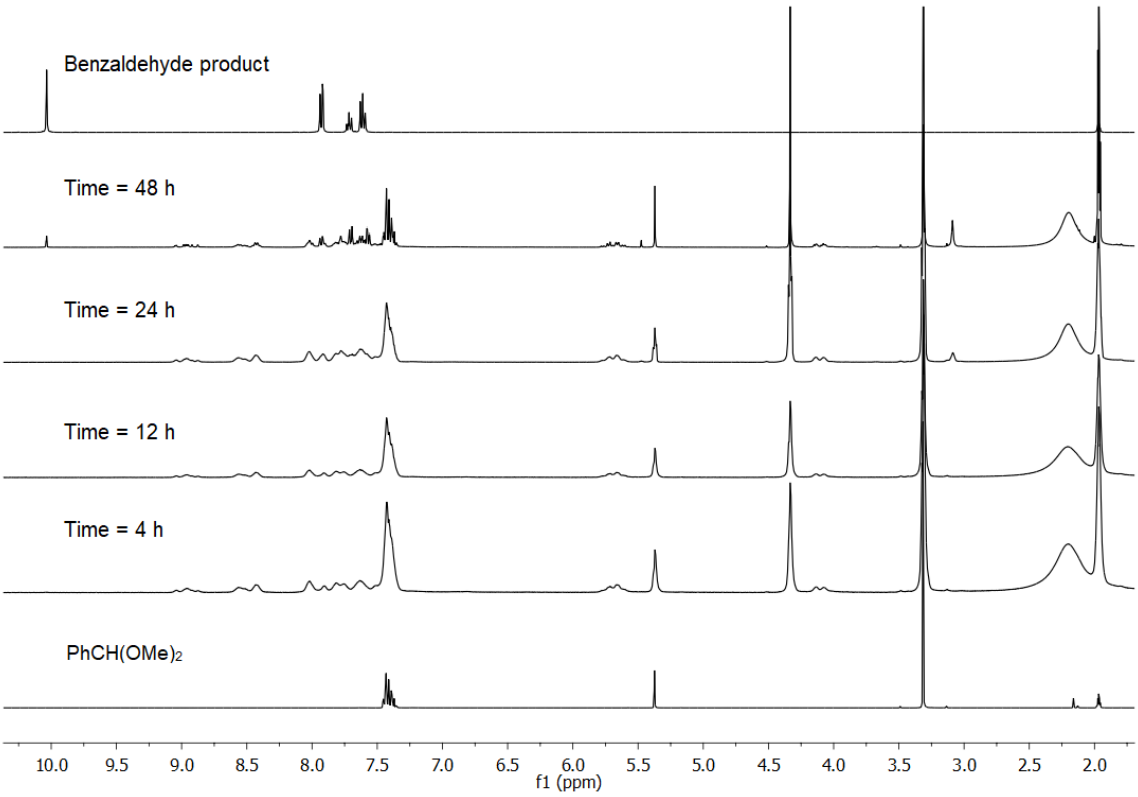

Figure 8.65. ^{1}H NMR spectrum of $PhCH(OMe)_2$ hydrolysis over time using 0.042 mol.-eq. unfunctionalized fluorene cage **6.3**, heated at 50 °C (CD_3CN, 400 MHz, 298 K). No change in the 1H NMR spectrum was observed when the reaction was performed at 23 °C.

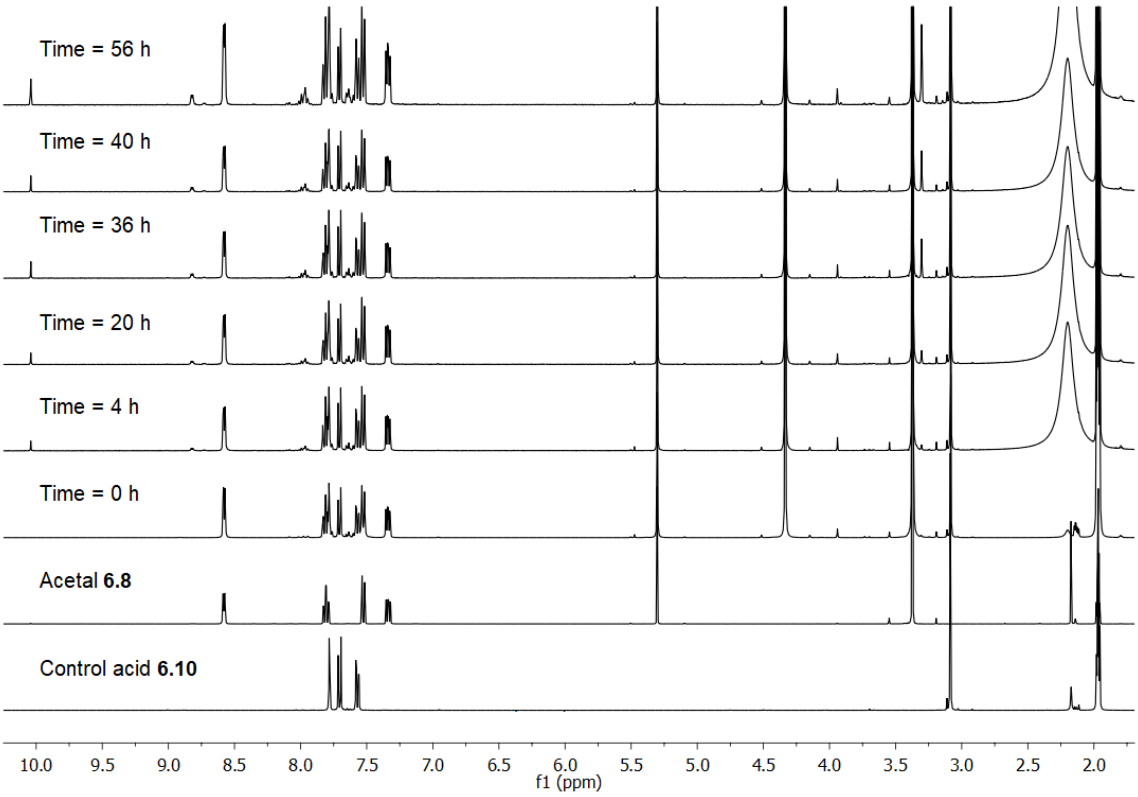

Figure 8.66. ^{1}H NMR spectrum of pyridyl acetal **6.8** hydrolysis over time using 0.25 mol.-eq. 2,7-dibromofluorenyl diacid catalyst **6.10** at 77 °C (CD_3CN, 400 MHz, 298 K).

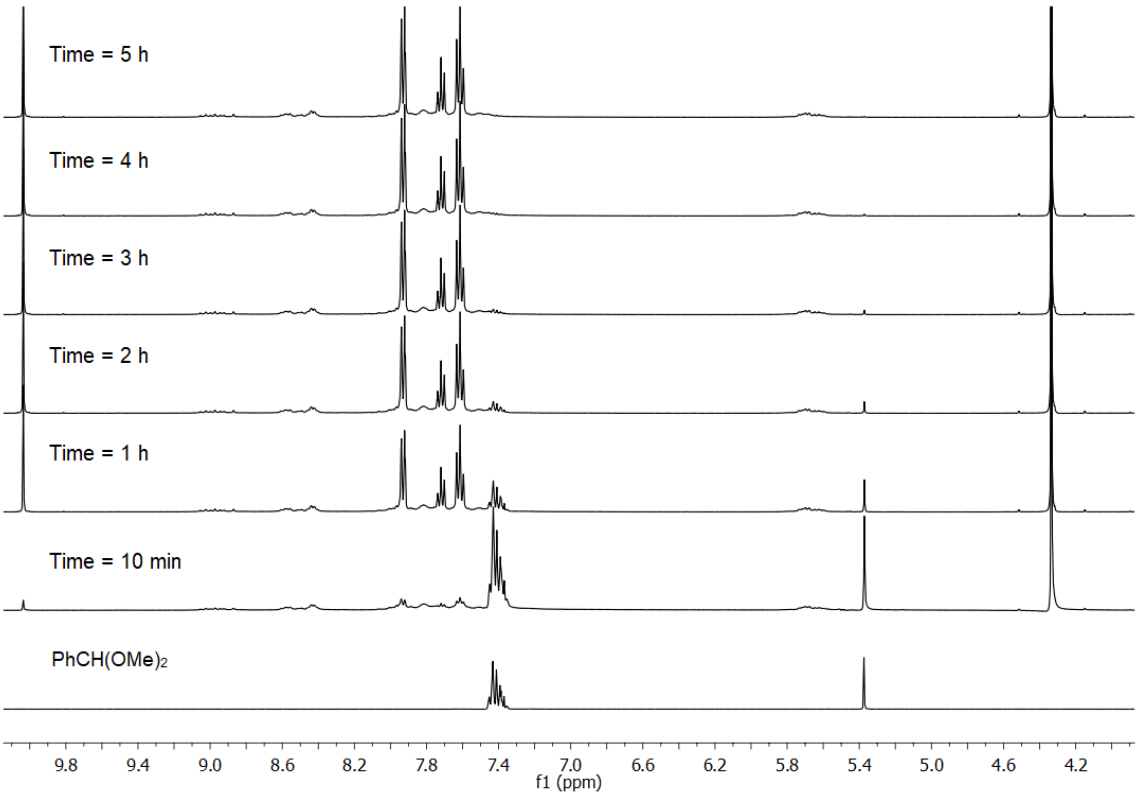

Figure 8.67. ^{1}H NMR spectrum of $PhCH(OMe)_2$ hydrolysis over time with 4.1 mol % cage catalyst **6.7** at room temperature (CD_3CN, 400 MHz, 298 K).

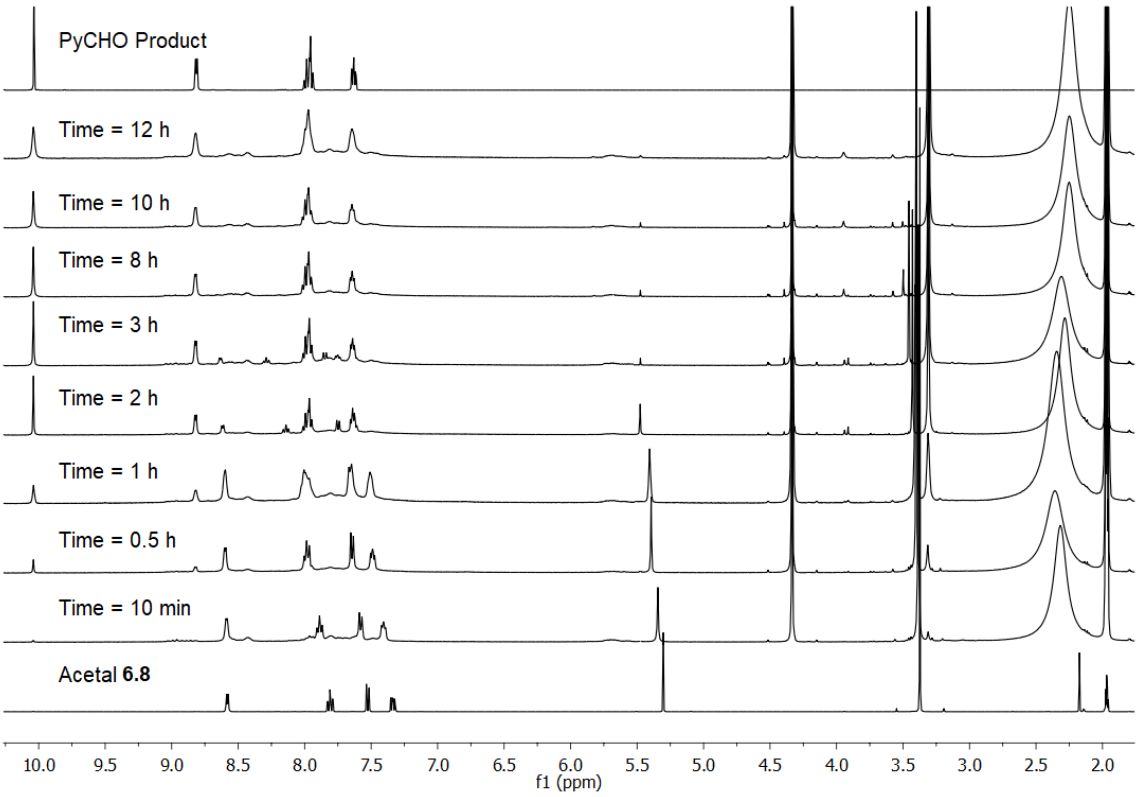

Figure 8.68. ^{1}H NMR spectrum of pyridyl acetal **6.8** hydrolysis over time with 4.1 mol % cage catalyst **6.7** at 77 °C (CD_3CN, 400 MHz, 298 K).

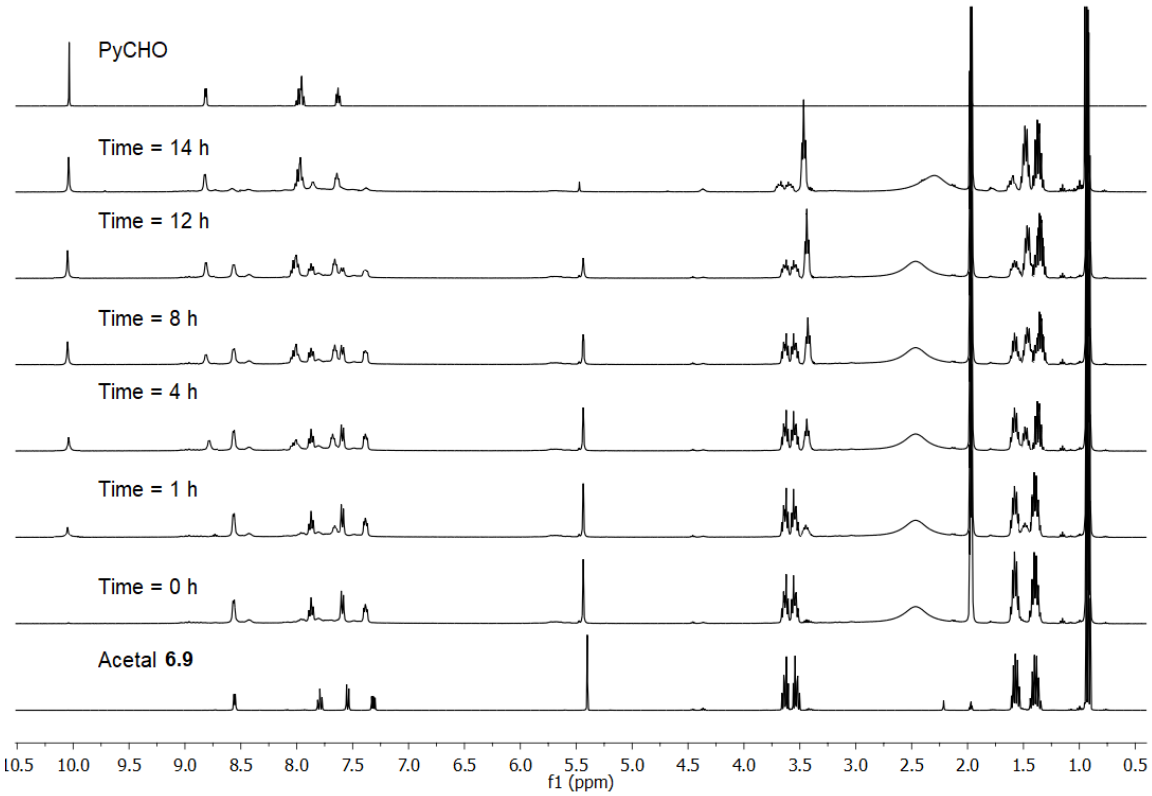

Figure 8.69. ^{1}H NMR spectrum of pyridyl acetal **6.9** hydrolysis over time with 4.1 mol % cage catalyst **6.7** at 77 °C (CD_3CN, 400 MHz, 298 K).

8.13 Selected Spectra from Chapter 7

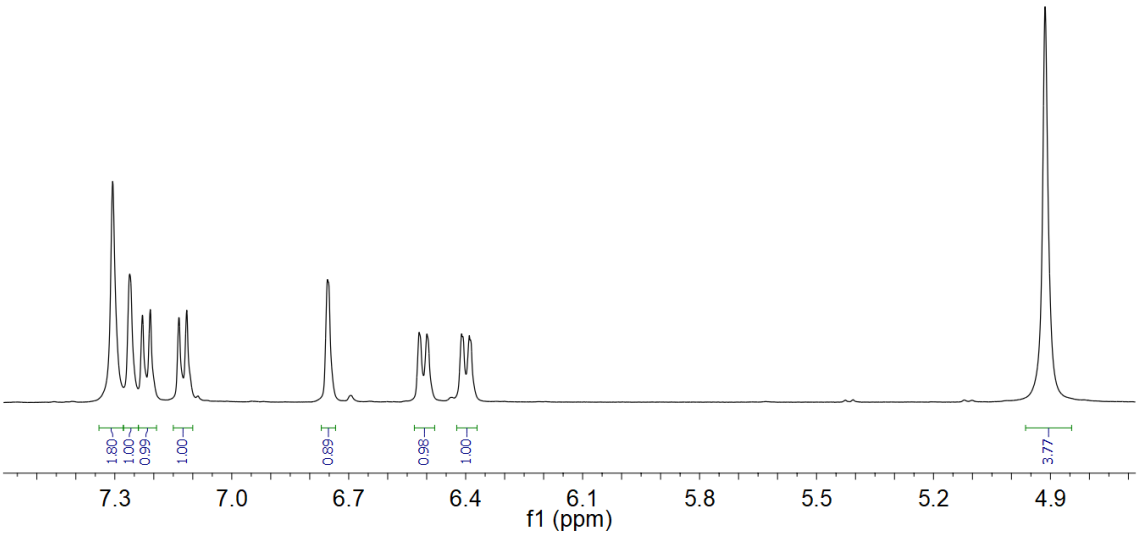

Figure 8.70. ^{1}H NMR spectrum of dianiline **7.1** (DMSO-d_6, 400 MHz, 298 K).

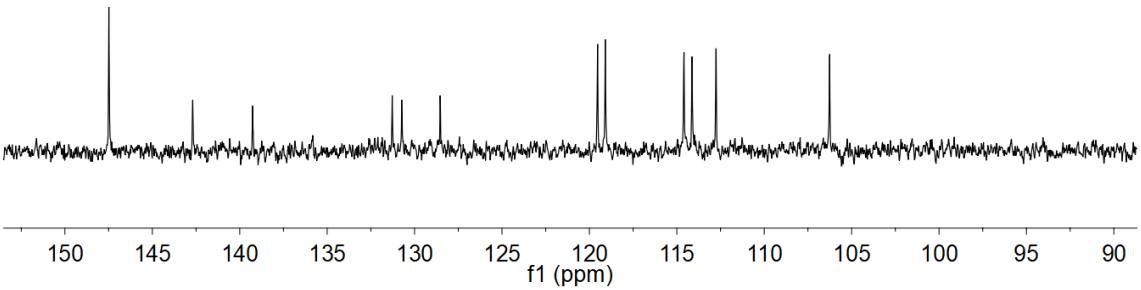

Figure 8.71. ^{13}C NMR spectrum of dianiline **7.1** (DMSO-d_6, 400 MHz, 298 K).

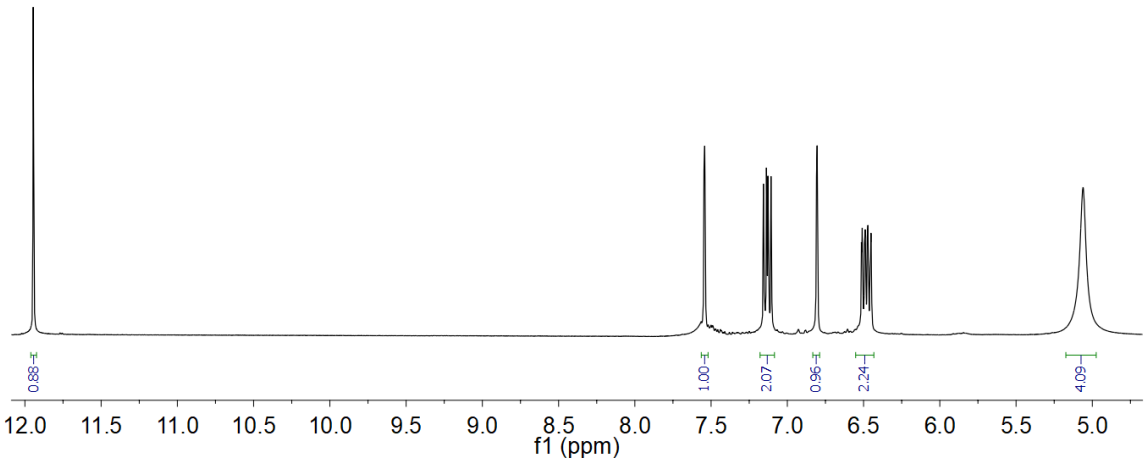

Figure 8.72. ^{1}H NMR spectrum of dianiline **7.2** (DMSO-d_6, 400 MHz, 298 K).

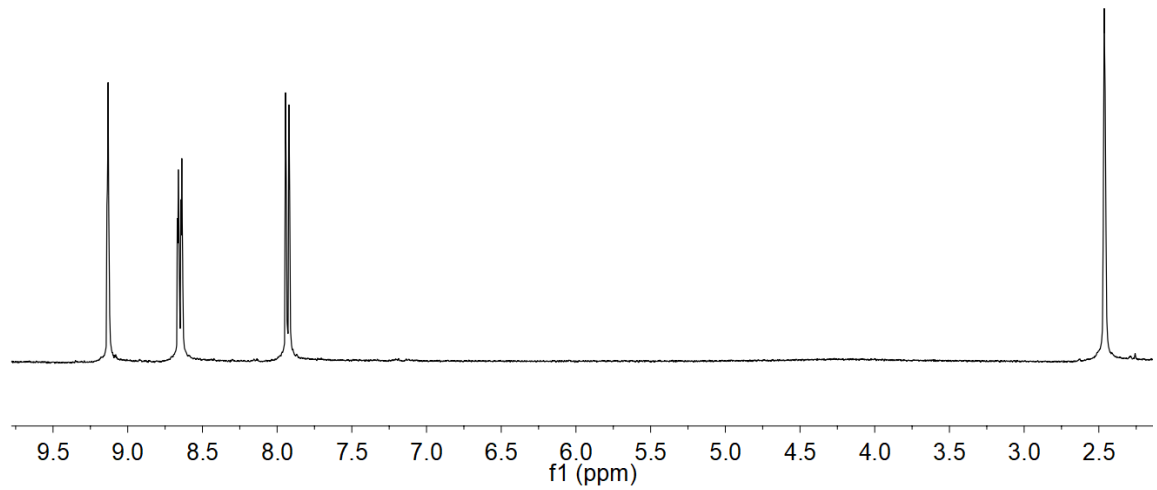

Figure 8.73. ^{1}H NMR spectrum of thioketone **7.4** (DMSO-d_6, 400 MHz, 298 K).

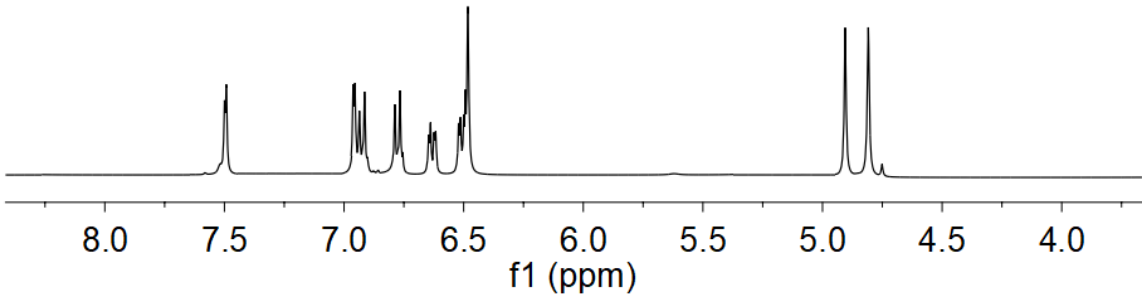

Figure 8.74. ^{1}H NMR spectrum of dianiline **7.7** (DMSO-d_6, 400 MHz, 298 K).

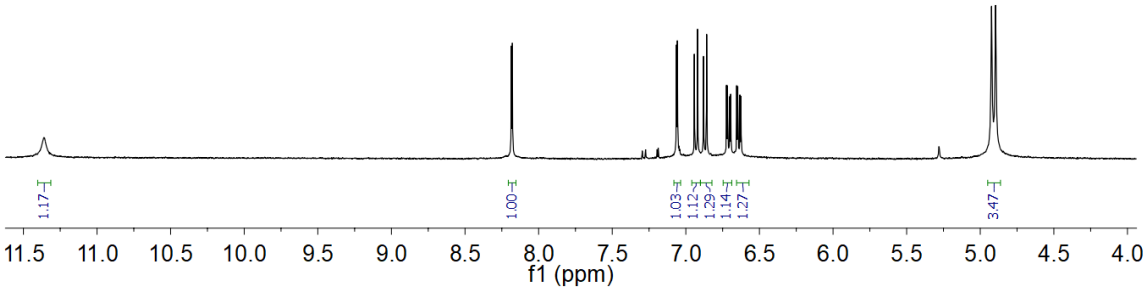

Figure 8.75. ^{1}H NMR spectrum of dianiline **7.8** (DMSO-d_6, 400 MHz, 298 K).

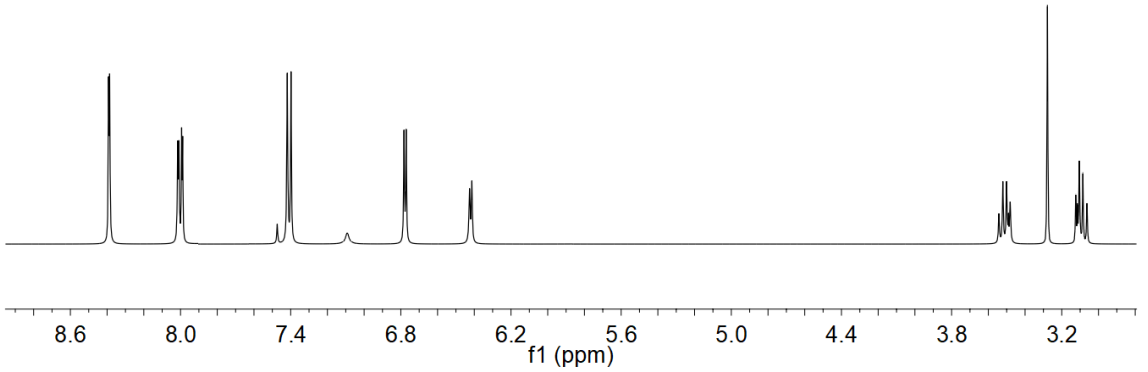

Figure 8.76. ^{1}H NMR spectrum of compound **7.9** (DMSO-d_6, 400 MHz, 298 K).

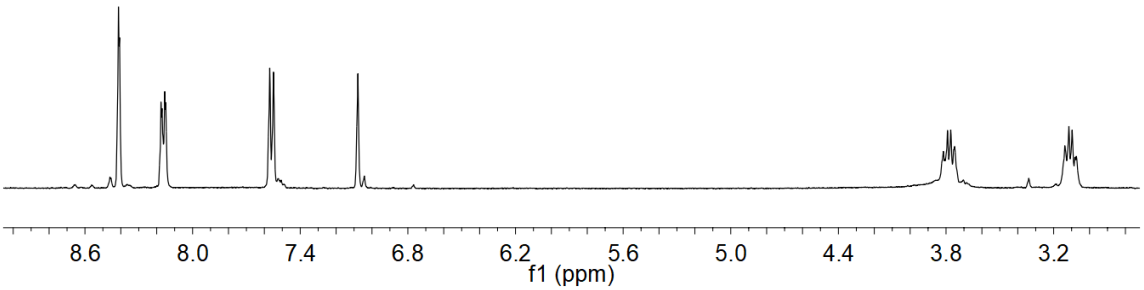

Figure 8.77. ^{1}H NMR spectrum of compound **7.10** (DMSO-d_6, 400 MHz, 298 K).

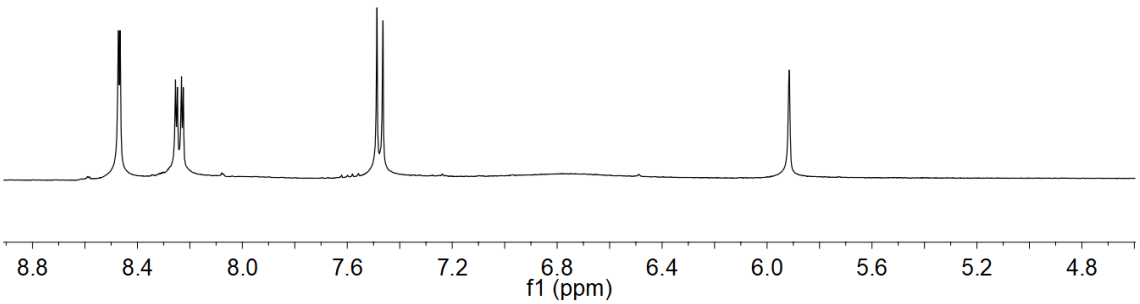

Figure 8.78. ^{1}H NMR spectrum of compound **7.11** (DMSO-d_6, 400 MHz, 298 K).

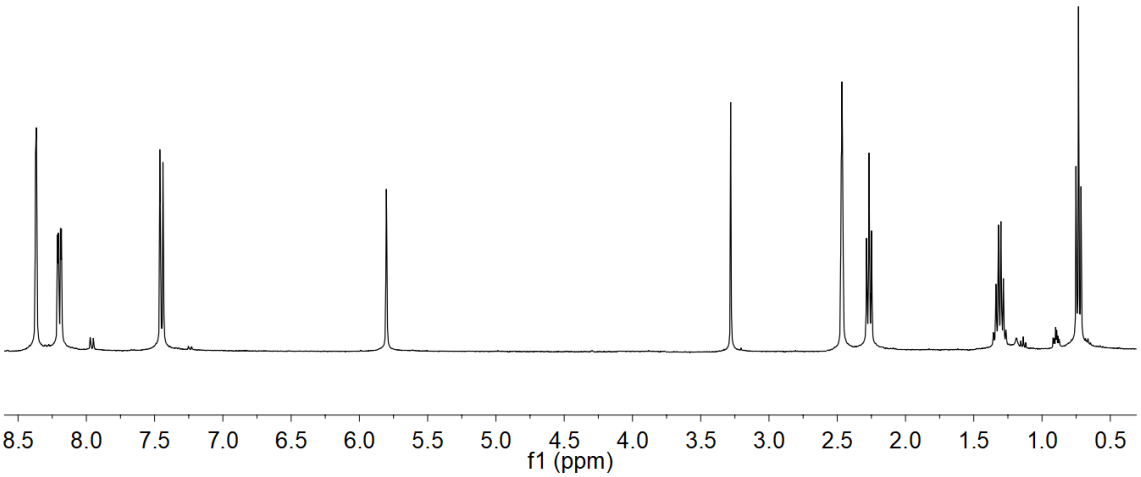

Figure 8.79. ^{1}H NMR spectrum of compound **7.12** (DMSO-d_6, 400 MHz, 298 K).

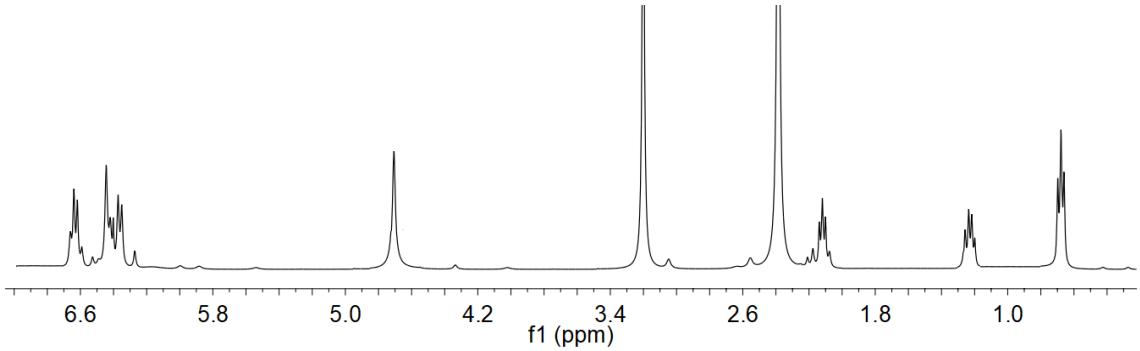

Figure 8.80. ^{1}H NMR spectrum of dianiline **7.13** (DMSO-d_6, 400 MHz, 298 K).

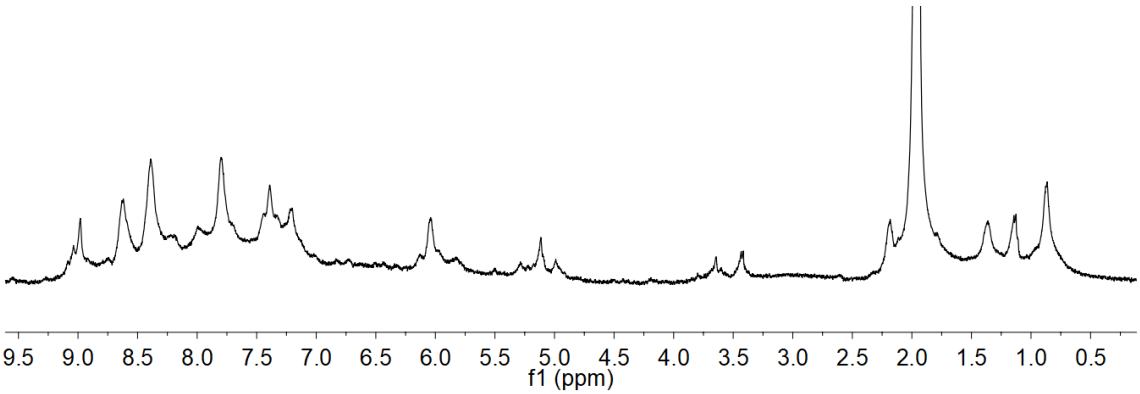

Figure 8.81. ^{1}H NMR spectrum of complex **7.14** (CD_3CN, 400 MHz, 298 K).

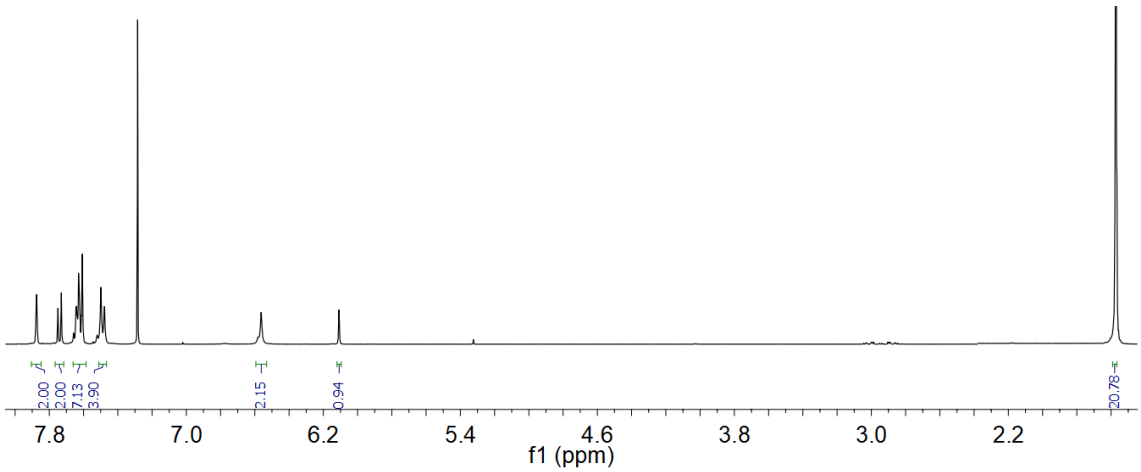

Figure 8.82. ^{1}H NMR spectrum of compound **7.15** ($CDCl_3$, 400 MHz, 298 K).

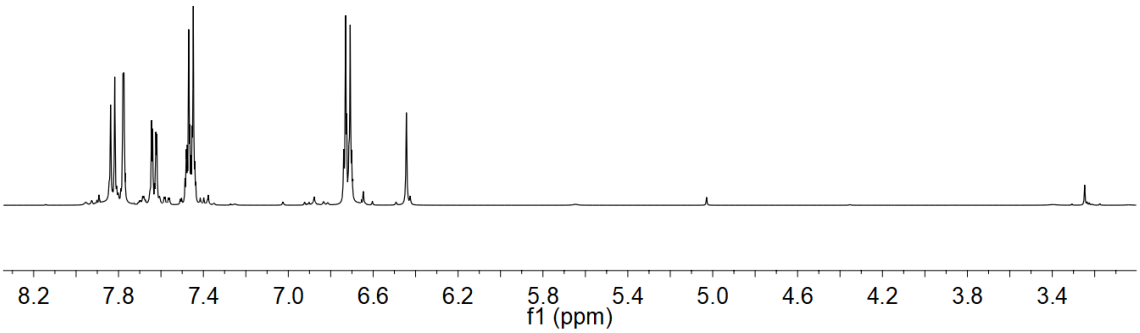

Figure 8.83. ^{1}H NMR spectrum of dianiline **7.16** ($CDCl_3$, 400 MHz, 298 K).

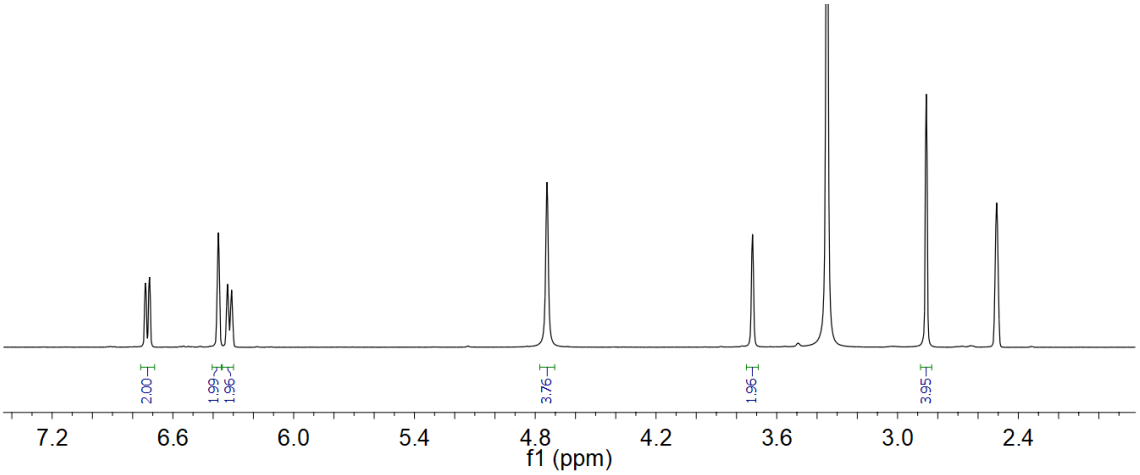

Figure 8.84. ^{1}H NMR spectrum of dianiline **7.17** (DMSO-d_6, 400 MHz, 298 K).

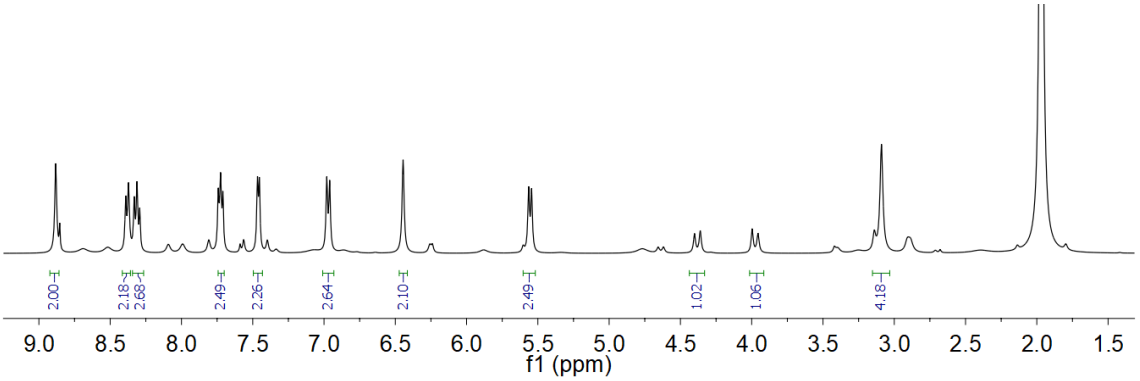

Figure 8.85. ^{1}H NMR spectrum of complex **7.18** (CD_3CN, 400 MHz, 298 K).

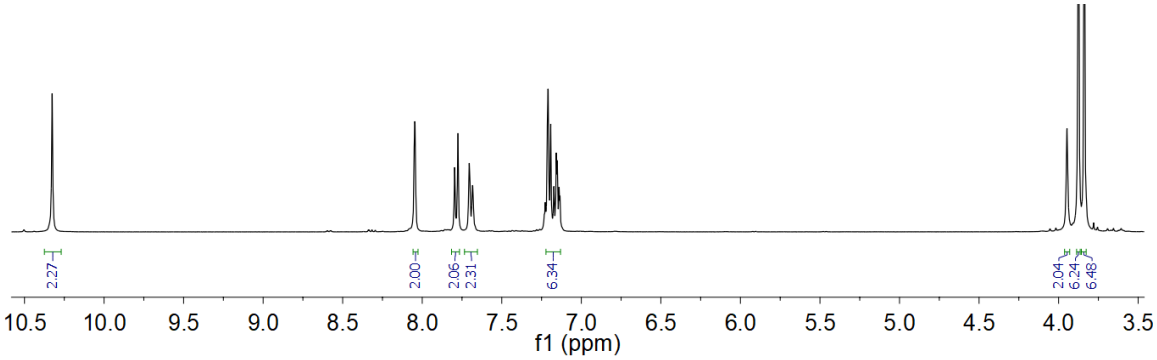

Figure 8.86. ^{1}H NMR spectrum of compound **7.43** (DMSO d_6, 400 MHz, 298 K).

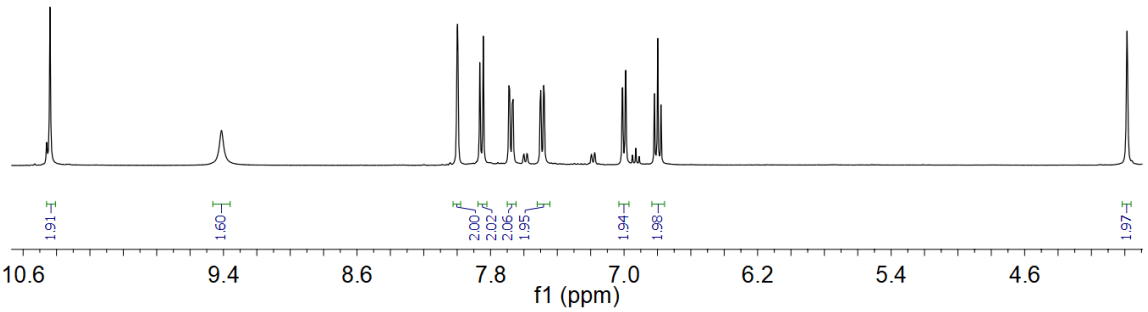

Figure 8.87. ^{1}H NMR spectrum of dianiline **7.44** (DMSO-d_6, 400 MHz, 298 K).

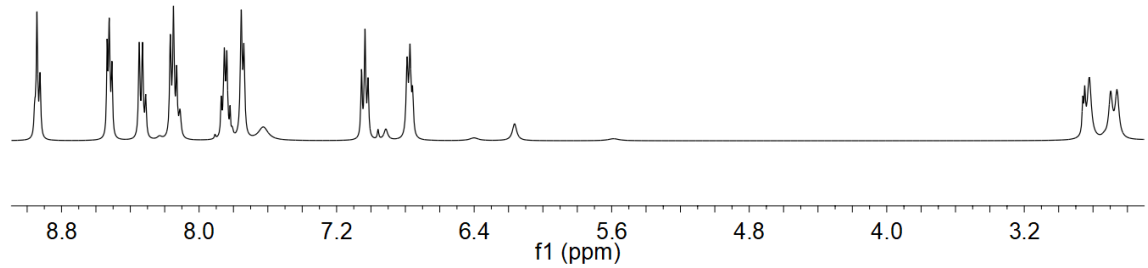

Figure 8.88. ^{1}H NMR spectrum of complex **7.45** (CD_3CN, 400 MHz, 298 K).

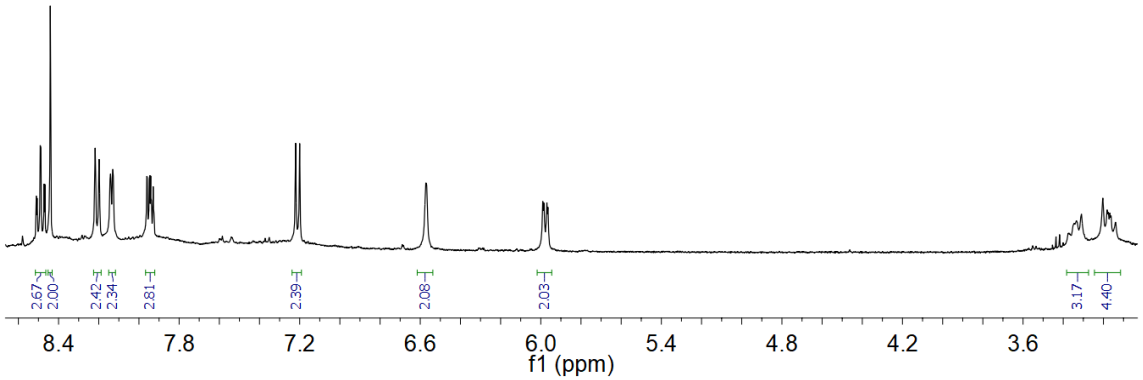

Figure 8.89. ^{1}H NMR spectrum of complex **7.46** (CD_3CN, 400 MHz, 298 K).

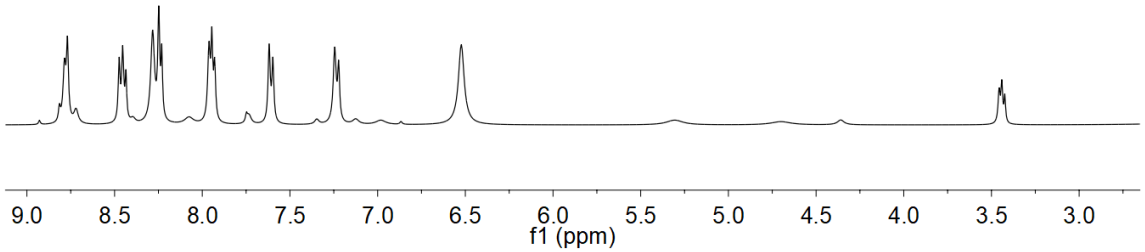

Figure 8.90. ^{1}H NMR spectrum of complex **7.47** (CD_3CN, 400 MHz, 298 K).

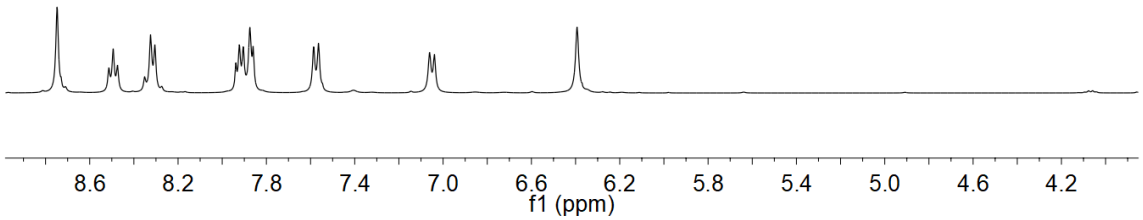

Figure 8.91. ^{1}H NMR spectrum of complex **7.48** (CD_3CN, 400 MHz, 298 K).

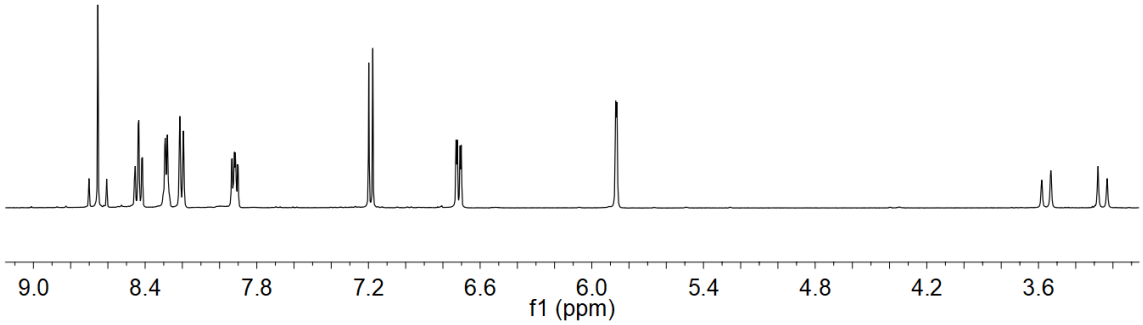

Figure 8.92. ^{1}H NMR spectrum of complex **7.49** (CD_3CN, 400 MHz, 298 K).

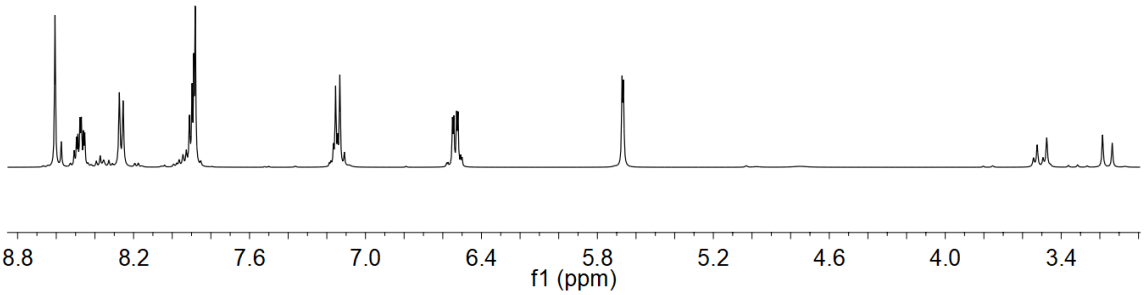

Figure 8.93. ^{1}H NMR spectrum of complex **7.50** (CD_3CN, 400 MHz, 298 K).

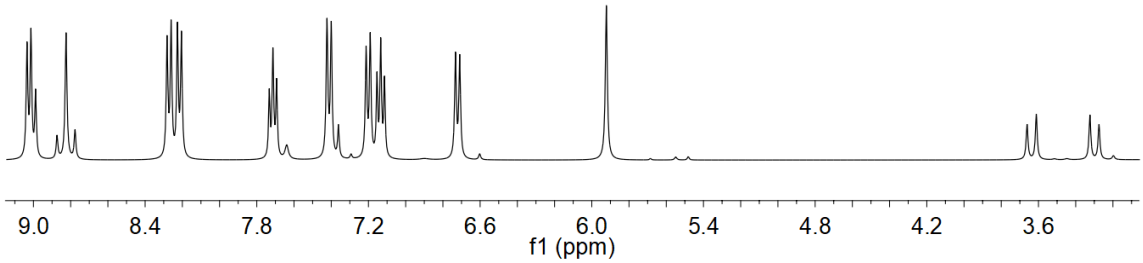

Figure 8.94. ^{1}H NMR spectrum of complex **7.51** (CD_3CN, 400 MHz, 298 K).

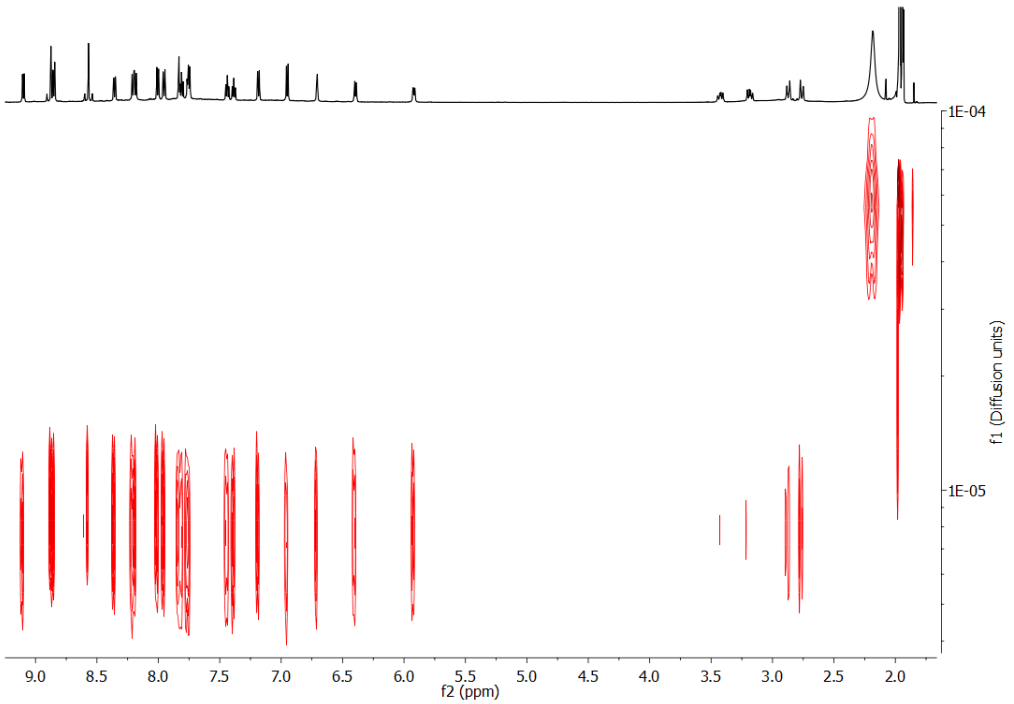

Figure 8.95.[1]H DOSEY spectrum of complex **7.52** (CD_3CN, 600 MHz, 298 K, Δ = 100 ms, δ = 2.6 µs, Diffusion constant = $2.17x10^{-9}$ m^2/s for **7.52** vs. $9.72x10^{-9}$ m^2/s for solvent).

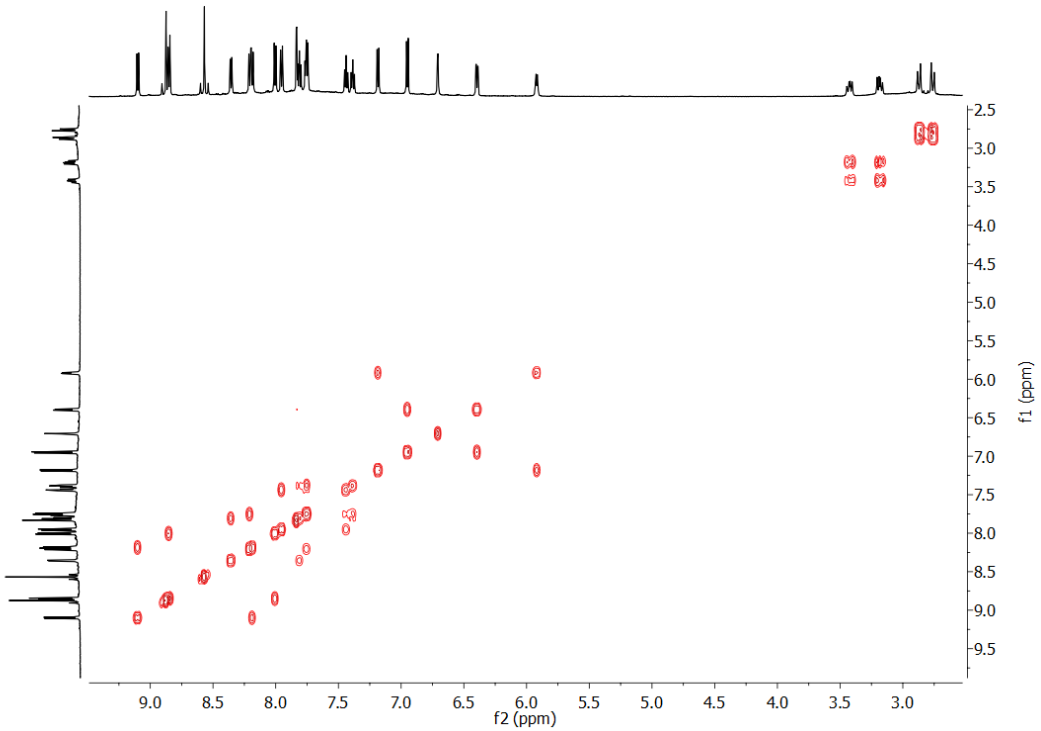

Figure 8.96. gCOSY spectrum of complex **7.52** (CD_3CN, 400 MHz, 298 K).

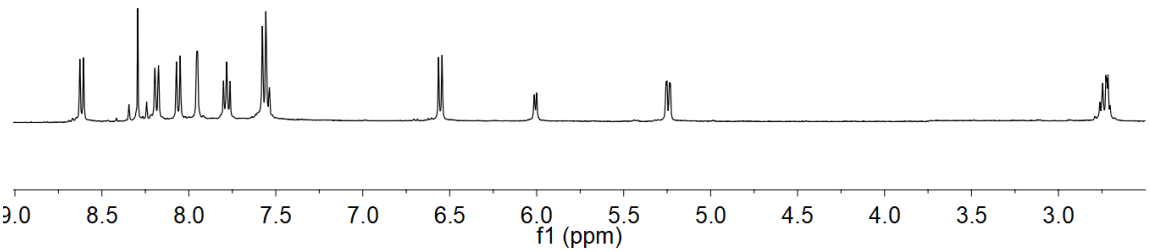

Figure 8.97. ^{1}H NMR spectrum of complex **7.53** (CD_3CN, 400 MHz, 298 K).

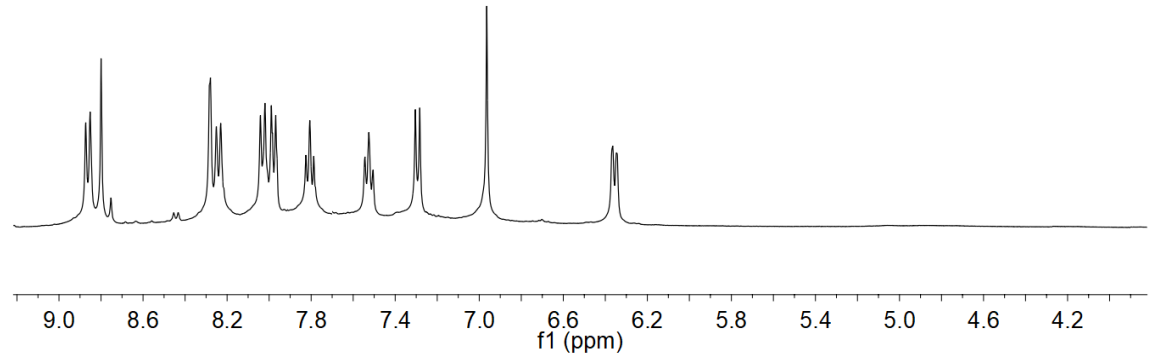

Figure 8.98. ^{1}H NMR spectrum of complex **7.54** (CD_3CN, 400 MHz, 298 K).

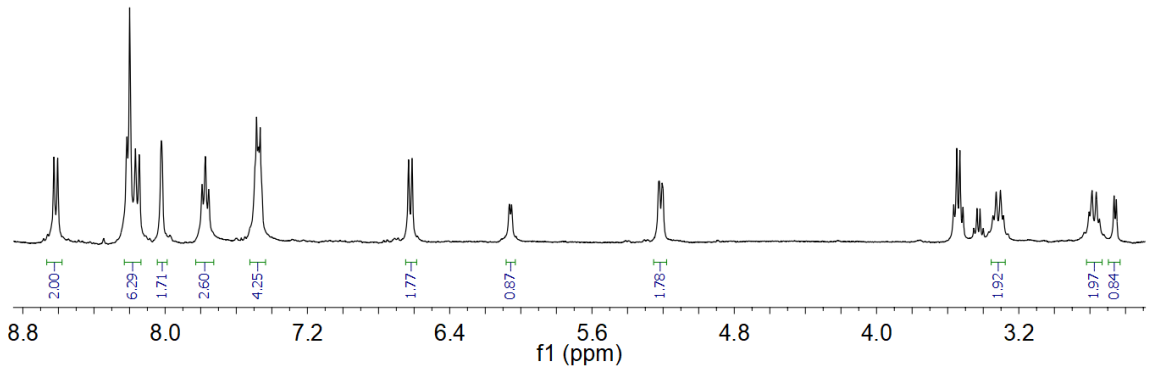

Figure 8.99. ^{1}H NMR spectrum of complex **7.55** (CD_3CN, 400 MHz, 298 K).

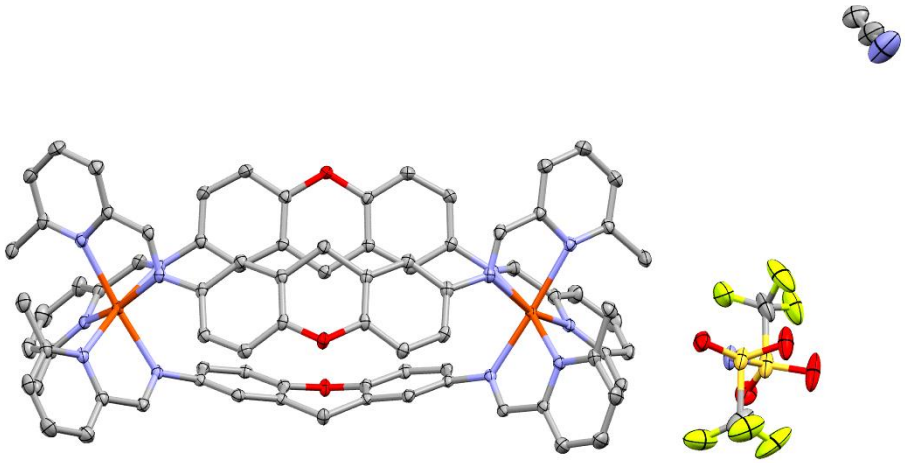

Figure 8.100. ORTEP structure of **7.56** (slow diffusion of diethyl ether into acetonitrile, diffracted at 100 K).

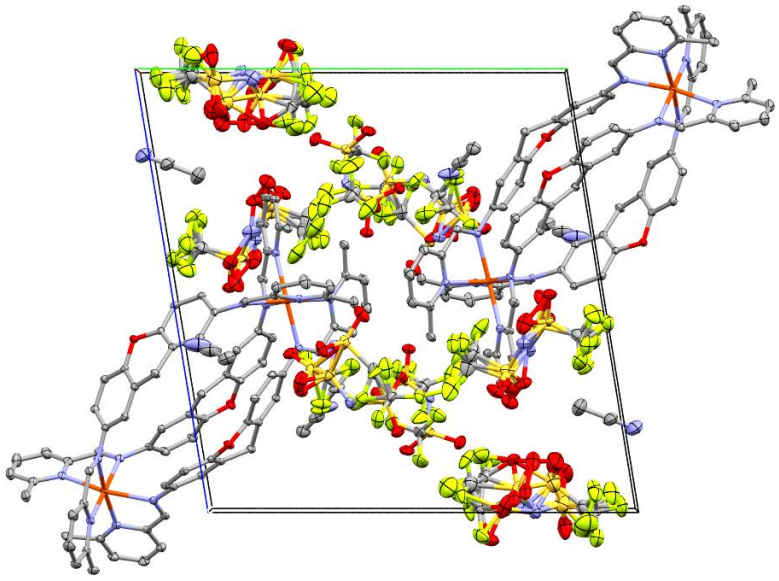

Figure 8.101. Unit cell of **7.56** (slow diffusion of diethyl ether into acetonitrile, diffracted at 100 K).

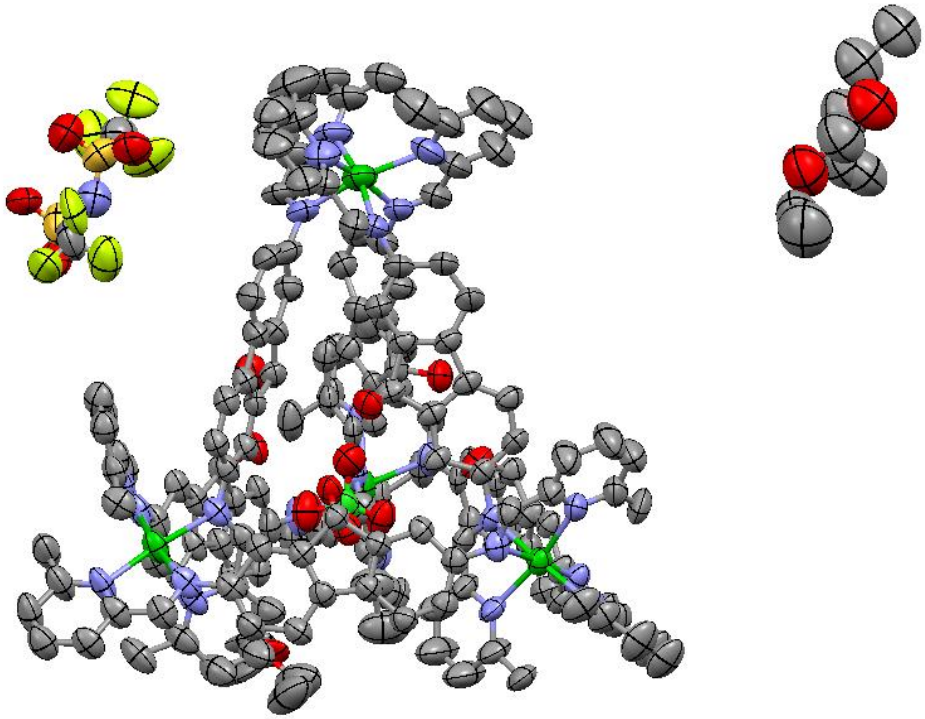

Figure 8.102. ORTEP structure of **7.57** (slow diffusion of diethyl ether into acetonitrile, diffracted at 150 K).

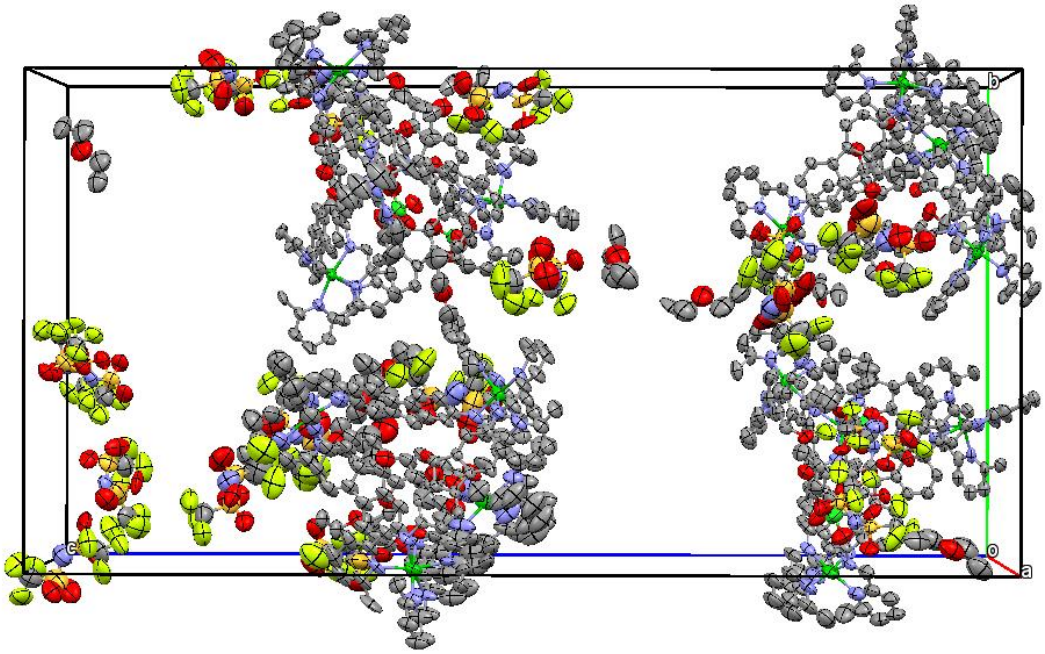

Figure 8.103. Unit cell of **7.57** (slow diffusion of diethyl ether into acetonitrile, diffracted at 150 K).

8.14 References

1. Patiny, L.; Borel, A. “ChemCalc: A Building Block for Tomorrow’s Chemical Infrastructure.” *J. Chem. Inf. Model.*, **2013**, *53*, 1223-1228.

2. Dewar, M. J. S.; Zoebisch, E. G.; Healy, E. F.; Stewart, J. J. P. “Development and Use of Quantum Mechanical Molecular Models. 76. AM1: A New General-Purpose Quantum Mechanical Molecular Model.” *J. Am. Chem. Soc.,* **1985**, *107*, 3902-3909; calculations performed on SPARTAN 06, Wavefunction Inc.

3. Young, M. C.; Johnson, A. M.; Hooley, R. J. “Self-Promoted Post-Synthetic Modification of Metal–Ligand M_2L_3 Mesocates.” *Chem. Commun.* **2014**, *50*, 1378-1380.

4. Holloway, L. R.; McGarraugh, H. H.; Young, M. C.; Sontising, W.; Beran, G. J. O.; Hooley, R. J. "Structural Switching in Self-Assembled Metal-Ligand Helicate Complexes via Ligand-Centered Reactions." *Chem. Sci*. **2016**, *7*, 4423-4427.

5. Holloway, L. R.; Bogie, P. M.; Lyon, Y.; Julian, R. R.; Hooley, R. J. "Stereoselective Postassembly CH Oxidation of Self-Assembled Metal-Ligand Cage Complexes." *Inorg. Chem*. **2017**, *56*, 11435-11442.

6. Young, M. C.; Holloway, L. R.; Johnson, A. M.; Hooley, R. J. A Supramolecular Sorting Hat: Stereocontrol in Metal-Ligand Self-Assembly by Complementary Hydrogen Bonding. *Angew. Chem. Int. Ed.* **2014**, *53*, 9832-9836.

7. Holloway, L. R.; Bogie, P. M.; Lyon, Y.; Ngai, C.; Miller, T. F.; Julian, R. R.; Hooley, R. J. “Tandem Reactivity of a Self-Assembled Cage Catalyst with Endohedral Acid Groups.” *J. Am. Chem. Soc*. **2018**, *140*, 8078-8081.

8. *APEX 2*, version 2014.1-1, Bruker (2014), Bruker AXS Inc., Madison, Wisconsin, USA.

9. *SAINT*, version V8.34A, Bruker (2012), Bruker AXS Inc., Madison, Wisconsin, USA.

10. *SADABS*, version 2012/1, Bruker (2012), Bruker AXS Inc., Madison, Wisconsin, USA.

11. *SHELXTL*, version 2013/4, Bruker (2013), Bruker AXS Inc., Madison, Wisconsin, USA.